Fourth International Reservoir Characterization Technical Conference

Proceedings

Sponsored by
Department of Energy,
BDM-Oklahoma, Inc.,
and
American Association of Petroleum Geologists

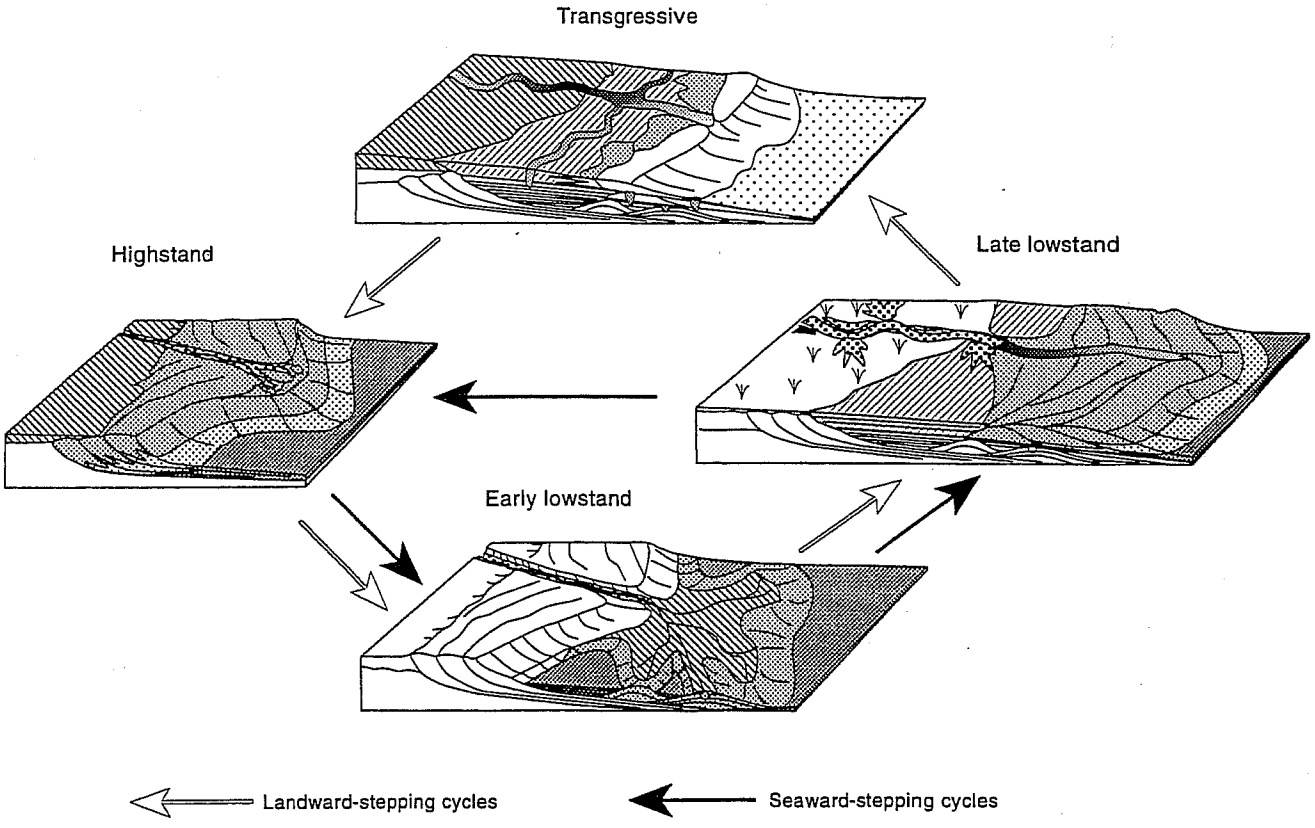

Wyndham Greenspoint Hotel
Houston, Texas • March 2 - 4, 1997

Fourth International Reservoir Characterization Technical Conference

Proceedings

Sponsored by
Department of Energy,
BDM-Oklahoma, Inc.,
and
American Association of Petroleum Geologists

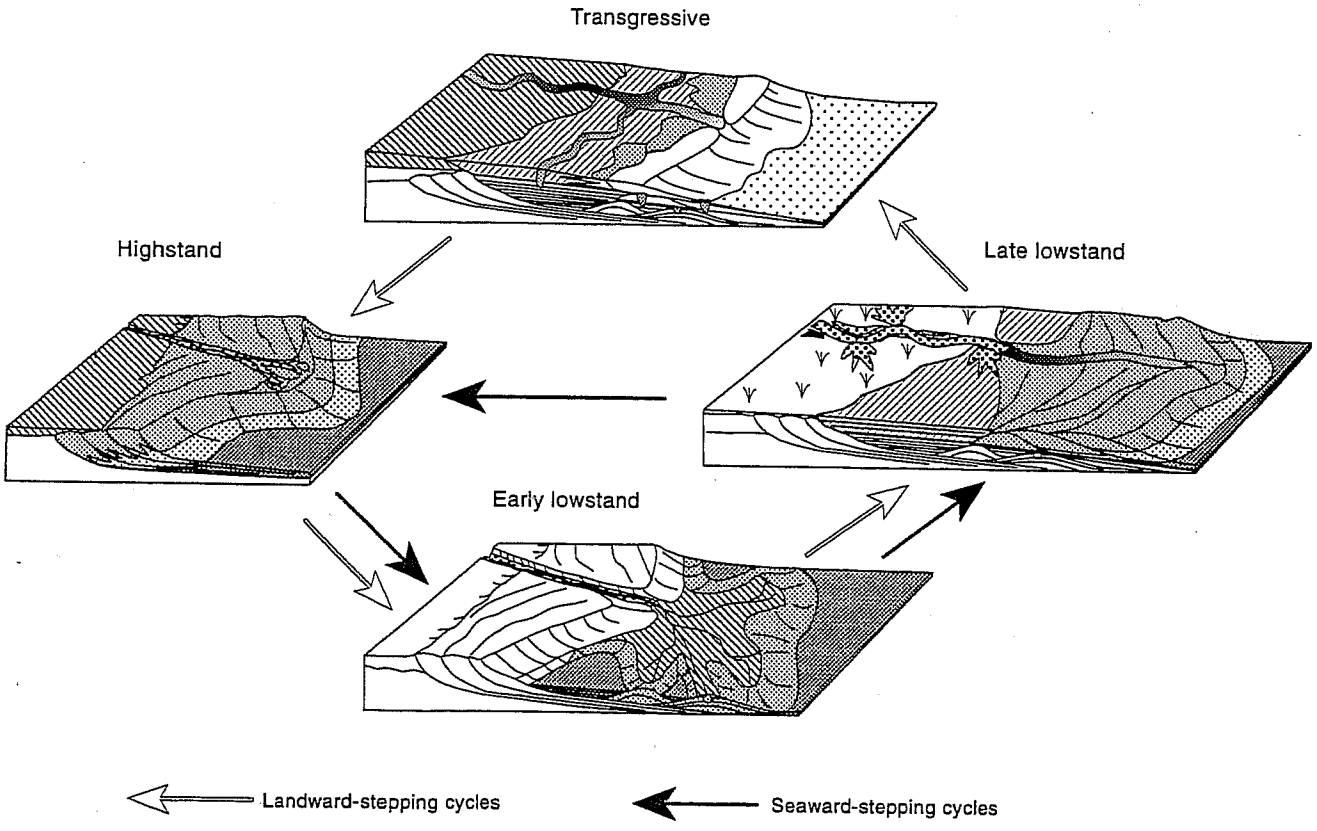

Wyndham Greenspoint Hotel
Houston, Texas • March 2 - 4, 1997

DISCLAIMER

This report was prepared as an account of work sponsored by an agency of the United States Government. Neither the United States Government nor any agency thereof, nor any of their employees, makes any warranty, expressed or implied, or assumes any legal liability or responsibility for the accuracy, completeness, or usefulness of any information, apparatus, product, or process disclosed, or represents that its use would not infringe privately owned rights. Reference herein to any specific commercial product, process, or service by trade name, trademark, manufacturer, or otherwise does not necessarily constitute or imply its endorsement, recommendation, or favoring by the United States Government or any agency thereof. The views and opinions of authors expressed herein do not necessarily state or reflect those of the United States Government.

This report has been reproduced directly from the best available copy.

Available to DOE and DOE contractors from the Office of Scientific and Technical Information, P.O. Box 62, Oak Ridge, TN 37831; prices available from (615) 5768401.

Available to the public from the National Technical Information Service, U.S. Department of Commerce, 5285 Port Royal Rd., Springfield VA 22161

Cover figure is from Paul R. Knox and Mark D. Barton,
Bureau of Economic Geology, University of Texas at Austin
(see paper beginning on page 411)

Susan Jackson and Michael Fowler co-chaired the DOE Class Workshop that consisted of six poster and oral sessions. Proceedings of the DOE Class Workshop are available in a separate volume.

We sincerely thank Phillips Petroleum Company for sponsoring the social hour on Sunday, March 2, 1997. Thanks also go to AAPG for their financial assistance with the registration process. A particular thanks goes to Susan Hayden, conference secretary. No conference can be a success without a dedicated Steering Committee. Ours consisted of the following:

Steve Begg
BP Exploration

Tom Burchfield
BDM-Oklahoma, Inc.

Jack Caldwell
Geco-Prakla

Lifu Chu
University of Tulsa

Robert Finley
Bureau of Economic Geology, University of Texas

Dominique Guerillot
IFP

Neil Humphreys
Mobil Oil Corporation

Susan Jackson
BDM-Oklahoma, Inc.

Jerry Jensen
Heriot-Watt University

Mohan Kelkar
University of Tulsa

Bob Lemmon
DOE/BPO

Charles Mankin
Oklahoma Geological Survey

Yi Nan Qiu
RIPED

Rick Schatzinger
BDM Petroleum Technologies

Eve Sprunt
Mobil Oil Corporation

Ray Sulak
Phillips Petroleum Company

Ganesh Thakur
Chevron Petroleum Technology Company

Min Tham
BDM-Oklahoma, Inc.

Lynn Watney
Kansas Geological Survey

Paul Worthington
Gaffney, Cline & Associates

David Zornes
Phillips Petroleum Company

Rick Schatzinger
Steering Committee Chairman
BDM Petroleum Technologies

PREFACE

This volume contains the Proceedings of the Fourth International Reservoir Characterization Technical Conference held March 2-4, 1997 at the Wyndham Greenspoint Hotel, Houston, Texas. The Department of Energy Bartlesville Project Office (DOE/BPO), BDM-Oklahoma, Inc., and the American Association of Petroleum Geologists (AAPG) were co-sponsors of the event. The theme for the conference was Advances in Reservoir Characterization for Effective Reservoir Management. Thomas C. Wesson, DOE/BPO, and Thomas E. Burchfield of BDM-Oklahoma, Inc., were Conference Co-Chairmen. The opening address was given by Dr. Olivier Guillon, Deputy Director of Research and Development, Elf Aquaitaine Production. Luncheon speakers included Dr. Mark McElroy, Division Manager of E&P, Phillips Petroleum Company and Dr. Leif Hinderaker, Senior Advisor for Reservoir Technology at the Norwegian Petroleum Directorate (NPD). On Sunday, March 2, 1997, the DOE Class Workshop kicked off with tutorials by Dr. Steve Begg (BP Exploration) and Dr. Ganesh Thakur (Chevron). Tutorial presentations are not included in these Proceedings but may be available from the authors.

The conference consisted of four half-day sessions with each session consisting of 6 presentations and an alternate. Poster sessions were presented on the evenings of Monday, March 3, and Tuesday, March 4. Session Topics and co-chairs were as follows:

Data Acquisition--Co-Chairs: Eve Sprunt, Mobil Oil Corporation, and Jack Caldwell, Geco-Prakla

Reservoir Modeling--Co-Chairs: Robert Finley, Bureau of Economic Geology, and Mohan Kelkar, University of Tulsa

Scaling Reservoir Properties--Co-Chairs: Steve Begg, BP Exploration, and Jerry Jensen, Heriot-Watt University

Managing Uncertainty--Co-Chairs: Michael Fowler, BDM Petroleum Technologies, and Ganesh Thakur, Chevron Petroleum Technology Company

Poster Session--Co-Chairs: Lifu Chu, University of Tulsa, and Dominique Guerillot, IFP

Effect of Wettability on Scale-Up of Multiphase Flow from Core-Scale to Reservoir Fine-Grid-Scale.....543

Y. C. Chang, V. Mani, and K. K. Mohanty

Adaptive Upscaling with the Dual Mesh Method.....563

Dominique Guerillot and S. Verdiere

Upscaling Vertical Permeability within a Fluvio-Aeolian Reservoir.....583

S. D. Thomas, P. W. M. Corbett, and J. L. Jensen

Use of Geostatistic Techniques to Describe a Reservoir to be Submitted into a Secondary Recovery Process Field Case: "Eocene B-Inferior/VLG-3659, Ceuta, Venezuela".....603

Thamara Hernandez and W. Poquioma

How Incorporating More Data Reduces Uncertainty in Recovery Predictions.....605

F. P. Campozana, L. W. Lake, and K. Sepehrnoori

Evaluation of Field Development Plans Using 3-D Reservoir Modeling.....625

D. Seifert, J. Newberry, C. Ramsey, and J. Lewis

Improved Characterization of Reservoir Behavior by Integration of Reservoir Performance Data and Rock Type Distributions.....645

D. K. Davies, R. K. Vessell, L. E. Doublet, and T. A. Blasingame

The Role of Reservoir Characterization in the Reservoir Management Process (as Reflected in the Department of Energy's Reservoir Management Demonstration Program).....671

Michael L. Fowler, M. A. Young, M. P. Madden, and E. L. Cole

Advanced Reservoir Characterization for Improved Oil Recovery in a New Mexico Delaware Basin Project.....703

D. F. Martin, R. P. Kendall, E. M. Whitney, R. A. Hardage, B. A. Stubbs, B. J. Uszynski, and W. W. Weiss

Non-Parametric Transformations for Data Correlation and Integration: From Theory to Practice 377

Akhil Datta-Gupta, Guoping Xue, and Sang Heon Lee

A New Approach to Integrate Seismic and Production Data in Reservoir Models 397

Ahmed Ouenes, A. Chawathé, and W. W. Weiss

Predicting Interwell Heterogeneity in Fluvial-Deltaic Reservoirs: Outcrop Observations and Applications of Progressive Facies Variation Through a Depositional Cycle 411

Paul R. Knox and M. D. Barton

Reducing Uncertainty in Geostatistical Description with Well Testing Pressure Data 443

A. C. Reynolds, Nanqun He, and D. S. Oliver

A Quantitative Method for Measuring the Quality of History Matches 463

Tom S. Shaw and R. M. Knapp

Study on Fine Geological Modeling of the Fluvial Sandstone Reservoir in Daqing Oilfield 483

Zhao Hanqing

A Combination of Streamtube and Geostatistical Simulation Methodologies for the Study of Large Oil Reservoirs 487

Avi Chakravarty, A. S. Emanuel, and J. A. Bernath

The Ardross Reservoir Gridblock Analogue: Sedimentology, Statistical Representivity, and Flow Upscaling 489

P. S. Ringrose, G. E. Pickup, J. L. Jensen, and M. Forrester

Use of Element Model to Evaluate Transmissibility Reduction Due to Barriers 509

T. Svanes, D. South, and O. M. Drønen

Quick Evaluation of Multiple Geostatistical Models Using Upscaling with Coarse Grids: A Practical Study 521

Pierre M. Lemouzy

Multiscale Heterogeneity Characterization of Tidal Channel, Tidal Delta, and Foreshore Facies, Almond Formation Outcrops, Rock Springs Uplift, Wyoming.....199

Richard Schatzinger and L. Tomutsa

Well Test Imaging—A New Method for Determination of Boundaries From Well Test Data.....219

Bruce A. Slevinsky

An Efficient Permeability Scaling-Up Technique Applied to the Discretized Flow Equations.....237

Denise Urgelli and Yu Ding

A Simple Method to Estimate Interwell Autocorrelation.....259

J. Sant'Anna Pizzaro and L. W. Lake

Extracting Maximum Petrophysical and Geological Information from a Limited Reservoir Database.....279

Maqsood Ali, A. Chawathé, A. Ouenes, M. Cather, and W. W. Weiss

Towards an Integrated Petrophysical Tool for Multiphase Flow Properties of Core Samples.....301

Roland Lenormand

Flow Units from Integrated WFT and NMR Data.....319

Ekrem Kasap, M. Altunbay, and D. Georgi

New Developments in High-Resolution Borehole Seismology and Their Application to Reservoir Development and Management.....333

Björn N. P. Paulsson

A Direct Method for Determining Complete Positive and Negative Capillary Pressure Curves for Reservoir Rock Using the Centrifuge.....347

E. A. Spinler and B. A. Baldwin

Reservoir Characterization Based on Tracer Response and Rank Analysis of Production and Injection Rates.....359

B. Refunjol and L. W. Lake

Compartmentalization Analysis Using Discrete Fracture Network Models 115

P. LaPointe, T. Eiben, W. Dershowitz, and E. Wadleigh

Characterization of Dynamic Change of Fan-Delta Reservoir Properties in Water-Drive Development 135

Wu Shenghe, Xiong Qihua, and Liu Yuhong

Calculation of Large-Scale Relative Permeabilities from Stochastic Properties of the Permeability Field and Fluid Properties 137

Roland Lenormand and M. R. Thiele

Statistical Analysis of Surface Lineaments and Fractures for Characterizing Naturally Fractured Reservoirs 139

Genliang Guo, S. George, and R. P. Lindsey

Transient Productivity Index for Numerical Well Test Simulations 159

G. Blanc, D. Y. Ding, A. Ene, T. Estebenet, and D. Rahon

Approaches to Identifying Reservoir Heterogeneity and Reserve Growth Opportunities from Subsurface Data: The Oficina Formation, Budare Field, Venezuela 177

D. S. Hamilton, S. K. Raeuchle, M. H. Holtz, M. Uzcategui, and T. Jimenez

Characterization of Oil and Gas Reservoirs and Recovery Technology Deployment on Texas State Lands 179

R. Tyler, R. P. Major, M. H. Holtz, H. S. Hamlin, and S. P. Dutton

High-Resolution Reservoir Geological Modeling Using Outcrop Information 181

Zhang Changmin, Lin Kexiang, Liu Huaibo, and Qiu Yinan

Characterization and Estimation of Permeability Correlation Structure from Performance Data 183

I. Ershaghi and M. Al-Qahtani

2D X-Ray Scanner and Its Uses in Laboratory Reservoir Characterization Measurements 185

Dan Maloney and K. Doggett

CONTENTS

Seismic Signatures of the Lodgepole Fractured Reservoir in Utah-Wyoming Overthrust Belt 1

Jorge O. Parra, H. Collier, and B. Angstman

Putting Integrated Reservoir Characterization into Practice—In-House Training 19

F. M. Wright Jr., D. A. Best, and R. T. Clarke

Study on Detailed Geological Modeling for Fluvial Sandstone Reservoir in Daqing Oil Field 21

Zhao Hanqing, Fu Zhiguo, and Lu Xiaoguang

Application of Fractal in Reservoirs Refined Description for EOR Test Regions 23

Li Yue, Duan Yong-Gang, and Li Yong

3-D Description of Fracture Surfaces and Stress-Sensitivity Analysis for Naturally Fractured Reservoirs 39

S. Q. Zhang, D. Jiao, Y. F. Meng,and Y. Fan

Integrated Reservoir Characterization: Improvement in Heterogeneities Stochastic Modeling by Integration of Additional External Constraints 55

B. Doligez, H. Beucher, F. Geffroy, and R. Eschard

Facies Architecture of the Bluejacket Sandstone in the Eufaula Lake Area, Oklahoma: Implications for the Reservoir Characterization of the Bartlesville Sandstone 73

Liangmiao Ye and Kexian Yang

Reservoir Compartmentalization and Management Strategies: Lessons Learned in the Illinois Basin 93

J. P. Grube, J. E. Crockett, B. G. Huff, H. E. Leetaru, D. G. Morse, B. Seyler, and E. O. Udegbunam

Petrofacies Analysis—The Petrophysical Tool for Geologic/Engineering Reservoir Characterization 95

W. L. Watney, W. J. Guy, J. H. Doveton, S. Bhattacharya, P. M. Gerlach, G. C. Bohling, and T. R. Carr

ERRATA SHEET

1. Figure 3 in the paper by Parra, Collier, and Angstman was inadvertently omitted. It is inserted between pages 12 and 13.

2. Pages 699–700 purposely omitted

3. Omit p. 714

4. Omit p. 726

Seismic Signatures of the Lodgepole Fractured Reservoir in Utah-Wyoming Overthrust Belt

by

Jorge Parra, Southwest Research Institute
Hughbert Collier, Tarleton University
Burke Angstman, Union Pacific Resource

ABSTRACT

In low porosity, low permeability zones, natural fractures are the primary source of permeability which affect both production and injection of fluids. The open fractures do not contribute much to porosity, but they provide an increased drainage network to any porosity. An important approach to characterizing the fracture orientation and fracture permeability of reservoir formations is one based upon the effects of such conditions on the propagation of acoustic and seismic waves in the rock.

We present the feasibility of using seismic measurement techniques to map the fracture zones between wells spaced 2400 ft at depths of about 1000 ft. For this purpose we constructed computer models (which include azimuthal anisotropy) using Lodgepole reservoir parameters to predict seismic signatures recorded at the borehole scale, crosswell scale, and 3D seismic scale. We have integrated well logs with existing 2D surfaces seismic to produce petrophysical and geological cross sections to determine the reservoir parameters and geometry for the computer models. In particular, the model responses are used to evaluate if surface seismic and crosswell seismic measurements can capture the anisotropy due to vertical fractures. Preliminary results suggested that seismic waves transmitted between two wells will propagate in carbonate fracture reservoirs, and the signal can be received above the noise level at the distance of 2400 ft. In addition, the large velocities contrast

between the main fracture zone and the underlying unfractured Boundary Ridge Member, suggested that borehole reflection imaging may be appropriate to map the fracture zone thickness variation and fracture distributions in the reservoir.

Introduction

Lodgepole field is the southernmost in a series of oilfields in the Overthrust Belt of southwestern Wyoming and neighboring Utah producing from the Jurassic Twin creek Formation. Union Pacific Resources (UPRC) has three fields in the play in Summit County, Utah: Lodgepole, Elkhorn, and Pineview. These three fields are shown in the overthrust field map of Utah and Wyoming in Figure 1.

Six horizontal and twelve vertical boreholes have been drilled in Lodgepole field. The field has produced 1,132 MBO. It is a depletion drive reservoir, but most of the wells have significant water production. The well location map (see Figure 2) shows the vertical and horizontal well paths. In particular, the map is showing the horizontal well path for the 34-1H Judd well and the seismic line CREA-25k that is used in the integration analysis.

Lodgepole was selected as the type field for this study because:

1. UPRC is continuing to drill horizontal wells in the field and they are interested in further characterizing the field.
2. An extensive database is available.
    a. Over 20 2D seismic lines are available. The lines are both parallel and perpendicular to the fracture orientation.
    b. UPRC recently ran a 4D seismic survey southwest of Lodgepole field. A small part of the survey overlaps the southwest edge of Lodgepole.

c. UPRC conducted an outcrop study of the fracture orientation in the Twin Creek formation.

d. Resistivity density, neutron, sonic, caliper, and gamma ray logs are available for almost all the vertical wells. As an example Figure 3 shows a suite of logs from vertical well 34-2. MWD gamma ray logs are available for every horizontal well and formation microscanner (FMS) logs have been run in three of them (35-2H, 4-2H and 34-1H).

e. A velocity survey and synthetic seismogram are available for the 35-1.

f. Cuttings are available for most wells, but no cores were taken in the field.

Stratigraphy

The Twin Creek Formation is approximately 1,500 feet thick in Lodgepole Field and is divided into seven members. The following descriptions of each member, beginning with the basal member, are taken from Bruce (1988):

Gypsum Springs. Approximately 50 feet of sabkha evaporites, red beds, and minor carbonates. In most places it serves as a barrier to hydrocarbon migration between the underlying Nugget Formation and the Twin Creek. Note: some workers given the Gypsum Springs formation status.

Sliderock. Approximately 90 feet of micritic limestone with thin beds of oolitic grainstone and thin shaly zones. No primary porosity has been preserved, but calcite-filled fractures are present.

Rich. Approximately 250 feet of argillaceous limestone that cleans upward. The upper 20 to 50 feet has some intergranular porosity and may be dolomitized.

Boundary Ridge. Approximately 50 feet of red siltstones and claystones with a sabkha character. It serves as a good marker bed in the Twin Creek Formation.

Watton Canyon. Approximately 250 feet of limestone with thin, tightly cemented oolitic zones. The limestones of the Watton Canyon are thinner bedded and more terrigeneous than the Rich Member.

Leeds Creek. Approximately 300 feet of interbedded argillaceous and relatively clean limestones. A highly radioactive unit near the top of the member is devitrified tuff.

Giraffe creek. Approximately 450 feet of micritic and oolitic carbonates. It becomes sandy toward the top.

The Twin Creek Formation represents a major marine transgression over the underlying Nugget Formation, which is eolain sandstones. The Nugget is one of the primary hydrocarbon producing reservoirs in the Overthrust Belt.

The Basan Preuss Silt, a 30 to 100 foot interval of tightly cemented quartz siltstone, overlies the Twin Creek Formation. The Preuss Salt overlies the siltstone. It varies from 20 to 300 feet in thickness.

Geologic Controls on Hydrocarbon Production

Virtually all the effective porosity in the Twin Creek Formation is from fractures. Existing vertical production comes from five members of the Twin Creek. The Gypsum Springs and Giraffe creek Members do not produce and production from the Leeds Creek Member has been limited. However, horizontal wells produce from fractured intervals in only the Rich and Watton Canyon members. In the Rich the upper 30 feet is the fractured interval.

The Watton Canyon is the most prolific hydrocarbon-producing member of the Twin Creek and it is also the most intensely fractured. The clean, shale-free section approximately 100 feet thick in the lower part of the Watton Canyon contains fractures. The main fractured zone is the lower 30-50 feet of this clean interval. An interval approximately 20 feet thick near the base of the Watton canyon is the primary target for most of UPRC's horizontal wells, including the 34-1H in Section 34.

Based on outcrop studies, FMS logs, and production data, the fractures run NW-SE. Fracturing was produced by faulting and tight folding of the hanging wall of the Absaroka Thrust sheet (Bruce, 1988). The Gypsum Springs Member served as a detachment surface between the Nugget and Twin creek in the thrusting process. The trapping mechanisms is structural closure on asymmetrical anticlines in the hanging wall. The geometry of the Watton canyon member of the Twin Creek Formation is given by the structural map and the structural cross-section shown in Figures 4 and 5.

Study Area

Lodgepole field extends over six sections. Section 34 in the center of the field was chosen as the initial study area for this project. The section contains three vertical and two horizontal well, with all of the data types listed above.

Structural cross sections were constructed with the logs from the vertical wells in Section 34. The cross sections center on the Watton Canyon and Boundary Ridge Members, which contain the fractured intervals in the Twin Creek Formation. The cross sections include the acoustic velocity, bulk density, gamma ray, and caliper curves. These cross-sections are given in Figures 6 and 7.

In the fractured interval within the Watton Canyon sonic velocity ranges from 18,500-20,000 feet/second and bulk density ranges from 2.6 to 2.75 g/cm^3. The upper boundary does not appear

to have a significant change in sonic velocity and the lower boundary is a shale with a sonic velocity of 16,000-17,000 feet/second.

For most of the fractured interval in the Rich, sonic velocities range from 18,800 to 21,000 feet/second and bulk density ranges from 2.65 to 2.8 g/cm^3. The interval is bounded above by a shale with a sonic velocity of 16,000 feet/second and below by a shaly limestone with a velocity of approximately 18,000 feet/second. The fractured interval is relatively clean (i.e. shale-free). The upper 15 feet of the fractured interval appears to be dolomite, which accounts for the corresponding higher bulk densities and may also explain, at least in part, the higher sonic velocities. The fractured interval in the Rich has ore shale than the fractured interval in the Watton Canyon.

Future Petrophysical Analysis

A petrophysical analysis of the logs and a petrographic analysis of the cuttings in selected wells in Section 34 will be conducted in order to ascertain the factors controlling horizontal and vertical distribution of fractures, relationships between petrophysical properties an fracture density and distribution, and the extent to which matrix porosity contributes to hydrocarbon production. Lateral fracture distribution is being quantified with the FMS log of horizontal well 34-1H. Petrographic analysis of the cuttings from the same well are being analyzed in order to ascertain the factors controlling fracture distribution. These data will be correlated with lateral variations observed on the 2D seismic lines.

Preliminary Integration of Seismic and Well Log Data

The seismic line CREA-25k was selected because follow the horizontal path of well 34-1H Judd. This well and well 34-2 are plotted in the migrated seismic section given in Figure 6. A synthetic seismogram was produced using the compressional wave velocity log and the density log

from well 34-2. The synthetic was superimposed on the migrated seismic line together with the geological boundaries defined by the well logs in Figure 7. Both Figures 6 and 7 show the horizontal path of well 34-1H in the Watton Canyon intercepting the fractured zone define in cross-section shown in Figure 3. The Watton Canyon is the most important geological unit which upper and lower boundaries correlate with the sonic, density and gamma logs, and seismic events in the seismic section of Figures 6 and 7. In fact, the synthetic seismogram fit reasonably well at the well position 34-1H Judd in " time-depth" on the seismic section. For example the top of the Watton Canyon is at 1600 ms and the top of the Rich Member is at 1640 ms.

In general the petrophysical boundaries defined by the well logs correlate with the seismic events in the seismic section. The seismic signatures associated with the Watton Canyon suggests lateral velocity changes between wells 34-1H and 34-2. There is an small change in thickness of the Watton Canyon up to about 27 traces from well 34-2 to well 34-1H. Following this event a different signature having similar characteristics is observed below the horizontal path which is approaching the vertical position of well 34-2. This event is associated the petrophysical characteristics of the Rich Member in the region below the Watton Canyon .

The fractured zones are located in the bottom part of the Watton Canyon Member and in the top of the Rich Member, where these fractured zones are intercepted by well 34-2. Both fractured zones are associated with low gamma ray counts. The top fractured zone in the Watton Canyon is separated from the bottom fractured zone by the a 50-foot Boundary Ridge Member formed by siltstones and claystones. A reflection event associated with this boundary is observed in the seismic sections of Figures 6 and 7 and is below the horizontal path of well 34-1H. This analysis suggests that the Watton Canyon in the region between both wells under consideration are associates with the

"trough"- reflection response ,which may be caused by the presence of the fractured zone containing vertical fractures. This fractured zone is intercepted by the horizontal well in the bottom part of the Watton Canyon. The FMS logs recorded in the horizontal well intercepted vertical fractures having a variable fracture density distribution.

Computer Models

In order to confirm the above interpretation , computer models will be produced for the geological units intercepted by well 34-2 and the fracture zones of interest. The fractures will be modeled assuming the axis of anisotropy perpendicular to the fractures. Synthetic seismograms will be produced considering the geometry of the formations and the rock physical properties determined from well logs. As a comparison synthetic seismograms will be produced for a model containing only the geological boundaries without the fractures. This modeling effort will determine if fractures zones can be detect using surface seismic in the Lodgepole field. This will be done by comparing both synthetic seismograms with the observed migrated seismic data.

In addition the fractured model based on the above geometry will be used to calculate synthetic interwell seismic response by assuming a seismic source in well 34-1H and three-component detectors in well 34-2. This modeling effort will determine the feasibility of transmitting and detecting interwell seismic waves in the Lodgepole formation. Also we will determine if fractures or fracture zones can be delineated using interwell seismic methods. In particular, we expect that small target zones can be image by using cross well methods of measurements. Several models will be produced to analyze the seismic signature characteristics associated with the vertical fractures that will be modeled assuming azimuthal anisotropy. To analyze the seismic waves time-frequency will be applied to the data to separate signatures of fractured zone from others associated with the different

geological units. This seismic analysis will be applied to the observed and calculated surface seismic data as well.

Conclusions

Correlation between the lithology and the well logs and the migrated seismic data from Lodgepole field served to identify seismic events associated with geological units of interest. A fractured zone in the Watton Canyon correlates with seismic signatures observed in the seismic section. Computer models including the fracture zones are proposed to confirm the qualitative interpretation at the Lodgepole field. In addition, computer models will be produced to determine the feasibility of detecting fracture zones using interwell seismic measurement techniques between wells at the Lodgepole field.

References

Bruce, C.L., 1988, Jurassic Twin Creek Formation: a fractured limestone reservoir in the Overthrust Belt, Wyoming and Utah: Rocky Mountain Association of Geologists, pp. 105-120.

Parra, J.O., 1995, A feasibility study of high-resolution reverse VSP and interwell seismic methods for hydrocarbon reservoir characterization: The Log Analysts, May-June, pp. 64-81.

Parra, J.O., Zook, B.J., and Collier, H.A., 1996, Interwell seismic logging for formation continuity at the Gypsy test site, Oklahoma: Journal of Applied Geophysics. v. 35, pp. 45-62.

Parra, J.O., 1996, Characterization of fracture reservoirs using static and dynamic data: from sonic and 3D seismic to permeability distribution: September Quarterly Report, U.S. Department of Energy, Contract No. DE-AC22-94PCp1008; SwRI Project 15-7939.

Captions

Figure 1. Regional map showing location of Overthrust Field.

Figure 2. Location map showing horizontal well path for the 35-1H Judd and seismic line CREA-25k.

Figure 3. Well log display for well 34-2 Judd including gamma ray, deep lateral log, compressional wave velocity and density-neutron porosity.

Figure 4. Structural map on top of Watton Canyon member of the Twin Creek Formation.

Figure 5. Structural cross-section along traverse AA′.

Figure 6. A structural cross-section through the Wells 34-2 and 34-1 at the Lodgepole field.

Figure 7. A structural cross-section through the wells 34-2 and 34-3 at the Lodgepole field.

Figure 8. Migrated seismic section CREA-25k along horizontal well path of well 34-1H Judd.

Figure 9. Migrated seismic section CREA-25k of Figure 8 with synthetic seismogram inserted at well location 34-2 Judd.

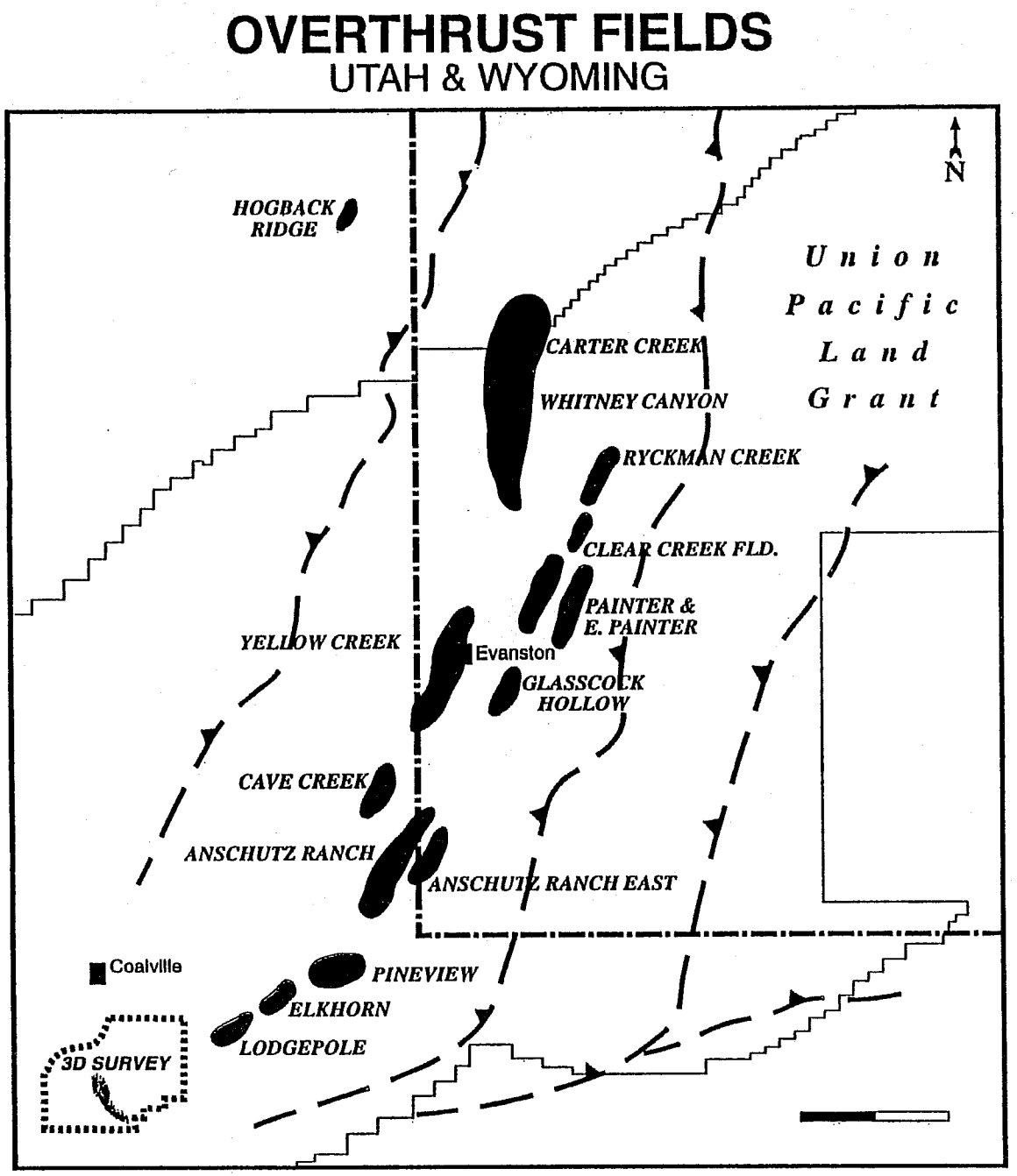

Figure 1. Regional map showing location of Overthrust Field.

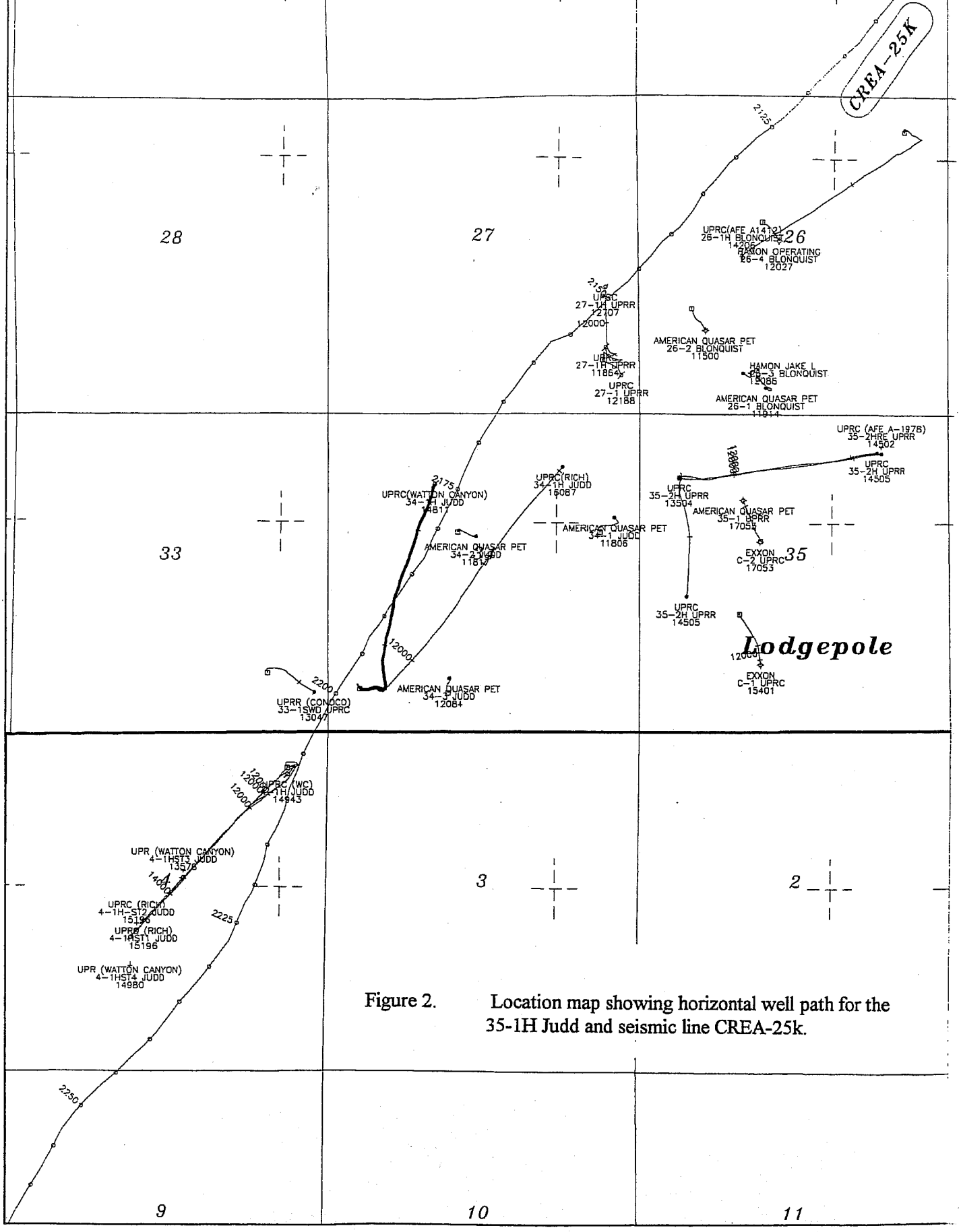

Figure 2. Location map showing horizontal well path for the 35-1H Judd and seismic line CREA-25k.

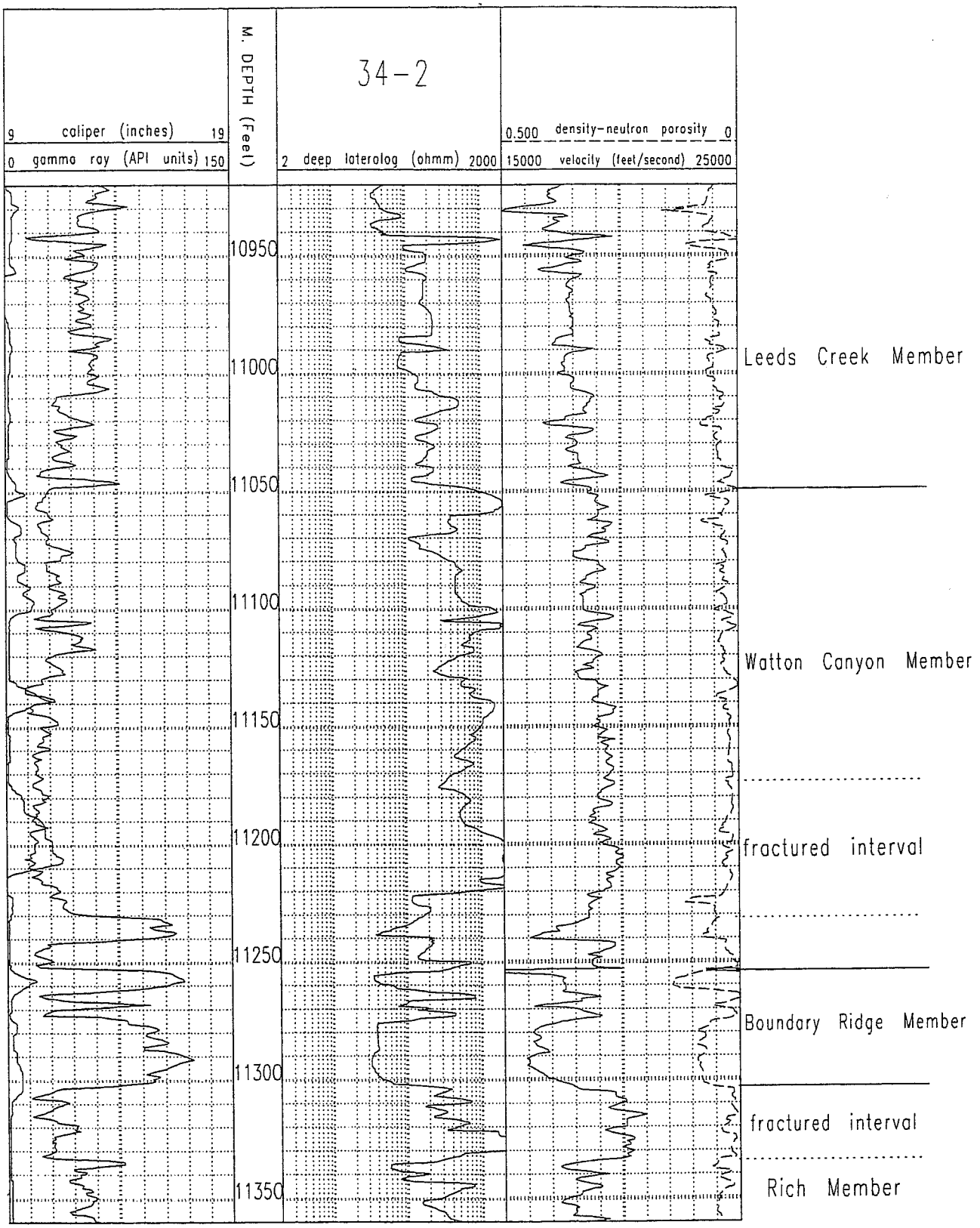

Figure 3. Well log display for well 34-2 Judd including gamma ray, deep lateral log, compressional wave velocity and density-neutron porosity.

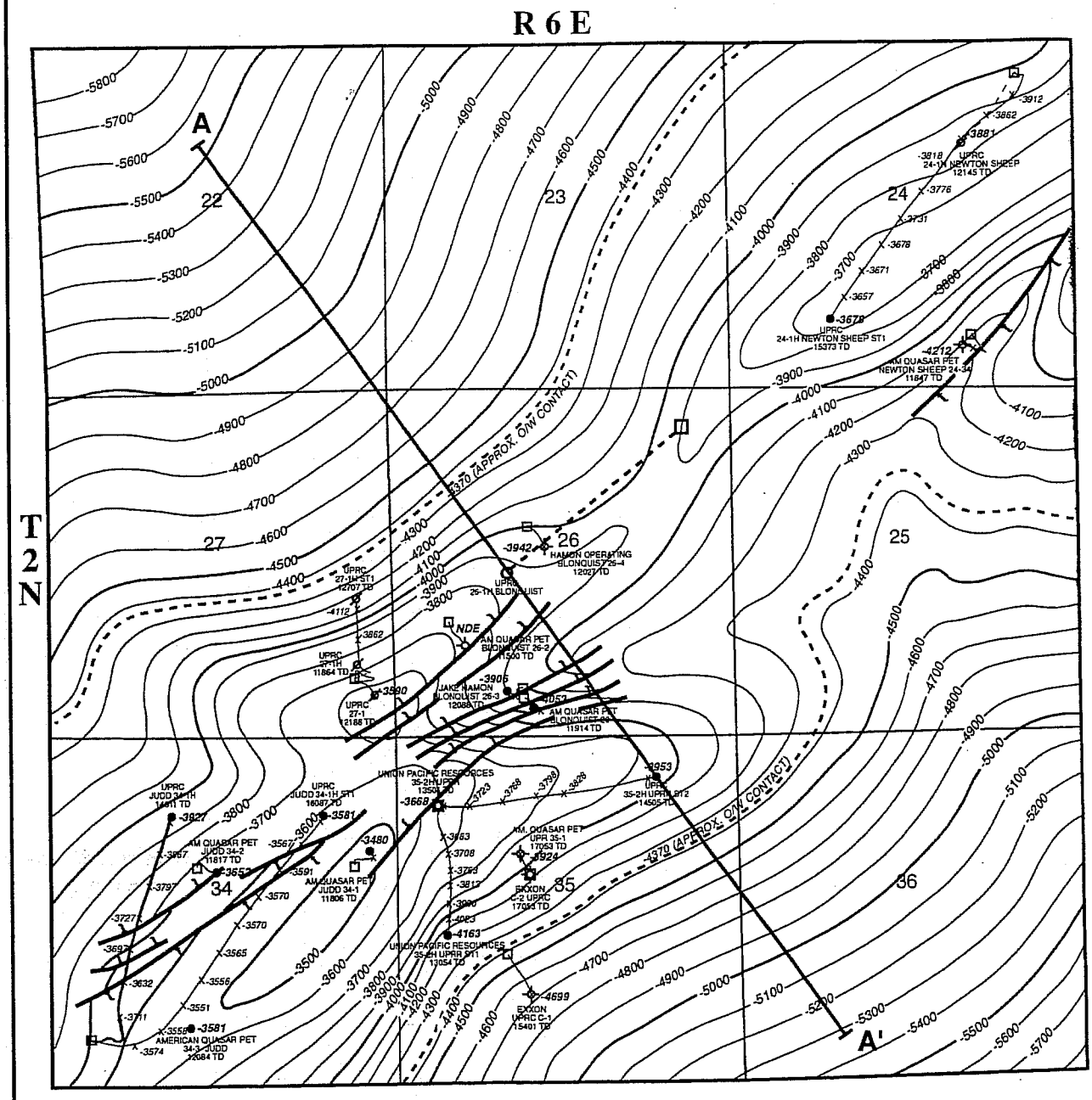

Figure 4. Structural map on top of Watton Canyon member of the Twin Creek Formation.

LODGEPOLE FIELD
SUMMIT COUNTY, UTAH

STRUCTURE MAP
TOP WATTON CANYON MEMBER
TWIN CREEK FM.

N

0 1000' 2000' 3000'

CI= 100'
March, 1996

STRUCTURAL CROSS-SECTION A-A'

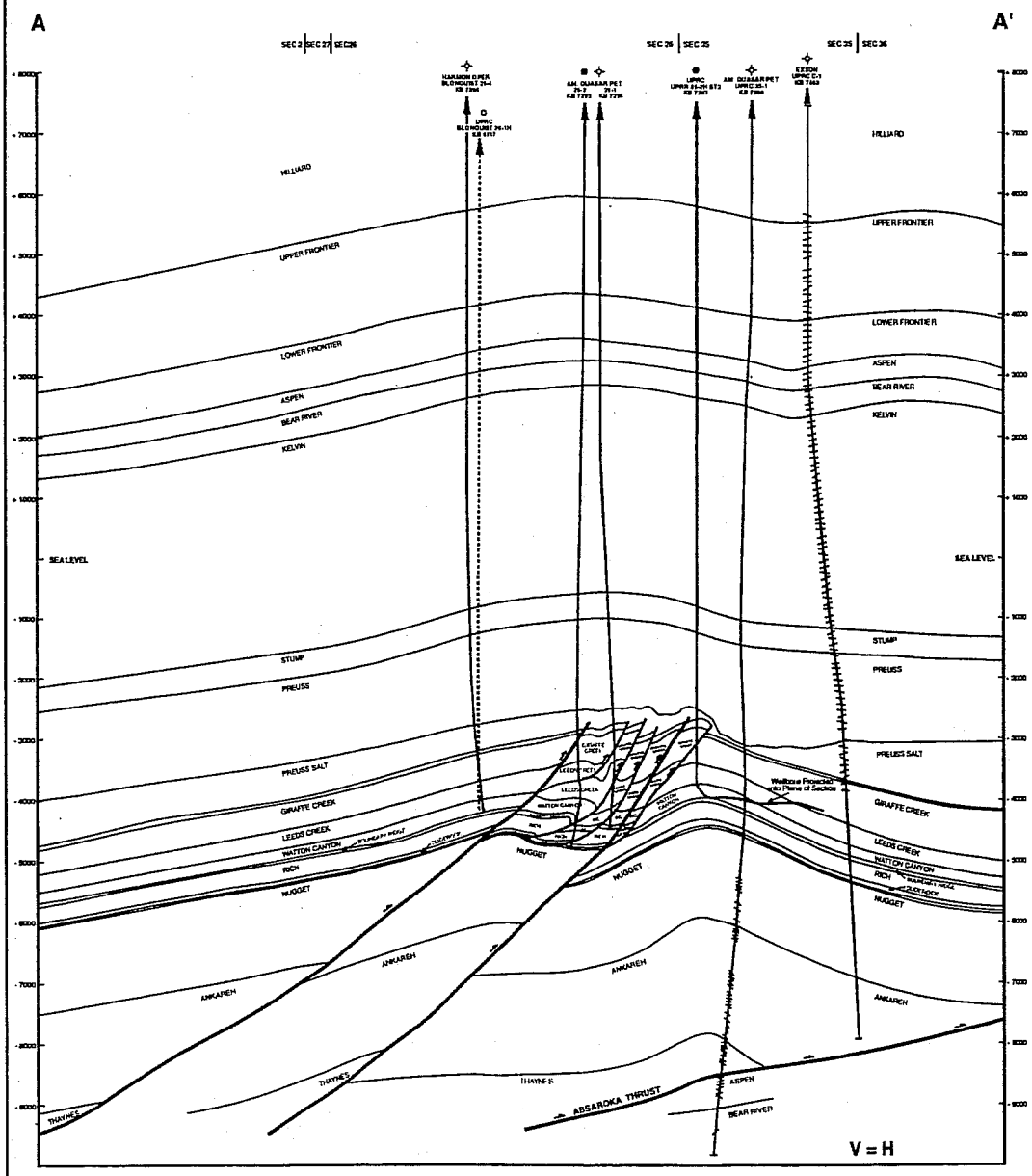

Figure 5. Structural cross-section along traverse AA'.

LODGEPOLE FIELD
SUMMIT COUNTY, UTAH

STRUCTURAL CROSS-SECTION
A-A'

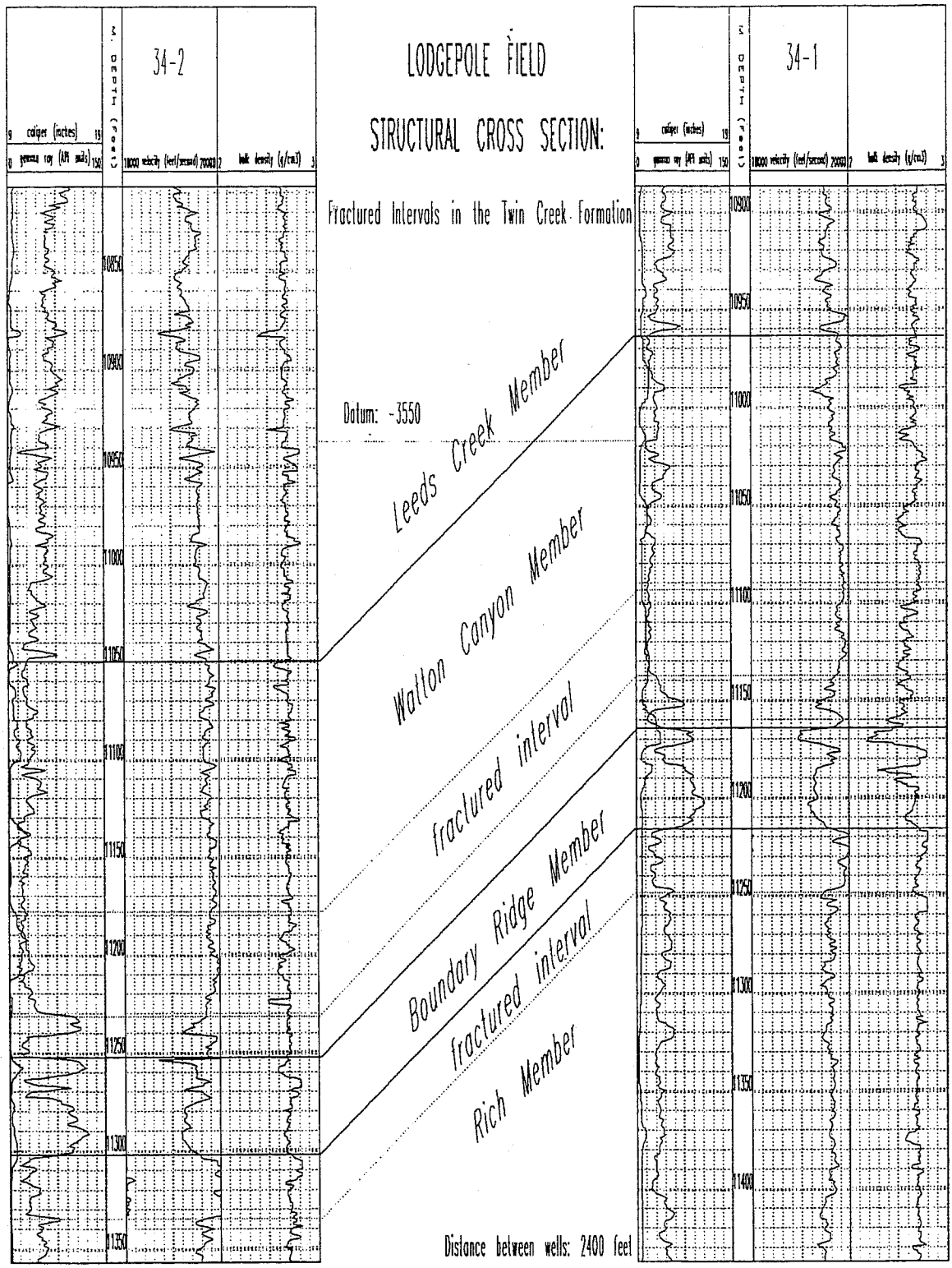

Figure 6. A structural cross-section through the Wells 34-2 and 34-1 at the Lodgepole field.

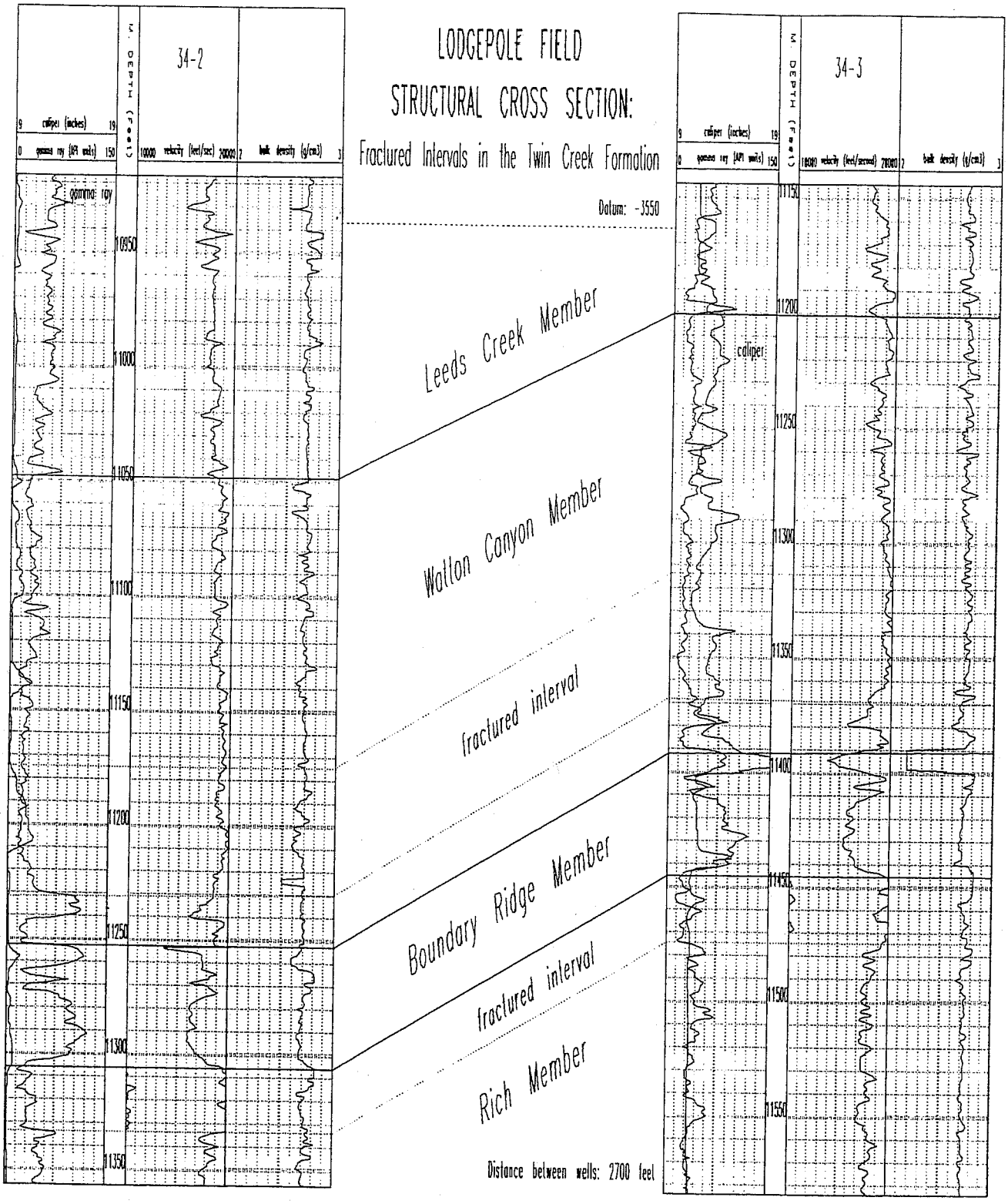

Figure 7. A structural cross-section through the wells 34-2 and 34-3 at the Lodgepole field.

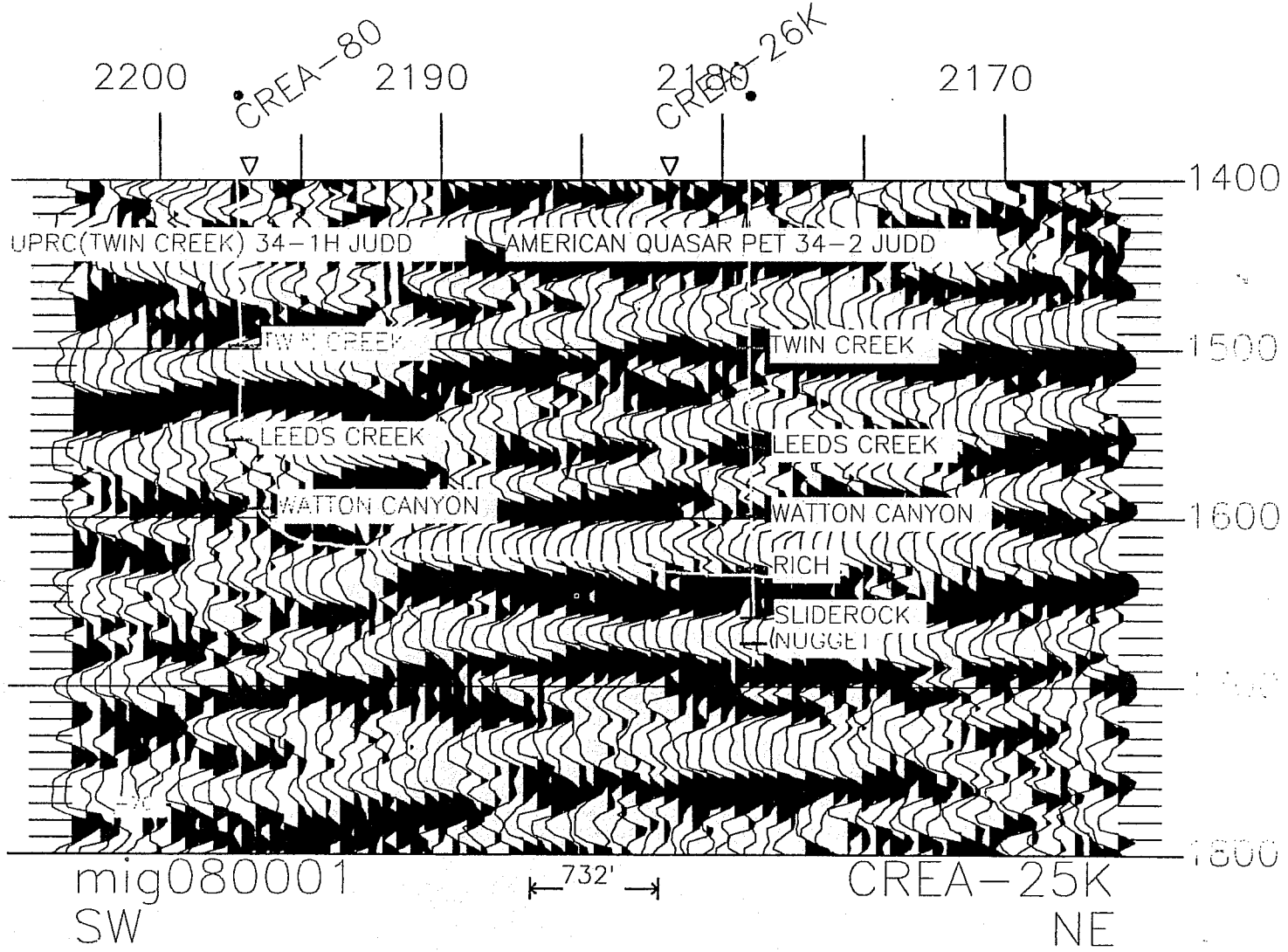

Figure 8. Migrated seismic section CREA-25k along horizontal well path of well 34-1H Judd.

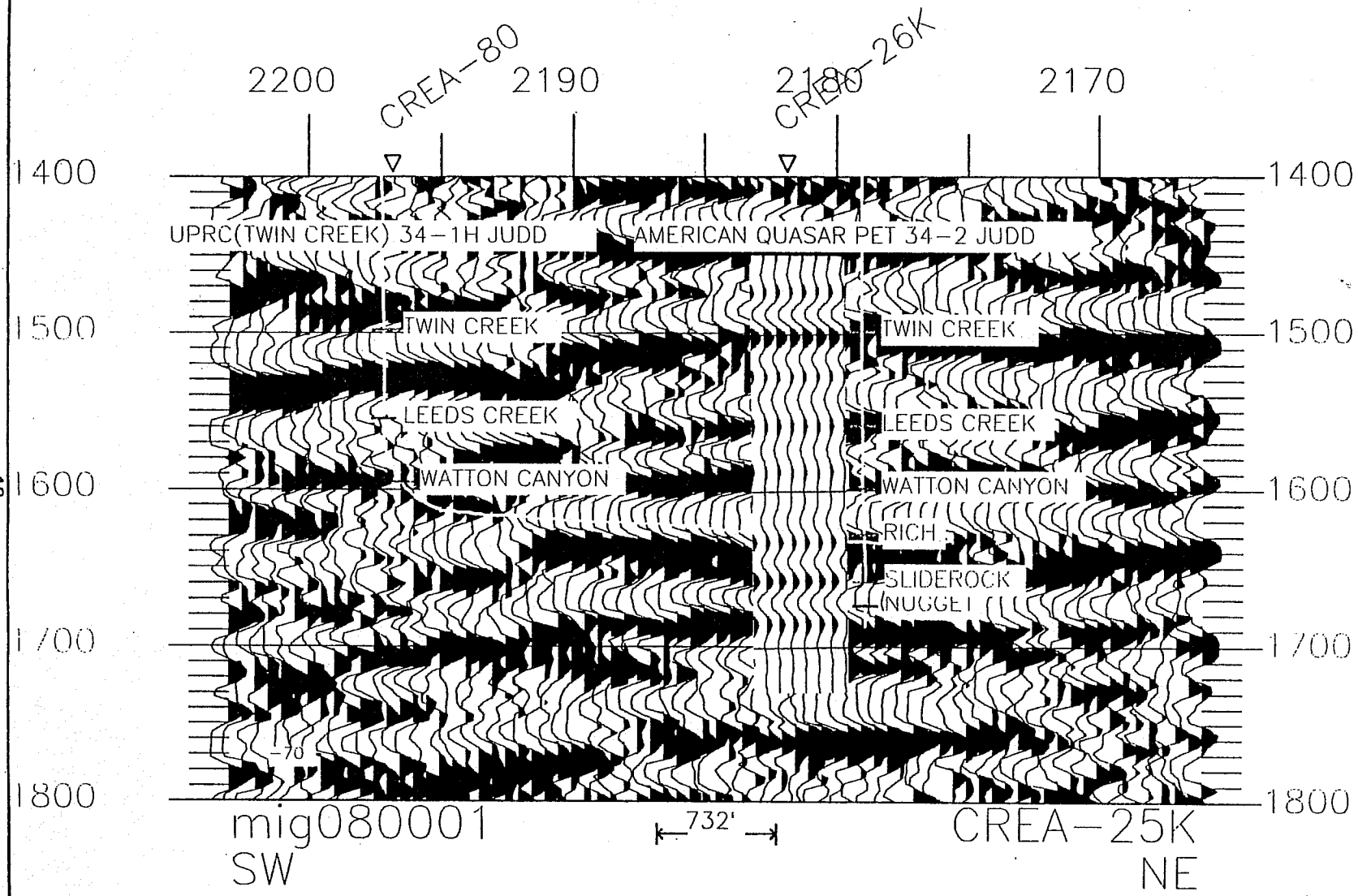

Figure 9. Migrated seismic section CREA-25k of Figure 8 with synthetic seismogram inserted at well location 34-2 Judd.

Putting Integrated Reservoir Characterization into Practice — In House Training

Dr. F. M. Wright, Jr., D. A. Best; R. T. Clarke
Mobile Exploration and Producing Technical Center
P.O. Box 819047
Dallas, TX 75381

ABSTRACT

The need for even more efficient reservoir characterization and management has forced a change in the way Mobil Oil provides technical support to its production operations. We've learned that to be successful, a good understanding of the reservoir is essential. This includes an understanding of the **technical** and **business** significance of reservoir heterogeneities at different stages of field development. A multi-disciplinary understanding of the business of integrated reservoir characterization is essential and to facilitate this understanding, Mobil has developed a highly successful "Reservoir Characterization Field Seminar". Through specific team based case studies that incorporate outcrop examples and data the program provides participants the opportunity to explore historic and alternative approaches to reservoir description, characterization and management. We explore appropriate levels and timing of data gathering, technology applications, risk assessment and management practices at different stages of field development. The case studies presented throughout the course are a unique element of the program which combine real life and hypothetical problem sets that explore how different technical disciplines interact, the approaches to a problem solving they use, the assumptions and uncertainties contained in their contributions and the impact those conclusions may have on other disciplines involved in the overall reservoir management process. The team building aspect of the course was an added bonus.

Study on Detailed Geological Modelling for Fluvial Sandstone Reservoir in Daqing Oil field

Zhao Hanqing; Fu Zhiguo; Lu Xiaoguang
Institute of Petroleum Exploration and Development
Daqing, China 163712

ABSTRACT

Guided by the sedimentation theory and knowledge of modern and ancient fluvial deposition and utilizing the abundant information of sedimentary series, microfacies type and petrophysical parameters from well logging curves of close spaced thousands of wells located in a large area. A new method for establishing detailed sedimentation and permeability distribution models for fluvial reservoirs have been developed successfully. This study aimed at the geometry and internal architecture of sandbodies, in accordance to their hierarchical levels of heterogeneity and building up sedimentation and permeability distribution models of fluvial reservoirs, describing the reservoir heterogeneity on the light of the river sedimentary rules. The results and methods obtained in outcrop and modern sedimentation studies have successfully supported the study.

Taking advantage of this method, the major producing layers (PI_{1-2}), which have been considered as heterogeneous and thick fluvial reservoirs extending widely in lateral are researched in detail. These layers are subdivided into single sedimentary units vertically and the microfacies are identified horizontally. Furthermore, a complex system is recognized according to their hierarchical levels from large to small, meander belt, single channel sandbody, meander scroll, point bar, and lateral accretion bodies of point bar.

The achieved results improved the description of areal distribution of point bar sandbodies, provide an accurate and detailed framework model for establishing high resolution predicting model. By using geostatistic technique, it also plays an important role in searching for enriched zone of residual oil distribution.

Application of Fractal Theory in Refined Reservoir Description for EOR Pilot Area

Yue Li Xin Jiang Petroleum Institute , P.R. China , Yonggang Duan and Yun Li
Southwest Petroleum Institute . P.R. China , Yuan Lu Xin Jiang Petroleum Institute , P.R. China

Acknowledgments

I would like to thank Xin jiang petroleum exportation and development research institute to support this project. I would also like to thank Dr. Di Jiao and yi-li Kang for exchanging idea to writing this paper.

Abstract

A reliable reservoir description is essential to investigate scenarios for successful EOR pilot test. Reservoir characterization includes formation composition, permeability, porosity, reservoir fluids and other petrophysical parameters. In this study, various new tools have been applied to characterize Kilamayi conglomerate formation. This paper examines the merits of various statistical methods for recognizing rock property correlation in vertical columns and gives out methods to determine fractal dimension including R/S analysis and power spectral analysis. The paper also demonstrates that there is obvious fractal characteristics in conglomerate reservoirs of Kilamayi oil fields . Well log data in EOR pilot area are used to get distribution profile of parameters including permeability, porosity, water saturation and shale content .

Introduction

Three dimensions geologic modeling of a reservoir requires the ability to detect the short and long range correlation of properties. Fractal provide a method for implementation of specific conceptual models to address the problem of heterogeneity mapping in geologic structure. While many natural entities have been demonstrated to follow fractal models, the universal application to all phenomena has not been established yet[1] . Efforts have been underway to synthesize various observations related to geologic system and to examine the applicability of fractal models[2],[3].

As pointed out by Hewett[1] , because of the inverse relationship between the variance and the lag , the R/S methodology is the best suited to long-range correlation estimation . As shown by Mandelbrot[4], fractal dimension D is related to Hurst exponent by D=2-H for fBM signals. Many studies have been published describing porosity well logs as fGn[5][6][7][8] . All of these authors used the R/S analysis, and several used many more of the tools. The discovery that well logs often have a fGn character was made by Hewett[1] He reported an H value of 0.855 . Aasum et al [8] analyzed 18 wells from a single unit. They used both R/S and variogram analysis . They found fGn with H varying between 0.70 and 0.94 for logs of both porosity and

the logarithm of permeability . Crane and Tubman [6] analyzed three horizontal wells and four vertical wells in a carbonate formation . They found all the logs to be fGn. H ranges between 0.88 and 0.89 for the vertical wells and between 0.85 and 0.93 for the horizontal wells . Taggart[7] analyzed a well from the Bowen/Surat Basin, a well from the Hutton Sandstone in the Jackson Field, and two wells from in Windalia Sandstone, Barrow Island. He found H values of 0.82, 0.82, and 0.8 .

This paper will review some of the important results of the statistical theories of reservoir properties and discuss their implications for modeling the influence of reservoir heterogeneity. Thirteen vertical wells are analyzed , the properties of fractal distributions is shown in conglomerate reservoirs at first time . This paper also gives out a fractal interpolation method for both internals and for the plane . Fractal distribution of reservoir heterogeneity can be gained from EOR pilot area in Kilamayi oil field .

Basic Characterization of EOR Pilot Area

EOR pilot wellblock located Er Zhong area on north of Ki~Wu structure and south of north black oil mountain, distance from this area to Kilamayi is about ten kilometers(Fig .1). EOR pilot area has four units with five-spot well pattern and , total well number is 13 including 9 producer wells and 4 injection wells. Well spacing from injection to producer is 50 meters.

Well depth in this area is from 599 to 678 meters. Total thickness of the formation is about 65 meters, and glutenite thickness of pay zones is about 20 meters. The formation form bottom to top divided into five layers , that is s_7^4 , s_7^3 , s_7^2 , s_7^1 and s_6^4, s_7^4 , s_7^3 and s_7^2 are main production layers . In the study, main work targets are s_7^4 , s_7^3 layers in EOR pilot area .

The effective permeability of glutenite zone is average ($150\sim450\times10^{-3}\mu m^2$) (Table1), and the average effective porosity is 17%~21% . Permeability between wells is from $100\sim3000\times10^{-3}\mu m^2$. Table 1 shows that heotergenous distribution of permeability is serious and complicated .

Since formation conditions are very complicated, reservoir engineers can not exactly describe the physical properties of interwells using traditional geological and statistical method. At present , a better way of disposing random changing of reservoir parameters between wells is by fractal geometry method .

Methodologies

Details about the correlation methods examined in this studies are well documented in the literature's . The following is a very brief description of the various techniques .

<u>R/S Analysis Method (R/S)</u>

As introduced by Hurst[9],[10] and later on improved by Mandelbrot and Wallis[11],[12], the appropriate statistic for evaluating long-range statistical dependence is the rescaled range $R(x,\ell)/S(x,\ell)$, where $R(x,\ell)$ is the cumulated or "graded" range of a process between positions x+1 and $x+\ell$ after removal of the sample average and $S^2(x,\ell)$ is the corresponding sample variance. For any function Z(x) with equal sample spacing normalized to unity, with Zg(x), defined as the graded sequence[1]:

$$Zg(x)= \sum_{u=1}^{x} Z(u) \tag{1}$$

and given any lag $\ell>1$, $R(x,\ell)$ and $S^2(x,\ell)$ are defined as

$$R(x,\ell)= \mathrm{Max}_{0\le u\le \ell}\{Zg(x+u)-Zg(x)-(u/\ell)[Zg(x+\ell)-Zg(x)]\}$$
$$-\mathrm{Min}_{0\le u\le \ell}\{Zg(x+u)-Zg(x)-(u/\ell)[Zg(x+\ell)-Zg(x)\} \tag{2}$$

This is the maximum range of deviations of the graded function from its trend over the lag interval . the sample variance is

$$S^2(x,\ell)=1/\ell[\sum_{u=1}^{\ell} Z^2(x+u)]-[{}^1/\ell \sum_{u=1}^{\ell} Z(x+u)]^2 \tag{3}$$

The sequential range of fBM asymptotically obeys an ℓ^H scaling law . For process of fractional Gaussian noise Z(x) , the corresponding Zg(x) is fBM:

$$\lim_{\ell\to\infty}\ell^H R(x,\ell)/S(x,\ell)=\mathrm{Const} \tag{4}$$

The H coefficient can be obtained from a plot of $R(x,\ell)/S(x,\ell)$ vs. ℓ (Fig.2) .

<u>Power Spectral Density Analysis (PSD)[14]</u>

Applying a Fourier transform of finite samples

$$Z(f,\ell)=1/L\int_0^L z(x)e^{2\pi ifx}dx \tag{5}$$

Spectral density is defined: $S_Z(f)=L|Z(f,L)|^2$ for large L .

Further , we can express $S_Z(f)=C_H \frac{1}{f\beta}$. From fast Fourier transform we obtain S(f) , and f=(1:N/2)/N . β is obtained from the plot of log Sz~log f . As indicated by Hewett[1] and Barnsley et al [15] , for power law scaling distribution the grading of a sequence raises the β by 2 to β+2 . For an fGn signal β=2H-1 and for fBM signal , β=2H+1. For ideal data sets we can use β to judge the nature of the original

The Fractal Interpolation Method Between Wells in Section

In this paper, are employed to describe fractal distribution of heotergenous parameters between wells. The method shows as follow and in Fig.4 .

The first iterated step of interpolation is:

$$\sigma_1=\sigma_0/2^H \quad (7)$$

$$Z_{1,1}=Z_{1,0}+\sigma_1 \cdot R_{1,1} \quad (8)$$

$$Z_{2,1}=Z_{2,0}+\sigma_1 \cdot R_{2,1} \quad (9)$$

$$Z_{3,1}=[(Z_{1,0}+Z_{2,0})/2]+\sigma_1 \cdot R_{3,1} \quad (10)$$

The second iterated step is :

$$\sigma_2=\sigma_1/2^H \quad (11)$$

$$Z_{1,2}=Z_{1,1}+\sigma_2 \cdot R_{1,2} \quad (12)$$

$$Z_{2,2}=Z_{2,1}+\sigma_2 \cdot R_{2,2} \quad (13)$$

$$Z_{3,2}=Z_{3,1}+\sigma_2 \cdot R_{3,2} \quad (14)$$

$$Z_{4,2}=[(Z_{1,1}+Z_{3,1})/2]+\sigma_2 \cdot R_{4,2} \quad (15)$$

$$Z_{5,2}=[(Z_{2,1}+Z_{3,1})/2]+\sigma_2 \cdot R_{5,2} \quad (16)$$

. . . . . .

repeat above step

where:

$Z_{1,0}$、$Z_{2,0}$ — the initial iterated values determined by log data ;

H— Hurst exponent , the slope of lnR/S ~ lnτ curve ;

i— section location ;

j— the number of iterated ;

$Z_{i,j}$— well log data in ith location and jth iteration;

σ_0^2— inital variance, obtained by all data point of well log ;

$R_{i,j}$ — a random number of obeying distributions of N(0,1), it must be randomly generated at position of difference and iteration times of difference .

Fractal Interpolation Method for a Unit with Five-spot Well in Plane

Specific operation adopted Pyramid method , as Figure 5 shown , first defined a value of certain number point in the figure, included value of four top point a 、 b 、 c and d , then conducted random factal

interpolation for other point in figure, value of middle point e was defined by a and b, the same as defining value of i point by four points of e、f、g and h, interpolation function follows as describing above, as continue weight interpolation until there are value of all point of having put up grey degree can not conduct interpolation.

Example: Analysis OF Well Log Data

Calculation Hurst Exponent (H)

In geological column, because of sequencing of various lithologies, establishment of long rang correlation requires a composite model incorporating various sections of a particular lithology To test the validity of these methods, a series of numerical experiments are conducted R/S method is used to calculate fractal dimension of single well, well log curves of 13 wells from EOR pilot area in Kalamyi conglomerate reservoirs are collected. Curves include eight kinds of well log, such as AC, DEN, RXO, CAL, CNL, GR, SP. Through comparing and analyzing, we select proximity log curve to calculate Hurst exponent (H). These samples are taken at intervals of 0.125 m from proximity log curve which depth is from 650~680 meters for each well. Figure 1 is shown the behavior of the rescaled range for this sequence, along with a least squares fit of the values for $\ell>20$ and a reference line with a slope of 1/2. Clearly, this sequence exhibits long-run interdependence and shows no sign of "breaking" to an $\ell^{1/2}$ behavior for large ℓ. The least square method is used to determine Hurst exponent (H) in the R/S analysis. Table 2 shows that values of Hurst exponent (H) are ranged from 0.8428 to 0.955, average value is 0.8936. Although Hurst exponent is different from 13 wells, difference value for Hurst exponent is not very large. Permeability of EOR pilot area for $s_7^4 \sim s_7^3$ layers forms at the same condition. Table 3 not only shows that pertophyiscal properties and from process of EOR pilot area for $s_7^4 \sim s_7^3$ are the same ,but also changing frequency for well of composition and permeability. The larger value of Hurst exponent, the more serious permeability changing and heotergenous of pay zone.

Selecting and Treating Data for Interwells Profile Distribution

Based on the same reason as calculating Hurst exponent, well log curves are selected. Well log curves must be the same interval and 8 points per meter. Fractal interpolation can be processed between wells. After fractal interpolation of each point between two wells are processed, obtaining new interpolation points will be covered whole well profiles. Fig.5 to Fig.8 show the distributed results of ptrophysical

parameters , these parameters include permeability, porosity, shale content, water saturation. In the Fig 5, fractal interpolation results of permeability in section show that permeability of conglomerate formation distributes characteristic of skip changing compound rhyme.

Selecting and Treating Data for Plane Distribution

Because of selecting pyramid random interpolation methods, every zone of each wells only use one data. Therefore, data must be treated for each layer . The method as follow:

(1) At the first, for well intervals of 650~680 meters, we divided it into four intervals from top to bottom according to s_7^{3-1}, s_7^{3-2}, s_7^{3-3}, s_7^{4-1}.

(2) In each intervals, mean and mean square deviation of corresponding parameters were obtained by arithmetic average method for all well logs interpretation results of this interval .

(3) Hurst exponent , mean and mean square deviation of parameters will be input computer program for selecting mine zones of five wells in plane area and data is shown in table 3. Plane distribution graph of heterogeneous parameters can be carried out for this layer. Fig.9 to Fig 12 shows distributing results of petrophysical parameters. Fig.9 shows that permeability distribution characteristic of fractal interpolation is the same as the well performance analysis results. Fig.5 also shows more detail characteristic of changing permeability than traditional geology analysis methods.

Conclusion

1. The self-similar statistics of random fractal provide a good tool for reservoir property distributions.
2. Through R/S method , this sequence exhibits long-run interdependence and fractal characteristics for EOR pilot area in conglomerate reservoirs of Kilamayi oil fields .
3. In EOR pilot area, Hurst exponent (H) ranges from 0.8428 to 0.955. H is higher than sandstone reservoirs ,this result show that there is very serious heotergenous for conglomerate formation.
4. Random fractal property distributions can be processed with fractal interpolation both in section and in plane.
5. Through fractal property distributions , results from fractal interpolation is the same as geology and well performance analysis results. Because shale content is lower , it is not obvious that shale content affects formation heotergenous. It is very obvious that water saturation affects formation heotergenous.

Reference

[1] Hewett, T.A., " Fractal Distributions of Reservoir Heterogeneity and Their Influence on Fluid Transport " , SPE 15386, 61th Ann . Tech . Con . of SPA , New Orleans , Oct . 5-8 , 1986

[2] Goggin, D.J., Chandler, M.A., Kocurek, G. and Lake, L.W., Permeability Transects of Eolian Sands and Their Use in Generating Random Permeability Fields , SPE Formation Evaluation, March 1992

[3] Perez, G. and Chopra, A.K., Evaluation of Fractal Model to Describe Reservoir Heterogeneity and Performance, SPE 22694, 66th Ann. Tech. Conf. of SPE, Dallas, Oct..6-9,91

[4] Mandelbrot, B.B., The Fractal Geometry of Nature , Freeman, New York, 1983.

[5] H . H . Hardy , SPE Paper 23968 , presented at SPE Permian Basin Oil and Gas Recovery Conf, Midland , Texas(1992)

[6] S.E . Crane and K . M . Tubman , SPE Paper 20606 , SPE Ann . Tech . Conf . , New Orleans (1990)

[7] I.J. Taggart and H.A.Salisch , APEA Journal 31 (1991) 377-385

[8] Y.Aasum, M.G.Kelkar, and S.Gupta, SPE Formation Evaluation. 6 (1991) 11-19

[9] Hurst, H.E., Long-Term Storage Capacity of Reservoirs , Trans. Am. Soc. Civil Engrs., 116, 770-808, 1951

[10] Hurst, H.E. , Methods of Using Long-Term Storage in Reservoirs , Proc.Inst. Civil Engrs., Part I

[11] M andelbrot, B.B. and Wallis, J.R., Computer Experiments with Fractional Gaussian Noises Part I , Part II and Part III , Water Res., Vol.5 , No. 1 , 228-267, Feb. 1969

[12] M andelbrot, B.B. and Wallis, J.R., Some Long-Run Properties of Geophysical Records , Water Res., Vol. 5, No.2, 321-340, April, 1969

[13] M andelbrot, B.B. and Wallis, J.R., Robustness of the Rescaled Range R/S in the Measurement of Nobcyclic Long Run Statisatical Dependence, Water Res., Vol.5 , No. 5 , 967-988, Oct. 1969

[14] Chanson Du and Ira . Ershaghi , " A Critical Evalution of Short and Long Range Correlation Methods for Heterogeneous Rocks " , SPE 26422

[15] Barnsley, M.F. AND dEVANEY, r.., Mandelbrot, B.B., Peitgen, H.O., Dietmar,S. and Voss, R.F., The Science of Fractal Images, Editors: Peitgen, H.O.and Dietmar,S., Springer-Verlag, New York, 1988

[16] H . H . Hardy Richard A . Beier , " Fractals in Reservoir Engineering " , 1994, World Scientific Publishing Co. . Ltd

[17] H . H . Hardy , in Reservior Characterization III , ed . B. Linvile (Penn Well, Tulsa, Oklahoma, 1993) pp. 787- 797

[18] James R . Wallis and Nicholas C . Matalas , " Small Sample Peroperties of H and K — Estimation of Hurst Coefficient H " , Water Resources Research , vol . 6 , No .6 , December 1970 , P 1583 ~ 1594

[19] T.A. Hewett and R . A . Behrens , " Conditional Simulation of Reservoir Heterogeneity with Fractals " , SPE Formation Evaluation , September 1990

[20] A.S. Emanuel,G.K. Alameda , R.A.Behrens and T.A. Hewett . , "Reservior Performance Prediction Methods Based on Fractal Geostatistic " , SPE 16971

[21] K. Aasum ,et al ., " An Application to Geostatistics and Fractal Geometry for Reservoir Characterization " , SPE/DOE 202578

Table 1 Statistical Permeability Data in layers

layer	K_{max} (md)	K_{min} (md)	K average (md)	K_{max}/K_{min}	K_{max}/K average
S^{3-1}_7	3851.39	14.66	775.78	262.71	4.96
S^{3-2}_7	2667.77	41.98	474.36	63.55	5.62
S^{3-13}_7	3035.29	35.02	979.51	86.67	3.10
S^{4-1a}_7	3327.18	14.83	890.29	224.36	3.74
S^{4-1b}_7	1165.19	2.01	251.18	579.70	4.66

Table 2 Results of calculating for each well

Well Number	Hurst Exponent (H)	Fractal dimension D=2-H
ES2001	0.8953	1.1047
ES2002	0.8503	1.1497
ES2003	0.8428	1.1572
ES2004	0.9550	1.0450
ES2005	0.8661	1.1339
ES2006	0.9277	1.0723
ES2007	0.9490	1.051
ES2008	0.8476	1.1524
ES2009	0.9301	1.0699
ES2010	0.8452	1.1548
ES2011	0.8732	1.1268
ES2012	0.9036	1.0964
ES2013	0.9309	1.0691
Average	0.8936	1.1064

Table 3 Data of plane interoplation for 13 wells

Well No.	K	σ	ϕ	σ	Sn	σ	Sw	σ	Layer
ES2001	269.0277	16.0840	18.8357	2.2043	7.0938	3.1639	60.7047	1.8226	s73-1
	——	——	——	——	——	——	——	——	s73-2
H=0.8953	379.5630	123.9028	18.1250	2.2850	6.8388	2.3954	63.2433	2.8687	s73-3
	337.7500	197.4371	23.5940	2.8359	6.0593	3.2880	55.8657	4.5594	s74
ES2002	277.9311	155.3707	18.1070	2.6570	7.5611	2.2240	60.5276	7.5490	s73-1
	111.8500	80.0004	18.5262	1.7391	8.3887	1.4209	63.4625	1.4336	s73-2
H=0.8503	89.7618	66.9357	16.1527	1.4546	8.3769	1.3781	68.6300	2.2408	s73-3
	256.4025	121.1720	15.1800	1.9456	6.3004	2.0822	68.1691	4.9847	s74

Well No.	K	σ	ϕ	σ	Sn	σ	Sw	σ	Layer
ES2003	401.7933	205.0750	14.9244	1.9780	7.8533	1.0982	67.6688	5.2185	s_7^{3-1}
	364.1133	39.2511	16.7800	1.6347	8.2659	1.2387	69.3683	2.5875	s_7^{3-2}
H=0.8428	513.2025	52.4408	15.2025	1.1165	8.0833	0.2101	66.3683	2.3350	s_7^{3-3}
	363.0382	95.6365	16.4000	1.5114	6.6847	2.3359	62.4582	3.9765	s_7^{4}
ES2004	240.4241	224.1621	17.8166	4.6464	10.082	0.7315	63.6591	2.9919	s_7^{3-1}
	232.7564	128.7264	16.2005	2.6450	9.3105	1.3458	59.0422	2.9482	s_7^{3-2}
H=0.9550	430.5052	163.0341	18.4817	1.9726	8.0311	1.7758	60.5005	4.6405	s_7^{3-3}
	350.1173	59.8491	18.3873	1.8235	8.6986	0.6811	59.0680	2.5969	s_7^{4}
ES2005	276.5617	303.2599	14.9733	4.0234	8.0195	1.2777	64.1576	8.0810	s_7^{3-1}
	73.2700	14.3116	14.6000	0.6001	8.5320	0.4465	74.1300	0.9735	s_7^{3-2}
H=0.8661	319.5375	39.9016	16.4618	1.0671	8.6381	0.1809	63.6162	1.5753	s_7^{3-3}
	354.6451	93.0542	14.5268	2.4211	6.9644	2.0437	66.8641	4.4036	s_7^{4}
ES2006	373.1433	87.4120	21.1841	1.9759	5.3091	3.0340	52.9091	4.4289	s_7^{3-1}
	191.6018	103.8214	17.9018	1.8527	9.8031	0.9499	61.1412	4.4076	s_7^{3-2}
H=0.9277	347.6300	91.7451	18.5693	1.1643	7.5081	1.2105	60.3812	3.4665	s_7^{3-3}
	338.3848	123.0444	16.6417	2.2949	8.1374	1.6112	65.1780	3.3291	s_7^{4}
ES2007	241.2969	78.4363	21.2015	0.8185	9.5023	2.2037	59.6584	3.0625	s_7^{3-1}
	294.9906	10.5557	17.4480	0.8666	6.5500	0.9521	62.2520	1.9783	s_7^{3-2}
H=0.9490	302.6016	51.4266	15.9444	1.8574	7.1583	1.1563	65.3777	1.4307	s_7^{3-3}
	272.2869	202.7579	16.9736	1.2289	7.4877	1.2691	63.4594	2.6126	s_7^{4}
ES2008	362.4566	80.3914	14.8133	0.8418	5.6655	1.7598	66.4966	2.1858	s_7^{3-1}
	246.2661	70.1039	14.1046	0.8728	9.8307	2.1065	70.8800	3.3861	s_7^{3-2}
H=0.8476	341.4429	209.7518	15.1917	0.9774	8.7700	2.2245	67.6188	1.3355	s_7^{3-3}
	424.9042	138.6820	15.1442	0.5102	8.1431	2.1724	64.2147	3.8748	s_7^{4}
ES2009	159.9045	88.3213	18.1263	0.4320	7.0754	1.5391	62.8990	2.1110	s_7^{3-1}
	210.6360	76.6998	18.0440	0.3359	6.3200	0.9258	62.3600	1.4753	s_7^{3-2}
H=0.9301	440.1980	138.5119	14.6726	1.2875	7.4380	2.6987	66.0300	2.1406	s_7^{3-3}
	349.9820	115.7455	17.4580	0.4565	8.5140	0.6725	62.7593	1.4034	s_7^{4}
ES2010	51.8114	81.2770	17.9900	0.5009	5.2285	1.2827	63.7357	0.5675	s_7^{3-1}
	152.5252	31.1206	15.1331	2.7413	9.2163	0.4109	71.5694	4.1118	s_7^{3-2}
H=0.8452	229.2321	140.6519	17.9704	1.4953	7.7965	1.5078	63.7960	2.9686	s_7^{3-3}
	296.2800	124.6636	16.8632	1.5563	7.2123	2.2676	64.4830	3.0813	s_7^{4}
ES2011	207.6220	42.5704	18.0140	1.2001	10.908	1.1445	61.4140	2.9999	s_7^{3-1}
	This layer is no data								s_7^{3-2}
H=0.8732	282.3596	103.8016	20.0914	0.6859	7.8151	2.4490	58.0870	3.1349	s_7^{3-3}
	362.6090	75.2518	18.9676	1.3420	8.5985	1.3425	59.3961	3.0466	s_7^{4}
ES2012	423.1691	100.2563	15.5666	1.4665	8.3466	1.4813	65.0941	3.4369	s_7^{3-1}
	354.1805	50.7182	18.0060	1.8815	8.8438	1.0248	61.9327	2.0129	s_7^{3-2}
H=0.9036	357.3427	47.1262	16.3772	1.0617	8.6354	0.6461	62.9845	3.2771	s_7^{3-3}
	345.3111	67.0954	16.5222	0.8015	7.0357	2.1377	61.0971	4.0414	s_7^{4}
ES2013	250.7463	53.0052	18.0000	2.1690	10.028	0.6488	57.7900	6.1884	s_7^{3-1}
	64.1075	13.8398	17.3246	1.3631	9.8246	0.9649	68.0766	1.8972	s_7^{3-2}
H=0.9309	217.8220	42.9408	18.7375	1.8279	7.8476	0.7523	55.9892	1.6721	s_7^{3-3}
	242.1605	67.2135	18.0922	1.0426	6.6966	2.5572	57.1694	3.1952	s_7^{4}

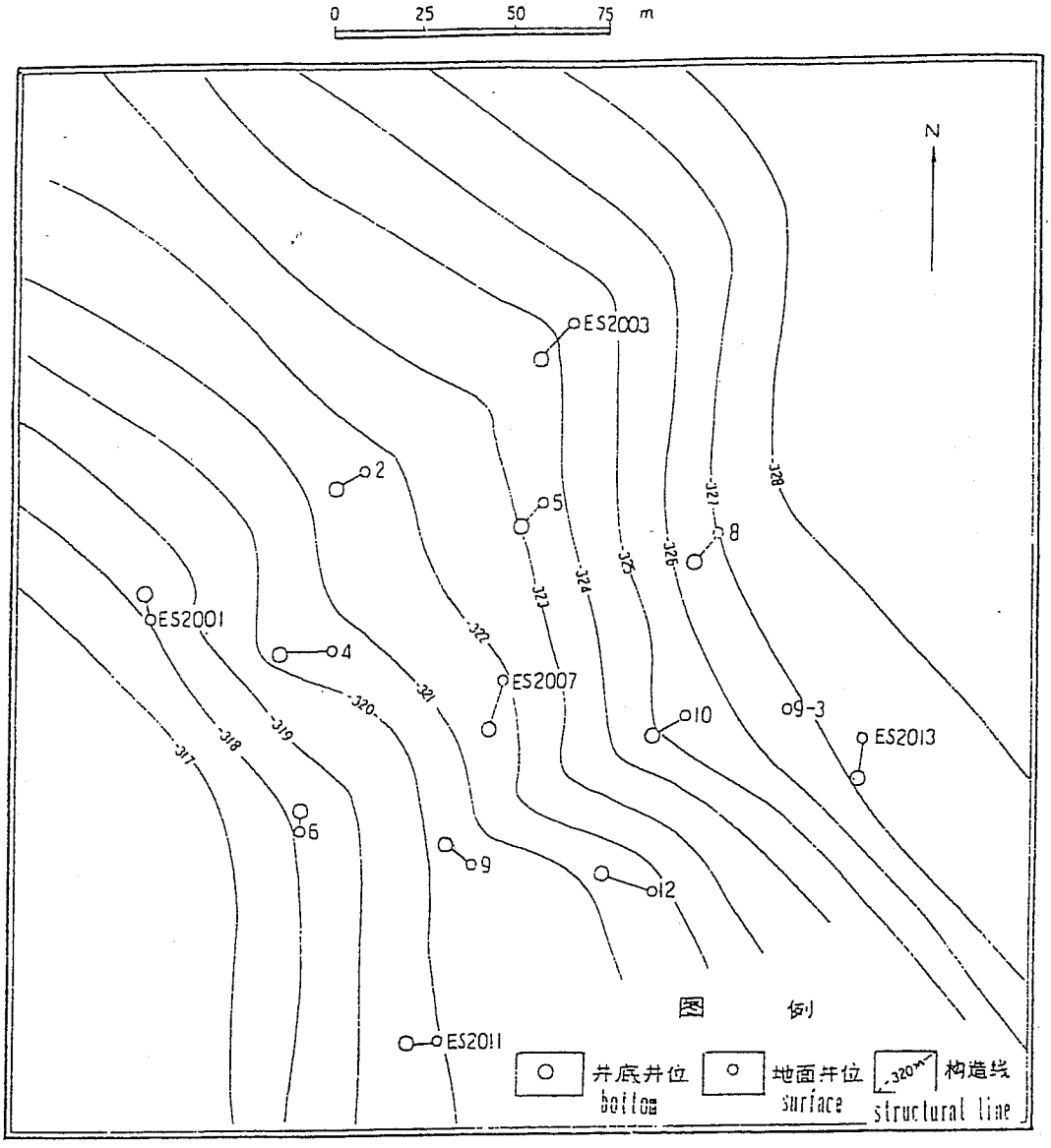

Fig 1: Top of structure contour line graph

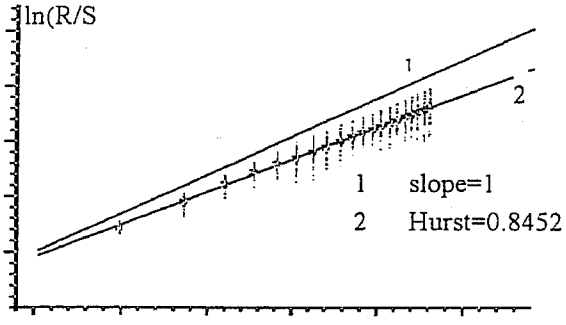

Fig 2: R/S analysis of normalized sequence for ES 2010 well

Fig 3. Schematic figure of random fractal interwells
(a) The rough shape of mountain before interpolation
(b) The final shape of mountain after interpolation

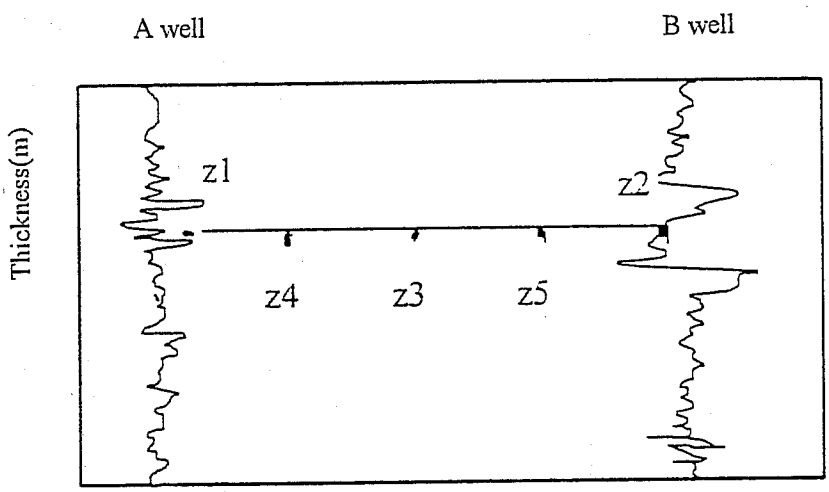

Fig 4. Random fractal interpolation of interwells in section

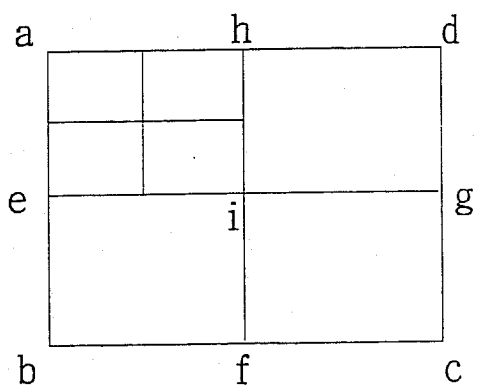

Fig 5. Random fractal interpolation of Pyramid in plane

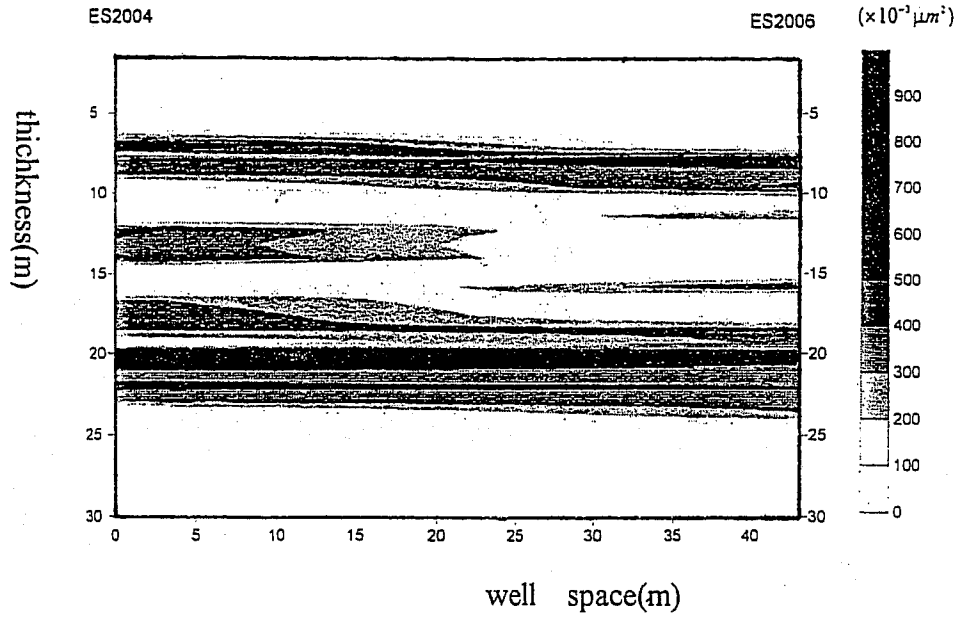

Fig. 6 Permeability distribution of between wells(ES2006~ES2004)

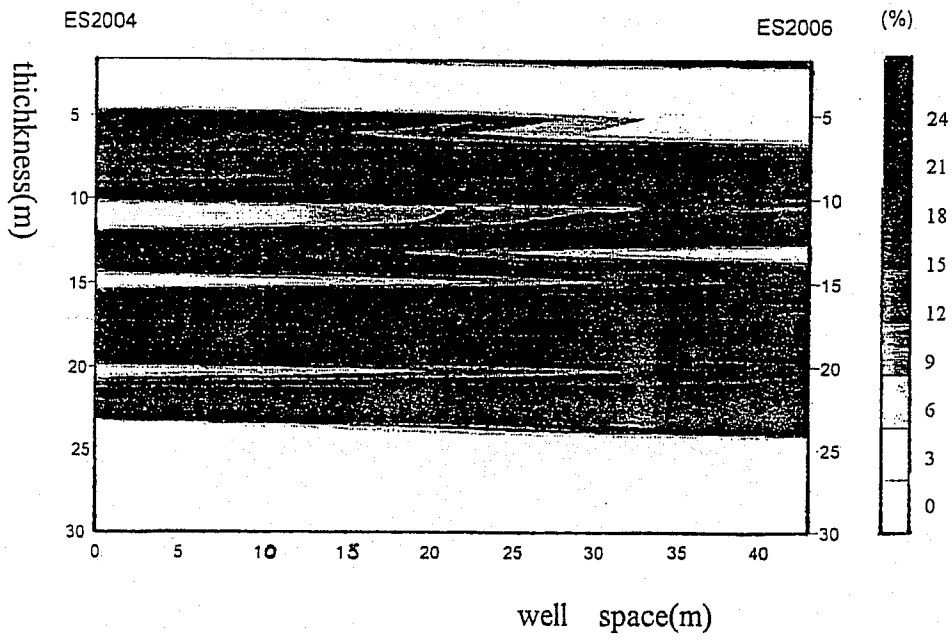

Fig .7 Porosity distribution of between wells(ES2006~ES2004)

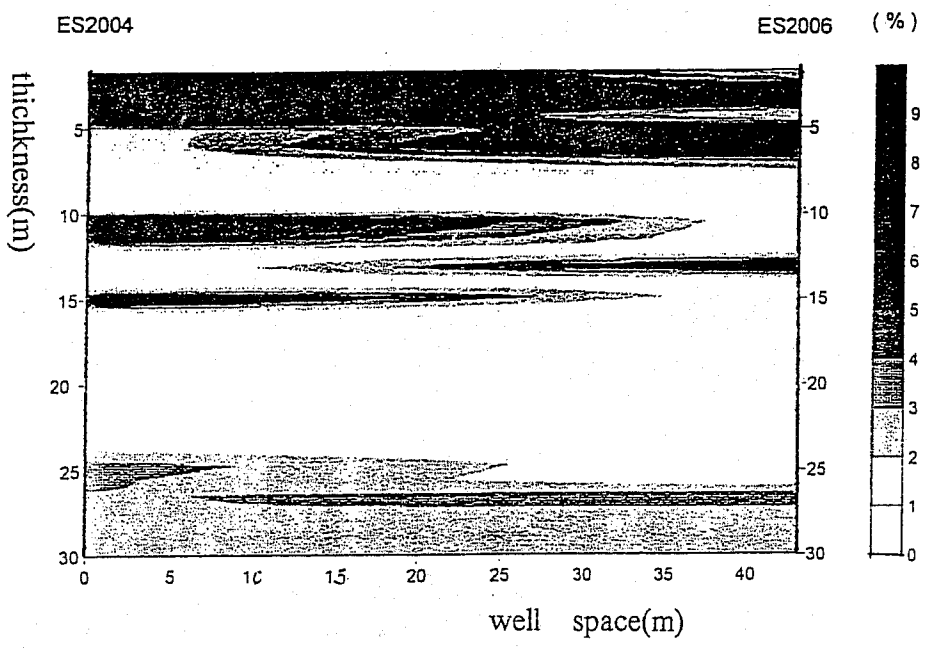

Fig. 8 Shale content distribution of between wells(ES2006~ES2004)

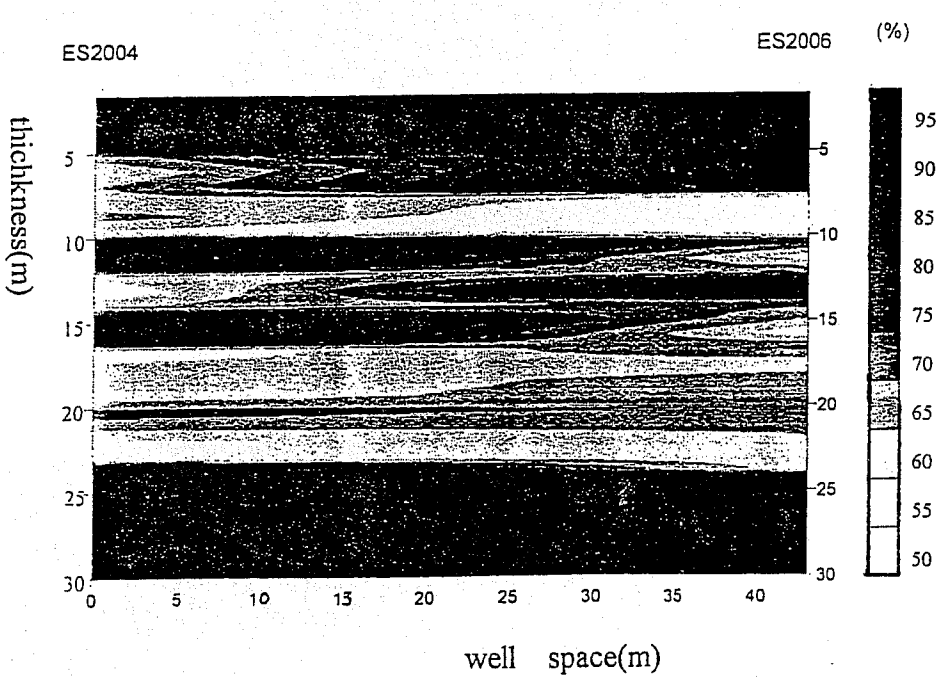

Fig. 9 Water saturation distribution of two well(ES2006~ES2004)

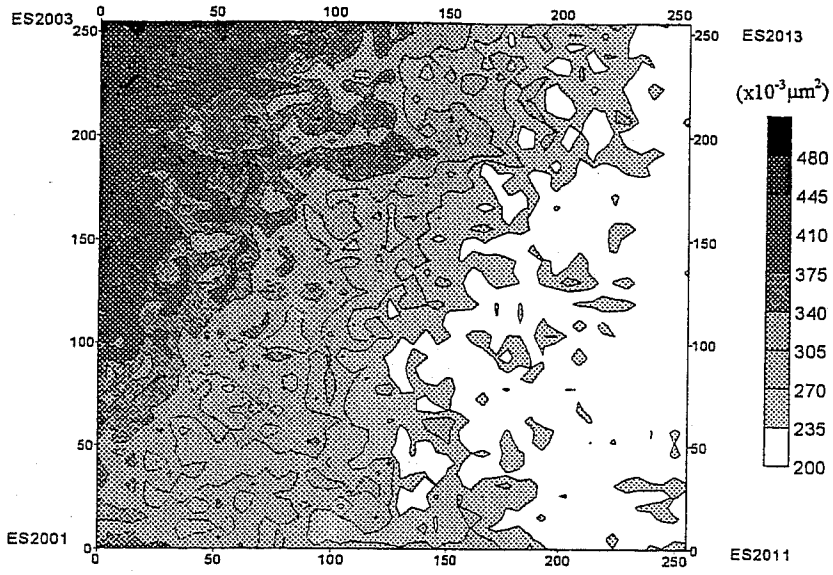

Fig . 10 Permeability distribution of plane for one unit(S_7^{3-3})

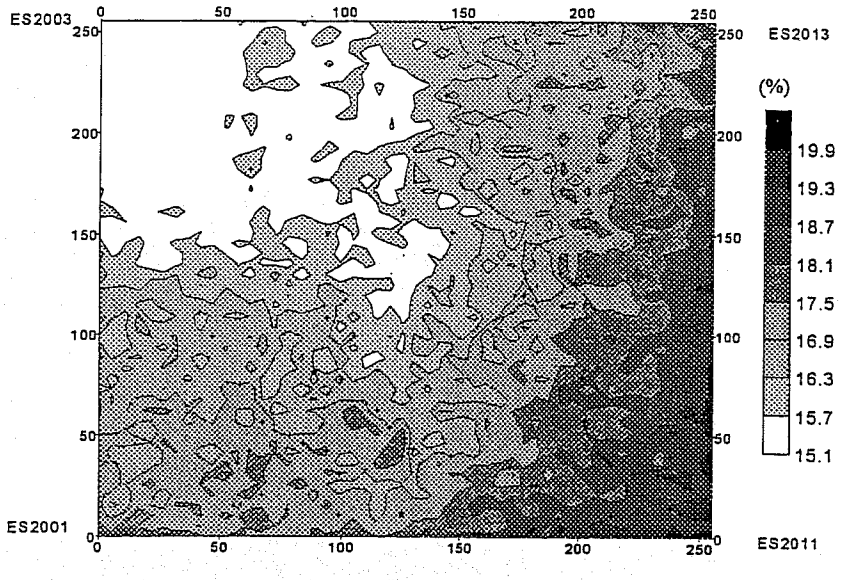

Fig . 11 Porosity distribution of plane for one unit (S_7^{3-3})

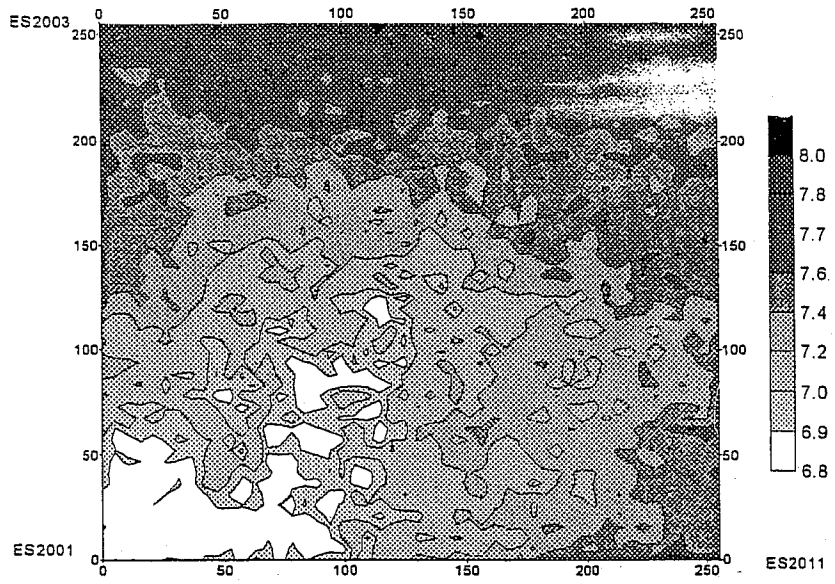

Fig . 12 Shale content distribution of plane for one unit (S_7^{3-3})

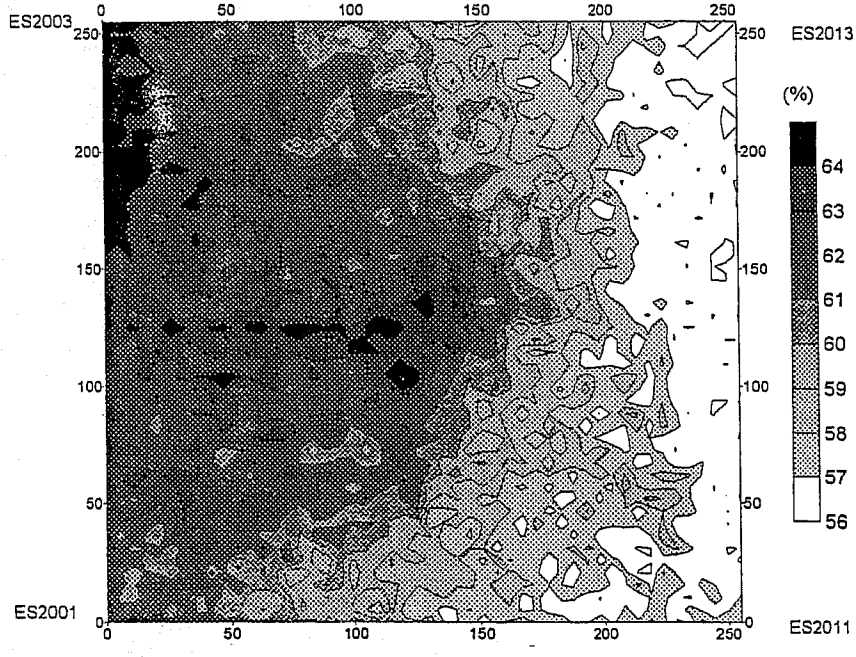

Fig. 13 Saturation distribution of plane for one unit (S_7^{3-3})

3-D Description of Fracture Surfaces and Stress-Sensitivity Analysis for Naturally Fractured Reservoirs

S.Q. Zhang, D. Jiao, Y.F. Meng, Southwest Petroleum Institute, China, and
Y. Fan, U. of Tulsa at NIPER

Acknowledgments

The authors acknowledge State Key Laboratory of Oil and Gas Reservoir Geology and Exploitation, China, for funding this research. Special thanks go to Profs. Su Wangyong and Li Lusen for their experimental plan and valuable discussion.

Abstract

Three kinds of reservoir cores (limestone, sandstone, and shale with natural fractures) were used to study the effect of morphology of fracture surfaces on stress sensitivity. The cores, obtained from the reservoirs with depths of 2170 to 2300 m, have fractures which are mated on a large scale, but unmated on a fine scale. A specially designed photoelectric scanner with a computer was used to describe the topography of the fracture surfaces. Then, theoretical analysis of the fracture closure was carried out based on the fracture topography generated. The scanning results show that the asperity has almost normal distributions for all three types of samples. For the tested samples, the fracture closure predicted by the elastic-contact theory is different from the laboratory measurements because plastic deformation of the asperities plays an important role under the testing range of normal stresses. In this work, the traditionally used elastic-contact theory has been modified to better predict the stress sensitivity of reservoir fractures. Analysis shows that the standard deviation of the probability density function of asperity distribution has a great effect on the fracture closure rate.

Introduction

The term "dual-porosity reservoir" often refers to a naturally fractured formation which has two distinct porosity types: matrix porosity and fracture porosity. The matrix has low permeability but relatively large storage capacity, whereas the fracture has high permeability with small storage capacity. In such naturally fractured reservoirs, many petrophysical properties, such as permeability and compressibility, are controlled by the fracture closure stress. Since fractures are major channels of

hydrocarbon flow, the fracture aperture determines the transport capability of hydrocarbons. Clearly, understanding fracture closure and its changes under different normal stresses is indispensable in characterizing fractured reservoirs. It is also important for controlling formation damages during drilling and well completion, because mud invasion can be effectively controlled by adding some appropriate fiber particles to the drilling and completion fluids if the fracture aperture under reservoir conditions is known.

Historically, studies on wells in dual-porosity reservoirs have considered two kinds of models for the matrix-fracture fluid transfer: the pseudo steady-state flow (Warren and Root, 1963) and the transient matrix flow (de Swaan, 1976. Kasemi, 1969). These models have been in wide use for well production performance and well treatment interpretations (Ehlig-Economides et al., 1994). However, the description of the fractures using assumption of parallel planes is not sufficient to study the fracture closure under normal stresses. In reality, a fracture has rough surfaces with some tortuosity. The surface roughness is dependent on formation deposition environment and history. Initially, some contacts of asperities on the fracture surfaces exist. The stress sensitivity is governed by the density and distribution of asperities on the fracture surface. In order to understand fracture closure under normal stress, topography of the fracture surface must be analyzed in detail.

Study of a fracture closure under the normal stresses is based on Hertz's elastic-contact theory. Using the assumption that asperities on fracture surfaces are spheres and the contacts between the asperities are elastic, Yamada et al. (1978a, 1978b) proposed a mathematical equation that describes the relation between the applied stress and the fracture closure:

$$p_n = \frac{16\pi}{15} n_1 n_2 E' \sqrt{R_1 R_2 R_t} \int_0^{Z_a} \int_0^{Z_a - Z_1} \left(Z_a - Z_1 - Z_2\right)^{5/2} \varphi(Z_1)\varphi(Z_2) dZ_1 dZ_2 \quad \text{.....(1)}$$

where

$$\frac{1}{E'} = \frac{1-\gamma_1^2}{E_1} + \frac{1-\gamma^2{}_2}{E_2}$$

$$R_t = R_1 + R_2$$

p_n = applied stress

E_1, E_2 = Young's modulus

γ_1, γ_2 = Poisson's ratio

R_1, R_2 = radius of curvature asperities

n_1, n_2 = number of asperities per unit area

Z_a = overlapped distance between two surfaces

$\varphi(Z_1), \varphi(Z_2)$ = probability density function

Brown and Scholtz (1985, 1986) measured surface profiles of both contact sides, and composed them into a composite profile. Then, the composite surface was intersected with a plane to investigate the fracture closure. Surface topographical parameters were obtained from the composite profiles by a random process. Figure 1 shows the principle of a composite surface. According to Brown and Scholtz's theory, the contacts between the composite surface and the plane are in elastic range. Therefore, Eq. (2) can be used to compute the fracture closure at the applied normal stress.

$$p = \frac{4n}{3}\Psi E' \sqrt{\beta}\int_{d_0-\delta}^{\infty}\left(Z - d_0 + \delta\right)^{3/2}\varphi(Z)dZ \quad \text{.....(2)}$$

where

p = normal stress

n = total number of asperities per unit area

Ψ = mean value of tangential stress correction factor (≈ 1)

E' = mean value of elastic constant

$\sqrt{\beta}$ = mean value of square root of curvature term

δ = joint closure

$\varphi(Z)$ = probability density function

d_0 = distance between reference planes at $p = 0$

In this study, a specially designed photoelectric scanner with a computer, as shown in Fig. 2, was used to generate 3-D topographic pictures of fracture surfaces. We regard a data point on the composite surface as a summit when that point is higher than the surrounding four points. Then, the initial aperture of the surface, asperity distribution, and mean curvature of the asperities are calculated. Elastic-contact

theory was adapted to predict the fracture closure under the normal stress. Compressing fracture closure tests were made to verify the numerical results. Eq. (2) was used to perform theoretical analysis.

Experiments and Results

For the samples tested, fracture surfaces are mated on a large scale, but unmated on a fine scale. The relative position of both surfaces is very important. Before experiments, both fracture surfaces were twisted in order to get the maximum mate. Three kinds of cores (limestone, sandstone, and shale with natural fractures) were analyzed. The tested cores have a diameter of 105 mm, and their detailed physical properties are presented in Table 1.

Fig. 3 shows a scanning result of the sandstone fracture surfaces. One of them has been turned 180° and overlapped with another to produce a composite surface. From this composite surface, the description of the 3-D distribution of a fracture surface morphology, density of the asperity, mean radius of curvature of asperities, and probability density function of the asperity distribution can be obtained. Eq.(2) is then used to predict fracture closures.

In order to verify the theoretical predictions, experimental measurements of the fracture closure with the same cores under applied normal stresses were conducted. Fig. 4 shows a schematic of the compressing tests. During the measurements, the extensometer was placed between the fractures. Normal stresses applied to the formation cores were gradually increased at a constant rate, and the displacement was recorded until the stress reaches the designed value. Then, the stresses were gradually reduced, and the displacement is recorded again. Such tests were repeated for two or three cycles. In the same way, the extensometer was used to measure the displacement of the rock matrix under the same normal stress for nonfractured cores. Consequently, the fracture closure can be obtained by subtracting the rock matrix displacement from the fractured displacement. Figs. 5 to 8 present the results of measured fracture closure curves for the different core samples. In this study, the shale sample broke at 3 MPa; therefore, no detailed data were analyzed.

Discussion

All three experimental results (Figs. 5 to 8) have indicated hysteresis effects in the fracture closure when loading and unloading applied stresses. In the first cycle of tests, the rock deformation is the largest, possibly due to further mating of the two surfaces, and causing plastic deformation of surface asperities. Once the normal stress is applied, the fracture surfaces cannot be separated easily. In the

second and the third cycles of the tests, smaller hysteresis effects were observed. The data measured in the second or third cycles were compared with those predicted by the model. Figs. 9 and 11 show the comparison of experimental and theoretical results. The model predictions cannot match the experimental measurements, especially in the low normal stress range. These computations are based on input of the 3-D composite surface before loading tests. However, after the loading experiments, the parameters obtained from scanning fracture surfaces changed significantly. For instance, the mean square root of the asperity summits can differ by a factor of 2 to 3 before and after loading tests. Such differences are directly caused by the plastic deformation of the asperities. The core samples used contain 5 to 8% clays, which are soft and therefore easily deform plastically, even under relatively low stresses.

Figs. 12 to 14 show measurements of fracture closure and the model predictions using the parameters obtained after the loading tests. (Table 2 presents the parameters after loading tests.) The model predictions are in good agreement with the experimental measurements. It appears that the plastic deformation of the asperities is an important factor in predicting the fracture closure.

The model proposed by Brown and Scholtz (1985) assumes that the contact among the asperities is purely elastic. This may be true for hard materials such as quartz and granite, but reservoir rocks contain clays which easily deform permanently. Even at low applied stress, the local stress may exceed the elastic limit, and results in plastic deformation. For the samples tested, Eq. (2) is not valid because the contribution of the plastic deformation is significant. However, after the permanent deformations, Eq. (2) can accurately predict fracture closures for reservoir rocks. Ironically, in terms of reservoir engineering, the initial fracture apertures, which are determined by the original morphology of the fracture surfaces under the reservoir conditions, are most interested in determining fracture closure. Therefore, Eq. (2) needs to be modified to properly predict fracture closure.

Figs. 15 to 17 show that closure and normal stress have the following empirical relationship:

$$\delta = A + B \ln p \qquad (3)$$

where A is a correlation constant that is related to the initial aperture of a fracture (at $p = 0$). B is also a constant related to deviation of the asperity distribution. Generally, smaller values of B mean the composite surface is relatively less rough or the asperities height is more uniform and more asperities contact each other at a given normal stress. As a result, the resistance to fracture closure is larger than

that with a higher value of B. In Figs. 15, 16 and 17, the means of curvatures are 26 μm, 5 μm and 8 μm, respectively. For Fig. 15, the closure is more sensitive to the normal stress than the others. Therefore, the deviation of the probability density function of the composite topography has a larger effect on fracture closure. Eq. (3) also implies that for a given composite surface, the closure should be more rapid at lower values of the applied stress, and should be gradually slowed down with an increase in the applied stress, because more and more asperities come into contact and the resistance to closure increases.

Conclusions

1. A photoelectric scanner designed to investigate fracture surfaces is an effective tool to characterize the morphology of fracture surfaces. With the scanner combined with a computer imaging technique, the asperity density, mean radius of curvature, and probability density function can be accurately determined for reservoir formations.
2. Because clays in the formation rock are easily deformed permanently, even at a relatively low normal stress, the fracture closure predicted by the model using elastic-contact theory differs from laboratory measurements. The permanent deformation of the asperities changes the topography of the fracture surfaces significantly. Elastoplastic contact theory should be used to predict the fracture closure for reservoir formations.
3. The deviation of probability density function of the asperity distribution has a significant effect on the fracture closure rate. Larger values of deviation causes more rapid fracture closure.

References Cited

Brown, S. R. and Scholtz, C. H., 1985, "The Closure of Random Elastic Surfaces in Contact", *Journal of Geophysical Research*, v. 90, p 5531-5545.

Brown, S. R. and Scholtz, C. H., 1986, "Closure of Rock Joints", *Journal of Geophysical Research*, v. 91, p 4939-4948.

De Swaan, O.A., 1976, "Analytic Solutions for Determining Naturally Fractured Reservoir Properties by Well Testing" *SPEJ*, p 117-122.

Ehlig-Economides, C.A., Fan, Y. and Economides, M.J., 1994, "Interpretation of Fracture calibration Tests in Naturally Fractured Reservoirs", paper SPE 28690 presented at the SPE International Petroleum Conference of Mexico held in Veracruz, Mexico, 10-13 October, 1994.

Kasemi, H., 1969, "Pressure Transient Analysis of Naturally Fractured Reservoirs With Uniform Fracture Distribution", *SPEJ*, p 451-458.

Warren, J.E. and Root, P.J., 1963, "The Behavior of Naturally Fractured Reservoirs", *SPEJ*, p245-255.

Yamada, K., Takeda, N., Kagami, J., and Naoi, T., 1978a, "Surface Density of Asperities and Real Distribution of Asperity Heights on Rubbed Surface", *Wear*, v. 47, p5-20.

Yamada, K., Takeda, N., Kagami, J., and Naoi, T., 1978b, "Mechanisms of Elastic Contact and Friction between Rough Surfaces", *Wear*, v. 48, p15-34.

Table 1— Mechanical Properties and Topographical Data of Composite Surfaces Before Loading Experiments.

Samples	Rock Type	Young's Modulus E (10^4 MPa)	Poisson's Ratio γ	Asperity Density n ($10^{-8}/mm^{-2}$)	Mean Square Root, $\sqrt{\beta}$ ($\sqrt{\mu m}$)	Standard Deviation σ (μm)	Initial Aperture d_0 (μm)
A	Limestone	6.1	0.33	323	240	81	243
B	Shale	1.5	0.15	32	781	196	
C	Sandstone	3.2	0.2	4.1	2300	202	606
D	Limestone	6.8	0.31	263	203	92	276

Table 2— Mechanical Properties and Topographical Data of Composite Surfaces After Loading Experiments.

Samples	Rock Type	Young's Modulus E (10^4 MPa)	Poisson's Ratio γ	Asperity Density n ($10^{-8}/mm^{-2}$)	Mean Square Root, $\sqrt{\beta}$ ($\sqrt{\mu m}$)	Standard Deviation σ (μm)	Initial Aperture d_0 (μm)
A	Limestone	6.1	0.33	367	73	20	60
C	Sandstone	3.2	0.2	52	411	91	273
D	Limestone	6.8	0.31	213	86	26	78

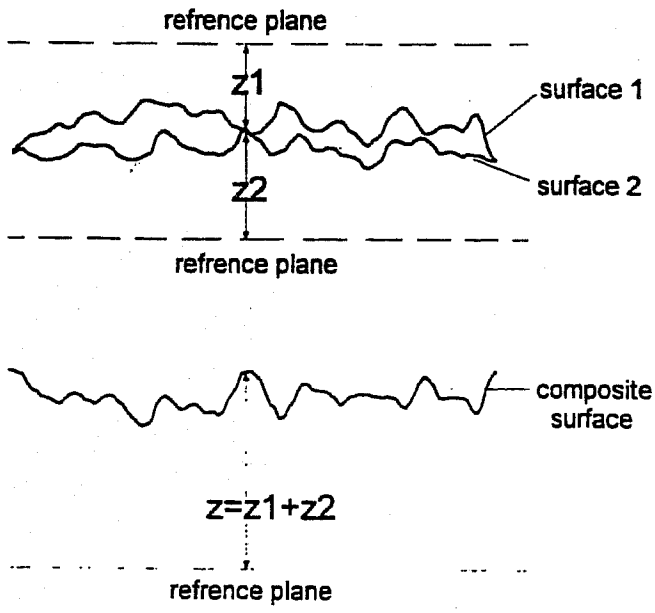

Fig. 1—Schematic of a composite surface profile.

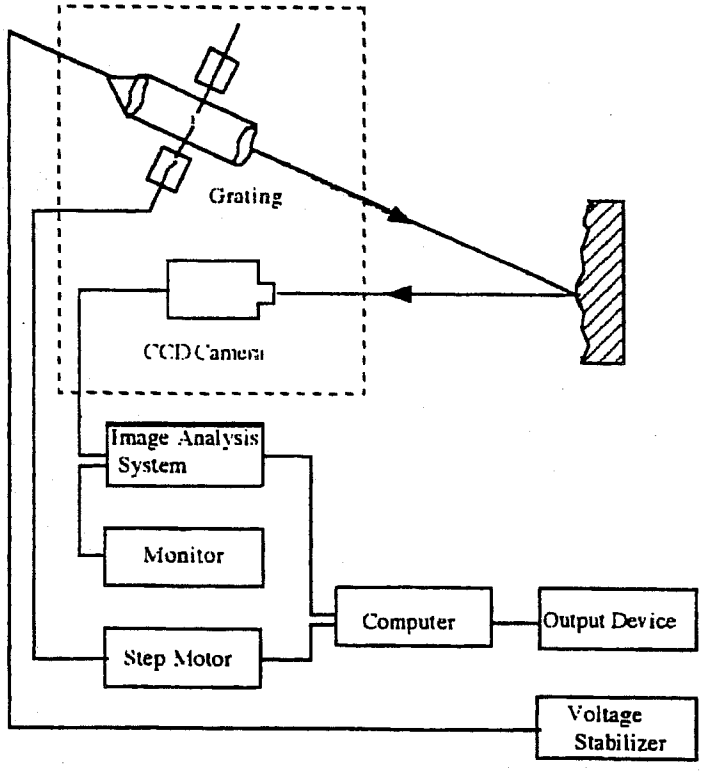

Fig. 2—Schematic of photoelectric scanning system.

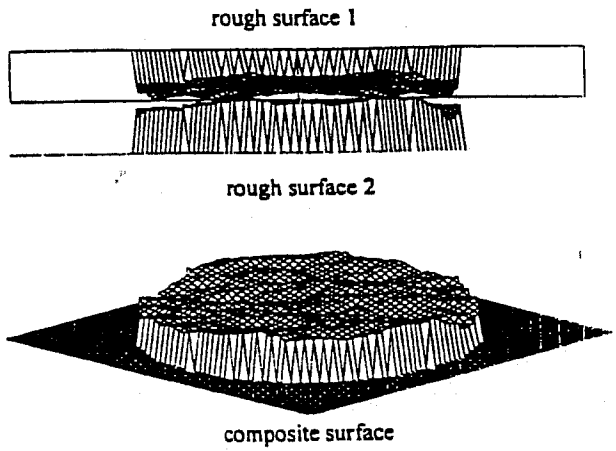

Fig. 3—Photoeletic scanning results of sandstone fracture.

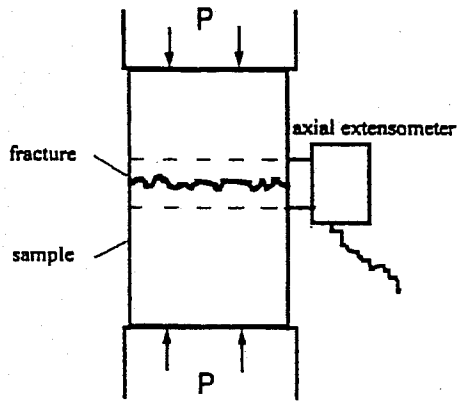

Fig. 4—Schematic of the compressing test.

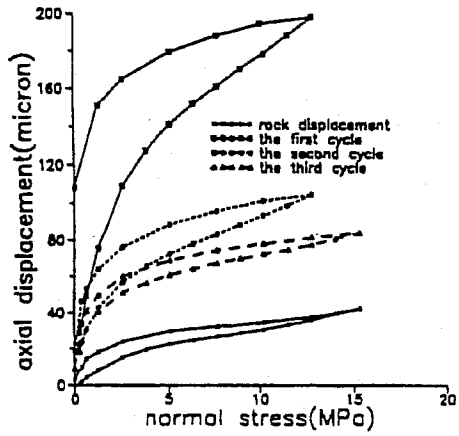

Fig. 5—Fracture closure curves of sample A (limestone).

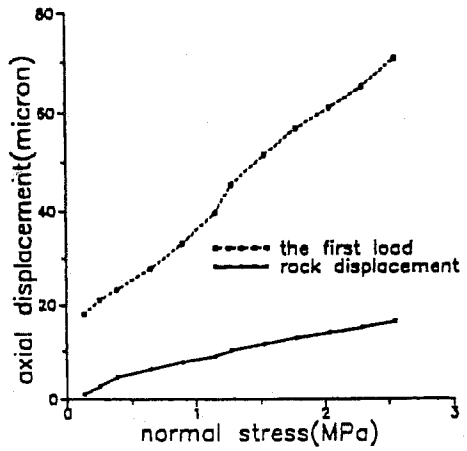

Fig. 6—Fracture closure curves of sample B (shale).

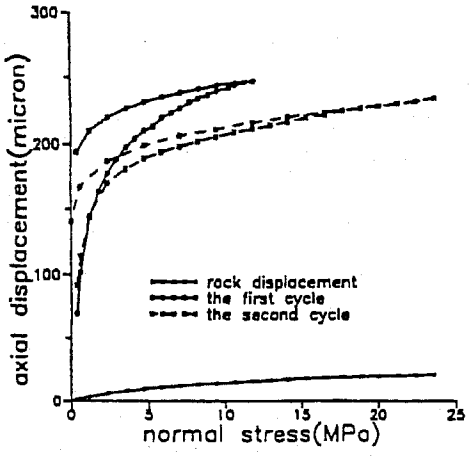

Fig. 7—Fracture closure curves of sample C (sandstone).

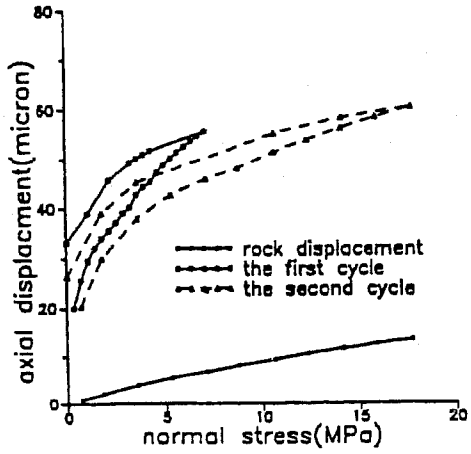

Fig. 8—Fracture closure curves of sample D (limestone).

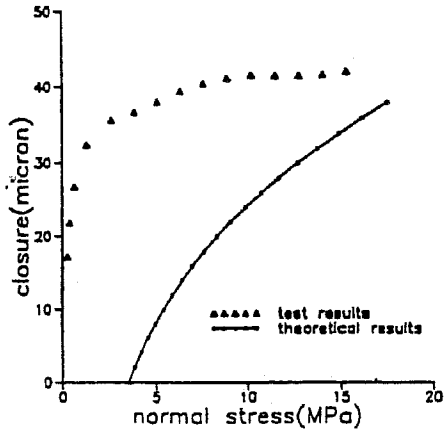

Fig. 9—Comparison of tests and theoretical results for sample A (surface parameters obtained before loading).

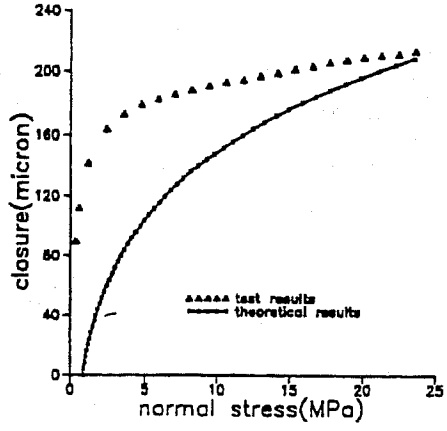

Fig. 10—Comparison of test and theoretical results for sample C (surface parameters obtained before loading).

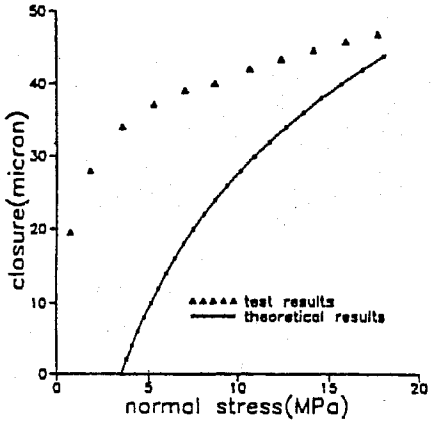

Fig. 11—Comparison of test and theoretical results for sample D (surface parameters obtained before loading).

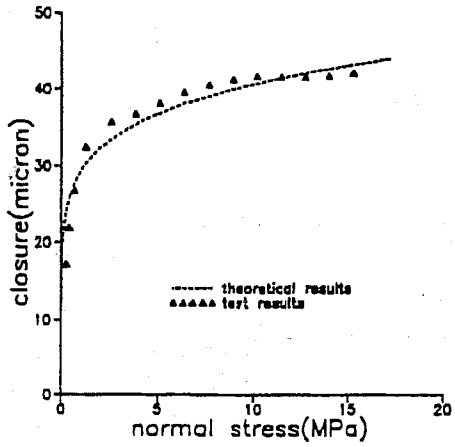

Fig. 12—Comparison of test and theoretical results for sample A (surface parameters obtained after loading).

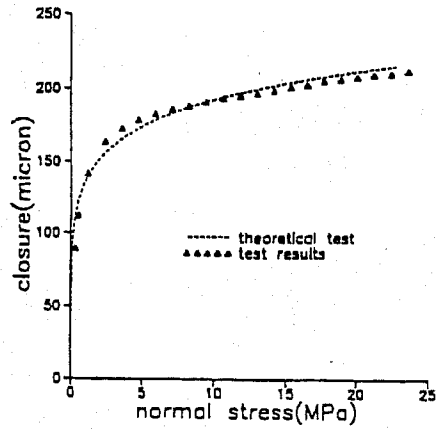

Fig. 13—Comparison of test and theoretical results for sample C (surface parameters obtained after loading).

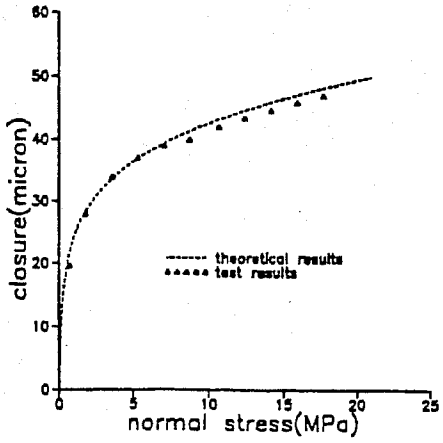

Fig. 14—Comparison of test and theoretical results for sample D (surface parameters obtained after loading).

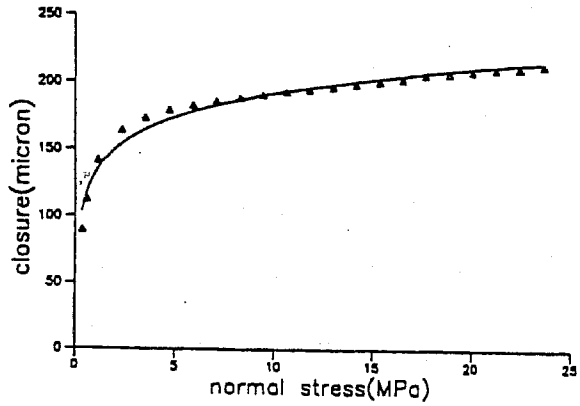

Fig. 15—Curve fitting of fracture closure for sample C $(\delta = 131 + 26\ln p)$.

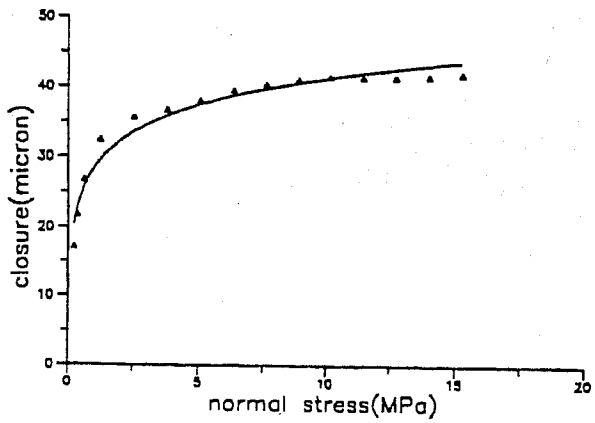

Fig. 16—Curve fitting of fracture closure for sample A $(\delta = 28 + 5\ln p)$.

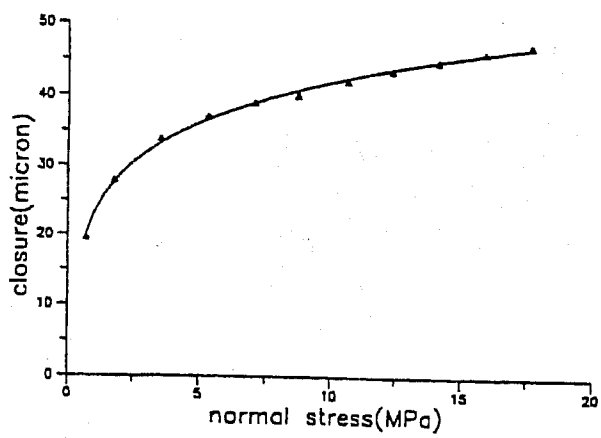

Fig. 17—Curve fitting of fracture closure for sample D $(\delta = 23 + 8\ln p)$.

Fig. 1—Schematic of a composite surface profile.

Fig. 2—Schematic of photoelectric scanning system.

Fig. 3—Photoeletic scanning results of sandstone fracture.

Fig. 4—Schematic of the compressing test.

Fig. 5—Fracture closure curves of sample A (limestone).

Fig. 6—Fracture closure curves of sample B (shale).

Fig. 7—Fracture closure curves of sample C (sandstone).

Fig. 8—Fracture closure curves of sample D (limestone).

Fig. 9—Comparison of tests and theoretical results for sample A (surface parameters obtained before loading).

Fig. 10—Comparison of test and theoretical results for sample C (surface parameters obtained before loading).

Fig. 11—Comparison of test and theoretical results for sample D (surface parameters obtained before loading).

Fig. 12—Comparison of test and theoretical results for sample A (surface parameters obtained after loading).

Fig. 13—Comparison of test and theoretical results for sample C (surface parameters obtained after loading).

Fig. 14—Comparison of test and theoretical results for sample D (surface parameters obtained after loading).

Fig. 15—Curve fitting of fracture closure for sample C $(\delta = 131 + 26\ln p)$.

Fig. 16—Curve fitting of fracture closure for sample A $(\delta = 28 + 5\ln p)$.

Fig. 17—Curve fitting of fracture closure for sample D $(\delta = 23 + 8\ln p)$.

Integrated reservoir characterization: Improvement in heterogeneities stochastic modelling by integration of additional external constraints.

B.Doligez(*), H.Beucher(**), F.Geffroy(**), R.Eschard(*) & Heresim group (*) (**)
(*) Institut Francais du Pétrole, 1&4 av. de Bois Préau, BP311 -92506- Rueil Malmaison -France
(**) Centre de Géostatistique, 35 rue Saint Honoré -77305- Fontainebleau Cédex- France

Abstract:

The classical approach to construct reservoir models is to start with a fine scale geological model which is informed with petrophysical properties. Then scaling-up techniques allow to obtain a reservoir model which is compatible with the fluid flow simulators.

Geostatistical modelling techniques are widely used to build the geological models before scaling-up. These methods provide equiprobable images of the area under investigation, which honour the well data, and which variability is the same than the variability computed from the data. At an appraisal phase, when few data are available, or when the wells are insufficient to describe all the heterogeneities and the behaviour of the field, additional constraints are needed to obtain a more realistic geological model. For example, seismic data or stratigraphic models can provide average reservoir information with an excellent areal coverage, but with a poor vertical resolution.

New advances in modelisation techniques allow now to integrate this type of additional external information in order to constrain the simulations. In particular, 2D or 3D seismic derived information grids, or sand-shale ratios maps coming from stratigraphic models can be used as external drifts to compute the geological image of the reservoir at the fine scale.

Examples are presented to illustrate the use of these new tools, their impact on the final reservoir model, and their sensitivity to some key parameters.

1 - Introduction

Reservoir characterization techniques involve more and more geosciences integration for a better recovery of hydrocarbons. However, in such reservoir integrated studies, the available data are of different kinds. Generaly, qualitative structural and sedimentological models are constructed, in order to give the general framework of the reservoir layering, using methods as sequence stratigraphy or regional geology synthesis, and only provide soft informations and global trends.

Quantitative data are also of different kinds and resolution scales. They could be splitted into different categories:

- the well data, which are 1D, with a high resolution along the vertical, but a very sparse lateral density generaly integrate a lot of parameters, . One problem is to synthetize all this information in a suitable database,

- the seismic data are generaly lateraly continuous and good for mapping. On the other hand, they have only a poor vertical resolution, and are difficult to be interpreted in terms of geological parameters. Moreover, at a reservoir scale, the precision of the picking is of primary importance for the construction of the reservoir layering. New methods based on the interpretation of seismic parameters in terms of reservoir properties using multivariate statistics can give some keys to merge these different sources of information. In favourable cases, seismic can also provide informations on lithological, petrophysical or fluid variations between the wells.

- other geological "soft" data as qualitative geological interpretations can help to introduce some rules or constraints in the models. Also, the stratigraphic modelling provides trends of lateral facies evolution and of their lithological components in a studied area.

Geostatistical modelling techniques are widely used to build the geological models at the fine scale within predefined sedimentary units. Geostatistic tools are also well adapted to deal with data of various resolution scale, and seem to be efficient for their integration.

Heresim is such a geostatistical tool, developed by IFP and CG which algorithm is based on the truncated gaussian method (Matheron et al., 1987, Ravenne et al., 1990). New advances in modelling techniques allow now to integrate average geological parameters grids, derived from seismic data or from stratigraphic models, to build 3D matrices of proportions which are used in the non stationary conditional simulations.

Some examples will illustrate these new methods, and point out the influence of these additional external constraints on the petrophysical properties distribution in the final reservoir grid.

2 - Principles of the methodology

2-1 - Some preliminary recalls

The methodology implemented into Heresim has already been presented in other papers (Ravenne et Beucher, 1988, de Fouquet et al., 1988, Galli et al., 1990, Eschard et al 1991, Doligez et al., 1992...). The main purpose is to provide to the reservoir engineers several equiprobable images of a reservoir which may be used for fluid flow simulations. Heresim is both a methodology and a geostatistical tool for reservoir characterization. The underlaying philosophy is that the description of the petrophysical heterogeneities of a reservoir is directly linked to the description of the lithofacies heterogeneities. The main steps of the method, illustrated on figure1, are the following:

1/ a database compilation, and the construction of a conceptual geological model,

2/ the lithofacies reservoir simulations in a high resolution grid

3/ the petrophysical properties attribution on these fine-scaled images

4/ the scaling-up of petrophysical properties in a coarser grid which will be the input for fluid flow simulators.

The sedimentological interpretation of the well data and concepts from sequence stratigraphy allow to define the main sedimentary units of the studied reservoir, their geometries, and the chronostratigraphic horizons which can be used as reference level for a flattening. In some cases, the units may also be defined as proportional, when the beds are concordant with the limits of the units, in case of differential subsidence for example.

For each unit, which are simulated independantly, the proportion curves and variograms are first computed, to characterize qualitatively and quantitatively the spatial variability of the sedimentary facies. In particular, the vertical proportion curve represents a cumulated histogram of the proportions of the lithofacies present on the discretized wells, computed at each stratigraphic level, parallely to the reference level of the considered unit, as illustrated in figure 2. It characterizes the vertical distribution of the lithotypes in the reservoir unit. The horizontal proportion curve is a projection of the cumulated proportions of each facies computed well by well and projected on an horizontal line. It allows to appreciate the degree of lateral variability of the facies within the studied unit.

The lithofacies simulation are made using a stationary simulation of a gaussian random function which is truncated level by level using thresholds, which are directly linked to the proportions of the lithofacies on each level. The equiprobable simulations honour the well data, and the global variograms and proportion curves computed from the simulated blocks are the same than those computed from the well data.

Originally, Heresim worked with an horizontal stationarity hypothesis for the lithofacies distribution, which means that the geological lateral variations are averaged across the field. In that case, the simulation algorithm uses constant thresholds, level by level, to truncate the gaussian function which is generated, as illustrated on figure 3.a. In this process, the thresholds are directly linked to the lithotypes proportions given by the vertical proportion curves.

Depending on the values of the gaussian function, compared to the different thresholds, it is possible to attribute a lithofacies value in each space location.

This horizontal stationarity hypothesis may be valid in some cases, when the facies distribution does not show any major trend in the simulated area. But this hypothesis is often not geologicaly satisfactory, especially when few well controls are available, or when the wells cannot be considered to be representative of the field behaviour. For these reasons, a non-stationary version of the software has been developed which allows to take into account in the simulations not only the vertical but also the horizontal trends of the facies repartition. Instead of defining only one vertical proportion curve, which represents the main vertical facies sequences in the unit, and which is used to define the truncation thresholds of the gaussian function level by level, the method deals in that case with a 3D proportion function which represents the mean spatial variations of the facies. The truncation thresholds of the gaussian function are then varying through space, as illustrated on figure 3.b, and the corresponding lithofacies values follow these variations.

2-2 - Building a 3D block of proportions

Different ways are possible to estimate the 3D functions of proportions, in a regular block support, from well data and possibly additional external data which may be qualitative or quantitative. A first approach is to divide the reservoir into several zones to each of which a representative vertical proportion curve is attributed, or where the mean proportions of lithofacies are estimated from initial vertical proportion curves.

The partition of the reservoir may be based on geological criteria, or on qualitative seismic interpretation using seismic facies analysis techniques. This methodology mainly uses pattern recognition techniques and statistical tools to rely each seismic trace of the field to a class, itself linked to a group of wells and thus to a vertical proportion curve (Johann et al, 1996, Fournier and Derain 1995, Fournier 1995). The result of such an analysis is a zonation of the studied field,

with an associated probability of assignment of the traces to the different classes. In other cases, this zonation may also be defined using a conceptual geological model which allows to recognize different depositional environments in different areas of the field, and their lateral extension, again associated to an uncertainty coefficient.

In other cases, the 3D block of proportions can be computed directly from the well data, if the wells are considered to be representative of the behaviour of the reservoir, or from initial vertical proportion curves (computed from the wells or imported from analogue examples). The principle remains to compute smooth or mosaic 3D functions of lithofacies proportions on block support, using more or less refined geostatistical methods, as illustrated on the next diagram:

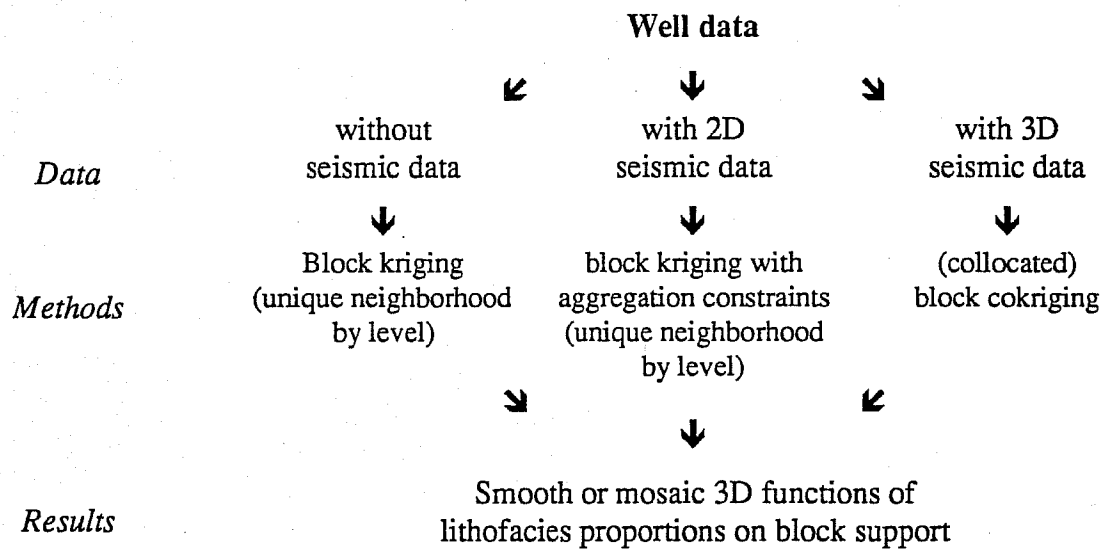

The estimation of the proportions from the well data or from initial vertical proportion curves may be done using an ordinary kriging method. If an additional information is available, derived from seismic or from a geological model, the kriging system is written with an additional constraint on the sum of the proportions of the facies in each cell of the 3D proportions block. Moreover, stratigraphic modelling techniques provide some quantitative maps of mean

lithofacies thicknesses which may be used as external drift for the proportions estimations (Joseph et al., 1996). In the same way, statistical calibration techniques of seismic attributes allow now in some cases to convert seismic attributes into proportions or thicknesses of lithofacies.

The different techniques may be mixed, and representative vertical proportion curves may be attributed in some zones, and estimated by kriging in other parts, taking into account wells data and these eventual additional external constraints.

The choice of the methodology mainly depends on the available data (Mouliere et al, 1996). The computation by zones is specific to the cases when the information, geological as well as derived from seismic is qualitative, or when the transition between the reservoir zones is very rapid. Generaly, the kriging methods and the use of these 3D functions of lithofacies proportions allow to obtain more realistic results than those obtained with the stationary algorithm. It is to notice that their estimation from initial vertical proportion curves is very flexible, as it allows to introduce some qualitative knowledge on the field, even if it is combined with a quantitative information.

2-3- Simulations

The non stationary algorithm is an extension of the stationary one. In the non stationary case, the thresholds which are used to truncate the gaussian function are now dependant on the location of the considered point of computation. In this option, the transition between lithofacies may vary and does not necessarily follow the sequential order of the facies.

Once the lithofacies grids are built, the process remains the same as in the stationnary case to translate the geological information into petrophysical values, and then to homegeneize these properties into coarser cells which will be the framework for the fluid flow simulations.

Porosities and permeabilities are assigned to the fine scale grid, according to experimental values distributions and regression laws depending on each lithofacies. The last step is to define a reservoir grid and to scale-up the petrophysical properties in this coarser grid, using algebraic and numeric methods, in order to get an adequate grid for fluid flow computations.

It seems obvious that the more the lithofacies simulations will be realistic, the better the petrophysical properties heterogeneities will be constrained, and the impact on the final reservoir grid properties will be important. The following application will illustrate this methodology.

3 - Applications on the Mesa Verde example

3-1- stationary simulations

This case study is extracted from an outcrop database collected in the MesaVerde area in the framework of a joined Elf, GDF, IFP and Total project. The geological interpretation of the 3D outcrop (campanian series of Colorado) in terms of chronostratigraphy and lithostratigraphy allowed to define the main genetic units, their limits and reference levels, and the lithofacies corresponding to three main depositional environments (Eschard et al., 1993, Homewood et al., 1992). For the demonstration purpose, we focussed on a seaward stepping wedge of littoral sediment, which corresponds to an overall progradation punctuated by transgressive events. In such a sequence, the lateral transition between coastal plain, foreshore, shoreface and offshore presents a typical non-stationary configuration. The conceptual seaward stepping stacking pattern model is shown on figure 1.a. After the extraction from the data base of ten representative wells from field sections and geological interpretation, we first used the stationary algorithm to simulate the 3D block, as a single relative unit, named PLO, for Point Lookout Sandstone.

The wells have been described using seven lithofacies, corresponding to two main depositional environments, a marine sequence (offshore, upper and lower shoreface, foreshore) and a

continental sequence (washover, channels and floodplain shales). From this numerical database, the main geostatistical parameters have been quantified, the vertical proportion curve, shown on figure 4, the horizontal and vertical variograms, and the lithofacies simulations performed.

It is to notice that the vertical proportion curve is also a powerful tool which helps to control the geological interpretations and hypotheses. In figure 4 for example, the main geological features of the studied unit may be analysed, with a transition of the sedimentary system from a marine pole to a continental pole.

The display of a lithofacies block diagram on figure 1.b shows that the results may be considered as globally correct, when compared to the conceptual geological model. This is due to overestimated values of the horizontal ranges of the variogram model, in order to recover the main bodies continuities. But in details, the real geometry of the clinoforms and of the shales is smoothed when compared to the real case, and most of the permeability barriers of the reservoir are not simulated, especially in the north-south direction.

Petrophysical values have then been attributed to each cell of this 3D block using a model which has been defined for each lithofacies using core analyses (figure 1.c shows the same block informed with petrophysical values). Then a scaling-up has been computed on a coarser grid as displayed on figure 1.d.

3-2 Comparison between stationary and non stationary simulations

In order to compare both approaches, we performed an other set of simulations, using the non stationary approach, from the same dataset. We computed 3D blocks of proportions as the one displayed on figure 5, using a set of six initial vertical proportion curves, which have been kriged level by level in order to fill the 3D block of proportions. This figure 5 may be described as an horizontal map of the unit PLO, which has been divided into regular blocks, each of them being filled with a vertical and local proportion curve computed using a block kriging with aggregation

constraints method. If we compare on figure 6 the same north-south cross section, obtained using the two algorithms, stationary and non stationary, it appears that the result is now much closer from the conceptual model if we use the non stationary approach than if we use the stationary one, and respects the main facies transitions.

After attribution of the same petrophysical model on both images and scaling-up on a simple reservoir mesh, the comparison of the horizontal permeabilities maps on a chosen layer of the reservoir (layer 7, figure 7.a, from a stationary model, figure 7.b, from a non stationary model) evidences the differences in the final results. This display points out the importance of the initial fine scale model heterogeneities on the reservoir model, and thus on the fluid flow simulations. With the stationary approach, the permeability heterogeneities are scattered throughout the field, whereas with the non stationary simulation, a trend is evidenced from the low permeabilities in the southern part of the field to the higher permeabilities in the north.

4 - Conclusions

New algorithms in geostatistical simulations allow now to better integrate more and more external constraints and data in order to obtain more precise images of a reservoir under investigation. In particular, the use of 3D functions of proportions of lithofacies instead of a single vertical proportion curve allows to take into account and to integrate both qualitative or quantitative informations derived from seismic or geological models.

The use of the non stationary algorithm in the lithofacies simulation of a reservoir becomes very powerful as the heterogeneities are more accurately simulated. The scaling-up process will take into account the petrophysical properties heterogeneities at the fine scale, which are directly linked to the lithofacies ones.

References Cited:

Doligez B., Ravenne C., Lemouzy P., Galli A., 1992: Une méthodologie pour une étude intégrée des réservoirs: des données de puits aux simulations d'écoulement en utilisant des outils géostatistiques. Pétroles et Techniques, n.372, p.43-47.

Eschard R., Doligez B., Rahon D., Ravenne C., Leloch G., and Heresim Group, 1991: A new approach for reservoirs description and simulation using geostatistical methods. In proceedings: Advances in resrvoir technology, characterization, modelling and management, Edinburg.

Eschard R., Tveiten B., Desaubliaux G., Lecomte JC., Van Buchem F., 1993: High resolution sequence stratigraphy and reservoir prediction of the Brent group (Tampen Spur area) using an outcrop analogue (Mesaverde group, Colorado). In: Subsurface reservoir characterization from outcrop observations. R.Eschard, B.Doligez Eds, Editions Technip, Paris, p.35-52.

de Fouquet C., Beucher H., Galli A., Ravenne C., 1988: Conditional simulation of random sets. Application to an argillaceous sandstone reservoir. 3rd International Geostatistics Congress, Avignon. M.Armstrong ed: Geostatistics, v.2, Kluwer, Academic Publishers, Dordrecht, p.517-530.

Fournier F., 1995: Integration of 3D seismic data in reservoir stochastic simulations: a case study. SPE 30564.

Fournier F. and Derain J.F., 1995: A statistical methodology for deriving reservoir properties from seismic data, Geophysics, v.60, n.5, p.1437-1450.

Galli A., Guerillot D., Ravenne C., and Group Heresim., 1990: Combining geology, geostatistics and multiphase flow for 3D reservoir studies. In: 2nd European Conference on the Mathematics of Oil recovery, Arles. D.Guerillot and O.Guillon eds, Editions Technip, p.11-19.

Homewood P., Guillocheau F., Eschard R., Cross T., 1992: Corrélations haute résolution et stratigraphie génétique: une démarche intégrée. Bull. Elf Acquitaine Production, F-31360, Boussens.

Johann P., Fournier F., Souza O., Eschard R., Beucher H., 1996: 3D stochastic modeling constrained by well and seismic data on a turbidite field. SPE 36501.

Joseph P., Eschard R., Doligez B., Granjeon D., 1996: 3D stratigraphic modelling, a new way to constrain geostatistical reservoir simulation. EAEG Amsterdam.

Matheron G., Beucher H., de Fouquet C., Galli A., Ravenne C., 1987: Conditional simulation of the geometry of Fluvio-Deltaic reservoirs. SPE 16753.

Mouliere D., Beucher H., Hu L.Y., Fournier F., Terdich P., Melchiori F., Grifi G., 1996: Integration of seismic derived information in reservoir stochastic modeling using truncated gaussian approach. Geostatistical Congress of Wollongong, Australia.

Ravenne C., Galli A., Beucher H., Eschard R., Guérillot D., and Heresim group, 1990: Outcrop studies and geostatistical modelling of a middle Jurassic Brent analogue. In proceedings of: The European Oil and Gas conference, Altavilla Milicia, Palermo, Sicily, Italia.

Ravenne C. et Beucher H., 1988: Recent development of sedimentary bodies in a fluvio-deltaic reservoir and their 3D conditional simulations. SPE 18310.

Figure captions:

Figure 1: the main steps of the Heresim methodology (stationary simulation)

Figure 2: example of computation of a vertical proportion curve

Figure 3: truncation of a gaussian function. Comparison between stationary and non stationary approach.

Figure 4: experimental vertical proportion curve computed for the PLO unit

Figure 5: 3D proportion block computed for the PLO unit from initial proportion curves

Figure 6: comparison between the stationary and the non stationary approach on a north-south lithological section of the PLO unit.

Figure 7: comparison of scaled-up horizontal permeability maps resulting from the stationary and non stationary approaches.

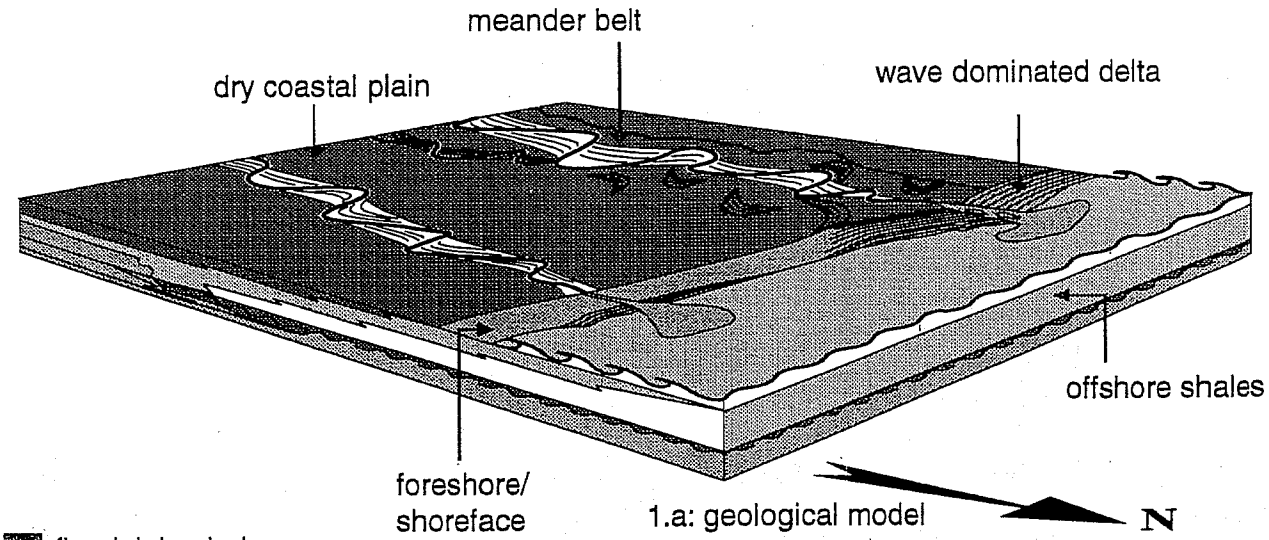

1.a: geological model

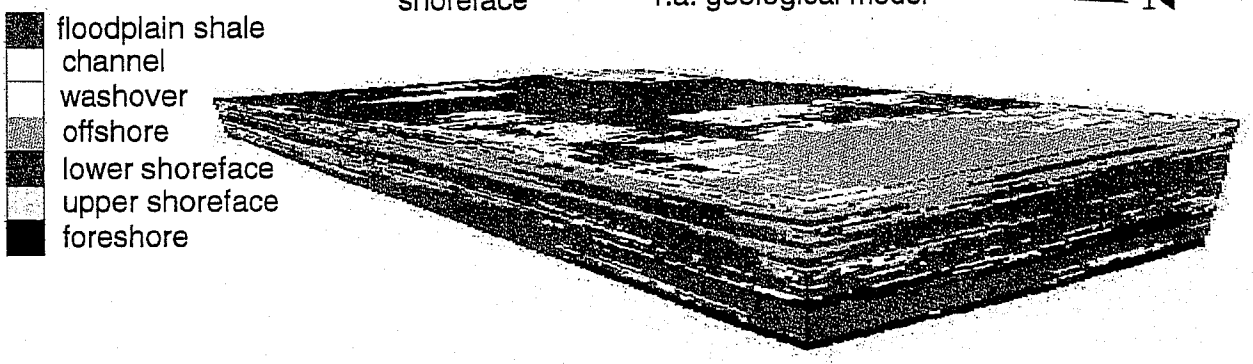

1.b: lithofacies simulation

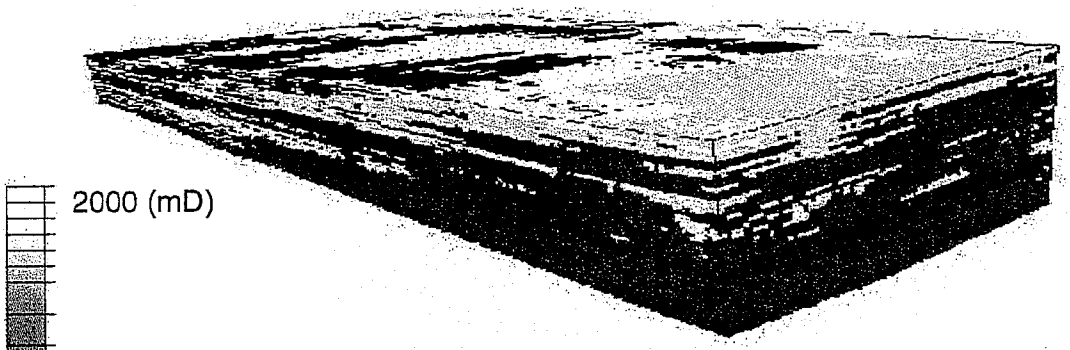

1.c: petrophysical properties attribution
(horizontal permeability Kx)

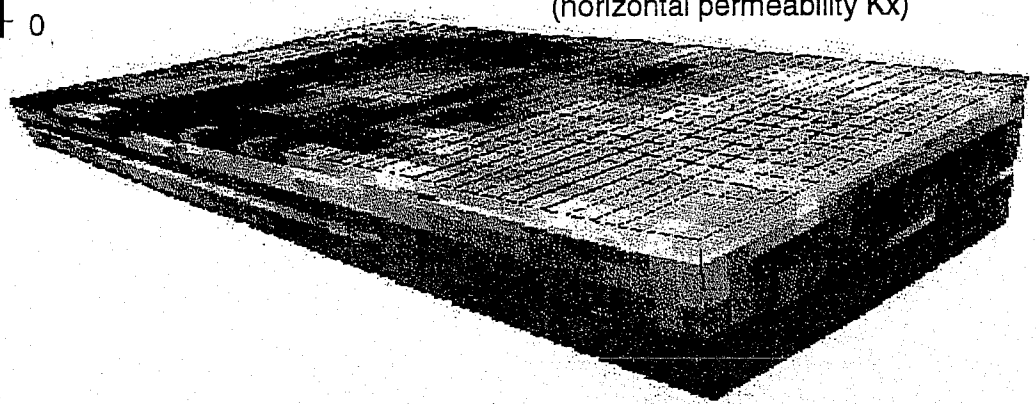

1.d: scaling-up (Kx)

figure 1

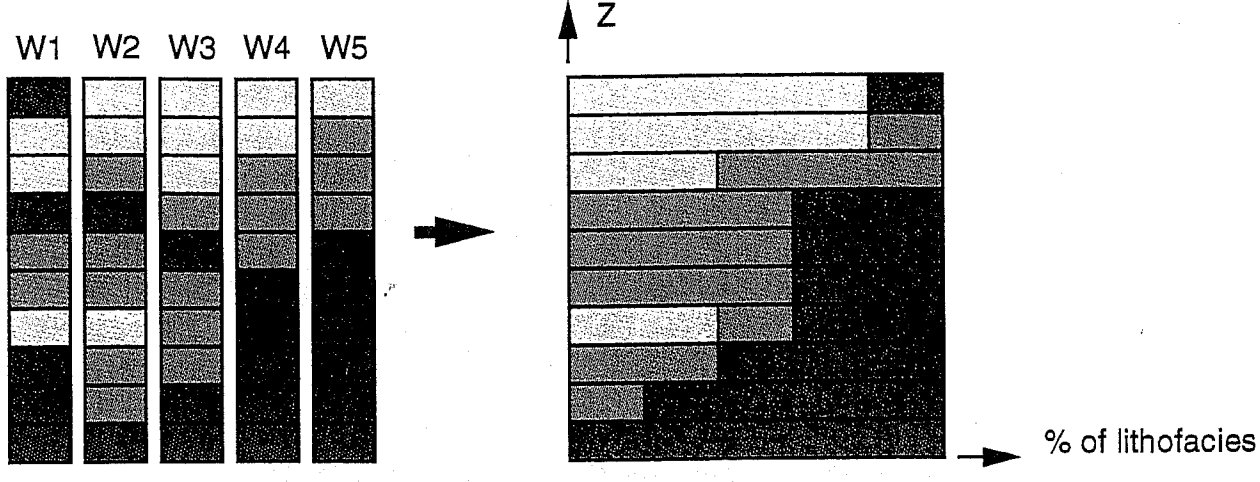

example of computation of a vertical proportion curve from five wells

figure 2

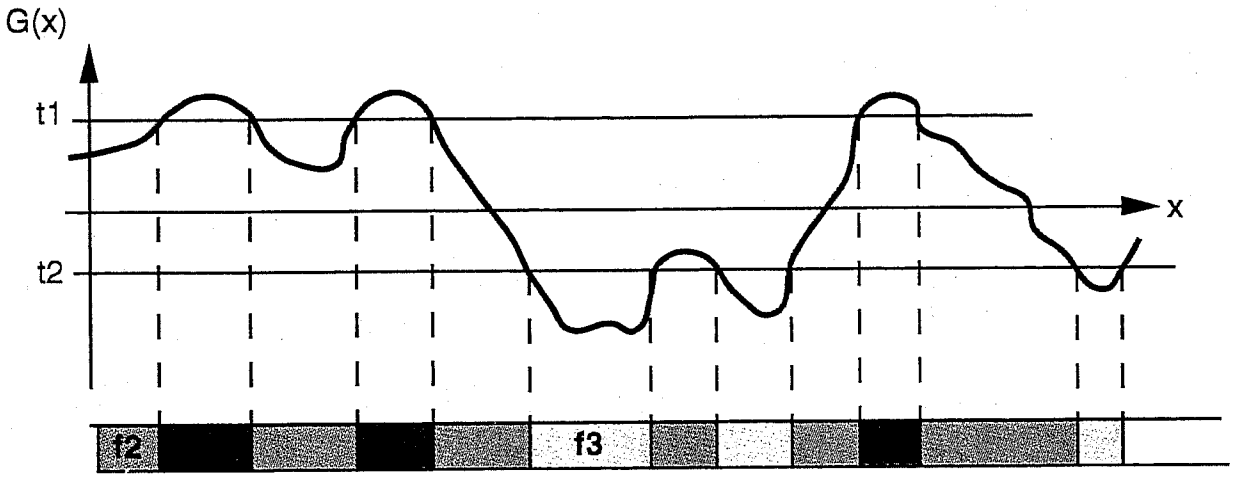

3.a: stationary case-
truncation of a gaussian function by constant thresholds t1 and t2,
and associated lithofacies f1, f2 and f3

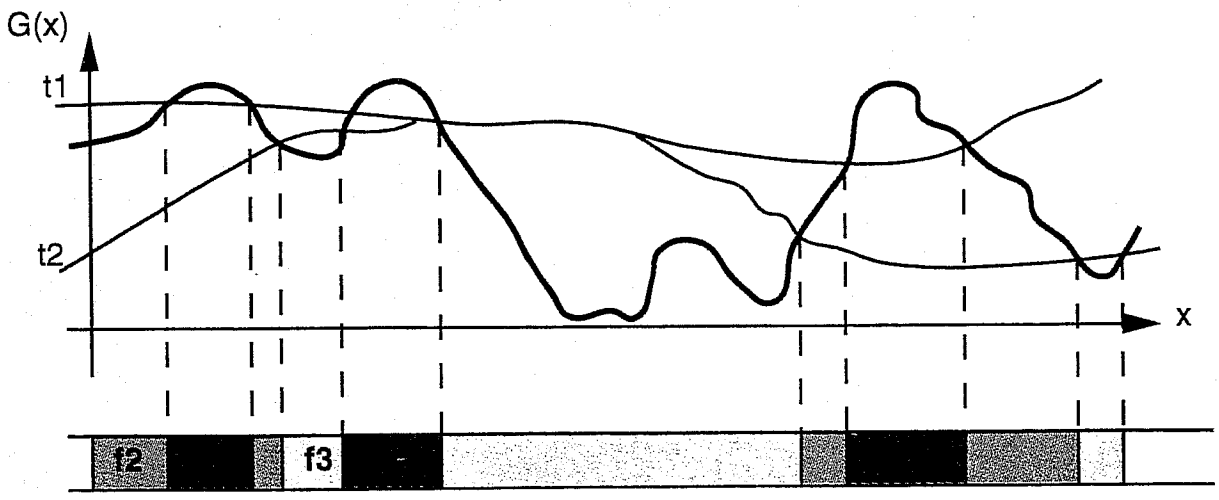

3.b: non stationary case-
truncation of a gaussian functionby thresholds t1(x) and t2(x),
and associated lithofacies f1, f2 and f3

figure 3

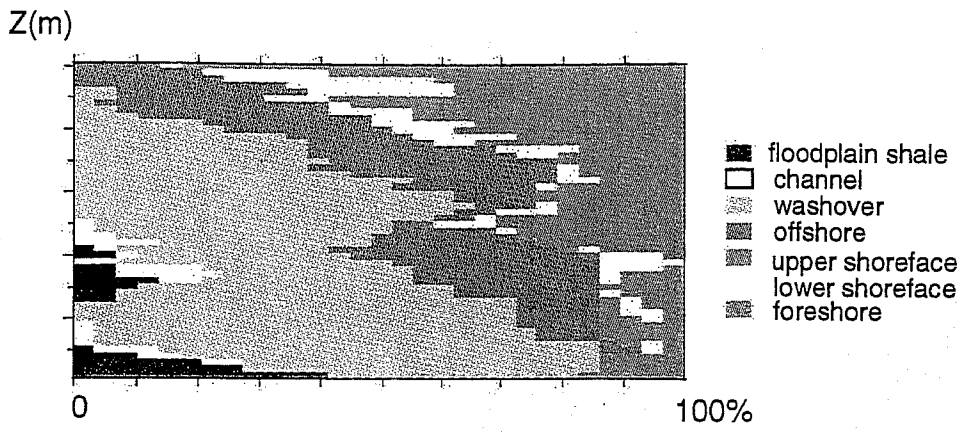

figure 4

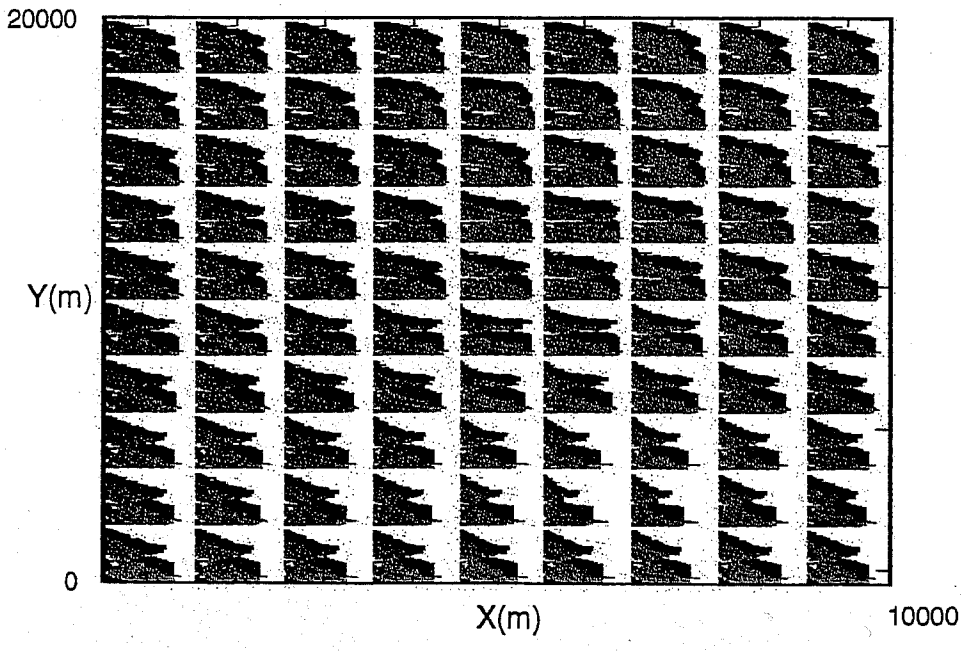

figure 5

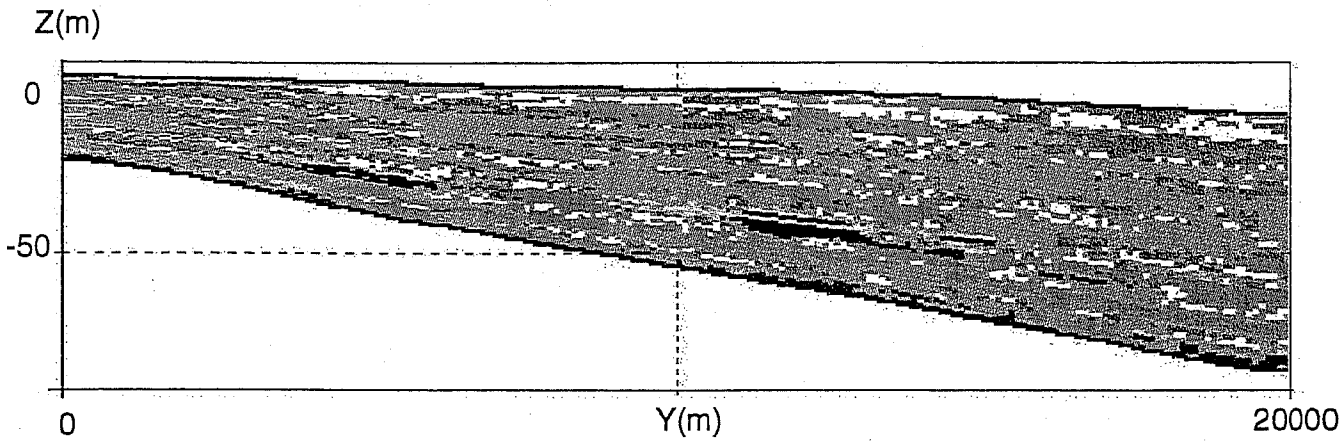

stationary simulation - NS section

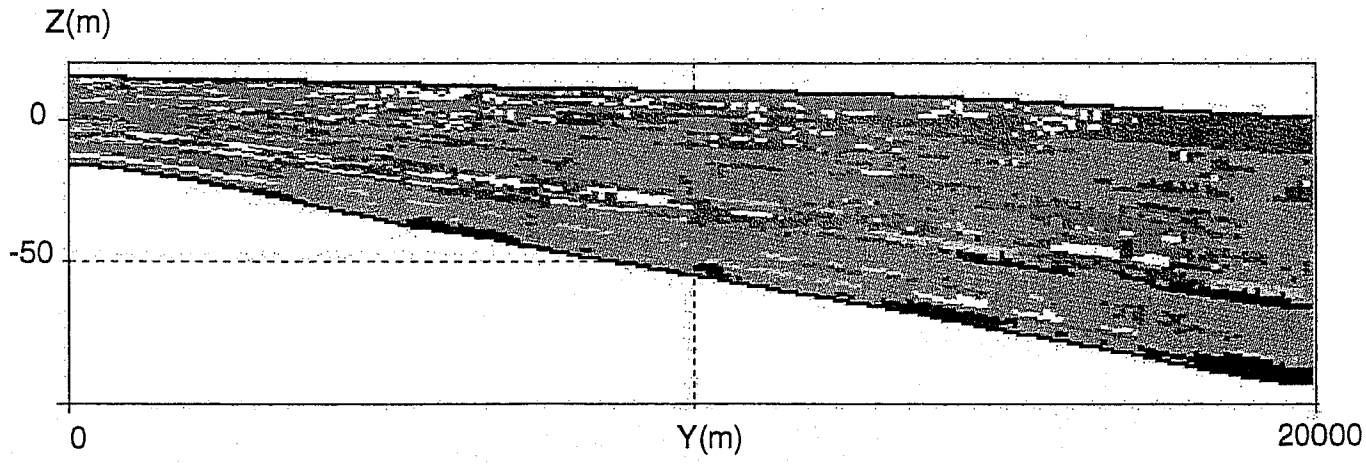

non stationary simulation - NS section

figure 6

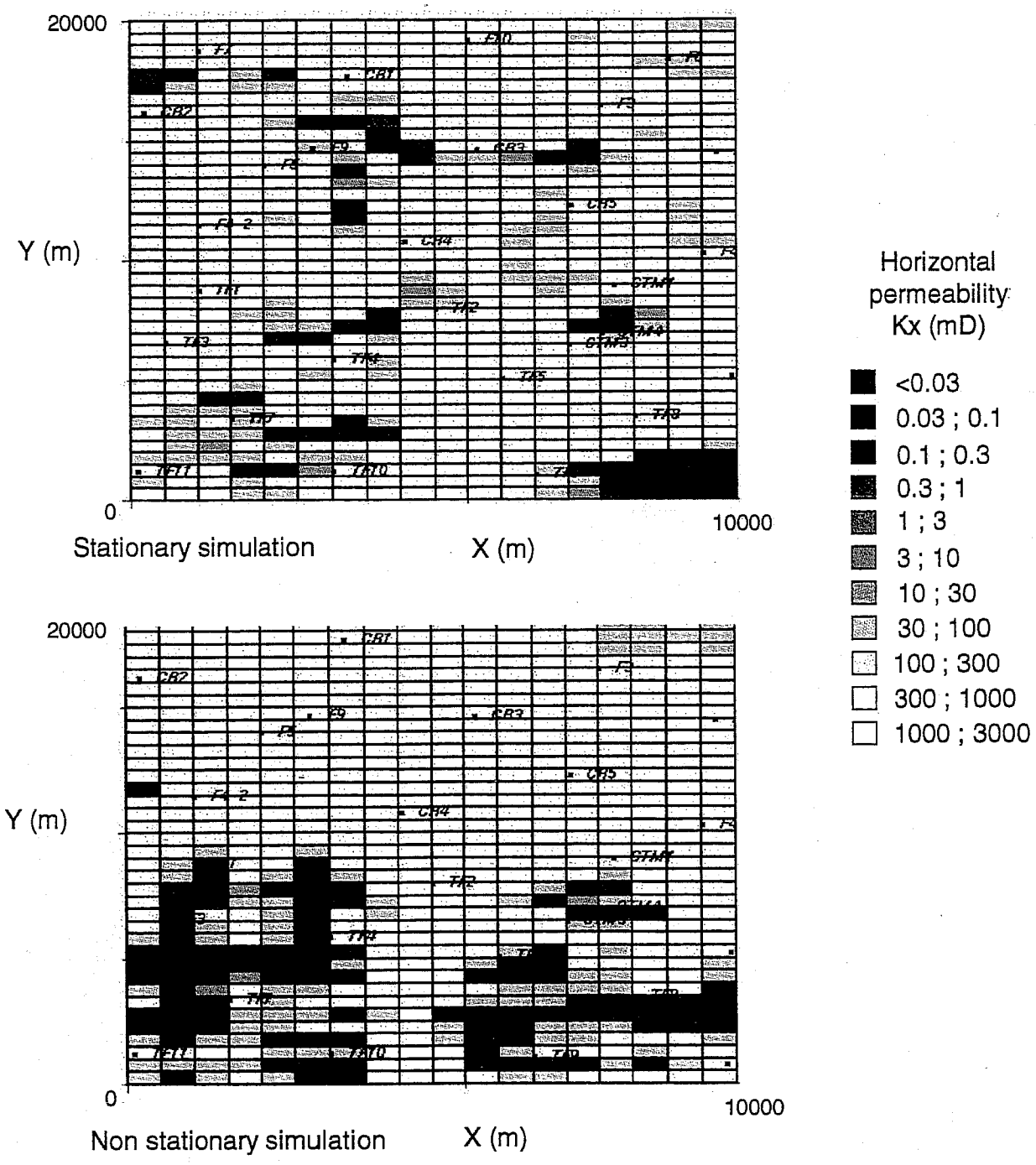

Scaled-up horizontal permeabilities - layer 7

figure 7

Facies Architecture of the Bluejacket Sandstone in the Eufaula Lake Area, Oklahoma: Implications for the Reservoir Characterization of the Bartlesville Sandstone

Liangmiao Ye and Kexian Yang
Department of Geosciences, The University of Tulsa, Tulsa, Oklahoma

Acknowledgments

The results presented here were partially supported by an industry-government partnership funded under US Department of Energy Contract No. DE-FC22-93BC14951 and by the Research Office of The University of Tulsa under Student Research Grant Program. We are grateful to Amoco Production Company Technology Center, Tulsa for allowing access to their microresistivity imaging interpretation facility, and core analysis facilities. We also thank D. Kerr and R. Tillman who provided valuable insights and helpful discussion.

Abstract

Outcrop studies of the Bluejacket Sandstone (Middle Pennsylvanian) provide significant insights to reservoir architecture of the subsurface equivalent Bartlesville Sandstone. Quarry walls and road cuts in the Lake Eufaula area offer excellent exposures for detailed facies architectural investigations using high-precision surveying, photo mosaics. Directional minipermeameter measurements are being conducted. Subsurface studies include conventional logs, borehole image log, and core data.

Reservoir architectures are reconstructed in four hierarchical levels: multi-storey sandstone, i.e. discrete genetic intervals; individual discrete genetic interval; facies within a discrete genetic interval; and lateral accretion bar deposits. In both outcrop and subsurface, the Bluejacket (Bartlesville) Sandstone comprises two distinctive architectures: a lower braided fluvial and an upper meandering fluvial.

Braided fluvial deposits are typically 30 to 80 ft thick, and are laterally persistent filling an incised valley wider than the largest producing fields. The lower contact is irregular with local relief of 50 ft. The braided-fluvial deposits consist of 100-400-ft wide, 5-15-ft thick channel-fill elements. Each channel-fill interval is limited laterally by an erosional contact or overbank deposits, and is separated vertically by discontinuous mudstones or highly concentrated mudstone interclast lag conglomerates. Low-angle parallel-stratified or trough cross-stratified medium- to coarse-grained sandstones volumetrically dominate. This section has a blocky well log profile.

Meandering fluvial deposits are typically 100 to 150 ft thick and comprise multiple discrete genetic intervals. Channel-fill facies width/thickness ratio for a given discrete genetic interval is from 30 to 60. Channel-fill facies successions include: a basal trough cross-stratified, medium-grained sandstone; a medial epsilon cross-stratified fine-grained sandstones with numerous mudstone drapes; an upper mudstone. Well log profile is typically a serrated bell shape. Splay facies is up to 20 ft thick and consists of ripple-stratified and lesser trough cross-stratified, medium-grained sandstones separated by laterally persistent thin mudstones. Floodplain mudstones laterally and vertically segment, with the exception of very limited areas, channel-fill and splay sandstones into reservoir compartments.

Introduction

The Middle Pennsylvanian Bartlesville (Bluejacket) Sandstone extends from southeastern Kansas across the northeastern Oklahoma platform and into the Arkoma foreland basin. The Bartlesville Sandstone has been a major oil producer in Oklahoma for more than 90 years, producing more than 2 billion bbl oil since the discovery of a number of fields back to the early 1900's. However, estimates of recovery of OOIP are as low as 20% for many Bartlesville-producing fields/reservoirs, despite post-primary recovery attempts (Welch, 1989).

The reason for poor recoveries is clearly attributed to complex reservoir architecture, which is very difficult to properly characterize with conventional subsurface information only. Static and dynamic data obtained from analogous outcrop is critical to reconstructing reliable reservoir models and developing effective reservoir management strategies.

This study offers detailed description of Bluejacket Sandstone road cuts and quarry walls in the Eufaula Lake area and characterization of selected reservoir units in Glenn Pool field, Oklahoma. The intent is to illustrate the usefulness of outcrop information to proper subsurface reservoir modeling.

A. Regional Depositional Framework

This section highlights key points regarding the regional depositional framework in both earlier view and our new interpretation, serving as background information for understanding the detailed study.

Extensive previous geological studies on the Bartlesville Sandstone have been conducted since late in the last century. Most recent systematic study of the depositional origin and framework was completed in late 1960's (Saitta, 1968; Saitta and Visher, 1968; Phares, 1969; Visher and Saitta and Phares, 1971), which concluded that the Bartlesville/Bluejacket Sandstone is part of a large fluvial-deltaic complex deposited in essential as a single regressive interval (figure 1).

However, regional scale to reservoir scale investigation in both outcrop and subsurface in a area over 2000 square miles in northeastern Oklahoma reveals that Bartlesville Sandstone is a mainly fluvial incised valley-fill deposited in a transgressive manner from a lower braided fluvial to an upper tidal-influenced meandering fluvial. Sequence stratigraphic analysis illustrates that the whole Bartlesville Sandstone incised valley-fill section consists of two sequence stratigraphic architectural elements: 1) the lower lowstand system tract, 40-150 ft, composed of braided fluvial deposits and distal lowstand delta; 2) the upper transgressive system tract, 70-100 ft, composed of meandering fluvial, estuarine tidal, and shallow marine deposits. The regional Inola Limestone marker, capping the Bartlesville Sandstone interval, is equivalent to a condensed section which represents maximum flooding (figure 2).

This new interpretation is supported by following observations:

1. Outcrop survey illustrates that a type-1 sequence boundary exists at the base of Bartlesville Sandstone, indicated by subaerial erosion of underlying Savanna Shale and basinward facies shift from pure marine shale below to braided fluvial deposits above. Core facies and log facies interpretation validate the facies shift.

2. Well log correlation shows Bartlesville Sandstone thickens at the expense of the Savanna Shale. The incised valley extends from north to south over 120 miles within Oklahoma, and is 4-5 miles wide in

Washington County to over 40 miles wide in the Eufaula Lake area. The thickness of Bartlesville Sandstone interval varies from 120-250 ft within the valley to less than 30 ft outside the valley.

3. Well log analysis observes a usually very sharp base, a interval with blocky log response at the lower part, and a fining-upward sequence at the upper part of Bartlesville Sandstone throughout the study area. Core and outcrop facies interpretation indicates that sedimentary facies transition upwards from braided fluvial, to meandering, to tidal-influenced meandering, to tidal estuarine and shallow marine deposits (figure 2). Same sequence of facies variation may be observed horizontally from north to south. This pattern of facies association clearly indicates that Bartlesville Sandstone is deposited in a transgressive manner. The regional Inola Limestone marker, capping the Bartlesville Sandstone interval, represents maximum flooding.

B. Study Areas

Self Unit

Self Unit is a 160 acre tract in southern part of Glenn Pool oil field, which was discovered in 1905 about 20 miles south of Tulsa, Oklahoma (The Bartlesville Sandstone here is therefore called Glenn Sand, Kuykendall and Matson, 1992). The Self Unit has been developed with 82 wells drilled to date. Data available includes: 41 conventional logs, 1 microresistivity borehole image log, 1 whole core, and porosity and permeability measurements from 9 cores.

Glenn Sand in Self Unit is about 130 ft thick. Detailed well log correlation resulted in the division of Glenn Sand into 6 discrete genetic intervals (explained later) descending from A to F. Core and log facies interpretation shows that DGI A through E are meandering fluvial channel-fill and crevasse splay sandstones and floodplain mudstones, and F braided fluvial sandstones.

Tract 7 and Adjacent Area

Tract 7 and adjacent area, located about one mile north of Self Unit, covers about 1000 acres. About 300 wells have been drilled. However, only 119 logs are available for study. As what was done in the Self Unit, the Glenn Sandstone is divided into 7 DGIs descending from A to G. DGI G is absent in the Self Unit because of the base relief of the incised valley. Log facies analysis indicates that DGI A through E again are meandering fluvial channel-fill and crevasse splay sandstones and floodplain mudstones. DGI F and G are braided fluvial sandstones.

Figure 3 shows the location of Glenn Pool field, Self Unit, and Tract 7 and adjacent areas.

Checotah Road Cut

This is a road cut surface on the Oklahoma Highway 266, 6.5 miles east of Checotah. The road cut extends 680 ft east-west, and is about 50 ft tall. Being normal to the general paleo-current direction (north to south), the road cut exposes a transverse cross section. With the dip of 50-60 degree, the road cut is mostly accessible for detailed investigation. Detailed facies interpretation was performed based on observations on the lithology, physical structures, and current orientations. Spatial configuration of facies element boundaries were measured using an infra-based precision survey system.

Comparative study of outcrop and subsurface equivalent leads to a believe that this road cut is sedimentologically analogous to middle-upper part of the Glenn Sand.

Eufaula Dam Cliff

This is a vertical cliff at the north end of Eufaula Dam. The cliff includes two segments--west leg, extending northwest-southeast, 70 ft tall and 850 ft long; and east leg, extending approximately southwest-northeast, 60-70 ft tall and 400 ft long. Both legs are oblique to general north-south flow direction. For this road cut, detailed observations can be done only for the lower part of the section because of limited accessibility. However, architectural element boundaries down to level of single channel-fill facies can be identified and surveyed precisely from distance.

This section, composed of braided fluvial deposits, is believed to be sedimentologically analogous to lower (DGI F and G) Glenn Sand reservoirs. Location of these two outcrops is shown on figure 1.

Reconstruction of Reservoir Architectures

One important concept in modern reservoir characterization is that reservoir architectures are of hierarchical features (Miall, 1985; Jordan and Pryor, 1992). A fluvial pay zone like Bartlesville Sandstone usually consists of multiple DGIs, one DGI is composed of several different facies, and one facies is made up of different subfacies and/or facies elements, and so on. Proper documentation of heterogeneity at each level of reservoir architectures is critical to better management planning for mature reservoirs.

A. Facies Architecture Hierarchy

Level 1: Multi-Storey Sandstone- Discrete Genetic Intervals

DGI (discrete genetic interval) is defined as a collection of contiguous facies that were deposited in a brief discrete increment of time (Kerr and Jirik, 1990). For the case of fluvial Glenn Sand, one DGI is equivalent to one fluvial rhythmic sequence which consists of all channel-fill and associated facies deposited in the same time period.

First level of hierarchical reservoir architectures deals with the stacking pattern of multiple discrete genetic intervals. Figure 4 (a) shows the vertical relationship of different DGIs surveyed from Checotah road cut. Eight DGIs are present here. One DGI basically represents one channel sequence and its equivalent deposits. For most of the DGIs, the upper part (i.e. upper channel subfacies and floodplain mudstone) has been eroded by overlying DGIs. Middle channel subfacies are mostly preserved except for DGI 5 and 6. Horizontally, DGI 8 is truncated by DGI 7, and DGI 4, 5, 6 are truncated by DGI 3. Top of DGI 7 is partially eroded by DGI 3. All these indicate that different discrete genetic intervals are not well separated vertically. Even though the rip-up clast shale, mud pebbles common on the bottom of channel-fill may function as flow barrier/baffles between different DGIs.

In comparison, vertical separation of different DGIs are much more evident in the subsurface. Figure 4 (b) is a cross section cut in the middle of Self Unit to illustrate that at most cases, different DGIs of Glenn Sand are separated by 1-5 ft floodplain mudstones. However, one DGI cutting into the other is observed in the subsurface too.

Other important observation in this level of hierarchical architectures is that the thickness of each DGI is decreasing upwards for both outcrop and subsurface, as shown in figure 5. For Glenn Sand reservoirs in Self Unit, maximum thickness of one DGI decreases upwards from 33 ft of DGI E to 22 ft of DGI A. For Checotah road cut, thickness of a individual DGI decreases upwards from 23 ft (DGI 8) to 7 ft (DGI 1). Thinning upward in both outcrop and subsurface implies one aspect of their similarities and also supports the interpretation that Bartlesville Sandstone is deposited in a transgressive manner.

Level 2: Individual Discrete Genetic Interval

As stated earlier, DGI (discrete genetic interval) is defined as a collection of contiguous facies that were deposited in a brief discrete increment of time (Kerr and Jirik, 1990). From sedimentological point of view, one DGI represents a brief episode of sedimentation which deposited a genetically related 3-D volume of sedimentary rocks. From oil development point of view, DGI represents the smallest subsurface mappable unit. DGI concept is critical for detailed and accurate reservoir characterization.

For the fluvial Bartlesville Sandstone, one DGI is commonly made of three facies: channel-fill sandstone, splay sandstone, and floodplain mudstone. These three facies are identified in all meandering DGIs recognized in the subsurface (figure 6 & 7). In the outcrop (figure 4-a), splay deposits only appear in DGI 2 and 6, floodplain mudstone is recognized in DGI 5 only. The lower presence of floodplain mudstone and splay sandstone in outcrop is probably due to the 2-D nature of the road cut, and their low volume percentages.

The relationship between these three facies elements are better shown in the facies map constructed for the Glenn Sand reservoirs. As shown in these maps (figure 6, 7), channel fill facies constitutes the main framework of the system. Channels extend generally from north to south, which is consistent to regional paleo-current direction. Channels may bifurcate or merge as they proceed. Splay is deposited as a result of bank-breaking during flooding, thus develops on the margin of channels and spreads outward in a fan-like shape. Floodplain mudstone occurs between channels and/or splays, or on top of channels. Therefore floodplain mudstones laterally and vertically segment channel-fill and splay sandstones into reservoir compartments.

Level 3: Facies Within a Discrete Genetic Interval

Third level of hierarchical reservoir architectures deals with individual channel-fill, splay and floodplain facies. Figure 8 are the first-hand description of these facies on both outcrop and cores of Glenn Sandstone.

1. Meandering Channel-Fill Facies

Checotah road cut and upper part of Glenn Sand are mainly composed of meandering channel-fill deposits, which are characterized by: a general fining-upward texture; upward decrease in scale of physical sedimentary structures; upward increase in proportion of mudstone interbeds. In the core and outcrop, channel-fill facies were subdivided into:

Lower channel-fill subfacies: well to moderately sorted, medium-grained sandstone with medium-scale (2 to 8 inch) cross stratification. Mudstone drapes common on cross strata. Rip-up clast shale and mud pebbles commonly occur on the bottom part.

Middle channel-fill subfacies: moderately sorted, lower medium-grained to poorly sorted, silty fine-grained sandstones with horizontal to low-angle parallel stratification and ripple lamination. Medium- to very thin-bedded (1 to 6 inch) mudstones to silty mudstones drape lateral accretion surfaces. Dip direction of lateral accretion surfaces rotate progressively upwards in response to the migration of lateral accretion bars.

Upper channel-fill subfacies: mudstone to silty claystone.

2. Splay Facies

Coarsening-upward texture from fine-grained to medium-grained sandstone. Upward increase in stratal thickness in lower levels only; otherwise, irregular vertical stacking of thick to thin beds (3 to 25 inch). Ripple lamination and low-angle parallel bedding dominate; medium-scale cross stratification and contorted bedding less common. Thin bedded (1 to 3 inch) mudstones interstratified with sandstones throughout.

3. Floodplain Facies

Deposited in floodplain area are usually clays, mudstone, silts, in corresponding to the relative quiet environment which characterize the floodplain environments. These lithologies usually functions as impermeable barriers to fluid flow in the reservoir.

4. Braided Channel-Fill Facies

DGI F of Self 82 core of Glenn Sand are interpreted as braided fluvial channel-fill deposits characterized by moderately to well sorted, generally structureless (but less commonly parallel-bedded), upper medium- to lower coarse-grained sandstone. In Glenn Pool field, thickness of braided fluvial deposits varies from 30 to 80 ft depending on local relief of the base contact, i.e. base of the incised valley. This section has a blocky well log profile and is laterally persistent filling the incised valley. Figure 6, 7 shows thickness pattern of DGI F and G braided sandstone in the Self Unit. Internal architectures could not be reconstructed through well log analysis because of its excellent vertical and horizontal continuity and lack of continuous mudstones or shales.

Interpretation of this massive DGI F sandstone as braided fluvial deposits was really assured by outcrop study. Similar thick-bedded, structureless rocks have been observed in the lower part of Bluejacket Sandstone outcrops in the Eufaula Dam area. These "massive" thick sandstones laterally transition to well cross-stratified and/or parallel-bedded thick sandstone in short distance; they are highly channelized, showing unidirectional paleoflow and vary greatly in thickness according to the position relative to the channel thalwegs. Figure 9 displays a outcrop section of the braided fluvial deposits. The figure indicates that braided fluvial deposits are actually made of many individual channels which are stacked together and cross-cutting each other horizontally and vertically, resulting in a widespread distribution. Each channel-fill is characterized by relatively uniform lithology and sedimentary structures.

Most channel-fills are limited laterally by erosional contacts and rarely by overbank fines. There is little shale occurring between and within channels, even though discontinuous mudstones or concentrated mudstone interclast lag conglomerates at the bottom of channels may act as vertical flow baffles.

Totally 25 individual braided channels are recognized in the Eufaula Dam Cliff. Figure 10 shows the braided channel-fill is 100-400-ft wide, and 5-15-ft thick. The widespread, continuous blocky interval of the lower Bartlesville Sandstone is actually made of numerous number of braided channels smaller than the meandering channels constituting much more isolated upper Bartlesville Sandstones.

Level 4: Subfacies of Channel-Fill Facies

As stated above, meandering channel-fill facies were subdivided into lower, middle, and upper channel-fill subfacies. In meandering fluvial system, lateral accretion bar deposits of middle channel-fill subfacies are most prominent component of channel-fill deposits. Its special depositional process and resultant heterogeneity are always interesting topics. The very unique characteristics of lateral accretion bar depositional processes is that the bar migrate or accrete laterally as the depositional process proceeds. Lateral migration process are pulsative as indicated by interbedding of lateral accretion dunes and lateral accretion mud drapes. Thus, the distribution of lateral accretion mud drapes is the key factor for the reservoir heterogeneity.

Core and log facies interpretation indicate that DGI C is made up of lateral accretion bar deposits at the location of well Self 82. The dip azimuths of the lateral accretion surfaces as indicated in microresistivity image acquired for this well show a progressive upward rotation from 200° to 146°. Such rotation suggests that the channel thalweg locally increased in sinuosity with growth of the bar. Further evaluation of the microresistivity log allows for extrapolation of lateral accretion mud drapes in DGI C (Ye and Kerr, 1995). Average vertical spacing of lateral accretion surfaces and average structure-corrected dip angle can be estimated from the image. Based on a simple geometric argument, number of lateral accretion mudstone drapes in a given horizontal distance can be predicted. The expected distribution of lateral accretion mud drapes can be reconstructed assuming lateral continuity and reasonable curvature development of the bar (see Kerr, Ye, Aviantara, and Martinez, this volume).

B. Width/Thickness Ratio

Width/Thickness ratio is a very useful parameter for subsurface facies geometry prediction. Many authors have tried to relate the width and thickness and found out they are not linearly related (Schumm, 1963; Leeder, 1973). It is commonly accepted that the ratios is 60 to 120 for meandering belts, and 40-60 for braided channel-fills.

As shown on figure 10, meandering channels are usually 200-1500 ft wide and 10-35 ft thick; and braided channels are normally 50-400 ft wide and 5-15 ft wide. Figure 10 displays the ratios for the meandering channels (30-80) and braided channels (15-50), including both outcrop and subsurface data. Results show the observed ratios are slightly lower than published number, which could be due to the fact that real widths of channels are underestimated when they are cut or eroded by other channels.

C. Porosity and Permeability

Figure 11 is the profile of porosity and permeability measured for Self 82 core. Both lab measurements and minipermeameter measurements are shown for comparison. It shows that the porosity and permeability are strongly DGI related. Descending from DGI A to F, porosity increases from about 8% to about 23%, lab-permeability increases from less than 0.1 md to more than 300 md. For this reason, channel-fill facies in one DGI may be of poorer reservoir than splay sandstone in other DGIs.

From the nine cored wells in the Self Unit, the relationship between facies/subfacies and petrophysical properties within a given DGI suggests that splay sandstones may have higher porosity and permeability than channel-fill sandstones. However, this difference may not be significant because samples are biased toward high porosity and permeability intervals.

Minipermeameter measurements are taken in a spacing of 0.2-0.5 ft (figure 11), in comparison to 1-3 ft for lab measurements. All the mini-permeability values reflect only horizontal permeability due to fixed orientation of slabbing surface. Two points can be made from comparison of mini-permeability and lab-permeability: First, the lab measurement and minipermeameter measurements are close to each other. Statistical analysis illustrates that when permeability is higher than 1 md, the mini-permeability values are systematically 25% lower than lab permeabilties measured in the core of same depth. It indicates that mini-permeameter is a reliable tool for measuring permeability for rocks with permeability larger than 1 md. The value difference could be attributed to the residual oil existing in the core. Second, the general trends of permeability variations are exactly matched by both measurements. However, different level of detailed variations are represented, because of the different sampling scales of these two measurements. Therefore, mini-permeabilities could represent reservoir better than lab-permeabilities. Plug measurements are generally biased toward to good reservoir qualities.

Analysis of the relationship between lab-measured vertical and horizontal permeabilities (K_v and K_h) has shown that K_v/K_h ratio increases downward from about 0.3 to 0.9 (figure 12), indicating lower Bartlesville Sandstone is more homogeneous than upper Bartlesville Sandstone. K_v/K_h ratios for both meandering channel-fill sandstone and splay sandstone are close to each other (0.3-0.5 for both); however, braided fluvial deposit (DGI F) has highest K_v/K_h ratio (about 0.8 to 0.9), indicating that braided fluvial deposit is less heterogeneous. These differences in K_v/K_h ratio also imply that fluid flow in vertical direction in lower Bartlesville Sandstone reservoirs is more important than that for upper Bartlesville Sandstone reservoirs.

Conclusions

1. Reservoir architectures are hierarchical features. This concept allows proper and logical description of reservoir heterogeneity. Four hierarchical levels of reservoir architectures are recognized in both outcrop and subsurface studies of Bartlesville Sandstone. These four levels are: multi-storey sandstone-discrete genetic intervals; discrete genetic interval; channel fill, splay and floodplain facies; and lateral accretion bar deposit.

2. Outcrop provides significant insights to reservoir architecture of the subsurface equivalent in terms of facies distribution, and reservoir architecture. However, a "DGI" recognized in the subsurface

may actually be amalgamation of more than one DGIs which can be clearly identified in outcrop but hard to be differentiated in the subsurface conditions.

3. Minipermeameter measurements of permeability are quite reliable in comparison with lab plug measurements. Its reliability, convenience and low cost allow description of very detailed level of permeability changes. Outcrop could offer excellent place for developing a database of three dimensional permeability variations.

References Cited

Jordan, D. W., and W. A. Pryor, 1992, Hierarchical levels of heterogeneity in a Mississippi river meander belt and application to reservoir systems, AAPG bulletin, V76, N10, p1601-1624.

Kerr, D., and L. A. Jirik, 1990, Fluvial architecture and reservoir compartmentalization in the Oligocene Middle Frio formation, South Texas, Gulf Coast Association of Geological Societies, V XL, 8p.

Kuykendall, M. D. and T. E. Matson, 1992, Glenn Pool field, Northeast Oklahoma platform, AAPG treatise of petroleum geology--atlas of oil and gas fields, (stratigraphic traps III), p155-188.

Leeder, M. R., 1973, Fluviatile finning-upwards cycles and the magnitude of palaeochannels", Geology Magazine, V 110, N 3, p 265-276.

Miall, A.D., 1985, Architectural-element analysis: a new method of facies analysis applied to fluvial deposits, Earth Science Review, N22, p261-308.

Phares, R. S., 1969, Depositional framework of the Bartlesville sandstone in northeastern Oklahoma, M.S. thesis, 56p, university of Tulsa.

Saitta, S., 1968, Bluejacket Formation-A subsurface study in northeastern Oklahoma: M. S. Thesis, The University of Tulsa, Tulsa, OK, 142 p.

Schumm, S. A., 1963, Sinuosity of alluvial rivers on the Great Plains, GSA Bulletin, V 74, p 1089-1099.

Saita., S., and G. S. Visher, 1968, Subsurface of the southern portion of the Bluejacket delta, A guidebook to the Bluejacket-Bartlesville sandstone, Oklahoma City Geological Society, 72p, 1968.

Visher, G. S., S. B. Saitta, and R. S. Phares, 1971, Pennsylvanian delta patterns and petroleum occurrence in eastern Oklahoma. AAPG Bulletin, V55, No.8 , p 1206-1230.

Welch, R. A., 1989, Berryhill Glenn Sand Unit, ARCO Reservoir Engineering Report.

Ye, L. and D. Kerr, 1995, Use of microresistivity image logs in the detailed reservoir architecture reconstruction of Glenn Sandstone, Glenn Pool field, northeastern Oklahoma: Transactions of the 1995 AAPG Mid-Continent Section Meeting, Tulsa, OK, Tulsa Geological Society, p 203-213.

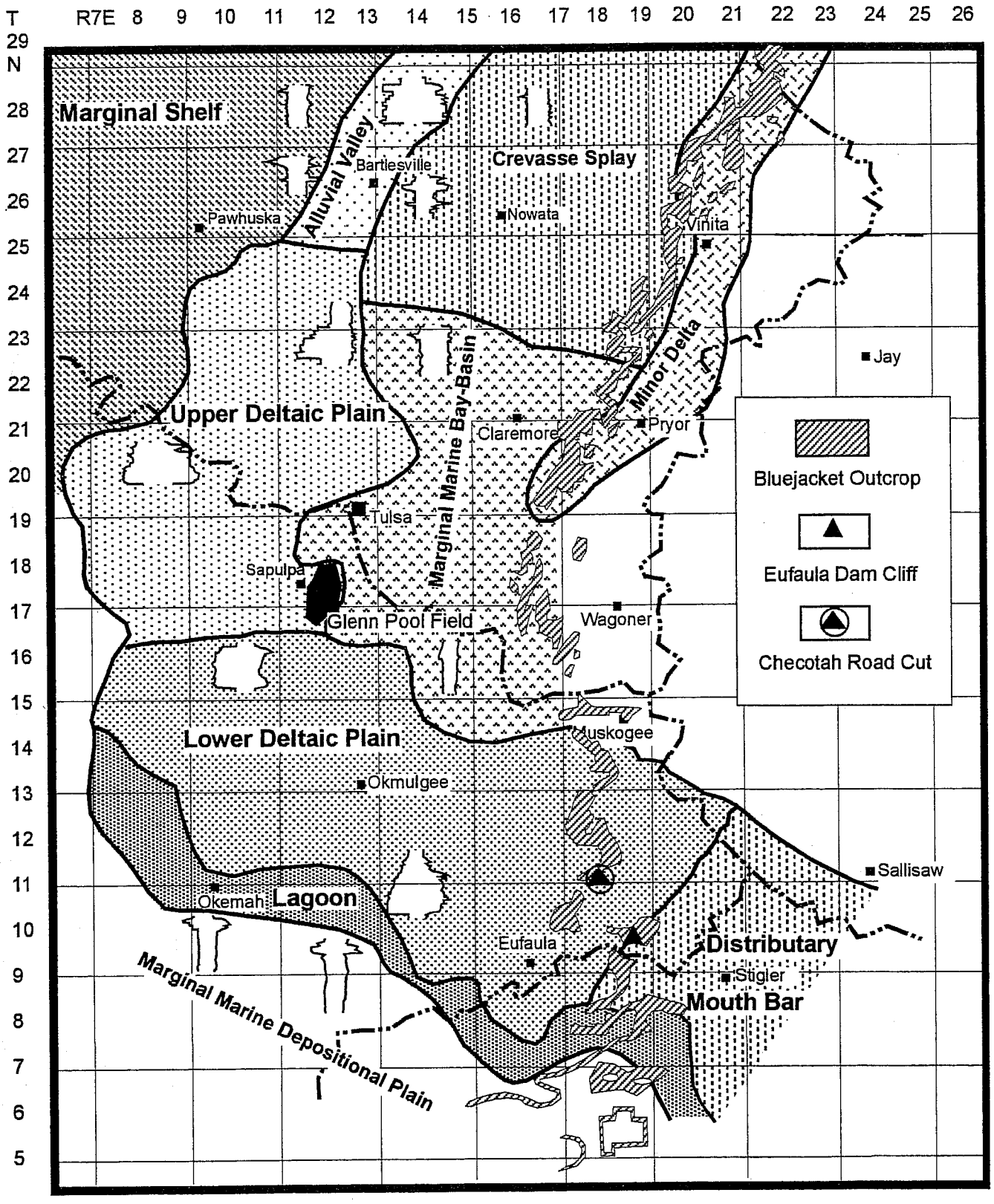

Figure 1 Well Log Patterns and Environmental Reconstruction

(modified from Visher, et al., 1971)

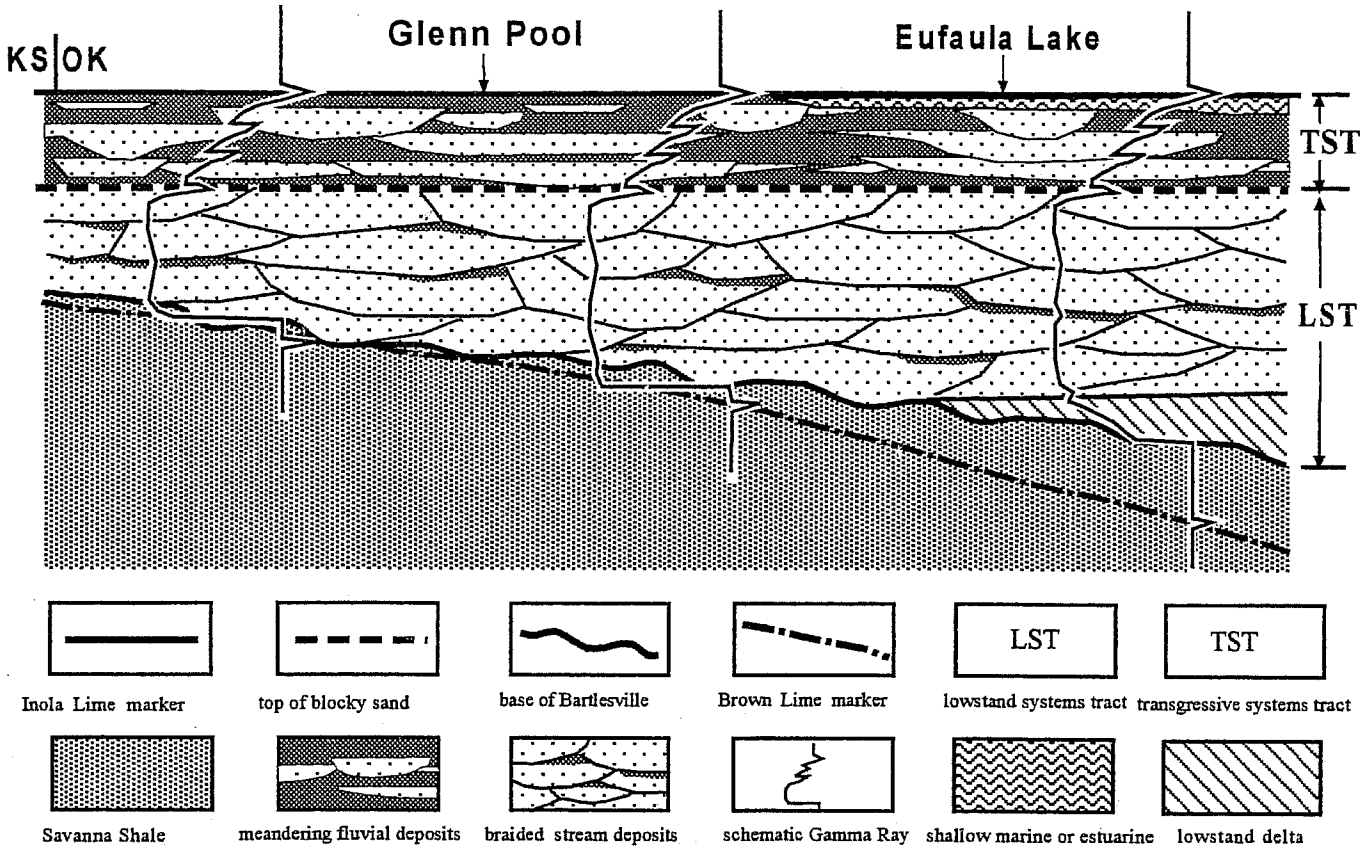

Figure 2 Regional Sequence Stratigraphic Architecture of Bartlesville Sandstone Expressed in Schematic Longitudinal Cross Section

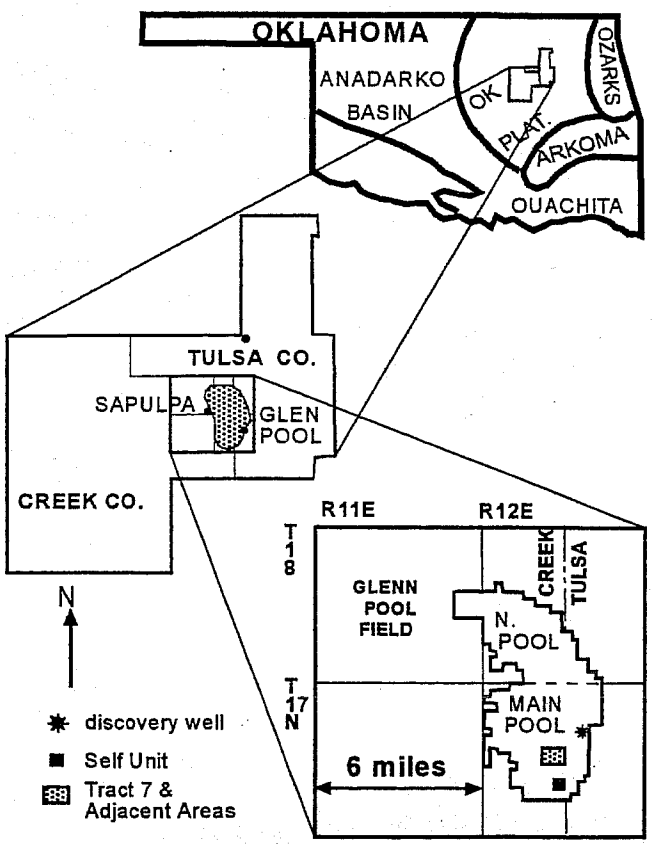

Figure 3 Geographic Location of Glenn Pool field, Self Unit, and Tract 7 and Adjacent Areas

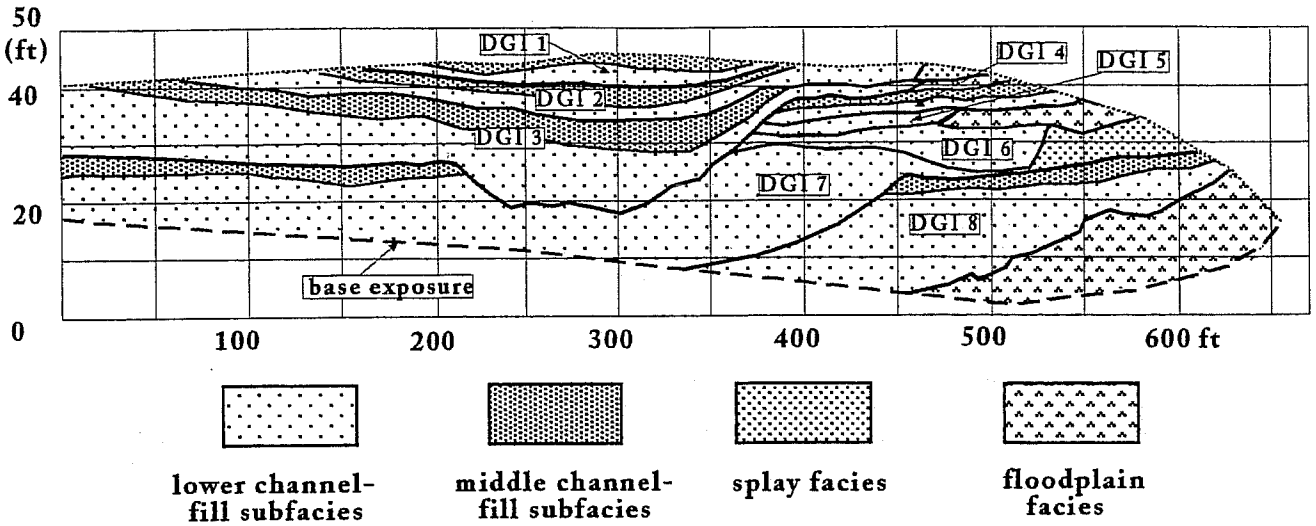

Figure 4 (a) Facies Architecture and Geometry Surveyed on Checotah Road Cut

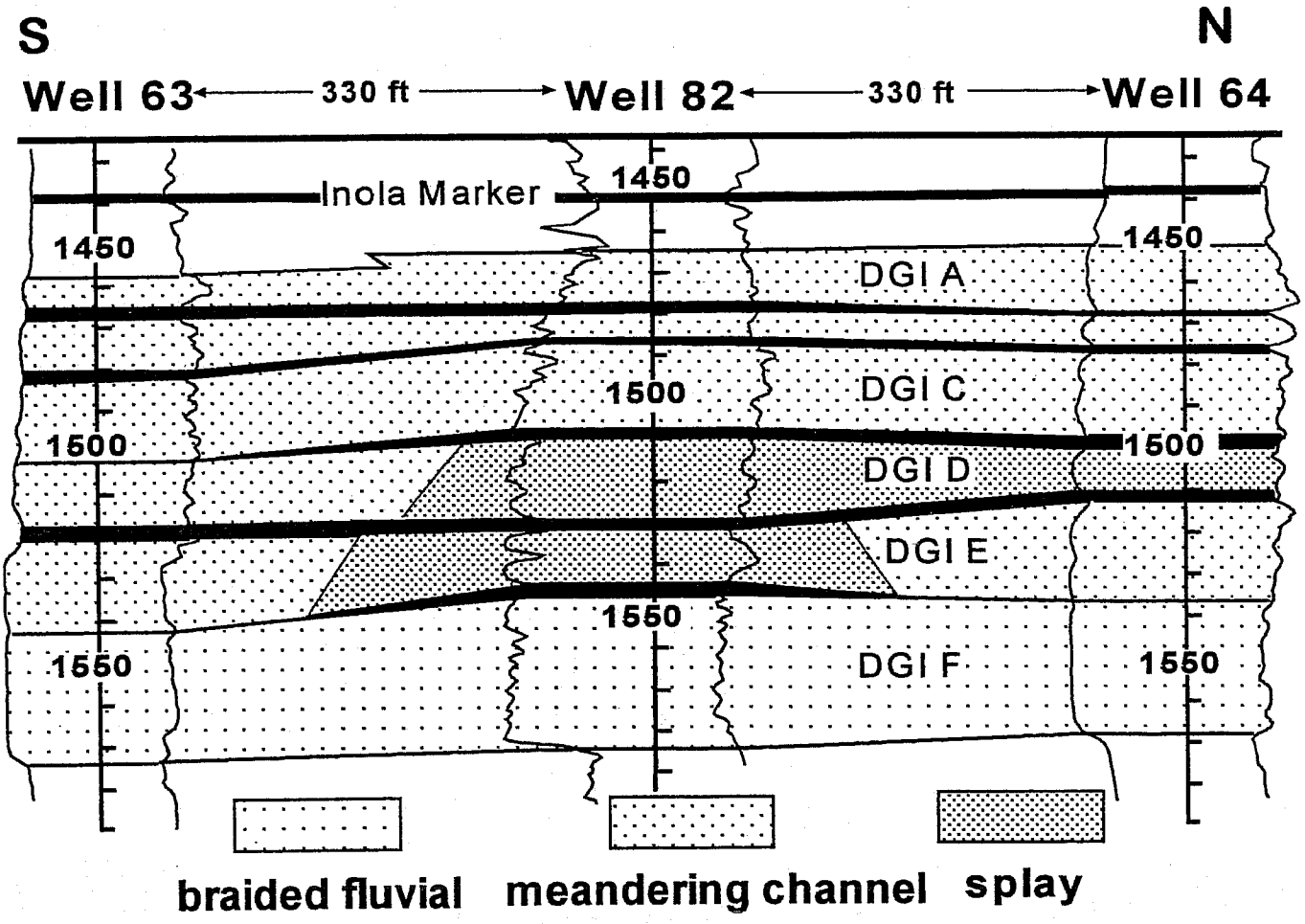

Figure 4 (b) A N-S Cross Section Cut in the Middle of Self Unit Showing DGIs and Facies Distribution

Figure 5 Thinning-Upward Sequence of Meandering Fluvial Deposits Shown by Upward-Decrease of Maximum Thickness for Each DGI

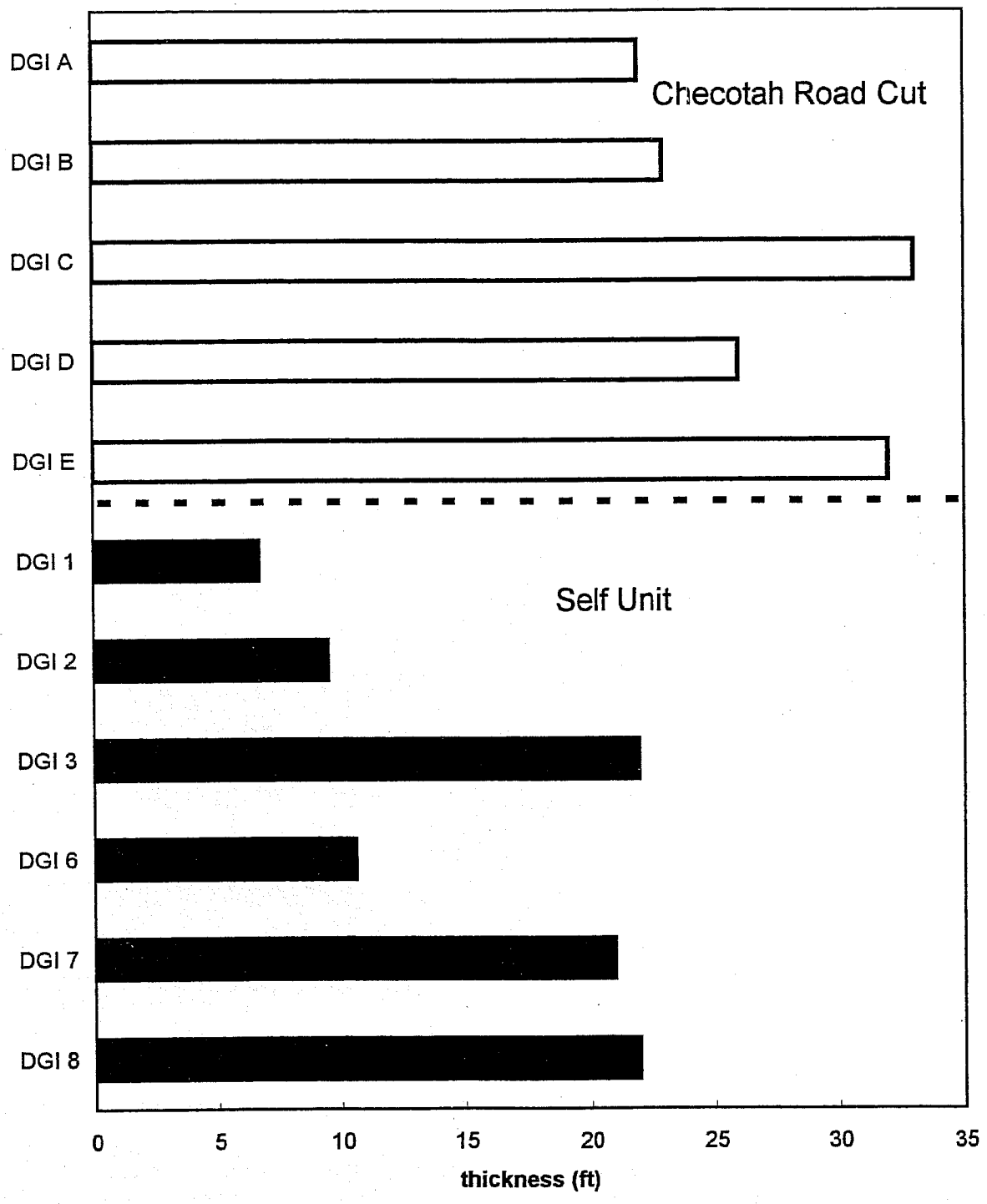

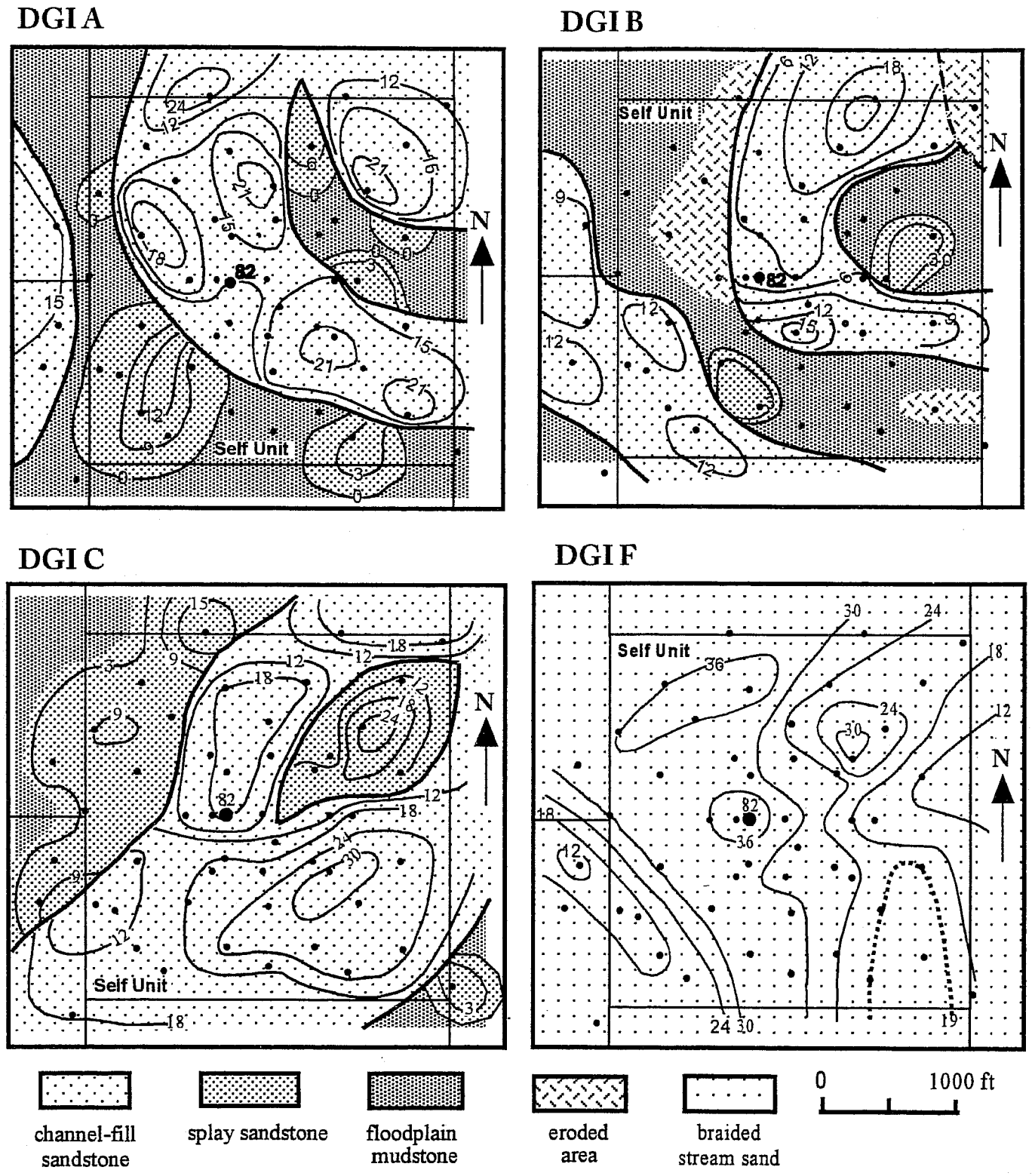

Figure 6 Net Sand Isopach and Facies Map, Self Unit

(thickness in ft)

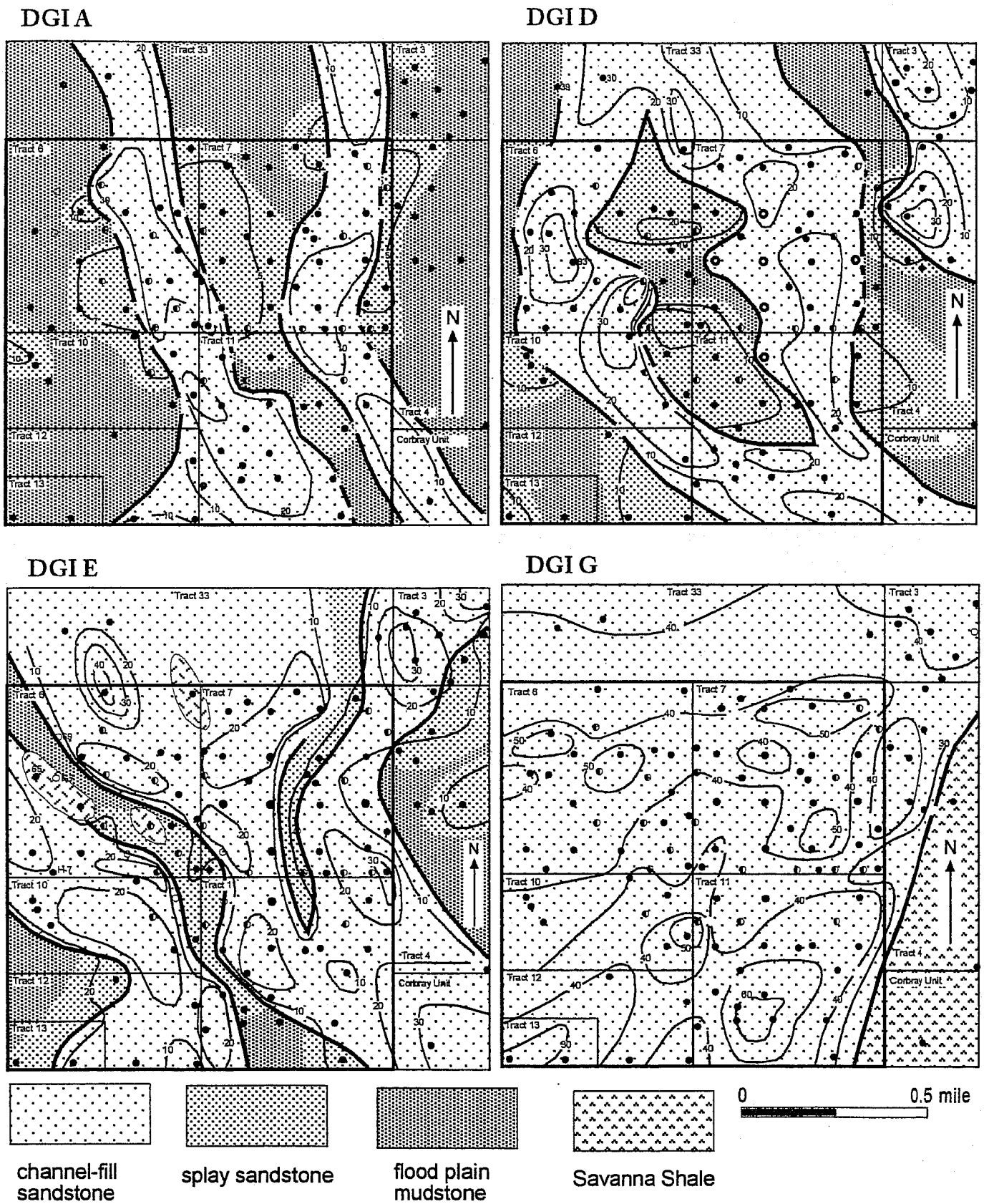

Figure 7 Net Sand Isopach and Facies Map, Tract 7 & Adjacent Areas (thickness in ft)

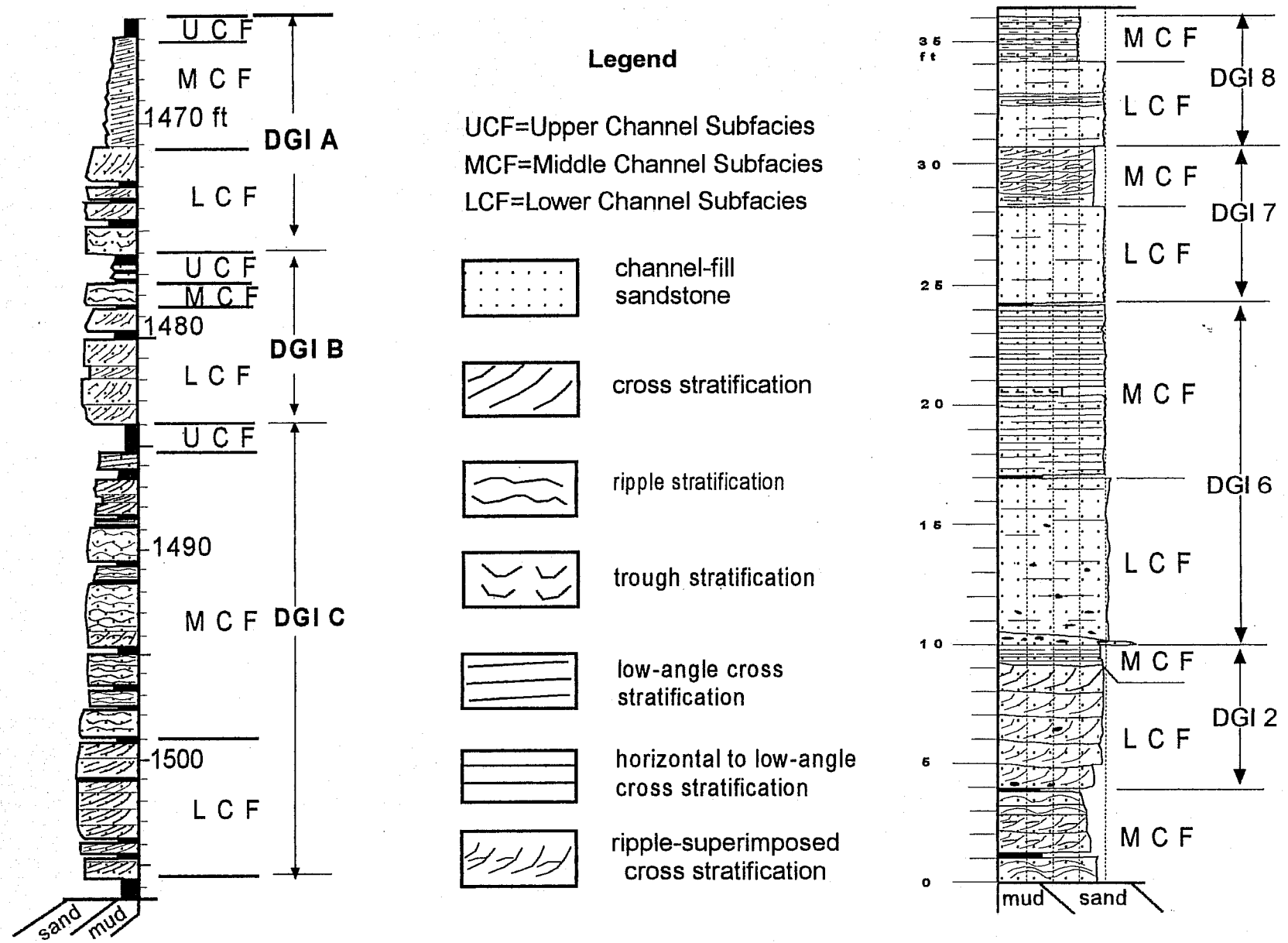

Figure 8 Sedimentological Description of Upper Part of Self 82 Glenn Sand (left) and Checotah Bluejacket Sandstone Road Cut (right)

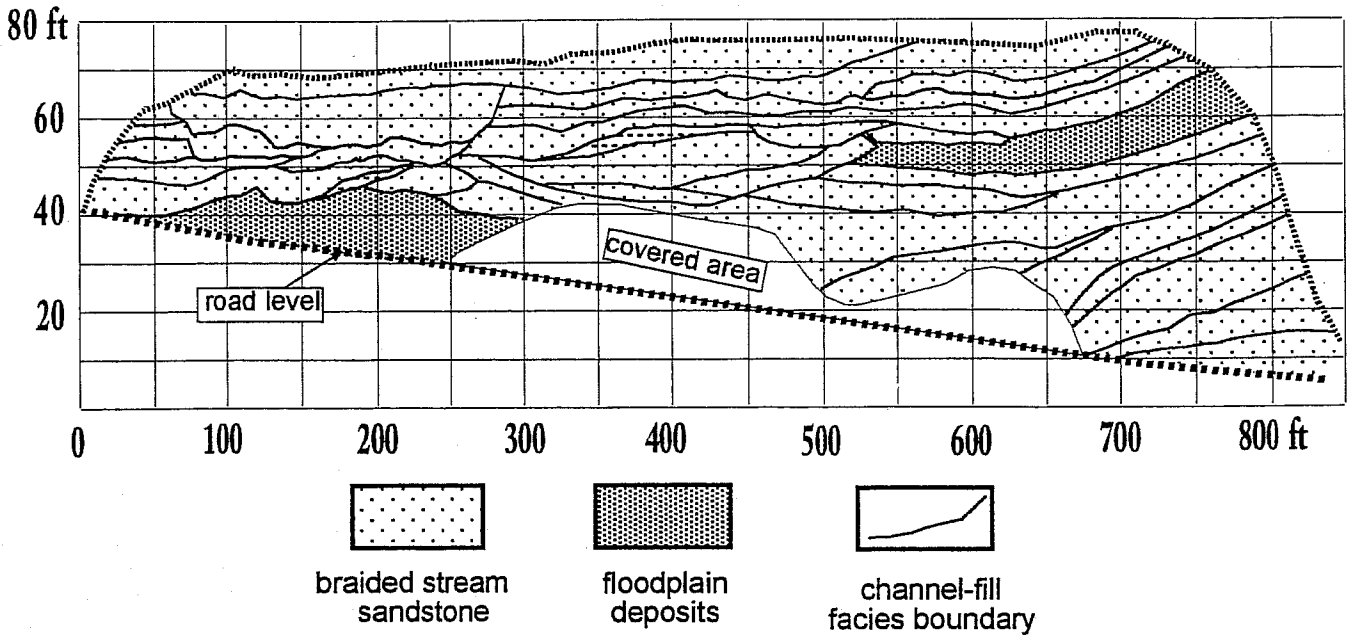

Figure 9 Distribution & Stacking Pattern of Braided Channel Deposits Surveyed on the West Leg of Eufaula Dam Cliff

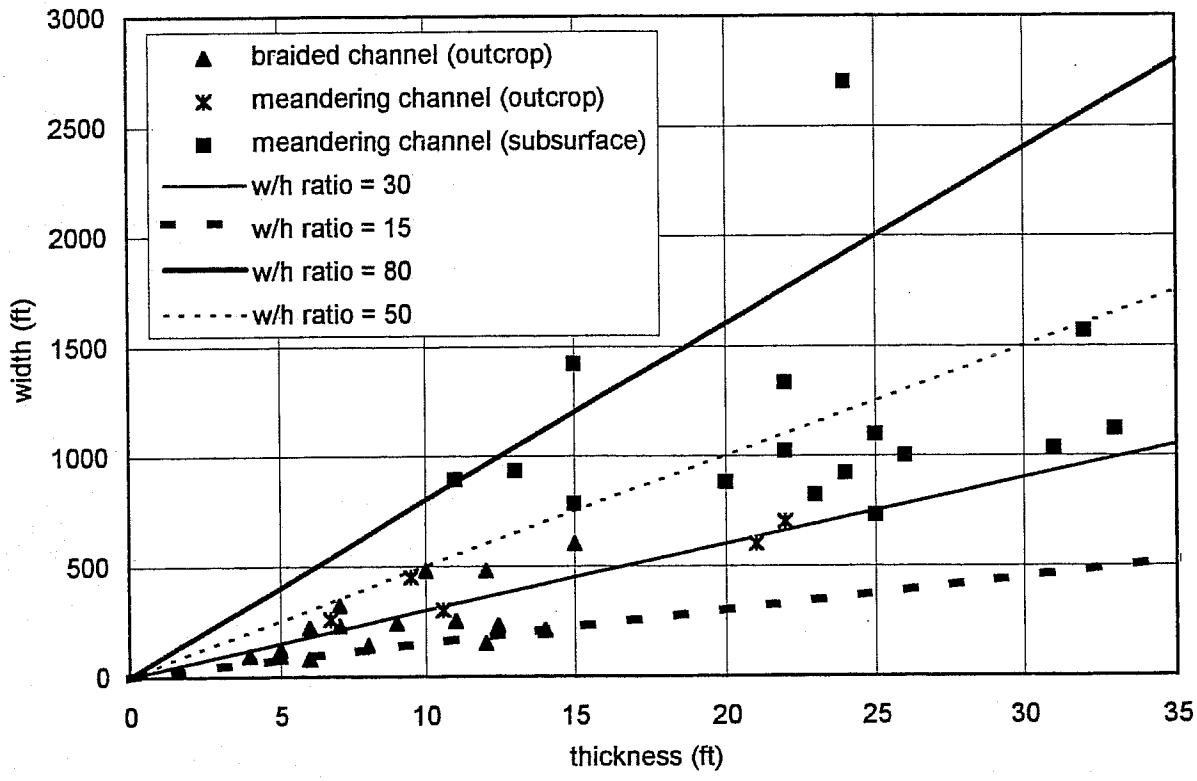

Figure 10 Channel-Fill Thickness vs. Width

Figure 11 Self 82 Core Porosity and Permeability Profile

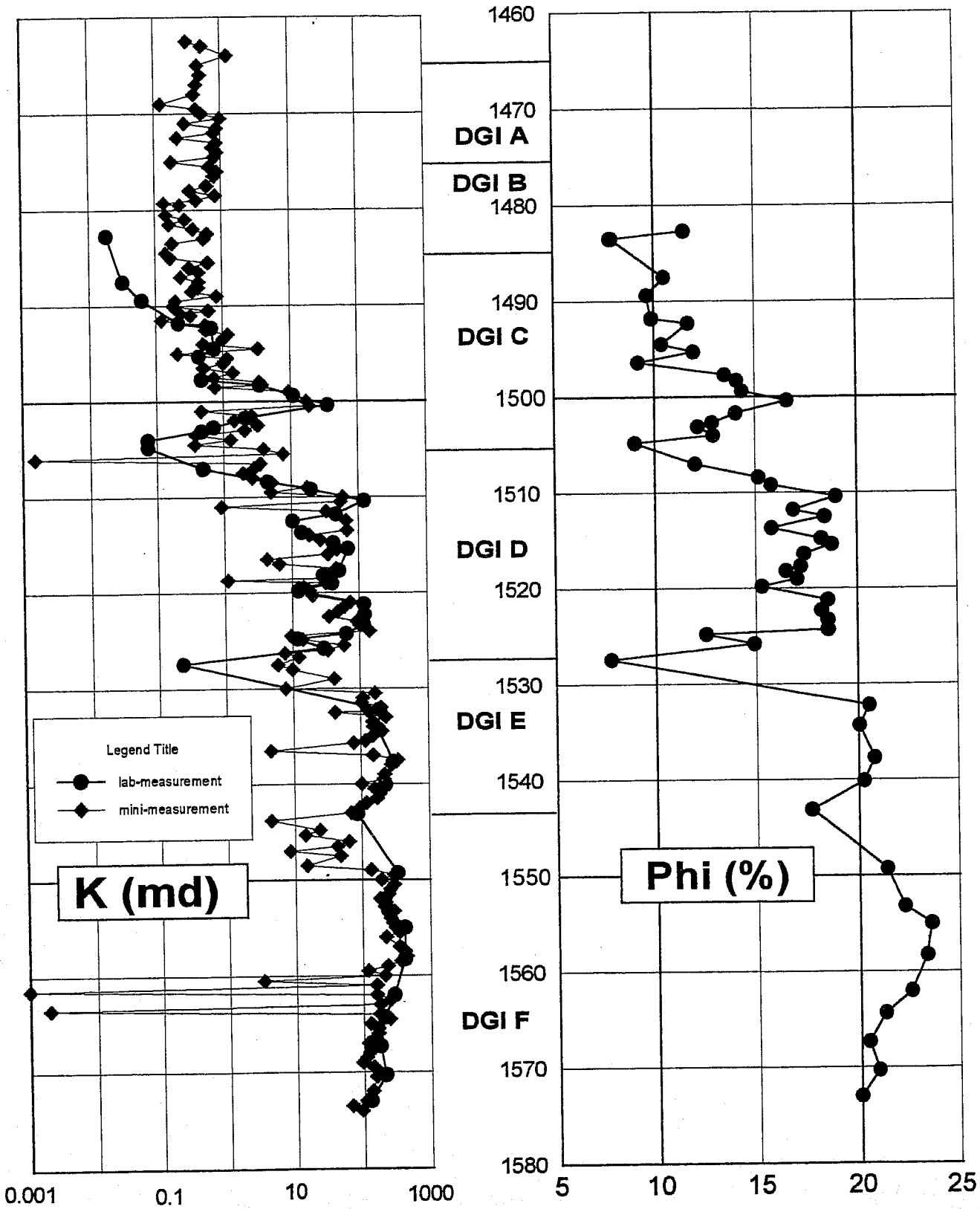

Figure 12 Kh vs. Kv for different DGIs and Facies

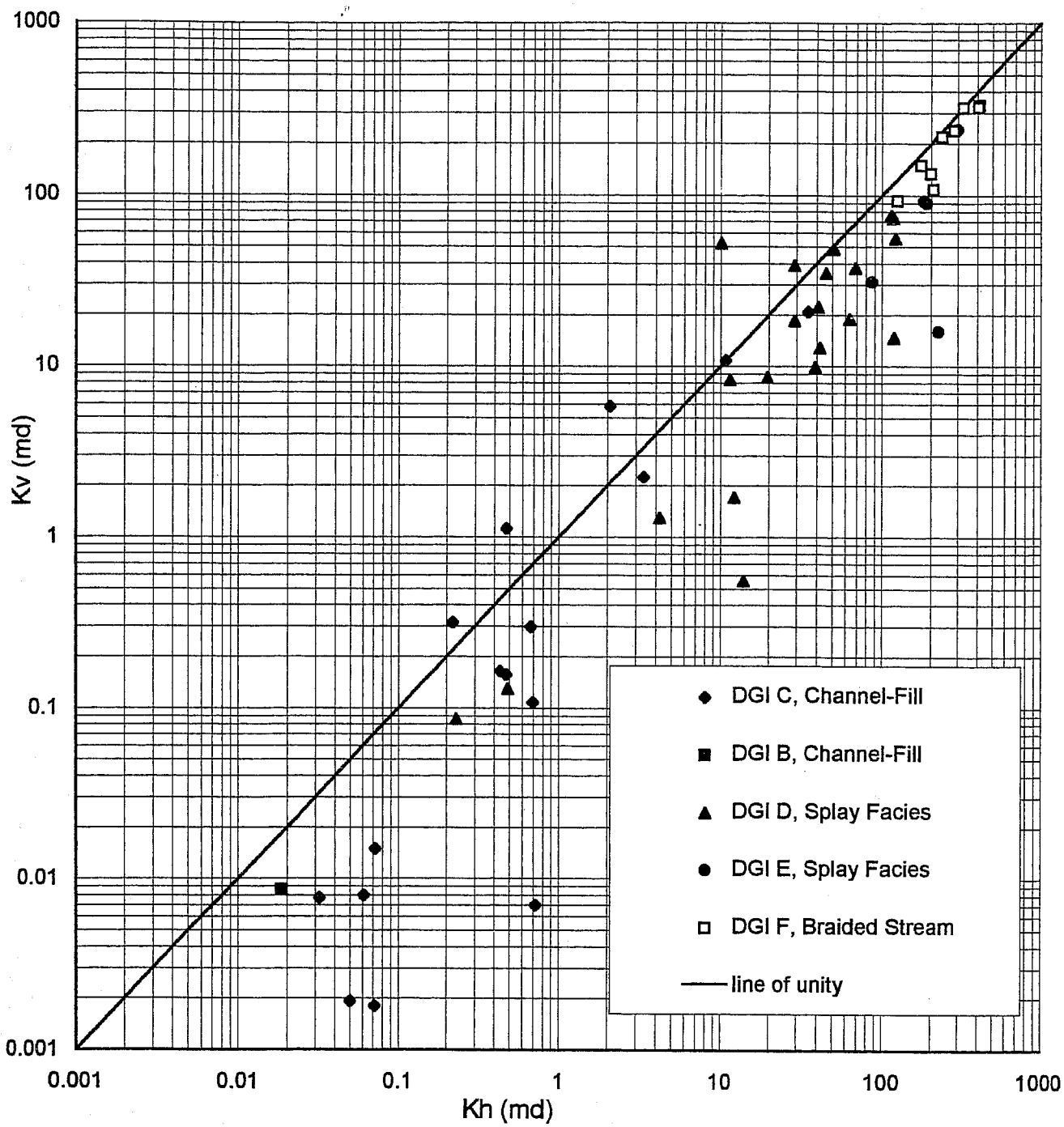

RESERVOIR COMPARTMENTALIZATION AND MANAGEMENT STRATEGIES: LESSONS LEARNED IN THE ILLINOIS BASIN

J. P. Grube, J. E. Crockett, B. G. Huff, H. E. Leetaru,
D. G. Morse, B. Seyler, and E. O. Udegbunam

A research project jointly sponsored by the U.S. Department of Energy and the Illinois State Geological Survey focused on the Cypress and Aux Vases Formations (Mississippian), major clastic reservoirs in the Illinois Basin. Results from the research showed that understanding the nature and distribution of reservoir compartments, and using effective reservoir management strategies, can significantly improve recovery efficiencies from oil fields in this mature basin. Compartments can be most effectively drained where they are geologically well defined and reservoir management practices are coordinated through unified, compartment-wide, development programs.

Our studies showed that the Cypress and Aux Vases reservoirs contain lateral and vertical permeability barriers forming compartments that range in size from isolated, interlaminated sandstone and shale beds to sandstone bodies tens of feet in thickness and more than a mile in length. Stacked or shingled, genetically similar sandstone bodies are commonly separated by thin impermeable intervals that can be difficult to distinguish on logs and can, therefore, cause correlation problems, even between wells drilled on spacing of less than ten acres. Lateral separation of sandstone bodies causes similar problems. Reservoir compartmentalization reduces primary and particularly secondary recovery by trapping pockets of by-passed or banked oil. Compartments can be detected by comparing recovery factors of genetically similar sandstone bodies within a field; using packers to separate commingled intervals and analyzing fluid recoveries and pressures; making detailed core-to-log calibrations that identify compartment boundaries; and analyzing pressure data from waterflood programs.

Petrofacies Analysis - The petrophysical tool for geologic/engineering reservoir characterization

Watney, W.L., W.J. Guy, J.H. Doveton, S. Bhattacharya, P. M. Gerlach, G. C. Bohling, T. R. Carr
Kansas Geological Survey, 1930 Constant Avenue - Campus West, Lawrence, Kansas 66047

Acknowledgments

Several grants that have supported the petrofacies project and utilized its developments over the past few years including the "Petrofacies Analysis Project" with the Kansas Technology Enterprise Corporation and industrial consortium, "Development and Demonstration of An Enhanced, Integrated Spreadsheet-based Well Log Analysis Software," Subcontract No. G4S60821 with BDM-Oklahoma and industry consortium, "Shaben Field -- Class II Field Demonstration Project, " Contract No. DE-FC22-94PC14987, and "Digital Petroleum Atlas," Contract No. DE-FG22-95BC14817, both supported by the Department of Energy.

Abstract

Petrofacies analysis is defined as the characterization and classification of pore types and fluid saturations as revealed by petrophysical measures of a reservoir. The word "petrofacies" makes an explicit link between petroleum engineers' concerns with pore characteristics as arbiters of production performance, and the facies paradigm of geologists as a methodology for genetic understanding and prediction. In petrofacies analysis, the porosity and resistivity axes of the classical Pickett plot are used to map water saturation, bulk volume water, and estimated permeability, as well as capillary pressure information, where it is available. When data points are connected in order of depth within a reservoir, the characteristic patterns reflect reservoir rock character and its interplay with the hydrocarbon column. A third variable can be presented at each point on the crossplot by assigning a color scale that is based on other well logs, often gamma ray or photoelectric effect, or other derived variables. Contrasts between reservoir pore types and fluid saturations will be reflected in changing patterns on the crossplot and can help discriminate and characterize reservoir heterogeneity.

Many hundreds of analyses of well logs facilitated by spreadsheet and object-oriented programming have provided the means to distinguish patterns typical of certain complex pore types (size and connectedness) for sandstones and carbonate reservoirs, occurrences of irreducible water saturation, and presence of transition zones. The result has been an improved means to evaluate potential production such as bypassed pay behind pipe and in old exploration holes, or to assess zonation and continuity of the reservoir.

Petrofacies analysis is applied in this example to distinguishing flow units including discrimination of

pore type as an assessment of reservoir conformance and continuity. The analysis is facilitated through the use of color cross sections and cluster analysis.

Introduction

Reservoir characterization and modeling are ongoing procedures utilized as the reservoir is developed. Well log data and occasional cores provide the fundamental stratigraphic information critical to delineating flow units, a primary objective of reservoir characterization. Flow units are correlatable and mapable regions in the reservoir that control fluid flow. Their distinction is usually centered on comparing permeability and porosity information. This classification is refined as fluid recovery, pressure data or chemical fingerprinting become available. Often times, particularly in older fields, production is commingled and cannot be used to substantiate flow units. Moreover, the costs of extensive fluid and pressure testing are not economic. The question examined here is whether the traditional definition of flow units can be modified to include additional information obtained from basic suites of well logs. An approach referred to as petrofacies analysis is described that extends the use of well logs to maximize information that relates to pore type and fluid flow. In particular, the utility of distinguishing vertical and lateral trends and patterns of irreducible bulk volume water, water saturation, and porosity is evaluated as a tool to improve the definition of flow units using well logs. Petrofacies are defined as portions of the reservoir that exhibit distinctive geological facies and petrophysical attributes.

Selecting flow units from core and log data is subjective due to judging whether reservoir conformance (interconnection) and lateral continuity exist without actual fluid flow information (Willhite, 1986). Consistent, explicitly defined steps must be developed between wells to ensure that the procedure is robust and can be repeated and improved as more information becomes available.

The initial task is correlating the reservoir interval and establishing stratigraphic subdivisions and lithofacies. Next, the correlated stratigraphic intervals are mapped with the subsurface control to test coherency of the data. At this stage, porosity and permeability data are integrated with stratigraphic units and lithofacies to define porous and permeable flow units. This information is then compared with the production and test data to check for consistency and correlations.

An intermediate step proposed here is to extract further information about pore types and fluid saturations utilizing petrofacies analysis. The analysis is based on the Pickett plot and delineation of depth-based trends and patterns in porosity, resistivity, water saturation, and bulk volume water (BVW). Thousands of analyzes of this type have demonstrated a well know fact, that porosity varies considerably due to varying pore

type and capillarity. Furthermore, the use of "rules of thumb" values for effective porosity and saturation cutoffs are inadequate to address today's needs to improve oil recovery from existing fields.

While porosity may vary little, saturations and productivity can be considerably different when pore types change. Alternatively, changes in water saturation and BVW may vary closely with elevation of the reservoir, suggesting fluid continuity and reservoir conformance as well as serving as an additional tool in evaluating lateral reservoir continuity. Added information on pore types, vertical reservoir conformance, and fluid/reservoir continuity provided by petrofacies analysis is important in assessing flow units and ensuring robust reservoir modeling.

Petrofacies analysis is used in this example to extend an initial stratigraphic analysis of a sandstone reservoir in an attempt to define flow units. The ultimate objective of this reservoir characterization will be to conduct a reservoir simulation of the field to help evaluate future production options.

Study Area

Petrofacies analysis was applied to a Lower Morrow (Lower Pennsylvanian) sandstone reservoir in Arroyo Field, Stanton County, Kansas (Township 29 South - Range 41 West)(Figure 1). Arroyo Field, operated by J.M. Huber Corporation, is a prolific field, discovered in 1992 through application of subsurface methods. Cumulative production exceeds 651,000 barrels of oil and 21 billion cubic feet of natural gas. Arroyo Field is a combination structural stratigraphic trap, currently containing 6,240 proven productive acres with 24 oil and gas wells and 3 dry holes. The field contains two reservoirs, the Lower Morrow sandstone and the St. Louis Limestone (oolite). The Lower Morrow sandstone is located at approximately 1715 m (5,400 ft) below the surface. The sandstone ranges from 0 to 19 m (0 to 60 ft) thick and is lenticular throughout the field (Figure 2). The porosity of the sandstone ranges up to 20% and averages 14%. All positions of the sandstone have been perforated in the field, some wells reported as only gross intervals. Initial reservoir pressure was 1,434 psi.

The upper portion of the sandstone has produced only natural gas and the lowest portion has produced significant amounts of both oil and gas. No water has been produced in any of the wells. Also, no oil:water contact has been recognized. The reservoir drive appears to be gas expansion.

A considerable amount of supporting data on Arroyo Field including digital well logs, completion reports, and interpretive maps, cross sections, and synthetic seismograms are included in a digital publication of this field on the Kansas Geological Survey's Digital Petroleum Atlas located on the Survey's Internet Home Page (URL=http://crude2.kgs.ukans.edu/DPA/Arroyo/arroyoMain.html).

The lenticular Lower Morrow sandstone is comprised of a series of upward-coarsening shoreface deposits that are mostly confined to within one-half mile wide meandering valley, up to 48 m (150 ft) deep (Figure 1). The sandstone was previously correlated and subdivided into five separate sandstone-dominated genetic units (1, 3, 5, 9, 11) using gamma ray, porosity, and resistivity logs and one spectral gamma ray log. Each genetic unit is delineated by bounding surfaces usually characterized by abrupt changes in lithofacies. Each genetic unit is believed to represent temporally distinct episodes deposition, i.e., a genetic unit. Only several of the genetic units are developed at any particular location in the field (Figure 2).

The sandstones were deposited in a meandering valley system. Maps of each genetic unit record episodes of infilling of this valley, each unit with varying geometries and sand abundance and quality. The lowest sandstones are more limited in distribution, filling only the lowest (deepest) portions of the valley, while the higher sandstones locally extend beyond the confines of the valley. For these reasons, the stratigraphic distribution was believed to be a controlling factor on flow unit definition.

Methodology

Volumetric properties of pore space and fluid saturation can be calculated from porosity logs (density, neutron, or sonic) and resistivity logs using the standard Archie equations. When plotted on a double-logarithmic plot of porosity versus resistivity (a "Pickett plot"), additional information on pore size and fluid producibility may be deduced by the use of pattern recognition informed by basic reservoir engineering principles. A "template" Pickett plot is shown in Figure 3 for the Upper Morrow in the Arroyo Field. A "water line" (Ro) expresses the theoretical resistivity-porosity coordinates of all zones that are completely saturated with water. The water line is established by the first Archie equation that links the "formation factor". F (the ratio of the resistivity of the completely water-saturated rock, Ro, to the resistivity of the formation water, Rw) to the porosity of the rock:

$$F = R_o/R_w = a/phi^m$$

using an Arroyo Field formation water resistivity, Rw, of 0.04 ohm-m and Archie parameter values of a=1 and m=1.8, which express pore geometry in the Morrow sandstone. Contours for different values of water saturation parallel the water line, with a spacing determined by the saturation exponent, n (generally with a value of about 2 in water-wet rocks) in the second Archie equation:

$$I = R_t/R_o = 1/Sw^n$$

where I is the "resistivity index" and Rt is the actual resistivity of the rock. Lines can also be drawn on the plot that are contours of bulk volume water (BVW), where water content is expressed as a proportion of the total rock, rather than in terms of the pore space as is the case with saturation.

The disposition of crossplotted zones with respect to the log axes of resistivity-porosity and the computed reference axes of water saturation and bulk volume water (BVW) gives useful clues on both pore type and producibility. These properties can be seen when relating Pickett plots to production histories (Figure 3) from some example wells in the Arroyo Field. Notice how overall well performance is determined to a large extent by higher porosities and lower water saturations. However, the location of the data-cloud with respect to the BVW contours reflects the pore size and likely water-cut. Lower values of BVW are matched with coarser pores; higher values of BVW are linked with either finer pores and/or zones with coarse pores and producible water. In terms of data-cloud shape, a classic reservoir profile would show zones high in the reservoir at "irreducible" water saturation and relatively low BVWs with a progressive increase in bulk volume water with increasing depth and descent into the transition zone. Some aspects of this ideal character are shown in the plots in Figure 4, where the four wells have been arranged from most productive at the top to least productive at the bottom. Notice that the bottom example was not completed for production, but abandoned because a DST yielded nothing but salt water. The associated Pickett plot shows a rather ragged scatter of mostly low-porosity zones with high water saturations that probably reflect residual hydrocarbon saturations. This pattern is common at the margins of fields as is this well and contrasts with an idealized situation far away from fields where zones are completely water-saturated and form a trend on a Pickett plot that conforms closely to the water line(Ro).

The Pickett (porosity-resistivity) cross plots are the fundamental components in the petrofacies analysis. The connection of data points by depth and the ability to annotate the data points with a third variable help establish relationships between the petrophysical response and the geology -- lithologies, stratigraphic units, and structure, i.e., the petrofacies. Template lines identify minimum BVW and associated water saturations and porosities on the Pickett plot. This, in turn, helps to correlate the geology to fluid-related parameters and delineate specific changes in fluids and variations in the pores between the different wells.

The definition of flow units might be refined to include regions of similar/related BVW and pore type using the petrofacies analysis. Often, permeability data are either lacking or are limited to averaging from core-log porosity and permeability correlations. In these cases, assessment of pore type using petrofacies analysis may help to provide novel constraints to flow units, lacking other substantial data. Of course, production and transient test data and geochemical tests are necessary to more definitively constrain the definition of flow units.

A west-to-east cross section was chosen to further characterize the sandstone reservoir using the petrofacies analysis approach (Figure 2). The cross section crosses the valley in two places, separated by a intervening high area.

The questions addressed in this analysis include 1) Is additional evidence available to confirm or reject the continuity of sandstones across the intervening high region residing between the valleys? 2) What is the evidence of vertical conformance and lateral continuity? 3) How do properties of the sandstones compare on either side of the valley? 4) Can the definition of flow units be improved? 5) How do the flow units compare with the detailed stratigraphic subdivisions?

In addition to the stratigraphic analysis, the procedure included three operations 1) construct Pickett plots for each of the wells on the cross section, 2) perform a cluster analysis of basic petrophysical data to independently define similar reservoir properties, 3) prepare a series of color cross sections of selected petrophysical variables with datums on sea level elevation and a stratigraphic marker (Middle Morrow limestone located above the sandstone), and 4) integrate this information to define flow units -- compare with stratigraphic zonation, Pickett plots, color log cross sections, cluster analysis, and well productivities.

Results

The digital data from five well logs comprising an west-to-east cross section in Arroyo Field were examined utilizing petrofacies analysis. The standard well log cross section was shown earlier in Figure 2. The objective was to compare well data on the cross section to test for evidence of lateral continuity. The cross section would suggest that some of the units are continuous. Units that are not shown as continuous may also be connected from outside of the plane of the cross section.

Pickett plots

LAS (log ascii standard) digital well log files were read into an Excel-Visual Basic program called PfEFFER to generate the Pickett cross plots. The initial Pickett cross plots provide a visual differentiation of the variation in the porosity, resistivity, water saturation, and bulk volume water. Permeability lines are annotated on the crossplots, estimated using empirical relationship between water saturation and porosity developed by Timur. The relationship holds for clean sandstones when water saturations are at irreducible values. We believe that to be the case here.

The crossplot with points annotated with gamma ray values indicate that points with higher gamma ray

values are located on the left side of the crossplot at BVWs in excess of 0.06 (Figure 5). This location presumably represents more shaly and finer pores. The permeability lines are not applicable to these points.

The reservoir has no water leg and no water has been produced. The points are annotated by stratigraphic interval and form rather tight clusters or bands for each stratigraphic unit (Figure 6). The clustering of points in distinct stratigraphic intervals and accompanying lower water saturations suggest that these zones are near their respective minimum BVWs. Also, the bands of points closely correspond to particular stratigraphic zones. Also, the bands parallel water saturation lines. This pattern is ascribed to changing minimum BVW and pore size within a zone. These relationships have implications to fluid flow. If any portions of the reservoir were in a gas or oil:water transition zone, the bands of points may have more likely paralleled porosity lines, if the pore type was not changing. However, this is not seen and no wells have experienced any water-cut oil or gas production.

The interwell comparison of the clusters and bands for each stratigraphic interval easily illustrate changes and similarities. The variations suggest possible changes in pore type and evidence for reservoir continuity or lack thereof.

Cluster Analysis

Some the boundaries between stratigraphic units involve sand on sand and may not present barriers to flow, but changes in transmissibility. Also, the internal variability in sandstone units may present further heterogeneity that can retard fluid flow. Cluster analysis was used to examine the similarity among petrophysical data. The method provides a consistent automated treatment of the data to aid in comparing considerable amounts of data among the zones and wells. Ward's Method was selected as the clustering technique. The method consists of a series of clustering steps that begins with "t" clusters each containing one object. The clustering ends with one cluster containing all objects. At each step, a merger of two clusters is made that results in the smallest increase in the variance (Romesburg, 1984).

The petrophysical variables included in the cluster analysis are gamma ray, deep induction resistivity, Pe, water saturation, BVW, and apparent permeability using the Timur equation,

$$ka = 1x10^4 * phi^{4.5}/Sw^2.$$

This apparent permeability is a minimum estimate when Sw is greater than irreducible Sw. Phi (porosity) and Sw are fractional values in this equation. Shaly intervals were assigned to zero permeability (removing depth intervals where gamma ray exceeded 60 API units and neutron minus density porosity was

greater than one). Depth was also included within the cluster analysis as an adjacency constraint to enhance spatial continuity.

Six separate agglomeration of points were selected from the cluster analysis of each well. Several criteria were used to determine this number. First, the number is not large so as to produce too many groups and thus probably complicate reservoir modeling. Second, the cluster dendrogram for each well show good separation of groups at this level. Third, the number is comparable to the stratigraphic divisions and might show useful groupings and comparison.

The assigned groupings derived from cluster analysis were first compared by depth with the petrophysical data and stratigraphic zonation. The boundaries between the stratigraphic intervals and the cluster assigned groupings generally coincide. The clustering identified a moderate amount of smaller scale heterogeneity within each stratigraphic interval (Figure 7). However, the general finding is that each stratigraphic interval is dominated by only one or two assigned cluster groupings.

The posting of assigned cluster groups as an attribute on the Pickett plot further indicates a close correspondence between stratigraphic units and assigned cluster grouping, e.g., Figure 8. The cluster analysis can be adapted in the spreadsheet environment to help facilitate consistent, rapid assignment of cluster groups and further aid in flow unit assessment.

Color Cross Sections

Flow units are assigned to zones in the reservoir with similar permeability and porosity and which also exhibit some degree of lateral continuity. Flow units are inferred to control fluid flow and confirmation is sought to substantiate these units. Petrophysical variation within individual well profiles has been described up to this point, focused on vertical conformance. The question remains as to the extent of lateral continuity. Flow units may not be everywhere present, but are anticipated to be correlatable in the field to some degree. This continuity is ultimately established using petrophysical data, fluid recovery, pressure and fluid chemistry. The suites of petrophysical variables including BVW can be used to evaluate laterally continuity. Continuous trends or constancy of properties of the sandstone and correlations with structural elevation suggest possible fluid continuity in the reservoir.

Computer-assisted generation of color cross sections based on original digital well log sampling of 0.16 m (0.5 ft) provides the means to observe and evaluate detailed subtle changes in reservoir character and substantially assist in assessing continuity and assigning flow units. The cross sections are generated with a

elevation (subsea) or stratigraphic datum.

Cross sections for key petrophysical parameters were generated including gamma ray, permeability calculated with the Timur equation (apparent permeability filtered on gamma ray and neutron-density shale indicators), Pe (photoelectric effect) from the Lithodensity log, porosity, water saturation, BVW, and deep induction resistivity. Each petrophysical variable is presented as a structural and stratigraphic cross section placed side by side, the later with a datum at the top of the Middle Morrow limestone. Stratigraphic units are identified and correlated. Perforated intervals are shown alongside each well profile.

The five wells in the cross section are perforated in two distinct intervals, a lower interval restricted to stratigraphic unit #1 in the Lauman 28-1 and Kendrick 22-1. Also, the lowest part of unit #3 in the Santa Fe 2-21 is suggested to be part of the lower interval and may possibly be recorrelated with unit #1.

The lower interval produces significant amounts of oil and gas. The upper perforated interval includes stratigraphic units #3, #5, #9, and #11. The upper interval produces natural gas and minor amounts of oil from the Santa Fe 2-11 and Santa Fe 2-22. This difference suggests that the reservoirs are separate. The lower and upper sandstones are isolated by a prominent shaly interval according to the gamma ray and photoelectric logs (Figure 9).

On closer inspection of the gamma ray cross section, the stratigraphic units can be distinguished with the help of the correlation lines. However, there is considerable variation in the internal properties of the stratigraphic units (Figure 9). This variation persists in the other parameters. The stratigraphic units generally appear to delineate most of the petrophysical variation except for several possible re-correlations. These recorrelations are based on further analysis.

Porosity varies from 15 to 20% in the Lauman well to 0-8% in the Kendrick (Figure 10). Apparent permeability calculated from the Timur equation and filtered on gamma ray and neutron shale indicators shows considerable changes on the cross section (Figure 11). The permeability and porosity are both higher on the west. Permeability ranges between 10 and 100 millidarcies (md) in the Lauman 28-1 on the west side to 0.1 to 1 md in the Kendrick 22-1 on the east side.

High permeability and porosity correlate well with a trend of increased natural gas production and decreased oil production in the Lauman 28-1 with 2.5 billion cubic feet of gas and 75,000 barrels of oil. In comparison, the Kendrick 22-1 well on the east and lowest side of the cross section recovered less gas, one billion cubic feet, but more oil, over 120,000 barrels. Permeability varies considerably in thin streaks near the base of the Kendrick 22-1 well. Unit #1 is separated from the overlying sandstones by a thicker shaly interval.

Unit #3 is also thick in the paleovalleys on either side of a central high. Santa Fe #2-21 is perforated in the basal part of a thin sandstone that is in close proximity to the lower interval, unit #1. This zone in Santa Fe 2-21 has produced 12.7 million m^3 (450 million ft^3) of gas and nearly 50,000 barrels of oil. Production values are less than Lauman and Kendrick, but the mixed production is similar to the recoveries noted in unit #1, suggesting that they are a common reservoir in the deeper portions of the paleovalleys.

Production from perforations in the upper interval in Santa Fe 21-1 and Santa Fe 22-2 are notably different. Santa Fe 21-1 has realized 16.1 million m^3 (570 million ft^3) of gas from the upper zone and has been declining relatively rapidly to 1 million cubic feet per month. In contrast, the Santa Fe 22-2 well has produced nearly three times more gas at 1.8 billion cubic feet and its production has declined to only 0.51 million m^3 (18 million ft^3) per month. Both wells have produced for nearly 3 years at the time the production figures were reported.

Conclusions

The stratigraphic units serve as adequate means to classify flow units in this reservoir with added refinements using petrofacies analysis. Petrofacies analysis utilizes Pickett plots to decipher reservoir properties of each stratigraphic unit. Cluster analysis provide as consistent means to further delineate reservoir properties. The boundaries of the clustered groups are commonly those of the stratigraphic units. The clustered groups provide further subdivisions of the reservoir rock that could be used to classify finer-scale flow units. Color cross sections further substantiate the use of the stratigraphic divisions as basic templates for distinguishing flow units. The color cross sections are a representative of the original digitized well log data and provide the means to precisely subdivide the stratigraphic units. The petrofacies analysis should be useful in future considerations when evaluating improved petroleum recovery options.

References Cited

Romesburg, H.C., 1984, Cluster Analysis for Researchers: Belmont, California, Lifetime Learning Publications, 334 p.

Willhite, G.P., 1986, Waterflooding: SPE Textbook Series Volume 3: Richardson, Texas, Society of Petroleum Engineers, Richardson, 326 p.

Figure Captions

Figure 1. Index map of Arroyo Field identifying cross section (Figure 2). Map include (a) with well names and (b) an isopachous map of the Lower Morrow interval (top Middle Morrow limestone to top Mississippian).

Figure 2. West-to-east stratigraphic well log cross section through Arroyo Field containing Lauman 28-1, Santa Fe 21-1, Santa Fe 22-1, Santa Fe 22-2, and Kendrick 22-1. Datum of section is Middle Morrow limestone. Correlated stratigraphic intervals are correlated through the Lower Morrow sandstone interval. Line of cross section is shown on Figure 1.

Figure 3. A "template" Pickett plot for the Upper Morrow sandstone in Arroyo Field.

Figure 4. Pickett plots and corresponding production histories for the Upper Morrow sandstone in Arroyo Field.

Figure 5. Pickett plot of Lower Morrow sandstone in the Santa Fe 22-1 annotated with gamma ray.

Figure 6. Pickett plot of Lower Morrow sandstone in the Santa Fe 22-1 annotated with stratigraphic units shown in type log in Figure 2.

Figure 7. Display of well log suite from the Santa Fe 22-1 well accompanied by derived information including water saturation (SW), bulk volume water (BVW), permeability derived from Timur equation (Timur k), stratigraphic units, and amalgamation groups from cluster analysis.

Figure 8. Pickett plot of Lower Morrow sandstone in the Santa Fe 22-1 annotated with amalgamation groups from cluster analysis.

Figure 9. East-to-west gray-level versions of color cross section depicting gamma ray variation across Arroyo Field. The section includes same wells as Figure 2, except direction is reversed. Left cross section is a structural version with a sea-level datum and right cross section is a stratigraphic cross section with a datum on the top of the Middle Morrow limestone overlying the Lower Morrow sandstone.

Figure 10. East-to-west gray-level versions of a color cross section depicting porosity variation across Arroyo Field. The section includes same wells as Figure 2, except direction is reversed. Left cross section is a structural version with a sea-level datum and right cross section is a stratigraphic cross section with a datum on the top of the Middle Morrow limestone overlying the Lower Morrow sandstone.

Figure 11. East-to-west gray-level versions of a color cross section depicting permeability variation across Arroyo Field. The section includes same wells as Figure 2, except direction is reversed. Left cross section is a structural version with a sea-level datum and right cross section is a stratigraphic cross section with a datum on the top of the Middle Morrow limestone overlying the Lower Morrow sandstone.

Fig. 1

a)

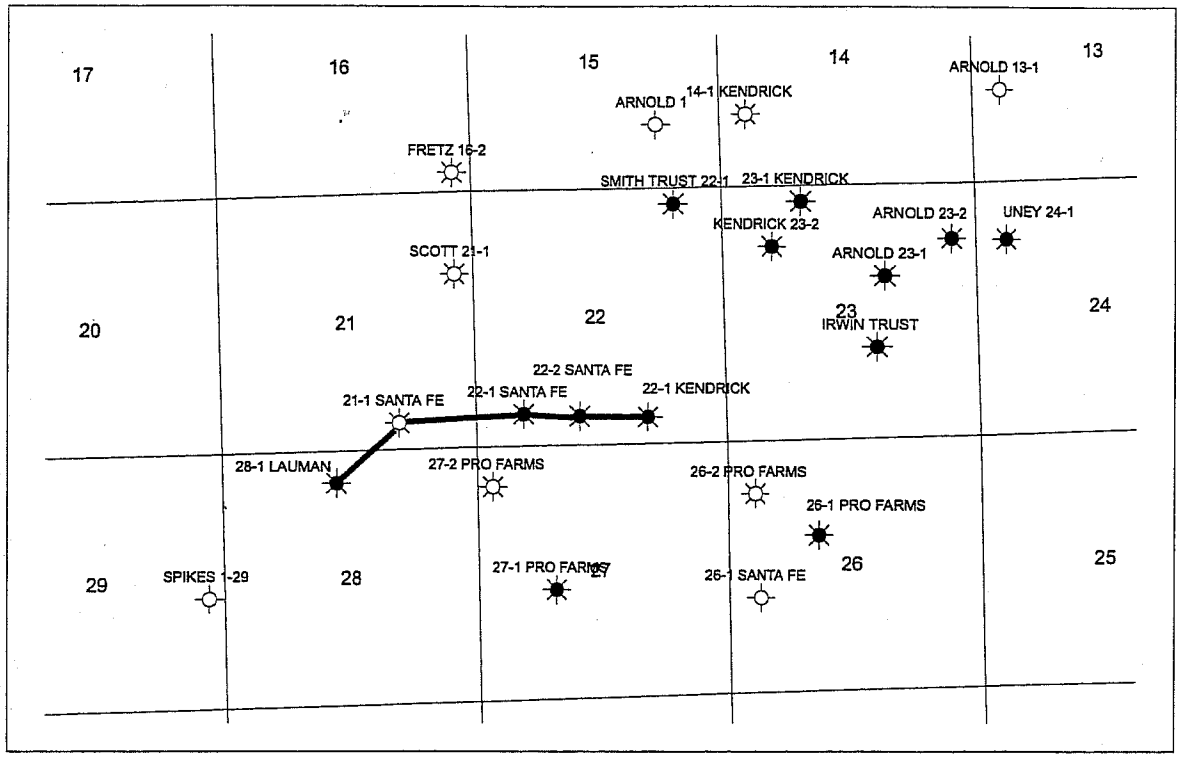
17
16
15
14
13
ARNOLD 13-1
ARNOLD 1
14-1 KENDRICK
FRETZ 16-2
SMITH TRUST 22-1
23-1 KENDRICK
KENDRICK 23-2
ARNOLD 23-2
UNEY 24-1
SCOTT 21-1
ARNOLD 23-1
20
21
22
23
IRWIN TRUST
24
22-2 SANTA FE
21-1 SANTA FE
22-1 SANTA FE
22-1 KENDRICK
28-1 LAUMAN
27-2 PRO FARMS
26-2 PRO FARMS
26-1 PRO FARMS
29
SPIKES 1-29
28
27-1 PRO FARMS
27
26-1 SANTA FE
26
25

b)

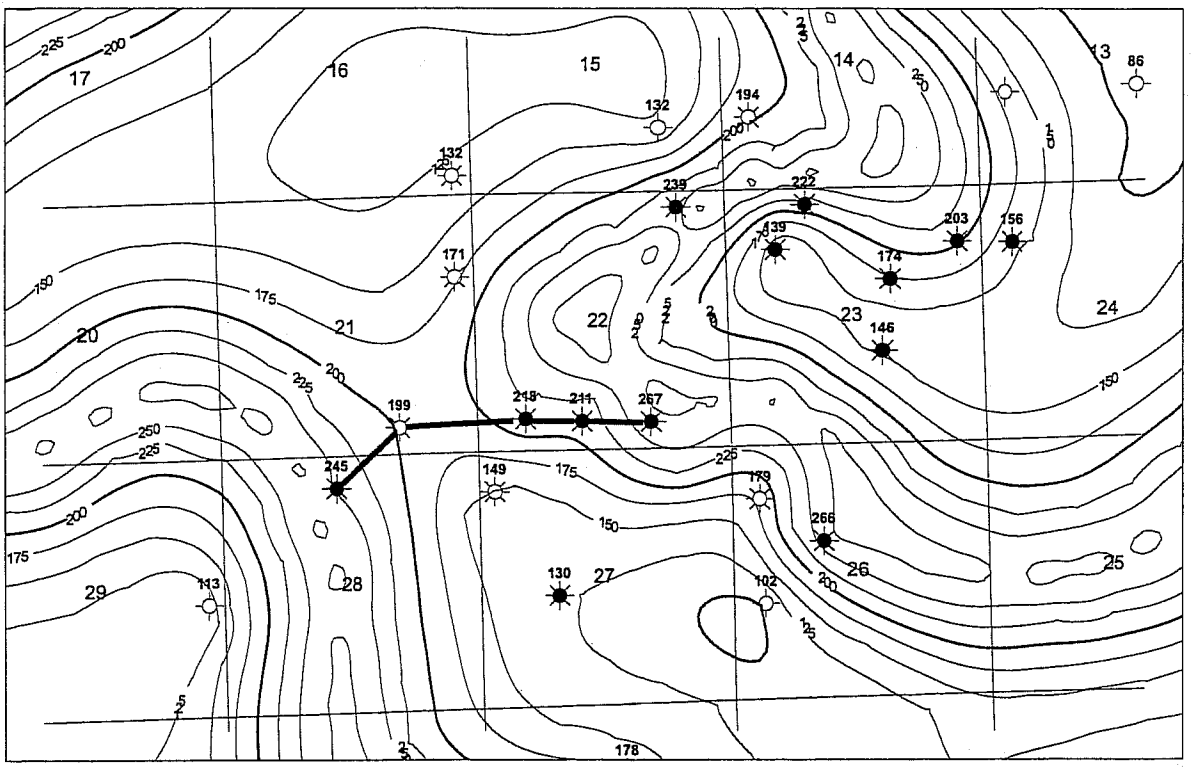
17
16
15
14
13
86
132
194
132
239
222
203
156
171
139
174
20
21
22
23
24
146
199
218
211
267
245
149
179
266
29
143
28
130
27
102
26
25
178

Fig. 2

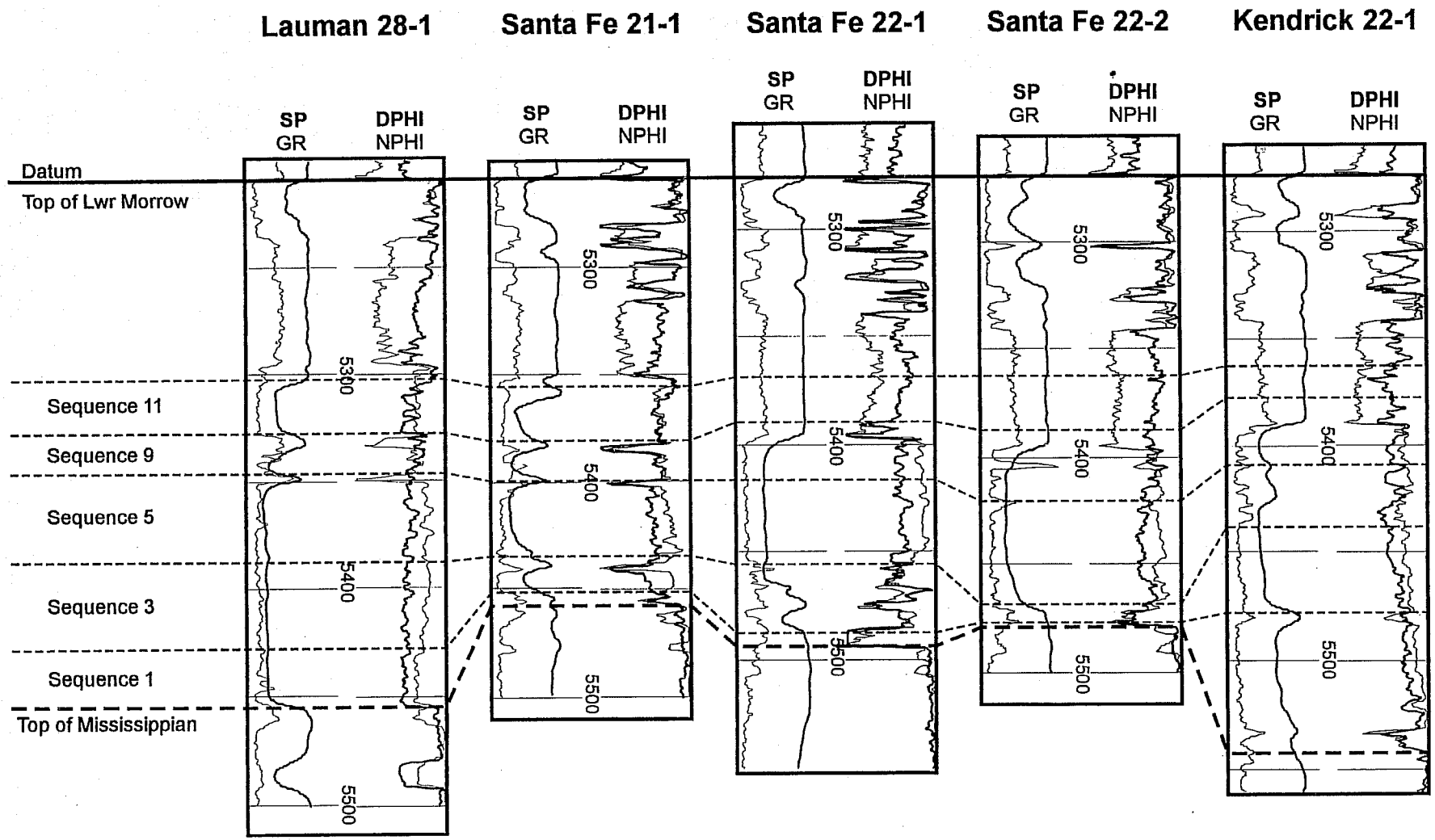
Lauman 28-1
Santa Fe 21-1
Santa Fe 22-1
Santa Fe 22-2
Kendrick 22-1
SP
GR
DPHI
NPHI
Datum
Top of Lwr Morrow
Sequence 11
Sequence 9
Sequence 5
Sequence 3
Sequence 1
Top of Mississippian
5300
5400
5500

Fig. 3

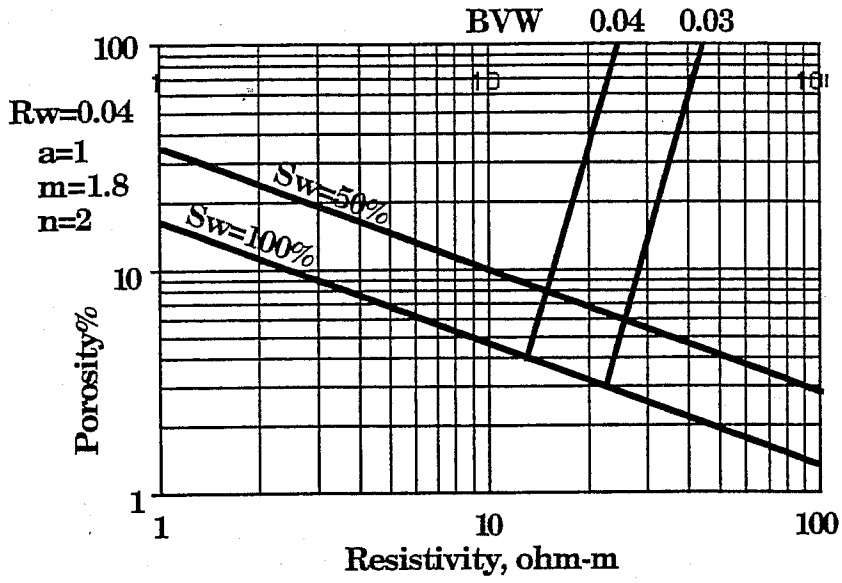
BVW
0.04
0.03
100
10
1
Rw=0.04
a=1
m=1.8
n=2
Sw=50%
Sw=100%
Porosity%
1
10
100
Resistivity, ohm-m

Fig. 4

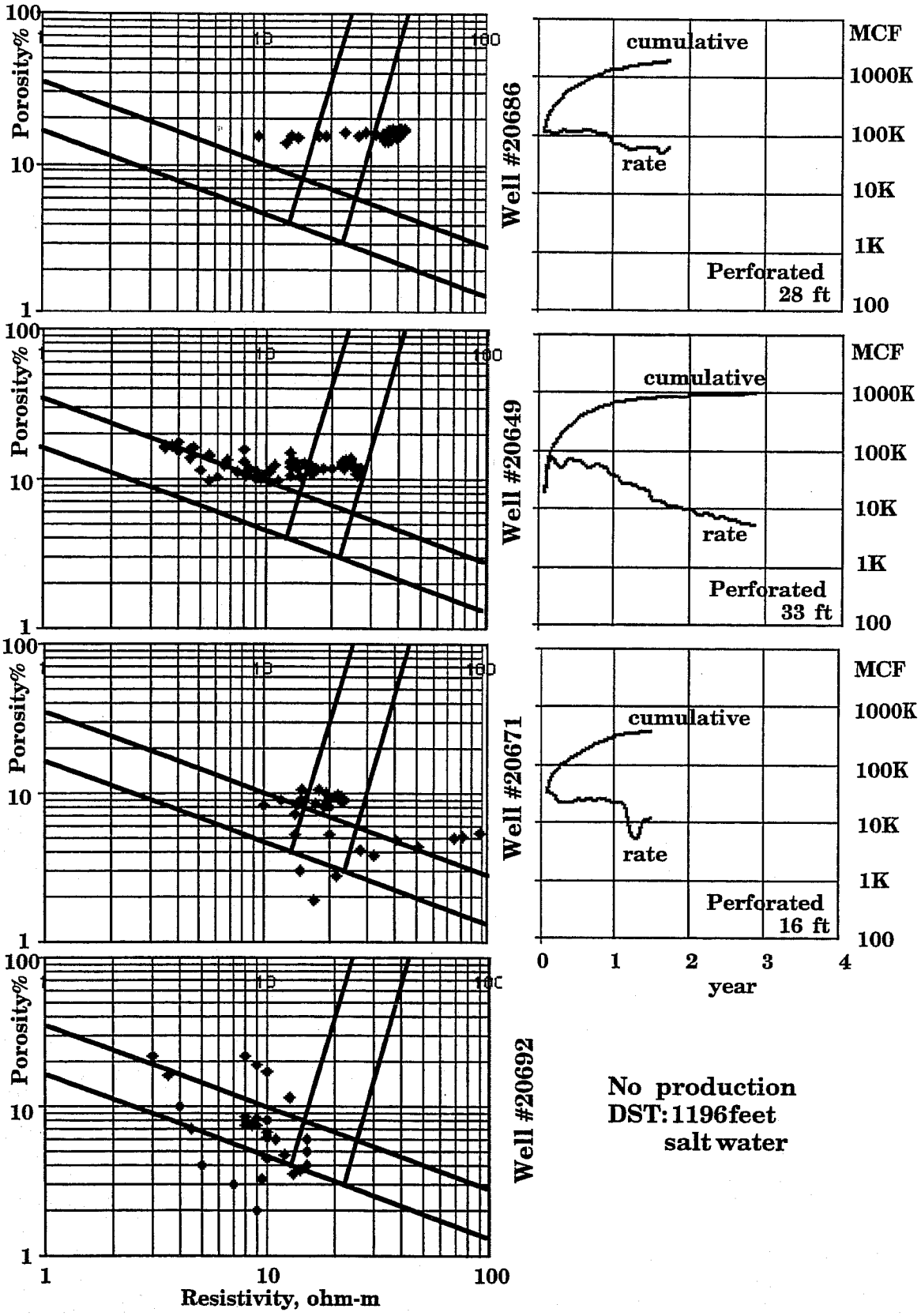
Porosity%
100
10
1
Well #20686
Well #20649
Well #20671
Well #20692
cumulative
rate
MCF
1000K
100K
10K
1K
100
Perforated 28 ft
Perforated 33 ft
Perforated 16 ft
0
1
2
3
4
year
No production
DST: 1196feet
salt water
Resistivity, ohm-m

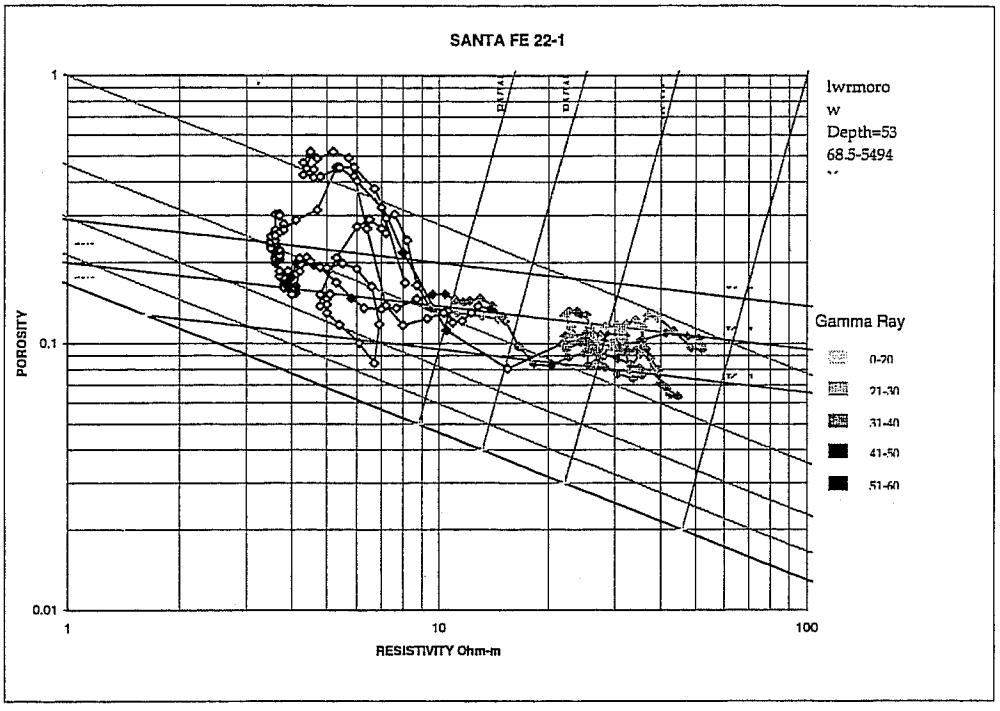
SANTA FE 22-1
lwrmoro
w
Depth=53
68.5-5494
Gamma Ray
0-20
21-30
31-40
41-50
51-60
POROSITY
1
0.1
0.01
1
10
100
RESISTIVITY Ohm-m

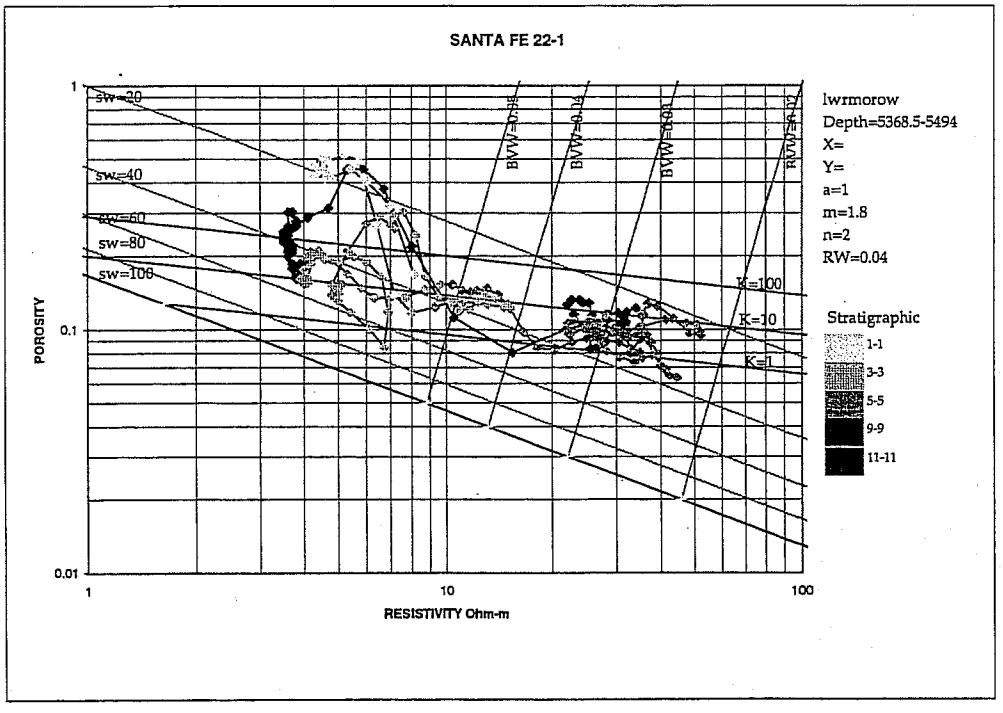
SANTA FE 22-1
lwrmorow
Depth=5368.5-5494
X=
Y=
a=1
m=1.8
n=2
RW=0.04
sw=20
sw=40
sw=60
sw=80
sw=100
K=100
K=10
K=1
Stratigraphic
1-1
3-3
5-5
9-9
11-11
POROSITY
1
0.1
0.01
1
10
100
RESISTIVITY Ohm-m

WELL: SANTA FE 22-1
FILE: D:\PFEFFER2\ARROYO\CROSSS-1\22-1SANT\20640-B.TXT

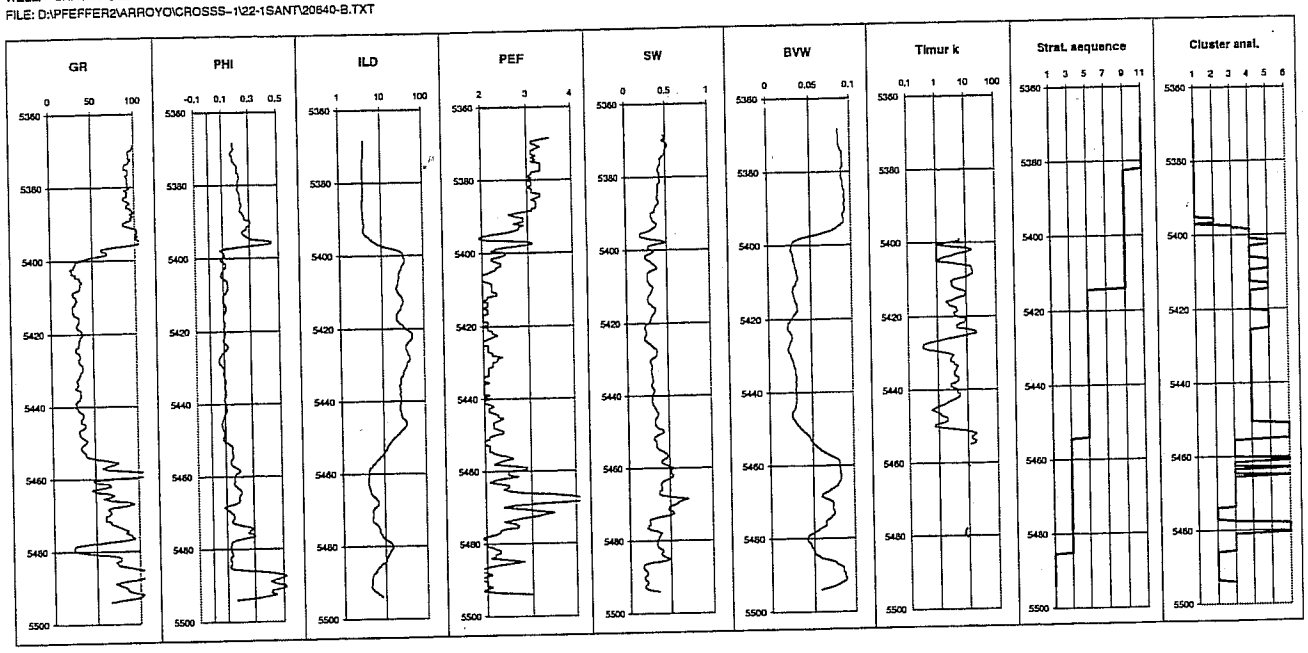

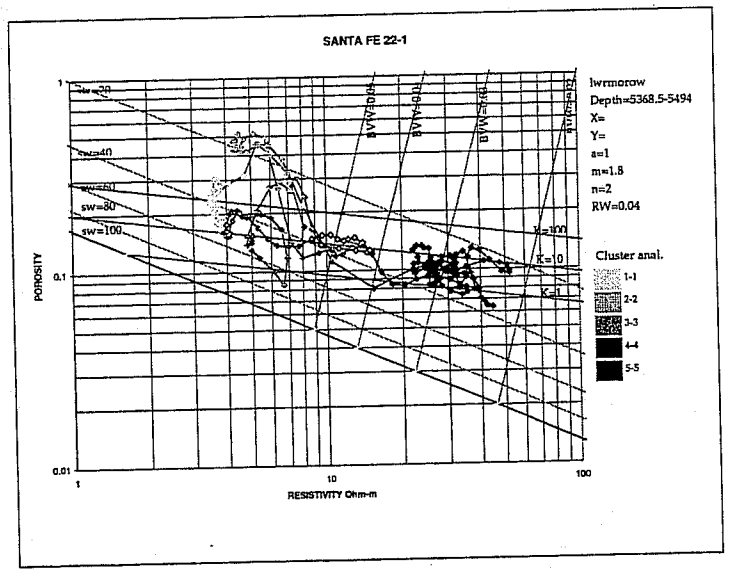

Fig. 9

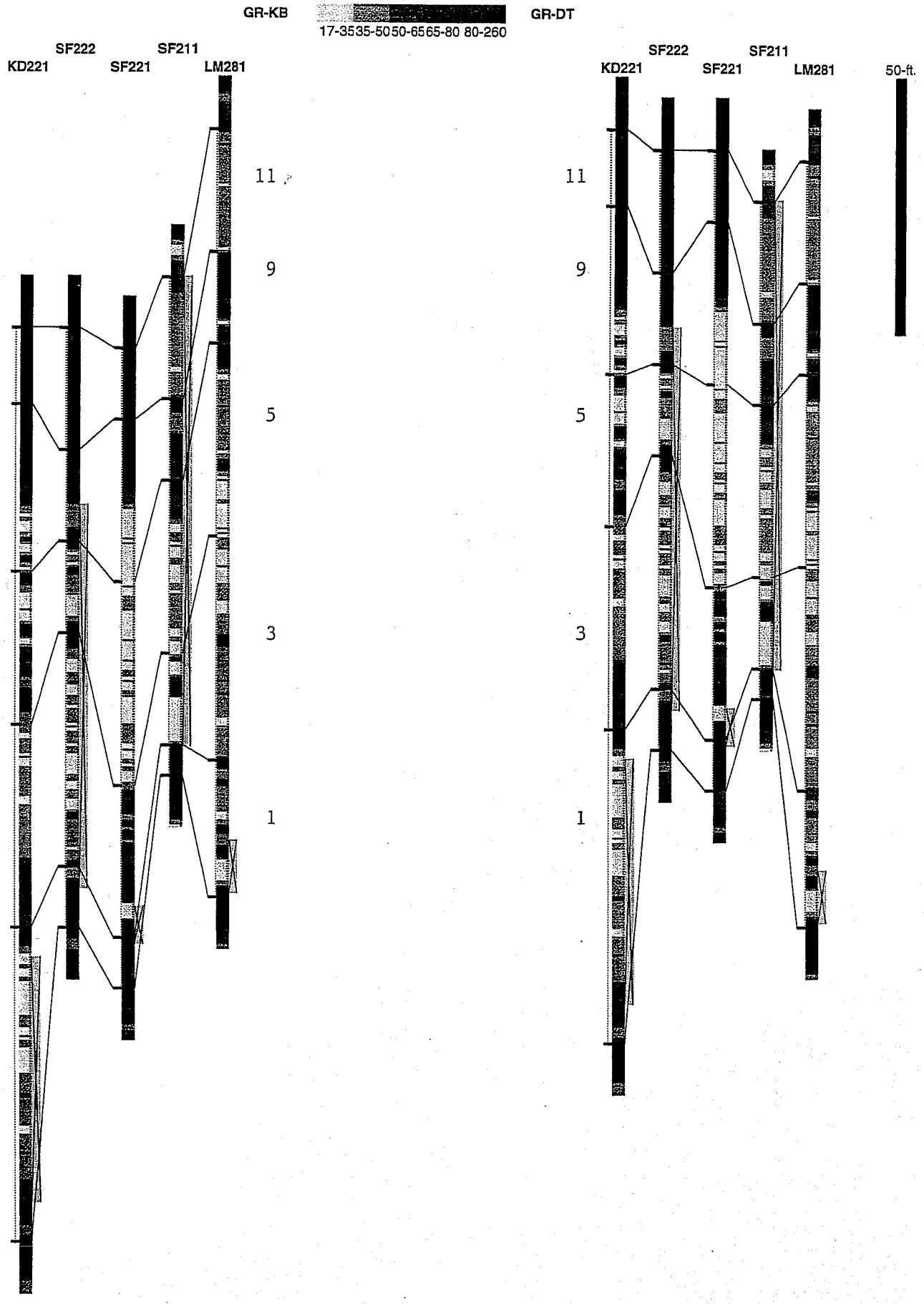
GR-KB
17-35 35-50 50-65 65-80 80-260
GR-DT
KD221
SF222
SF221
SF211
LM281
11
9
5
3
1
KD221
SF222
SF221
SF211
LM281
50-ft.
11
9
5
3
1

Fig. 16

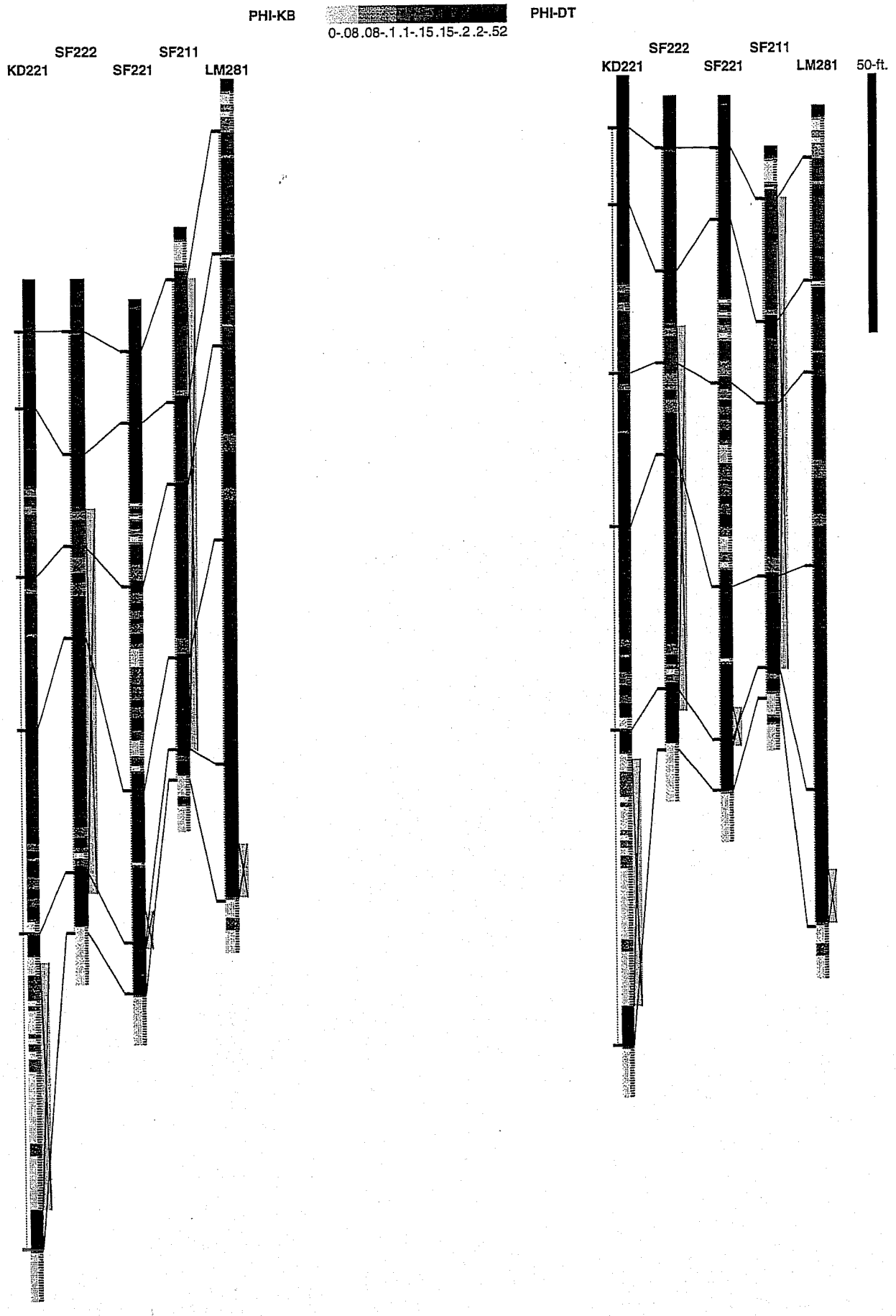
PHI-KB
0-.08 .08-.1 .1-.15 .15-.2 .2-.52
PHI-DT
KD221
SF222
SF221
SF211
LM281
KD221
SF222
SF221
SF211
LM281
50-ft.

Fig. 11

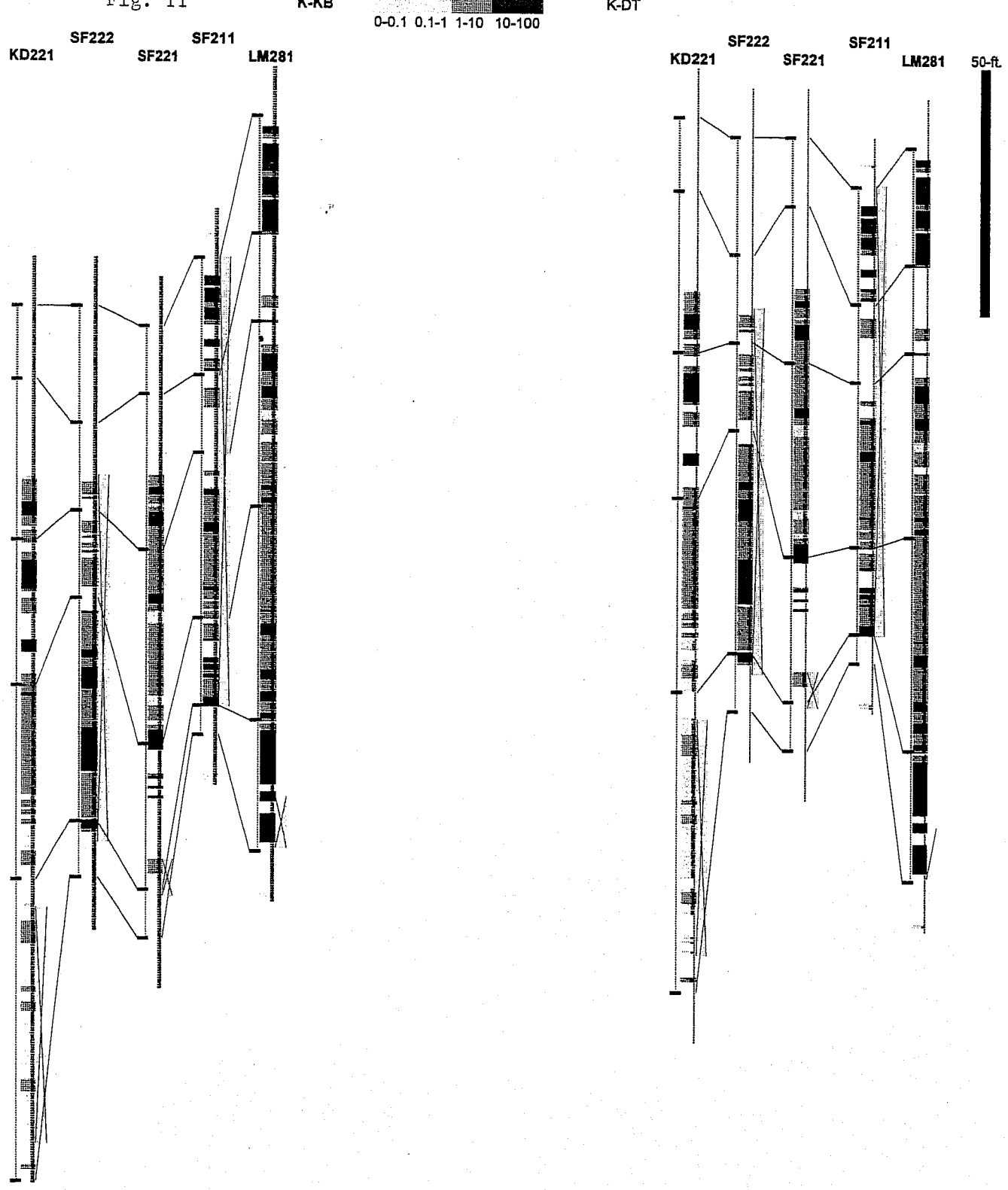
K-KB
0-0.1 0.1-1 1-10 10-100
K-DT
KD221
SF222
SF221
SF211
LM281
KD221
SF222
SF221
SF211
LM281
50-ft

Compartmentalization Analysis using Discrete Fracture Network Models

Paul R. La Pointe*, Thorsten Eiben*, William Dershowitz*, Eugene Wadleigh+

* Golder Associates Inc., 4104 - 148th Ave. N.E., Redmond, WA, 98052

+ Marathon Oil Company, Mid-Continent Region Production U.S., P.O. Box 552, Midland, TX 79702

ACKNOWLEDGMENTS

This research is supported by the U.S. Department of Energy, National Institute for Petroleum and Energy Research (DOE/NIPER) under contract number #G4S51728.

ABSTRACT

This paper illustrates how Discrete Fracture Network (DFN) technology can serve as a basis for the calculation of reservoir engineering parameters for the development of fractured reservoirs. It describes the development of quantitative techniques for defining the geometry and volume of structurally controlled compartments. These techniques are based on a combination of stochastic geometry, computational geometry, and graph theory. The parameters addressed are compartment size, matrix block size and tributary drainage volume. The concept of DFN models is explained and methodologies to compute these parameters are demonstrated.

1. INTRODUCTION

In fractured reservoirs, the low permeability rock matrix holds the storage for the hydrocarbons while the high permeability fracture system provides the pathways to produce them. The amount of hydrocarbon that can be produced therefore is a function of the fracture network connectivity and geometry.

For fractured reservoirs the quantity and rate of fluid movement between the rock mass and a well often significantly departs from what a porous continuum model of the system might indicate (La Pointe and Dershowitz 1994). High initial production (IP) rates may drop dramatically over the first months of production. Estimates of recoverable hydrocarbons based upon dynamic and mass balance calculations may differ substantially. A key parameter in this context is reservoir compartmentalization, i.e. the division of the reservoir in not or only poorly connected regions. A petroleum reservoir that is compartmentalized either increases the cost of production or reduces the quantity of oil that is ultimately recovered. This economic cost has spawned renewed interest in understanding reservoir compartmentalization and methods to engineer compartmentalized reservoirs (e.g. Ortoleva, 1994).

Compartmentalization may arise due to a variety of structural and depositional geological processes (Ortoleva, 1994). One process which has not been well-studied but occurs widely is compartmentalization due to the finite extent of poorly connected fracture networks. One reason that this compartmentalization process has not been studied more thoroughly is that tools have only recently become available.

Recently, a new method to study flow and transport in fractured rock has evolved to the point that it provides a useful way to study fractured reservoir compartmentalization. This method is based upon Discrete Fracture Network (DFN) models. DFN models are three-dimensional stochastic or combined stochastic/deterministic realizations of the fractures in a rock mass. Fracture properties such as orientation, size, intensity, location and transmissivity can be conditioned to match either observed fracture statistics or structural models related to folding, faulting or in-situ stress.

The DOE/NIPER research project *"Fractured Reservoir Discrete Fracture Network Technologies"*, undertaken by Golder Associates, Marathon Oil Co. and The Massachusetts Institute of Technology, will develop and demonstrate technologies for improving recovery from fractured oil reservoirs. The project focuses on applying DFN-technology to tertiary recovery processes. The research is designed to use information gathered during a field trial of Thermally-Assisted-Gravity-Segregation (TAGS) at the Yates field in West Texas.

This paper presents some preliminary results of this research showing how DFN models might be used for the analysis of reservoir compartmentalization.

2. DFN MODELS

DFN models, like all models, idealize the fracturing in a reservoir. While conventional dual-continuum models simplify fracture geometry in order to better model transient multiphase flow behavior, DFN models focus on realistic fracture geometries while simplifying the flow physics (Figure 1).

Each type of modeling strategy has its strengths and weaknesses, and there is some useful overlap in these modeling approaches. However, when fracture networks dominate rock mass permeability, DFN models will significantly out-perform conventional models based on effective continuum properties (La Pointe et al., 1996b). This is because network geometry and the connectivity structures that result control the scale at which wells can communicate with each other, how much matrix can be accessed by a well, and the rate of advective flow, mass transport and heat conduction. The effects of multiphase flow or other physical processes, though also important, are second-order effects for these applications.

DFN models are stochastic or a combination of deterministic and stochastic fractures. Large-scale faults are easily identified from seismic profiles, geological mapping, lineament analyses and well logs/core. These large-scale faults are either significant flow conduits or act as barriers due to stratigraphic offset or mineralization. Since large-scale

faults are known and because they are important, they are treated as deterministic features. This means that the DFN model will have each large- scale fault represented in the location that it occurs, and with the geometry and fluid flow characteristics that have been measured or inferred. Every stochastic realization of the entire DFN model will have these deterministic features whose properties will remain unchanged throughout all of the realizations.

However, there are many medium- and small-scale faults and joints that are not detected by seismic or remote sensing imagery, or encountered in wells. Yet these faults and large joints form important flow conduits through the rock mass. It is possible to derive statistical distributions necessary for the construction of DFN models for these smaller faults and joints, as detailed for example in Dershowitz et al. (1996). These fractures constitute the stochastic portion of the DFN model, since their locations, orientations, etc. are assigned as a random sample from the statistical distributions for each realization.

The statistical distributions of fracture properties may vary in different regions. Structural models abound that relate fracture intensity, orientation, permeability and location according to the structural geology of folds, faults or in-situ stress fields thought to have produced the fractures (e.g. Stearns 1971, Stearns and Friedman 1972, Suppe 1983, Mitra 1993). Advanced DFN modeling software (Dershowitz et al., 1996) incorporates this type of conditioning.

Because the resulting DFN models contain a stochastic component, it is possible to generate multiple statistical realizations of the faults and joints. These realizations can then be used to calculate the statistics for any parameter, such as compartment size and shape, and also to carry out sensitivity studies to determine what factors control compartment size. This makes the DFN approach particularly useful for economic decision analysis.

3. METHODOLOGIES FOR CALCULATING RESERVOIR ENGINEERING PARAMETERS FROM DISCRETE FRACTURE NETWORKS

Once a DFN realization has been created, the calculation of practical reservoir engineering parameters is a straightforward, although numerically sophisticated, process. First, it is necessary to determine which fractures intersect to form networks, and to determine whether these networks intersect a well. Elementary graph theory algorithms can be used to identify completely isolated fracture networks or networks that are weakly connected to other networks. This intersection information can be stored as either an *adjacency matrix* or an *adjacency list* (Sedgewick, 1990).

Based on the intersection information various parameters can be computed. In the current stage of the project there are three parameters calculated from the DFN model:

Compartment size is defined only by the fracture network geometry. It gives the oil in place which is associated with a connected fracture system. In combination with a recovery factor it can serve as a rough quantitative measure of how much oil or gas can be produced by a well.

Matrix block shape and size also is a purely geometrical parameter. It gives a measure of the typical undisturbed volume of rock matrix in a fractured reservoir. Fluid flow within such a block will be purely dependent upon the matrix properties.

Drainage volume is a more precise quantity and important for the ultimate recovery of hydrocarbon from a producing well and for the rate of movement and shape of the heat front during steam injection. It describes the estimated volume of matrix that a fracture system intersected by a well can access. The drainage volume therefore is related to both compartmentalization and matrix block size.

4. COMPARTMENT SIZE

4.1 EFFECT OF COMPARTMENTALIZATION ON FIELD DEVELOPMENT PLANNING

The "size" of a compartment formed by a fracture network may be defined in different ways, depending upon the reservoir engineering application. For example, the horizontal cross-section of each compartment relates to how efficient a particular well pattern will be in accessing potentially recoverable oil. The number of wells, representing an economic cost, needs to be balanced against the estimated ultimate recovery (EUR) that can be produced from those wells. If many compartments are missed by a proposed well pattern, then potentially recoverable hydrocarbons are being left in the ground. Alternatively, a well pattern that already produces from most of the reservoir compartments will not benefit from an infill drilling program.

Compartmentalization as it relates to economically efficient well patterns can be assessed by computing the horizontal dimensions and area of all of the fracture compartments in a series of DFN realizations. From these Monte Carlo realizations of a model, it is possible to compute a cumulative probability graph for compartment cross-sectional area. Such a graph provides an estimate of the mean acreage of the reservoir which a well could access. This acreage provides an indication whether a particular well pattern spacing will probably miss intersecting a number of compartments, whether each compartment is typically intersected by numerous wells (and thus may be economically inefficient), or whether the number of wells balances compartment access with drilling costs.

While it is usually possible to identify large-scale fault-bounded reservoir compartments from seismic or production histories, it is far more difficult to assess the compartmentalization due to joint network geometry and connectivity, for which seismic information is of little use. Joint network compartmentalization is often suspected when static and dynamic calculations of recoverable oil or gas do not agree, and there is no evidence for fault-offset or other types of fault-related compartmentalization.

Figures 2 and 3 illustrate the effect compartmentalization has on the connectivity within a reservoir. Figure 2 shows the DFN of a compartmentalized and intensively fractured rock mass. By looking at the figure one would expect all areas of the reservoir to be well connected. Figure 3, however, displays the same fracture network but only shows that portion of the network which is connected directly or indirectly to one of the 5 wells.

4.2 COMPARTMENTALIZATION ANALYSIS

The computation of the volume and horizontal extent of joint network compartments is a three-step process:

Step 1. Identify individual fracture networks within the DFN model

Step 2. Compute the bounding surface for each identified network

Step 3. Calculate the volume within the bounding surface and the horizontal extent of the network

While it would be possible to compute the "bounding box" for a network, and use this box volume and horizontal cross-section as surrogates for compartment volume and horizontal extent, this would lead to an overestimation in most cases of both volume and cross-section. This in turn would produce overestimates of the ultimate recovery from wells, and suggest greater well spacings and recovery efficiencies than would actually be the case. To reduce the potential for overestimates, it is necessary to calculate a bounding surface that better approximates the outer limits of the network. A convex hull meets these requirements.

A convex hull is essentially a bounding surface with certain advantageous mathematical properties. For points with three-dimensional spatial coordinates, the convex hull is a convex polyhedron, which has the minimum volume of all possible convex polyhedra that bound the point set. Figure 4 shows such a three-dimensional convex hull calculated using the QuickHull algorithm and the Qhull software package (Barber et al., 1995) for the central well shown in Figure 3. In Figure 5, the horizontal projection of the hull is

shown. The resulting data can easily be used to compute the volume and cross-sectional area of each hull.

5. MATRIX BLOCK SIZE

The fracture surface area of matrix blocks within a simulation grid cell influences the rate and quantity of fluids that can move between the matrix and the fracture system. The Z-dimension of matrix blocks influences gravity drainage mechanisms. The shape of the matrix blocks influences the choice of sugar cube, matchstick or slab idealization. A realistic description of block size and shape in a way that can be implemented in existing dual porosity simulators will benefit not only the thermal simulation TAGS processes, but also non-thermal simulations of injection or production in fractured reservoirs.

5.1 BLOCK SIZE ANALYSIS

Two DFN algorithms have been developed to compute matrix block shape and size that are :

1. Based on geologically realistic three-dimensional fracture systems, and
2. Provide output in the form required by conventional dual-porosity simulators.

The first algorithm is a fast computational method to compute blocks based upon fracture spacing distributions in several directions. Its main advantage is that the calculation is computationally fast. Its disadvantage is that it assumes that block x, y and z dimensions are uncorrelated. This algorithm is referred to as the *multidirectional spacing distribution algorithm* (Figure 6).

For each realization of the discrete fracture model, a series of randomly-located lines in selected directions are generated. The location of fractures intersected by each line is recorded. This leads to a spacing frequency distribution in several directions. Typically, the directions include the vertical direction, in order to calculate the vertical dimension of blocks for gravity drainage considerations, and in two or three orthogonal directions that relate to simulator grid layering geometry and the fracture system.

The spacing probability distributions are multiplied together using Monte Carlo sampling techniques to produce a frequency distribution of block volumes and surface areas. This is carried out by selecting X, Y and Z spacing values at random with selection probability proportional to their frequency, and multiplying them together to create a prismatic block volume.

The second algorithm is based upon graph theory and, again, uses convex hulls. This algorithm is therefore referred to as the *convex hull algorithm*. It is based upon computing the convex hull of points lying on fractures bounding or partially bounding a matrix block.

The convex hull algorithm is more computationally intensive, but measures the actual dimensions of the blocks, rather than reconstructing blocks stochastically from spacing frequencies. Thus, any correlation among block dimensions or non-prismatic block shapes are considered appropriately. The algorithm's accuracy is governed by two factors: whether in fact the matrix blocks are convex; and how many points are required to accurately characterize the convex block. The algorithm as implemented allows the user to specify the number of points for characterizing the convex block.

Test cases (La Pointe et al., 1996b) suggest that both the multi directional spacing (MDS) and convex hull (CH) algorithms provide reliable and consistent estimates of fracture surface area, at least for simple fracture geometries. The CH algorithm appears to provide better estimates of the mean volume of matrix blocks when block dimensions are partially correlated. Since jointing in many sedimentary rocks is characterized by pseudo-periodic spacings (e.g., La Pointe and Hudson, 1985), it may be preferable to use the CH algorithm to estimate block volumes. On the other hand, the geometric construction of a convex hull from a sparse data set creates hulls with slightly greater average Z-dimensions than the MDS algorithm. In both test cases 1 and 2, the MDS algorithm provided more accurate estimates of the Z-dimension. Thus, both algorithms have proven useful and necessary to provide estimates of matrix block parameters, and neither alone is completely satisfactory.

6. DRAINAGE VOLUME

The tributary drainage volume for a well is that volume of the matrix that can be drained by the fracture network connected to a well or heated up by steam injection. The drainage volume takes into account both the geometry of the fracture network and the physical processes of advective flow, transport, diffusion and heat conduction. Tributary drainage volume is related to both block size and compartmentalization.

6.1 DRAINAGE VOLUME ANALYSIS

The algorithm developed to compute the tributary drainage volume is divided into two steps:

Step 1. Identify the fracture networks connected to the well or perforated zone of interest

Step 2. Estimate the volume of matrix within the network that could be produced

While the procedure for step 1 is the same as for the compartmentalization analysis, step 2 can become extremely complex. The task is to predict which portion of the matrix volume is close enough to a fracture, given the pressure drawdown within the matrix block, to be able to contribute to production.

Different ways could be used to accomplish step 2. If the fracture network is very dense, then the volume of the matrix accessed by the fracture network will be closely approximated by the volume of the convex hull enclosing the network. In essence, this means that the tributary drainage volume is equal to the compartment volume. The same conclusion applies if the matrix permeability is sufficiently large to allow production to take place from all of the matrix volume.

In less dense fracture networks where the typical matrix block size is large, some or maybe most of the volume inside the convex hull will be too far from any of the fractures to be easily produced. For these cases, the user can specify an average drainage percentage. It is possible to compute this percentage with the help of the blocksize information

derived earlier. The average drainage percentage is then used to reduce the convex hull volume.

Another approach to exclude matrix that might not be efficiently produced through pressure depletion drainage is to surround each fracture in the network with a polygon that is calculated from the area of the fracture and the distance away from the fracture over which drainage might be effective (Figure 7). This leads to a prism that encloses the fracture. For pressure depletion mechanisms, the fracture forms the midplane of the prism. An obvious problem with this algorithm is to avoid double-counting the volume where there is overlap between the prisms. Calculations based upon solid geometry to compute the volume while accounting for the overlap are highly time-consuming for the number of fractures that might commonly be encountered in a fracture network. A simpler method has been devised which is much more efficient, though not as numerically exact (La Pointe et al. 1996b).

Computing the drainage volume is a critical reservoir engineering parameter. For computing the ultimate recovery, it is necessary to combine the static parameters like compartment volume and block size with the dynamics involved in the flow of fluids from the matrix into the fracture system. Because of the time dependent pressure distribution within a matrix block the drainage volume will also be time dependent. This corresponds to the step from volumetric oil in place estimation to dynamic ultimate recovery calculation using reservoir simulation.

Nonetheless, the measures described above will provide an estimate of the recoverable reserves from a reservoir. They offer an advantage, however, that a large number of realizations can be run, and so the uncertainty relating to simplification can be quantified in a clear and straightforward manner. The alternative of carrying out hundreds of numerical fluid flow simulations requires substantially greater, and perhaps prohibitive, computing times.

7. SUMMARY AND OUTLOOK

The ongoing DOE/NIPER research project "*Fractured Reservoir Discrete Fracture Network Technologies*" is developing technologies for improving recovery from fractured oil reservoirs. This paper illustrates some preliminary results of this effort. The work thus far has concentrated on the development of methodologies and algorithms which can be used to extract valuable parameters from fracture network information for the use in reservoir engineering tasks. It has been shown how Discrete Fracture Network models can be used to calculate parameters like compartment size, matrix block size and tributary drainage volume.

At the time of the submission of this paper, the methods described are undergoing an intense verification process (La Pointe et al. 1996b). In the next step, the methods will be used on field data from the Yates field.

8. REFERENCES

Barber, C. B., D.P. Dobkin, and H.T. Huhdanpaa, 1995. The Quickhull Algorithm for Convex Hulls. ACM Transactions on Mathematical Software.

Dershowitz, W., G. Lee, J. Geier, T. Foxford, P. La Pointe and A. Thomas, 1996. FracMan Interactive Discrete Feature Data Analysis, Geometric Modeling, and Exploration Simulation: User Documentation Version 2.5. Golder Associates Inc., Redmond, WA.

La Pointe, P.R., and J. Hudson, 1985. Characterization and Interpretation of Rock Joint Patterns. GSA Special Paper 199. GSA, Denver.

La Pointe, P.R., and Dershowitz, W.S., 1994. Discrete Fracture Approaches for Oil and Gas Applications. Proceedings: 1st North American Rock Mechanics Symposium, The University of Texas at Austin, June 1-3, 1994, p. 19-30.

La Pointe, P.R., Wallmann, P.C., and Follin, S., 1996a. Continuum Modeling of Fractured Rock Masses: Is it useful? Proceedings: Prediction and Performance in Rock Mechanics and Rock Engineering (EUROCK '96), Torino, Italy, September 2-5, 1996, p. 343-350.

La Pointe, P.R., Eiben, Th., and Dershowitz, W.S., 1996b. Fractured Reservoir Discrete Fracture Network Technologies. Research Report Reservoir Compartmentalization. Golder Assoc. Inc., Redmond, WA.

Mitra, S., 1993. Geometry and kinematic evolution of inversion structures. Bulletin American Association of Petroleum Geologists, Vol 77, p. 1159-1191.

Ortoleva, P.J.(ed), 1994. Basin Compartments and Seals. AAPG Memoir 61, American Assoc. of Petroleum Geologists, Tulsa.

Sedgewick, R., 1990. Algorithms in C. Addison-Wesley Pub. Co., Reading, MA.

Stearns, D. W. 1971. Mechanisms of drape folding in the Wyoming Province. Wyoming Geol. Assoc. Guidebook. Twenty-third Field Conference, p. 125-143.

Stearns, D. W. and Friedman, M. 1972. Reservoirs in fractured rock. Memoir 16, American Association of Petroleum Geologists, p. 82-106.

Suppe, J. 1983. Geometry and kinematics of fault-bend folding. American Journal of Science, Vol 283, p. 684-721.

LIST OF FIGURES

Fig. 1: Discrete Fracture Network model approach for a fractured rock mass

Fig. 2: DFN model of compartmentalized intensively fractured rock mass

Fig. 3: Production from compartmentalized intensively fractured reservoir

Fig. 4: Convex hull of fracture network connected to center well

Fig. 5: Horizontal projection of convex hull connected to center well

Fig. 6: Multi-Directional Spacing Algorithm

Fig. 7: Tributary Drainage Volume

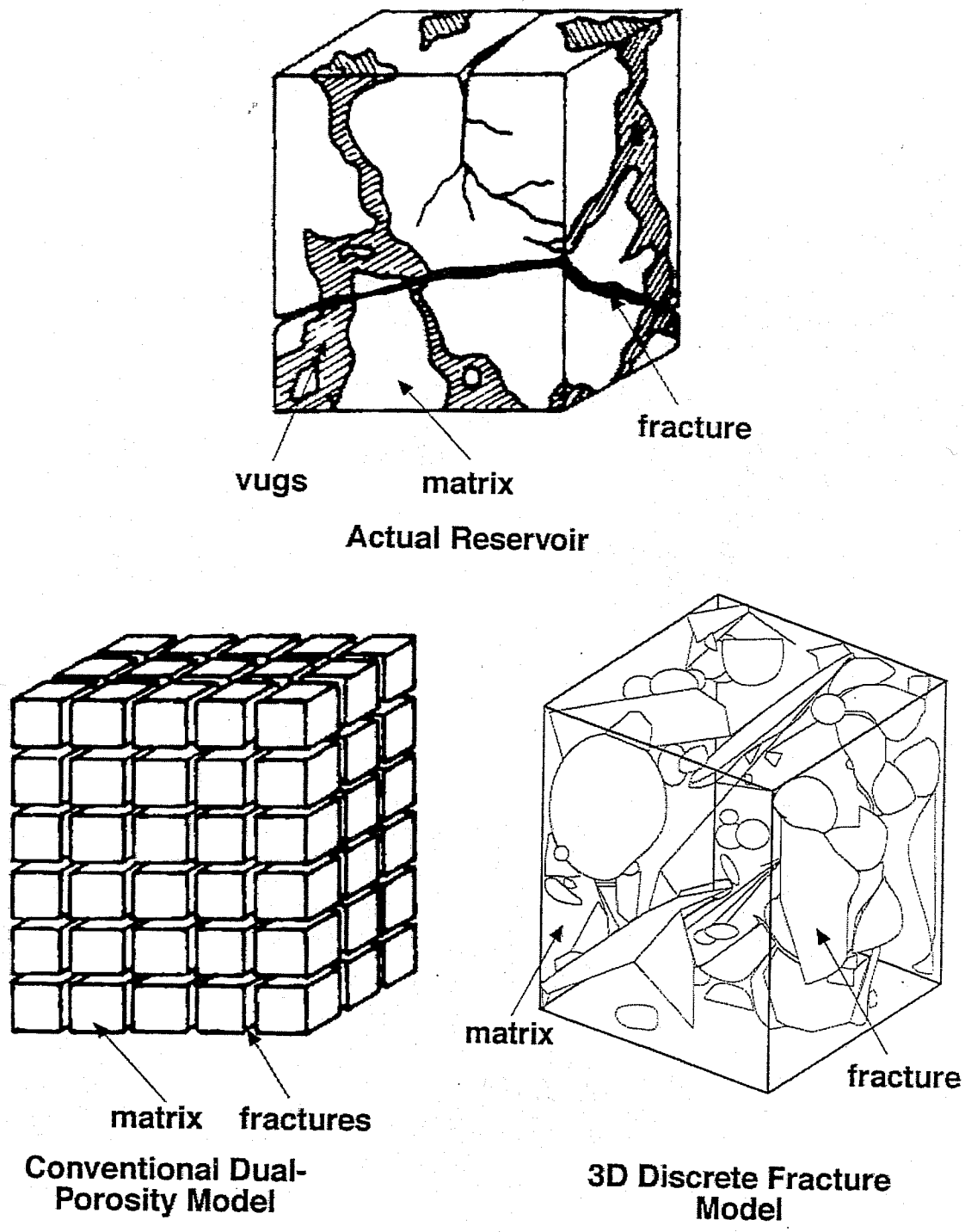

Fig. 1: Discrete Fracture Network model approach for a fractured rock mass

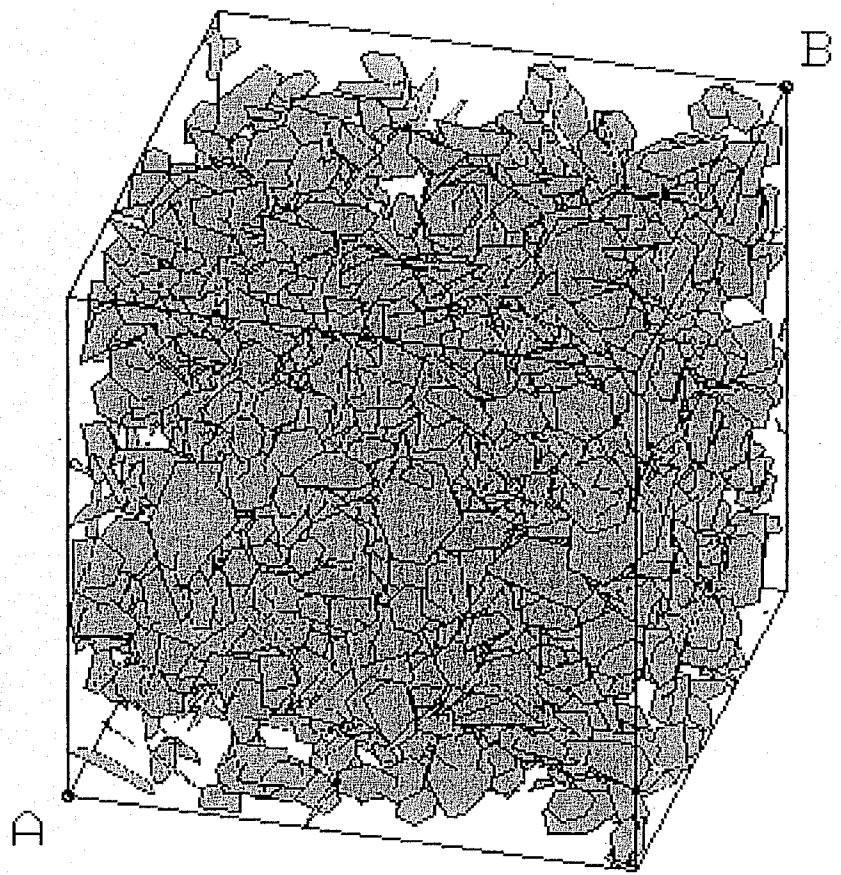

Fig. 2: DFN model of compartmentalized intensively fractured rock mass

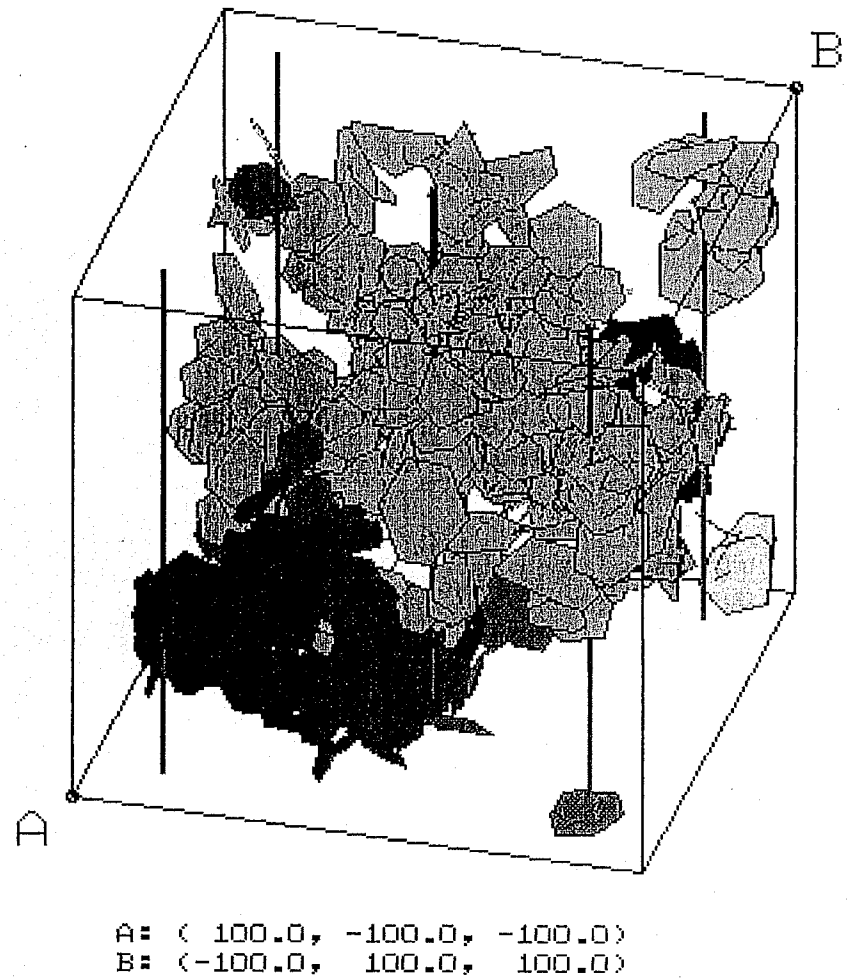

Fig. 3: Production from compartmentalized intensively fractured reservoir

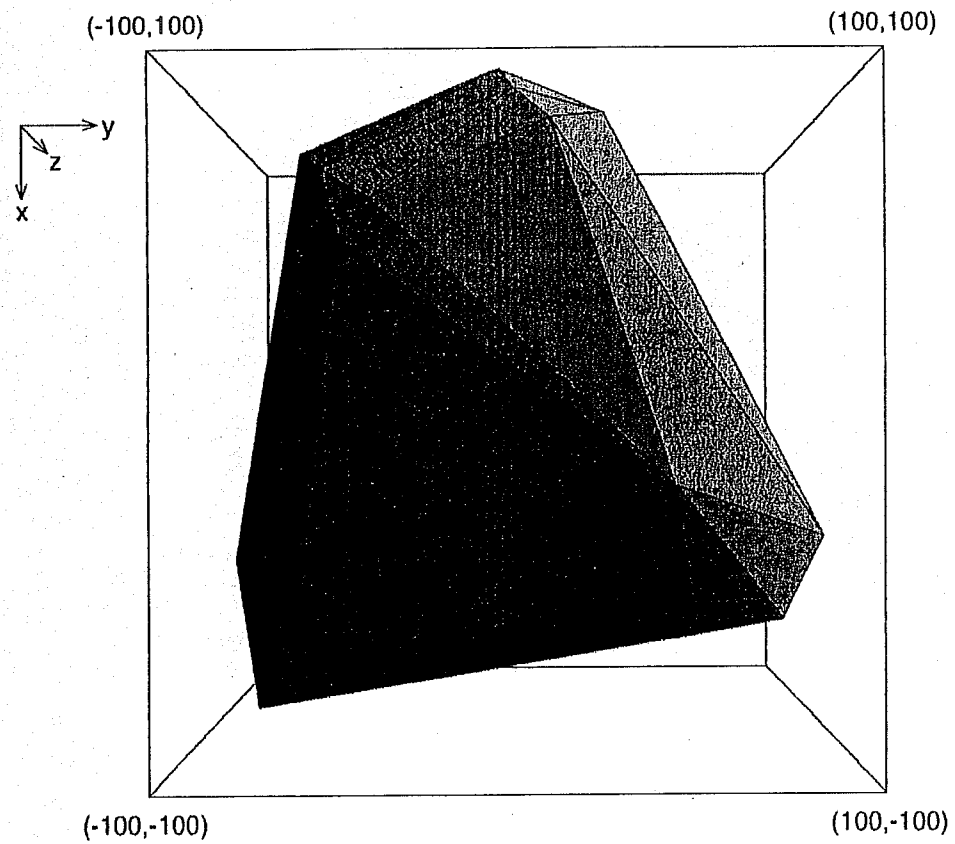

Fig. 4: Convex hull of fracture network connected to center well

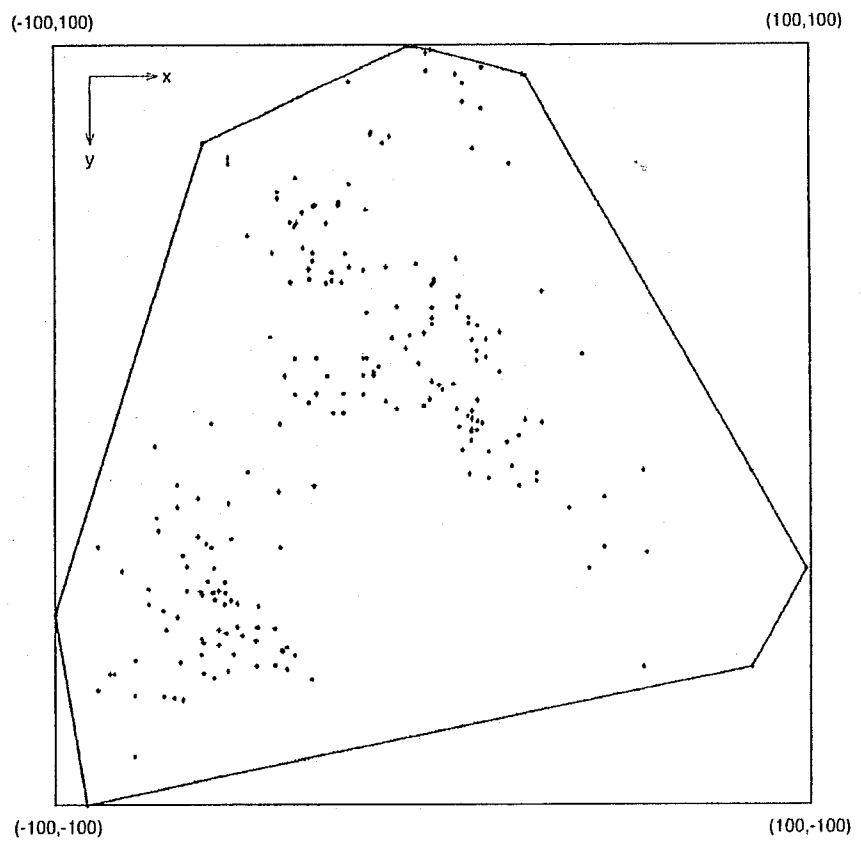

Fig. 5: Horizontal projection of convex hull connected to center well

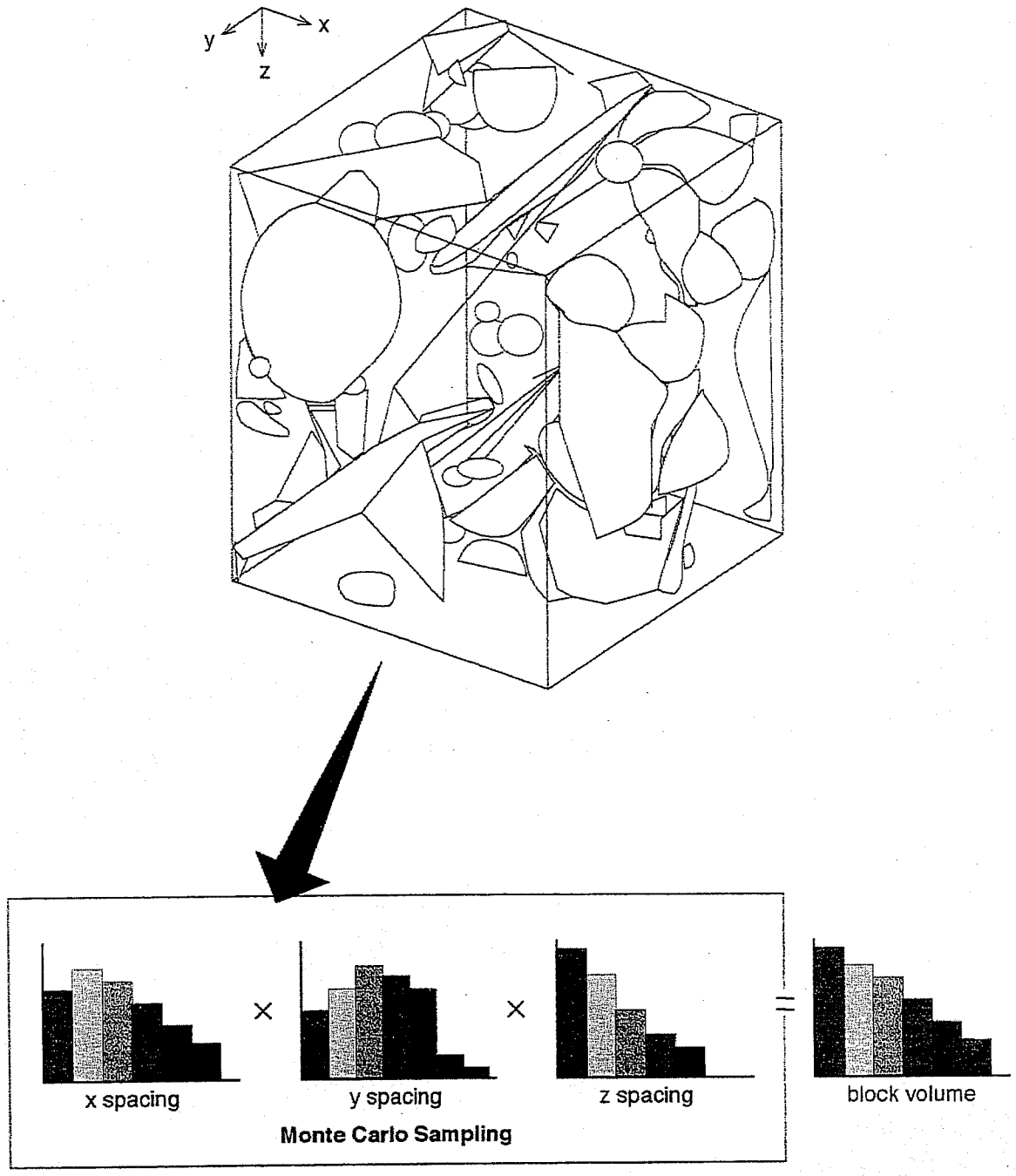

Fig. 6: Multi-Directional Spacing Algorithm

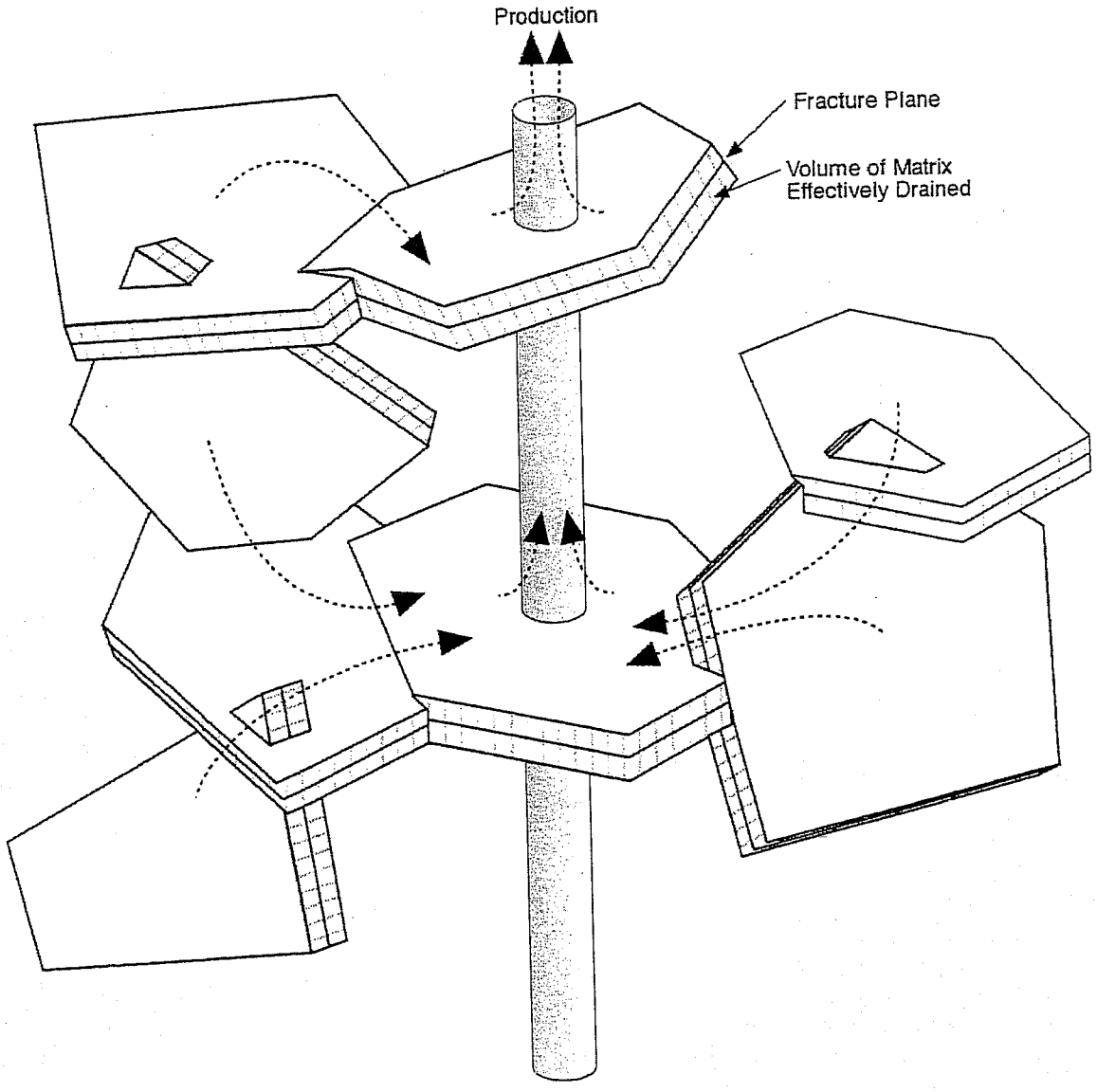

Fig. 7: Tributary Drainage Volume

Characterization of Dynamic Change of Fan-delta Reservoir Properties in Water-drive Development

Wu Shenghe; Xiong Qihua; Liu Yuhong
Department of Geosciences
University of Petroleum
Changping, Beijing P.R. China

ABSTRACT

Fan-delta reservoir in Huzhuangji oil field of east China, is a typical highly heterogeneous reservoir. The oil field has been developed by water-drive for 10 years, but the oil recovery is less than 12%, and water cut is over 90%, resulting from high heterogeneity and serious dynamic change of reservoir properties. This paper aims at the study of dynamic change of reservoir properties in water-drive development.

Through quantitative imaging analysis and mercury injection analysis of cores from inspection wells, the dynamic change of reservoir pore structure in water-drive development was studied. The results show that the "large pore channels" develop in distributary channel sandstone and become larger in water-drive development, resulting in more serious pore heterogeneity.

Through reservoir sensitivity experiments, the rock-fluid reaction in water-drive development is studied. The results show the permeability of some distal bar sandstone and deserted channel sandstone becomes lower due to swelling of I/S clay minerals in pore throats. On the other hand, the permeability of distributary channel and mouth bar sandstone become larger because the authigenic Koalinites in pore throats are flushed away with the increase of flow rate of injection water.

Well-logging analysis of flooded reservoirs are used to study the dynamic change of reservoir properties in various flow units. The distribution of remaining oil is closely related to the types and distribution of flow units.

Calculation of Large Scale Relative Permeabilities from Stochastic Properties of the Permeability Field and Fluid Properties

Roland Lenormand; Marco R. Thiele (Stanford University)
Institut Français du Pétrole
1 et 4 Avenue de Bois-Priau - B.P. 311
Rueil Malmaison 92506
Cedex, France

ABSTRACT

The paper describes the method and presents preliminary results for the calculation of homogenized relative permeabilities <Kr> using stochastic properties of the permeability field.

In heterogeneous media, the spreading of an injected fluid is mainly sue to the permeability heterogeneity and viscosity fingering. At large scale, when the heterogeneous medium is replaced by a homogeneous one, we need to introduce a homogenized (or pseudo) relative permeability <Kr> to obtain the same spreading. Generally, <Kr> is derived by using fine-grid numerical simulations (Kyte and Berry). However, this operation is time consuming and cannot be performed for all the meshes of the reservoir. We propose an alternate method which uses the information given by the stochastic properties of the field without any numerical simulation.

The method is based on recent developments on homogenized transport equations (the "MHD" equation, Lenormand SPE 30797). The MHD equation accounts for the three basic mechanisms of spreading of the injected fluid:

1) Dispersive spreading due to small scale randomness, characterized by a macrodispersion coefficient D.
2) Convective spreading due to large scale heterogeneities (layers) characterized by a heterogeneity factor H
3) Viscous fingering characterized by an apparent viscosity ration M

In the paper, we first derive the parameters D and H as functions of variance and correlation length of the permeability field. The results are shown to be in good agreement with fine-grid simulations. The <Kr> are then derived a function of D, H and M. The main result is that this approach lead to a time dependent <Kr>. Finally, the calculated <Kr> are compared to the values derived by history matching using fine-grid numerical simulations.

Statistical Analysis of Surface Lineaments and Fractures for Characterizing Naturally Fractured Reservoirs

Genliang Guo and Stephen A. George, BDM Petroleum Technologies, and Rhonda P. Lindsey, DOE Bartlesville Project Office

Abstract

Thirty-six sets of surface lineaments and fractures mapped from satellite images and/or aerial photos from parts of the Mid-continent and Colorado Plateau regions were collected, digitized, and statistically analyzed in order to obtain the probability distribution functions of natural fractures for characterizing naturally fractured reservoirs. The orientations and lengths of the surface linear features were calculated using the digitized coordinates of the two end points of each individual linear feature. The spacing data of the surface linear features within an individual set were obtained using a new analytical sampling technique. Statistical analyses were then performed to find the best-fit probability distribution functions for the orientation, length, and spacing of each data set. Twenty-five hypothesized probability distribution functions were used to fit each data set. A chi-square goodness-of-fit test was used to rank the significance of each fit. A distribution which provides the lowest chi-square goodness-of-fit value was considered the best-fit distribution.

The orientations of surface linear features were best-fitted by triangular, normal, or logistic distributions; the lengths were best-fitted by PearsonVI, PearsonV, lognormal2, or extreme-value distributions; and the spacing data were best-fitted by lognormal2, PearsonVI, or lognormal distributions. These probability functions can be used to stochastically characterize naturally fractured reservoirs.

Introduction

The characterization of naturally fractured reservoirs has challenged geologists and engineers for decades. From a reservoir engineering point of view, the objective of characterizing a naturally fractured reservoir is to estimate the flow and storage capacity, both of which require a quantitative description of natural fracture characteristics. Unfortunately, subsurface natural fracture data are rarely available and very expensive to obtain. The scarcity of subsurface natural fracture data and our inability to cost-effectively acquire sufficient amount of them have prevented us from obtaining a realistic and quantitative description of subsurface fracture systems.

One technique for characterizing a naturally fractured reservoir, which may overcome the limitation in the availability of subsurface natural fracture data, is to stochastically simulate the subsurface fracture systems and numerically calculate their permeability tensor distributions (Guo et al. 1994). The reliability of this technique, however, rests on the validity of the probability distribution functions of natural fracture characteristics used in the stochastic simulations. Many attempts have been made to use surface fracture data mapped from outcrop studies to derive the probability distributions of natural fracture characteristics.

Studies show that natural fracture orientations have a normal or Arnold's hemispherical normal distribution for two-dimensional data and a Fisher-Von Mises distribution for three-dimensional data (Long et al. 1982, Cacas et al. 1990, Dverstorp et al. 1989, Belfield et al. 1995). Fracture lengths have been found by various investigators to have a lognormal, exponential, or power law distribution (Long et al. 1982, Cacas et al. 1990, Dverstorp et al. 1989, Baecher et al. 1977, Baecher 1983, Roulean et al. 1985, Heffer et al. 1990). The distribution functions which provide best fits to many fracture aperture data include normal and lognormal distributions (Long et al. 1982, Belfield et al. 1995, Snow 1970). As the most extensively investigated characteristic of natural fractures, fracture spacing is found to have an exponential, lognormal, Weibull, Gamma, or power law distribution (Long et al. 1982, Belfield et al. 1995, Baecher et al. 1977, Baecher 1983, Roulean et al. 1985, Heffer et al. 1990, Lorentz et al. 1991, Loosveld et al. 1992). These distribution functions were usually identified by best-fitting measured data to a few hypothesized distributions.

In this paper, we present the results of a statistical analysis of natural fracture characteristics using a large number of surface lineaments and fractures in the Mid-continent and Colorado Plateau regions collected and digitized from previous studies reported in the literature. Twenty-five different probability distribution functions (see the Appendix) are used to best fit the orientation, length, and spacing of each of the 36 fracture and/or lineament sets identified. A chi-square goodness-of-fit test is employed to identify the best fits. The abundance of surface lineaments and fractures and the list of 25 hypothesized distribution functions used in the statistical analysis will inevitably result in more reliable probability distributions for describing natural fracture characteristics.

Statistical Analysis Procedure

The basic data used in this study were obtained by digitizing the two end points of the surface linear features mapped from

satellite images and/or aerial photos of various parts of the Mid-continent and Colorado Plateau regions. Due to the nature of the data, only orientation, length, and spacing were analyzed. No data were available for aperture analysis. The following procedure was used for the statistical analysis of surface lineament and fracture characteristics:

- A rose diagram analysis for identifying the number of subsets in a surface lineament and/or fracture system.
- A filtering analysis for partitioning a surface-fracture system into subsets.
- A sampling analysis for collecting surface-fracture spacing data using a new analytical technique.
- A best-fit analysis for obtaining distribution functions for surface lineament and fracture orientation, length, and spacing.

In the following discussion, the surface fractures in Osage County, Oklahoma, are used to demonstrate the procedure for statistical analysis of surface-fracture characteristics.

Shown in Fig. 1 are the surface fractures in Osage County. They were mapped from satellite images and aerial photos (Guo et al. 1995). A rose diagram for these surface fractures was generated (see Fig. 2). This rose diagram shows that the surface fractures primarily consist of two sets trending northeast and northwest. Figs. 3 and 4 show the northeast- and northwest-trending surface fractures, after they are separated through a filtering analysis based on their orientations.

Within each subset, the orientation and length data are calculated using the digitized coordinates of the two end points for each surface fracture. The spacing data are obtained using an analytical sampling technique. The technique involves overlapping a set of uniform imaginary scanlines on top of an individual fracture set (see Figs. 5 and 6). The scanlines are oriented perpendicular to the average orientation of the fracture set. The intersection points along each imaginary scanline are then identified and sorted. The spacing data are obtained by calculating the distance between two adjacent intersection points along a scanline. After orientation, length, and spacing data are obtained for each fracture set, they are fitted to 25 hypothesized probability distributions. A chi-square goodness-of-fit test is used to identify the best-fit distributions.

Fig. 7 shows the histogram and best-fit orientation distribution of the northeast-trending surface fractures. A total of 2,046 data points were used in the analysis. A triangular distribution, TRIANG(-1.47, 37.38, 95.63), appears to provide the best fit to the data, although a normal distribution, NORMAL(43.59, 19.80), also fits the data closely. Similarly, Fig. 8 shows the histogram and best-fit orientation distribution of the northwest-trending surface fractures. There are 1,322 surface fractures in this set. The orientations of this set of surface fractures were best-fitted by a logistic distribution, LOGISTIC(128, 12.01).

As shown in Fig. 9, the length data of the northeast-trending surface fractures, were best-fitted by a PearsonVI distribution, PearsonVI(11.35, 4.54, 1480). Fig. 10 shows the histogram and best-fit length distribution for the northwest-trending surface fractures. A PearsonVI distribution, PearsonVI(8.95, 3.95, 1500), provides the best fit, but a lognormal2 distribution, LOGNORM2(8.20, 0.60), also fits the data very well.

The spacing data of the northeast-trending surface fractures, were best-fitted by a lognormal2 distribution, LOGNORM2(8.21, 1.11). The histogram, best-fit distribution, and statistical parameters of the northeast-trending surface-fracture spacing data are shown in Fig. 11. Similar results were also obtained for the spacing data of the northwest-trending surface fractures, as shown in Fig. 12. A lognormal2 distribution, LOGNORM2(8.64, 1.18), is the best-fit distribution.

Statistical Analysis of Surface Lineaments and Fractures in Northeastern Arizona

A photogeological interpretation study was conducted in the Cameron and the Black Mesa Basin areas in northeastern Arizona (Guo et al. 1995). Over 50,000 surface fractures were mapped from aerial photos and subsequently digitized. In addition, large-scale surface lineaments were collected and digitized in the general northeastern quarter of Arizona (Lepley 1977). Using the statistical analysis procedure discussed in the previous section, the characteristics of the surface lineaments and fractures in northeastern Arizona were statistically analyzed.

Surface Lineaments in Northeastern Arizona. Fig. 13 is a rose diagram for the surface lineaments in northeastern Arizona. The surface lineaments apparently can be partitioned into four subsets, including two major sets trending northeast and northwest and two minor sets trending east and north. Figs. 14 to 17 show the histograms, best-fit orientation distributions, and sample data statistics for the four sets of the surface lineaments. A normal distribution provides the best fit to the orientation data of the east-trending surface lineaments; whereas those of the northeast-, north-, and northwest-trending surface lineaments were best-fitted by three triangular distributions.

The results of a statistical analysis on the corresponding length data are given in Figs. 18 to 21. The length data of the east- and north-trending surface lineaments were best-fitted by two PearsonV distributions; those of the northeast- and northwest-trending surface lineaments were best-fitted by two PearsonVI distributions.

Similarly, the results of a statistical analysis on the corresponding spacing data are given in Figs. 22 to 25. The spacing data of the east-trending surface lineaments were best-fitted by a PearsonVI distribution; those of the northeast-, north-, and northwest-trending surface lineaments were best-fitted by three lognomal2 distributions.

Surface Fractures in the Cameron Area in Northeastern Arizona. Over 6,100 surface fractures were mapped from aerial photos in the Cameron area in northeastern Arizona (Guo et al. 1995). Fig. 26 is a rose diagram for those surface fractures. From this rose diagram, three subsets were identified, including two major sets trending northeast and north-northeast and a minor set trending east. The histograms, best-fit orientation distributions, and sample data statistics for the

three sets of the surface fractures are shown in Figs. 27 to 29. The orientation data of the northeast-trending surface fracture set were best-fitted by a normal distribution, whereas those of the other two fracture sets were best-fitted by two triangular distributions.

Figs. 30 to 32 show the results of a statistical analysis on the corresponding three sets of surface fracture length data in the Cameron area. A PearsonVI distribution appears to provide the best fit to the length data of the east-trending fracture set; two loglogistic distributions provide the best fits to the other two fracture sets.

Similarly, Figs. 33 to 35 show the histograms, best-fit distributions, and sample data statistics for the spacing data of the three sets of surface fractures in the Cameron area. A lognormal distribution provides the best fit to the spacing data of the east-trending surface fracture set. Those of the northeast- and north-northeast-trending surface fractures were best fitted by two lognormal2 distributions.

Surface Fractures in the Black Mesa Basin Area in Northeastern Arizona. Over 44,000 surface fractures were mapped from aerial photos of the Black Mesa Basin area in northeastern Arizona (Guo et al. 1995). Fig. 36 shows a rose diagram of these surface fractures. Four subsets were identified from Fig. 36 trending east, northeast, north-northeast, and northwest. A statistical analysis was performed on the orientations of these four sets of surface fractures. The results are given in Figs. 37 to 40. The orientation data of the east- and northeast-trending fractures were best-fitted by two normal distributions. Those of the north-northwest-trending fractures were best fitted by a triangular distribution, whereas those of the northwest-trending fractures were best-fitted by a chi-square distribution.

Similarly, the length data of the four sets of surface fractures were also statistically analyzed. The results are shown in Figs. 41 to 44. It appears that the length data of the east- and northwest-trending surface fractures in this area were best-fitted by two PearsonVI distributions. Those of the northeast-trending surface fractures were best-fitted by an extreme-value distribution, whereas those of the north-northwest-trending surface fractures were best-fitted by a lognormal2 distribution.

Figs. 45 to 48 show the results of a statistical analysis on the spacing data of the four sets of surface fractures in the Black Mesa Basin area. A lognormal distribution appears to provide the best fit to the spacing data of the northwest-trending surface fractures, but those of the other three sets were best-fitted by lognormal2 distributions.

Statistical Analysis of Surface Lineaments and Fractures in the Mid-continent Region

A large number of surface lineaments and fractures were also collected and digitized from many previous studies of various parts of the Mid-continent region (Guo et al. 1996). Using the procedure discussed earlier, best-fit statistical distribution functions were obtained for the surface lineament and fracture characteristics in this region through extensive best-fitting analyses.

Surface Lineaments in Northeastern Oklahoma. Fig. 49 is a rose diagram for the surface lineaments in northeastern Oklahoma (Burchett et al. 1983). From this rose diagram, one can see that the surface lineaments in this area can be partitioned into five subsets oriented east-northeast, north-northeast, north, north-northwest, and northwest. Figs. 50 to 54 show the histograms, best-fit distributions, and sample data statistics for the five sets of the surface lineament orientation data. The orientations of the east-northeast-, north-northeast-, and north-northwest-trending surface lineaments in this area were best-fitted by normal distributions. Those of the north- and northwest-trending surface lineaments were best-fitted by triangular distributions.

The histograms, best-fit distributions, and sample data statistics of the corresponding lengths for the five sets of surface lineaments in the northeastern Oklahoma are shown in Figs. 55 to 59. It appears that PearsonV or PearsonVI distributions provide the best fits to the five sets of the lineament length data.

The spacing data for the surface lineaments in northeastern Oklahoma were also analyzed. The results are shown in Figs. 60 to 64. Inverse Gaussian, lognormal, lognormal2, and PearsonVI distributions appear to provide best fits to the five sets of the spacing data.

Surface Lineaments in Eastern Kansas. Fig. 65 shows a rose diagram of the surface lineaments in eastern Kansas (Burchett et al. 1983). Three major subsets can be identified from this diagram. They are oriented in the northeast, north-northwest, and northwest directions. Figs. 66 to 68 show the histograms, best-fit distributions, and sample data statistics of the orientation data. A triangular, a normal, and a chi-square distribution provide the best-fit probability distribution functions for the orientation data of the surface lineaments in eastern Kansas.

The corresponding length data were also analyzed. The results are shown in Figs. 69 to 71. One can see that the lengths of the surface lineaments in eastern Kansas are best-fitted by lognormal, PearsonVI, and PearsonV distributions.

The results of a statistical analysis on the corresponding spacing data are shown in Figs. 72 to 74. Lognormal2 and PearsonVI distributions were found to provide the best fits to the three sets of spacing data for the surface lineaments.

Surface Lineaments in Eastern Nebraska and Western Iowa. Fig. 75 is a rose diagram of the surface lineaments in eastern Nebraska and western Iowa (Burchett et al. 1983). Clearly, the lineaments can be partitioned into three sets, oriented in northeast, north and northwest. A statistical analysis of the lineament orientations shows that triangular distributions provide the best fits to the three sets of surface lineaments in the area. Figs. 76 to 78 show the histograms, best-fit distributions, and sample data statistics.

Similarly, a statistical analysis was also performed on the corresponding three sets of length and spacing data. The results for the length data analysis are given in Figs. 79 to 81. PearsonVI distributions appear to provide the best fits to the length data. The results for the spacing data analysis are shown in Figs. 82 to 84. An inverse Gaussian, a PearsonVI, and a lognormal distribution are the best-fitted spacing distributions for the surface lineaments in eastern Nebraska and western Iowa.

Surface Lineaments and Fractures in Western Oklahoma. Fig. 85 shows a rose diagram of the surface lineaments and fractures in western Oklahoma (Collins et al. 1974). From this figure, the surface lineaments and fractures can apparently be partitioned into three subsets trending in northeast, north, and northwest. Figs. 86 to 88 show the histograms, best-fit distributions, and sample data statistics for the three sets of the orientation data. A logistic, a normal, and a triangular distribution provide the best fits to the orientation data.

The results of a statistical analysis on the three sets of length data are given in Figs. 89 to 91. A lognormal, a lognormal2, and a PearsonV distribution appear to provide the best fits to the length data. The corresponding three sets of spacing data were sampled and statistically analyzed. The results are shown in Figs. 92 to 94. The spacing data were best-fitted by three lognormal2 distributions.

Surface Lineaments and Fractures in Western Kansas. Fig. 95 shows a rose diagram of the surface lineaments and fractures in western Kansas (Cooley 1984). The surface linear features in this area can be divided into two subsets trending northeast and northwest, although there appears an insignificant set trending north. Upon being partitioned into two sets, the orientation data were statistically analyzed. The best-fitted distributions are a triangular distribution for the northeast-trending set and a logistic distribution for the northwest-trending set. The histograms, best-fit distributions, and sample data statistics for the orientation data are shown in Figs. 96 and 97.

Similarly, the corresponding length and spacing data are also analyzed. The results for the two sets of the length data are shown in Figs. 98 and 99. PearsonVI distributions appear to provide the best fits to the length data. The results for the spacing data are shown in Figs. 100 and 101. The spacing data are also best-fitted by PearsonVI distributions.

Surface Lineaments and Fractures in the Hugoton Gas Field. Fig. 102 is a rose diagram of the surface lineaments and fractures in the western Hugoton Gas Field in southwestern Kansas and the Oklahoma Panhandle (Swanson et al. 1990). It is clear from this rose diagram that the surface linear features in this area can be partitioned into two subsets trending northeast and northwest. Figs. 103 and 104 show the histograms, best-fit distributions, and sample data statistics for the two sets of orientation data. A logistic and a triangular distribution appear to provide the best fits to the orientation data.

Similar analyses were also performed on the corresponding length and spacing data. The results for the length data are given in Figs. 105 and 106. A lognormal2 and a PearsonVI distributions were found to provide the best fits to the two sets of length data. The results for the spacing data are shown in Figs. 107 and 108. The best-fitted distributions are a lognormal2 distribution for the spacing data of the northeast-trending linear features, and a Weibull distribution for the spacing data of the northwest-trending linear features.

Surface Fractures in the Northern Forest City Basin. Fig. 109 shows a rose diagram of the surface fractures in northern Forest City Basin in southwestern Iowa (Herman et al. 1986). The surface fractures in this area appear to consist of two subsets trending east and north-northeast. The results of a statistical analysis on the orientation data are given in Figs. 110 and 111. A triangular and a normal distribution provide the best fits to the two sets of orientation data.

Figs. 112 and 113 show the histograms, best-fit distributions, and sample data statistics for the corresponding length data. A logistic and an extreme-value distribution give the best fits to the two sets of length data.

Similarly, the results for an analysis of the corresponding spacing data are shown in Figs. 114 and 115. The best-fitted distributions for the two sets of spacing data are an exponential distribution for the east-trending surface fractures and a lognormal2 distribution for the north-northeast-trending surface fractures.

Surface Lineaments and Fractures in Northeastern Iowa. Fig. 116 shows a rose diagram of the surface lineaments and fractures in northeastern Iowa (Chen 1992). Three subsets can be identified trending east, northeast, and northwest. Figs. 117 to 119 show the histograms, the best-fit distributions, and the sample data statistics for the three sets of orientation data. A PearsonV and two triangular distributions provide the best fits to the three sets of orientation data.

Similarly, Figs. 120 to 122 show the results of a statistical analysis on the corresponding length data. The best-fitted distributions are a triangular distribution for the lengths of the east-trending linear features, a PearsonV distribution for the lengths of the northeast-trending linear features, and an extreme-value distribution for the lengths of the northwest-trending linear features.

The results of a statistical analysis on the corresponding spacing data are shown in Figs. 123 to 125. A Weibull, a PearsonV, and a PearsonVI distribution provide the best fits to the three sets of spacing data for the surface lineaments and fractures in northeastern Iowa.

Discussions on the Statistical Distributions of Surface Lineaments and Fractures

The surface lineaments and fractures mapped from nine areas in the Mid-continent region and three areas in the northeastern Arizona were collected, digitized, and statistically analyzed in this paper. In all, 36 sets were identified based on their orientations. The best-fit distributions were obtained for the orientation, length, and spacing of each set.

Fig. 126 shows the best-fit distributions and their frequencies for the orientations of the 36 sets of surface lineaments and fractures. Triangular, normal, and logistic distributions provided the best fits to 33 of the 36 sets of the orientation data. The best-fit distributions and their frequencies for the corresponding 36 sets of the length data are shown in Figure 127. PearsonVI, PearsonV, lognormal, and extreme-value distributions provided the best fits to 30 of the 36 sets of length data. Similarly, the best-fit distributions and their frequencies for the corresponding 36 sets of spacing data are given in Fig. 128. Lognormal2, PearsonVI, and lognormal distributions provided the best fits to 30 of the 36 sets of spacing data.

Comparing the results of this study to those of the previous studies reviewed earlier in this paper, one can notice both consistency to a certain degree and significant discrepancies between them. Many probability distribution functions identified in the previous studies, such as normal distribution for orientation data, lognormal distribution for length data, and lognormal and Weibull distributions for spacing data, also provided best fits to some of the 36 sets of surface lineaments and fractures. However, these distribution functions only fitted a few of the 36 sets of data. Different from previous studies, this study shows triangular distributions are the most significant type of probability functions for describing natural fracture orientation data, followed by normal and logistic distributions (see Fig.126). PearsonVI distributions are the most significant type of probability functions for describing natural fracture length data, followed by PearsonV, lognormal2, and extreme-value distributions (see Fig. 127). Natural fracture spacing data, as shown in Fig. 128, appear to be best characterized by lognormal2 distribution, followed by PearsonVI and lognormal distributions.

The probability distribution functions identified in this study for describing natural fracture characteristics were obtained through an extensive statistical analysis of a large number of surface lineaments and fractures, and using 25 different hypothesized probability functions during best fitting. We believe they provide realistic descriptions of natural fracture orientation, length, and spacing. However, these distribution functions must be conditioned using any available subsurface fracture data before they can be used for stochastic simulations of natural fractures in a naturally fractured reservoir.

Conclusions

In this paper, we presented the results of an extensive statistical analysis of natural fracture characteristics using a huge number of surface lineaments and fractures mapped in the Mid-continent and Colorado Plateau regions. The following conclusions are obtained:

Natural fracture orientations are best described by triangular and normal distributions, followed by logistic, chi-square, and PearsonV distributions. Triangular and normal distributions are, by far, the most significant distributions for characterizing natural fracture orientation data.

Natural fracture lengths are best described by PearsonVI and PearsonV distributions. Other favorable distribution functions for characterizing natural fracture length data include extreme-value, lognormal2, lognormal, loglogistic, logistic, and triangular distributions.

Natural fracture spacing data are best described statistically by lognormal2 and PearsonVI distributions followed by lognormal, inverse Gaussian, Weibull, exponential, and PearsonV distributions.

The probability distribution functions identified for characterizing natural fracture characteristics using surface lineaments and fractures must be calibrated using any available subsurface fracture data before they can be used for stochastic simulations of subsurface natural fracture systems in a naturally fractured reservoir.

References

1. Baecher, G.B., Lanney, N.A., and Einstein, H.H. 1977. "Statistical Description of Rock Properties and Sampling," presented at the 18th U.S. Symp. on Rock Mechanics, Energy Resources and Excavation Technology, 1977, 5C1-1.
2. Baecher, G.B., 1983. "Statistical Analysis of Rock Mass Fracturing," *Math. Geol.* (Vol. 15, No. 2, 1983) 329.
3. Belfield, W.C., and Sovich, J.P. 1995. "Fracture Statistics from Horizontal Wellbores," *JCPT* (Vol. 34, No. 6, June 1995) 47.
4. Burchett, R.R., Luza, K.V., Van Eck, O.J., and Wilson, F.W. 1983. *Seismicity and Tectonic Relationships of the Nemaha Uplift and Midcontinent Geophysical Anomaly*, Division of Health, Siting and Waste Management, Office of Nuclear Regulatory Commission.
5. Cacas, M.C., *et al.*,1990. "Modeling Fracture Flow with a Stochastic Discrete Fracture Network: Calibration and Validation 1. The Flow Model," *Water Resources Research* (Vol. 26, No. 3, March 1990) 479.
6. Chen X. 1992. "Applications of Remote Sensing and GIS Techniques for Environmental Geologic Investigation, Northeastern Iowa," PhD thesis, University of Iowa.
7. Collins, R.J., McCown, F.P., Stonis, L.P., Petzel, G.J., Everett, J.R. 1974. *An Evaluation of ERTS Data for the Purposes of Petroleum Exploration*, final report prepared for Goddard Space Flight Center.
8. Cooley, M.E. 1984. *Linear Features Determined from Landsat Imagery in Western Kansas*, U.S. Geological Survey Open-File Report 84-241.
9. Dverstorp, B., and Andersson, J. 1989. "Application of the Discrete Fracture Network Concept with Field Data: Possibilities of Model Calibration and Validation," *Water Resources Research* (Vol. 25, No. 3, March 1989) 540.

10. Guo, G., and Carroll, H.B. 1995. *A New Methodology for Oil and Gas Exploration Using Remote Sensing Data and Surface Fracture Analysis*, NIPER/BDM-0163, Aug. 1995.
11. Guo, G., and George, S.A. 1996. *An Analysis of Surface and Subsurface Lineaments and Fractures for Oil and Gas Exploration in the Midcontinent Region*, NIPER/BDM-0223, March 1996.
12. Guo, G., and Evans, R.D., 1994. "Geologic and Stochastic Characterization of Naturally Fractured Reservoirs," SPE 27025 presented at the 1994 SPE III Latin American & Caribbean Petroleum Engineering Conference, Buenos Aires, Argentina, April 27-29.
13. Heffer, K.J., and Bevan, T.G. 1990. "Scaling Relationships in Natural Fractures: Data, Theory, and Application," SPE 20981 presented at the 1990 European Petroleum Conference held in Hague, Netherlands, Oct. 22-24.
14. Herman, J., Etzler, P.J., Wilson, M.L., and Vincent, R.K. 1986. "Remote Sensing Study of the Mid-continent Geophysical Anomaly in Iowa," Paper presented at the Society of Mining Engineers Fall Meeting, St. Louis, Missouri, Sep. 7-10, 1986.
15. Lepley, L.K. 1977. *Landsat Lineament Map of Arizona with Emphasis on Quaternary Fractures*. University of Arizona Bureau of Geology and Mineral Technology Open-File Report 77-2.
16. Long, J.C.S., Remer, J.S., Wilson, C.R., and Witherspoon, P.A. 1982. "Porous Media Equivalents for Networks of Discontinuous Fractures," *Water Resources Research* (Vol. 18, No. 3, June 1982) 645.
17. Loosveld, R. J. H., and Franssen, R.C.M.W. 1992. "Extensional vs. Shear Fractures: Implications for Reservoir Characterization," SPE 25017 presented at the 1992 SPE European Petroleum Conference held in Cannes, France, Nov. 16-18.
18. Lorentz, J.C., and Hill, R.E. 1991. "Subsurface Fracture Spacing: Comparison of Inferences from Slant/Horizontal Core and Vertical Core in Mesaverde Reservoirs," SPE 21877 presented at the 1991 Rocky Mountain Regional Meeting and Low-Permeability Reservoirs Symposium held in Denver, April 15-17.
19. Rouleau, A., and Gale, J.E. 1985. "Statistical Characterization of the Fracture System in the Stripa Granite, Sweden," *Int. J. Rock Mech. Min. Sci. & Geomech.* Abstr. (Vol. 22, No. 6, 1985) 353.
20. Snow, D.T., 1970. "The Frequency and Apertures of Fractures in Rock," *Int. J. Rock Mech. Min. Sci.* (Vol. 7, 1970) 23.
21. Swanson, D.C., and Shannon, P.J. 1990. "Landsat Interpretation Useful in Hugoton Gas Field," *World Oil* (January 1990) 108.

Appendix. Probability Density Functions

$BETA(\alpha_1,\alpha_2)$: $$f(x)=\frac{x^{\alpha_1-1}(1-x)^{\alpha_2-1}}{B(\alpha_1,\alpha_2)}$$

where $B(x_1,x_2)=\int_0^1 t^{x_1-1}(1-t)^{x_2-1}dt$

$BINOMIAL(n,p)$: $$f(x)=\binom{n}{x}p^x(1-p)^{n-x}$$

$CHISQ(v)$: $$f(x)=\frac{x^{\frac{v}{2}-1}e^{\frac{-x}{2}}}{2^{\frac{v}{2}}\Gamma\left(\frac{v}{2}\right)}$$

$ERF(h)$: $$f(x)=\frac{h}{\sqrt{\pi}}e^{-h^2x^2}$$

$ERLANG(m,\beta)$: $$f(x)=\frac{\beta^{-m}x^{m-1}e^{\frac{-x}{\beta}}}{\Gamma(m)}$$

$EXPON(\beta)$: $$f(x)=\frac{e^{\frac{-x}{\beta}}}{\beta}$$

$ExtremeValue(a,b)$:
$$f(x)=\left(\frac{1}{b}\right)\exp\left(-\frac{x-a}{b}\right)\exp\left[-\exp\left(-\frac{x-a}{b}\right)\right]$$

$GAMMA(\alpha,\beta)$: $$f(x)=\frac{\beta^{-\alpha}x^{\alpha-1}e^{\frac{-x}{\beta}}}{\Gamma(\alpha)}$$

$GEOMET(p)$: $$f(x)=p(1-p)^x$$

$HYPERGEO(n,D,M)$: $$f(x)=\frac{\binom{D}{x}\binom{M-D}{n-x}}{\binom{M}{n}}$$

$InverseGaussian(\lambda,\mu)$: $$f(x)=\left(\frac{\lambda}{2\pi x^3}\right)^{\frac{1}{2}}\exp\left(\frac{-\lambda(x-\mu)^2}{2\mu^2x}\right)$$

$LOGISTIC(\alpha,\beta)$: $$f(x)=\frac{z}{\beta(1+z)^2}$$

where $z=\exp\left[\frac{-(x-\alpha)}{\beta}\right]$

$LOGLOGISTIC(\alpha,\beta,\gamma)$: $$f(x)=\frac{\alpha\left(\frac{x-\gamma}{\beta}\right)^{\alpha-1}}{\beta\left[1+\left(\frac{x-\gamma}{\beta}\right)^{-\alpha}\right]^2}$$

$LOGNORM(\mu,\sigma)$: $$f(x)=\frac{1}{x\sqrt{2\pi\sigma_1^2}}\exp\frac{-(\ln x-\mu_1)^2}{2\sigma_1^2}$$

where $\mu_1=\ln\left(\frac{\mu^2}{\sqrt{\sigma^2+\mu^2}}\right)$ and $\sigma_1=\sqrt{\ln\left(\frac{\sigma^2+\mu^2}{\mu^2}\right)}$

$LOGNORM2(\mu,\sigma)$: $$f(x)=\frac{1}{x\sqrt{2\pi\sigma^2}}\exp\frac{-(\ln x-\mu)^2}{2\sigma^2}$$

$NEGBIN(s,p)$: $$f(x)=\binom{s+x-1}{x}p^s(1-p)^x$$

$$NORMAL(\mu,\sigma): \quad f(x)=\frac{1}{\sqrt{2\pi\sigma^2}}e^{\frac{-(x-\mu)^2}{2\sigma^2}}$$

$$PARETO(\theta,a): \quad f(x)=\frac{\theta a^{\theta}}{x^{\theta+1}}$$

$$PearsonV(\alpha,\beta): \quad f(x)=\frac{x^{-(\alpha+1)}\exp\left(-\frac{\beta}{x}\right)}{\beta^{-\alpha}\Gamma(\alpha)}$$

$$PearsonVI(\alpha_1,\alpha_2,\beta): \quad f(x)=\frac{\left(\frac{x}{\beta}\right)^{\alpha_1-1}}{\beta B(\alpha_1,\alpha_2)\left(1+\frac{x}{\beta}\right)^{\alpha_1+\alpha_2}}$$

$$POISSON(\lambda): \quad f(x)=\frac{e^{-\lambda}\lambda^{x}}{x!}$$

$$RAYLEIGH(b): \quad f(x)=\frac{x}{b^2}\exp\left(-\frac{x^2}{2b^2}\right)$$

$$Student'sT(\upsilon): \quad f(x)=\frac{\Gamma\left(\frac{\upsilon+1}{2}\right)}{(\pi\upsilon)^{\frac{1}{2}}\Gamma\left(\frac{\upsilon}{2}\right)\left[1+\frac{x^2}{\upsilon}\right]^{\frac{\upsilon+1}{2}}}$$

$$TRIANG(a,b,c): \quad f(x)=\begin{cases}\frac{2(x-a)}{(b-a)(c-a)} & if \ a\le x\le b\\ \frac{2(c-x)}{(c-a)(c-b)} & if \ b\le x\le c\end{cases}$$

$$WEIBULL(\alpha,\beta): \quad f(x)=\alpha\beta^{-\alpha}x^{\alpha-1}e^{-(x/\beta)^{\alpha}}$$

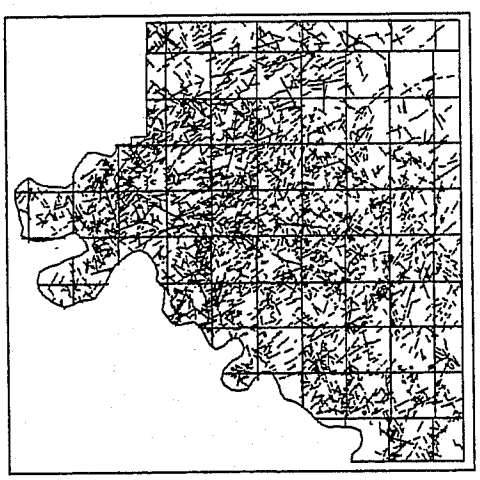

Fig. 1—Surface fractures in Osage County, Oklahoma.

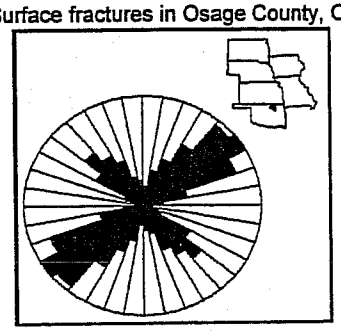

Fig. 2—A rose diagram of the surface fractures in Osage County, Oklahoma.

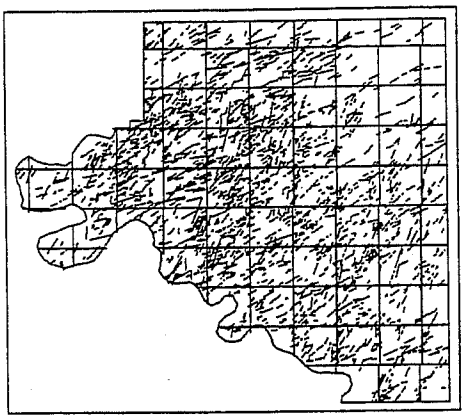

Fig. 3—Northeast-trending surface fractures in Osage County, Oklahoma.

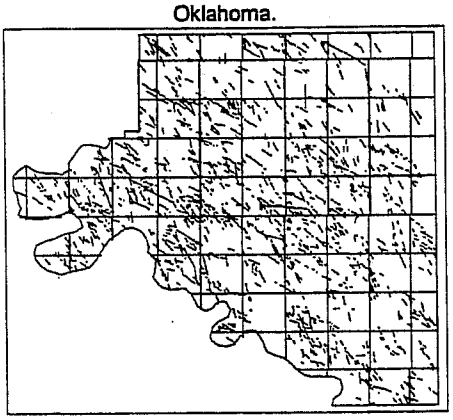

Fig. 4—Northwest-trending surface fractures in Osage County, Oklahoma.

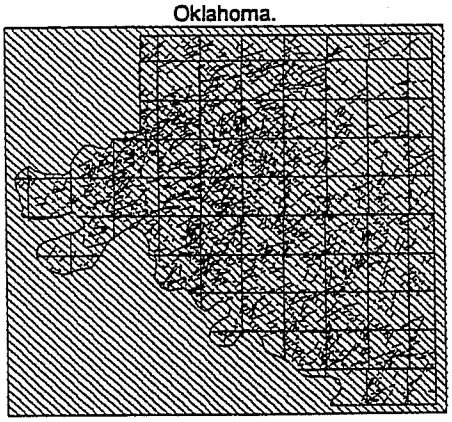

Fig. 5—The northeast-trending surface fractures and a set of imaginary scanlines in Osage County, Oklahoma.

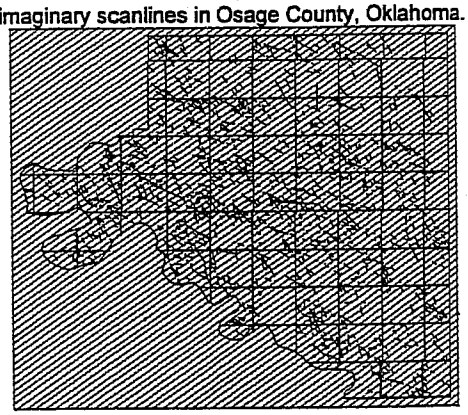

Fig. 6—The northwest-trending surface fractures and a set of imaginary scanlines in Osage County, Oklahoma.

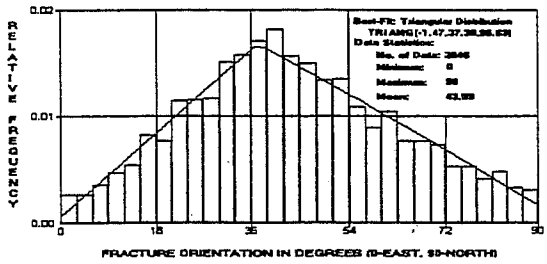

Fig. 7—The histogram and best-fit orientation distribution of the northeast-trending surface fractures in Osage County, Oklahoma.

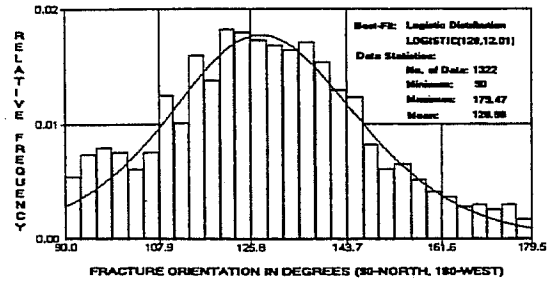

Fig. 8—The histogram and best-fit orientation distribution of the northwest-trending surface fractures in Osage County, Oklahoma.

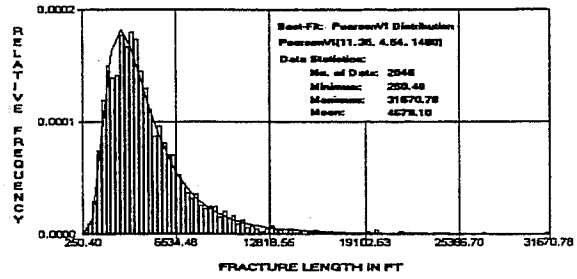

Fig. 9—The histogram and best-fit length distribution of the northeast-trending surface fractures in Osage County, Oklahoma.

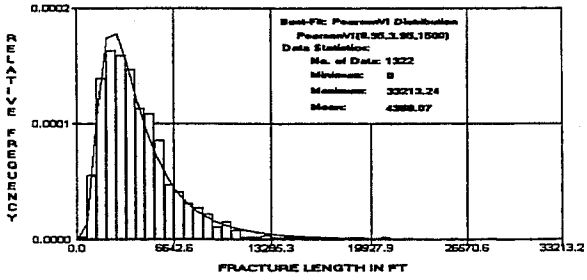

Fig. 10—The histogram and best-fit length distribution of the northwest-trending surface fractures in Osage County, Oklahoma.

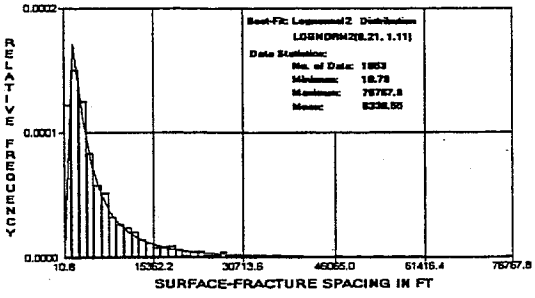

Fig. 11—The histogram and best-fit spacing distribution of the northeast-trending surface fractures in Osage County, Oklahoma.

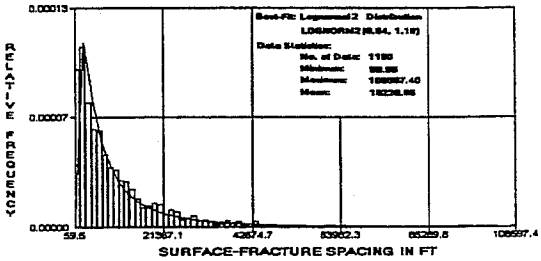

Fig. 12—The histogram and best-fit spacing distribution of the northwest-trending surface fractures in Osage County, Oklahoma.

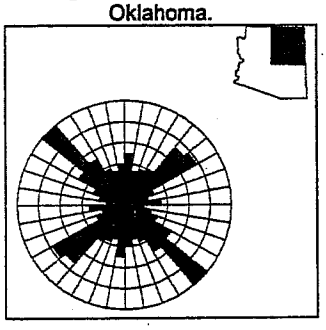

Fig. 13—A rose diagram of the surface lineaments in northeastern Arizona.

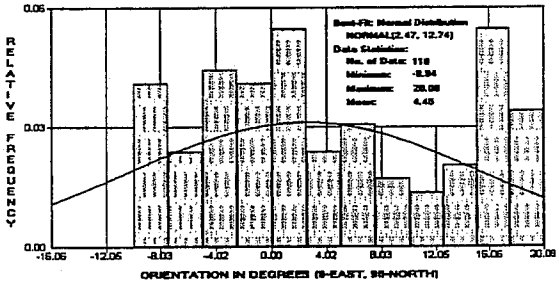

Fig. 14—The histogram and best-fit orientation distribution of the east-trending surface lineaments in northeastern Arizona.

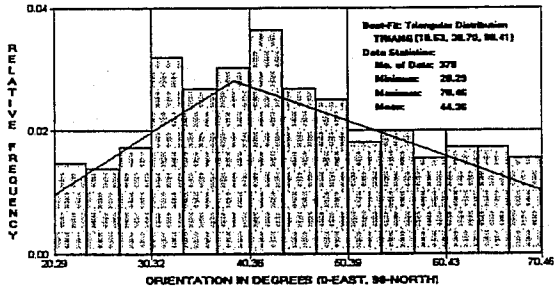

Fig. 15—The histogram and best-fit orientation distribution of the northeast-trending surface lineaments in northeastern Arizona.

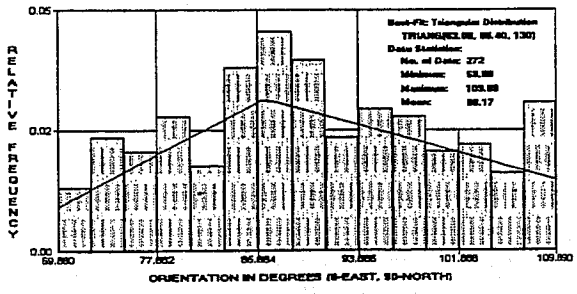

Fig. 16—The histogram and best-fit orientation distribution of the north-trending surface lineaments in northeastern Arizona.

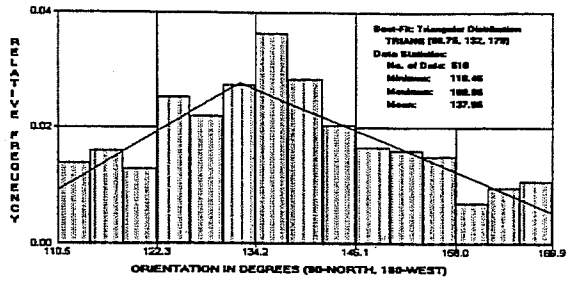

Fig. 17—The histogram and best-fit orientation distribution of the northwest-trending surface lineaments in northeastern Arizona.

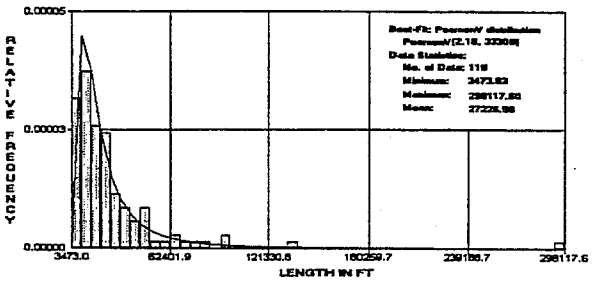

Fig. 18—The histogram and best-fit length distribution of the east-trending surface lineaments in northeastern Arizona.

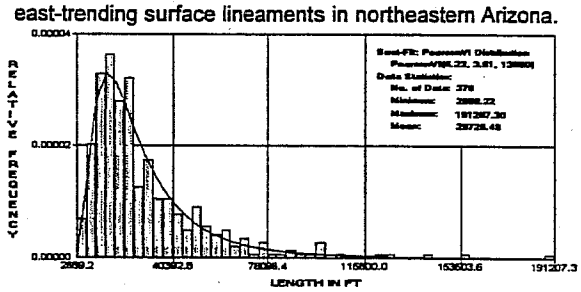

Fig. 19—The histogram and best-fit length distribution of the northeast-trending surface lineaments in northeastern Arizona.

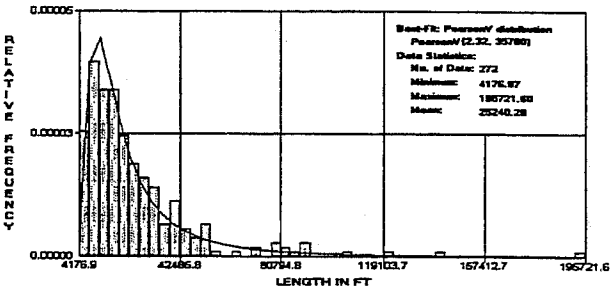

Fig. 20—The histogram and best-fit length distribution of the north-trending surface lineaments in northeastern Arizona.

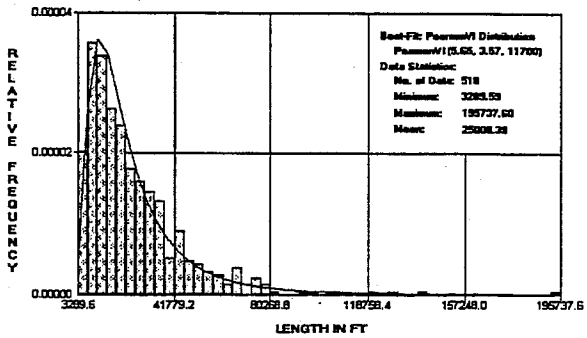

Fig. 21—The histogram and best-fit length distribution of the northwest-trending surface lineaments in northeastern Arizona.

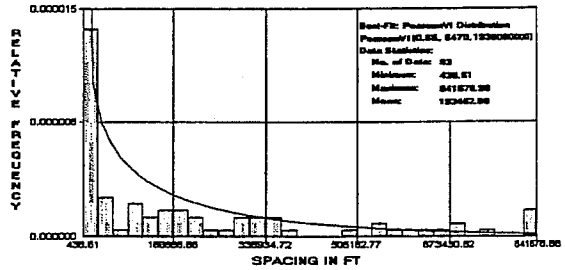

Fig. 22—The histogram and best-fit spacing distribution of the east-trending surface lineaments in northeastern Arizona.

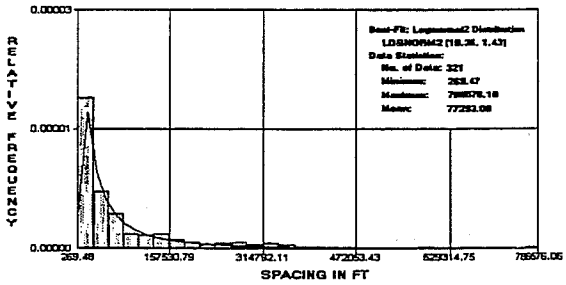

Fig. 23—The histogram and best-fit spacing distribution of the northeast-trending surface lineaments in northeastern Arizona.

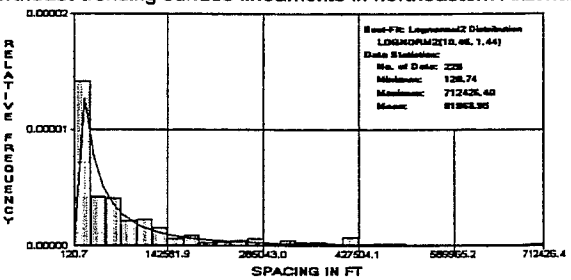

Fig. 24—The histogram and best-fit spacing distribution of the north-trending surface lineaments in northeastern Arizona.

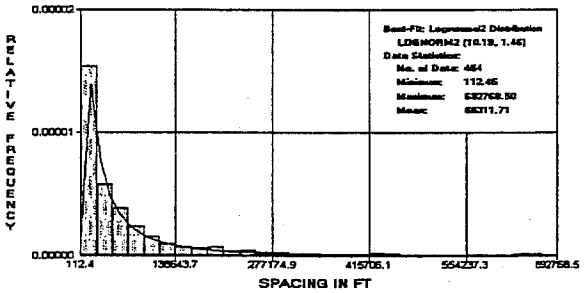

Fig. 25—The histogram and best-fit spacing distribution of the northwest-trending surface lineaments in northeastern Arizona.

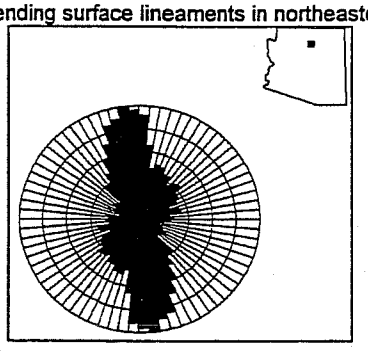

Fig. 26—A rose diagram of the surface fractures in the Cameron area in northeastern Arizona.

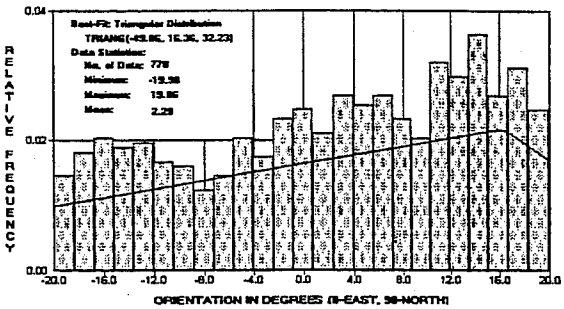

Fig. 27—The histogram and best-fit orientation distribution of the east-trending surface fractures in the Cameron area.

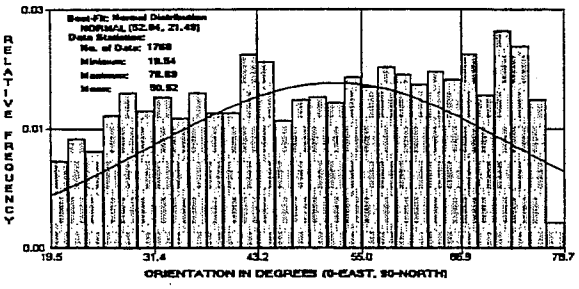

Fig. 28—The histogram and best-fit orientation distribution of the northeast-trending surface fractures in the Cameron area.

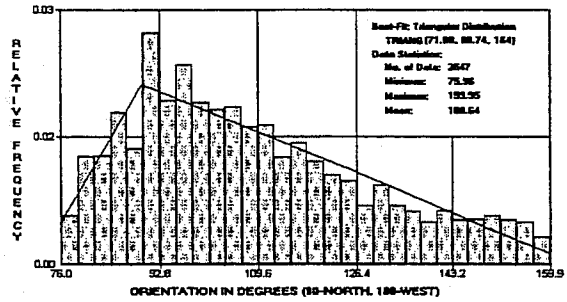

Fig. 29—The histogram and best-fit orientation distribution of the north-northwest-trending surface fractures in the Cameron area.

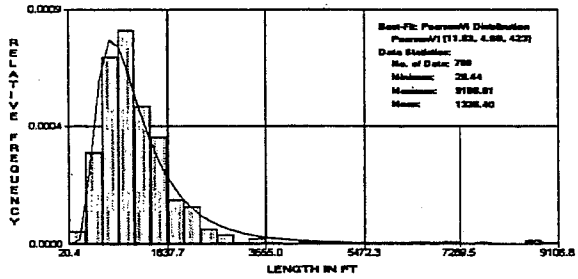

Fig. 30—The histogram and best-fit length distribution of the east-trending surface fractures in the Cameron area.

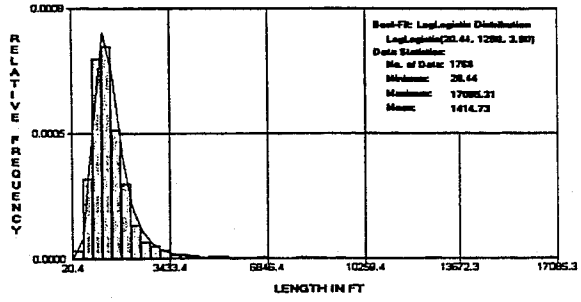

Fig. 31—The histogram and best-fit length distribution of the northeast-trending surface fractures in the Cameron area.

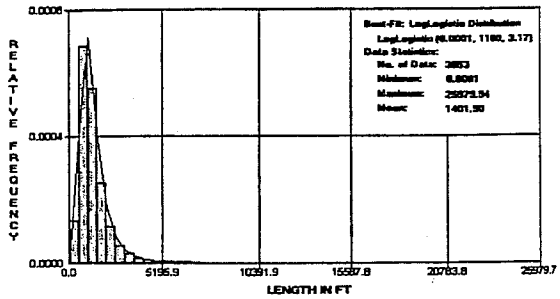

Fig. 32—The histogram and best-fit length distribution of the north-northwest-trending surface fractures in the Cameron area.

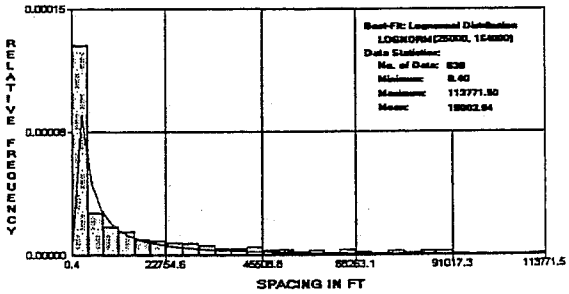

Fig. 33—The histogram and best-fit spacing distribution of the east-trending surface fractures in the Cameron area.

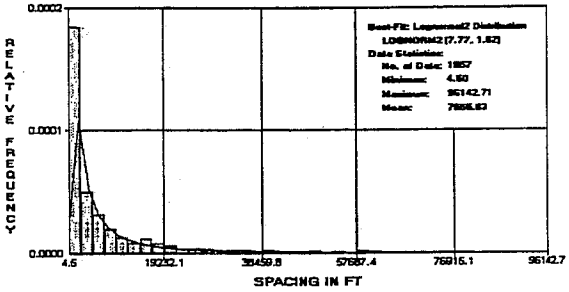

Fig. 34—The histogram and best-fit spacing distribution of the northeast-trending surface fractures in the Cameron area.

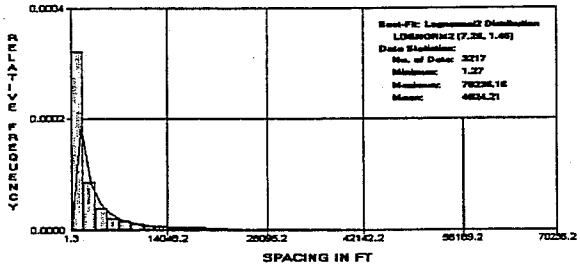

Fig. 35—The histogram and best-fit spacing distribution of the northwest-trending surface fractures in the Cameron area.

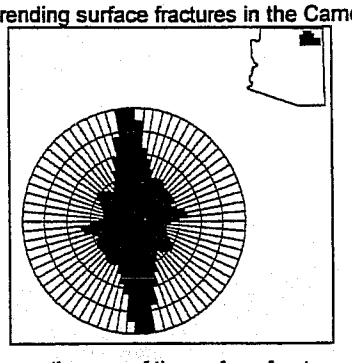

Fig. 36—A rose diagram of the surface fractures in the Black Mesa Basin area in northeastern Arizona.

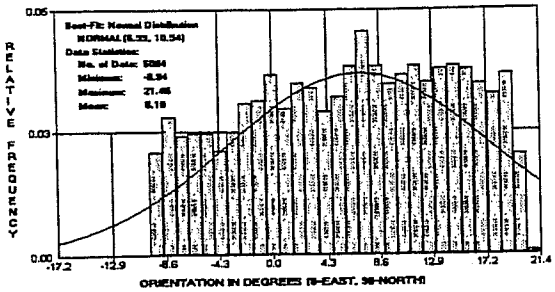

Fig. 37—The histogram and best-fit orientation distribution of the east-trending surface fractures in the Black Mesa Basin area.

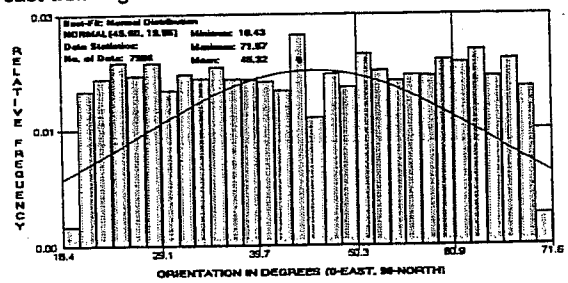

Fig. 38—The histogram and best-fit orientation distribution of the northeast-trending surface fractures in the Black Mesa Basin area.

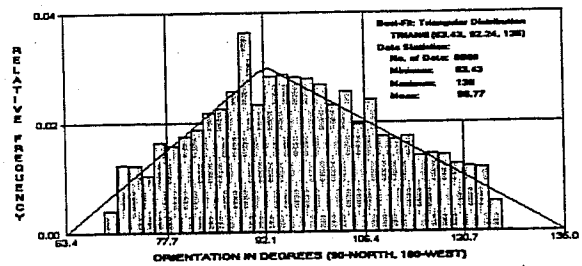

Fig. 39—The histogram and best-fit orientation distribution of the north-northwest-trending surface fractures in the Black Mesa Basin area.

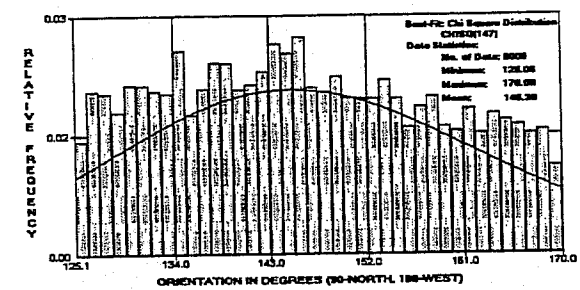

Fig. 40—The histogram and best-fit orientation distribution of the northwest-trending surface fractures in the Black Mesa Basin area.

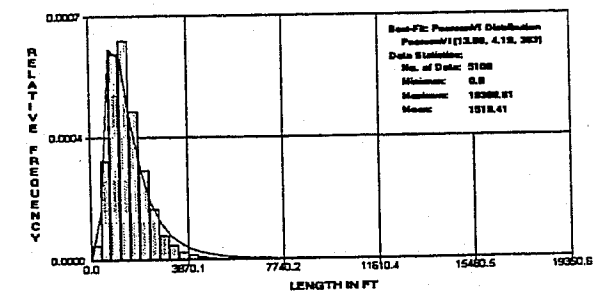

Fig. 41—The histogram and best-fit length distribution of the east-trending surface fractures in the Black Mesa Basin area.

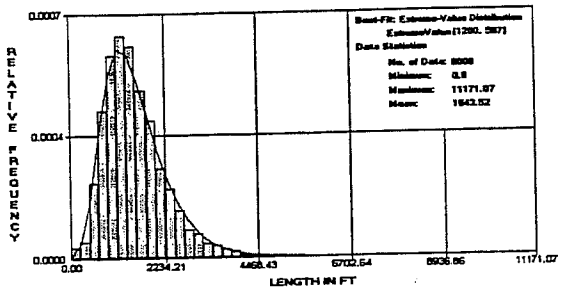

Fig. 42—The histogram and best-fit length distribution of the northeast-trending surface fractures in the Black Mesa Basin area.

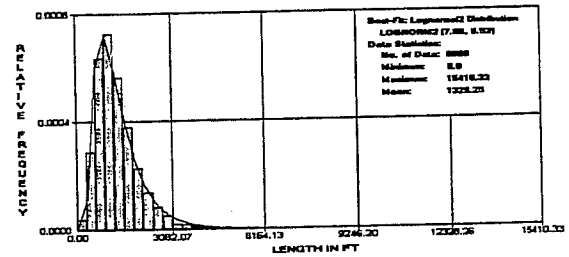

Fig. 43—The histogram and best-fit length distribution of the north-northwest-trending surface fractures in the Black Mesa Basin area.

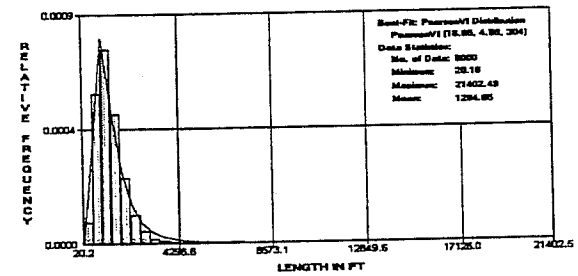

Fig. 44—The histogram and best-fit length distribution of the northwest-trending surface fractures in the Black Mesa Basin area.

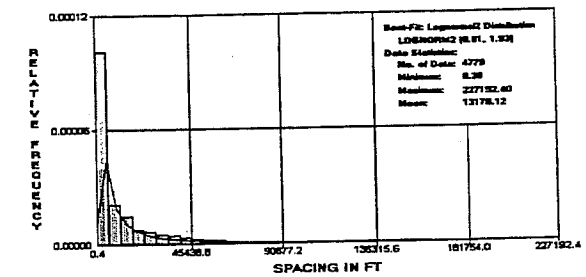

Fig. 45—The histogram and best-fit spacing distribution of the east-trending surface fractures in the Black Mesa Basin area.

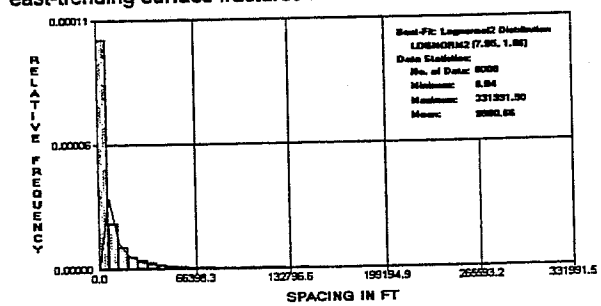

Fig. 46—The histogram and best-fit spacing distribution of the northeast-trending surface fractures in the Black Mesa Basin area.

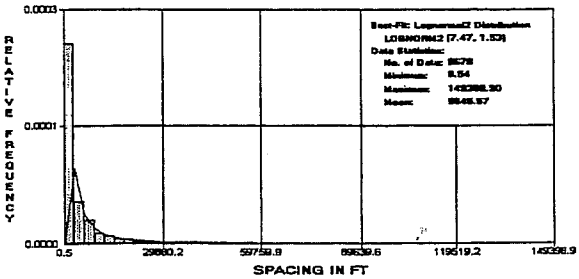

Fig. 47—The histogram and best-fit spacing distribution of the north-northwest-trending surface fractures in the Black Mesa Basin area.

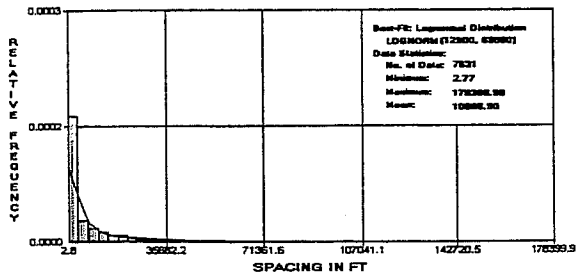

Fig. 48—The histogram and best-fit spacing distribution of the northwest-trending surface fractures in the Black Mesa Basin area.

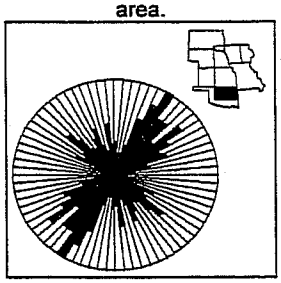

Fig. 49—A rose diagram of the surface lineaments in northeastern Oklahoma.

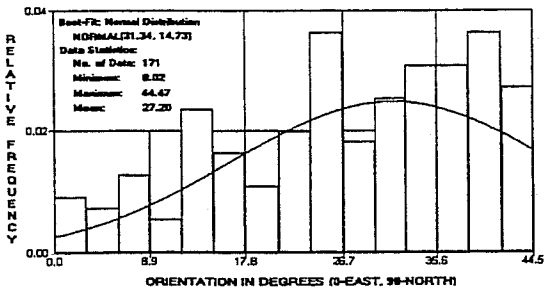

Fig. 50—The histogram and best-fit orientation distribution of the east-northeast-trending surface lineaments in northeastern Oklahoma.

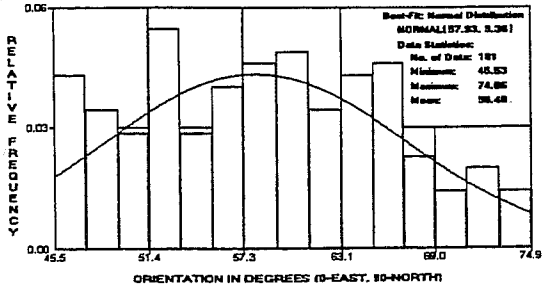

Fig. 51—The histogram and best-fit orientation distribution of the north-northeast-trending surface lineaments in northeastern Oklahoma.

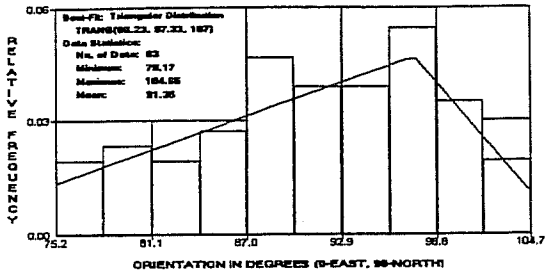

Fig. 52—the histogram and best-fit orientation distribution of the north-trending surface lineaments in northeastern Oklahoma.

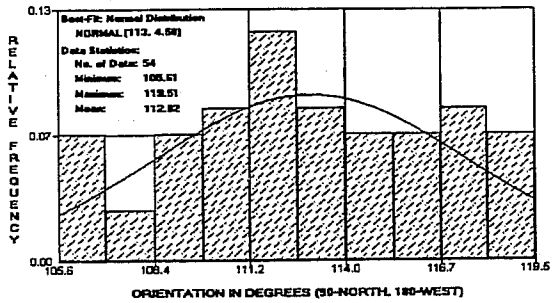

Fig. 53—The histogram and best-fit orientation distribution of the north-nothwest-trending surface lineaments in northeastern Oklahoma.

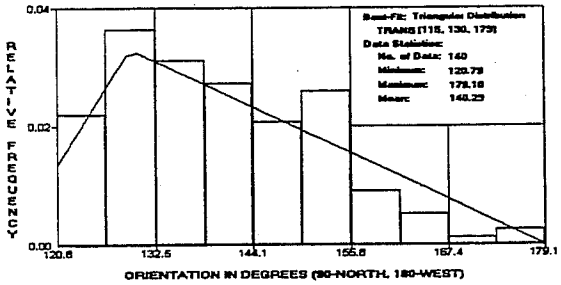

Fig. 54—The histogram and best-fit orientation distribution of the northwest-trending surface lineaments in northeastern Oklahoma.

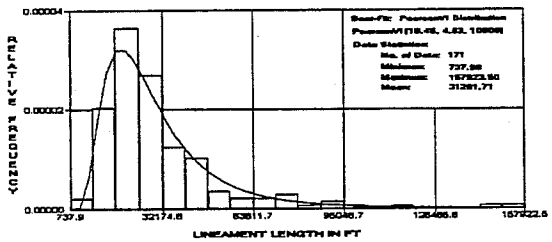

Fig. 55—The histogram and best-fit length distribution of the east-northeast-trending surface lineaments in northeastern Oklahoma.

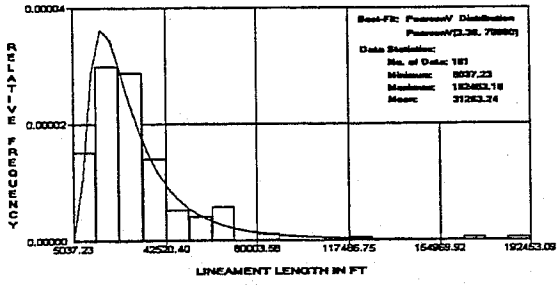

Fig. 56—The histogram and best-fit length distribution of the north-northeast-trending surface lineaments in northeastern Oklahoma.

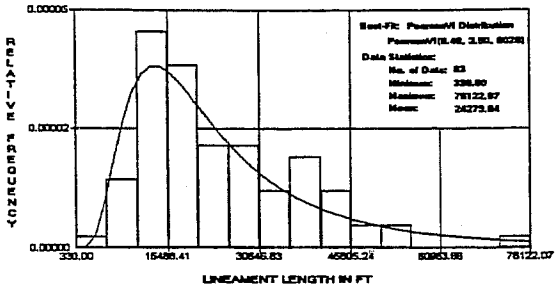

Fig. 57—The histogram and best-fit length distribution of the north-trending surface lineaments in northeastern Oklahoma.

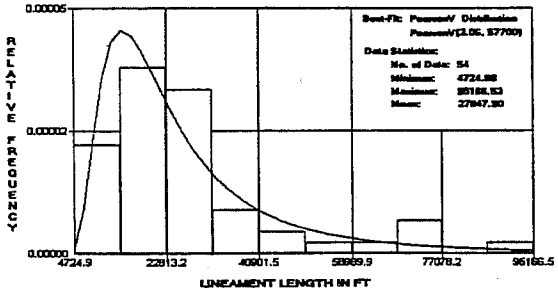

Fig. 58—The histogram and best-fit length distribution of the north-northwest-Trending Surface Lineaments in Northeastern Oklahoma.

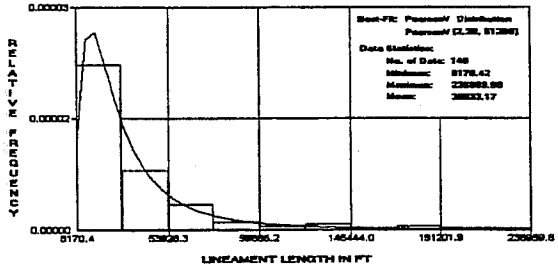

Fig. 59—The histogram and best-fit length distribution of the northwest-trending surface lineaments in northeastern Oklahoma.

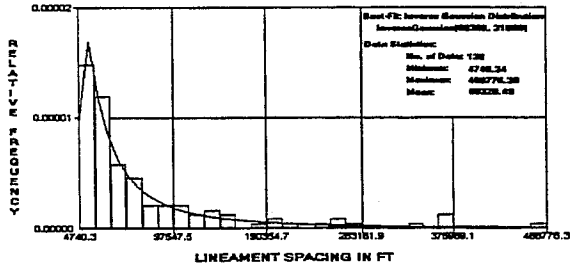

Fig. 60—The histogram and best-fit spacing distribution of the east-northeast-trending surface lineaments in northeastern Oklahoma.

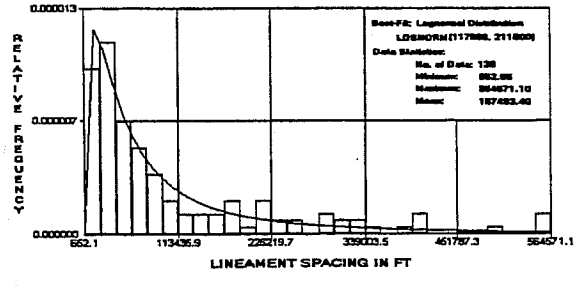

Fig. 61—The histogram and best-fit spacing distribution of the north-northeast-trending surface lineaments in northeastern Oklahoma.

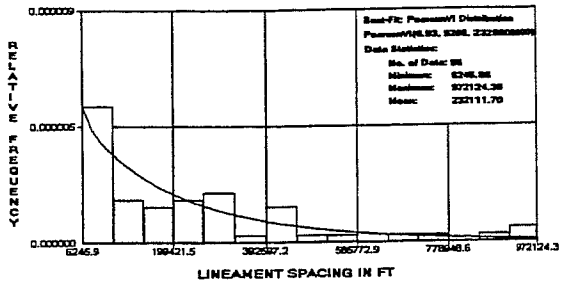

Fig. 62—The histogram and best-fit spacing distribution of the north-trending surface lineaments in northeastern Oklahoma.

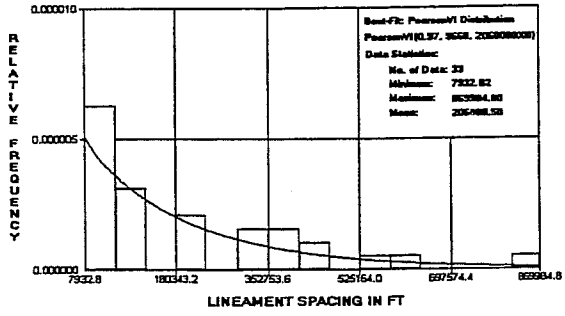

Fig. 63—The histogram and best-fit spacing distribution of the north-northwest-trending surface lineaments in northeastern Oklahoma.

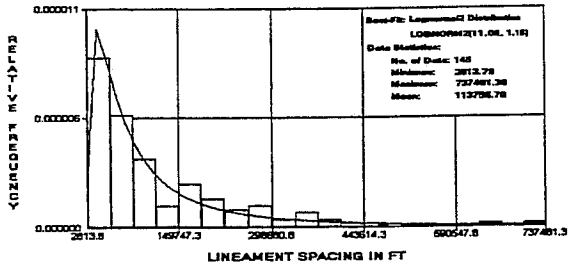

Fig. 64—The histogram and best-fit spacing distribution of the northwest-trending surface lineaments in northeastern Oklahoma.

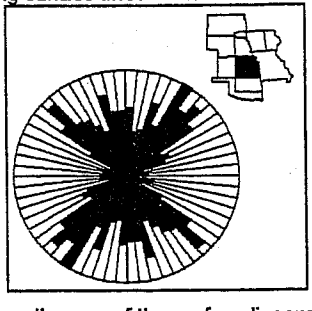

Fig. 65—A rose diagram of the surface lineaments in eastern Kansas.

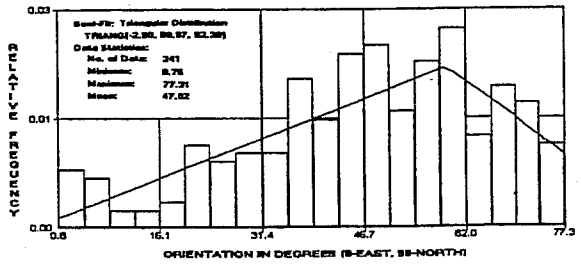

Fig. 66—The histogram and best-fit orientation distribution of the northeast-trending surface lineaments in eastern Kansas.

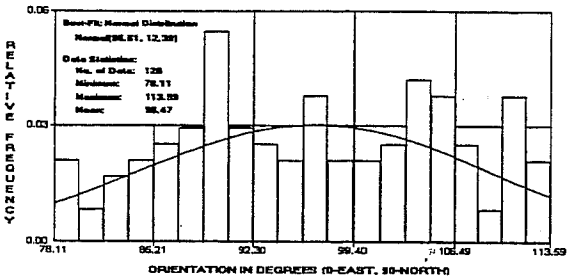

Fig. 67—The histogram and best-fit orientation distribution of the north-northwest-trending surface lineaments in eastern Kansas.

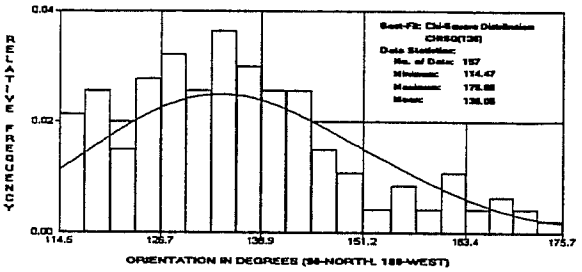

Fig. 68—The histogram and best-fit orientation distribution of the northwest-trending surface lineaments in eastern Kansas.

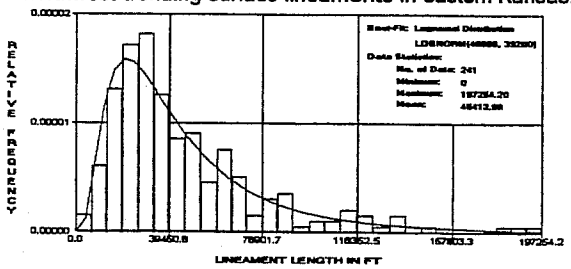

Fig. 69—The histogram and best-fit length distribution of the northeast-trending surface lineaments in eastern Kansas.

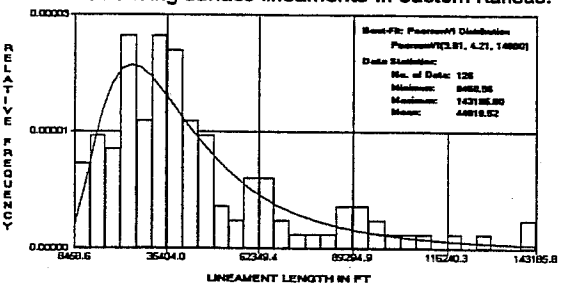

Fig. 70—The histogram and best-fit length distribution of the north-northwest-trending surface lineaments in eastern Kansas.

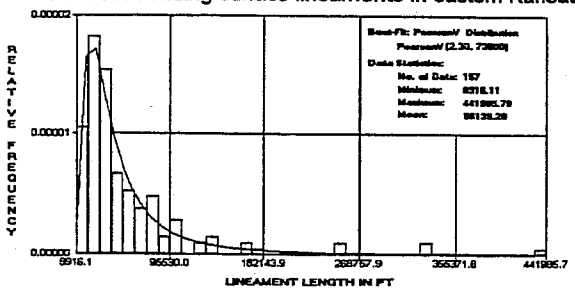

Fig. 71—The histogram and best-fit length distribution of the northwest-trending surface lineaments in eastern Kansas.

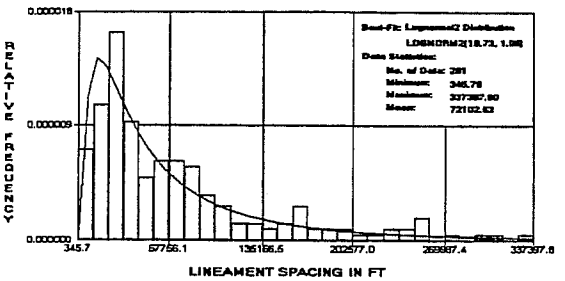

Fig. 72—The histogram and best-fit spacing distribution of the northeast-trending surface lineaments in eastern Kansas.

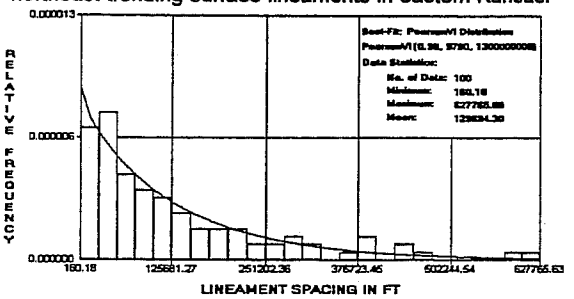

Fig. 73—The histogram and best-fit spacing distribution of the north-northwest-trending surface lineaments in eastern Kansas.

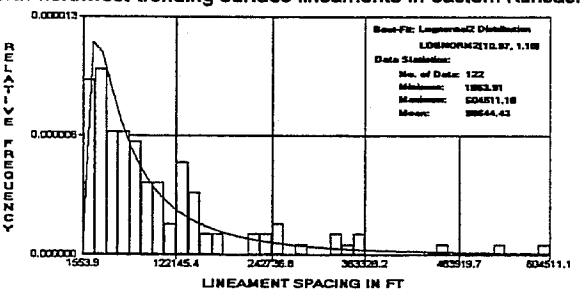

Fig. 74—The histogram and best-fit spacing distribution of the northwest-trending surface lineaments in eastern Kansas.

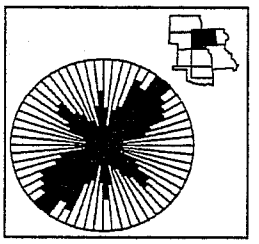

Fig. 75—A rose diagram of the surface lineaments in eastern Nebraska and western Iowa.

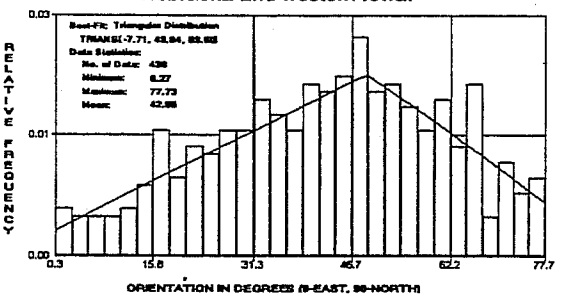

Fig.76—The histogram and best-fit orientation distribution of the northeast-trending surface lineaments in eastern Nebraska and western Iowa.

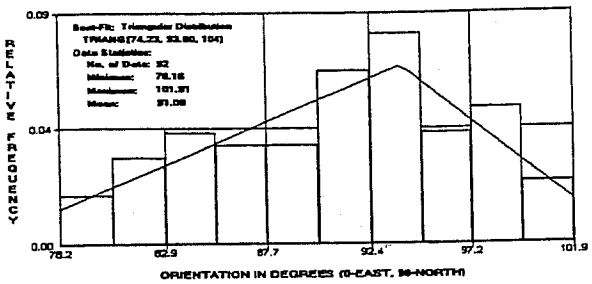

Fig. 77—The histogram and best-fit orientation distribution of the north-trending surface lineaments in eastern Nebraska and western Iowa.

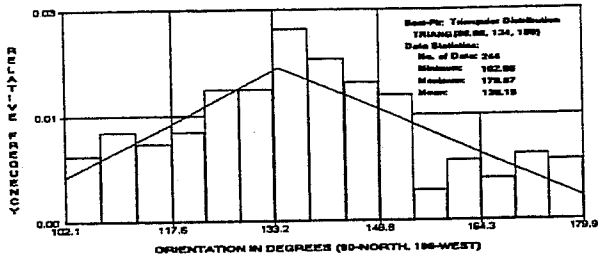

Fig. 78—The histogram and best-fit orientation distribution of the northwest-trending surface lineaments in eastern Nebraska and western Iowa.

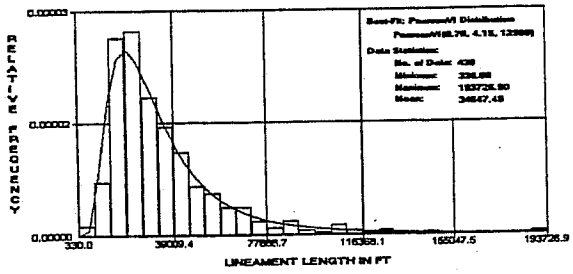

Fig. 79—The histogram and best-fit length distribution of the northeast-trending surface lineaments in eastern Nebraska and western Iowa.

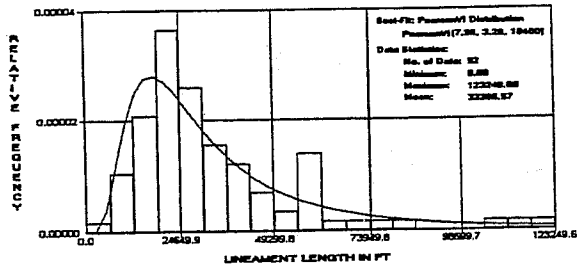

Fig. 80—The histogram and best-fit length distribution of the north-trending surface lineaments in eastern Nebraska and western Iowa.

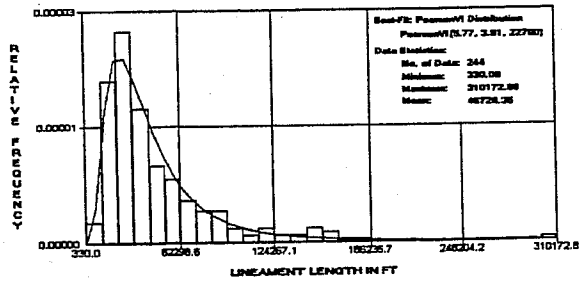

Fig. 81—The histogram and best-fit length distribution of the northwest-trending surface lineaments in eastern Nebraska and western Iowa.

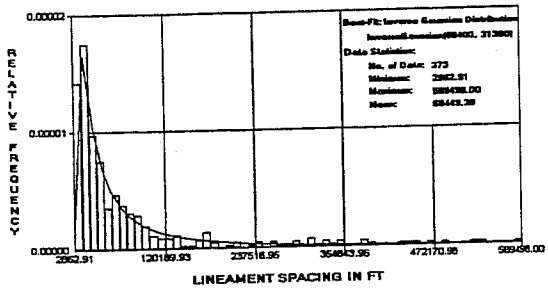

Fig. 82—The histogram and best-fit spacing distribution of the northeast-trending surface lineaments in eastern Nebraska and western Iowa.

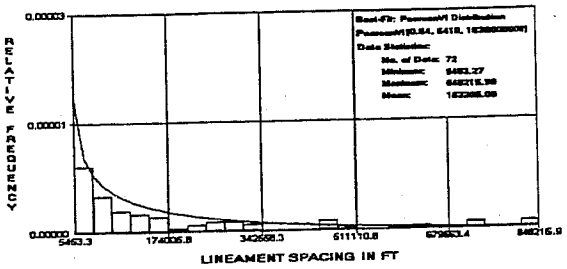

Fig. 83—The histogram and best-fit spacing distribution of the north-trending surface lineaments in eastern Nebraska and western Iowa.

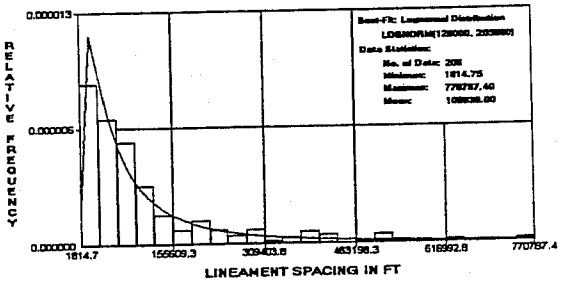

Fig. 84—The histogram and best-fit spacing distribution of the northwest-trending surface lineaments in eastern Nebraska and western Iowa.

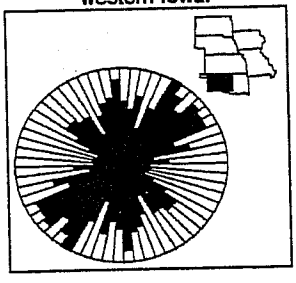

Fig. 85—A rose diagram of the surface lineaments and fractures in western Oklahoma.

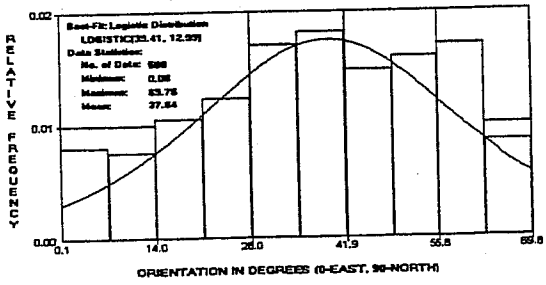

Fig. 86—The histogram and best-fit orientation distribution of the northeast-trending surface lineaments and fractures in western Oklahoma.

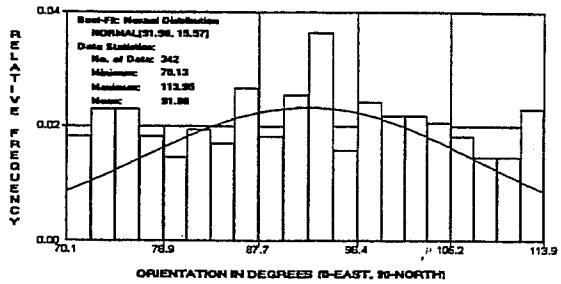

Fig. 87—The histogram and best-fit orientation distribution of the north-trending surface lineaments and fractures in western Oklahoma.

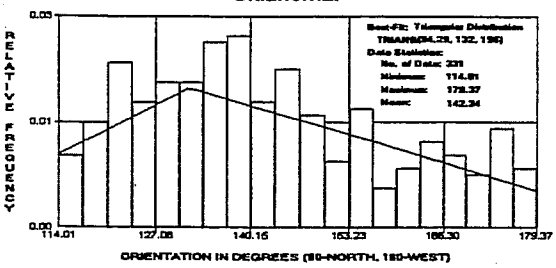

Fig. 88—The histogram and best-fit orientation distribution of the northwest-trending surface lineaments and fractures in western Oklahoma.

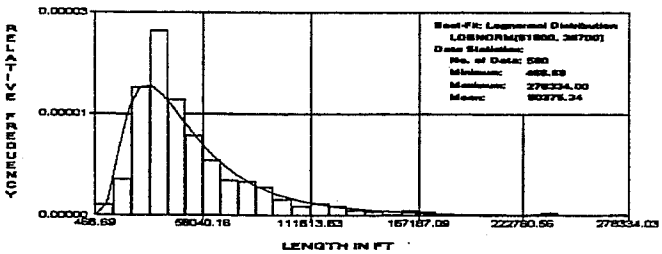

Fig. 89—The histogram and best-fit length distribution of the northeast-trending surface lineaments and fractures in western Oklahoma.

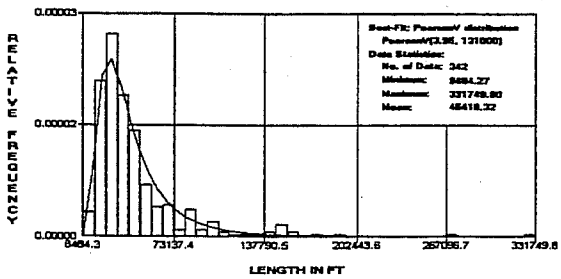

Fig. 90—The histogram and best-fit length distribution of the north-trending surface lineaments and fractures in western Oklahoma.

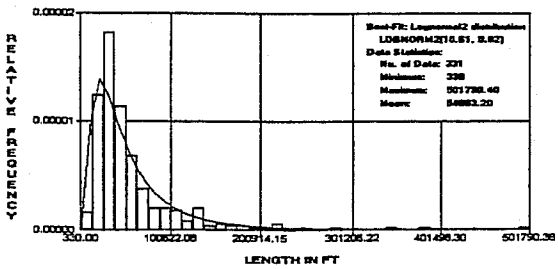

Fig. 91—The histogram and best-fit length distribution of the northwest-trending surface lineaments and fractures in western Oklahoma.

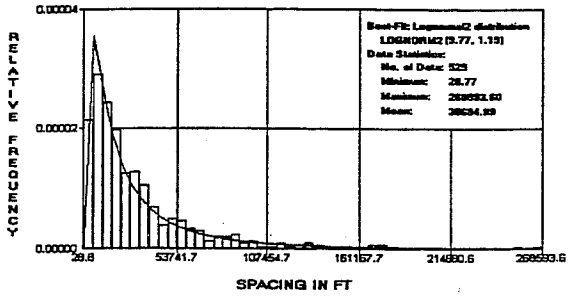

Fig. 92—The histogram and best-fit spacing distribution of the northeast-trending surface lineaments and fractures in western Oklahoma.

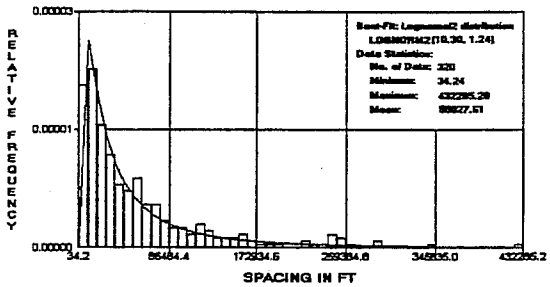

Fig. 93—The histogram and best-fit spacing distribution of the north-trending surface lineaments and fractures in western Oklahoma.

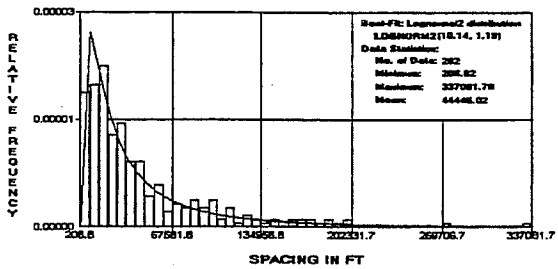

Fig. 94—The histogram and best-fit spacing distribution of the northwest-trending surface lineaments and fractures in western Oklahoma.

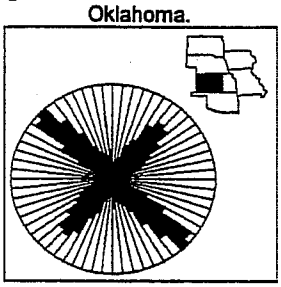

Fig. 95—A rose diagram of the surface lineaments and fractures in western Kansas.

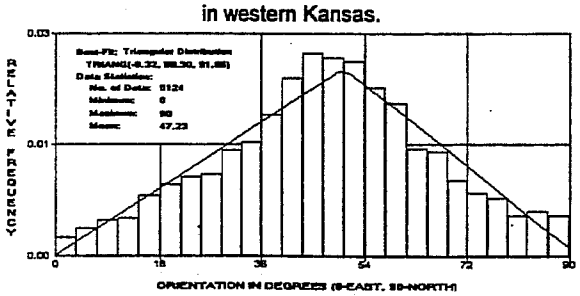

Fig. 96—The histogram and best-fit orientation distribution of the northeast-trending surface lineaments and fractures in western Kansas.

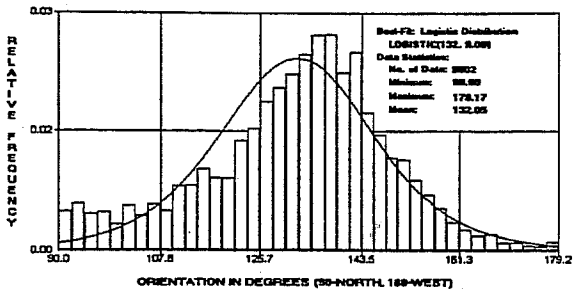

Fig. 97—The histogram and best-fit orientation distribution of the northwest-trending surface lineaments and fractures in western Kansas.

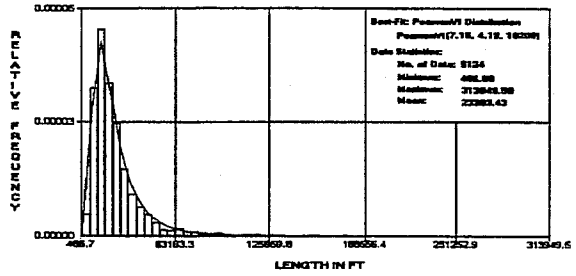

Fig. 98—The histogram and best-fit length distribution of the northeast-trending surface lineaments and fractures in western Kansas.

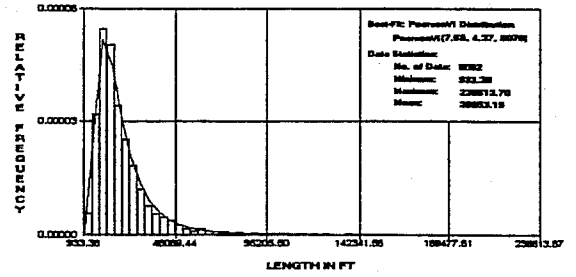

Fig. 99—The histogram and best-fit length distribution of the northwest-trending surface lineaments and fractures in western Kansas.

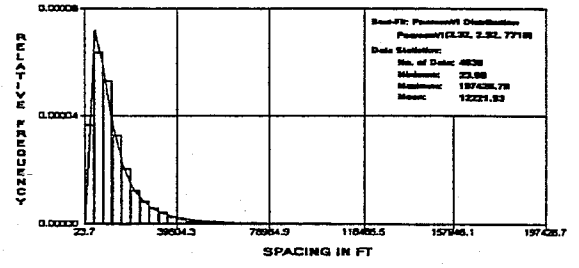

Fig. 100—The histogram and best-fit spacing distribution of the northeast-trending surface lineaments and fractures in western Kansas.

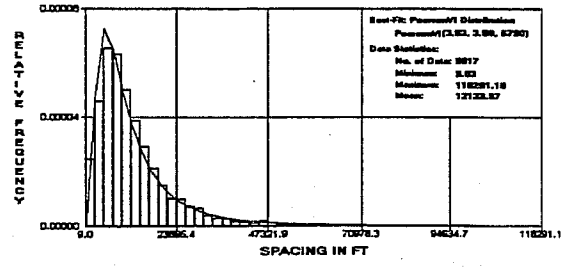

Fig. 101—The histogram and best-fit spacing distribution of the northeast-trending surface lineaments and fractures in western Kansas.

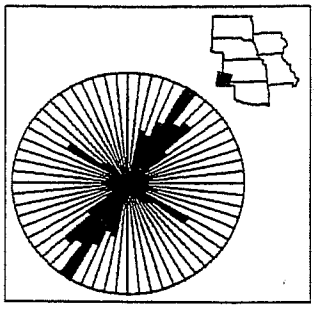

Fig. 102—A rose diagram of the surface lineaments and fractures in the western Hugoton Gas Field.

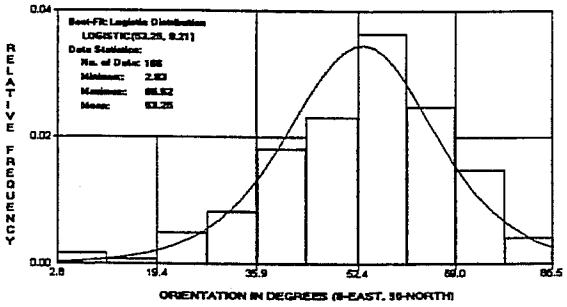

Fig. 103—The histogram and best-fit orientation distribution of the northeast-trending surface lineaments and fractures in the western Hugoton Gas Field.

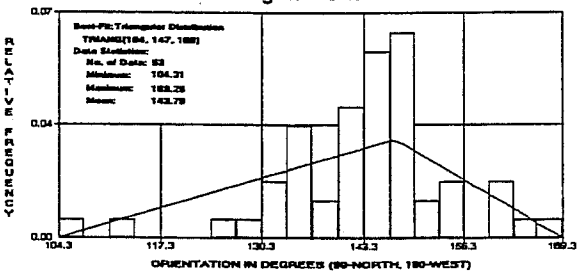

Fig. 104—The histogram and best-fit orientation distribution of the northwest-trending surface lineaments and fractures in the western Hugoton Gas Field

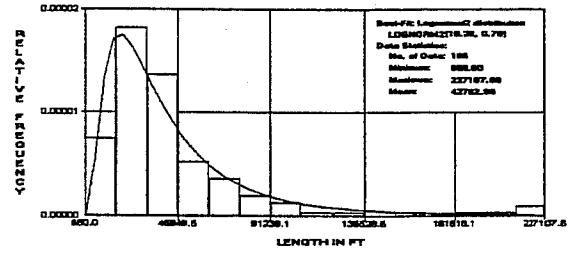

Fig. 105—The histogram and best-fit length distribution of the northeast-trending surface lineaments and fractures in the western Hugoton Gas Field.

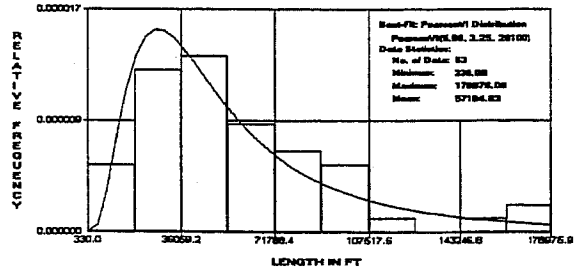

Fig. 106—The histogram and best-fit length distribution of the northwest-trending surface lineaments and fractures in the western Hugoton Gas Field.

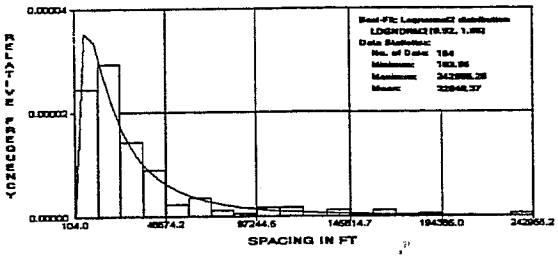

Fig. 107—The histogram and best-fit spacing distribution of the northeast-trending surface lineaments and fractures in the western Hugoton Gas Field.

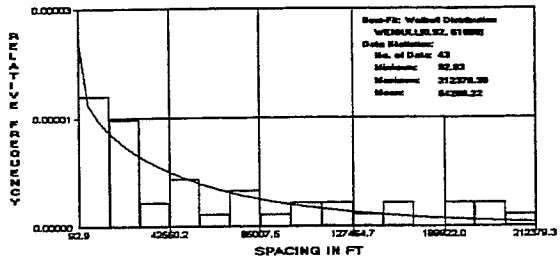

Fig. 108—The histogram and best-fit spacing distribution of the northwest-trending surface lineaments and fractures in the western Hugoton Gas Field.

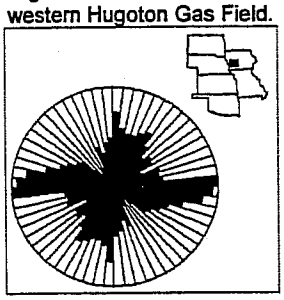

Fig. 109—A rose diagram of the surface fractures in northern Forest City Basin.

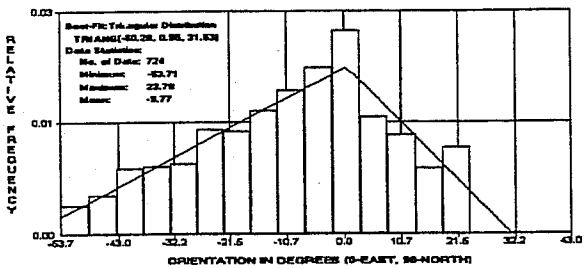

Fig. 110—The histogram and best-fit orientation distribution of the east-trending surface fractures in northern Forest City Basin.

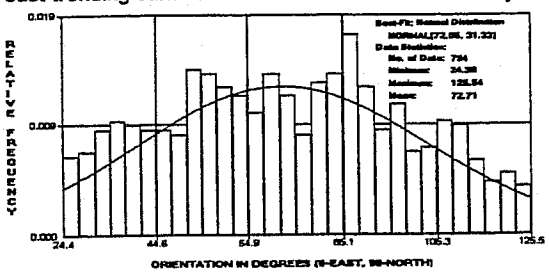

Fig. 111—The histogram and best-fit orientation distribution of the north-northeast-trending surface fractures in northern Forest City Basin.

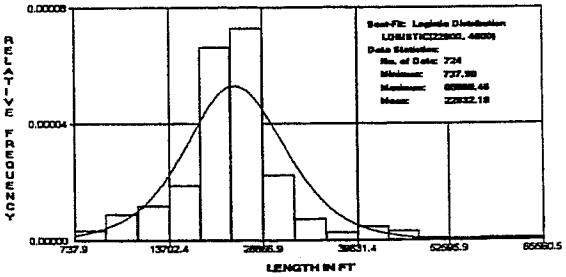

Fig. 112—The histogram and best-fit length distribution of the east-trending surface fractures in northern Forest City Basin.

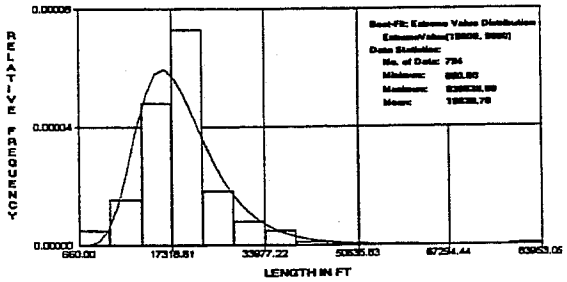

Fig. 113—The histogram and best-fit length distribution of the north-northeast-trending surface fractures in northern Forest City Basin.

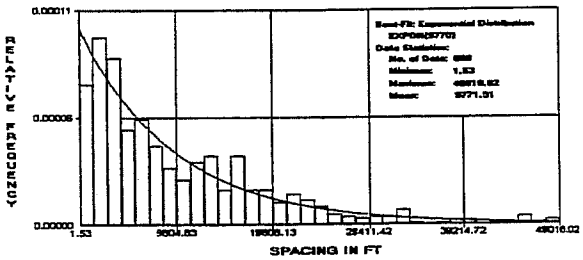

Fig. 114—The histogram and best-fit spacing distribution of the east-trending surface fractures in northern Forest City Basin.

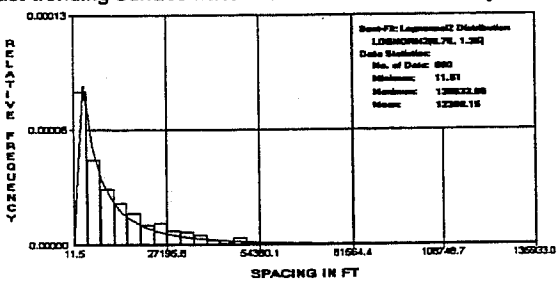

Fig. 115—The histogram and best-fit spacing distribution of the north-northeast-trending surface fractures in northern Forest City Basin.

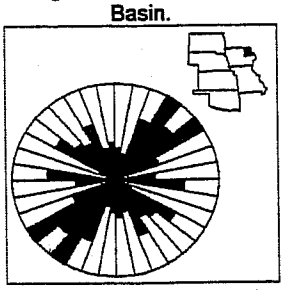

Fig. 116—A rose diagram of the surface fractures in northeastern Iowa.

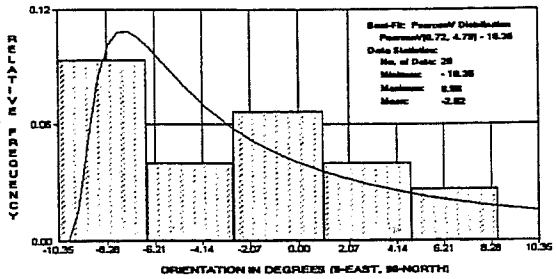

Fig. 117—The histogram and best-fit orientation distribution of the east-trending surface fractures in northeastern Iowa.

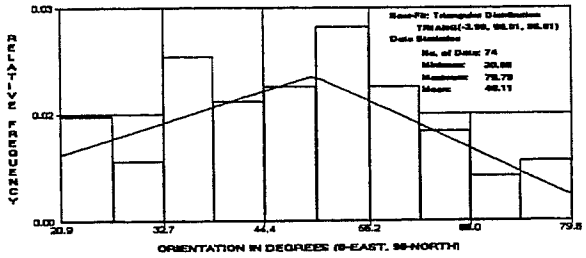

Fig. 118—The histogram and best-fit orientation distribution of the northeast-trending surface fractures in northeastern Iowa.

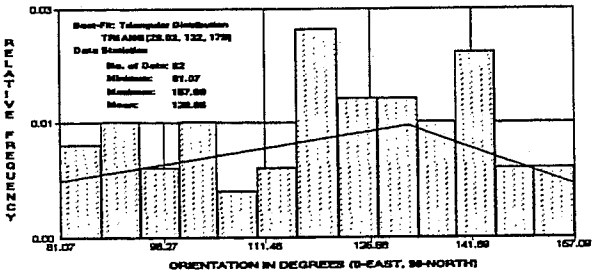

Fig. 119—The histogram and best-fit orientation distribution of the northwest-trending surface fractures in northeastern Iowa.

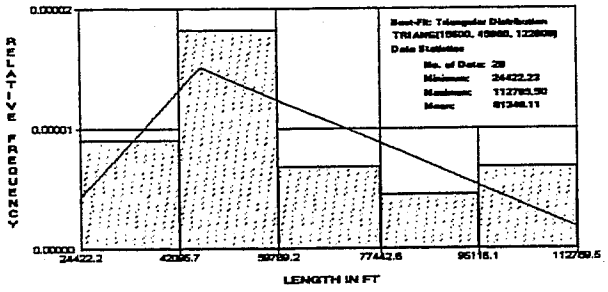

Fig. 120—The histogram and best-fit length distribution of the east-trending surface fractures in northeastern Iowa.

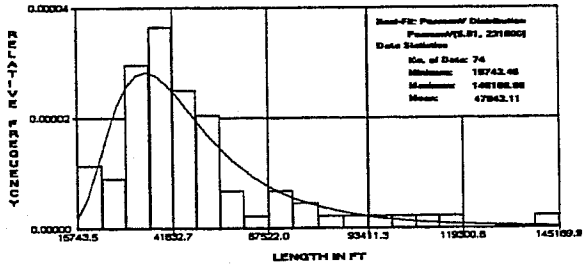

Fig. 121—The histogram and best-fit length distribution of the northeast-trending surface fractures in northeastern Iowa.

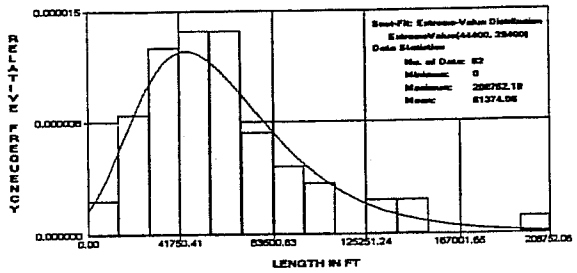

Fig. 122—The histogram and best-fit length distribution of the northwest-trending surface fractures in northeastern Iowa.

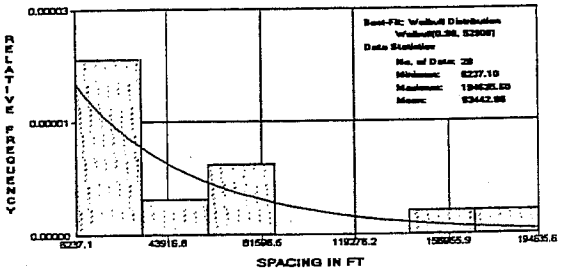

Fig. 123—The histogram and best-fit spacing distribution of the east-trending surface fractures in northeastern Iowa.

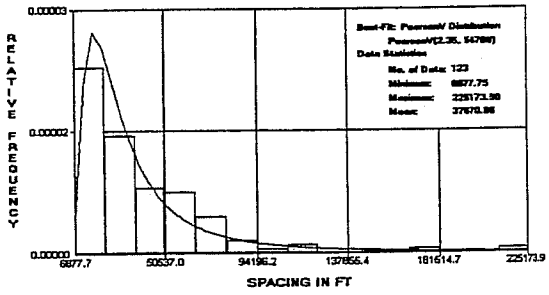

Fig. 124—The histogram and best-fit spacing distribution of the northeast-trending surface fractures in northeastern Iowa.

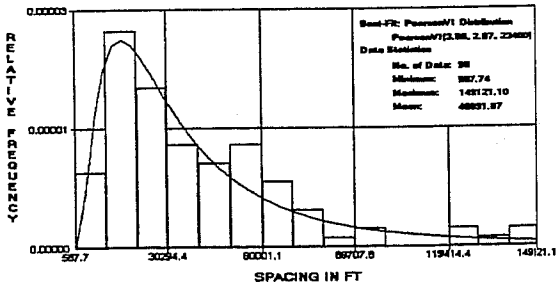

Fig. 125—The histogram and best-fit spacing distribution of the northwest-trending surface fractures in northeastern Iowa.

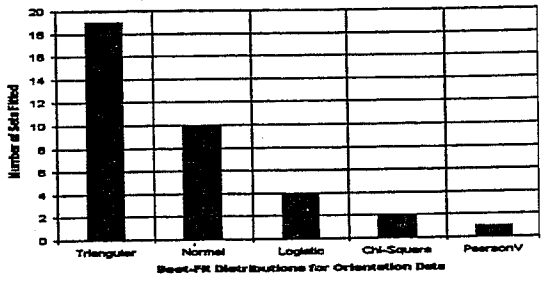

Fig. 126—The best-fit distributions for the orientations of 36 sets of surface lineaments and fractures based on chi-square goodness-of-fit tests.

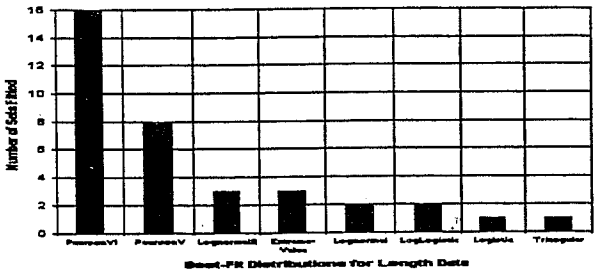

Fig. 127—The best-fit distributions for the lengths of 36 sets of surface lineaments and fractures based on chi-square goodness-of-fit tests.

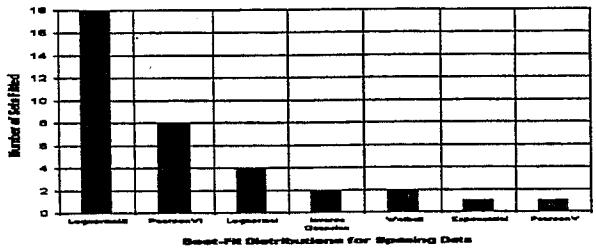

Fig. 128—The best-fit distributions for the spacing of 36 sets of surface lineaments and fractures based on chi-square goodness-of-fit tests.

TRANSIENT PRODUCTIVITY INDEX FOR NUMERICAL WELL TEST SIMULATIONS

G. BLANC
D.Y. DING
A. ENE
T. ESTEBENET
D. RAHON

INSTITUT FRANÇAIS DU PÉTROLE
PAU, FRANCE

ACKNOWLEDGEMENTS

This work has been done within the framework of an ARTEP project sponsored by ELF, the Institut Français du Pétrole and TOTAL. The authors would like to thank both ARTEP and the Institut Français du Pétrole for their permission to publish this work. They would also like to thank L. Piacentino for his help.

ABSTRACT

The most difficult aspect of numerical simulation of well tests is the treatment of the Bottom Hole Flowing (BHF) Pressure. In full field simulations, this pressure is derived from the Well-block Pressure (WBP) using a numerical productivity index which accounts for the grid size and permeability, and for the well completion. This productivity index is calculated assuming a pseudo-steady state flow regime in the vicinity of the well and is therefore constant during the well production period.

Such a pseudo-steady state assumption is no longer valid for the early time of a well test simulation as long as the pressure perturbation has not reached several grid-blocks around the well. This paper offers two different solutions to this problem :

- The first one is based on the derivation of a Numerical Transient Productivity Index (NTPI) to be applied to Cartesian grids ;
- The second one is based on the use of a Corrected Transmissibility and Accumulation Term (CTAT) in the flow equation.

The representation of the pressure behavior given by both solutions is far more accurate than the conventional one as shown by several validation examples which are presented in the following pages.

INTRODUCTION

Need for better numerical Well Test simulation

Analytical well test solutions have been extensively used for a long time by reservoir engineers to interpret their well tests results. In the field of hydrogeology, C. V. Theis (1935), offered one of the first solutions to the problem of the lowering of the piezometric surface under the effect of the rate and duration of a discharge well. Theis' solution was based on the use of the Exponential Integral or Ei function and is still being used by petroleum engineers. Hundreds of papers have been published since that date to account for more complex reservoir models, well completion and test designs. An SPE monograph has summarized the practical aspects of pressure transients (Volume 5 by Earlougher Jr. R. C). Two SPE Reprint Series have been also published (Volume No. 9, *Pressure Analysis Methods*, Volume No. 14, *Pressure Transient Testing Methods*). Published more recently, R. Horne's book gives the status of the knowledge in the 90's.

Despite this abundance of solutions, there are many cases where the analytical solutions no longer apply. Heterogeneous reservoirs with complex in boundaries and complex well geometry are examples where numerical model simulation is the only way to compute the pressure transient. Geostatistical modeling, which is now widely used by geoscience engineers to fill in reservoir simulation grids, also requires numerical reservoir simulation (Blanc G., 1995 and 1996).

In the meantime the well testing technology has been improved allowing bottom hole shut down and early time pressure recording. This is where the need for more and more precise numerical BHF Pressure simulation becomes evident.

Numerical simulation of Well Tests

The pressure behavior of a single-phase flow in a 3D reservoir is governed by the following equation:

$$\frac{\partial}{\partial x_i}\left(\frac{k_i}{\mu}\frac{\partial(P+\rho g z)}{\partial x_i}\right) = \phi c_t \frac{\partial P}{\partial t} + q \quad \text{(1)}$$

where :

P	is the pressure
i	is the axis index
x_i	coordinates (x_1, x_2, x_3, stands for x, y, z)
k_i	is the directional permeability
μ	is the fluid viscosity
ρ	is the fluid density
g	is the gravity
ϕ	is the porosity
c_t	is the total rock and fluid compressibility
q	is a sink term

SIMTESTW is the IFP numerical well test simulation program that uses the 7-point finite-difference scheme of Equation (1). The grid-block system is Cartesian irregular and dead cells are used to simulate complex shapes.

Discretization of Equation (1) in space and time, for a grid-block i and at time step n, is:

$$\sum_j \frac{T_{ij}}{\mu}\left[\left(P_j^n - P_i^n\right) + \rho g\left(z_j - z_i\right)\right] = \phi c_t V i \frac{P_i^n - P_i^{n-1}}{t^n - t^{n-1}} + \delta_{ip} Q_p \quad \text{(2)}$$

where:

j is the index of all neighbors of grid-block i

$\Delta x_i, \Delta y_i$ and Δz_i are the size of the rectangular grid-block i

T_{ij} is the transmissibility between grid-blocks i and j (harmonic average of $\Delta z_i \times k_i$ products)

V_i is the volume of grid-block $i = \Delta x_i \times \Delta y_i \times \Delta z_i$

Q_p is the rate of the well p

δ_{ip} is equal to 1 when grid-block i contains the well p and 0 elsewhere

P^n, is then the solution vector of the following matrix equation:

$$A^n \times P^n = B^n \quad (3)$$

where:

A^n is the 7-band matrix of the system of discretized equations at time n

P^n is the vector of the pressure map at time n

B^n is the vector column of the right-hand side of the system of discretized equations at time n

This program can handle vertical, horizontal or complex wells operated at an imposed rate or at an imposed BHF Pressure. The management of the well completion is flexible enough to allow the user to open or close any grid-block to the flow during the simulation time.

Previous Works - PEACEMAN Numerical Productivity Index (NPI)

Steady State flow

The problem of getting the BHF Pressure from the well grid-block pressure has been addressed by Peaceman D. W. (1978).

Peaceman has shown that the steady state grid-block pressure P_b at the well location, computed using a square grid-block system ($\Delta x_i = \Delta y_i = \Delta L$) in a homogeneous, isotropic and infinite reservoir (permeability = k, porosity = ϕ, compressibility c_t) produced at constant flow rate by a vertical well, is the same as would be observed at a dummy well of radius ro given by :

$$r_0 = 0.198 \times \Delta L \quad (4)$$

When these conditions apply, the BHF Pressure can be obtained using a Numerical Productivity Index (NPI), which relates the grid-block pressure P_0 to the BHF Pressure P_{wf} according to:

$$P_{wf} = P_0 - \frac{Q_b}{NPI} \quad (5)$$

NPI can be computed using the steady state radial flow equation between ro and rw :

$$NPI = \frac{2\pi \times \Delta z_i k}{\mu \ln(\frac{r_w \times e^{-S}}{r_o})} \quad (6)$$

where :

rw is the well radius

S is the well skin

Each well can then be assigned a well bore storage C which relates the well rate Q to the sand face rate Q_{sf} applied to the reservoir as follows:

$$Q_{sf} = Q + C \times \frac{\Delta P_{wf}}{\Delta t} \quad (7)$$

where :

ΔP_{wf} is the pressure drop within the well during the time step Δt

Unsteady State Flow

Peaceman (1978) has also shown that, for unsteady state flow, and when a pseudo steady state flow regime is reached near the well, *ro* can be derived from the following equation :

$$r_0 = \Delta L\left[4t_D \exp(-\gamma - 4\pi p_{Db})\right] \quad (8)$$

where :

γ is the Euler's constant

$t_D = \dfrac{k}{\phi \mu c_t \Delta L^2} \times t$ is the dimensionless time related to ΔL ..... (9)

$p_D = \dfrac{kh}{Q\mu} \times p$ is the dimensionless pressure, p_{Db} rely to rate Q_b..... (10)

Peaceman (1978) concluded that when t_D>1, *ro* computed from equation (4) is close enough to the value given by relation (4), and that equation can therefore be applied in most full field simulation cases.

Previous Works - IFP Transmissibility Correction Multiplier (TCM)

Peaceman's work has been extended to many more complex conditions by the author himself (1983,1990 and 1994) and by several others. All these works are based on the derivation of a better NPI or on the evaluation of numerical pseudo skin to be used with relations (5) and (6).

Recently a new method has been proposed by Ding Y. et al (1993 & 1995a) for improving the well modeling in non standard configurations such as non-uniform Cartesian grids, flexible grids and off-center wells. The principle of this method is to improve the flow representation around the well by modifying the transmissibility in the near well region. This approach, referred to as the Transmissibility Correction Multiplier (TCM) approach, is particularly suited to 3D well modeling as shown by Ding (1995b).

Within this approach the pressure p_0 corresponding to a radius r_0 is obtained using equivalent transmissibility T_{eq} which links p_0 to the pressure of adjacent grid-blocks through equivalent distances (Figure 1). The following transmissibilities must be used instead of the conventional harmonic average ones :

$$T_{eq,i} = k\Delta z_i \frac{\Delta y_0}{L_{eq,i}} \text{ and with } L_{eq,i} = \Delta y_0 \frac{\ln\left(\frac{\Delta x_0 + \Delta x_i}{r_0}\right)}{\phi_i} \quad \text{for i=1 and 3} \quad (11)$$

$$T_{eq,i} = k\Delta z_i \frac{\Delta x_0}{L_{eq,i}} \text{ and with } L_{eq,i} = \Delta x_0 \frac{\ln\left(\frac{\Delta y_0 + \Delta y_i}{r_0}\right)}{\phi_i} \quad \text{for i=2 and 4} \quad (12)$$

The radius r_0 can be chosen by the user and the BHF Pressure is obtained using relation (6).

This method can be easily implemented in conventional numerical simulators, provided that they allow transmissibility multipliers.

TRANSIENT NUMERICAL PRODUCTIVITY INDEX (TNPI)

Generalities

In order to investigate how the Peaceman approach behaves at early time we simulated a pumping test on a vertical well producing a homogeneous "infinite" reservoir using a regular square (10m×10m) grid system. Table 1 shows all the properties of the test, referred to as Reference Case 1.

Figure 2 is a semi-log plot of the results showing the grid-block pressure p_o, the BHF Pressure p_{wf} derived from relation (5) and (6), and the Ei analytical solution. This figure points out the following facts :

- At late time of the test, the Peaceman approach provides a very good BHF Pressure (less than 1% of error).
- At early time, the pressure perturbation has not yet reached the neighbor blocks and all the produced fluid comes from the well-block capacity. The well-block draw-down pressure is negligible compared to the r_o-r_w steady state correction and then the corresponding BHP Pressure is higher than the analytical one.
- In between these two periods, the neighbor blocks start providing an increasing part of the well rate, and the BHF Pressure is lower than the analytical one to compensate for the delay at early time.

The second question addressed concerns the influence of the grid-block size on the BHF Pressure and on its derivative. To do so, the previous draw-down test was simulated using a set of different grid sizes ΔL : 20m×20m, 10m×10m, 5m×5m and 1m×1m. Figure 3, which represents a log-log plot of the BHF Pressure and its derivative versus the time, shows all the results together with the Ei analytical solution. This Figure shows that :

- Decreasing the mesh size leads, as expected, to better results at earlier time.
- An equivalent "well bore storage effect" appears at early time when nearly all the produced fluid comes from the well-block capacity.

This phenomena leads two more questions :

- Is there any rule to calculate the maximum mesh size to be used in order to get clean results from any given pressure recording time ?
  Figure 4, which gathers results calculated using various grid-block size and reservoir permeability, is a log-log plot of dimensionless BHF Pressure and its derivative versus dimensionless time computed using Δx^2 (relations (9) and (10)). This figure shows that for $t_D > 2.6$ the derivative is flat, as expected by the analytical solution of the fluid flow equation. This time, which was determined as the one from which the apparent well-block storage ends, leads to the relation :

$$t \geq 2.6\Delta L^2 \times \frac{\phi \mu c_t}{k} \quad \text{(13)}$$

- Is it possible to use the mesh storage to simulate well bore storage whenever the numerical simulation program does not account for such a condition ?
  Figure 5 is the derivative plot of the PIE well test interpretation program which has been used to interpret the results of the ΔL=20 m grid-block simulation. For such a grid the well-block capacity is equal to $\Delta x \times \Delta y \times \Delta z \times \phi \times c_t$ that is 0.8 m^3/bar, and the interpretation leads to a close 0.737 m^3/bar. However the shape of the pressure derivative shows a huge discrepancy between the behavior of a true well bore storage (solid line) and the apparent well block storage (dash line), pointing out that the latter can be used to simulate the former.

Derivation of the Transient Numerical Productivity Index

Three different attempts have been made to correct the early time problem coming from the use of the NPI steady state grid-block correction. Reference Case 1 (described in Table 1) has been used to check for their validity. A one-layer system made of square (20m×20m) grid-blocks has been selected for all numerical simulations. The well bore storage and skin are both equal to 0.

The Peaceman_Ei correction

The first attempt was to use a unsteady state radial flow equation between *ro* and *rw* to compute the *NPI* as follows :

$$NPI = \frac{4\pi \times \Delta z_i k}{Ei\left(-\frac{r_0^2}{4kt}\right) - Ei\left(-\frac{r_w^2}{4kt}\right)} \quad \text{with} \quad r_0 = 0.198 \times \Delta L \quad \text{.....} \quad (14)$$

The corresponding BHF Pressure and its derivative which are shown in Figure 7 are far better than the conventional ones. The pressure is relatively correct compared to the analytical Ei solution. The early part of the apparent well-block storage was removed from the derivative which still shows a "wave" before the stabilization.

The Peaceman Explicit Transient correction

The main drawback of the first attempt seems to come from the use of a constant equivalent radius r_o. We then extended the Peaceman transient analysis of r_0, using relation (8), far more toward the early time than Peaceman did. Figure 6 shows that the ratio $r_0/\Delta x$ first grows rapidly up to a maximum of 0.3 for t_D=0.01 and then decreases down to the 0.198 limit value.

The corresponding BHF Pressure and its derivative are referred to as $r_{0(t)}$_explicit in Figure 7. Compared to the analytical Ei solution, the pressure is not as good as that achieved by the Peaceman_Ei, the derivative being far better than the previous one.

The full TNPI correction

The previous correction is based on a pseudo-steady state approximation of the transient flow equation corresponding to a pseudo-steady state flow regime around the well. The approximation allows the explicit derivation of r_0.

To be more accurate we used the full transient Ei solution. The r_0 radius was obtained using a Newton method of solution. Figure 6 shows that the corresponding radius is close to the previous one when the dimensionless time t_D becomes greater than 0.2. Earlier than 0.2, the two radii are slightly different. The BHF pressure and derivative computed using this new radius are referred to as NTPI in Figure 7. They both correspond well with the analytical solution.

Validation of the NTPI correction

Three different Reference Cases (Tables 3 to 5) were used to check for the validity of the full NTPI proposed correction.

The first validation was used to check for the accuracy of the proposed NTPI correction in the case of partial well penetration in a homogeneous reservoir. The last two validations were devoted to multiple rate tests such as Drill Stem Tests (DST) and build-up tests. As demonstrated earlier, the correction works properly when the well rate is constant, but it vanishes when the well is shut-down as

does the conventional Peaceman approach. To by-pass this limitation we used a constant rate simulation to derive a « kernel» pressure which was then used as the reference pressure response for a superposition (rate convolution) program. By doing so, any kind of multiple rate test can be simulated, even if it includes shut-down periods. This method can only be applied when the permeability, the porosity and the compressibility are not pressure or fluid saturation dependent, i.e. when the equation (1) is linear (necessary validity condition of the superposition theorem).

Reference Case3 - Homogeneous Reservoir - Draw-down test - Partial penetration

A 10 m thick homogeneous reservoir is produced at constant rate by a well that is perforated in the top 2 m. The grid-block system is made of square (20m×20m) grids 2m thick, the numerical model is made of 10 layers. Table 3 shows all the characteristics of this reference case.

Figure 8 gives the results of the simulation. The computed BHF Pressure as well as its derivative are close to the analytical one computed by the analytical well test interpretation program PIE down to 0.2 s. The derivative is far better than the one computed with the conventional Peaceman correction.

Reference Cases 4 - Three-layer reservoir - DST - Partial penetration

Reference Case 4 is a 3-layer reservoir for which the characteristics are shown in Table 4. There are 3 layers in the numerical model (one per reservoir layer) which are made of square grid-blocks (20m×20m×2m). The purpose of this case was to check for the validity of the superposition method proposed to simulate build-up flow periods of a DST. The simulated DST is made of three flow periods of 7 hours followed by a build-up of more than 100 hours (Table 4). The well is only perforated in the middle layer of the reservoir. The results of the simulated build-up, which are represented in Figure 9, correspond well with those given by the analytical program. The improvement of the conventional Peaceman correction is very significant in the 10^3 first seconds of the build-up.

Reference Case 5 - Three- layer reservoir - DST - Full penetration

Reference Case 5 is also a 3-layer reservoir for which the characteristics are shown in Table 5. The grid-block system is the same as the one used in Reference Case 4. The purpose of this case was to check for the validity of the superposition method with and without the presence of a well bore storage for a full penetration well. The two simulated build-ups are represented in Figures 10 and 11. They both correspond well with the analytical program results. When there is no well bore storage the improvement of the proposed correction is also very significant, as previously observed with Reference Case 4.

TRANSMISSIBILITY and ACCUMULATION Correction Multipliers (TACM)

Derivation of the Transmisibility and Accumulation Correction Multiplier

The Transmissibility Correction Multiplier which is based on a steady state flow regime was also improved to account for the short time period when the well flow rate is essentially produced from the well-block by the « volume storage », that is, by the term :

$$c_t \phi \int_{V_0} \frac{\partial p}{\partial t} dV \quad \text{.....} \quad (15)$$

However, as p_0 is expected to be the pressure corresponding to the radius r_0, the « volume storage » variation will be approximated by :

$$c_t \phi V_0 \frac{\partial p_0}{\partial t} = -c_t \phi V_0 \frac{q\mu}{4\pi kh} \frac{e^{-\frac{r_0^2}{4kt}}}{t} \quad \text{(16)}$$

where the well block pressure is assumed to be equal to :

$$p_0 = p_i + \frac{q\mu}{4\pi hk} Ei\left(-\frac{r_0^2}{4kt}\right) \quad \text{(17)}$$

so that the derivative :

$$\frac{\partial p_0}{\partial t} = -\frac{q\mu}{4\pi kh} \frac{e^{-\frac{r_0^2}{4kt}}}{t} \quad \text{(18)}$$

is independent of the integration variables on V_0. This approximation is not accurate enough for short time period. To improve this calculation, we introduce the Accumulation Correction coefficient for volume storage by determining the coefficient β such that :

$$\begin{aligned} -\beta c_t \phi V_0 \frac{q\mu}{4\pi kh} \frac{e^{-\frac{r_0^2}{4kt}}}{t} &= c_t \phi \int_{V_0} \frac{\partial p}{\partial t} dV \\ &= -c_t \phi \frac{q\mu}{4\pi kh} \int_{V_0} \frac{e^{-\frac{r^2}{4kt}}}{t} dr \end{aligned} \quad \text{(19)}$$

The result is as follows :

$$\beta = \frac{1}{V_0} \int_{V_0} e^{-\frac{(r^2 - r_0^2)}{4kt}} dr \quad \text{(20)}$$

Validation of the TACM correction

Reference Case2 - Homogeneous Limited Reservoir - Draw-down test - Full penetration

The validity of the full TACM correction was first checked with the Reference Case 2 (this case is the same as the Reference Case 1 but for a limited reservoir, as shown on Tables 1 and 2). Figure 12 shows that, while the early time improvement obtained with the TACM correction is not as good as the full NTPI one, it is still better than the pure Peaceman_Ei correction and it is close to the one obtained with the Peaceman Explicit Transient correction.

Reference Case3 - Homogeneous Reservoir - Draw-down test - Partial penetration

Reference Case 3 simulation confirms the previous conclusions for early time as illustrated on Figure 12: NTPI gives better results than TACM. On the contrary, the TACM correction works better than the NTPI one for late times. This is the result of the use of the transmissivity multipliers which have proven to be more accurate than the conventional Peaceman approach in steady state flow conditions (i.e. for late test times) as demonstrated by DING Y. (1994).

CONCLUSIONS

The main conclusions from this work are the following :

The Peaceman approach can be used for numerical well test simulation as long as the following relation between the petrophysical properties, the time and the grid-block size is fulfilled :

$$t \geq 2.6\Delta L^2 \times \frac{\phi \mu c_t}{k}$$

This relation is true if and only if the well is located at the center of a local 5x5 square grid system within which the reservoir is isotropic and homogeneous.

For the simulation of early time two approaches have been proposed :

- The Numerical Transient Productivity Index correction which has been validated on several reference case and has proven to give far better results than the conventional Peaceman approach.

- The Transmissibility and Accumulation Correction Multipliers is not as good as the previous one but is still far better than the conventional Peaceman approach. However, the use of transmissibility multipliers gives a better simulation of late time.

For both approaches, the simulation of multiple rate and build up tests, must be done using the rate convolution of a constant rate simulation. This approach is only valid when the permeability, the porosity and the compressibility are not pressure or fluid saturation dependent.

This work indicates that the combination of the NTPI approach and the transmissibility multipliers would probably give both better early and late times than the previous approaches for the numerical simulation of well tests.

Nomenclature

c_t	=	total compressibility, Lt^2/m, 1/bars
C	=	well bore storage, , m^3/bar
$\Delta x, \Delta y, \Delta z$	=	grid-block dimension, L,m
h	=	reservoir thickness, L, m
k	=	permeability, L^2, mD
NPI	=	numerical productivity index, L^4t/m
P	=	pressure, $m/L\,t^2$, bar
q	=	sink term, L^3/t
Q	=	well flow rate, L^3/t, m^3/d
r_w	=	well radius, L, cm
r	=	Peaceman equivalent radius, L, cm
S	=	well skin
t	=	time, t
T	=	transmissibitity,L^2/t
V_i	=	grid block volume, L^3, m^3
β	=	accumulation multiplier
ϕ	=	porosity, fraction
μ	=	fluid viscosity, m/Lt, cp
ρ	=	fluid density, m/L^3, g/cm^3

REFERENCES

BLANC, G. *et al.*, Numerical Well Tests Simulations in Heterogeneous Reservoirs. Poster presented at AAPG, Nice 95.

BLANC, G. & al, 1996, Building Geostatistical Models Constrained by Dynamic Data". SPE 35478 presented at the SPE/NPF European Conference held in Stavanger, Norway, 16-17 April 1996.

DING Y., RENARD, G. and WEILL, L., Representation of Wells in Numerical Reservoir Simulation, paper SPE 29123, presented at the 13 th SPE Symposium on Reservoir Simulation, San Antonio, Feb. 12-15, 1995.

DING Y., and RENARD, G., A New Representation of Wells in Numerical Reservoir Simulation SPERE, May 1994, p. 140.

DING Y., A Generalized 3D Well Model for Reservoir Simulation, paper SPE 30724, presented at the SPE Annual Technical Conference help in Dallas, USA, Oct. 22-25, 1995.

EARLOUGHER, LR. C. Jr., 1977. Advances in Well Test Analysis. Monograph Volume 5 of the Henry L. Doherty Series. Published by Society of Petroleum Engineers of AIME , New York , Dallas.

LEE, John, 1982. Well Testing. SPE Textbook Series, vol. 1. Published by Society of Petroleum Engineers of AIME , New York , Dallas.

PEACEMAN, D. W., 1978, Interpretation of Well-block Pressures in Numerical Reservoir Simulation: in Transactions of AIME, 1978, p253.

PEACEMAN, D. W., 1983, Interpretation of Well-block Pressures in Numerical Reservoir Simulation with Non Square Grid-Blocks and Anisotropic Permeability. SPEJ (June), p531.

PEACEMAN, D. W., 1990, Interpretation of Well-block Pressures in Numerical Reservoir Simulation, part 3 - Off Center and Multiple Wells Within a Well Block, SPERE, May 1990, p.1990.

PEACEMAN, D. W., 1995, A New Method for Representing Multiple Wells with Arbitrary Rates in Numerical Reservoir Simulation, paper SPE 29120, presented at the 13 th SPE Symposium on Reservoir Simulation, San Antonio, Feb. 12-15, 1995.

PIE - Well Test Analysis, User's Manual, S.M.C. limited, June 1994.

SPE Reprint Series N° 9, 1967, Pressure Analysis Methods. Published by Society of Petroleum Engineers, Dallas, Texas.

SPE Reprint Series N° 14, 1980, Pressure Transient Testing Methods. Published by Society of Petroleum Engineers, Dallas, Texas.

THEIS, C. V. , 1935, The relationship Between the Lowering of the Piezometric Surface and the Rate and Duration of Discharge Well Using Ground-Water Storage. Trans. Amer. Geophysical Union, vol. 16, pages 515-524.

FIGURES

Figure 1 - Well-block pressure calculation - TCT method
Figure 2 - Conventional BHF Pressure computation (Reference Case 1- 10m×10m grid-blocks)
Figure 3 - Conventional BHF Pressure and Derivative Plot computation (Reference Case 1)
Figure 4- Well-block size effects on Conventional BHF Derivative computation (Reference Case 1)
Figure 5 - Apparent Well-Block storage (Reference Case 1- 20m×20m grid-blocks)
Figure 6 - Equivalent Well-block radius versus time
Figure 7 - Summary of NPI transient corrections (Reference Case 1 - 10m×10m grid-blocks)
Figure 8 - Homogeneous reservoir - Partial penetration (Reference Case 3- 20m×20m grid-blocks)
Figure 9 - 3 Layers - Partial penetration (Reference Case 4 - 20m×20m grid-blocks)
Figure 10 - 3 Layers - Full penetration - no WBS (Reference Case 5 - 20m×20m grid-blocks)
Figure 11 - 3 Layers - Full penetration - WBS (Reference Case 5 - 20m×20m grid-blocks)
Figure 12 - Homogeneous reservoir - CTAT Correction (Reference Case 2 - 20m×20m grid-blocks)

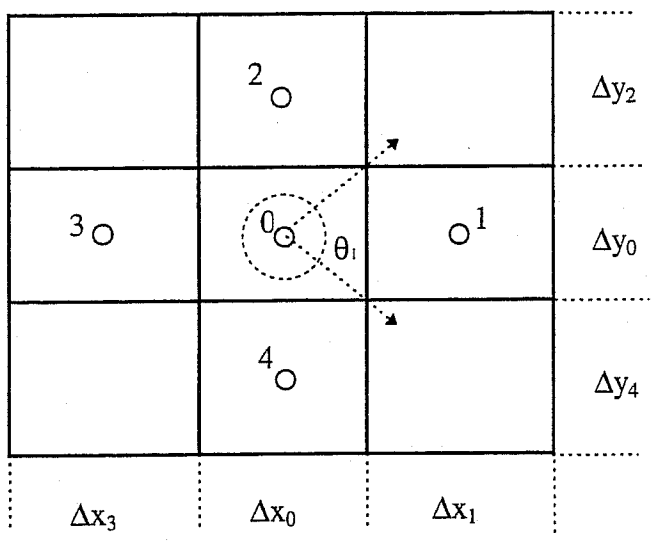

Figure 1 - Well-block pressure calculation - TCT method

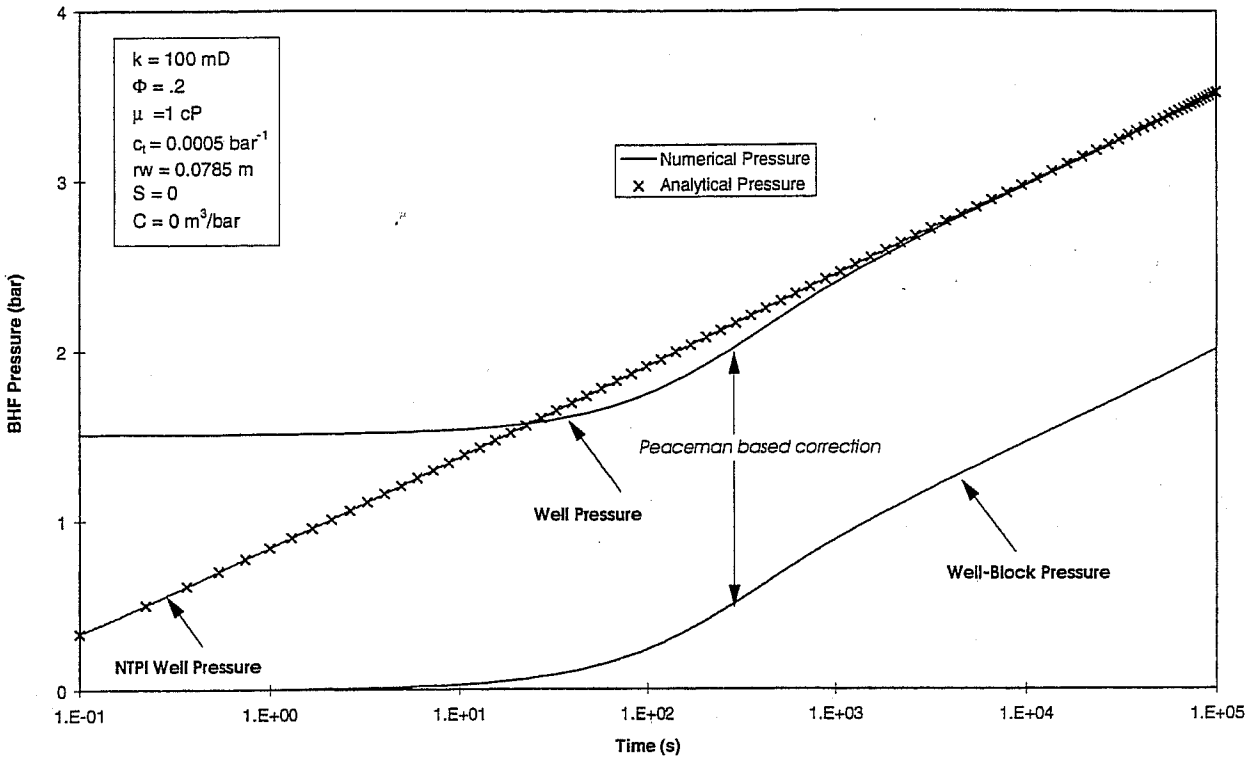

Figure 2 - Conventional BHF Pressure computation (Reference Case 1- 10m×10m grid-blocks)

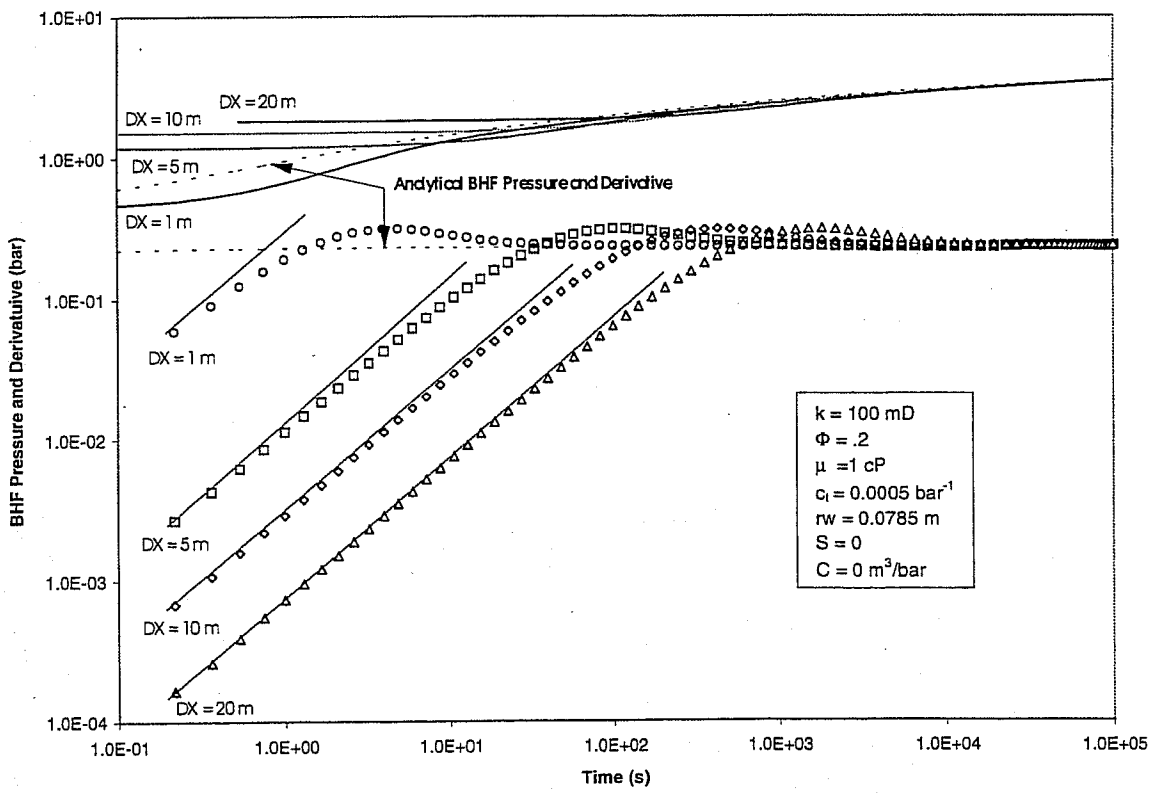

Figure 3 - Conventional BHF Pressure and Derivative Plot computation (Reference Case 1)

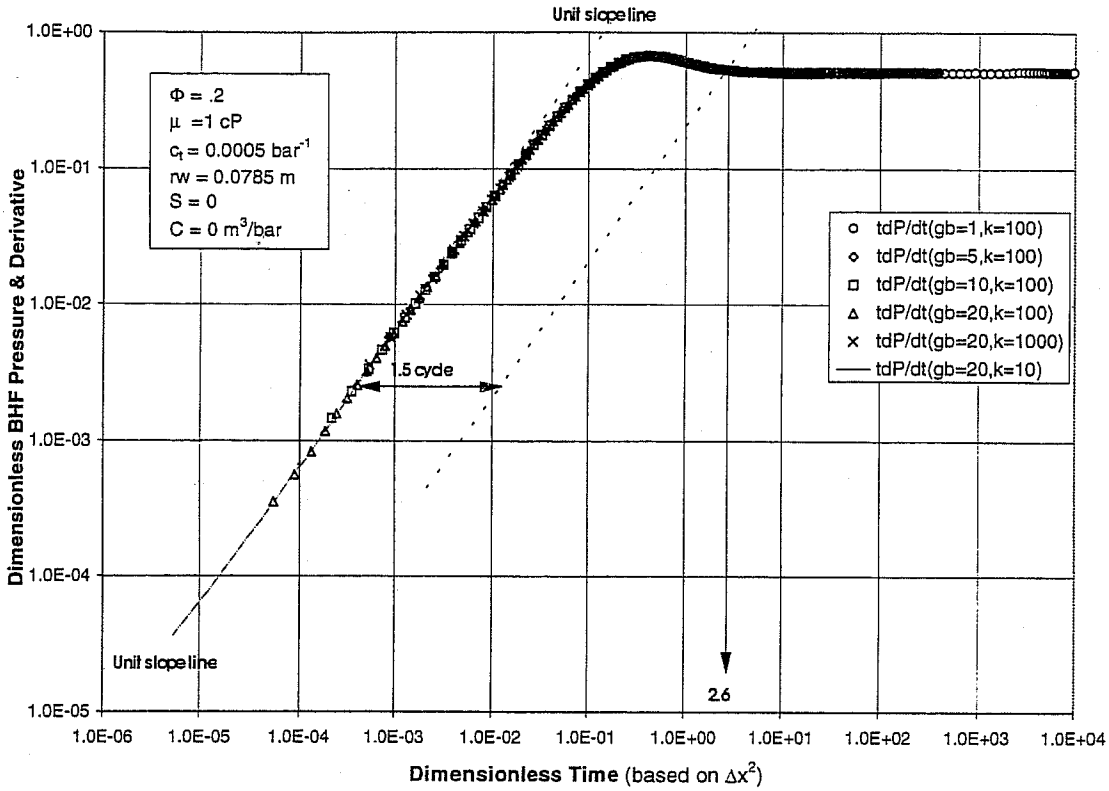

Figure 4- Well-block size effects on Conventional BHF Derivative computation (Reference Case 1)

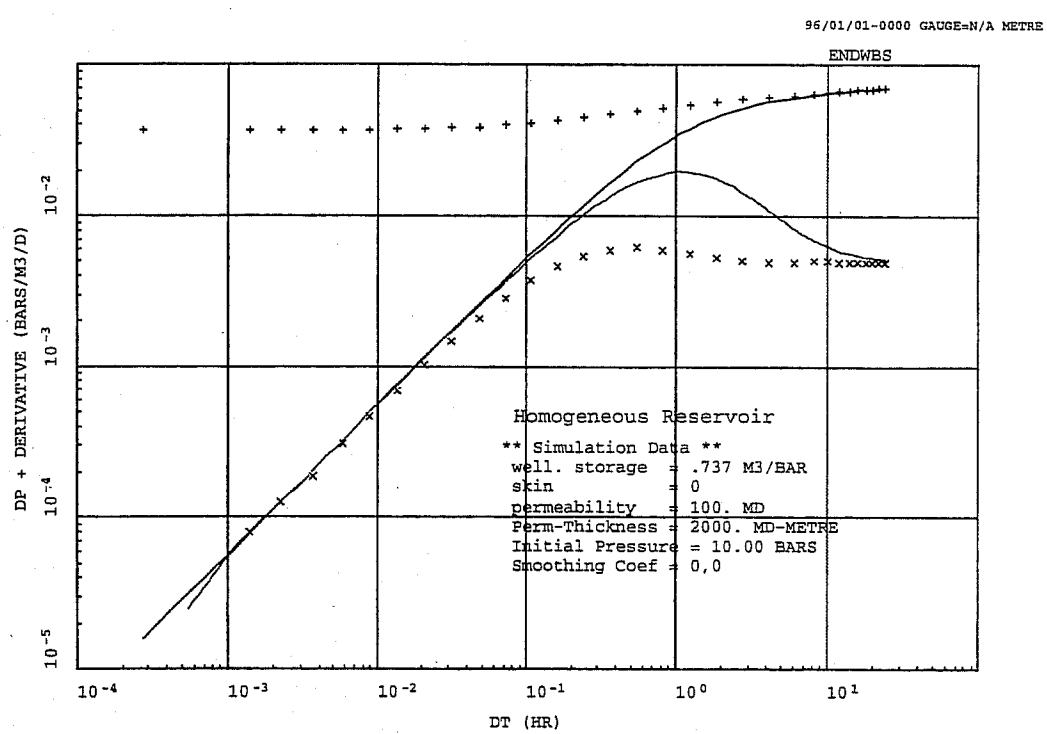

Figure 5 - Apparent Well-Block storage (Reference Case 1- 20m×20m grid-blocks)

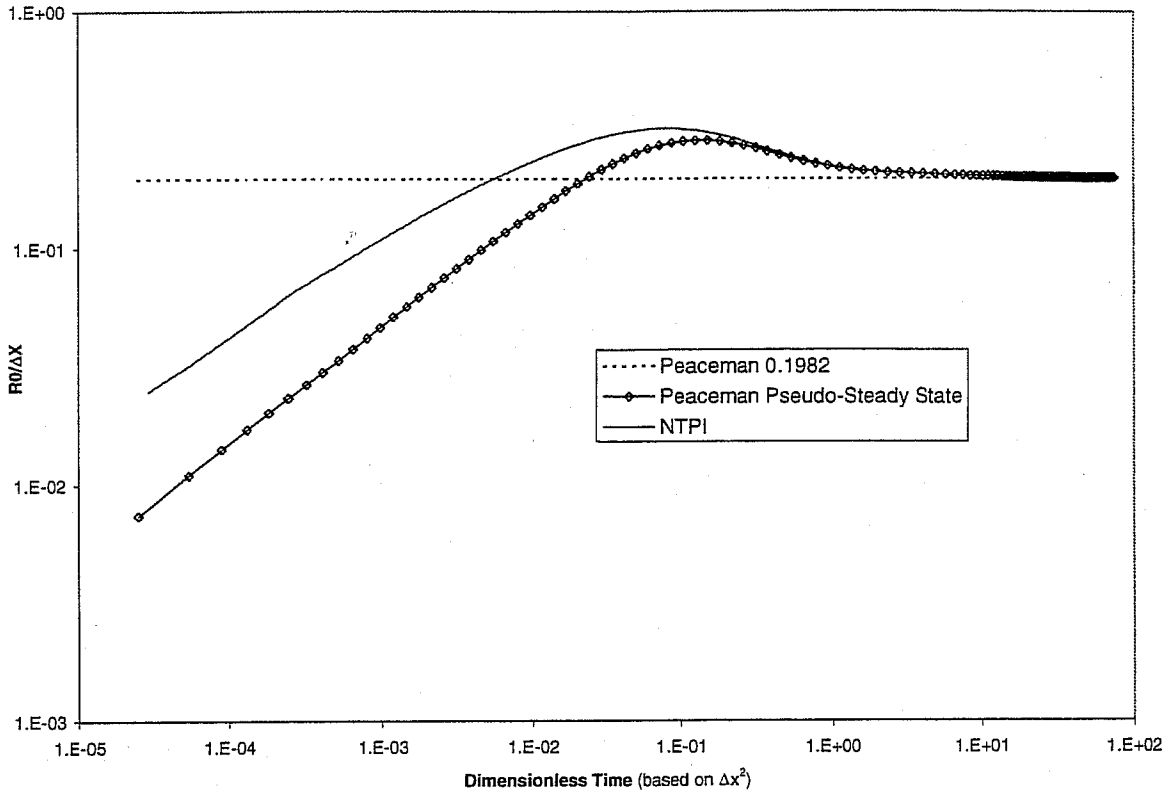

Figure 6 - Equivalent Well-block radius versus time

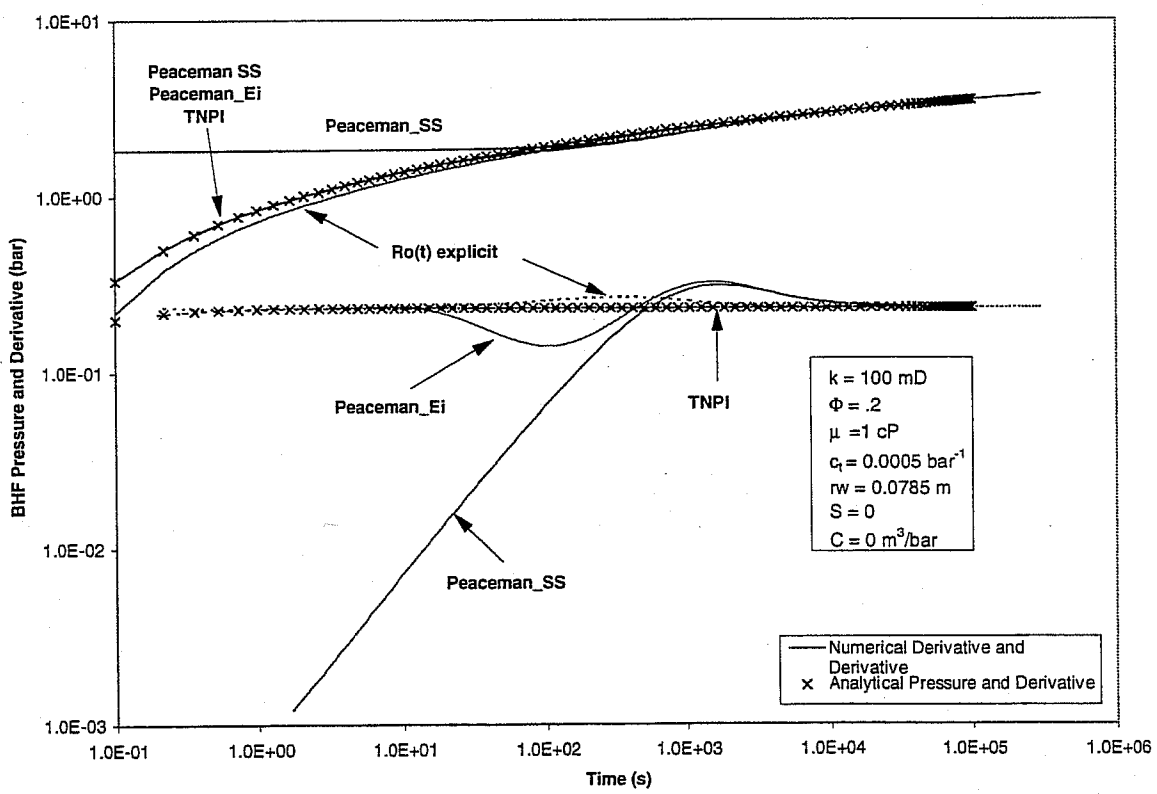

Figure 7 - Summary of NPI transient corrections (Reference Case 1 - 10m×10m grid-blocks)

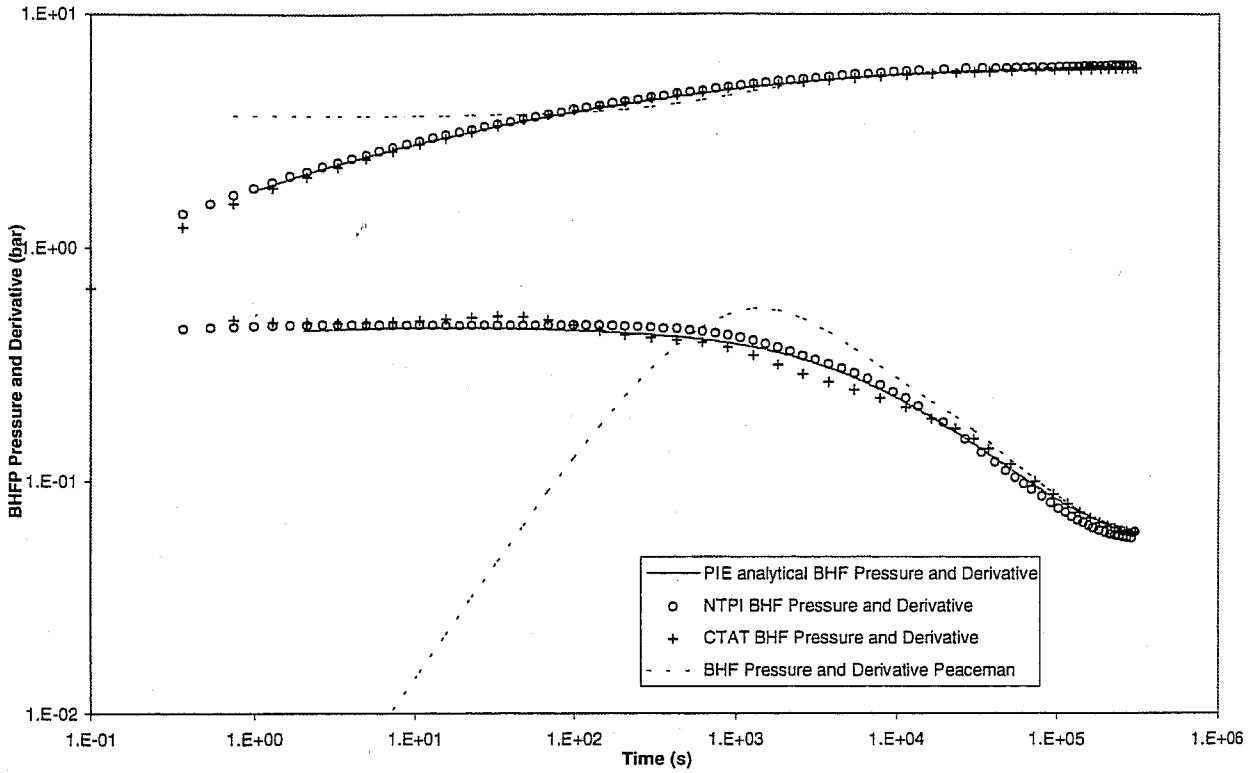

Figure 8 - Homogeneous reservoir - Partial penetration (Reference Case 3- 20m×20m grid-blocks)

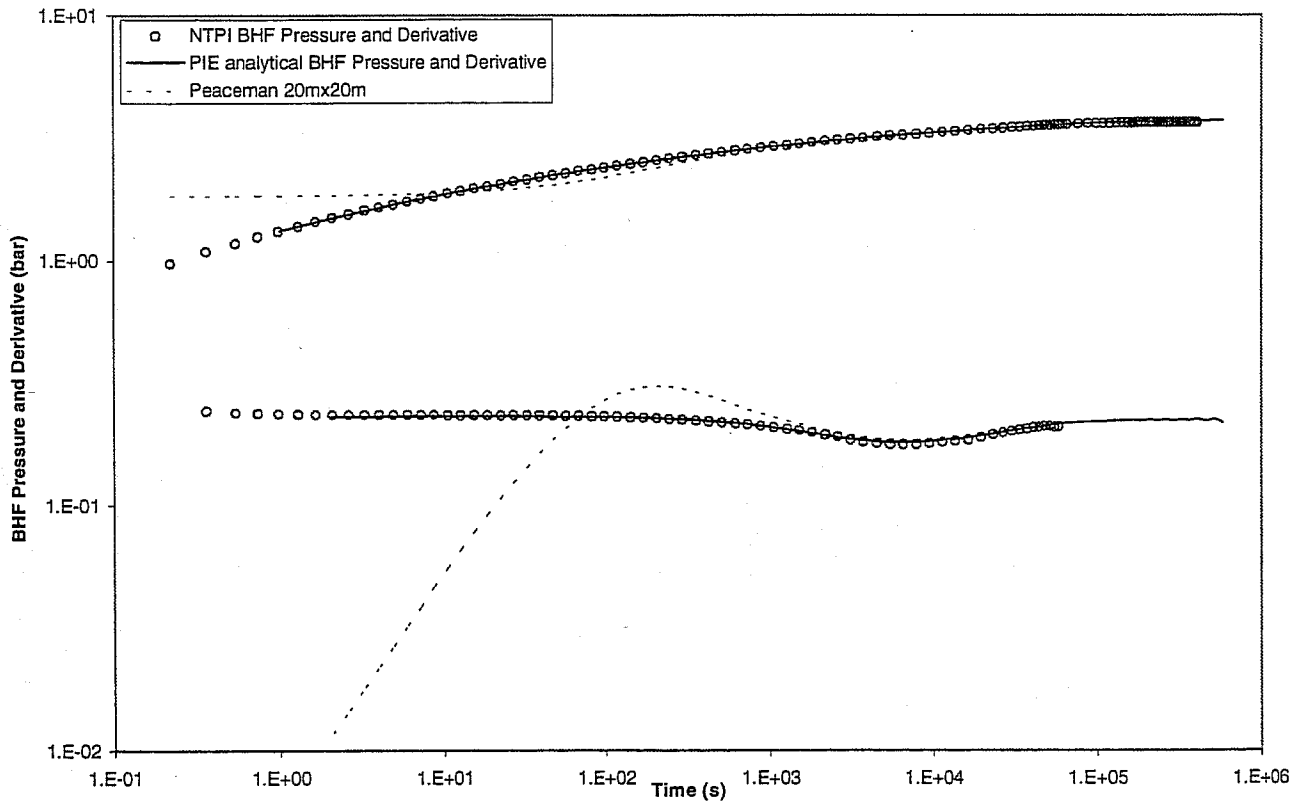

Figure 9 - 3 Layers - Partial penetration (Reference Case 4 - 20m×20m grid-blocks)

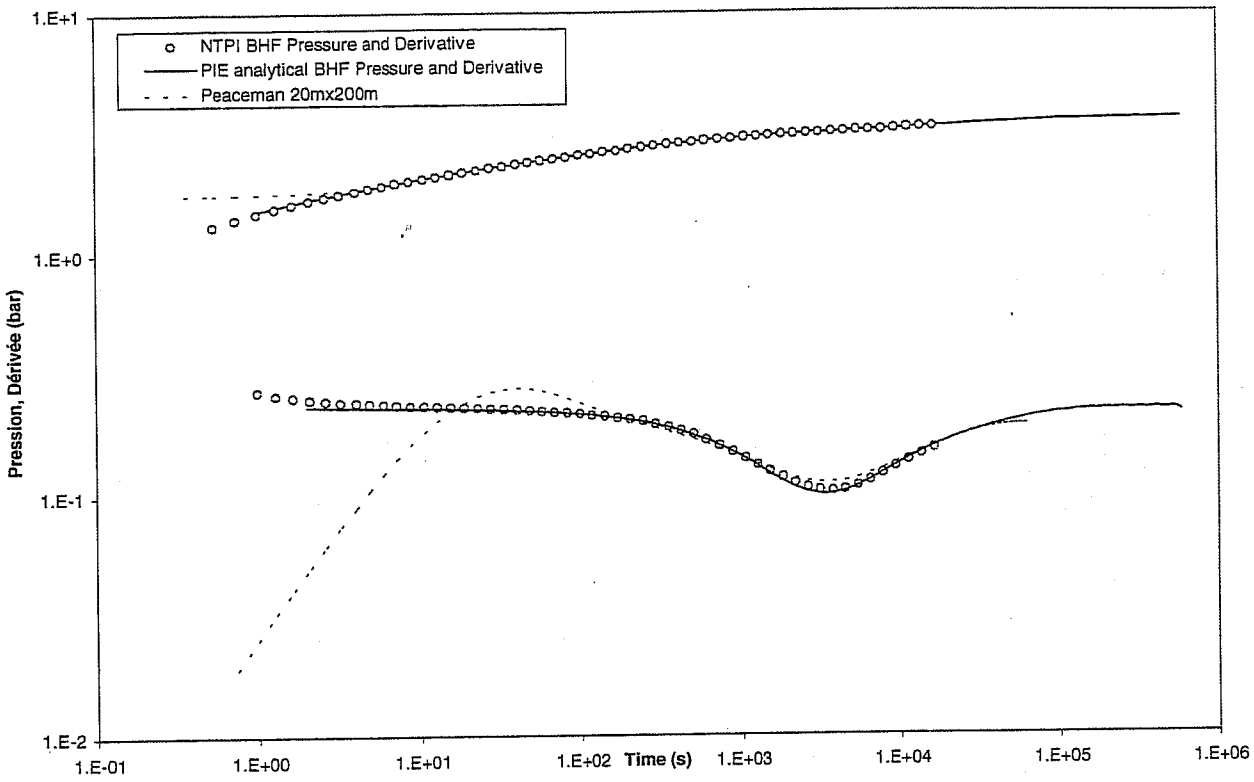

Figure 10 - 3 Layers - Full penetration - no WBS (Reference Case 5 - 20m×20m grid-blocks)

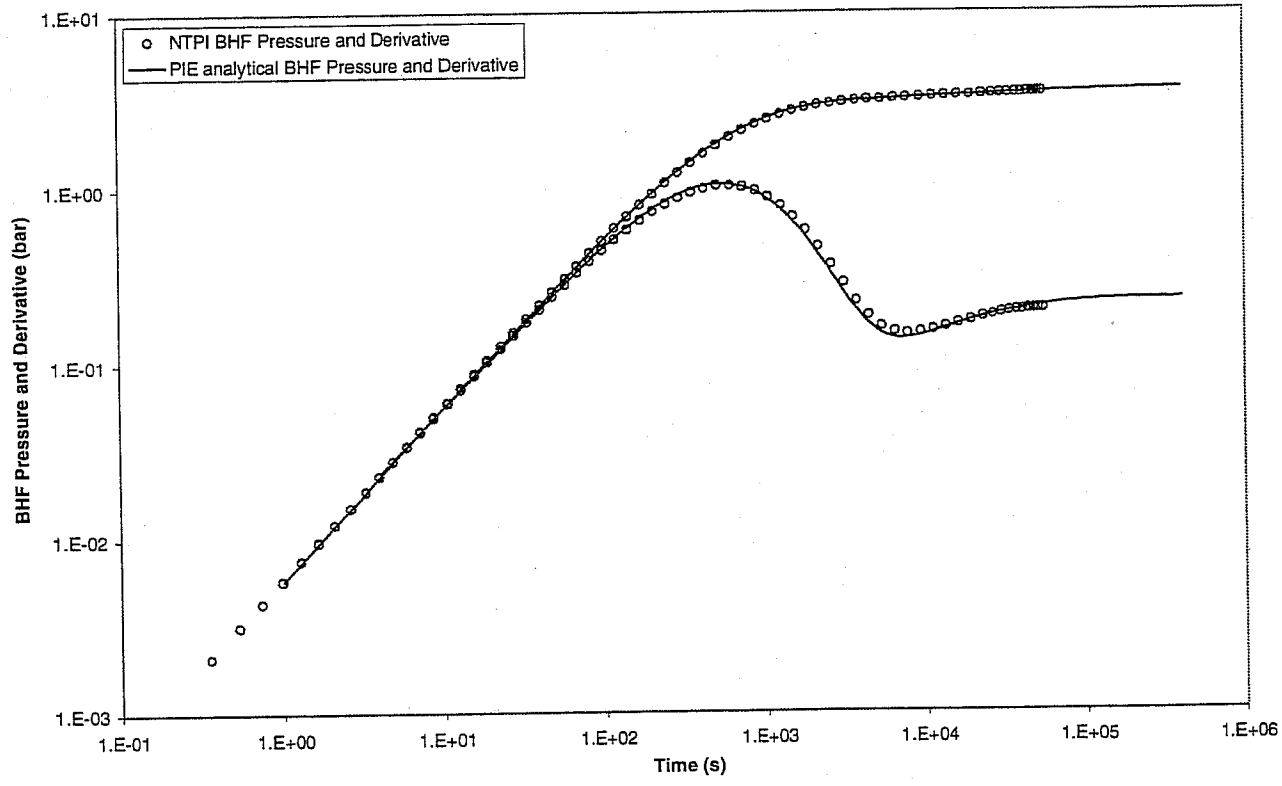

Figure 11 - 3 Layers - Full penetration - WBS (Reference Case 5 - 20m×20m grid-blocks)

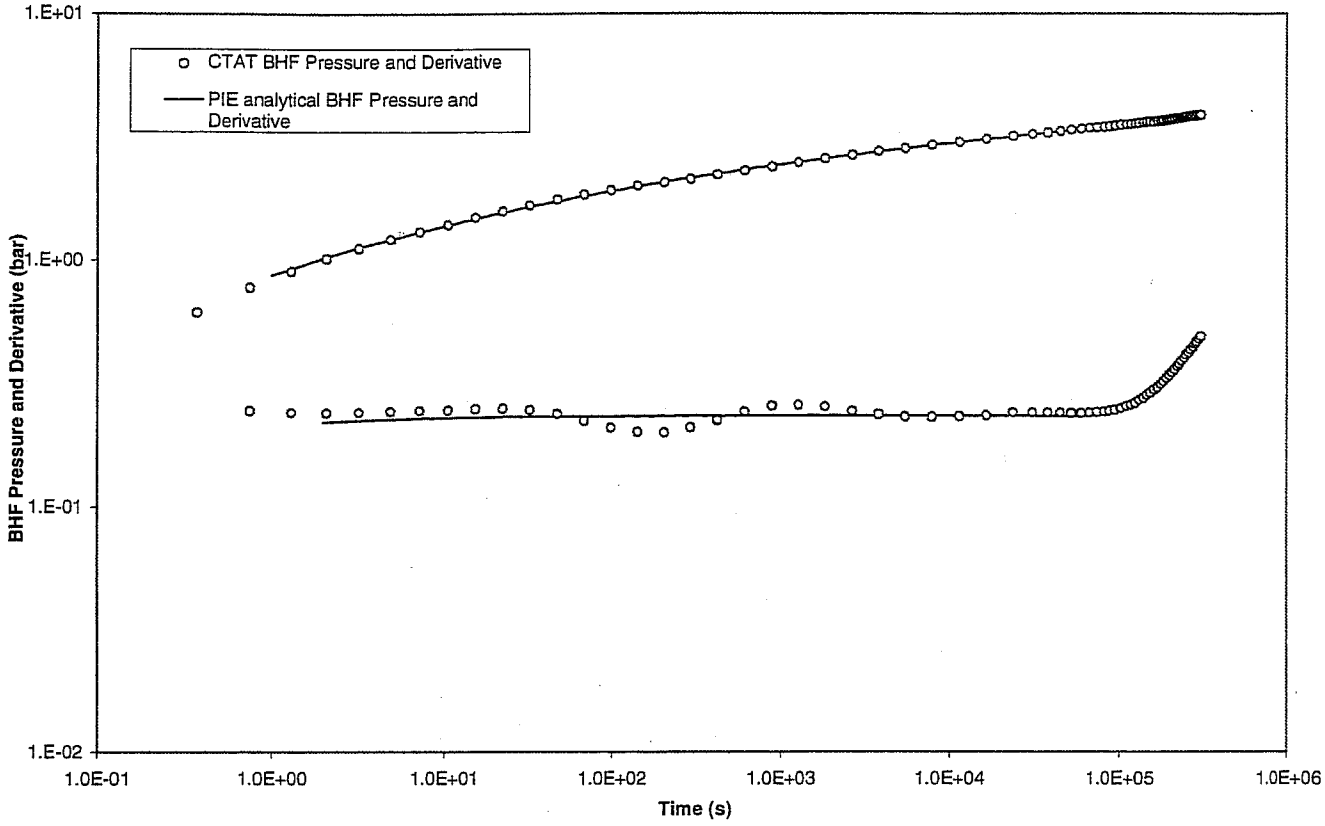

Figure 12 - Homogeneous reservoir - CTAT Correction (Reference Case 2 - 20m×20m grid-blocks)

TABLES

Table 1 - Reference Case 1 - Characteristics

(corresponding to figures 2,3,4,5 and 7)

Reservoir - one layer - infinite	k (mD)	ϕ (fraction)	c_t (1/bar)	h (m)
	100	.20	$5\ 10^{-4}$	20

Fluids	μ (cPo)	ρ (g/cm^3)	Bo (m^3/m^3)
	1	1	1

Well	rw (m)	S	C (m^3/bar)
	0.0785	0	0

Test	type	duration (s)	rate (m^3/d)
	Pumping test	10^5	50

Table 2 - Reference Case 2 - Characteristics

(corresponding to figure 12)
Same as Table 1 but Reservoir limited 1020mx1020m

Table 3 - Reference Case 3 - Characteristics

(corresponding to figure 8)

Reservoir - 8 layers - infinite	k_h (mD)	k_v (mD)	ϕ (fract.)	c_t (1/bar)	h (m)
all layers	100	10	.20	$5\ 10^{-4}$	10

Fluids	μ (cPo)	ρ (g/cm^3)	Bo (m^3/m^3)
	1	1	1

Well	skin	rw = 0.0785 m
layer 1	0	S = 0
layer 2 to 8	closed	C = 0 m^3/bar

Test	Type	duration (s)	rate (m^3/d)
	pumping test	$5\ 10^5$	50

Table 4 - Reference Case 4 - Characteristics

(corresponding to figures 9)

Reservoir - 3 layers - infinite - c_t=5 10^{-4} bar	k_h (mD)	k_v (mD)	ϕ (fraction)	h (m)
layer 1	10	.1	.08	2
layer 2	1000	1	.25	2
layer 3	30	.3	.12	2

Fluids	μ (cPo)	ρ (g/cm^3)	Bo (m^3/m^3)
	1	1	1

Well	skin	rw = 0.0785 m
layer 1	closed	S = 0
layer 2	0	C = 0 m^3/bar
layer 3	closed	

Test	duration (h)	rate (m^3/d)
flow period 1	7	10
flow period 2	7	30
flow period 3	7	50
flow period 4	112	0 build up

Table 5- Reference Case 5 - Characteristics

(corresponding to figures 10 and 11)

Reservoir - 3 layers - infinite - c_t=5 10^{-4} bar	k_h (mD)	k_v (mD)	ϕ (fraction)	h (m)
layer 1	10	.1	.20	2
layer 2	1000	1	.05	2
layer 3	30	.3	.20	2

Fluids	μ (cPo)	ρ (g/cm^3)	Bo (m^3/m^3)
	1	1	1

Well	skin	rw = 0.0785 m
layer 1	0	S = 0
layer 2	0	C= 0 m^3/bar - fig 10
layer 3	0	C = 0.1 m^3/bar - fig 11

Test	Same as Reference case 4

Approaches to Identifying Reservoir Heterogeneity and Reserve Growth Opportunities from Subsurface Data: The Oficina Formation, Budare Field, Venezuela

D. S. Hamilton; S. K. Raeuchle; M. H. Holtz, M. Uzcategui; T. Jimenez
Bureau of Economic Geology
10100 Burnet Road
Austin, TX 78758

ABSTRACT

We applied an integrated geologic, geophysical, and engineering approach devise to identify heterogeneities in the subsurface that might lead to reserve growth opportunities in our analysis of the Oficina Formation at Budare field, Venezuela. The approach involves 4 key steps: 1) Determine geologic reservoir architecture; 2) Investigate trends in reservoir fluid flow; 3) Integrated fluid flow trends with reservoir architecture; and 4) Estimate original oil-in-place, residual oil saturation, and remaining mobile oil, to identify opportunities for reserve growth.

There are three main oil-producing reservoirs in the Oficina Formation that were deposited in a bed-load fluvial system, an incised valley-fill, and a barrier-strandplain system. Reservoir continuity is complex because, in addition to lateral facies variability, the major Oficina depositional systems were internally subdivided by high-frequency stratigraphic surfaces. These surfaces define times of intermittent lacustrine and marine flooding events that punctuated the fluvial and marginal marine sedimentation, respectively. Syn and post depositional faulting further disrupted reservoir continuity. Trends in fluid flow established from initial fluid levels, response to recompletion workovers, and pressure depletion data demonstrated barriers to lateral and vertical fluid flow caused by a combination of reservoir facies pinchout, flooding shale markers, and the faults.

Considerable reserve growth potential exists at Budare field because the reservoir units are highly compartment by the depositioinal heterogeneity and structural complexity. Numerous reserve growth opportunities were identified in attics updip of existing production, in untapped or incompletely drained compartments, and in field extensions.

Characterization of Oil and Gas Reservoirs and Recovery Technology Deployment on Texas State Lands

Roger Tyler; R. P. Major; M. H. Holtz; H. Scott Hamlin; S. P. Dutton
University of Texas
University Station, Box X
Austin, TX

ABSTRACT

Texas State Lands oil and gas resources are estimated at 1.6 BSTB of remaining mobile oil, 2.1 BSTB or residual oil, and nearly 10 Tcf of remaining gas. An integrated, detailed geologic and engineering characterization of Texas State Lands has created quantitative descriptions of the oil and gas reservoirs, resulting in delineation of untapped, bypassed compartments and zones of remaining oil and gas. On Texas State Lands, the knowledge gained from such interpretative, quantitative reservoir descriptions has been the basis for designing optimized recovery strategies, including well deepening, recompletions, workovers, targeted infill drilling, injection profile modification, and waterflood optimization. The State of Texas Advanced Resource Recovery program is currently evaluating oil and gas fields along the Gulf Coast (South Copano Bay and Umbrella Point fields) and in the Permian Basin (Keystone East, Ozona, Geraldine Ford and Ford West fields). The program is grounded in advanced reservoir characterization techniques that define the residence of unrecovered oil and gas remaining in select State Land reservoirs. Integral to the program is collaboration with operators in order to deploy advanced reservoir exploitation and management plans. These plans are made on the basis of a thorough understanding of internal reservoir architecture and its controls on remaining oil and gas distribution. Continued accurate, detailed Texas State Lands reservoir description and characterization will ensure deployment of the most current and economically viable recovery technologies and strategies available.

High Resolution Reservoir Geological Modelling Using Outcrop Information

Zhang Changmin; Lin Kexiang; Liu Huaibo; Qiu Yinan
Department of Geology
Jianghan Petroleum Institute
Jingsha, Hubei, China 434102

ABSTRACT

This is China's first case study of high resolution reservoir geological modelling using outcrop information. The key of the modelling process is to build a proto-type model and using the model as a geological knowledge bank. Outcrop information used in geological modelling including seven aspects: 1) Determining the reservoir framework pattern by sedimentary depositional system and facies analysis; 2) Horizontal correlation based on the lower and higher stand duration of the paleo-lake level; 3) Determining the model's direction based on the paleo-current statistics; 4) Estimating the sandbody communication by photomosaic and profiles; 6) Estimating reservoir properties distribution within sandbody by lithofacies analysis; 7) Building the reservoir model in sandbody scale by architectural element analysis and 3-D sampling. A high resolution reservoir geological model of Youshashan oil field has been built by using this method.

Characterization and Estimation of Permeability Correlation Structure from Performance Data

I. Ershaghi; M. Al-Qahtani
University of Southern California
Petroleum and Engineering Program
Los Angeles, CA 90089

ABSTRACT

In this study, the influence of permeability structure and correlation length on the system effective permeability and recovery factors of 2-D cross-sectional reservoir models, under waterflood, is investigated. Reservoirs with identical statistical representation of permeability attributes are shown to exhibit different system effective permeability and production characteristics which can be expressed by a mean and variance. The mean and variance are shown to be significantly influenced by the correlation length. Detailed quantification of the influence of horizontal and vertical correlation lengths for different permeability distributions is presented.

The effect of capillary pressure, P_{c1} on the production characteristics and saturation profiles at different correlation lengths is also investigated. It is observed that neglecting P_c causes considerable error at large horizontal and short vertical correlation lengths. The effect of using constant as opposed to variable relative permeability attributes is also investigated at different correlation lengths.

Next we studied the influence of correlation anisotropy in 2-D reservoir models. For a reservoir under five-spot waterflood pattern, it is shown that the ratios of breakthrough times and recovery factors of the wells in each direction of correlation are greatly influenced by the degree of anisotropy. In fully developed fields, performance data can aid in the recognition of reservoir anisotropy.

Finally, a procedure for estimating the spatial correlation length from performance data is presented. Both the production performance data and the system's effective permeability are required in estimating the correlation length.

2D X-RAY SCANNER AND ITS USES IN LABORATORY RESERVOIR CHARACTERIZATION MEASUREMENTS

by Dan Maloney and Kevin Doggett

BDM Petroleum Technologies

ABSTRACT

X-ray techniques are used in petroleum laboratories for a variety of reservoir characterization measurements. This paper describes the configuration of a 2D X-ray scanner and many of the ways in which it simplifies and improves accuracy's of laboratory measurements.

Linear X-ray scanners are most often used to provide descriptions of fluid saturations within core plugs during flow tests. We configured our linear scanner for both horizontal and vertical movement. Samples can be scanned horizontally, vertically, or according to horizontal and vertical grids. X-ray measurements are fast, allowing measurements of two- and three-phase fluid saturations during both steady- and unsteady-state flow processes. Rock samples can be scanned while they are subjected to stress, pore pressure, and temperature conditions simulating those of a petroleum reservoir.

Many types of measurements are possible by selecting appropriate X-ray power settings, dopes, filters, and collimator configurations. The scanner has been used for a variety of applications besides fluid saturation measurements. It is useful for measuring porosity distributions in rocks, concentrations of X-ray dopes within flow streams during tracer tests, gap widths in fracture flow cells, fluid interface levels in PVT cells and fluid separators, and other features and phenomena.

HARDWARE

Many have used X-rays to determine two- and three-phase fluid saturations in rocks.[1-11] The system used by the authors is based primarily on systems described by Oak, Potter, and others,[7-11] except that scans can be taken in both horizontal and vertical directions. Figure 1 is a general schematic of the X-ray scanner used by BDM Petroleum Technologies.[12,13] The figure shows the relative position of a sample with respect to the X-ray source and detector.

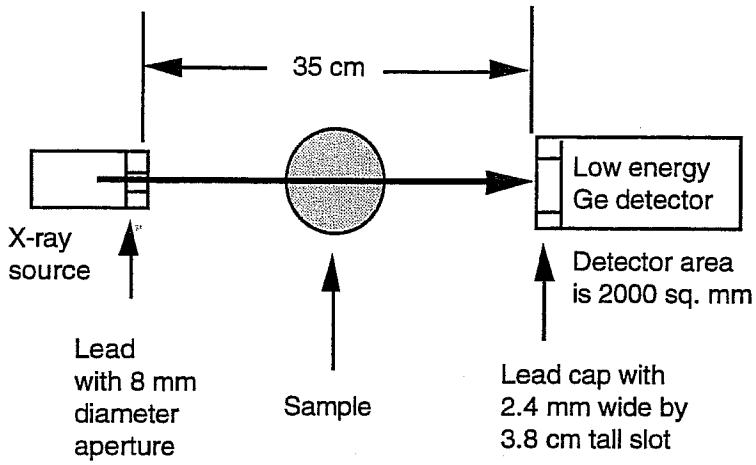

Figure 1 General schematic of the X-ray source and detector.

The X-ray source is a Philips PW2184/00 tungsten target XRF tube. The tube is rated for 3 kW at 100 kV, although normal operating conditions include voltages from 25 to 60 kVp and currents to 80 mA. The tube is normally operated with peak voltages close to but above the k-emission energies of X-ray dopes contained in test fluids. This yields maximum contrast between X-ray absorption characteristics of the test fluids. The tube is powered by a Philips XRG 3100 X-ray generator.

The portion of the tube that emits X-rays is housed within a thick, lead-lined stainless steel turret that has several collimation ports of different lengths. A lead shutter within the turret is normally closed unless a scan is taking place. The ends of the collimation ports are machined to accept cuvettes containing doped fluid solutions for beam conditioning.

A chiller is required to protect the tube from heat damage. The chiller used with this X-ray device was made by the Haskris Co.

The X-ray detector is a Canberra low energy germanium detector, which has a 2000 sq. mm area, 20 mm thickness, 0.5 mm Beryllium window, and the following resolution characteristics: FWHM at 5.9 keV of 400 eV and FWHM at 122 keV of 700 eV. The detector has an RC preamplifier. The detector electronics are cooled by liquid nitrogen using a 15 liter, horizontal integral cryostat. The 15 liter capacity provides about 10 days of operation before the cryostat must be refilled with liquid nitrogen. To prevent damage to the detector from a low liquid nitrogen condition, the preamplifier has a high-temperature inhibitor. Damage can also occur if full power is

suddenly applied to the deenergized detector. To protect against this occurrence, power to the detector passes through a pull-down switch that protects against sudden off-and-on power cycles during storms. An integrated signal processor, slave board, and software are used for multichannel data acquisition and analysis. These reside within a Gateway 486 computer.

The detector is surrounded by a lead shield. A thick lead cap was installed into the end of the detector shield between the detector and sample. The lead cap contains a slit that limits X-rays that reach the detector to only those which pass through the test sample. The slit is used to gain better resolution of position-specific X-ray intensities during linear X-ray scans. For scans on horizontal samples, the slit is positioned vertically. For scans on vertical samples, the slit is positioned horizontally. For samples in which X-ray scans are taken in 2 dimensions (vertical and horizontal), another lead cover with a 2 mm aperture is placed in front of the detector.

The X-ray tube and detector are mounted on an inverted U-shaped frame. The horizontal and vertical positions of this frame are controlled by drive screws and motors. Parker Compumotor indexers and motors along with other hardware are used to control horizontal and vertical movement of the scanning platform. The Compumotor indexers controlling the horizontal and vertical stages of the X-ray scanner are daisy-chained so that commands to change the scanner horizontal and vertical positions are sent through a single communication channel. The laboratory PC computer communicates with the indexers during X-ray scans. As a sample is scanned, the X-ray tube and detector move with respect to the stationary samples.

As previously stated, the laboratory computer is used for data acquisition and X-ray scanner control. The system uses LabVIEW, a software product by National Instruments, for these functions. The computer also controls pumps and other laboratory hardware, collects data from instruments, and performs calculations using measured data.

GENERAL X-RAY SCANNER OPERATION

Samples to be scanned are mounted within the scanning region of the X-ray device. The horizontal scan range is approximately 3 meters while the vertical scan range is approximately 0.6 m. An X-ray scan consists of a number of X-ray intensity measurements taken at discrete positions along the length and height of a sample. For small rock samples, scan increments of 0.1 to 0.5 cm

are often employed. A scanning pattern is determined for a sample during the initial stages of experimentation. Scan parameters are entered into the computer program. Thereafter, scans can be automatically programmed for specific time intervals.

When a scan is initiated, the X-ray device moves to the first measurement position. Upon reaching the first position, the scanner stops moving. The lead shutter opens, emitting X-rays. The intensities of X-rays that pass through the sample are measured by the detector. After the predefined count interval, which is usually about 5 seconds, the X-ray device moves to the next position. Intensities are measured at the second position, then the scanner moves again. This process continues until measurements have been recorded at each scan position. Upon completing the final measurement, the lead shutter closes. Scanning an 8 cm long sample at 15 positions takes about 2 minutes. Faster scans are also possible, making the device useful for determining changing saturations during unsteady-state tests.

The first sets of X-ray scans taken of a sample are used to correlate X-ray intensities to fluid contents or in situ rock fluid saturations. Once these correlations are established, they are entered into the scanning program. For subsequent scans, the correlation equations are used to calculate fluid saturations as soon as X-ray intensities are measured. Results are plotted on the computer's screen, providing a real-time image of the saturation conditions within the sample. Several experiments on different samples are often conducted at the same time. The only restriction here is that scan times have to be scheduled in a manner that avoids conflicts.

X-RAY TERMINOLOGY AND BASIC CALCULATIONS

X-ray measurements described in following sections of this report are for various X-ray tube voltage and current settings. Because the X-ray source is polychromatic, X-rays with a range of photon energies are emitted from the X-ray tube for particular X-ray generator settings. For this reason, the X-rays which pass through the sample and reach the detector also are over a range of photon energies.

Figure 2 shows intensities of X-ray photons that passed through a coreholder for various tube voltage and current settings.[12] A fairly broad band of X-rays pass through a sample during a typical X-ray scan. For example, for scans of figure 2 with the X-ray generator set to 55 kV, intense X-rays were within a range from about 40 keV to 60 keV with greatest intensity at around 55 keV.

Increasing the tube voltage shifts the region of greatest intensity to a higher photon energy and increases the relative intensities of the photons which emerge from the coreholder. Increasing the tube current while keeping the voltage constant generally increases the amplitude of the photon intensity distribution plot. Another way to increase intensities at the detector is to increase the area of the collimator, allowing greater numbers of photons to reach the detector. Decreasing the collimator area decreases the intensities of detected photons, but provides a better measure of the photons which pass through a specific region of the sample.

The X-ray detector is used to count the number of photons which emerge from the coreholder over a specified live-time interval (part of the total detector time is dead-time). Intensities are calculated by dividing the number of counts by the live-time interval in seconds.

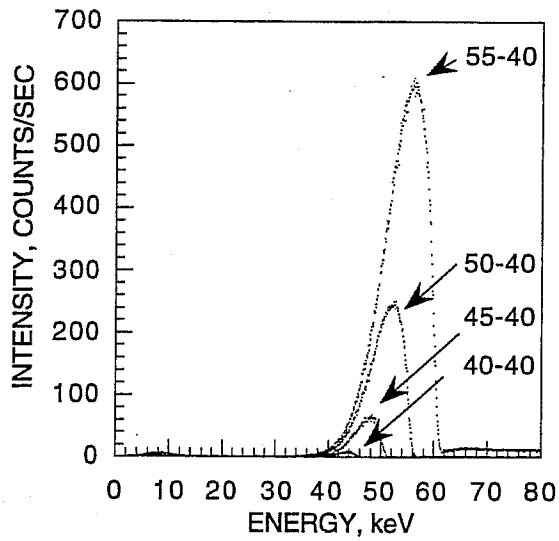

Figure 2 **X-ray results from scans through an aluminum coreholder of a Bluejacket sandstone plug. X-ray generator kV and mA settings (kV-mA) are shown from scans with different tube voltages.**

Lambert's Law is often cited[14,15] to relate intensities of X-rays which emerge from a sample to intensities of X-rays which are incident to the sample:

$$I = I_o e^{(-kx)} \tag{1}$$

where I is the emergent intensity, I_o is the incident intensity, k is the linear absorption coefficient of the sample, and x is the sample thickness. Taking natural logs of both sides of equation 1 and manipulating the result yields:

$$Ln(I) = -kx + Ln(Io) \tag{2}$$

When more than one absorber is in the X-ray beam path, the equation is:

$$I=Ioe(-k1x1 - k2x2 - ...) \quad (3)$$

For typical rock fluid saturation measurements, I_O, the X-ray absorption characteristics of the specific rock and coreholder assembly, and the X-ray path length are constants so that changes in Ln(I) result from changes in rock fluid saturations. As long as incident X-ray intensities remain constant throughout a particular flow experiment in which X-ray absorption techniques are used for fluid saturation measurements, a value for the incident intensity is not specifically required. However, knowledge of incident X-ray intensities are important when predicting X-ray absorption characteristics of experimental fixtures that have never been scanned before. X-ray scan results from this laboratory are usually described using natural logs of emergent X-ray intensities because this is the variable predominantly used for rock fluid saturation calculations.

X-Ray Calibrations

For tests in which two different fluids exist within the sample, one of the fluids is typically doped with an X-ray absorber, such as sodium iodide in the brine phase or bromodecane in the oil phase.

Figure 3 shows X-ray data from scans of a particular position within a rock sample when it was completely saturated with air, then oil, and finally with a doped brine.[16] The absorption characteristics of the sample change significantly with changes in fluid content. Figure 4 shows the result of taking the natural log of the integrated intensities under each curve to construct two-phase saturation calibrations. The figure shows correlations for air-brine and oil-brine fluid systems. Using these types of calibrations for each scan position within the rock, two-phase fluid saturations within rock samples can be easily determined from X-ray measurements. Figure 5 shows a typical result from a coreflood experiment. The saturation gradient toward the outlet end of the sample is probably indicative of a capillary end-effect.

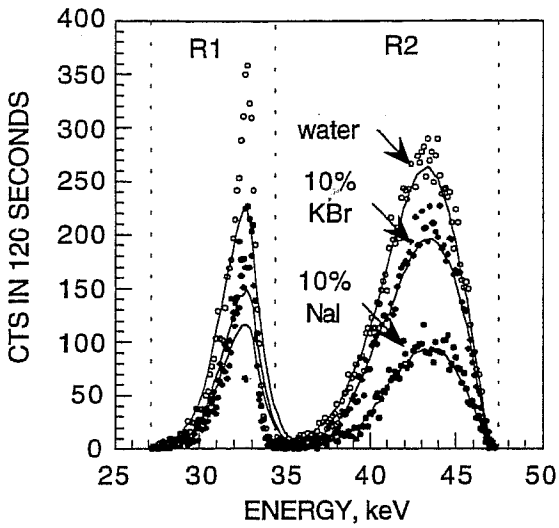

Figure 3 **X-ray scan data for one scan position with different saturating fluids.**

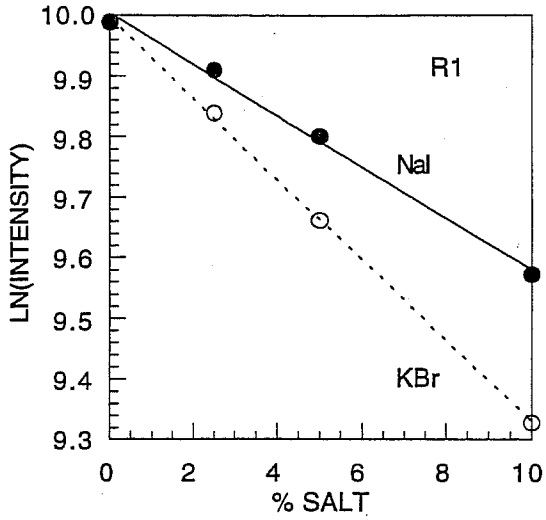

Figure 4 **Resulting X-ray correlations to fluid saturations.**

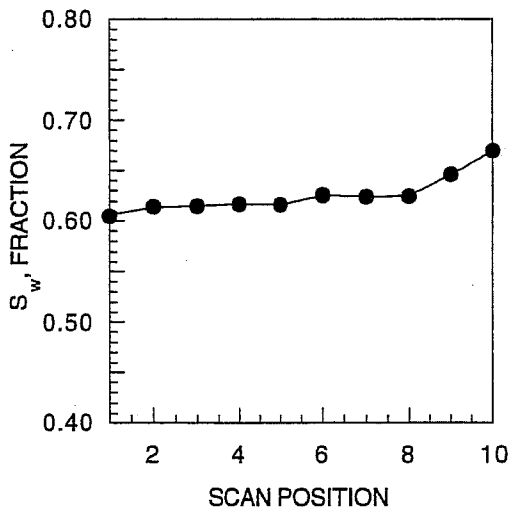

Figure 5 **Typical scan results showing an end-effect.**

For tests with three fluid phases, two of the fluids are doped with absorbers that have X-ray absorption edges at different energies. Additionally, the incident X-ray beam is filtered by passing it through an absorber that splits the distribution of intensities into two distinct regions. Figure 6 provides an example in which containers filled with water, water doped with potassium bromide, and water doped with sodium iodide were scanned using a filtered X-ray beam.[16] As shown, the dopes yield different absorption characteristics for each fluid on each side of the split. Figures 7 and 8 show how taking the natural log of the integrated intensities under each curve

provide sets of equations that can be used to determine three phase saturations from a single X-ray scan. Figure 9 graphically shows how these results are used to calculate three phase saturations. The beauty of this "dual energy" technique is that saturations for each of the three fluid phases are calculated from data measured during a single X-ray scan.

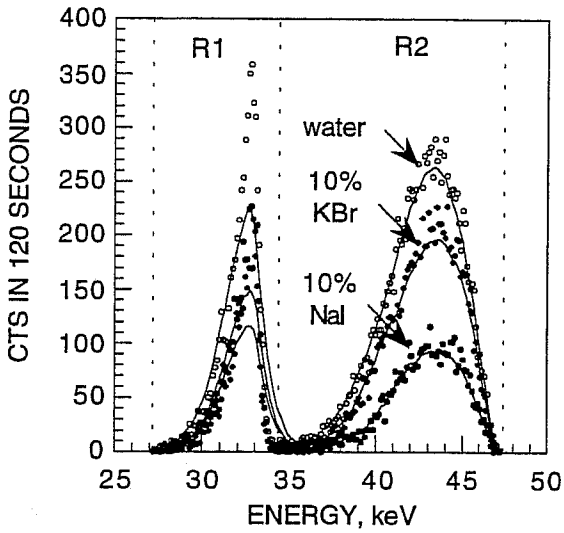

Figure 6 **Intensities from "dual energy" measurements.**

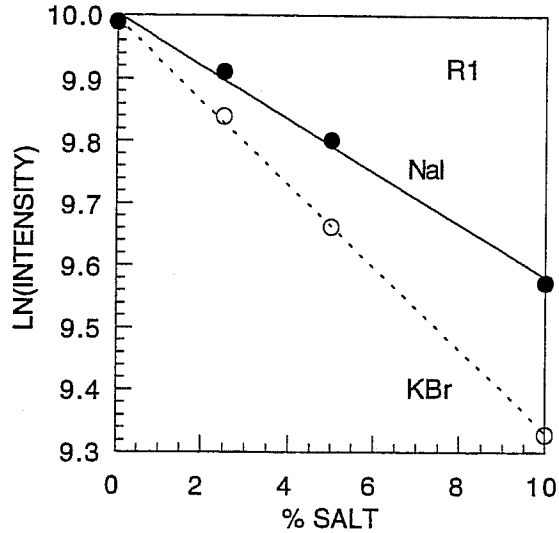

Figure 7 **Resulting X-ray range 1 correlations to saturations.**

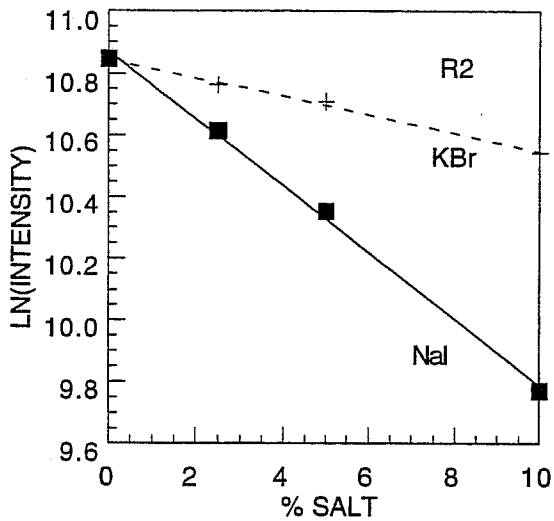

Figure 8 **Resulting X-ray range 2 correlations to saturations.**

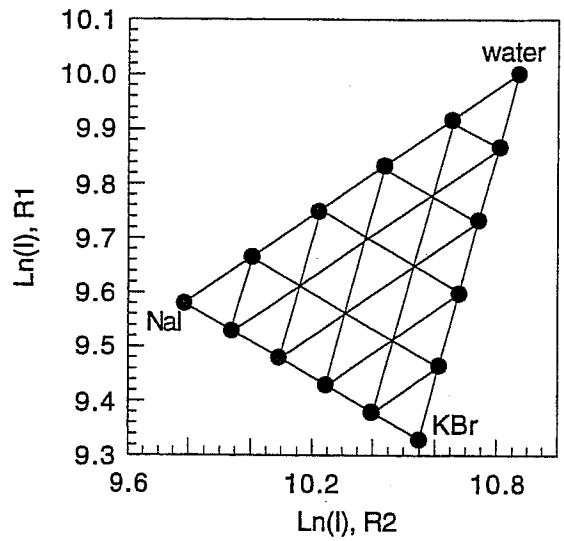

Figure 9 **Determination of three-phase saturations from range 1 and range 2 X-ray measurements.**

X-RAY SCANNER APPLICATIONS

The following lists some of the more novel measurements that have been performed using the scanner.

Corefloods

The X-ray scanner is commonly used for two and three-phase steady- and unsteady-state relative permeability tests and corefloods. Figure 10 shows a simple schematic of a closed-loop flow system that was used for three-phase measurements during a reservoir condition coreflood. Rock fluid saturations were determined by X-ray scanning the core plug through the coreholder. Produced fluid volumes were determined by vertically scanning the fluid separator.

As shown by figure 11, fluid interface levels within the separator are easily determined from X-ray results. The interface levels can be clearly defined from step-changes in X-ray intensities. The X-ray technique for measuring fluid volumes within a separator is effective even when the fluids mix or form emulsions. Scans of fluids within the separator can be used to determine linear X-ray absorption coefficients for the fluids "on the fly" so that X-ray calibrations can be adjusted for changes in fluid properties.[16] This type of X-ray technique is also applicable for PVT measurements and provides an added advantage in that windowless cells can be employed.

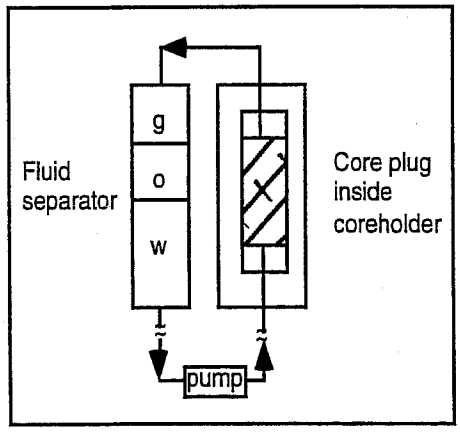

Figure 10 **Simple schematic of a closed-loop flow system.**

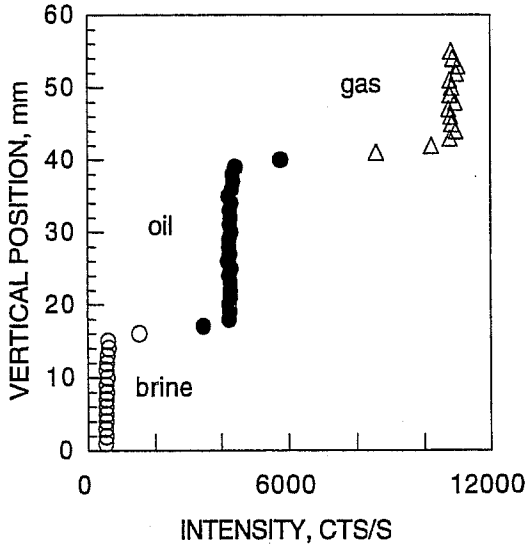

Figure 11 **Fluid interface level measurements from a separator scan.**

Porosity Distribution Imaging

Rock porosity distributions can be calculated from X-ray intensity measurements.[9] Software can be used to create images from the 2-D X-ray data. Figure 12 shows results for a 10 x 10 x 3 cm sandstone block.[17] The block was X-ray scanned while dry and then after it was saturated with brine. Intensity measurements were recorded at about 1000 horizontal and vertical positions. Differences in X-ray intensities for the dry and brine saturated sample and the total porosity were used to calculate porosity distributions. Permeabilities measured along the lower face of the dry sample by a probe permeameter are overlaid on the porosity map. This information simplified interpretations of results from subsequent spontaneous imbibition measurements.[17]

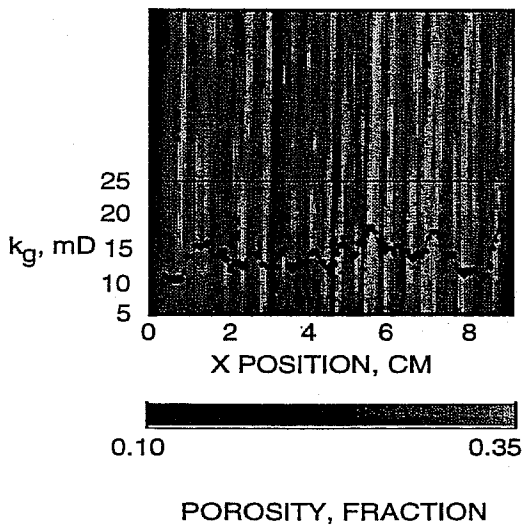

Figure 12 **Characteristics of a Berea Sandstone slab. Porosities were calculated from X-ray measurements of the dry and brine-saturated rock. Permeabilities were from probe minipermeameter measurements.**

Determination of Fluid Saturations Within Fracture Models

X-rays techniques are also particularly well suited for measurements of fluid flow properties in fractures or cracks. Figure 13 is a schematic of a plastic fracture model that was used for multiphase fluid flow measurements in fractures.[17,18] The fracture gap width within the cell was 790 μm. Flow properties and saturation distributions were measured as oil and brine flowed

upward through the cell. In addition to measurements of fluid saturations, the X-ray device was also found to be an effective tool for measuring the width of the open fracture. Fracture widths were measured with resolution to about 5 μm.

Figure 14 shows saturation profiles that were measured by the X-ray scanner during this steady-state relative permeability test. For each steady-state flow condition in this particular test, the oil flowed through a narrow stream in the center of the fracture. Contrary to what some might expect, the brine saturation was considerably different than the brine fractional flow.

Figures 15 and 16 provide comparisons of fracture relative permeabilities for two different fracture widths with vertical upward flow. As shown, relative permeabilities are considerably different for wide and narrow fractures. Differences in fluid densities and the direction of fluid flow had pronounced effects on results for the wide fracture. As shown by these results, the 2-D X-ray scanner was a useful tool for fracture relative permeability measurements. This X-ray application should help to resolve some of the questions concerning multiphase flow in fractures.

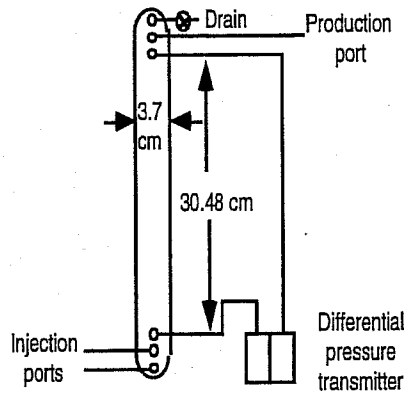

Figure 13 Simple fracture cell schematic.

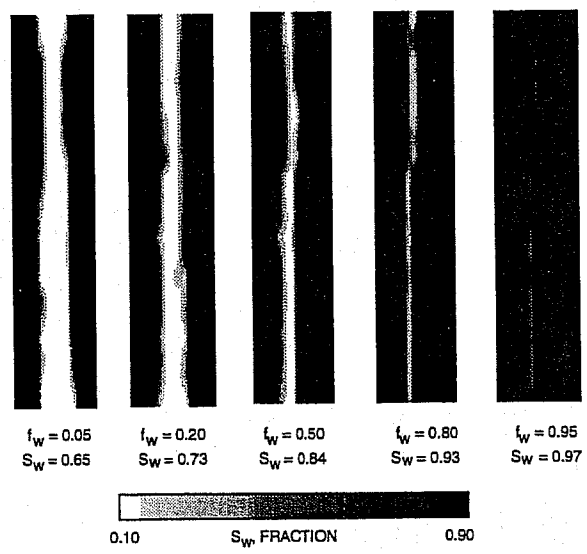

Figure 14 Two-phase oil-brine saturation profiles within a 790 μm wide fracture. Flow was vertically upward.

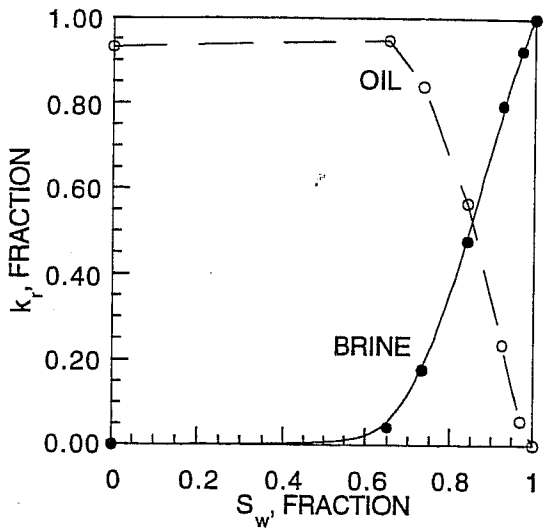

Figure 15 **Oil-brine relative permeability results, 790 μm fracture. The flow direction was upward.**

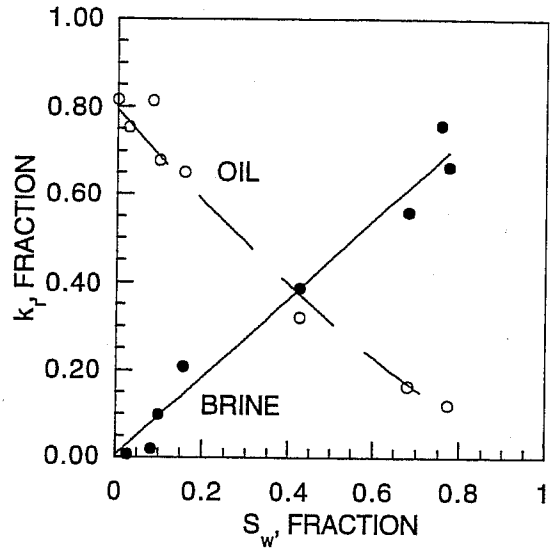

Figure 16 **Oil brine relative results, permeability results, 50 μm fracture. The flow direction was upward.**

Tracer Tests

The X-ray scanner is also useful during tracer tests to evaluate changes in in-situ rock fluid saturations as well as tracer concentrations in the effluent. With the X-ray generator set at its lowest tube power settings of 25 kV and 1 mA, X-ray scans of fluid-filled tubes were used to identify changes in salt concentrations in a brine.[16] Adding salt to the brine increased the X-ray attenuation appreciably, much like what happens when an X-ray absorber is added to a test fluid with higher tube power settings. This application provides flexibility for tracer tests when dopes or other unnatural compounds cannot be added to the rock fluids.

CONCLUSIONS

In conclusion, many types of rock and fluid characterization measurements are possible using a 2-D X-ray scanning device and appropriate X-ray power settings, dopes, filters, and collimator configurations. While linear scanners have traditionally been used for measuring fluid saturations in rocks, X-ray data from the scanner can also be used to create images of rock and fluid distribution characteristics. The scanner is useful for measuring porosity distributions in rocks, concentrations of X-ray dopes within flow streams during tracer tests, gap widths in fracture

flow cells, fluid interface levels in PVT cells and fluid separators, and other features and phenomena. In essence, X-ray scanners are powerful tools for a variety of applications in petroleum laboratories.

ACKNOWLEDGMENTS

The authors express appreciation to U.S. Department of Energy for supporting the preparation and publication of this paper. Many of the X-ray applications reported in this paper were developed during the performance of Department of Energy funded projects. We thank the management of BDM Petroleum Technologies for giving permission to publish this work.

REFERENCES

1. Boyer, R., F. Morgan and M. Muskat: A New Method for Measurement of Oil Saturation in Cores. Trans. AIME, vol. 170, 1947, pp. 15-33.
2. Morgan, F., J. McDowell, and E. Doty: Improvements in the X-ray Saturation Technique of Studying Fluid Flow. Petroleum Transactions, AIME, vol. 189, 1950, pp. 183-194.
3. Laird, A. and J. Putnam: Fluid Saturation in Porous Media by X-ray Technique. Petroleum Transactions, AIME, vol. 192, 1952, pp. 275-284.
4. Laird, A. and J. Putnam: Three Component Saturation in Porous Media by X-Ray Techniques. Petroleum Transactions, AIME, v. 216, 1959, pp. 216-220.
5. Schneider, F. and W. Owens: Sandstone and Carbonate Two- and Three-Phase Relative Permeability Characteristics. Soc. of Petr. Eng. Journal, March 1970, pp. 75-84.
6. Schneider, F. and W. Owens: Steady-state Measurements of Relative Permeability for Polymer/Oil Systems. Soc. of Petr. Eng. Journal, February 1982, pp. 79-86.
7. Oak, M. and R. Ehrlich: A New X-Ray Absorption Method for Measurement of Three-Phase Relative Permeability. Paper SPE 14420 presented at the 60th Annual Technical Conference and Exhibition of the Society of Petroleum Engineers, Las Vegas, NV, Sept. 22-25, 1985.
8. Oak, M., L. Baker, and D. Thomas: Three-Phase Relative Permeability of Berea Sandstone. Paper SPE/DOE 17370 presented at the 1988 SPE/DOE Symposium on Enhanced Oil Recovery, Tulsa, OK, April 17-20.
9. Potter, G. and D. Groves: Displacements, Saturations, and Porosity Profiles from Steady-State Permeability Measurements. Paper SPE 19679 presented at the 64th Annual Technical Conference and Exhibition of the Society of Petroleum Engineers, San Antonio, TX, Oct. 8-11, 1989.
10. Oak, M.: Three-Phase Relative Permeability of Water-Wet Berea. Paper SPE/DOE 20183 presented at the 1990 SPE/DOE Symposium on Enhanced Oil Recovery, Tulsa, OK, April 22-25.

11. Oak, M.: Three-Phase Relative Permeability of Intermediate-Wet Berea Sandstone. Paper SPE 22599 presented at the 66th Annual Technical Conference and Exhibition of the Society of Petroleum Engineers, Dallas, TX, Oct. 6-9, 1991.

12. Maloney, D. and K. Doggett: Advances in Steady- and Unsteady-State Relative Permeability Measurements and Correlations FY 1995. Report NIPER/BDM-0160 prepared under DOE contract DE-AC22-94PC91008, July 1995, pp. 21-28.

13. Maloney, D. and L. Tomutsa: Use of X-ray Scanners in Petroleum Research. Paper HD 31D-03 presented at the 1995 Fall Meeting of the American Geophysical Union, San Francisco, CA, Dec. 11-15, 1995.

14. Sproull, W.: X-rays in Practice. McGraw Hill, New York, 1946.

15. Bertin, E.: Principles and Practice of X-ray Spectrometric Analysis. Plenum Press, New York, 1970.

16. Maloney, D. and K. Doggett: Relative Permeability Research FY 1994. Report NIPER/BDM-0067 prepared under DOE contract DE-AC22-94PC91008, Sept. 1994, pp. 23-29.

17. Chang, M. and D. Maloney: Analytical Solutions and Experiments to Two-Phase Flow Problems of Naturally Fractured Reservoirs, Imbibition Transfer Function. Report NIPER/BDM-0171 prepared under DOE contract DE-AC22-94PC91008, Sept. 1995, p. 124.

18. Maloney, D., K. Doggett, and A. Sarkar: Laboratory Characterization of Oil Production Mechanisms in Fractured Rock. Report NIPER/BDM-0274 prepared under DOE contract DE-AC22-94PC91008, Sept. 1996, pp. 9-21.

Multiscale Heterogeneity Characterization of Tidal Channel, Tidal Delta and Foreshore Facies, Almond Formation Outcrops, Rock Springs Uplift, Wyoming

By
Richard A. Schatzinger and Liviu Tomutsa
BDM Petroleum Technologies
Bartlesville, Oklahoma

ABSTRACT

In order to accurately predict fluid flow within a reservoir, variability in the rock properties at all scales relevant to the specific depositional environment needs to be taken into account. The present work describes rock variability at scales from hundreds of meters (facies level) to millimeters (laminae) based on outcrop studies of the Almond Formation. Tidal channel, tidal delta and foreshore facies were sampled on the eastern flank of the Rock Springs uplift, southeast of Rock Springs, Wyoming. The Almond Fm. was deposited as part of a mesotidal Upper Cretaceous transgressive systems tract within the greater Green River Basin.

Bedding style, lithology, lateral extent of beds of bedsets, bed thickness, amount and distribution of depositional clay matrix, bioturbation and grain sorting provide controls on sandstone properties that may vary more than an order of magnitude within and between depositional facies in outcrops of the Almond Formation. These features can be mapped on the scale of an outcrop. The products of diagenesis such as the relative timing of carbonate cement, scale of cemented zones, continuity of cemented zones, selectively leached framework grains, lateral variability of compaction of sedimentary rock fragments, and the resultant pore structure play an equally important, although less predictable role in determining rock property heterogeneity. A knowledge of the spatial distribution of the products of diagenesis such as calcite cement or compaction is critical to modeling variation even within a single facies in the Almond Fm. because diagenesis can enhance or reduce primary (depositional) rock property heterogeneity. Application of outcrop heterogeneity models to the subsurface is greatly hindered by differences in diagenesis between the two settings.

The measurements upon which this study is based were performed both on drilled outcrop plugs and on blocks. One inch diameter plugs were taken at lateral spacing from 6 inches (15 cm) to 50 feet (16.5 meters) and vertical spacing from 3 inches (8 cm) to 5 feet (1.5 meters) to capture hierarchically stacked patterns of variations on the scale of meters to hundreds of meters. Probe permeameter permeability and x-ray CT porosity from outcrop blocks captured variations at the scale of a few mm to a few hundred mm. Conventional gas porosity and permeability measurements were performed on the plugs and were integral to mapping the distribution of petrophysical properties at the scale of the facies (tens to hundreds of meters). Microscopic scale heterogeneities such as grain size, pore distribution, authigenic cement content, and paragenetic stages were recorded using thin section point count methods and semi-automated petrographic image analysis.

INTRODUCTION

The Upper Cretaceous Almond Formation was deposited as a dominantly transgressive shoreline along the western margin of the North American Cretaceous Western Interior Seaway. It marks the uppermost phase of Mesaverde Group sedimentation (Fig. 1). In the area of the Rock Springs Uplift and eastward in the Washakie Basin the Almond Formation has typically been informally divided into lower (dominantly estuarine) and upper (dominantly marine) units (e.g. Van Horn, 1979). Almond sedimentation was markedly cyclical, particularly within the lower, estuarine section. Even within the upper marine section multiple periods of eastward regression of the shoreline can be mapped into the Washakie Basin (Krystinik and Mead, 1996). Within the greater Green River Basin area, especially the Washakie Basin, these sands comprise important gas and oil reservoirs (see Table 1 of Martinsen and Christensen, 1992). Rapid fluctuations of relative shoreline positions are typical in the upper Almond. Each regression was terminated by a rapid flooding event as the western margin of the Lewis Shale transgressed farther to the west. Regressive fluvial to alluvial plain deposits of the Ericson Sandstone lie immediately beneath the

Almond Formation in the study area (Fig. 2) where the Ericson's upper portion records the earliest phases of the overall shoreline retreat that occurred during late Cretaceous (Campanian) time.

The study area from which the samples for this report were collected is located on the eastern flank of the Rock Springs Uplift in southwestern Wyoming (Fig. 2). Excellent outcrops of Almond Formation that exhibit the lateral relationship between depositional facies are located immediately north of highway 430 in the SE 1/4 of the SW 1/4 of section 33, T. 16 N., R. 102 W, approximately 32 miles southeast of Rock Springs Wyoming. This area was called "outcrop G" in a detailed study of Almond coals and depositional environments by Roehler (1988). The paleogeography of the area during Almond deposition was that of an embayed shoreline created by progradation of deltas north and south of the area. Tidal forces were amplified within the Rock Springs Embayment so that the Almond in this area was deposited under mesotidal conditions (Roehler, 1988; Schatzinger, and others, 1992; and Van Horn 1979).

ROCK PROPERTY VARIATIONS AT VARIOUS SCALES

Outcrop Stratigraphic Cross Section

The coarsest scale of heterogeneity within the Almond Formation was evaluated by mapping the facies relationships at "Outcrop G". At this location 8 detailed geological profiles were measured over the lateral distance of more than 1,000 ft. Outcrop gamma ray profiles were collected at and between geologically described profiles and all of the profiles were correlated to produce a cross section that approximates the distance between wells with a 40 acre spacing. Photo mosaics were made to help trace out facies architecture and critical contacts were "walked out" on the outcrop. The critical southern half of this work is reproduced here as a stratigraphic cross section (Fig. 3). The lower portion of this cross section illustrates the northward pinchout of a major tidal inlet containing reservoir quality sands that are nearly 20 ft thick. The inlet channel overlies and cuts into adjacent foreshore sands (beach and welded swash bar). Just above the Pintail coal bed is a 30 ft thick section of non-reservoir marsh/lagoonal shales and thin, silty tidal creek deposits that contains a horizon with laterally extensive reservoir quality tidal channel sands.

Note that the architecture of this "horizon" consists of discontinuous tidal channels. In the strike parallel cross section presented here (Fig. 3) tidal channel units have geometries with average lateral extents of only 300-350 ft. In reality, tidal channels are often sinuous and highly elongate. If the three-dimensionality of the channels could be accounted for, they might be expected to have a greater extent than 300 ft, however, the meander loops of smaller backbarrier tidal channels are frequently cut off and abandoned at which time they fill in with clay plugs. If this geometry were present in a reservoir, log correlations for wells with as little as 10 acre spacing would almost certainly erroneously indicate a continuous reservoir unit. However, as can be seen in the stratigraphic cross section (Fig. 3) the discontinuity of tidal channels in the plane of this cross section creates a scale of heterogeneity that could lead to significant bypassed oil if a simple layercake model were used. One would clearly expect little sweep of this zone if an "injection well" was placed at the southernmost limit of this cross section. At the inter-facies scale, additional complexity to modeling fluid flow is created by the Oyster Marker Bed which is tightly cemented by calcite. Calcite cement supplied by the abundant oyster shells filled virtually all pore space in this bed very early in its diagenetic history creating a field-to-regional scale impermeable barrier to vertical flow of fluids (except along fractures). Although several reservoir quality sands are present in the stratigraphic cross section, the facies architecture illustrated at this outcrop would lead one to expect poor sweep and little cross flow with sands higher in the formation because of the marsh/lagoon shales and the calcite cemented Oyster Marker Bed deposits.

Petrophysical Properties from Plugs

The measurements upon which this study is based were performed both on drilled outcrop plugs from 9 depositional facies and on blocks collected from the Almond Formation at "locality G". One inch diameter plugs were taken at lateral spacing from 6 inches (15 cm) to 50 feet (16.5 meters) and vertical spacing from 3 inches (8 cm) to 5 feet (1.5 meters) to capture hierarchically stacked patterns of variations on the scale of meters to hundreds of meters. Plugs were subjected

to standard core analysis do determine porosity and permeability and to aid in mapping petrophysical property distribution within depositional facies.

When porosity and permeability for the various depositional facies was analyzed it was recognized that, in terms of reservoir quality sandstones, there were only two groups of facies: tidal delta sandstones and all other facies combined. A representative chart (Fig. 4) comparing the porosity and permeability of tidal delta, tidal channel and foreshore facies (beach and beach-welded swash bar) illustrates the significantly higher values for the tidal delta compared to the other facies which all have similar petrophysical properties. The plug data indicate average values of just greater than 1 darcy permeability and 31.5% porosity for the tidal delta compared to 226 md and 25.6% for tidal channels, 422 md and 27.3% for the beach, and 219 md and 25.3% for the beach-welded swash bar.

The structure of the porosity and permeability distribution (lamination, bedding, bedsets), however, is different in each of the facies. In this case the structure or geometry of the petrophysical property distribution rather than the scale of the heterogeneity would cause each of the major reservoir quality facies to react differently to fluid flow.

Semi-variograms were constructed from tidal delta, tidal channel, and foreshore (spit/swash bar) facies plug permeability data in order to investigate the structure of the petrophysical properties:

Beach semi-variograms: Permeability semi-variograms of plug data from the foreshore (beach) facies (not including the beach-welded swash bar) indicate horizontal correlation lengths of less than 1 ft and 7-8 feet. The data was collected essentially parallel to depositional strike. In an unmodified fore-beach the lateral correlation lengths would be expected to be much greater than 8 ft. It is believed that the Almond data indicate shorter lateral correlation lengths because the flat lying semi-parallel laminations are not well preserved and that some degree of diagenetic compartmentalization has occurred. Clay cement variations (related to partial leaching of skeletal sand grains) and relative differences in compaction are currently being investigated as primary causes of the 7-8 ft scale heterogeneity. Lateral correlation lengths of less than one foot

are believed to be due to grouping of laminae with similar permeability values, but may have to do with the minimal horizontal sample distance.

Beach-welded tidal swash bar semi-variograms: Permeability semi-variograms of data taken exclusively from the beach-welded tidal swash bar indicate a horizontal correlation length of approximately 7 ft. Planar-tabular foreset cross bedding with millimeter thick laminae are well preserved within this sub-facies. It is believed that the horizontal correlation length for the beach-welded swash bars correlates to the width of individual sand waves that were washed shoreward across the swash platform just downdrift of a tidal inlet to become welded onto the beachface.

Tidal channel semi-variograms: Permeability semi-variograms for the tidal channel facies indicate a vertical correlation length at approximately 4 ft and two lateral correlation lengths at approximately 2 feet and 10 ft. It is interesting, but probably accidental that the 4 ft vertical correlation length is twice the *thickness* of major bedsets within the measured tidal channels. It is likely that the 2 ft lateral correlation length reflects the scale of poorly-preserved foreset bedding within major bedsets. Well-preserved large scale lateral accretion surfaces mark the significant bedset boundaries within the tidal channel facies (illustrated below). Bedding within major tidal channel bedsets is poorly preserved, however, there is evidence from the photo-mosaics that the 10 ft. correlation length may represent the distance that bedding (ripple to dune-size sand waves) can be traced laterally within bedsets. Large, compacted clay clasts, clay-rich laminae, thin clay and carbonate cemented laminae and beds as well as imprints or organic material such as plant stems and other vegetation are abundant at the base of the tidal inlet channel where it cuts into laminated, white beach sands. Oysters and other molluscan remains are not abundant in the base of the inlet channel that was studied.

Tidal delta semi-variograms: Permeability semi-variograms of data from the tidal delta facies show a wide scatter, however, in both lateral and vertical directions, a correlation length of approximately 5 ft is found. additional samples are necessary to better resolve the variogram range. Raw permeability data taken along a single bedset boundary where lateral

spacing of samples was 5 ft over a distance of 450 ft indicates a well developed 20 ft cyclicity. This scale of cyclicity is only a fraction of the lateral extent of mapped major bedsets in the tidal delta facies. It is believed that the 20 ft cyclicity seen on raw permeability data reflects the frequency of beds (i.e. dune size sandwaves) within the major bedsets.

Bi-directional lamination between major beds and bedsets is moderately to well preserved. Broad, low angle festoon bedding is well preserved at major bedset surfaces. Iron oxide cements accentuate bedset boundaries and form concretionary layers that extend laterally for distances up to 50 ft.

Based on the permeability distribution of plug data and process driven geological interpretations the differences in permeability structure between depositional facies, therefore, is primarily related to the differing bedding styles present and enhancement of these heterogeneities by diagenetic processes.

Mapping Bedsets and Permeability Distribution

Tidal delta facies: Mapped bedsets within the tidal delta facies tend to extend laterally for 100 to more than 300 ft (Fig. 5) and are up to 3 ft thick. Permeability within bedsets follows the "grain" of the primary bedding direction and often exhibits significant differences across bedset surfaces (Fig 6). It was found that the permeability trend within major bedsets of this facies and others could not be properly interpreted based on widely spaced plugs (5 ft to 50 ft spacing) without first understanding the location of the bedset boundaries and the bedding direciton within the bedsets.

Thin sections indicate that the bedset boundaries, which are well preserved and very obvious on the outcrop, are enhanced by iron oxide and kaolinite cements, tighter packing with more long grain contacts, and have smaller pores than the sandstone beds on either side of the surface. The beds away from the bedset surfaces tend to have larger, clean pores that appear well connected, better grain and pore size sorting, and only local "clumps" of compacted rock fragments or partly clay-filled interparticle porosity.

Figure 7 displays X-ray CT and probe permeameter surface views from a block containing a tidal delta bedset boundary. The CT image was reconstructed from sections taken at 5 mm spacing. The probe permeameter measurements were performed on a grid 4 mm along laminations and 2 mm across laminations using a 3 mm ID and 6 mm OD tip. The X-ray attenuation values are consistent with the relatively high porosity values determined by plug measurements. They indicate a small porosity contrast between the bedset boundary and the rest of the rock, with the bedset boundary displaying the lower porosity. The probe permeameter measurements indicate a small permeability contrast between the bedset boundary and the rest of the rock with the bedset boundary displaying the lower permeability.

Tidal channel facies: Laterally accreting major bedsets within the tidal channel facies have average lateral dimensions (parallel to depositional strike) of approximately 150 ft (Fig.8).

Thin sections from the basal portion of a tidal inlet channel that cutinto an adjacent beach deposit exhibit very poor grain size sorting, widespread cm-thick layers containing iron oxide cements, finely crystalline calcite and siderite, and small, dirty appearing pores. The "dirty" appearance of the pores is caused by the presence of disseminated clays of two origins. Detrital clay-size particles within interparticle pore space originated from partly leached framework grains and compacted rock fragments. Authigenic kaolinite is also present within the pores, further reducing the permeability. Multiple layers of cm-thick channel fill were noted at the base of the inlet channel and all were poorl- to very poorly-sorted.

Figure 9 displays X-ray CT and probe permeameter surface views from a block containing a tidal channel/beach facies contact. The CT image was reconstructed from 4 mm thick sections taken at 5 mm spacing. The probe minipermeameter measurements were performed on a 5mm x 5mm grid using a 3 mm ID and 6 mm OD tip The X-ray attenuations are higher than in figure 7 indicating a lower average porosity and greater content of minerals with increased CT densities (such as iron oxide cement). The higher attenuations for to the tidal channel correspond to both a lower average porosity and more CT-dense mineralization while the beach displays a higher porosity and less diagenetic alteration. The probe permeameter measurements indicate a large

permeability contrast between the tidal channel and the beach facies, with the beach displaying permeabilities in the 150-500 mD range and the tidal chanel displaying permeabilities in the 20-150 mD range.

Foreshore facies: Bedsets were not recognized within the beach facies. However, within the 1 ft thick beach-welded swash bar closely spaced samples allowed us to map the permeability distribution (Fig. 10). Once again a primary knowledge of the bedding style (planar-tabular foreset cross bedding) was necessary to contour the permeability map correctly. Although the bedding within this unit is technically laminations (mm scale), several laminations with similar permeability values seem to be group together providing permeability layers that dip in the same direction as the bedding but less steeply.

Thin sections from the tidal swash bar facies show great variations in grain size, a relatively clean pore system with only minor amounts of interparticle clay cement, but an abundance of partly compacted soft rock fragments that tend to block pore throats.

CONCLUSIONS

Permeability distribution based on 1 inch diameter plugs collected within and between depositional facies corresponds to process driven geological explanations for the differences in permeability. The differences in petrophysical properties between bedsets and as well as between facies is primarily related to the differing bedding styles present and enhancement of these heterogeneities by diagenetic processes.

Distribution of petrophysical properties interpreted from reservoir quality sandstone blocks using CT and mini-permeameter analysis can be mapped at a scale approximately two orders of magnitude finer than that mapped using plugs. The CT and mini-permeameter data distribution can be explained through petrographic analysis. Both the large scale plug data and the detailed minipermeameter maps of sandstone blocks show similar ranges of permeability for the equivalent depositional facies based on our study of outcropping Almond Formaion barrier island sandstones. This correspondence implies that, for this system, if one correctly identifies the depositional facies and has an understanding of the facies architecture, then small sized samples are not a major hinderance to modeling the reservoir at a larger scale. Thus it is possible to provide a good approximation of scaled fluid flow*within this system* from cuttings, thin sections, or core plugs.

For our study we found that permeability dropped from approximately 1 darcy ("matrix" values) to 400-500 mD across tidal delta bedset boundaries. Matrix permeability for the tidal channel and foreshore (beach and beach-welded swash bar) are both on the order of 200-500 md. The drop in permeability across the facies contact between a tidal inlet channel deposit and the adjacent beach sandstones is 1-2 orders of magnitude.

REFERENCES

Krystinik, L .F., and R. H. Mead, 1996, Sequence stratigraphic and synsedimentary tectonic controls on reservoir compartmentalization in a transgressive sequence set: Almond Formation, southwest Wyoming: AAPG Annual Convention, Program with Abstracts, p. A79.

Martinsen, R. S., and G. Christensen, 1992, A stratigraphic and environmental study of the Almond Formation, Mesaverde Group, Greater Green River Basin, Wyoming, *in* C. E. Mullen, ed., Wyoming Geological Association Guidebook, Forty-Third Field Conference, p. 171-190.

Roehler, H., 1988, The Pintail coal bed and barrier bar G- A model for coal of barrier bar-lagoonal origin, Upper Cretaceous Almond Formation, Rock Springs Coal Field, Wyoming: USGS Professional Paper 1398, 60 p.

Schatzinger, R. A., M. J. Szpakiewicz, S. R. Jackson, M. M. Chang, B. Sharma, and M. K. Tham, 1992, Integrated geological-engineering model of Patrick Draw field and examples of similarities and differences among various shoreline barrier systems: DOE Report NIPER-575, 146 p.

Van Horn, M., 1979, Stratigraphic relationships and depositional environments of the Almond and associated formations east-central Flank of the Rock Springs Uplift, *in* Rocky Mountain Section SEPM Field Trip, Cretaceous of the Rock Springs Uplift, Wyoming, Sept. 21-23, p. 51-63.

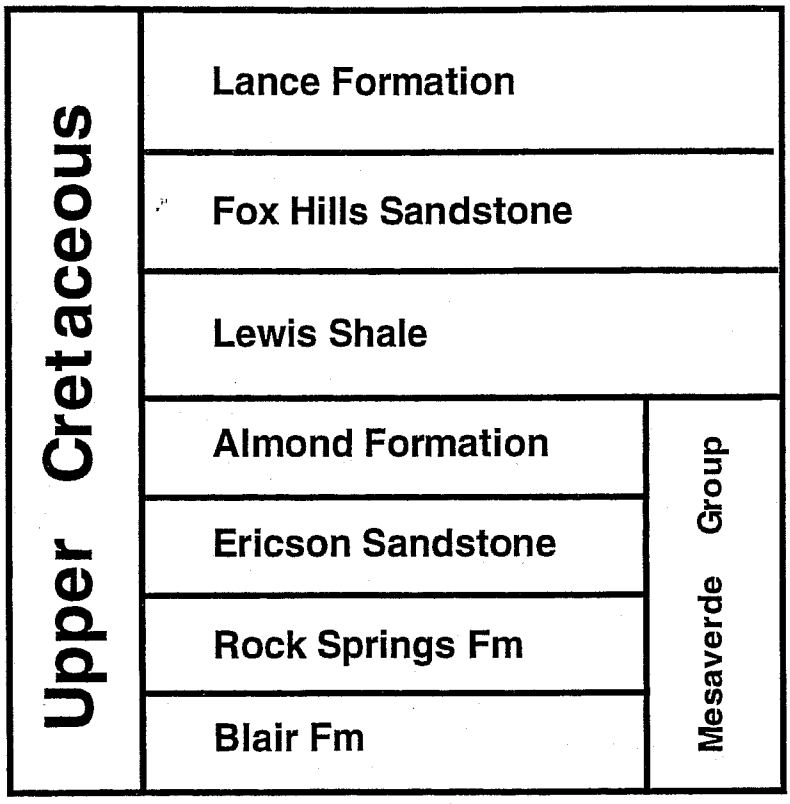

Figure 1. Stratigraphic column for outcropping Upper Cretaceous units in the study area.

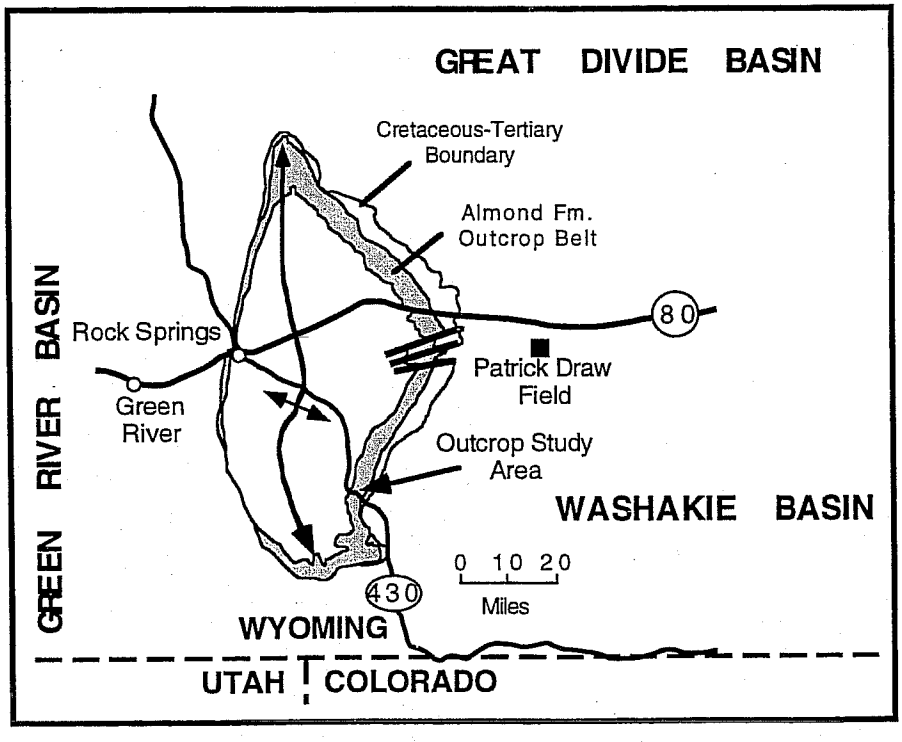

Figure 2. Location map of the study area on the eastern flank of the Rock Springs Uplift, southwestern Wyoming.

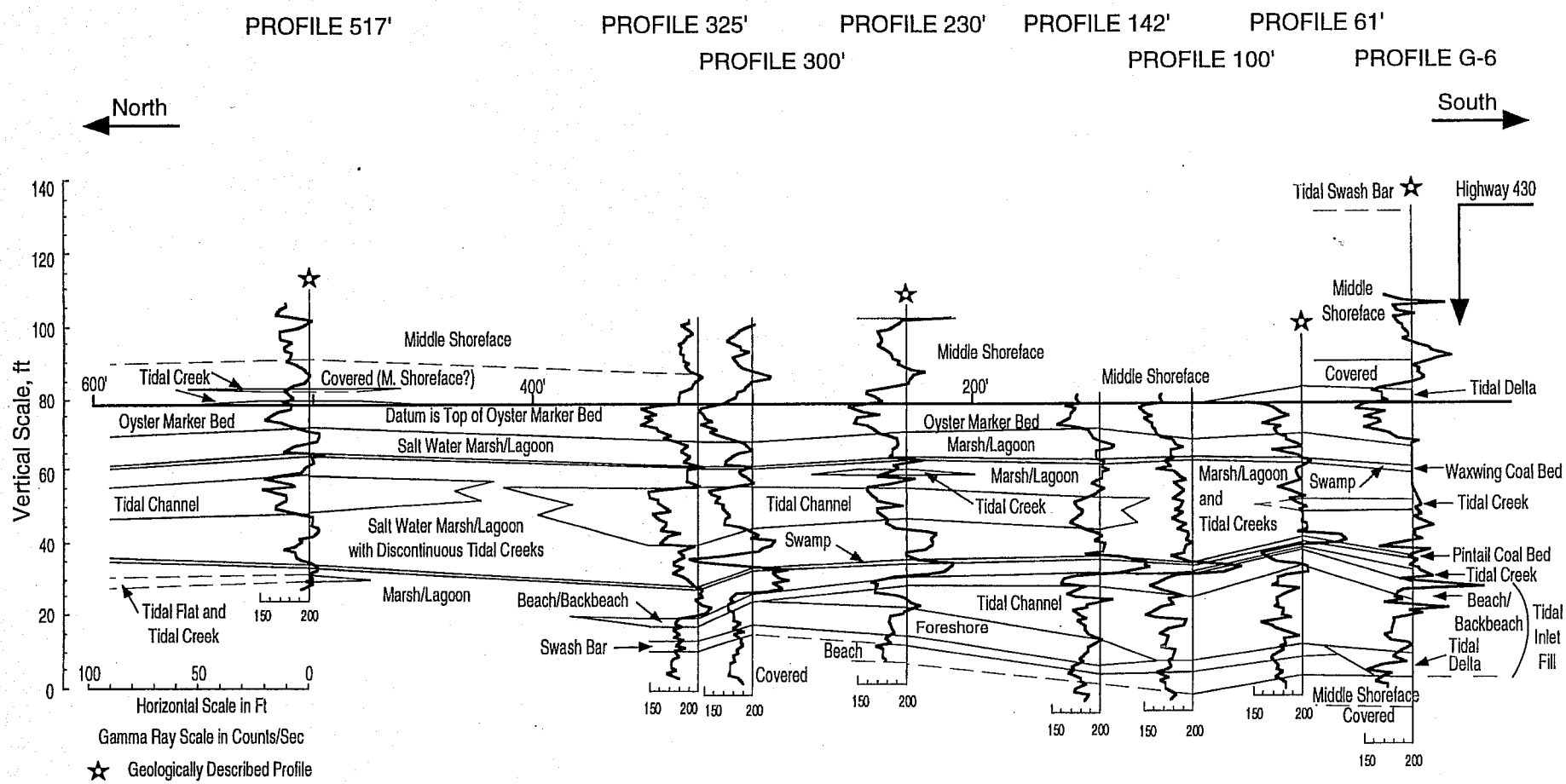

Figure 3. Outcrop stratigraphic cross section is nearly parallel to depositional strike. Note the breaks in tidal channel facies and the complexity of tidal inlet fill that can be found between distances much less than that of 40 acre well spacings.

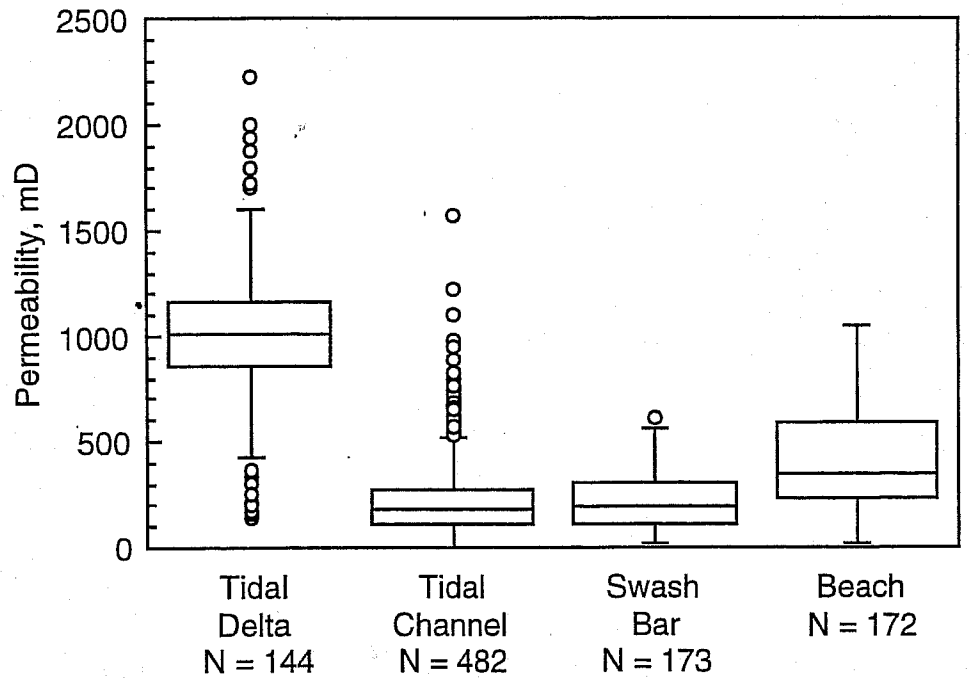

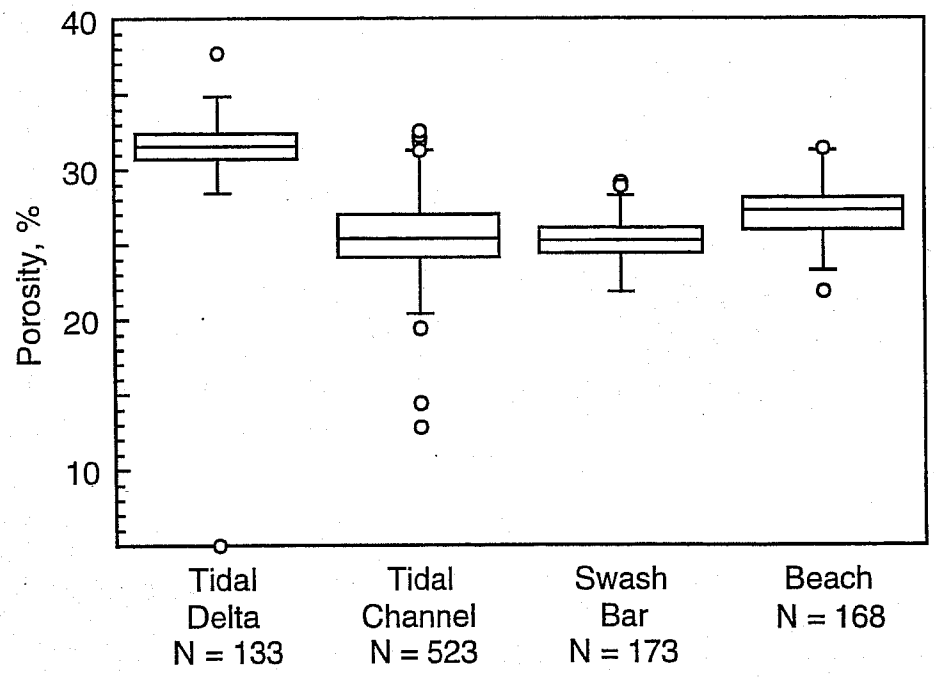

Figure 4. Comparison of porosity and permeability for outcrop facies samples. Box encloses 50% of the data centered about the median value. Lines extend to 95% value. Outliers beyond these ranges are indicated by circles. N = number of samples analysed.

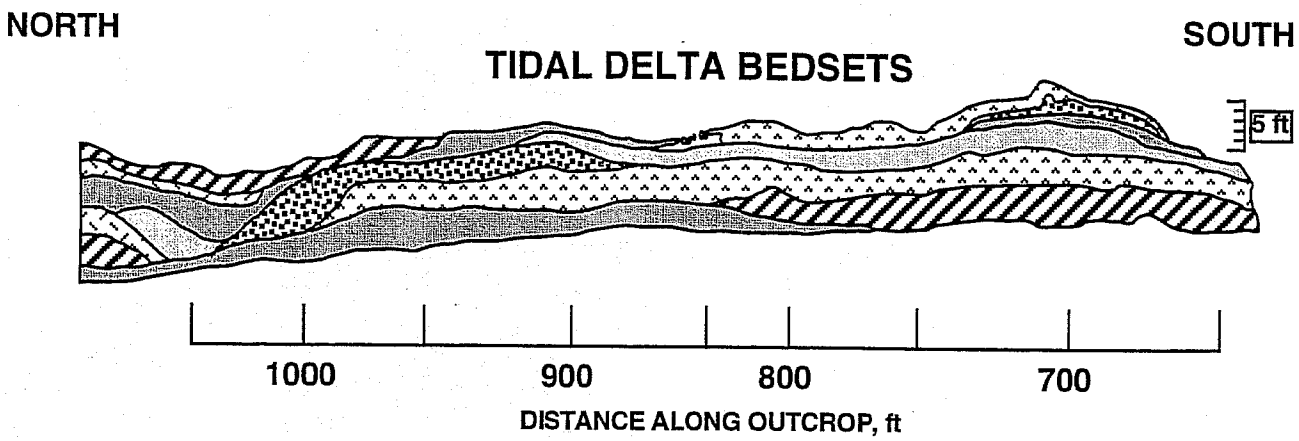

Figure 5. The lateral distribution of major bedsets within the tidal delta facies. Note that the lateral extent of bedsets is less typically less than 300 ft. Uneven horizontal scale is due to construction of cross section from photomosaic.

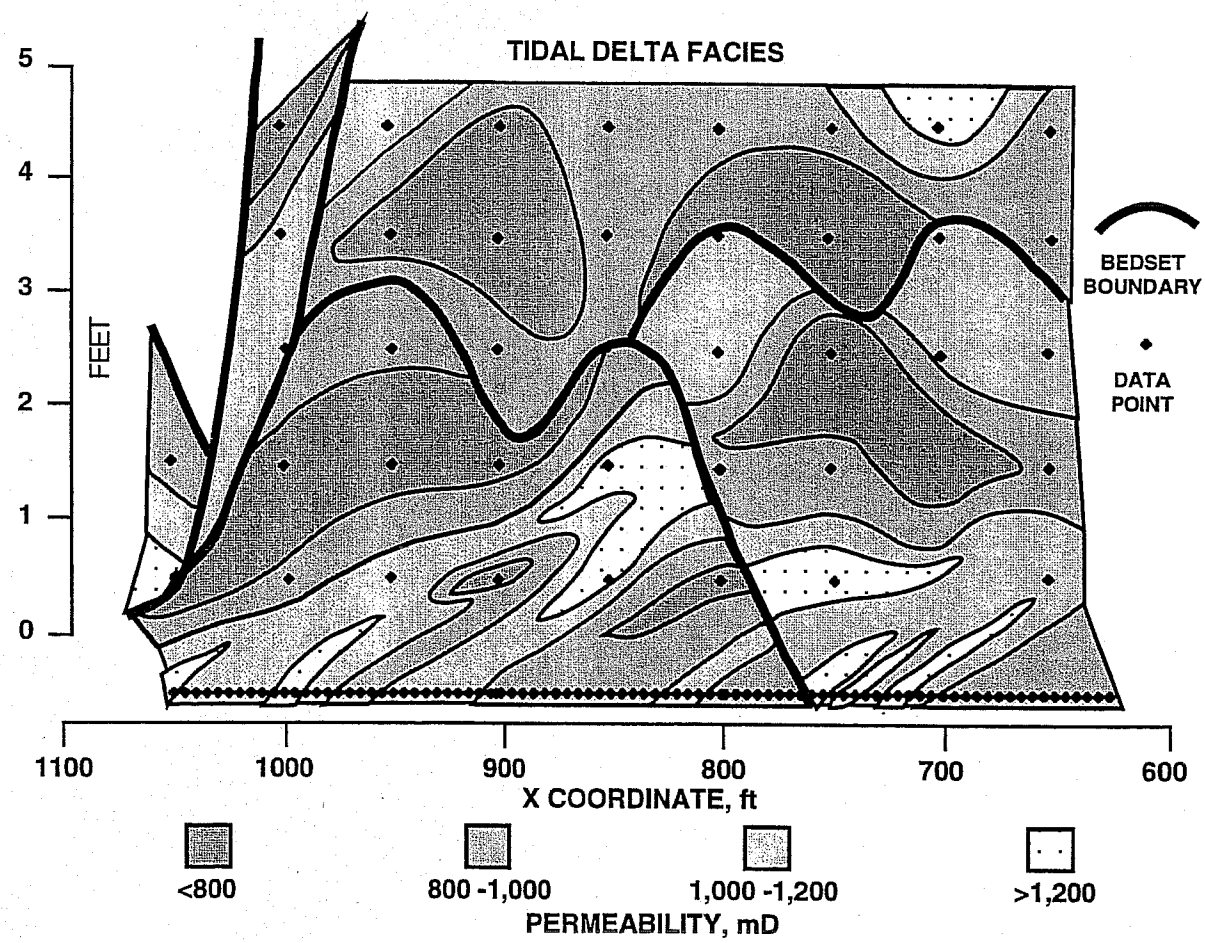

Figure 6. Distribution of permeability within major bedsets comprising the tidal delta facies.

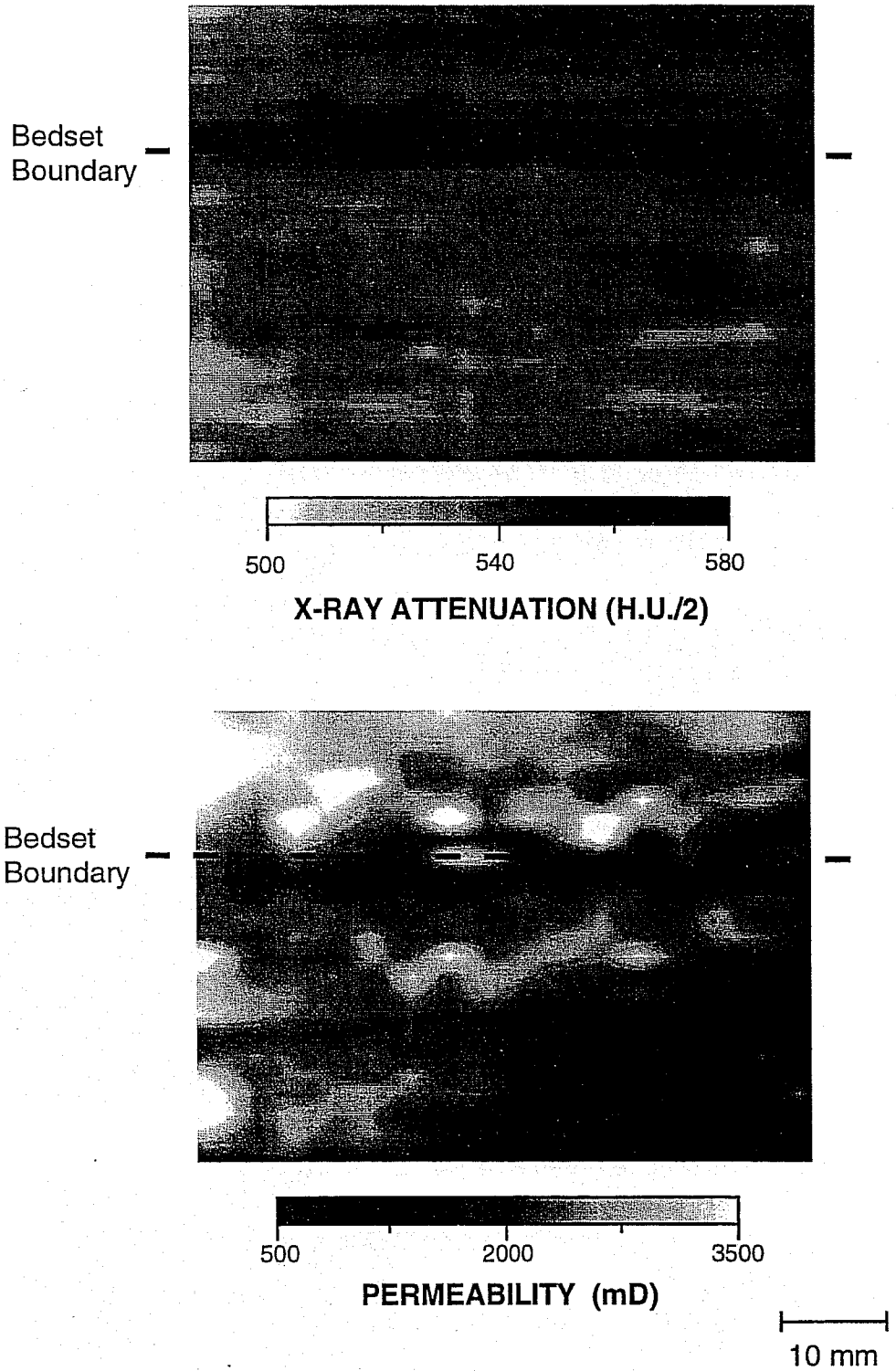

Figure 7. X-ray CT and Probe permeameter maps of a tidal delta bedset boundary. The CT image was reconstructed from sections taken at 5 mm spacing. The probe mini-permeameter measurements were performed on a grid 4 mm along laminations and 2 mm across laminations using a 3 mm ID tip.

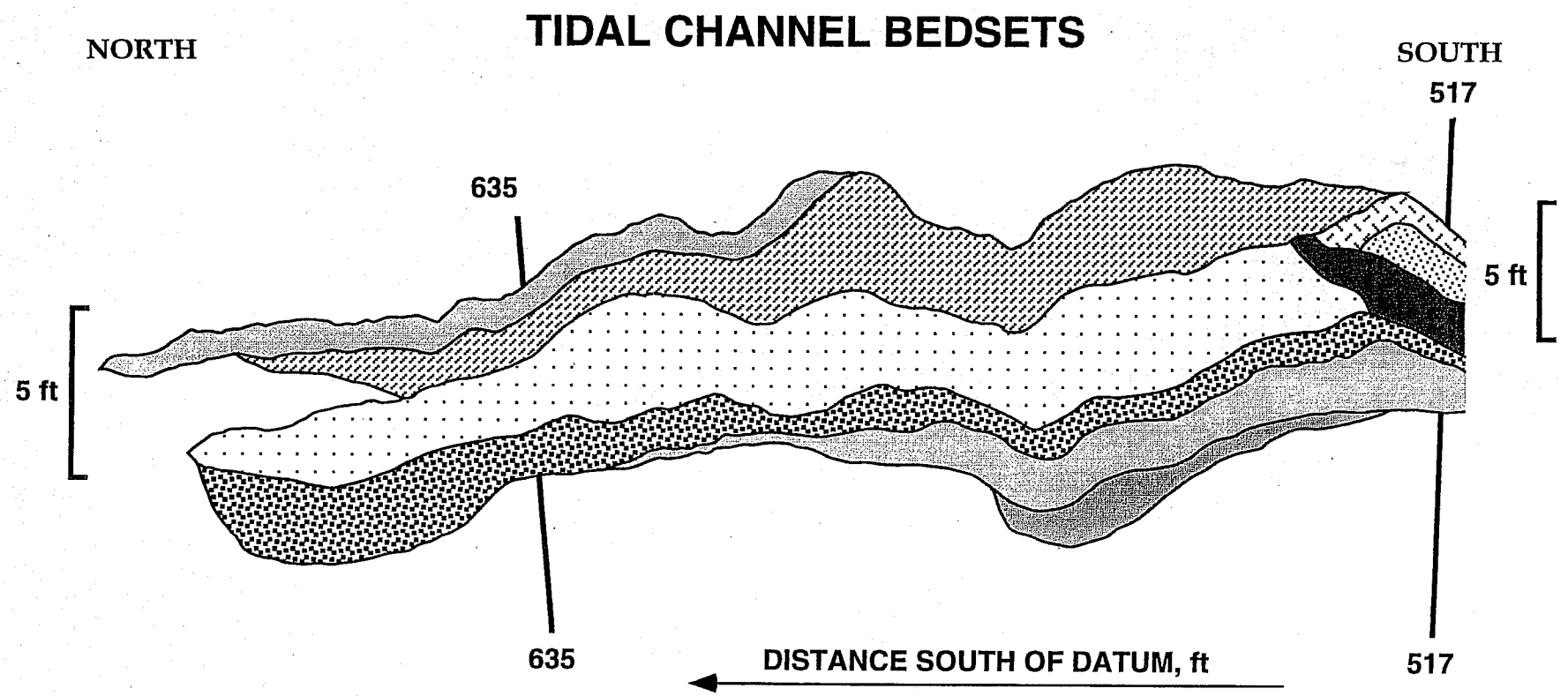

Figure 8. Distribution of laterally accreting major bedsets within the tidal channel facies. Note that fluids moving laterally through this facies would have to pass through more than one bedset boundary.

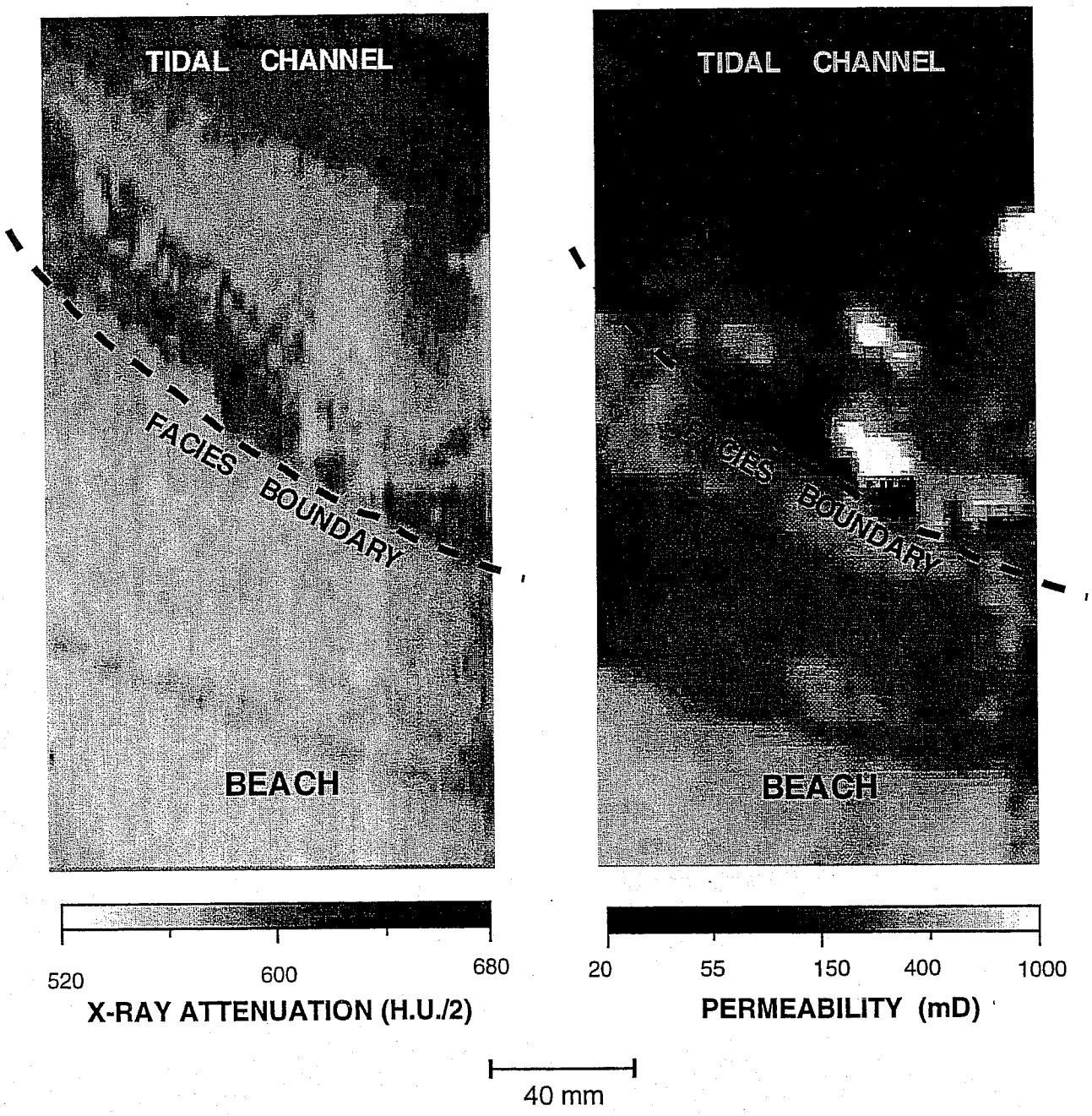

Figure 9. X-ray CT and Probe permeameter maps of a tidal channel/beach facies contact. The CT image was reconstructed from sections taken at 5 mm spacing. The probe mini-permeameter measurements were performed on a 5 mm by 5 mm grid, using a 3 mm ID tip.

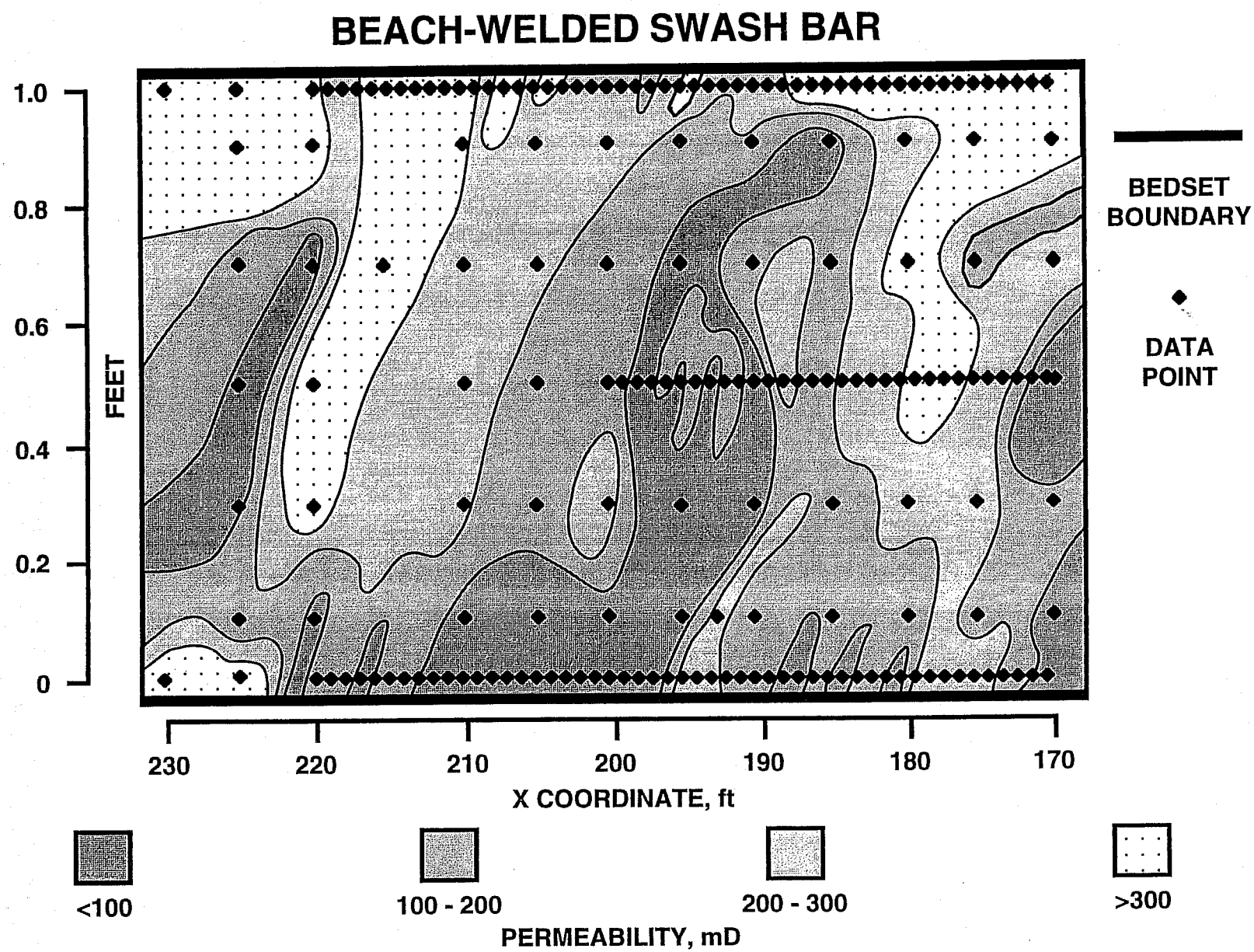

Figure 10. Map of the distribution of permeability within the tidal swash bar based on closely spaced one inch diameter outcrop plugs. Note northward dip (to the left) of permeability trend is in the same direction as the planar tabular cross bedding.

Well Test Imaging - A New Method for Determination of Boundaries From Well Test Data

Bruce A. Slevinsky, SPE, M. Sc., P. Eng.
Senior Reservoir Engineering Advisor
Petro-Canada

Acknowlegments
I would like to thank Petro-Canada for permission to publish this paper, and particularly Mike Danyluk and Duncan Robertson for their support in the development of the technique as Managers of the Technology Improvement Group. As well, I wish to thank all of my colleagues at Petro-Canada for their patience and willingness to share their well tests, geological and geophysical data, and scarce time to make the Well Test Imaging process so much better than it would be otherwise.

Abstract

A new method has been developed for analysis of well test data, which allows the direct calculation of the location of arbitrary reservoir boundaries which are detected during a well test. The method is based on elements of ray tracing and information theory, and is centred on the calculation of an instantaneous 'angle of view' of the reservoir boundaries. In the absence of other information, the relative reservoir shape and boundary distances are retrievable in the form of a Diagnostic Image. If other reservoir information, such as 3-D seismic, is available; the full shape and orientation of arbitrary (non-straight line or circular arc) boundaries can be determined in the form of a Reservoir Image. The well test imaging method can be used to greatly enhance the information available from well tests and other geological data, and provides a method to integrate data from multiple disciplines to improve reservoir characterization. This paper covers the derivation of the analytical technique of well test imaging and shows examples of application of the technique to a number of reservoirs.

Introduction

Conventional well test analysis methods determine the distance to boundaries using either a simplified technique outlined by Earlougher [(2)] or by regression on distance parameters in a mechanistic model of well test response as described by Gringarten [(3)]. The analytical technique for calculating distance for a single linear sealing fault involves the estimation of an intersection time, t_x, calculated from the intersection point of the two straight line segments of the Horner plot for the pressure buildup as illustrated in Figure 1. This intersection time is then substituted into equation 1 (from Earlougher [(2)])

$$L=0.01217(kt_x/(phi*mu*c_t))\text{^}.5 \qquad \text{eq. 1}$$

This represents approximately 42 percent of the equivalent radius of investigation at that particular

point in time,

$$Rinv=.029(kt/(phi*mu*c_t))^{.5} \qquad \text{eq. 2}$$

Multiple boundaries in the vicinity of a well can cause many different transient-test behaviours depending on the number, type, and orientation of the boundaries. Few general rules are given in the literature to resolve these differences. A simple example may show some of the difficulties:

1) two linear boundaries intersecting at right angles serve to produce three straight line segments showing slope doubling, and two intersection points on the Horner plot which can be interpreted to give the distances to the two boundaries, Figure 2,

while

2) two linear boundaries arranged parallel to each other produce a continuously increasing Horner plot characteristic of linear flow which cannot be readily interpreted to give the distances to the two boundaries using the technique described above, Figure 3.

In the computer-aided well test analysis technique based on mathematical models and regression analysis of the model parameters; the analyst selects an overall model based on near wellbore, reservoir flow character, and reservoir boundary parameters which are then 'solved' to fit the observed behaviour. The mathematical models usually involve solutions in Laplace space and inversions to real space, using multiple regression passes to converge to values which attempt to characterize the whole system of equations and effects. The mathematical background is complex, the numerical difficulty is significant, and the traditional handling of reservoir boundaries has been simplistic, involving linear bounding elements arranged as wedges or elements of a rectangle. Because the reservoir boundary effects usually occur late in time, the numerical approach above is dominated by near wellbore and reservoir character parameters, and there is usually significant uncertainty in the choice of the reservoir boundary model and the accuracy of the predicted boundary parameters. The development of well test imaging was targeted at increasing the understanding of boundary effects, removing limitations imposed by arbitrary linear boundary systems, and increasing the ease with which boundary data can be interfaced to other forms of data to increase the confidence in boundary distances and orientations.

Well Test Imaging - Theoretical Development

A) Information Theory and Boundary Type Curve Development

The development of well test imaging began with the use of a conventional well test analysis program, in its test design mode, to produce theoretical well test responses for simple boundary systems to deduce the behaviour of the boundary signal. The first case was a single linear boundary system under a variety of conditions of near wellbore, reservoir flow character, and boundary distance. The models were constructed in pairs

with and without the boundary effects to get a visual presentation of the impact of a boundary. A typical simple model with wellbore storage and skin, and a uniform homogeneous reservoir produces the log-log type curve responses of Figures 4 and 5. The boundary effects show up most clearly in the difference in the Bourdet derivative curves at the bottoms of these Figures.

Information theory indicates that we should attempt to isolate the effect of any input parameter by filtering out all of the extraneous information in a signal so that we can concentrate solely on the response to the input. In the case of the pairs of well test designs above, a simple way of removing the near wellbore and reservoir character effects was found by dividing the Bourdet derivative response of the case with boundary effects by the Bourdet derivative of the case without boundaries. This produces a very simple 'Boundary Ratio Type Curve' which has a value of 1.0 up to the point at which boundary interactions take place and a shift upward in response to boundary interactions, as shown on Figure 6, which was derived from Figures 4 and 5. When many well test designs are processed in this way it can be seen by inspection that the curves are all similar, Figure 7, and can be condensed into one curve, Figure 8, by a shift in the time scale. This implies geometric similarity for the single boundary problem with the time, t_0, being representative of the time for the boundary interaction to be perceived at the test well.

A similar set of well test designs was done for the case of two boundaries in the form of a wedge. The Boundary Ratio Type Curves for the case of a 60 degree wedge with the well on the centre-line are shown onFigure 9. The Boundary Ratio Type Curve was found to have a geometric similarity relationship similar to that seen in the single boundary case, Figure 10. For all of the wedge angle cases, the Boundary Ratio Type Curve approached an asymptotic limit value equal to,

$$\text{Wedge Boundary Ratio Limit} = 360/\text{Wedge included angle} \qquad \text{eq. 3}$$

as shown on Figure 11.

The final set of well test designs studied was the set of two parallel boundary 'channel flow' cases, shown on Figure 12. It was found again that only the short time behaviour showed differences which could be characterized by the position of the well between the two boundaries, but that all cases approached a linear, half slope on the log-log plot, limit behaviour. For a common ratio of distances to the two boundaries, a normalized type curve could be developed for each case as on Figure 13.

The strong geometric similarity behaviour of the sets of cases studied argues strongly that there is an underlying linkage in the physics of how the information about a boundary is sensed by the well test, and that this is linked to the flow and pressure transient behaviour of the reservoir. In particular, it can be concluded that the magnitude of the response seen on the Boundary Ratio Type Curve was independent of distance to the boundary, and represents a measure of the geometric properties of the boundary. The distance to the boundary appears to be related to the time scaling of the

boundary response.

B) Ray Tracing and Interpretation of Boundary Effects

A set of visualization experiments of a drawdown or buildup well test with a single boundary was conducted using a simple computer program which plotted the position of the radius of investigation as a function of time, under the assumption that the well test could be treated as a non-linear transient wave phenomenon. A composite sequence of these images is shown on Figure 14, illustrating that the effective wave position is dependent on the square root of the test time. The information about the first contact with the boundary (t=100) reaches the well at a time equal to 4 times the contact time (t=400). All of the information about the boundary, however, does not reach the test well at one time as seen on the type curves generated in the previous section. In order to determine just how all of the information reaches the well, the overall wave front was broken down into a number of rays or packets. In order for information on the boundary contact to propagate back to the test well it was necessary to assume that the boundary behaved in a manner similar to an elastic absorbtion and re-radiation rather than as a reflection, similar to the concepts used in interpreting seismic data. These subsequently re-radiated rays which pass information back to the source well, illustrated on Figure 15, have wave fronts that combine to form the overall front of Figure 14. Information is carried back to the test well along a straight line path, from the contact point to the test well, which arrive back at the test well at 4 times the contact time for each ray. Considering just the array of rays carrying information back to the test well over time as in Figures 16 and 17, it was observed that the rays passing through the test well formed an 'angle of view' of the boundary which asymptotically approached 180 degrees. Going back to equation 3 this also predicts the asymptotic Boundary Ratio Type Curve value for the single linear boundary.

If we assume that the instantaneous 'angle of view' of the boundary, AOV(t), is directly related to the Boundary Ratio Type Curve value through,

$$BRTC(t) = 360/(360-AOV(t)) \qquad \text{eq. 4}$$

it is possible to calculate a theoretical type curve for the single linear boundary case. This is accomplished by following the logic of Figure 18, which shows a ray with Rinv(t) just contacting the boundary. The value of the angle of view of the boundary is 2*theta which can be expressed through relationships with the radius of investigation with time

$$Rinv(t) = d_c*(t/t_c)^{.5} \qquad \text{eq. 5}$$

as

$$AOV(t) = 0 \quad \text{for } t<=4*t_c \qquad \text{eq. 6 a}$$

where t_c is the time to first contact with the boundary at which time $Rinv=d_c$

and therefore,

$$AOV(t) = 2*theta \quad \text{for } t>4*t_c \qquad \text{eq. 6 b}$$

$$= 2*\arccos(2*d_c/Rinv(t))$$

$$= 2*\arccos((4*t_c/t)^{\wedge}.5) \qquad \text{eq. 6c}$$

Therefore, an equation for the BRTC(t) for a single linear boundary can be expressed as,

$$BRTC(t) = 360/(360-2*\arccos((4*t_c/t)^{\wedge}.5)) \quad \text{for } t>4*t_c \qquad \text{eq. 7}$$

If we normalize this curve at $t_0=4*t_c$ then the resulting normalized type curve plot is shown on Figure 19, which can be compared with the normalized linear boundary ratio plot of Figure 8, derived from the well test design exercises which began the process. The approximate answer of equation 7 is a very close match to Figure 8, and has several desirable characteristics:

1) it is easy to evaluate
2) it has a clear physical interpretation
3) it is easily inverted

This same construction process can be used on the 60 degree wedge example and the parallel channel boundary to reconstruct approximations of those type curves as well, as shown on Figures 20, and 21.

Any arbitrary reservoir boundary system whether it is composed of straight lines or curves can be evaluated using the ray tracing methodology, to construct a Boundary Ratio Type Curve for that boundary system. Combined with any base line near wellbore and reservoir flow characteristic log-log type curve, this technique can generate an overall type curve for that reservoir and boundary system. Yeung et al [4] proposed a method to analyze the transient pressure behaviour of an arbitrarily shaped reservoir using a superposition in time approach which is much more time consuming and difficult than the method proposed above.

Inversion of a Well Test Response - Calculation of a Well Test Image

As useful as being able to construct a type curve for a given geometry may be, the bigger problem in well test analysis is the interpretation of the actual test response to determine the distance to and orientation of the boundaries observed in a well test. The simple form of equation 6 allows simple inversion; that is, for a given well test response, a picture of the boundary system can be created. The process starts by conducting a conventional analysis to produce the best possible match to the early time data to properly calibrate the near wellbore and reservoir flow characteristics. At this point we either do not match the boundary affected portion of the test or turn off the boundary effects once the best conventional match is achieved. The resulting difference between the model log-log type curve and the actual data represents the information or signal of the boundary. By dividing the actual reservoir response by the non-boundary predicted response we create the Boundary Ratio Type Curve as a function of time. As well, with most programs, the analysis method without boundaries will predict a radius of investigation for the whole test (i.e. $Rinv(t_{max})$) which will be used to calibrate distances for the calculations.

Given the Boundary Ratio Type Curve as a function of time, BRTC(t), the Angle of View of

the boundary as a function of time and radius of investigation can be determined by inverting equation 4,

$$AOV(t) = 360 - 360/BRTC(t) \qquad \text{eq. 8}$$

Given the Angle of View of the reservoir boundary system as a function of time, the distance to the reservoir boundary is determined as a function of the Radius of Investigation as a function of time. The distance to a reservoir boundary which will affect a given well test at a given time is exactly half of the radius of investigation at that point (since the information must travel back to the source well covering twice the distance)

$$Rinf(t) = Rinv(t)/2 \qquad \text{eq. 9}$$

This distance is called the Radius of Information in the terminology of this paper. Given $Rinv(t_{max})$, the Rinf(t) is calculated at each point from,

$$Rinf(t) = 0.5*Rinv(t_{max})*(t/t_{max})\text{^}.5 \qquad \text{eq. 10}$$

With Rinf(t) and the AOV(t), a picture of the reservoir surrounding a well can be drawn in the following manner. Beginning at the last point where the BRTC(t) is less than or equal to 1.0 ($t=t_0$), draw a circular arc at a radius equal to

$$Rinf(t_0)=0.5*Rinv(t_{max})*(t_0/t_{max})\text{^}.5 \qquad \text{eq. 11}$$

This represents the maximum radius of reservoir behaviour without boundary influences. At each point $t>t_0$, draw an arc of radius Rinf(t) from equation 10, through an angle of 360-AOV(t) showing the non-boundary containing reservoir as a function of time. Continue to draw these arcs until $t=t_{max}$ is reached. The resulting diagram, similar to a sonar display, will be an image or realization of the reservoir and, by difference, the boundary system. A Well Test Image drawn at this stage is called a Diagnostic Image, in that it can give you a general reservoir shape and distance to a boundary, but the picture may not be realistic or recognizable in terms of geological features which you might be able to recognize in other data. In order to make this picture more understandable in terms of our usual visualization processes and to help distinguish more complex systems when more than one boundary may be present, three standardized interpretation models have been devised:

a) Angular Model. Draw a tangent line to the circle at $Rinf(t_0)$, and draw all remaining arcs with one end placed on the tangent line.

b) Balanced Model. Draw a radial line from the centre of the circle of radius $Rinf(t_0)$ and centre all of the remaining arcs on this line.

c) Channel Model. Draw a tangent line to the circle at $Rinf(t_0)$ and a radial line perpendicular to it through the test well. Begin to draw arcs centred on the perpendicular line until the remaining arc ends fail to cross or contact the tangent line. At this point split the arc in half and place the two original ends on

the initial tangent line on opposite sides of the well and predict the position of the other boundary by tracing out the position of the newly cut arc ends.

The model descriptions above can be expressed mathematically, calculated, and displayed directly from the well test analysis. In many cases, all three models may produce results which are valid and need to be tested against other geological information. This merely illustrates that the well test data (and the information returned by a well test alone) may be insufficient to provide a unique answer to the question of boundary configuration.

Well Test Imaging - Examples

There are few examples in the literature with enough data to allow comparison of conventional and well test imaging approaches to the prediction of reservoir boundaries. One exception is the paper by Clark [1] on the Oseberg reservoir which shows the application of conventional techniques to predict two boundaries at right angles around well 30/6-13, Figure 22. Application of well test imaging to the raw data from the paper produces the log-log type curve of Figure 23, the BRTC(t) of Figure 24, and the well test image (Diagnostic Image) of Figure 25. The key difference is that the boundaries are found to be neither at right angles nor precisely linear and the distances to the boundaries are slightly different than those predicted conventionally. These differences could be significant in terms of interpretation of the alignment of the boundaries with known seismic or geological anomalies and illustrate how our dependence on fixed models of reservoir boundaries could alter our perception of the boundary system.

Another example of the application of the approach is taken from a Petro-Canada operated well in the Fireweed pool in northeastern British Colombia. This pool is a fractured and dolomitized carbonate reservoir containing gas, where reservoir quality and continuity are an issue. The well test log-log type curve for an initial well in a new area of the pool is shown on Figure 26. The Boundary Ratio type curve of Figure 27 shows some significant variations which were difficult to fit with conventional techniques (predicting two boundaries at right angles, but leaving a high residual error in the match). The Diagnostic Image of the test, Figure 28, shows a system with several 'steps' in the boundary system. We believe that these variations depict the underlying fracturing fabric of the reservoir and a conjugate set of lineaments which both create the reservoir and simultaneously set up internal reservoir boundaries. These considerations have influenced our application of horizontal well technology to develop the field using our knowledge of local tectonic history to orient the well test images in the preferred fracturing directions and to orient the horizontal wells along axes which allow the maximum number of lineaments to be contacted.

Well Test Image Enhancement - Integration of Geological and Geophysical Data

The problem of well test image solution uniqueness can be addressed in many ways, including:

a) fitting together of well test images of neighbouring wells which may image parts of the same boundary system, much like solving a jig-saw puzzle.

b) observing a well test at offsetting wells and interpreting the interference data to determine boundary orientations. The ray tracing methodology proposed above can be used to interpret the offset well response.

c) incorporating geological or geophysical information from other sources to fit against the well test images, to provide information on orientation of lineaments or depositional directions.

The experience of the last few years with well test imaging indicates that the integration with geological and geophysical data offers the most potential for significant improvement in the quality of the images. As well, it can lead to an improvement in the understanding of the characteristics of the boundaries in terms of their expression in the other data types.

Geological maps and 3-D seismic data represent excellent sources of information which can be integrated with well test imaging. As an example, an attribute of the 3-D seismic data (amplitude of a reflector, depth of a surface, slope of a surface), is contoured in the form of a 2-D map. The well location is marked on the map, and the well test image is superimposed at the same scale. As a first approximation, the whole image can be rotated and positioned so that the circular boundary of the radial flow reservoir region just contacts a likely lineament. This represents identification of the most likely boundary forming element in the region surrounding the well. The image is then rotated until the boundary image tangent to the radial region parallels the mapped lineament. Then the individual arc segments can be rotated to exactly contact the mapped boundary, because in most instances it is not perfectly linear. In many instances several mapped lineaments or potential boundary elements can be made to fit simultaneously, adding to the potential that a more unique match has been determined.

As an example of the application of the process, consider the well test shown on Figure 29, which has been modeled as well as possible to match the early time data. The difference between the match curve and the actual well test was used to create the Diagnostic Image shown on Figure 30. The angular model indicates a generally open-ended rectangular model with three no-flow boundaries. The slope of a surface near the level of this test was derived from 3-D seismic and is shown of Figure 31. Combining the Diagnostic Image and the 2-D map of the surface slope produced the Reservoir Image shown on Figure 32. This image very clearly identified the boundary forming critical slope of .12 to .20 m/m which is characteristic of fault boundaries in this field, and fit two prominent lineaments simultaneously. While the perception of the general character of the well test boundaries did not change, the additional work did allow the precise orientation of the open end of the system to be deduced and aided in the placement of a potential waterflood

support well. This same image can then be superimposed on other data representations; in the case of Figure 33 on the structure top of the zone derived from seismic, and presented in a 3-D mesh perspective to allow visualization of the effective reservoir around the well.

Other Uses of Well Test Images

The digital nature of the well test imaging process, allows a number of calculations to be carried out using the Rinf(t) and AOV(t) data generated by the analysis that would otherwise not be possible:

1) it is possible to integrate the area and volume swept by the test to show the area over which information was generated. This leads to a better descriptor of the volume affected by a well test than the Radius of Investigation. This can be used to develop an estimate of 'proved' reserves due to the test.

2) by constructing a line joining nearest neighbour ends of the concentric arcs of the well test a picture of the boundary alone can be generated.

3) an automated procedure for generation of simulation model grids with realistic boundaries can be set up since the region of reservoir around the well is known.

4) When multiple tests of several zones are conducted in a single well which shows fault boundaries, the images of each test can be stacked to provide a 3-D representation of the fault surfaces, as shown on Figure 34.

All of these applications are new to the field of well test analysis, and allow significant input to be provided to 3-D seismic and geological interpretations. Well test imaging provides a natural integrating mechanism for well test data which spans the gamut of reservoir characterization from 3-D seismic to reservoir simulation.

Conclusions

1) A new type curve, the Boundary Ratio Type Curve, is proposed as a way to characterize boundary influences and to measure the boundary signal in a well test.

2) Based on observation of the Boundary Ratio Type Curve characteristics, the magnitude of the response is concluded to be due to the geometric shape of the boundary which is characterized by the 'Angle of View' (AOV(t)) of the boundary; while the distances to the boundary contacts are represented by the time scaling of the response through the 'Radius of Information' (Rinf(t)).

3) The accuracy of the boundary calculations is limited only by the accuracy with which the underlying time and pressure measurements are made, and with modern gauges this can be down to the order of meters.

4) The well test images derived directly from AOV(t) and Rinf(t) with perhaps an analytical

model as a guide, Diagnostic Images, are non-unique.

5) Integration of the Well Test Image with geological or geophysical information can lead to enhanced images (Reservoir Images) which can resolve the uniqueness problem, and increase the quality of the interpretation overall.

6) Well Test Imaging can help to extract more information from well test data, enabling better quality interpretations and enhanced reservoir characterization that are unconstrained by simplistic straight-line boundary models.

7) Well Test Imaging provides a key element in the integration of well test data with geological and geophysical analyses, and reservoir engineering simulation in the reservoir characterization process.

Nomenclature

AOV	= angle of view
arccos	= inverse cosine ($\cos^{-1}$)
BRTC	= boundary ratio type curve value
ct	= total system compressibility [1/psi or 1/kPa]
k	= permeability [md]
L	= distance to a boundary
mu	= oil viscosity [cp or mPa.s]
phi	= porosity [frac]
Rinf	= radius of information
Rinv	= radius of investigation
t	= time
t_c	= time for radius of investigation to first contact with a boundary
t_0	= time for first boundary interaction to be sensed or measured at the test well
t_x	= intersection time, calculated from intersection of straight-line segments on Horner plot.
t_{max}	= maximum test time (shut-in or drawdown)
theta	= angle between the shortest distance between a well and a surface and the current ray contact with the surface

References Cited

1) Clark , D. G., Van Golf-Racht, Pressure-Derivative Approach to Transient Test Analysis: A High-Permeability North Sea Reservoir Example, SPE 12959, 1985
2) Earlougher, R. C. Jr., Advances in Well Test Analysis, SPE Monograph Vol. 5, pp. 124-125, 1977
3) Gringarten, A. C., Computer-Aided Well Test Analysis, SPE 14099, 1986
4) Yeung, Kacheong and Chakrabarty, Chayan; An Algorithm for Transient Pressure Analysis in Arbitrarily Shaped Reservoirs, Computers and Geosciences, Vol. 19, No. 3, pp 391-397, 1993

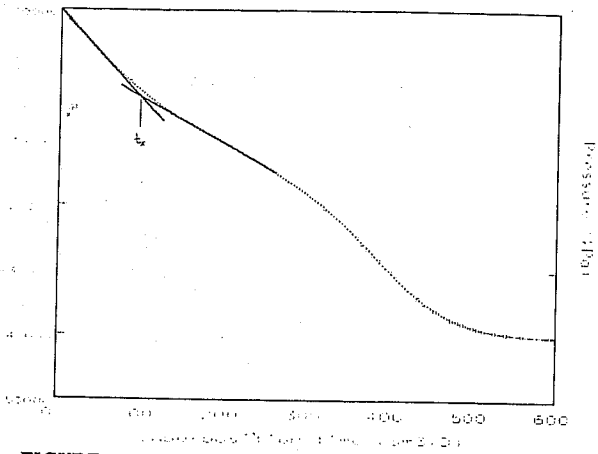

FIGURE 1: Intersection of Horner curve straight-line segments

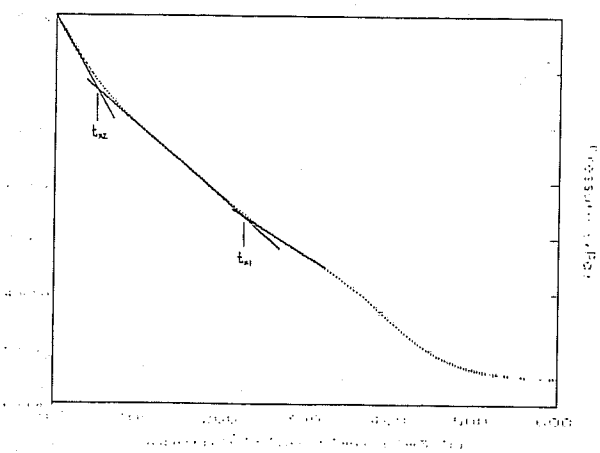

FIGURE 2: Horner curve for 2 boundaries at right angles

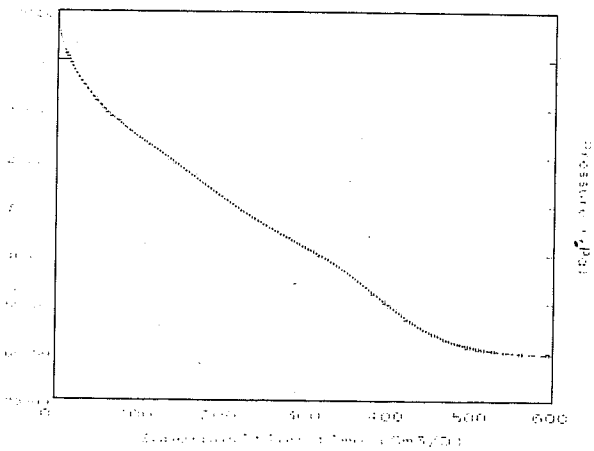

FIGURE 3: Horner curve for 2 parallel boundaries

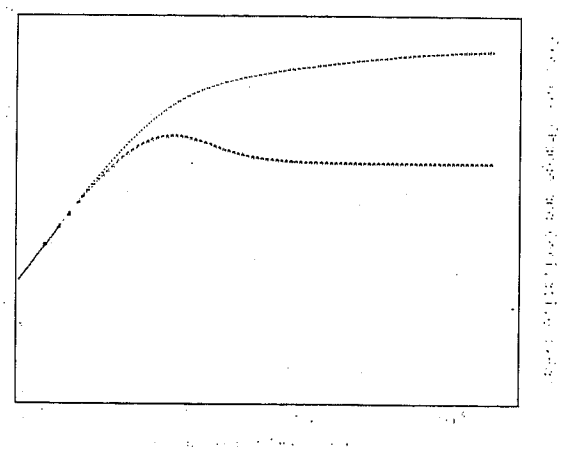

FIGURE 4: Log-log type curve for homogeneous reservoir

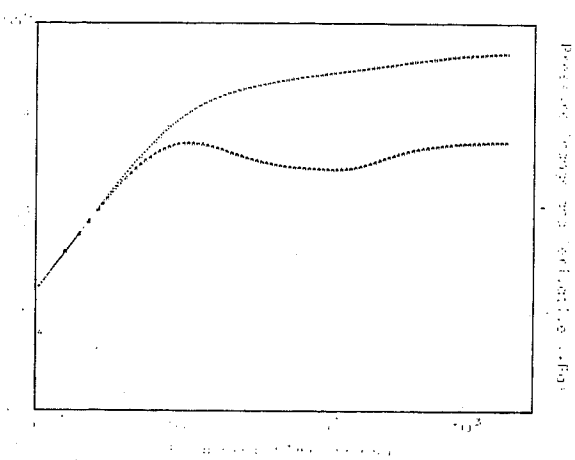

FIGURE 5: Log-log type curve for homogeneous reservoir with a single linear boundary

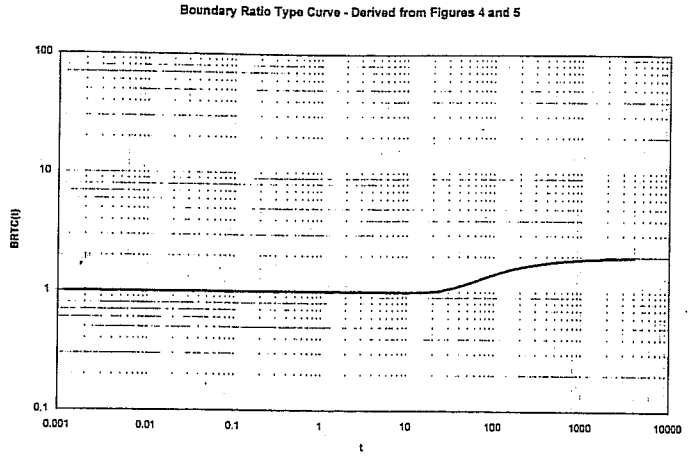

FIGURE 6: Boundary Ratio Type Curve for a single linear boundary

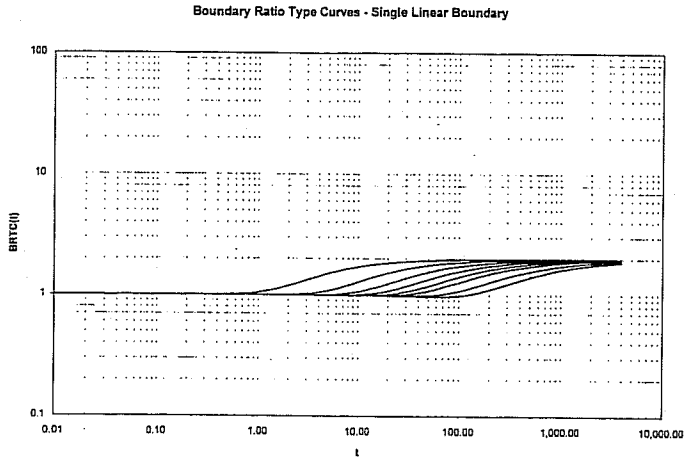

FIGURE 7: Boundary Ratio Type Curves for single linear boundary cases

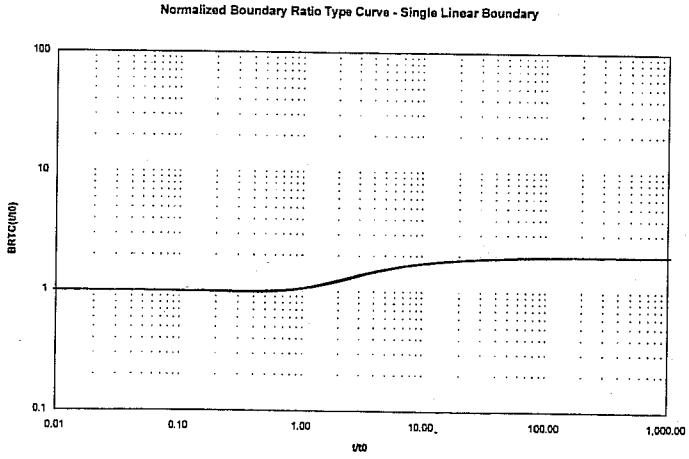

FIGURE 8: Normalized Boundary Ratio Type Curve - Single Linear Boundary

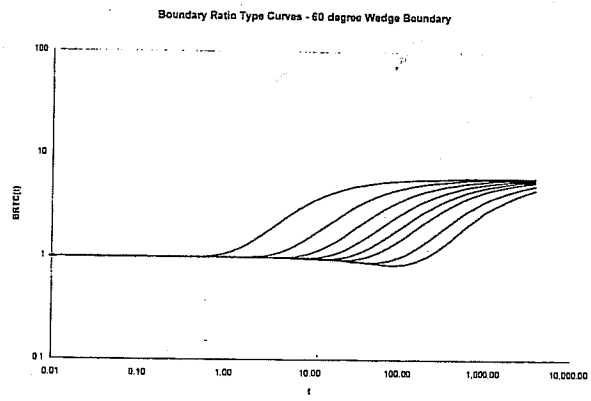

FIGURE 9: Boundary Ratio Type Curves - 60 degree Wedge Boundary

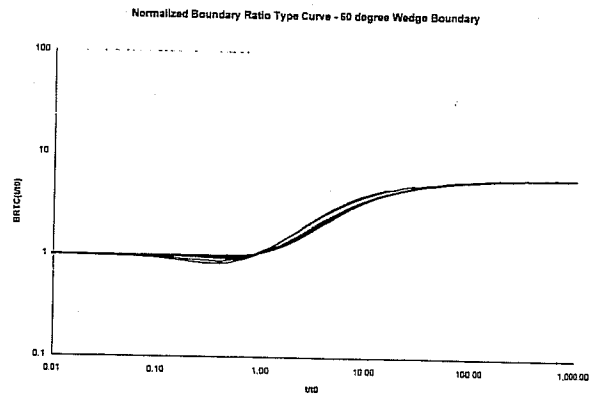

FIGURE 10: Normalized Boundary Ratio Type Curve - 60 degree Wedge Boundary

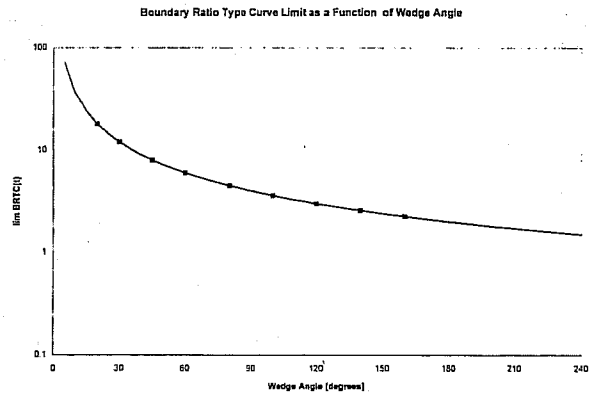

FIGURE 11: Boundary Ratio Type Curve Limit as a Function of Wedge Angle

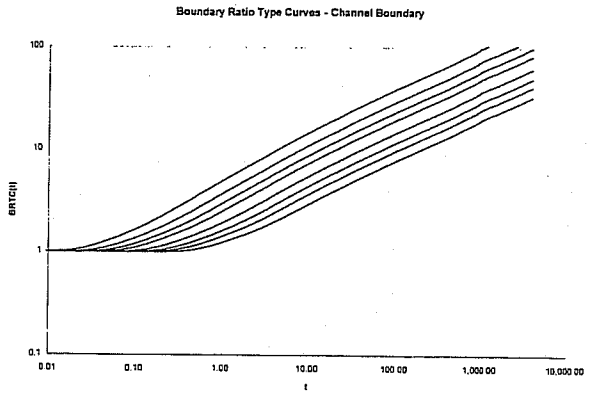

FIGURE 12: Boundary Ratio Type Curves - 2:1 Parallel Boundaries

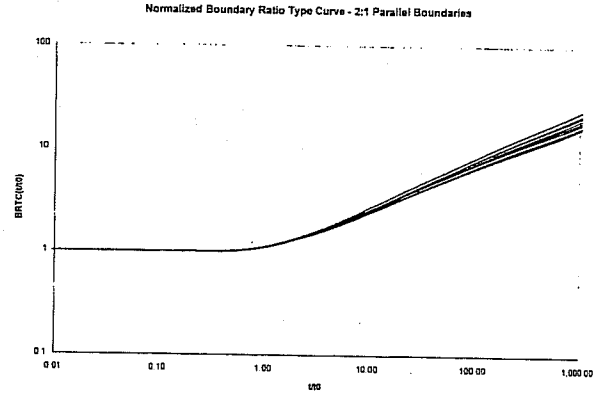

FIGURE 13: Normalized Boundary Ratio Type Curve - 2:1 Parallel Boundaries

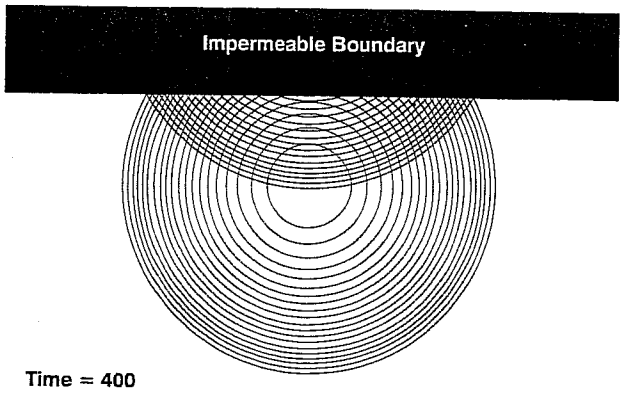

FIGURE 14: Composite Images of Rinv as a Function of Time

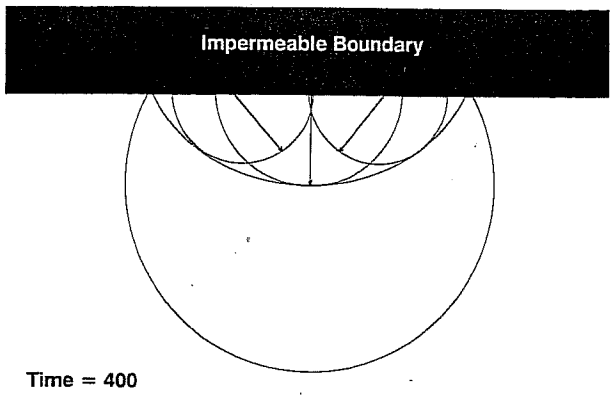

FIGURE 15: Assumed Boundary Interaction Wave Fronts

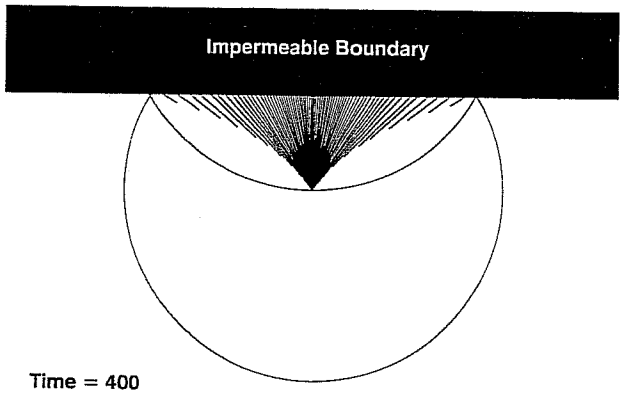

FIGURE 16: Rays Showing Boundary Interactions at Time t_0

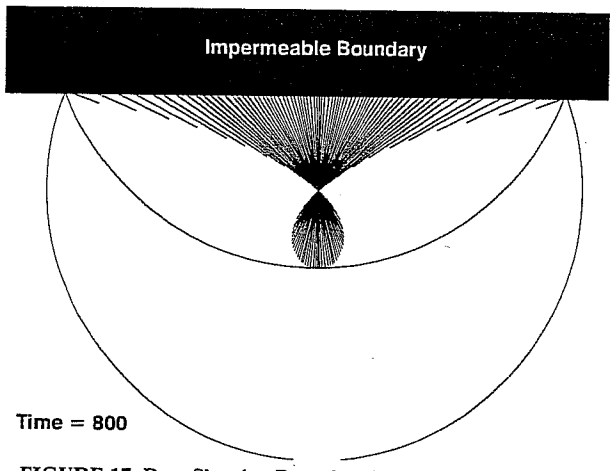

FIGURE 17: Rays Showing Boundary Interactions at Time $t>t_0$

Well Test Imaging - Elemental Boundary Contact

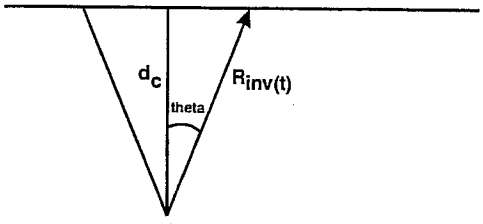

theta = arc cos $(d_c/R_{inv(t)})$

FIGURE 18: Diagram of Ray Interaction With Boundary at Time $t>t_c$

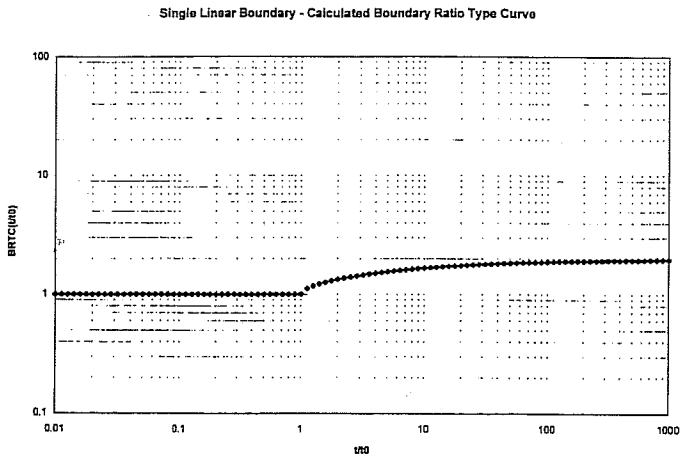

FIGURE 19: Calculated Normalized Boundary Ratio Type Curve for Single Linear Boundary

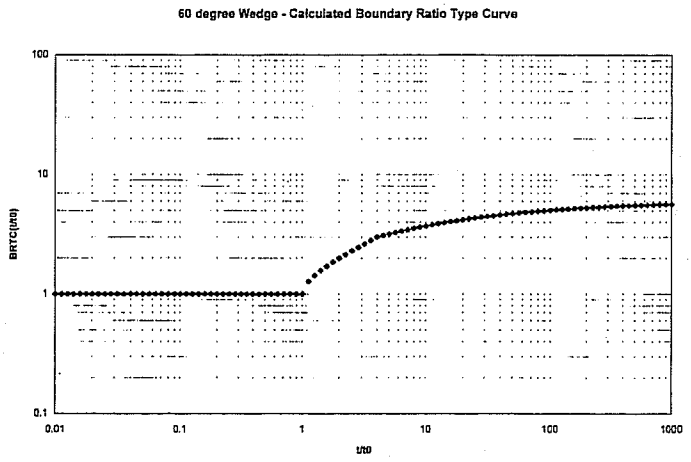

FIGURE 20: Calculated Normalized Boundary Ratio Type Curve for 60 degree Wedge Boundary

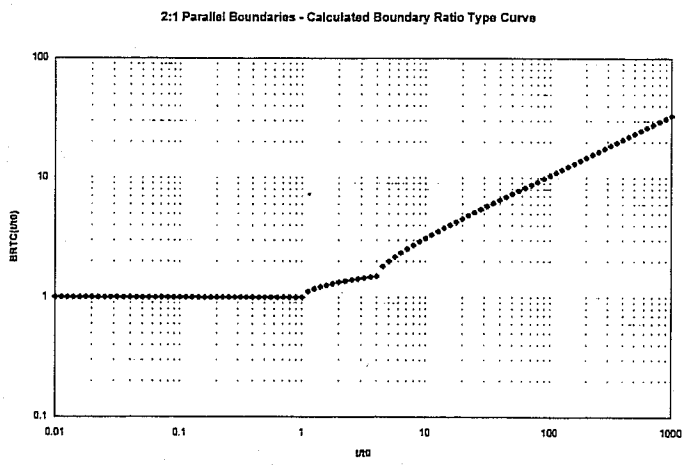

FIGURE 21: Calculated Normalized Boundary Ratio Type Curve for 2:1 Parallel Boundaries

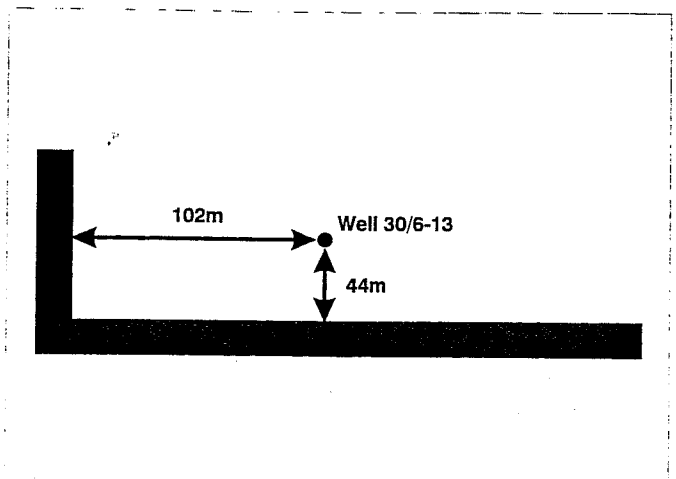

FIGURE 22: Conventional Boundary Prediction - Oseberg 30/6-13 after Clark et al

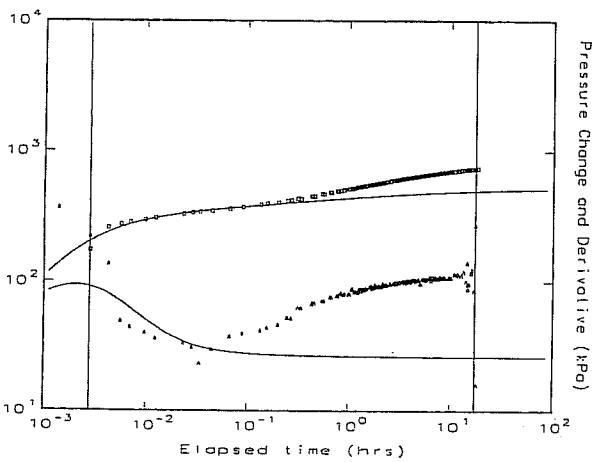

FIGURE 23: Oseberg 30/6-13 - Log-log Type Curve of Test B after Clark et al

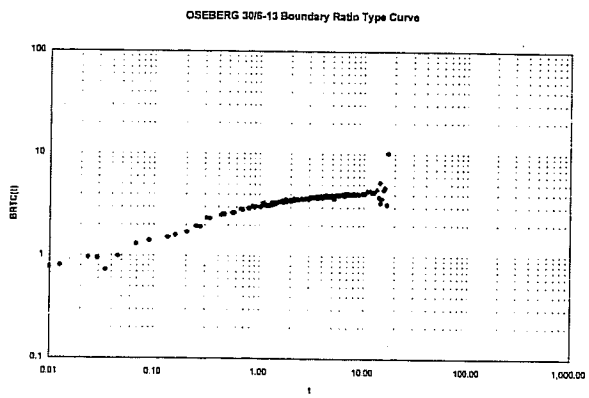

FIGURE 24: Oseberg 30/6-13 - Boundary Ratio Type Curve

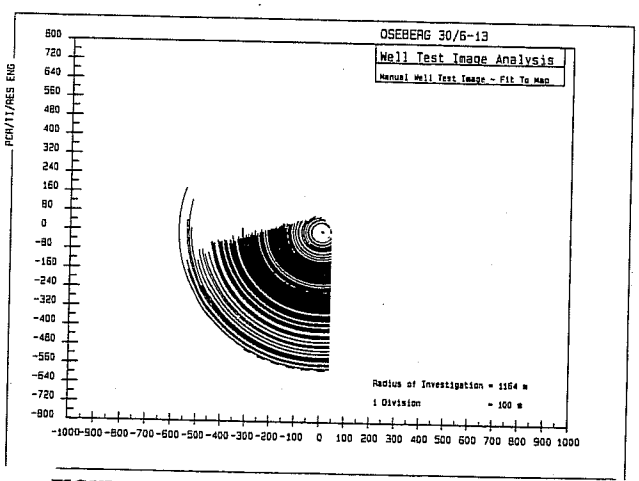

FIGURE 25: Oseberg 30/6-13 - Diagnostic Well Test Image

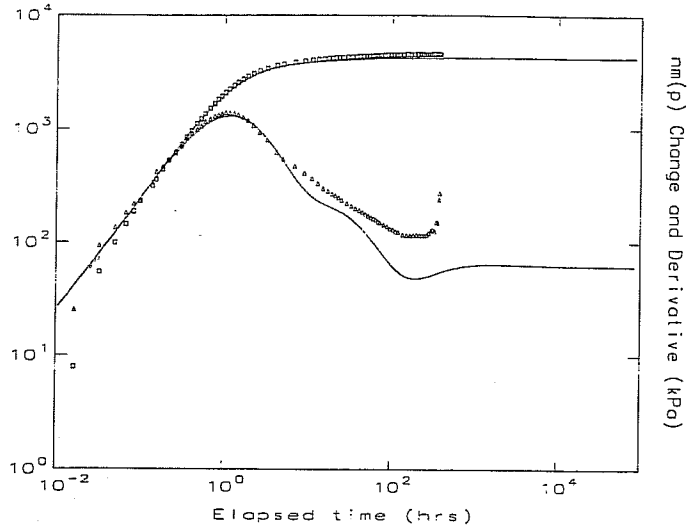

FIGURE 26: Fireweed b-6-A - Log-log Type Curve

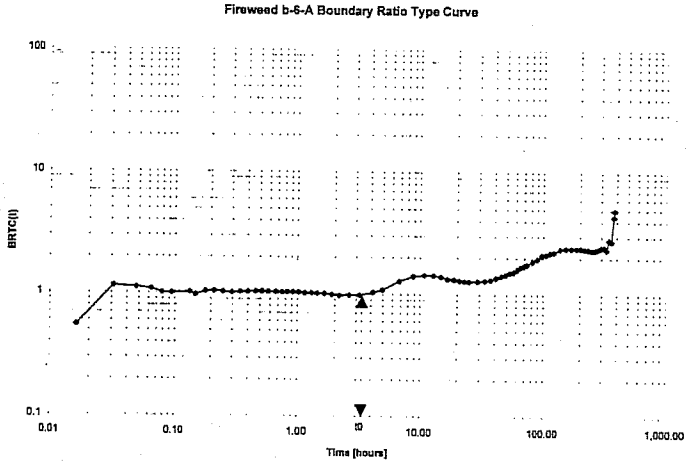

FIGURE 27: Fireweed b-6-A - Boundary Ratio Type Curve

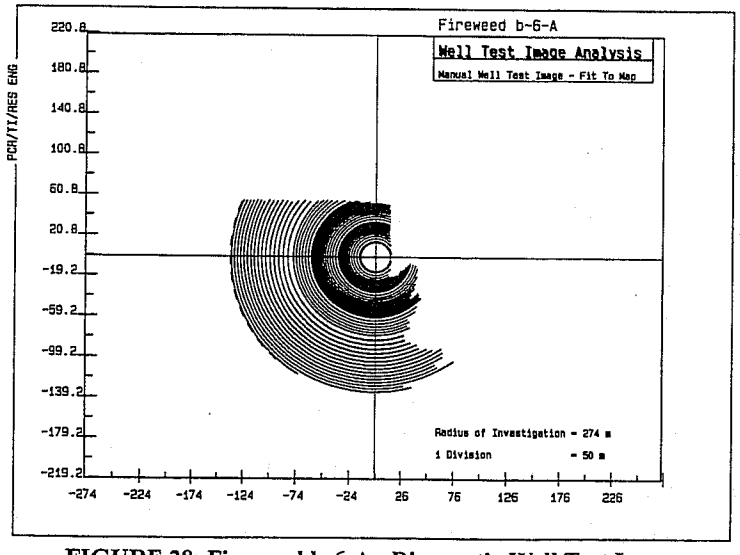

FIGURE 28: Fireweed b-6-A - Diagnostic Well Test Image

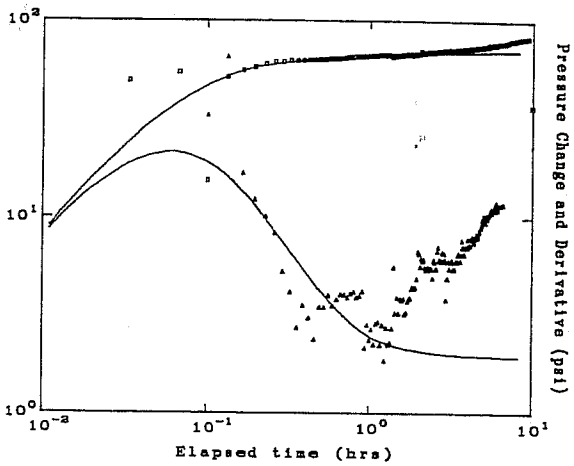

FIGURE 29: Example Well - Log-log Type Curve

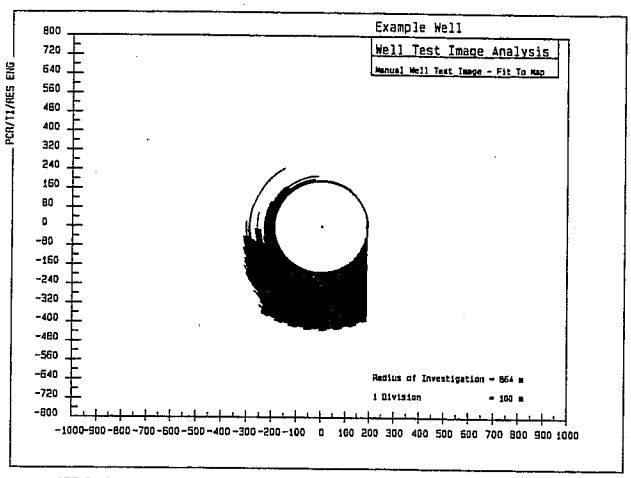

FIGURE 30: Example Well - Diagnostic Well Test Image

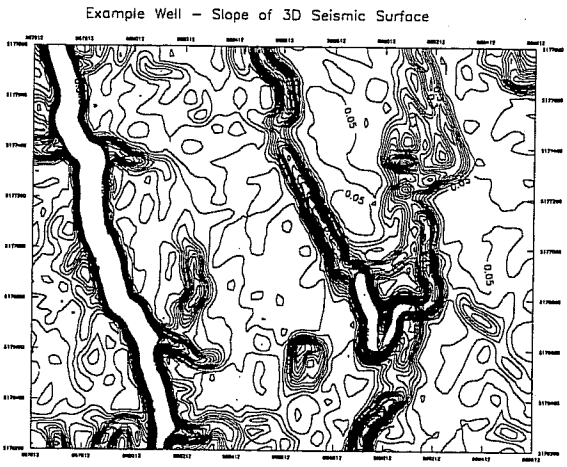

FIGURE 31: Example Well - First Derivative of 3-D Seismic Structure

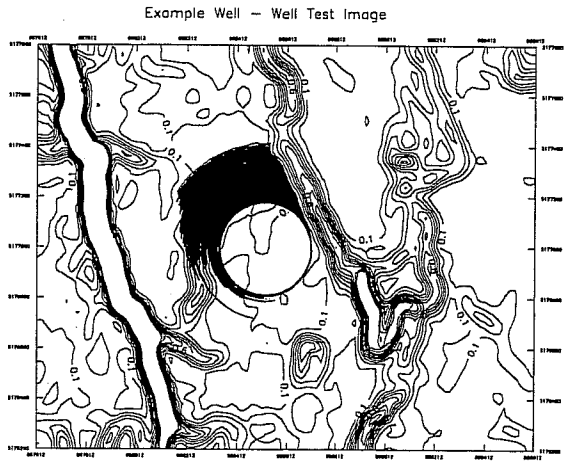

FIGURE 32: Example Well - Reservoir Image

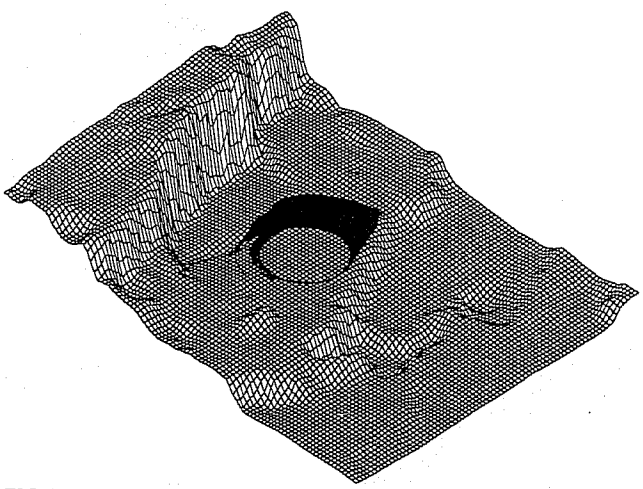

FIGURE 33: Example Well - Well Test Image Superimposed on 3-D Seismic Structure

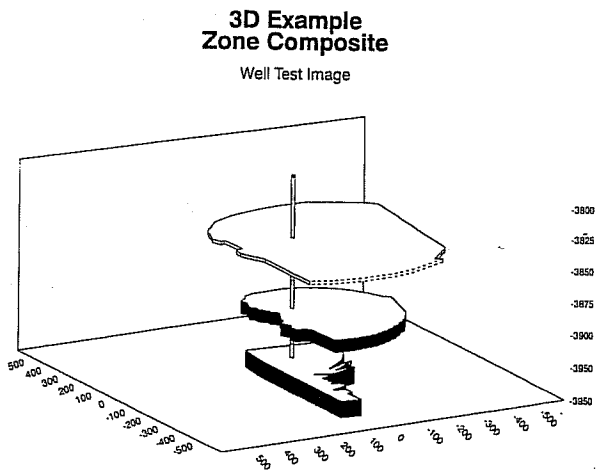

FIGURE 34: Example Well - 3-D Representation of Multiple Tests

An Efficient Permeability Scaling-up Technique Applied to the Discretized Flow Equations

Denise Urgelli
Yu Ding

Institut Français du Pétrole
Rueil Malmaison, France

Abstract

Grid-block permeability scaling-up for numerical reservoir simulations has been discussed for a long time in the literature. It is now recognized that a full permeability tensor is needed to get an accurate reservoir description at large scale. However, two major difficulties are encountered: 1) grid-block permeability cannot be properly defined because it depends on boundary conditions; 2) discretization of flow equations with a full permeability tensor is not straightforward and little work has been done on this subject.

In this paper, we propose a new method, which allows us to get around both difficulties. As the two major problems are closely related, a global approach will preserve the accuracy. So, in the proposed method, the permeability up-scaling technique is integrated in the discretized numerical scheme for flow simulation. The permeability is scaled-up via the transmissibility term, in accordance with the fluid flow calculation in the numerical scheme. A finite-volume scheme is particularly studied, and the transmissibility scaling-up technique for this scheme is presented.

Some numerical examples are tested for flow simulation. This new method is compared with some published numerical schemes for full permeability tensor discretization where the full permeability tensor is scaled-up through various techniques. Comparing the results with fine grid simulations shows that the new method is more accurate and more efficient.

I. Introduction

Reservoir heterogeneity can be described using geostatistical models. But these models generate the heterogeneity on million fine grid blocks, which leads to prohibitive computational costs for reservoir simulations. In order to reduce the number of grid blocks, averaging techniques are needed to scale-up the fine scale permeabilities to the larger scales appropriate for flow simulations and engineering calculations.

Generally, when the principal flow direction is not parallel to the grid-block axes, the effective permeability must be represented as a full tensor to capture the flow properties of the system. But this scaling-up procedure leads to two difficulties: 1) grid-block permeability cannot be properly defined because it depends on boundary conditions; 2) discretization of flow equations with a full permeability tensor is not straightforward. One of the solution is using a global approach to improve the accuracy.

Nowadays, more and more authors recommend the use of internodal permeabilities calculated at the center of the interface and not at the center of block. This calculation is equivalent to the calculation of transmissibilities, once the numerical scheme is fixed. Scaling-up of the transmissibility is more accurate than scaling-up of the permeability because the transmissibility is calculated directly with the fine scale permeability. Furthermore, reservoir simulators are incorporating as input the transmissibilities from each block to each of its neighbours.

The purpose of this paper is to present a new procedure for computing the equivalent transmissibility in the discretized flow equations. An application of this technique to a finite-volume type numerical scheme is detailed. In Section II, we give a non exhaustive review of scaling-up of full permeability tensor and discuss the different methods for the computation of transmissibilities. Then we present a new procedure to scale-up the transmissibility for a finite-volume scheme in Section III. Finally, we compare the results of the transmissibility scaling-up and the permeability scaling-up by two examples.

II. Review of scaling-up technique for single phase flow

II.1 Permeability scaling-up

The determination of the effective permeability in grid blocks has been discussed for a long time in the literature (*Warren and Price,* 1961). It is now recognized that a full block permeability tensor (*Bamberger*, 1977; *Durlofsky*, 1991; *Gautier and Noetinger*, 1994; *Guerillot et al.*, 1989; *Guerillot*, 1988; *Pickup and Sorbie*, 1994; *Samier*, 1990; *Wang et al.*) is needed to get an accurate reservoir description. In this section, several methods currently used are reviewed, and the advantages and disadvantages of these methods are analyzed.

Bamberger (1977) proposed to define the equivalent block permeability using an energy criterion. The equivalent permeability is determined using a bilinear form of the variational formula associated to the elliptic operator: $A = -div[k\nabla]$ and the bilinear form associated to the elliptic operator: $\tilde{A} = -div\left[K_{eq}\nabla\right]$. This method is based on the fact that the work realized by the viscous force in the heterogeneous media and in the equivalent homogeneous media must be equal. The energy criterion presents an immediate physical sense. This method is also studied by *Njifenjou* (1993, 1994).

conditions (*Guerillot,* 1988, 1989). A pressure gradient is imposed in the flow direction and a linear pressure in the two other opposite faces. This method allows to construct a non-symmetrical permeability tensor. This type of condition is equivalent to putting the block in a uniform large scale flow. This method takes into account the cross flow term, but it may lead to overestimating the grid-block permeability in some cases (*Galli et al.,* 1996).

The most successful approach to the computation of equivalent permeability tensor consists of using a periodic boundary condition (*Durlofsky* 1991). The permeability tensor is determined using a pressure gradient in the x-direction to obtain K_{eq}^{xx} and K_{eq}^{xy} and a pressure gradient in the y-direction to obtain K_{eq}^{yx} and K_{eq}^{yy}. This method is exact for infinitely repeated permeability structures. Periodic boundary conditions were also adopted by *Pickup and Sorbie* (1994) for their studies.

The periodic boundary condition was also applied by *Gautier and Noetinger* (1994) to the renormalization scaling-up technique (tensorial renormalization). The renormalization method was introduced by *King* (1989). The scaled-up permeability is calculated by a series of successive aggregations. *King* computes the permeability of an elementary cell of four meshes (in 2-D) with a finite difference approximation and with standard no flow boundary conditions. This method can be improved by the simplified renormalization where the general idea is to group the cells only two by two and to calculate the permeability of the cell pairs by applying the harmonic mean if the cells are in series, or the arithmetic mean if the cells are in parallel (*Le Loc'h,* 1987; *Kruel Romeu,* 1994). But the effective permeability is diagonal. If the non-diagonal terms are necessary, it is important to use the tensorial renormalization.

II. 2. Transmissibility scaling-up

The scaled-up block permeability will be integrated in the transmissibility terms in a numerical scheme for flow simulation on coarse grid blocks. However, it is difficult to determine accurately the transmissibility from the block permeability. Usually, the harmonic average of the block permeability is used for the transmissibility calculation (*Kruel Romeu and Noetinger,* 1995), but using the harmonic average might cause a loss of precision for 2-D problem. So, several authors proposed to directly scale-up the transmissibility from the fine grid heterogeneity (*White and Horne* , 1987; *Palagi*, 1992, 1993; *Kruel Romeu and Noetinger,* 1995; *Peaceman*, 1996).

White and Horne (1987) seem to be the first authors who considered the scaling-up of transmissibilities between grid blocks rather than the equivalent permeabilities of a grid block. They scaled-up the transmissibility on a global domain, which included all the fine grid blocks. Several boundary conditions are imposed on the whole domain to evaluate the transmissibility tensor between the connected blocks. The well conditions are particularly considered as one of the boundary conditions. Then the pressures and fluxes from fine scale simulations were

averaged and summed to obtain pressures and fluxes on a coarse scale. Using this pressures and fluxes on a coarse scale and the least square method, they determined macro transmissibilities. As the whole simulation domain is considered with different boundary conditions, the linear system will be solved several times on fine grid scale with all grid blocks, which might be very expensive in terms of computing time.

Palagi (1992) and *Palagi et al.* (1993) presented a scaling-up procedure for the permeability at the interface of Voronoi grid blocks. They used the power law average to calculate the homogenized permeability. The optimum value for the power law coefficient ω obtained by the minimum between the fine grid results and coarse grid results for various value of ω.

Kruel Romeu and Noetinger (1995) presented a numerical method with impermeable boundary conditions on rectangular grid blocks. The impermeable conditions consist of imposing a pressure drop between two opposite faces and no flow boundary on the remaining two faces. The *Kruel Romeu and Noetinger*'s method is equivalent to the calculation of the permeability in a block placed between the two blocks where the transmissibility are calculated.

More recently, *Peaceman* (1996) proposed a transmissibility scaling-up method on corner point geometry. For each coarse blocks, six half block transmissibilities are scaled-up. In a first step, *Peaceman* represents each half block as a rectangular block. To calculate the transmissibility on this rectangular block, he proposed a direct method which consist to use the impermeable boundary conditions and to calculate the flow through the block by solving sets of difference equations for the pressure. Then, he compares this direct method with the renormalization. He found that the renormalization is less accurate and less easy to implement than the direct method.

It is clear that using transmissibility scaling-up can give more accurate results than using permeability scaling-up. However, the *White and Horne*'s method needs to consider a global domain, which is CPU consuming. The other methods, which calculate locally the transmissibility, are limited to finite-difference type numerical scheme and do not fully incorporate the full tensor property. In this paper, we will present a transmissibility scaling-up technique related only to the local grid block for a finite-volume type method with a full tensor discretization.

III. Scaling-up of Transmissibility for a Finite-Volume Scheme

III.1 Finite-Volume Scheme

Consider a two-phase flow problem in 2-D:

$$\frac{\partial}{\partial t}\left(\frac{\Phi S_l}{B_l}\right) = \nabla(\lambda_l k \nabla p) - Q_l$$

where $l = w$ or o indicates the phase, λ is the mobility, and k is a full permeability tensor given by $k = \begin{pmatrix} k^{xx} & k^{xy} \\ k^{yx} & k^{yy} \end{pmatrix}$.

One of the difficulty for the numerical method is the discretization of the elliptic operator $\nabla(\lambda k \nabla p)$ with a full permeability tensor. We present a finite-volume type method for the discretization of this operator. Integrating on a considered grid block (i,j) and applying the Gauss divergence theorem (Figure 1), we have:

$$\int_{\Omega} \nabla(\lambda k \nabla p) d\Omega = -\sum_{m=1}^{4} \int_{\Gamma_m} \lambda k \nabla \vec{p}.\vec{n}.d\gamma$$

Without loss of generality, we will study the fluid flow calculation through the interface Γ_1:

$$F_1 = \int_{\Gamma_1} \lambda k \nabla \vec{p}.\vec{n}.d\gamma = \lambda_{i+1/2,j} \int_{Y_1}^{Y_2} (k^{xx} \frac{\partial p}{\partial x} + k^{xy} \frac{\partial p}{\partial y}) dy$$
$$= \lambda_{i+1/2,j}(F_{1a} + F_{1b})$$

where $F_{1a} = \int_{Y_1}^{Y_2} k^{xx} \frac{\partial p}{\partial x} dy$ represents the fluid flow through the interface Γ_1 by a force in x-direction and $F_{1b} = \int_{Y_1}^{Y_2} k^{xy} \frac{\partial p}{\partial y} dy$ represents the fluid flow through this interface by a force in y-direction. The last one is also called the cross flow for an uniform grid that $\Delta x = Cte$ and $\Delta y = Cte$. These two terms can be approximated by:

$$F_{1a} = \frac{\Delta y}{\Delta x} k^{xx}_{i+1/2,j}(p_{i+1,j} - p_{i,j})$$

and

$$F_{1b} = \frac{1}{4} k^{xy}_{i+1/2,j}(p_{i,j+1} + p_{i+1,j+1} - p_{i,j-1} - p_{i+1,j-1})$$

Finally, the fluid flow through the interface Γ_1 is calculated by:

$$F_1 = \lambda_{i+1/2,j}(T^{xx}_{i+1/2,j}(p_{i+1,j} - p_{i,j}) + \tfrac{1}{4} T^{xy}_{i+1/2,j}(p_{i,j+1} + p_{i+1,j+1} - p_{i,j-1} - p_{i+1,j-1}))$$

From this discretization, we observe that $T^{xx}_{i+1/2,j} = \frac{\Delta y}{\Delta x} k^{xx}_{i+1/2,j}$ represents the transmissibility (permeability) between the blocks (i,j) and $(i+1,j)$ and $T^{xy}_{i+1/2,j} = k^{xy}_{i+1/2,j}$ represents the cross transmissibility (permeability) between these two blocks. However, one of the difficulty is the determination of the transmissibility (permeability) at the interface, if the permeability is known on the grid block. In homogeneous media, these terms are well defined. But, in heterogeneous media, the interface permeability $k^{xx}_{i+1/2,j}$ or $k^{xy}_{i+1/2,j}$ are usually

unknown. To get an accurate transmissibility formula, one of the possibility is to calculate these terms directly from the scaling-up procedure.
For the fluid flow at the interface Γ_2, it can be calculated by:

$$F_2 = \lambda_{i,j+1/2}(T^{yy}_{i,j+1/2}(p_{i,j+1} - p_{i,j}) + \tfrac{1}{4}T^{yx}_{i,j+1/2}(p_{i+1,j} + p_{i+1,j+1} - p_{i-1,j+1} - p_{i-1,j}))$$

where $T^{yy}_{i,j+1/2}$ represents the transmissibility between the blocks *(i,j)* and *(i,j+1)* and $T^{yx}_{i,j+1/2}$ represents the cross transmissibility between these two blocks.
A complete discretization formula is given in Appendix 1.

III. 2 Transmissibility Scaling-up on a shifted block

A transmissibility scaling-up method was proposed by *White and Horne* (1987) for this kind of scheme. But their method needs to solve several linear systems in the whole domain with millions of fine grid blocks. So, it is very time consuming. In this section, we propose to scale-up the transmissibility which depends only on the local heterogeneity. The principle of the proposed technique is similar to the calculation of a full block permeability tensor, but the considered block is not the coarse grid block. The block is shifted. To calculate the transmissibility related to the flow in the x-direction, a shifted block is used as shown in Figure 2a. With a given scaling-up procedure, a permeability tensor $k_{i+1/2,j} = \begin{pmatrix} k^{xx}_{i+1/2,j} & k^{xy}_{i+1/2,j} \\ k^{yx}_{i+1/2,j} & k^{yy}_{i+1/2,j} \end{pmatrix}$ can be determined on this block, where $k^{xx}_{i+1/2,j}$ represents the permeability on the x-direction, and $k^{xy}_{i+1/2,j}$ represents the cross permeability on this direction. From this formula, we can determine the transmissibility terms for the flow in the x-direction for the finite-volume scheme with $T^{xx}_{i+1/2,j} = \frac{\Delta y}{\Delta x} k^{xx}_{i+1/2,j}$ and $T^{xy}_{i+1/2,j} = k^{xy}_{i+1/2,j}$.

In the same way, we can determine the transmissibility terms related to the flow in the y-direction. Calculating the permeability tensor $k_{i,j+1/2} = \begin{pmatrix} k^{xx}_{i,j+1/2} & k^{xy}_{i,j+1/2} \\ k^{yx}_{i,j+1/2} & k^{yy}_{i,j+1/2} \end{pmatrix}$ on the shifted block in the y-direction (Figure 2b), the transmissibility terms are $T^{yy}_{i,j+1/2} = \frac{\Delta x}{\Delta y} k^{yy}_{i,j+1/2}$ and $T^{yx}_{i,j+1/2} = k^{yx}_{i,j+1/2}$.

In the examples presented below, we use, for the transmissibility scaling-up procedure, the periodic boundary conditions which was successfully used for block permeability scaling-up. In fact, on the shifted block which can be refined by the user for a good affectation of fine scale heterogeneities, a pressure gradient is imposed on the faces perpendicular to the flow direction and the flow rates in the same direction are equal. On the other faces, pressures and

flow rates on opposite boundaries are equal. This can be expressed as follows (Figure 1) for pressure gradient in x-direction:

$$\begin{cases} p(x, y=0) = p(x, y=L) \text{ on } \Gamma_2 \text{ and } \Gamma_4 \\ q(x, y=0) = q(x, y=L) \text{ on } \Gamma_2 \text{ and } \Gamma_4 \\ p(x=0, y) = p(x=L, y) - Cte \text{ on } \Gamma_3 \text{ and } \Gamma_1 \\ q(x=0, y) = q(x=L, y) \text{ on } \Gamma_3 \text{ and } \Gamma_1 \end{cases}$$

Thus, the pressure and consequently the flow rate on each refined blocks are calculated using a 5-point scheme and an iterative solver. Imposing a pressure gradient Δp_x in the x-direction for a shifted block as shown in Figure 2a, the transmissibility (permeability) $T^{xx}_{i+1/2,j}$ can be determined by:

$$k^{xx}_{i+1/2,j} = \frac{Nx_r \Delta x_r \sum_{i_1=1}^{Nx_r} \sum_{j_1=1}^{Ny_r} q^{xx}_{i_1,j_1}}{\Delta p Ny_r \Delta y_r}.$$

Imposing a pressure gradient Δp_y in the y-direction for the same block, we can determine the cross transmissivity (permeability) term $T^{xy}_{i+1/2,j}$:

$$k^{xy}_{i+1/2,j} = \frac{Nx_r \Delta x_r \sum_{i_1=1}^{Nx_r} \sum_{j_1=1}^{Ny_r} q^{yy}_{i_1,j_1}}{\Delta p Ny_r \Delta y_r}$$

where Nx_r, Ny_r= number of the refined blocks in the x-, y-direction, respectively,

Δx_r, Δy_r= size of the refined blocks in the x-, y-direction, respectively.

To calculate $k^{yy}_{i,j+1/2}$ and $k^{yx}_{i,j+1/2}$, we use the same procedure for the shifted block as shown in Figure 2b.

It must be mentioned that the scaled-up transmissibility might strongly depend on the boundary condition as in the case of scaling-up the block permeability. But the transmissibility scaling-up can be considered as an improvement with respect to the block permeability scaling-up, since the transmissibility will not be determined again from the scaled-up block permeability. Moreover, we think that the effect of boundary condition might be less sensitive at the field scale and the flow simulation at the reservoir scale might be approximated by considering two kinds of flow pattern, as discussed by *Ding* (1995).

IV. Numerical Results

Two numerical examples are presented to compare this new transmissibility scaling-up method and several published permeability scaling-up methods. For the transmissibility scaling-up procedure, we use the periodic boundary condition (*Durlofsky*, 1991). For

permeability scaling-up, we use the periodic boundary condition (*Durlofsky*, 1991) and the optimized linear boundary condition (*Bamberger*, 1977). For the permeability scaling-up, the transmissibilities are calculated using an harmonic average for block permeability as presented in Appendix 1.

The general data is given in Table 1. To validate the proposed method, the flow is simulated using the fine scale isotropic permeability distribution. The fine scale simulation results are assumed to be the reference solution.

Example 1

The permeability distribution is given in Figure 3. This heterogeneity field is well-known and was studied by several authors (*Samier* 1990, *White and Horne* 1987, *Wang et al.*). They showed the necessary of using a full permeability tensor. Here, we will compare the transmissibility scaling-up method and some permeability scaling-up methods.

Two wells, one injector and one producer are placed at the corner of this field. Water is injected into the oil reservoir with a fixed flow rate. The results of water-cut curves are presented in Figure 4 and the results of saturation distribution are presented in Figure 5. All the coarse grid simulation results are very similar. But, we can observe that scaling-up of transmissibility, which uses periodic boundary conditions, gives slightly better results than the scaling-up of permeability. In this case, the improvement using transmissibility scaling-up is not significant. But, it proves that scaling-up of transmissibility is a good initiative.

Example 2

A field with parallel barriers of permeability is used as shown in Figure 6 with a strong permeability contrast. The fine grid has 99x99 grid blocks, and the coarse grid has 11x11 grid blocks. Water is injected into an oil reservoir. In this example, we have one injector and three producers. For the fine grid simulation, it is clear that the #3 producer produces the most because it is connected to the injector by a permeable layer, and the #2 producer produces less because it is separated by several "impermeable" zones. For coarse grid simulation, if the permeability is scaled-up on grid blocks, the phenomenon resulting from anisotropy might be homogenized in the transmissibility calculation. Figure 7 shows the water-cut. Even though using the transmissibility scaling-up gives the results far from the fine grid simulation, they are much better than using the permeability scaling-up method. Figure 8 and Figure 9 represent the saturation distribution and the pressure distribution, respectively for the fine grid and the coarse grid simulations with different scaling-up methods. It is clear that using transmissibility scaling-up gives the best result, which represents the same trend as fine grid simulation. The improvement of using transmissibility scaling-up is significant.

V. Conclusion

The scaling-up of transmissibility and permeability are discussed. Scaling-up of transmissibility is more accurate than scaling-up of permeability. A new transmissibility scaling-up procedure, which uses shifted blocks to calculate locally the transmissibility, is proposed for a finite-volume type numerical scheme with a full permeability tensor.

Some numerical examples are presented. The results show that using the transmissibility scaling-up improves the coarse grid simulation accuracy. In some cases, like a stratified field, this improvement is significant.

Appendix 1. Discretization of Elliptic Operator with a Full Permeability Tensor

According to the discussion in the section III.1, the elliptic operator can be discretized as:

$$\begin{aligned}
\Delta x\Delta y\, div(k\nabla p) = {} & \lambda_{i+1/2,j}(T^{xx}_{i+1/2,j}(p_{i+1,j}-p_{i,j})+ \\
& \tfrac{1}{4}T^{xy}_{i+1/2,j}(p_{i,j+1}+p_{i+1,j+1}-p_{i,j-1}-p_{i+1,j-1})) \\
& +\lambda_{i,j+1/2}(T^{yy}_{i,j+1/2}(p_{i,j+1}-p_{i,j})+ \\
& \tfrac{1}{4}T^{yx}_{i,j+1/2}(p_{i+1,j}+p_{i+1,j+1}-p_{i-1,j+1}-p_{i-1,j})) \\
& +\lambda_{i-1/2,j}(T^{xx}_{i-1/2,j}(p_{i-1,j}-p_{i,j})- \\
& \tfrac{1}{4}T^{xy}_{i-1/2,j}(p_{i,j+1}+p_{i-1,j+1}-p_{i,j-1}-p_{i-1,j-1})) \\
& +\lambda_{i,j-1/2}(T^{yy}_{i,j-1/2}(p_{i,j-1}-p_{i,j})- \\
& \tfrac{1}{4}T^{yx}_{i,j-1/2}(p_{i+1,j}+p_{i+1,j-1}-p_{i-1,j-1}-p_{i-1,j}))
\end{aligned}$$

In this formula, λ represents the mobility. It takes an upstream value according to the flow direction at the interface. For example,

$$\lambda_{i+1/2,j} = \begin{cases} \lambda_{i+1,j} & If\ \delta_{i+1/2,j} > 0 \\ \lambda_{i,j} & If\ \delta_{i+1/2,j} \le 0 \end{cases}$$

with $\delta_{i+1/2,j} = T^{xx}_{i+1/2,j}(p_{i+1,j}-p_{i,j}) + \tfrac{1}{4}T^{xy}_{i+1/2,j}(p_{i,j+1}+p_{i+1,j+1}-p_{i,j-1}-p_{i+1,j-1})$

This scheme is conservative, because the fluid flux through an interface is always the same for the discretization of the block in both sides ($\delta_{i+1/2,j} = \delta_{i\to i+1,j} = \delta_{i+1\to i,j}$).

In section III, we present a scaling-up procedure to calculate these transmissibility terms. However, if the block permeability is scaled-up, these transmissibility terms should be calculated depending on the block permeability value. For this case, we propose to use the harmonic average for the calculation, which is calculated by:

$$T^{xx}_{i+1/2,j} = \frac{\Delta y}{\Delta x}\frac{2k^{xx}_{i+1,j}k^{xx}_{i,j}}{k^{xx}_{i,j}+k^{xx}_{i+1,j}}$$

for the cross term $T^{xy}_{i+1/2,j}$ is calculated by:

$$T^{xy}_{i+1/2,j} = \frac{1}{2}\left[\frac{4k^{xy}_{i,j+1}k^{xy}_{i,j-1}k^{xy}_{i,j}}{k^{xy}_{i,j+1}k^{xy}_{i,j} + k^{xy}_{i,j+1}k^{xy}_{i,j-1} + k^{xy}_{i,j}k^{xy}_{i,j-1}} + \frac{4k^{xy}_{i+1,j+1}k^{xy}_{i+1,j-1}k^{xy}_{i+1,j}}{k^{xy}_{i+1,j+1}k^{xy}_{i+1,j} + k^{xy}_{i+1,j+1}k^{xy}_{i+1,j-1} + k^{xy}_{i+1,j}k^{xy}_{i+1,j-1}}\right]$$

This formula is used in the examples for the comparison with the block permeability scaling-up.

It cannot be written in the general standard nine-point scheme form (*Yanosik and McCracken*, 1979). However, for the single-phase flow modelling, the discretization formula can be written in a standard form, but it is a non-symmetrical scheme:

$$\begin{aligned}
-\int_{\partial\Gamma} k\nabla\bar{p}.\bar{n}.d\gamma \approx & \left[T^{xx}_{i+1/2,j} + \frac{T^{yx}_{i,j+1/2}}{4} - \frac{T^{yx}_{i,j-1/2}}{4}\right]\left(p_{i+1,j} - p_{i,j}\right) \\
& + \left[T^{xx}_{i-1/2,j} - \frac{T^{yx}_{i,j+1/2}}{4} + \frac{T^{yx}_{i,j-1/2}}{4}\right]\left(p_{i-1,j} - p_{i,j}\right) \\
& + \left[T^{yy}_{i,j+1/2} + \frac{T^{xy}_{i+1/2,j}}{4} - \frac{T^{xy}_{i-1/2,j}}{4}\right]\left(p_{i,j+1} - p_{i,j}\right) \\
& + \left[T^{yy}_{i,j-1/2} - \frac{T^{xy}_{i+1/2,j}}{4} + \frac{T^{xy}_{i-1/2,j}}{4}\right]\left(p_{i,j-1} - p_{i,j}\right) \\
& + \left[\frac{T^{xy}_{i+1/2,j}}{4} + \frac{T^{yx}_{i,j+1/2}}{4}\right]\left(p_{i+1,j+1} - p_{i,j}\right) \\
& + \left[-\frac{T^{xy}_{i+1/2,j}}{4} - \frac{T^{yx}_{i,j-1/2}}{4}\right]\left(p_{i+1,j-1} - p_{i,j}\right) \\
& + \left[-\frac{T^{xy}_{i-1/2,j}}{4} - \frac{T^{yx}_{i,j+1/2}}{4}\right]\left(p_{i-1,j+1} - p_{i,j}\right) \\
& + \left[\frac{T^{xy}_{i-1/2,j}}{4} + \frac{T^{yx}_{i,j-1/2}}{4}\right]\left(p_{i-1,j-1} - p_{i,j}\right)
\end{aligned}$$

Nomenclature

A = elliptic operator,

B = formation volume factor,

F = flow term,

K_{eq} = effective permeability tensor,

L = length of the shifted block,

Nx_r, Ny_r = number of the refined blocks in the x-,y-direction, respectively,

T = internodal transmissibility,

k = permeability tensor of fine grid block,

n = normal direction,

p = pressure,

Q = well flow rate,

u = Darcy filtration velocity,

Δx, Δy = size of the coarse grid block,

Δx_r, Δy_r = size of the refined block,

μ = fluid viscosity,

λ = mobility,

Φ = porosity,

δ = fluid flux,

Ω = domain,

$\partial\Omega = \Gamma$ = domain boundary,

ω = power law coefficient.

Subscript

i,j = indice of blocks in x-, y- direction, respectively,

o = oil phase,

w = water phase,

x,y = spatial directions.

Acknowledgements

We would like to thank P. Lemonnier and E. Delamaide for their encouragement and critical comment during the writing of this paper.

References

Bamberger, A., 1977, "Approximation des coefficients d'opérateurs elliptiques stables pour la G-convergence", rapport du Centre de Mathématiques Appliquées, École Polytechnique.

Ding, Y., 1995, "Scaling-up in the Vicinity of Wells in Heterogeneous Field", SPE n°29137 presented at the 13th SPE Symposium on Reservoir Simulation, 12-15 Feb., San Antonio, Texas.

Durlofsky, L.J., 1991, "Numerical calculation of equivalent grid block permeability tensors for heterogeneous porous media", Water Ressources Research, v. 27 (5), p. 699-708.

Galli, A., Goblet, P., Griffin, D., Ledoux, E., Le Loc'h, G., Mackay, R., Renard, P., 1996, "Quick upscaling of flow and transport related parameters", Technical Report.

Gautier, Y., Noetinger, B., 1994, "Preferential flow paths detection for heterogeneous reservoirs using a new renormalization technique", 4th European Conference on the Mathematics of Oil Recovery, 7-10 June, Roros, Norway.

Guerillot, D., 1988, "Composition des perméabilités absolues aux échelles intermédiaires pour les gisements d'hydrocarbures hétérogènes; application à un affleurement du Yorkshire; rapport d'avancement, IFP report n°36738.

Guerillot, D., Rudkiewicz, J. L., Ravenne, Ch., Renard, G. ,Galli, A., 1989, "An integrated model for computer aided reservoir description: from outcrop study to fluid flow simulations", presented at the IOR Symposium, Budapest, Hungary.

King, P.R., 1989, "The use of renormalization for calculating effective permeability", Transport in Porous Media, v. 4, p. 37-58.

Kruel Romeu, R., 1994, "Écoulement en milieux hétérogènes : prise de moyenne de perméabilités en régimes permanent et transitoire", PhD thesis, Université Paris VI, France.

Kruel Romeu, R., Noetinger, B., 1995, "Calculation of internodal transmissivities in finite difference models of flow in heterogeneous media", Water Ressources Research, v. 31, p. 943-959.

Le Loc'h, G., 1987, "Etude de la decomposition des perméabilités par des méthodes variationnelles", PhD thesis, Ecole Normale Superieure des Mines de Paris, France.

Njifenjou, A., 1993, "Éléments finis mixtes hybrides duaux et homogénéisation des paramètres pétrophysiques; application à l'étude numérique de l'écoulement en milieux poreux", PhD thesis, Université Paris VI, France.

Njifenjou, A., 1994, "Expression en termes d'énergié pour la perméabilité absolue effective", IFP review, v. 49 (4), p. 345-358.

Palagi, C., 1992, "Generation and application of Voronoi grid to model flow in heterogeneous reservoirs", PhD thesis, Stanford University, California.

Palagi, C. L., Ballin, P. R., Aziz, K., 1993, "The modelling of flow in the heterogeneous reservoirs with Voronoi grid", SPE n°25259 presented at the SPE Symposium on Reservoir Simulation, 28 Feb.-3 March, New Orleans, Louisiana.

Peaceman, D.W., 1996, "Effective transmissibilities of a gridblock by upscaling; why use renormalization?", SPE n°36722 presented at the SPE Annual Technical Conference and Exhibition, 6-9 Oct., Denver, Colorado.

Pickup, G. E., Sorbie, K. S.,1994, "Development and application of a new two phase scale up method based on tensor permeabilities", SPE n°28586 presented at the SPE Annual Technical Conference and Exhibition, 25-28 Sept., New Orleans, Louisiana.

Pickup, G. E., Sorbie, K. S.,1994, "The scale-up of two phase flow using permeability tensors", 4th European Conference on the Mathematics of Oil Recovery, 7-10 June, Roros, Norway.

Samier, P., 1990, "A finite element method for calculating transmissibilities in N-point difference equations using a non diagonal permeability tensor", 2nd European Conference on the Mathematics of Oil Recovery, 11-14 Sept., Arles, France.

Wang, J. T., Daltaban, T. S., Archer, J. S., "The use of permeability tensor in modelling heterogeneous and fractured flow media", SPE n°24503.

Warren, J.E., Price, H.S., 1961 : "Flow in heterogeneous porous media", SPEJ Sept., p. 153-169

White, C. D., Horne, R. N., 1987, Computing absolute transmissibility in the presence of fine scale heterogeneity", SPE n°16011 presented at 9th Symposium on Reservoir Simulation, 1-4 Feb., San Antonio, Texas.

Yanosik, J.L., McCracken, T.A., 1979 : "A nine-point finite difference reservoir simulator for realistic prediction of adverse mobility ratio displacements", SPEJ Agu., p. 253-262.

Figure captions:

Figure 1. Finite-volume scheme (on coarse grid block)

Figure 2. Transmissibility upscaling on shifted blocks

Figure 3. Heterogeneous field in example 1

Figure 4. Water cut for the production well in example 1

Figure 5. Water saturation distribution for example 1

Figure 6. Heterogeneous field in example 2

Figure 7. Water cut curves in example 2

Figure 8. Water saturation distribution for example 2

Figure 9. Pressure distribution for example 2

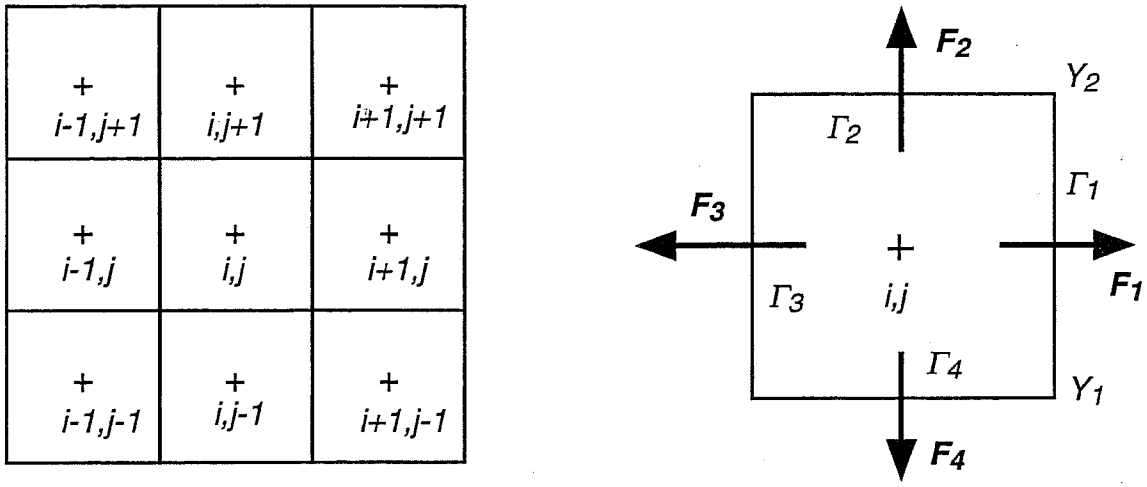

Figure 1. Finite-volume scheme (on coarse grid block)

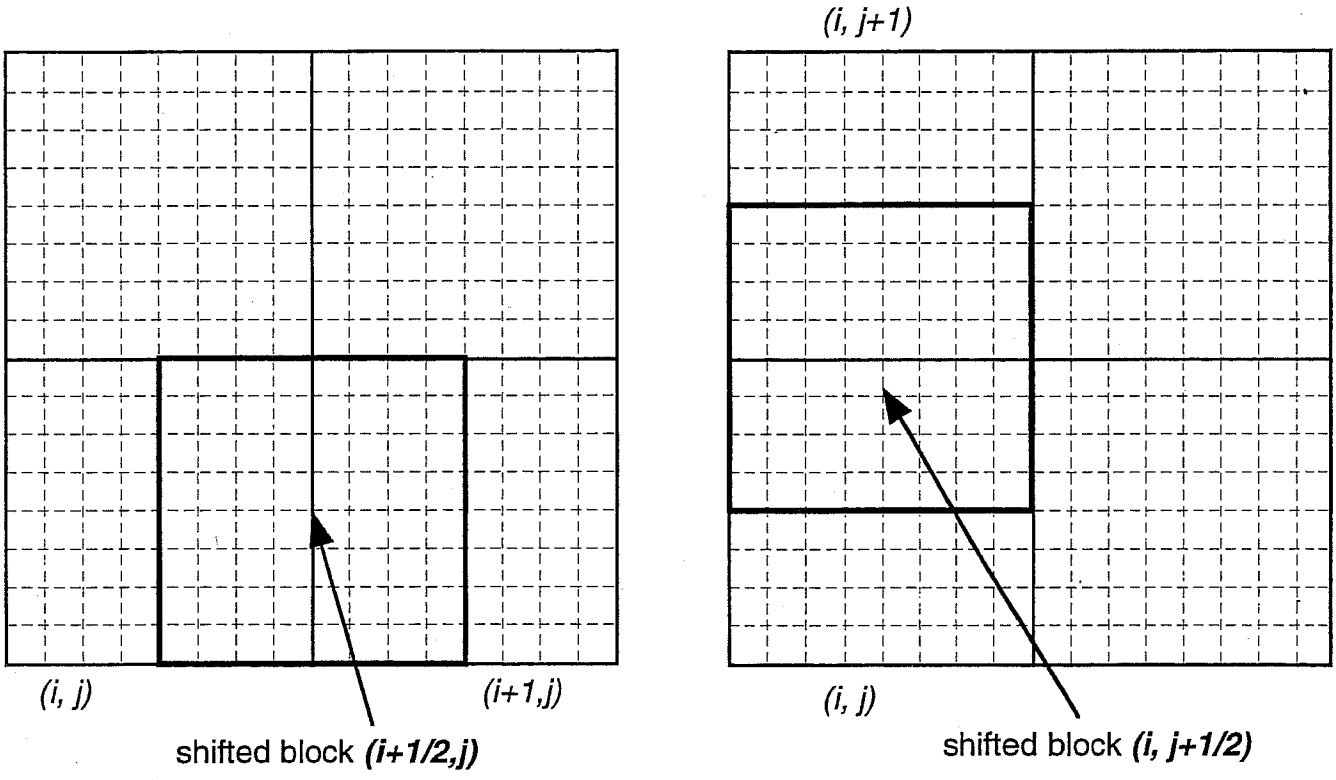

a). Scaling-up in *x*-direction

b). Scaling-up in *y*-direction

Figure 2. Transmissibility scaling-up on shifted blocks

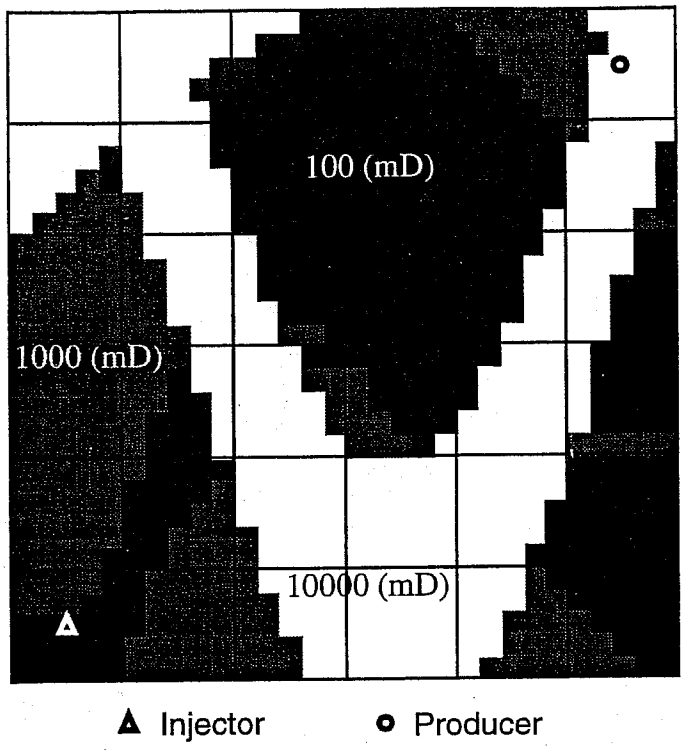

Figure 3. Heterogeneous field in example 1.

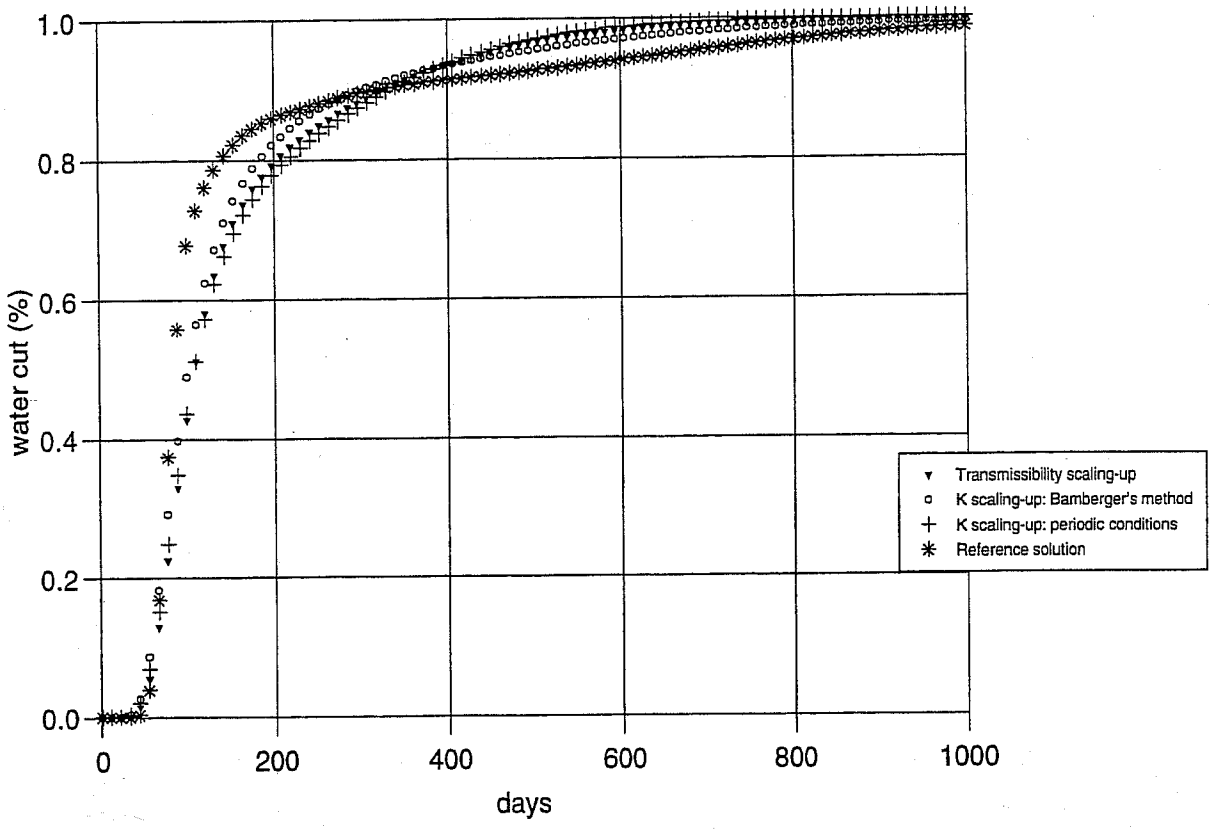

Figure 4. Water cut for production well in example 1.

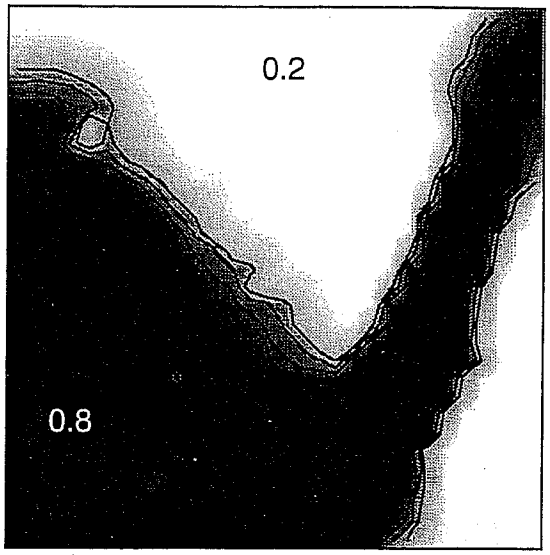

5a). Fine grid simulation

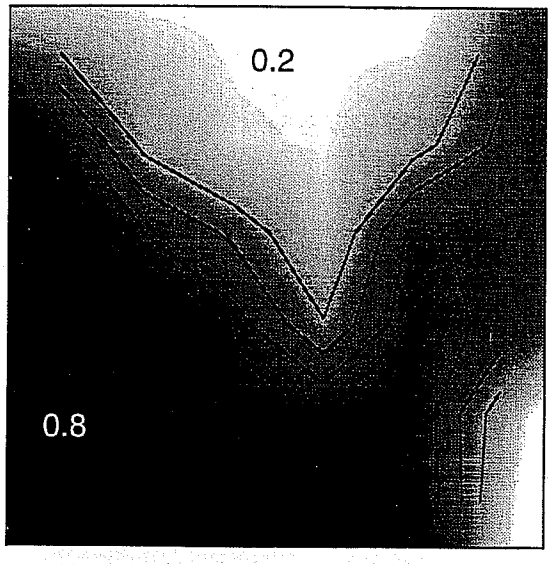

5b). Coarse grid simulation with transmissibility scaling-up

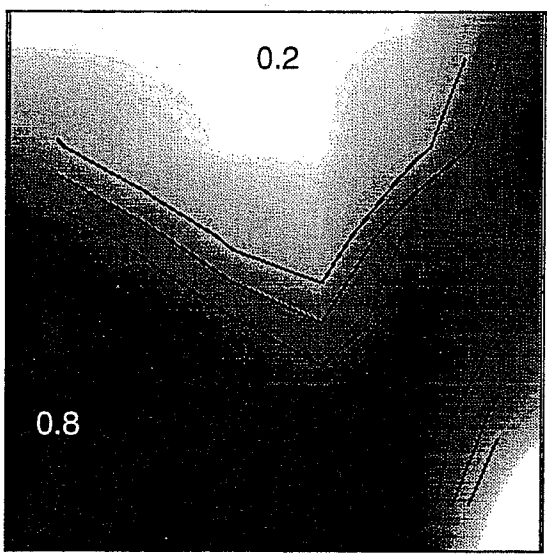

5c). Coarse grid simulation with permeability scaling-up using Bamberger's method

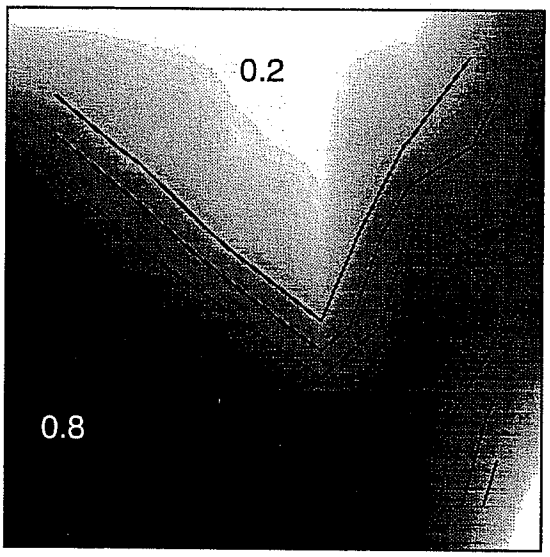

5d). Coarse grid simulation with permeability scaling-up using periodic boundary conditions

Figure 5. Water saturation distribution for example 1

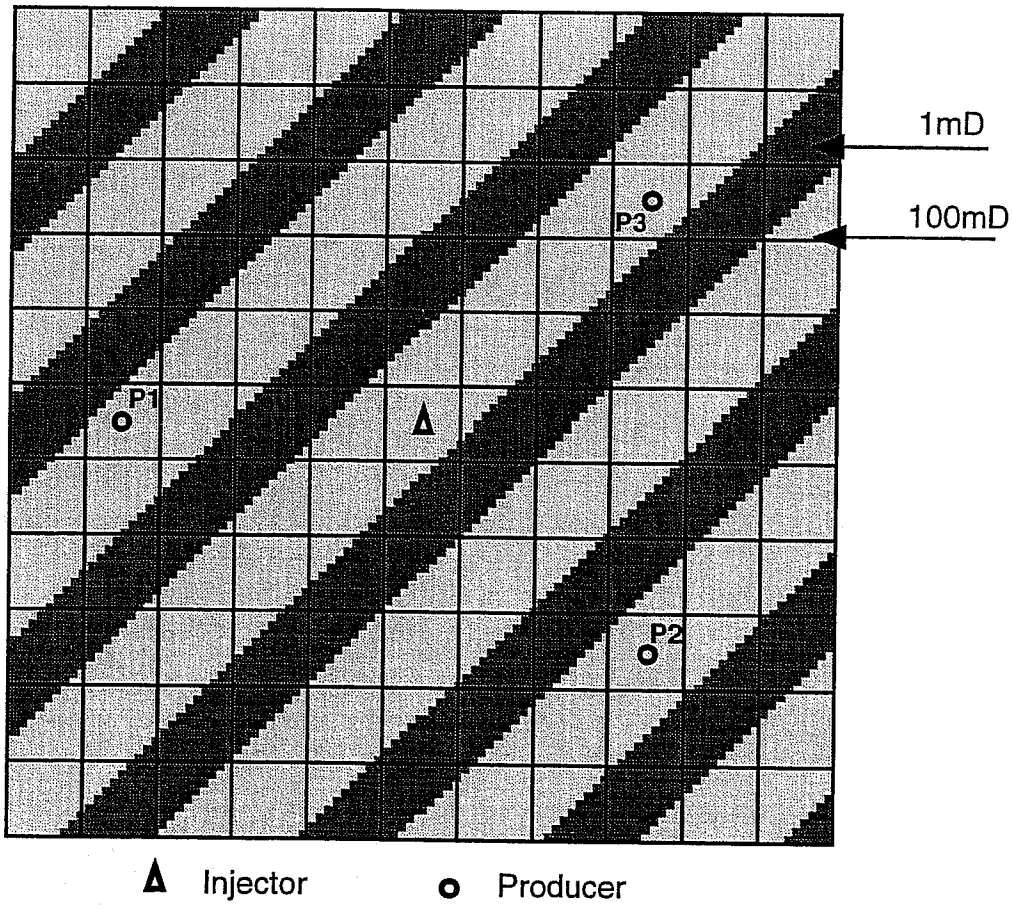

Figure 6. Heterogeneous field in example 2

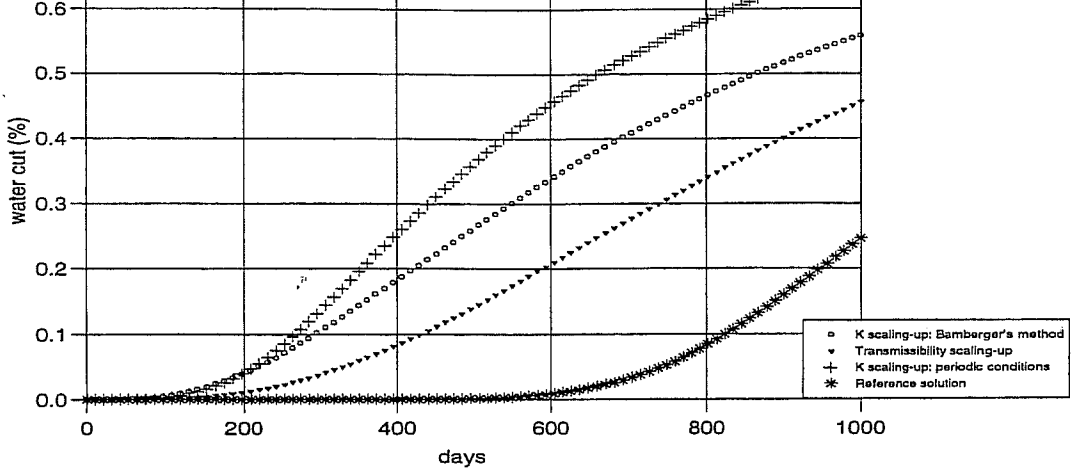

7a). Water cut for the production well P1

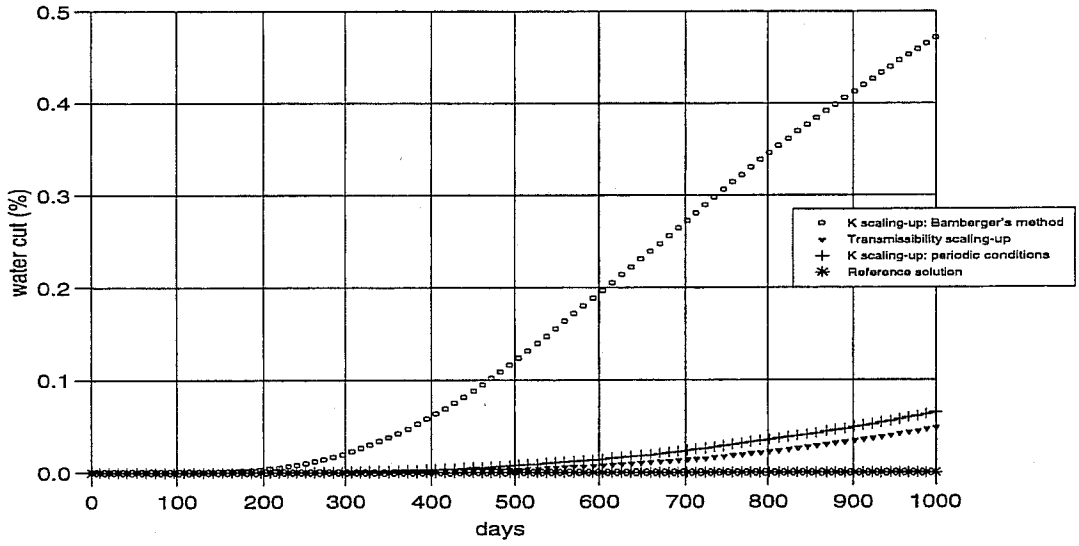

7b). Water cut for the production well P2

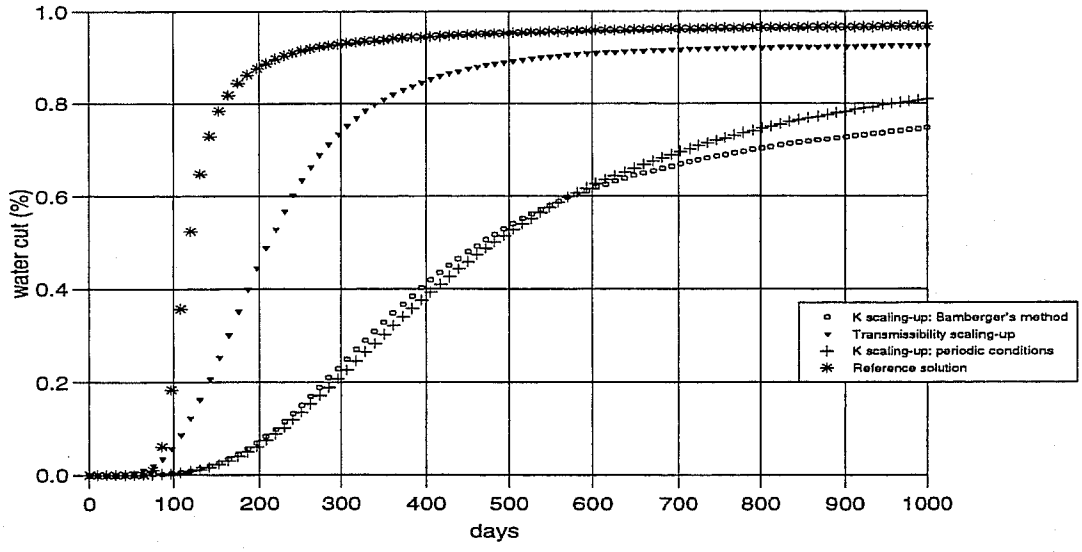

7c). Water cut for the production well P3

Figure 7. Water cut curves in example 2

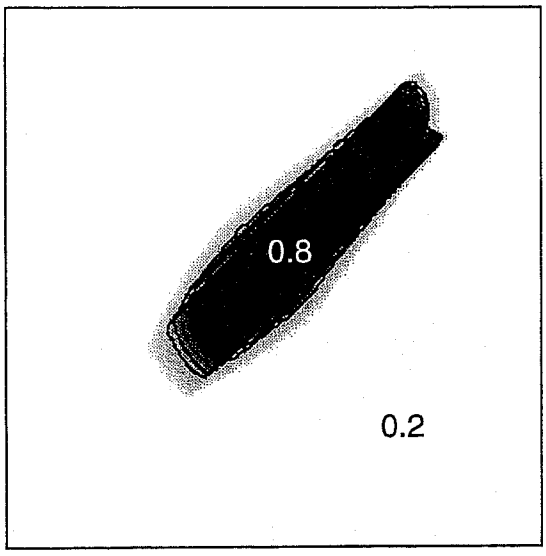

8a). Fine grid simulation

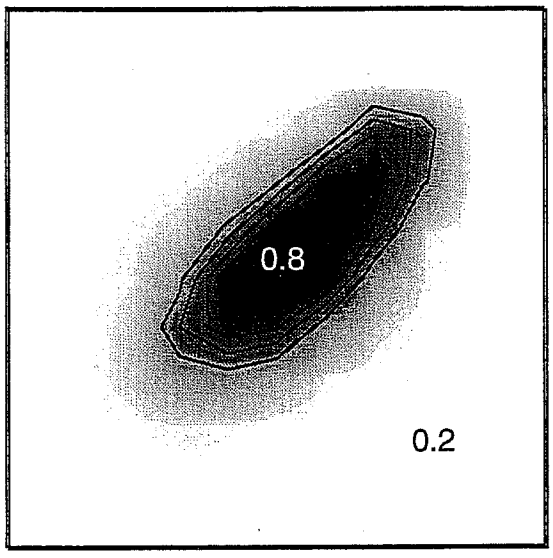

8b). Coarse grid simulation with transmissibility scaling-up

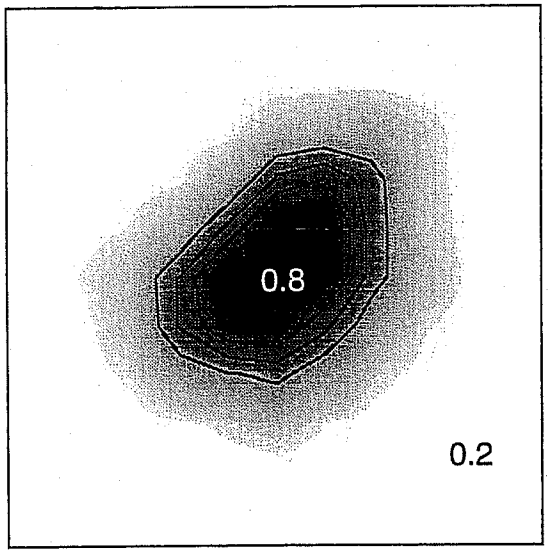

8c). Coarse grid simulation with permeability scaling-up using Bamberger's method

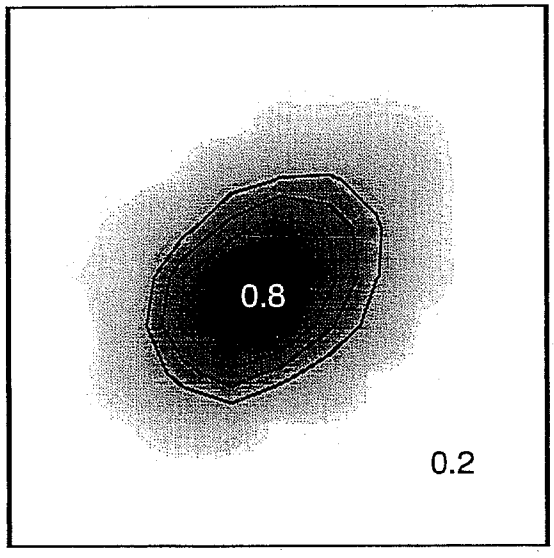

8d). Coarse grid simulation with permeability scaling-up using periodic boundary conditions

Figure 8. Water saturation distribution for example 2

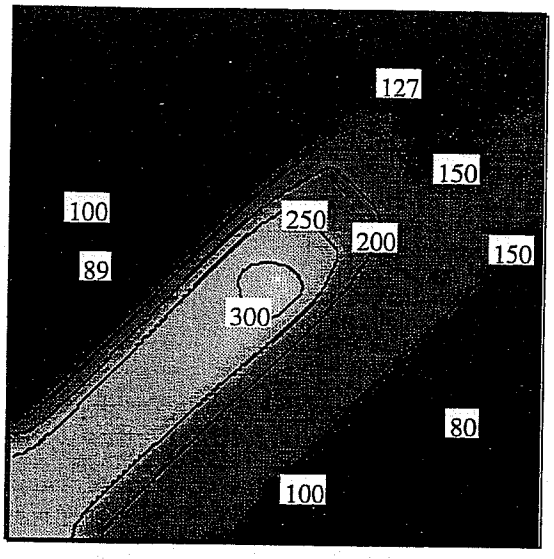

9a). Fine grid simulation

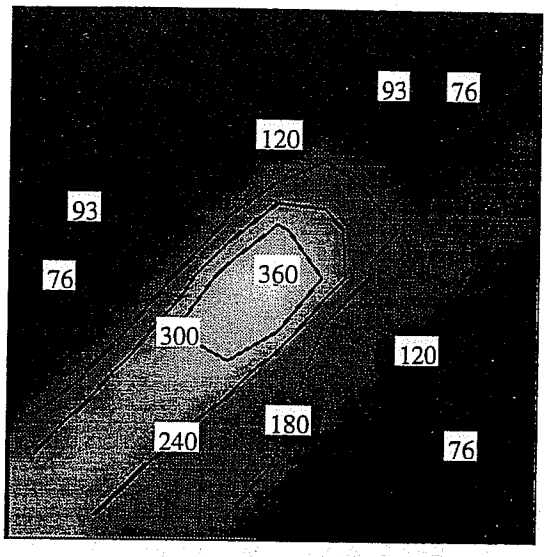

9b). Coarse grid simulation with transmissibility scaling-up

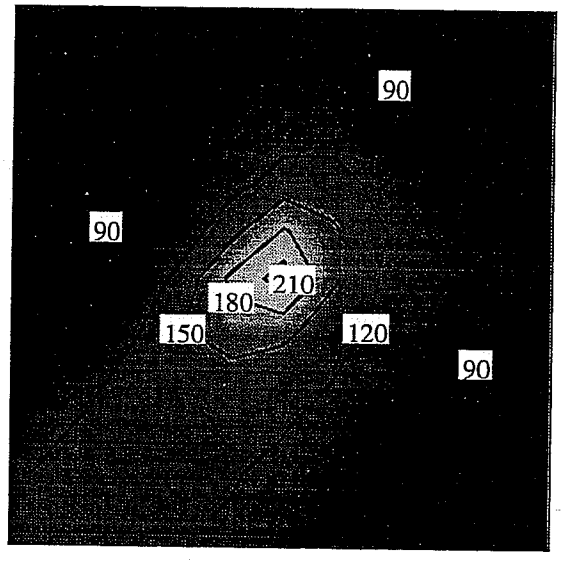

9c). Coarse grid simulation with permeability scaling-up using Bamberger's method

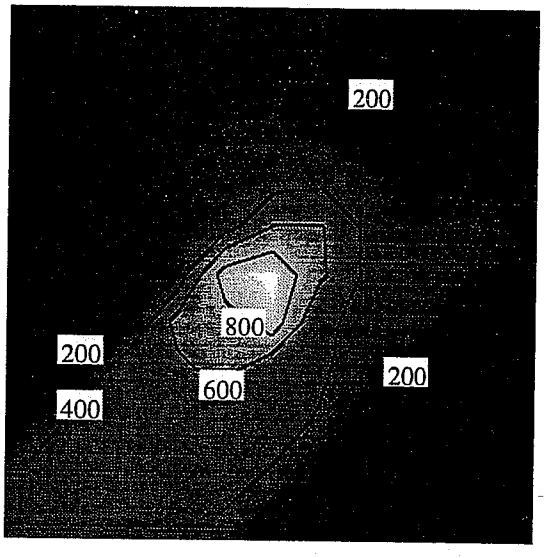

9d). Coarse grid simulation with permeability scaling-up using periodic boundary conditions

Figure 9. Pressure distribution for example 2

Parameter	Input data (S.I. unit)
Injection rate	0.00081 m^3/s
Production well pressure	$7x10^6$ Pa
Oil viscosity	0.001 Pa.s
Water viscosity	0.001 Pa.s
Initial/irreducible water saturation	0.2
Residual oil saturation	0.2
Porosity	0.2
Thickness	1 m
Areal Dimensions	300 m by 300 m for example 1 990 m by 990 m for example 2
Initial pressure	$85x10^5$ Pa

Table 1. Simulation input data

A SIMPLE METHOD TO ESTIMATE INTERWELL AUTOCORRELATION

Jorge O. S. Pizarro
Larry W. Lake
Department of Petroleum and Geosystems Engineering
The University of Texas at Austin

ABSTRACT

The estimation of autocorrelation in the lateral or interwell direction is important when performing reservoir characterization studies using stochastic modeling. This paper presents a new method to estimate the interwell autocorrelation based on parameters, such as the vertical range and the variance, that can be estimated with commonly available data.

We used synthetic fields that were generated from stochastic simulations to provide data to construct the estimation charts. These charts relate the ratio of areal to vertical variance and the autocorrelation range (expressed variously) in two directions. Three different semivariogram models were considered: spherical, exponential and truncated fractal.

The overall procedure is demonstrated using field data. We find that the approach gives the most self-consistent results when it is applied to previously identified facies. Moreover, the autocorrelation trends follow the depositional pattern of the reservoir, which gives confidence in the validity of the approach.

INTRODUCTION

The importance of reservoir characterization methods has been established in the last decade by reservoir studies that are based on stochastic models that account for the heterogeneity of the porous media.

A reliable study depends on prior quantification of the heterogeneity of the reservoir (Srivastava, 1994). The geostatistical approach describes the heterogeneity through averages, variances and autocorrelation. Although it has several advantages, when compared with

deterministic approaches, the confidence in geostatistical modeling will be a strong function of how well the input data represent reality. The horizontal autocorrelation, especially, is among the most critical of the parameters to be estimated; we propose a new procedure to estimate it in this paper. The method uses serial data from several vertical wells, as would exist from wells in mature projects.

MOTIVATION

There are in the literature several works stressing that the estimation of horizontal autocorrelation is important in achieving a good reservoir description. Lucia and Fogg (1990) stated that the principal difficulty in reservoir characterization is estimating the spatial distribution of petrophysical properties between vertical wellbores. These points have also been highlighted by Hewett (1986), Lemouzy *et al.* (1995) and Jensen *et al.*(1996).

Lambert (1981) calculated and tabulated Dykstra-Parsons coefficients (measures of heterogeneity) in both the horizontal and vertical directions from 689 wells in 22 fields. In 90 % of the cases, the ratio of the coefficients in the horizontal and vertical directions was less than one. This result, governed by the depositional trends observed in petroleum reservoirs, indicates a spatial dependence among these variables.

Figures 1 and 2 illustrate this idea in more detail. The figures show an idealized cross-section (x,z) that is being penetrated by several vertical cored wells. We can calculate two types of variances for the cross section. The *vertical* variance is the arithmetic average of the variances for each individual well; the *areal* variance is the variance of the well averages. A cross section that is strongly autocorrelated in the x direction will have a small areal variance; strong autocorrelation in the z direction will lead to a small vertical variance. The ratio of these two is a measure of the extent of autocorrelation in the respective directions.

If we quantify the relationship between the autocorrelation and the variances, in both directions, we will be able to estimate one parameter from the others. Therefore, the main idea behind our method is that the horizontal autocorrelation must depend on the ratio of the areal-to-vertical variances and the autocorrelation in the vertical direction. With a chart that expresses this relationship, one can estimate autocorrelation in the horizontal direction.

METHOD OF STUDY

This section states the approach used to estimate autocorrelation in the interwell region of a reservoir. In the following derivation, we focus on the estimation of horizontal autocorrelation

since, in most cases, vertical wells can provide information on autocorrelation in the vertical direction. We also restrict attention to the estimation of horizontal autocorrelation in permeability.

The autocorrelation will be a function of the type of model chosen to represent it. Three different theoretical semivariogram models were tested: spherical, exponential and truncated fractal (power-law). The fractal model usually does not have a finite autocorrelation, but we will truncate at some upper cutoff; hence, the use of *truncated* fractal.

The way we express autocorrelation depends on the model being used for it. For the spherical semivariogram model,

$$\gamma(h) = \mathrm{Cov}(0) \begin{cases} \frac{3}{2}\left(\frac{h}{a}\right) - \frac{1}{2}\left(\frac{h}{a}\right)^3 & 0 \le h \le a \\ 1 & h \ge a \end{cases} \tag{1}$$

autocorrelation is expressed by the range a. For the vertical direction $a = \lambda_z$; for the horizontal, $a = \lambda_x$. For the exponential model,

$$\gamma(h) = \mathrm{Cov}(0)\, e^{-\frac{h}{\lambda}} \tag{2}$$

we use the autocorrelation length. As before, for the vertical direction $\lambda = \lambda_z$; for the horizontal, $\lambda = \lambda_x$. For the truncated fractal fBm model,

$$\gamma(h) = \mathrm{Cov}(0) \begin{cases} h^{2H} & 0 \le h \le a \\ 1 & h \ge a \end{cases} \tag{3}$$

we use the cut-off length, a. For the vertical direction $a = \lambda_z$; for the horizontal, $a = \lambda_x$. We use the word *range* to generically express all three autocorrelation measures. Since a log-normal distribution is assumed for the permeability, all variances and averages are calculated on the logarithm of the permeability (ln k). In the above equations, Cov(0) stands for the sill, h the lag distance, and H the Hurst coefficient.

Formally, the vertical variance is the expectation of the conditional variances of Y(x,z) = ln(k(x,z):

$$\sigma^2_{vert} = E(\mathrm{Var}(Y(x_0, z)) \tag{4}$$

where $\mathrm{Var}(Y(x_0, z)$ indicates a z-direction variance conditioned to a fixed location x_0. As suggested in Fig. 2, σ^2_{vert} is estimated as

$$s^2_{vert} = \frac{1}{N_w}\sum_{i=1}^{N_w} Var(Y(i,j)) \qquad j = 1, \ldots, N_l \tag{5}$$

where i and j are the indices on the x and z directions, respectively. The areal variance is the variance of the conditional expectation of Y:

$$\sigma^2_{areal} = Var(E(Y(x_0, z)) \tag{6}$$

It is estimated as

$$s^2_{areal} = Var\left(\frac{1}{N_l}\sum_{j=1}^{N_l} Y(i,j)\right) \qquad i = 1, \ldots, N_w \tag{7}$$

See Jensen *et al.* (1996) for details on conditional variances and expectations.

Our approach consists of the generation of synthetic, equiprobable permeability fields using stochastic simulation and a statistical treatment of the obtained data.

There are several methods that can generate stochastic reservoir images (Srivastava, 1994). One is the matrix decomposition method (MDM). This method is an averaging technique based on the decomposition of the autocovariance matrix. The present study uses a program developed by Yang (1990) that performs simulations based on MDM.

The MDM can generate permeability fields for reservoir modeling, but several statistics must be known as input data. In this step, it is essential to quantify the geologic knowledge in terms of a few parameters that can characterize the static properties of the reservoir. In doing this some assumptions were necessary; we considered that the permeability distribution can be represented by a single log-normal distribution that obeys second-order stationarity. The log-normal assumption was corroborated by the work of several authors, which results are summarized in a paper by Jensen *et al.* (1987).

The generation of synthetic permeability fields provided the necessary data to describe the relation among all investigated parameters. Averaging results from several realizations will provide a good estimate for the actual value of λ_x.

TYPE-CURVE PROCEDURE

To perform the numerical experiments, we established the following procedure. First, we chose a rectangular cross section with 4,000 blocks, 200 blocks in the x direction and 20 in the z direction. The sampling procedure represents a reservoir with 11 vertical wells aligned in one

direction having a constant spacing between them. We later concluded that the difference in results caused by staggered wells is small (Pizarro, 1996). Therefore, the analysis can be used for irregularly spaced wells, provided the average spacing is used as the reference distance.

The ranges input to MDM were converted to dimensionless form to provide more generality to the results. The dimensionless horizontal autocorrelation was normalized by the interwell spacing; the total thickness (H) is the reference distance in the vertical direction. We sample the generated fields at a constant interval to generate the estimated variances.

In the stochastic simulations, the dimensionless ranges were varied between 0.1 and 100 in the x direction and from 0.1 to 2.0 in the z direction. This range is believed to describe the autocorrelation existing in most petroleum reservoirs.

To make the results accurately represent the expectations in Eqs. 5 and 7, several realizations were performed. For each realization, Y values in each well were collected in a table in which there were 11 columns in the horizontal direction (each corresponding to one well) and 20 lines in the vertical direction, representing layer values. For each well the arithmetic average of Y was calculated in the vertical direction as well as the variance in the vertical direction.

Once both areal and vertical variances are known, the calculation of the ratio between them is straightforward. Since all of the semivariances used in Eqs. 5 and 7 are directly proportional to the variance, the ratio will be a function only of λ_{x_D}, λ_{z_D} and the semivariogram model. Therefore, if s^2_{areal} and s^2_{vert} are calculated and λ_{z_D} is estimated from fitting a specific semivariogram model to the vertical data, λ_{x_D} can be estimated.

RESULTS

Here we present the simulation results used to build the type-curve charts. The procedure stated above was implemented and several simulations performed.

All fields were generated for $\sigma^2 = 1$, which is equivalent to $V_{DP} = 0.63$. Since both areal and vertical variances are derived from the autocovariance, their ratio is independent of σ^2 (Pizarro, 1996). We used the minimal number of realizations (N_R) that would provide stable results, $N_R = 50$ (Pizarro, 1996).

The results obtained are expressed in Figs. 3 to 5 for the spherical, exponential and truncated fractal semivariogram models, respectively. Each figure is a plot of s^2_{areal} / s^2_{vert} versus λ_{z_D} with λ_{x_D} as a parameter. The truncated fractal fBm plot uses a Hurst coefficient of 0.25, since this seems to fit various types of field data (Neumann, 1994). Each figure contains results from 3,500 MDM simulations, since we calculate the average of 50 realizations.

Validation The overall procedure cannot be validated since we only have analytical expressions for some limiting cases. We would need an extraordinary amount of field data to cover all the possible situations aside from the limiting cases. However, some insight into the results can be given by analyzing the available solutions.

The first result that can be compared is for the case when we have no autocorrelation in either the horizontal or vertical directions. This means that the permeability values are completely random with no spatial correlation. The central limit theorem states that no matter what distribution a group of independent random variables are from, the sample mean of these variables is approximately normally distributed. So, if $Y_1, Y_2, Y_3, \ldots, Y_N$ denote independent random variables each having the same mean, μ, and variance, σ^2, and $\overline{Y}$ equals the mean of N of these random variables, we will obtain

$$\overline{Y} = \frac{Y_1}{N} + \frac{Y_2}{N} + \cdots \frac{Y_N}{N} = \frac{1}{N}\sum_{i=1}^{N} Y_i \tag{8}$$

Applying the property that the variance of a sum of independent variables will be equal to the sum of the variance of each one, we obtain

$$\mathrm{Var}(\overline{Y}) = \frac{\sigma^2}{N} \tag{9}$$

According to this procedure, the variance of the mean can be approximated by the areal variance (s^2_{areal}). Hence, the above relation states that, for the case of an uncorrelated field ($\lambda_{x_D} = \lambda_{z_D} = 0$), the areal variance should be equal to

$$\sigma^2_{areal} = \frac{\sigma^2}{N_1} \tag{10}$$

When the number of layers (N_1) equals 20, the above expression gives $\sigma^2_{areal} = 0.050$. In the numerical experiments with MDM we obtained $s^2_{areal} = 0.047$, a good approximation.

Another way to validate the results is to make use of an analytic expression that describes the relationship between variances of properties measured at different scales. Several authors, including Neuman (1994), Lasseter *et al.* (1986) and Haldorsen (1986), have reported the effect of the scale on the measurement of heterogeneity. One of the strong points of geostatistics is its ability to represent this behavior. For instance, the permeability of a well can be measured from a series of core measurements representing blocks of a certain size, shape and orientation. As the

size of these blocks increases, the variance of the mean value within the blocks get smaller although they may have the same mean.

Krige's relationship (Journel and Huijbregts, 1978) can be adapted to the present application. If a mining deposit (D) is split up into blocks (V), the variance of the properties of these blocks will be called the block variance and be denoted by $\sigma^2_{(V/D)}$. The variance of point grades (O) within a block is expressed by $\sigma^2_{(O/V)}$. This relationship states that these variances can be related to the variance of point grades within a deposit ($\sigma^2_{(O/D)}$)

$$\sigma^2_{(V/D)} = \sigma^2_{(O/D)} - \sigma^2_{(O/V)} \tag{11}$$

In our application the block represents a well, the point grades will be core samples within each well, and the deposit will correspond to the reservoir. With this analogy, Krige's relationship will be

$$s^2_{areal} + s^2_{vert} = \sigma^2 \tag{12}$$

Figure 6 illustrates how each variance behaves with λ_{x_D} increasing from 0.1 to 100, when σ^2 equals 1, an exponential model is used, and $\lambda_{z_D} = 0.8$. The sum of s^2_{areal} and s^2_{vert} is constant and equals the value expected from Krige's relationship for all values of λ_{x_D}. The agreement between Eq. 12 and the numerical response is very good. The good agreement between analytical and numerical solutions indicates that the dependence on sample number is small.

The chart in Fig. 6 reveals, also, how both s^2_{areal} and s^2_{vert} behave with increasing λ_{x_D}. As described above, for small λ_{x_D}, s^2_{areal} reaches a maximum and s^2_{vert} a minimum. As λ_{x_D} becomes greater than one, s^2_{areal} declines while s^2_{vert} rises. For very large values of λ_{x_D}, the horizontal autocorrelation is so large that s^2_{areal} tends to zero while s^2_{vert} approaches the population variance (σ^2).

Krige's equation also provides an alternative way to develop the relationships expressed in the charts of Figs. 3 to 5. Knudsen and Kim (1978) showed that, using the definition of the autocovariogram (Cov(h)), the areal variance could be calculated by

$$\sigma^2_{(V/D)} = \frac{1}{V^2}\int_V\int_V \mathrm{Cov}(h)\,dv\,dv \tag{13}$$

where h stands for the distance between any two points in the volume V, and the above integrals represent an integration over a volume. However, the amount of effort to be spent in these integrations is excessive, which motivated us to adopt the numerical approach using MDM.

Discussion Here we discuss the results and interpret some features of the type charts. The differences in results among the three semivariogram models are related with the degree of autocorrelation that each model incorporates. As s^2_{areal}/s^2_{vert} represents a ratio between two variances, the effect of the autocorrelation model will depend on which of the variances controls the final result. One way to illustrate this effect is by plotting the dependence of $\sigma^2_{areal}/\sigma^2_{vert}$ on the Hurst coefficient for the truncated fractal model. This parameter represents the degree of autocorrelation among data.

Figure 7 shows how s^2_{areal}/s^2_{vert} can vary with H and λ_{x_D}, for $\lambda_{z_D} = 1$. For instance, considering a reservoir strongly autocorrelated in the horizontal direction ($\lambda_{x_D} = 100$), the larger the H, the smaller will be s^2_{areal}/s^2_{vert}. However, when dealing with smaller values of λ_{x_D}, the behavior of the vertical variance will control the ratio s^2_{areal}/s^2_{vert}. Therefore, as H increases, s^2_{areal}/s^2_{vert} also increases.

The charts in Figs. 3 to 5 also show that s^2_{areal}/s^2_{vert} increases when λ_{z_D} is greater than 0.1. However, in the horizontal direction, s^2_{areal}/s^2_{vert} decreases very slowly with the vertical autocorrelation until λ_{x_D} reaches 1.0. This behavior is the same for all three semivariogram models and shows that a field with $\lambda_{x_D} = 1$ will behave similarly to an uncorrelated field in this direction. This result is a consequence of the fact that s^2_{areal} depends strongly on horizontal autocorrelation only for ranges greater than the interwell spacing. Ranges smaller than one have only a slight effect on s^2_{areal}. This observation also illustrates that, as expected, it is impossible to estimate ranges smaller than the well spacing ($\lambda_{x_D} < 1$).

One limitation of this method is the variability of s^2_{areal}/s^2_{vert} among the 50 realizations. Figure 8 expresses how the results for $\lambda_{z_D} = 0.1$ and 0.5, obtained from the exponential model, vary with λ_{x_D}. The figure shows the average of 50 realizations and also curves representing plus or minus one standard deviation about the mean. The estimate of λ_{x_D} is more precise when it is large.

APPLICATION

We chose data from a particular field to demonstrate how the procedure works. The results represent an illustration of the method rather than a comprehensive analysis of the reservoir. A complete analysis requires additional effort and integration among geologists and reservoir engineers to interpret the results in the light of all the knowledge about the field.

We applied the procedure to the El Mar field, located in the Delaware Basin of West Texas and New Mexico (Fig. 9). This unit is currently operated by Burlington Resources Co.

The El Mar This field is located 30 km north of Mentone, Texas. The entire field covers approximately 40 km^2 with two-thirds of the field located in the western portion of Loving County, Texas, and the remainder in southwest Lea County, New Mexico. In this study, we investigated only the data from the El Mar (Delaware) Unit, which covers an area of 5 by 8 km and contains 175 wells.

The primary producing horizon is the Ramsey sand, which is composed of an upper "A" sand and a lower "B" sand separated by a shale laminae. These sandstones were deposited in deep water, probably by submarine-fan complexes formed by turbidity-current deposition during lowstands of sea level. Dutton *et al.* (1996) discuss this and other alternative models of Delaware sandstone deposition. The Ramsey formation lies at an average producing depth of 1500 m and the formation's weighted average porosity and permeability are, respectively, 23 % and 22 md. A description of other petrophysical properties of the Delaware Formation can be found in Jenkins (1961).

The difficulty in estimating the water saturation caused a large number of cored wells to be taken. This made it possible to find several cored wells aligned in the orthogonal directions of the field, leaving it in a favorable condition to perform the present analysis. We selected six wells aligned in the north-south direction and two more in the east-west, totaling three in this direction.

We selected the data from the eight wells and built a vertical semivariogram of Y for each. Most of the data analyzed were from Unit A because of the predominance of this unit in this part of the field. Our approach was to separate the data from both units, because they seem to have different petrophysical properties. We performed the analysis only for Ramsey A, since the amount of data for Ramsey B was less; only two wells, 1814 and 1824, have data that include core samples from both Units A and B. We later comment on the difference in the results if data from both units were grouped together for the analysis.

The goal here was simply a practical demonstration of the method. Therefore, we assumed that there were no problems concerning data acquisition and the further analysis was based on the semivariograms constructed with primary data. We also did not consider the possibility of nugget effects in the semivariogram fitting.

The procedure outlined above was performed to calculate the average values and the s^2_{areal} and s^2_{vert} for each set of data. To calculate λ_z, the experimental semivariograms must be fitted by a theoretical model. The difficulties and the importance of this step are well described in the literature by several authors, including Journel and Huijbregts (1978), Isaaks and Srivastava (1989), and Olea (1994).

Estimating λ_{z_D} We tested three different semivariogram models, trying to find the one that best described the experimental data.

The spherical semivariogram fit was considered poor. The second model tested was the truncated fBm fractal or power-law model. For the fitting, a value of H = 0.15 gave a better adjustment than the value of H = 0.25. Therefore, a new set of curves for the fractal model, analogous to the ones in Fig. 5, was generated for H = 0.15. The final result was better than the spherical fitting for most wells. The exponential model gave a fit close to that obtained with the fractal for most wells and reproduced a similar response for the ones in which the spherical model worked better. The results are summarized in Table 1 for the East-West (EW) section and in Table 2 for the North-South (NS) section. The average ranges in the vertical direction calculated with the spherical, exponential and fractal models were, respectively, 0.19, 0.08 and 0.32 for the EW direction, and 0.22, 0.10 and 0.33 for the NS direction.

Estimating λ_{x_D} Using these results and the ratio s^2_{areal}/s^2_{vert} for each direction, we enter the charts and interpolate λ_{x_D}, as shown in Fig. 10. The results shown in Table 3 for the spherical, exponential and fractal are, respectively, $\lambda_{x_D}\big|_{EW}$ = 1.2, 1 and 3, and $\lambda_{x_D}\big|_{NS}$ = 4, 2 and 6.

The results show anisotropy in the autocorrelation pattern of the El Mar field, at least along the directions indicated. The permeability range in the NS direction is at least twice that in the EW direction. This behavior roughly coincides with the depositional characteristic of the field, since the major axis of the turbidite channel is aligned with the northeast-southwest direction (Fig. 9).

A less rigorous approach would be to group the data from both units A and B together, instead of performing the analysis only for Unit A. Additional data from two wells (1814 and 1824) need to be considered. Since the wells in the EW section do not contain the Ramsey B sand only results from the NS section will change. The main difference is that the value of s^2_{areal} changes from 0.23 to 0.36, making s^2_{areal}/s^2_{vert} = 0.18 instead of 0.12. This change would led to the conclusion that the ranges were similar in both directions, in conflict with the depositional

pattern. This illustrates the importance of prior geological analysis of the data to be used in making the estimation.

Final Remarks The autocorrelation analysis of the El Mar field shows that answers obtained by using different semivariogram models can be different. These results were expected, since each model uses a different approach. Even when using the same model, different interpretations of the semivariogram data can lead to different values of horizontal autocorrelation. Although this seems a little strange at first, it may not have a great effect on a simulated flow response. Indeed, Fogg *et al.* (1991) referred to a study in which two ranges of 120 and 390 m caused significantly different permeability patterns but practically identical cumulative oil recoveries and water-oil rates, when used in simulation.

When calculating the data to construct the charts in Figs 3 to 5 we also derived a chart to correct the vertical variance, measured at the wells, to the value that should be used in conditional simulation studies. Recall that the vertical variance measured at the wells will be equal to the population variance only when there is no autocorrelation. Figure 11 shows how s^2_{vert}/σ^2 varies with λ_{z_D} and λ_{x_D}. The more vertically autocorrelated the permeability field is, the more the s^2_{vert} is different from σ^2.

Figure 12 shows an analogous result but expressed as the Dykstra-Parsons coefficient instead of the variance. To express the variance in terms of the V_{DP}, the chart is no longer general and depends on the population V_{DP}. Figure 12 considered a $V_{DP\,pop}$ of 0.9.

These charts can be used to correct data for input into stochastic simulation. For instance, from Fig.12, we can conclude that a sample V_{DP} of 0.85 ($s^2_{vert} = 3.6$) calculated from a reservoir with $\lambda_{z_D} = 0.3$ and $\lambda_{x_D} = 1.0$, given by the exponential model, will have a population $V_{DP\,pop} = 0.9$ ($\sigma^2 = 5.3$).

SUMMARY AND CONCLUSIONS

We developed a set of charts for estimating autocorrelation in the horizontal direction based on the ratio of areal-to-vertical variances, the vertical autocorrelation and the type of semivariogram model used.

The procedure was partially validated through a comparison of results; analytical solutions were available for some limiting situations. A field case was analyzed to demonstrate how the method can be applied. Data from eight wells in the El Mar field, Ramsey A sand, were used to estimate horizontal autocorrelation for two directions of the field.

Results from the El Mar analysis point out the anisotropy in the permeability distribution of this field. The autocorrelation ranges in the vertical direction were found to be between 0.1 and 0.3 of the sampled interval, depending on the type of model used. The horizontal range in the north-south direction varied between 2 and 6 times the mean well spacing, being at least twice the autocorrelation in the east-west direction. These results can be used in conditional simulations to generate the expected permeability pattern of this field.

The present approach seems to be an effective tool to be used, along with the geological knowledge of the facies continuity, for estimating the autocorrelation for the interwell region between vertical wells.

NOMENCLATURE

a	=	semivariogram range
Cov	=	covariance
D	=	mining deposit
E	=	expectation value
h	=	distance lag
H	=	Hurst coefficient
	=	reservoir thickness
k	=	permeability
N_l	=	number of layers
N_R	=	number of realizations
N_w	=	number of wells
O	=	point grades
s^2	=	estimation of the variance
V	=	volume of a block
V_{DP}	=	Dykstra-Parsons coefficient
Var	=	variance
Y	=	natural logarithmic of the permeability
λ	=	autocorrelation range (general)
	=	range (spherical model)
	=	correlation length (exponential model)
	=	truncated upper cutoff (fractal model)
μ	=	population mean

σ = population standard deviation

σ^2 = population variance

σ^2_{areal} = areal variance

σ^2_{vert} = vertical variance

Subscripts

D = dimensionless variable

EW = east-west direction

NS = north-south direction

O/D = point grades within a mining deposit

O/V = points grades within a block

pop = population values

V/D = blocks within a mining deposit

x,y,z = Cartesian coordinate directions

ACKNOWLEDGEMENTS

This work was supported, in part, by the Enhanced Oil Recovery Research Program of the Center for Petroleum and Geosystems Engineering at The University of Texas. Jorge Pizarro's support is provided by Petrobrás S.A.. Larry W. Lake holds the W.A. (Tex) Moncrief Centennial Chair. We thank Dr. I.H. Silberberg for his editorial comments and John Barnes with Burlington Resources for supplying the core data on the El Mar (Delaware) Unit.

REFERENCES

Dutton, S. P., Hovorka, S. D. and Cole, A. G.: "Application of Advanced Reservoir Characterization, Simulation, and Production Optimization Strategies to Maximize Recovery in Slope and Basin Clastic Reservoirs, West Texas (Delaware Basin)," Bureau of Economic Geology, The University of Texas at Austin (1996).

Fogg, G.E., Lucia, F.J. and Senger, R.K.: "Stochastic Simulation of Interwell-Scale Heterogeneity for Improved Prediction of Sweep Efficiency in a Carbonate Reservoir," *Reservoir Characterization II*, L. W. Lake, H. E. Carroll and T. C. Wesson (eds.), Academic Press, New York (1991).

Haldorsen, H.H.: "Simulation Parameter Assignment and the Problem of Scale in Reservoir Engineering," *Reservoir Characterization*, L. W. Lake and H. E. Carroll (eds.), Academic Press, New York (1986)

Hewett. T. A., "Fractal Distributions of Reservoir Heterogeneity and Their Influence on Fluid Transport," paper SPE 15386 presented at the 1986 Soc. Pet. Eng. Annual Tech. Conf. and Exhibition, New Orleans, LA, Oct. 5-8.

Isaaks, E. H. and Srivastava, R. M.: *Applied Geostatistics*, Oxford University Press, New York 1989.

Jenkins, R.E.: "Characteristics of the Delaware Formation," *J. Pet. Tech.* (Dec. 1961), 1230-1236.

Jensen, J.L., Hinkley, D.V. and Lake, L.W.: "A Statistical Study of Reservoir Permeability: Distributions, Correlations, and Averages," *SPE Formation Evaluation* (1987) **2** 461-468.

Jensen, J.L., Lake, L.W., Corbett, P.M.W. and Goggin, D.J.: *Statistics for Petroleum Engineers and Geoscientists*, PTR Prentice Hall, Englewood Cliffs, New Jersey (1996).

Journel, A. G. and Huijbregts, CH. J.: *Mining Geostatistics*, Academic Press, New York (1978).

Knudsen, H. P. and Young C. Kim. : "A Short Course on Geostatistical Ore Reserve Estimation," Department of Mining and Geological Engineering, College of Mines, The University of Arizona, Tucson, AZ (1978).

Lambert, M.E.: "A Statistical Study of Reservoir Heterogeneity," M.S. thesis, The U. of Texas at Austin (1981).

Lasseter, T. J., Waggoner, J. R., Lake, L. W.: "Reservoir Heterogeneities and Their Influence on Ultimate Recovery," *Reservoir Characterization* , L. W. Lake and H. E. Carroll (eds.), Academic Press, New York (1986)

Lemouzy, P. M., Parpant, J., Eschard, R., Bachiana, C., Morelon, I., Smart, B.: "Successful History Matching of Chaunoy Field Reservoir Behavior Using Geostatistical Modeling," paper SPE 30707 presented at the 1995 Soc. Pet. Eng. Annual Tech. Conf. and Exhibition, Dallas, TX, Oct. 22-25.

Lucia, F.J. and Fogg, G.E.: "Geologic/Stochastic Mapping of Heterogeneity in a Carbonate Reservoir," paper SPE 19597 presented at the 1989 Soc. Pet. Eng. Annual Tech. Conf. and Exhibition, San Antonio, TX, Oct. 8-11.

Neuman, S. P.: "Generalized Scaling of Permeabilities: Validation and Effect of Support Scale," *Geophysical Research Letters* (March 1994), **21**, 5, 349-352.

Olea, R. A.: " Fundamentals of Semivariogram Estimation, Modeling, and Usage," *Stochastic Modeling and Geostatistics*, J. M. Yarus and R. L. Chambers (eds.), AAPG (1994).

Pizarro, J. O. S.: Ph.D. dissertation in progress, The University of Texas at Austin (1996).

Srivastava, R. M.: "An Overview of Stochastic Methods for Reservoir Characterization," *Stochastic Modeling and Geostatistics*, J. M. Yarus and R. L. Chambers (eds.), AAPG (1994).

Yang, A. P.: "Stochastic Heterogeneity and Dispersion," Ph.D. dissertation, The U. of Texas at Austin (1990).

Table 1. Summary of results for the East-West cross section of the El Mar field.

	WELLS			
	1514	1513	1512	AVERAGE
Average of Ln (k) in vertical direction	1.15	2.25	2.17	1.86
Variance of Ln (k) in vertical direction	1.96	2.44	2.81	2.40
Vertical correlation range with spherical model	0.21	0.18	0.17	0.19
Vertical correlation length with exponential model	0.09	0.07	0.08	0.08
Vertical truncated upper cutoff with fractal model (H=0.15).	0.35	0.26	0.34	0.32

Table 2. Summary of results for the North-South cross section of the El Mar field.

	WELLS						AVERAGE
	1514	1524	1534	1532	1814	1824	
Average of Ln (k) in vertical direction	1.15	1.89	2.37	2.40	1.85	1.58	1.87
Variance of Ln (k) in vertical direction	1.96	1.47	0.46	2.09	4.00	1.71	1.95
Vertical correlation range with spherical model	0.21	0.20	0.23	0.20	0.22	0.24	0.22
Vertical correlation length with exponential model	0.09	0.08	0.12	0.09	0.11	0.11	0.10
Vertical truncated upper cutoff with fractal model (H=0.15)	0.35	0.28	0.30	0.34	0.42	0.30	0.33

Table 3. Summary of the results from autocorrelation analysis of the El Mar field.

SUMMARY	NORTH-SOUTH	EAST-WEST
Areal variance	0.23	0.37
V_{DP} areal	0.46	0.46
Vertical variance	1.95	2.40
V_{DP} vertical	0.75	0.79
Ratio areal/vertical variances	0.12	0.15
λ_{x_D} (Spherical model)	4	1.2
λ_{x_D} (Exponential model)	2	1
λ_{x_D} (Fractal model)	6	3

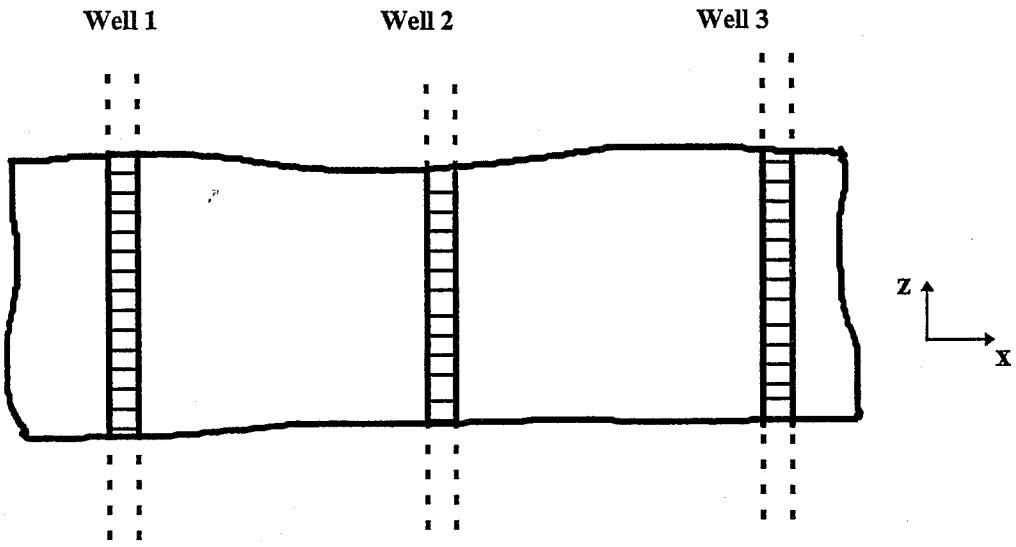

Figure 1. An idealized cross section (x,z) penetrated by vertical wells.

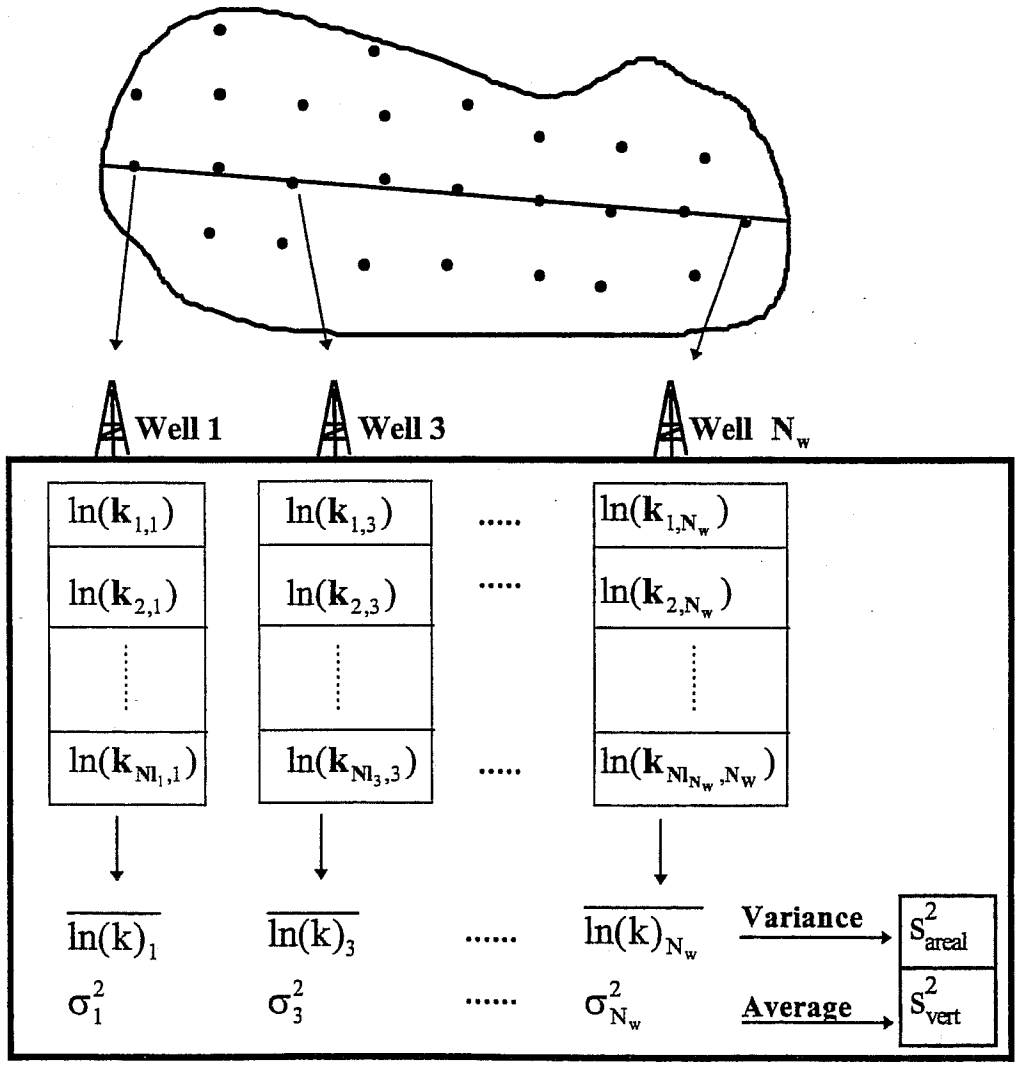

Figure 2. Schematic of the procedure to calculate the areal and vertical variances.

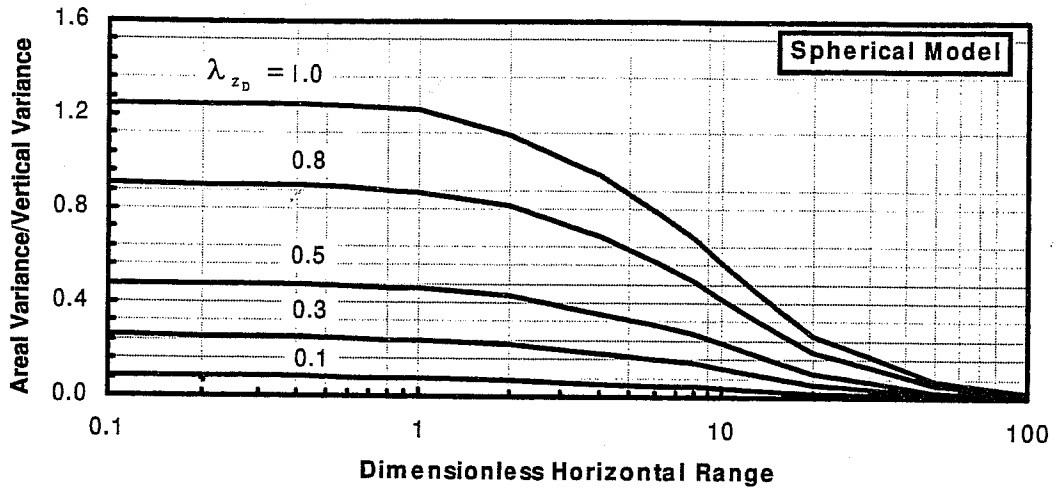

Figure 3. Autocorrelation chart for spherical semivariogram model obtained from 50 realizations.

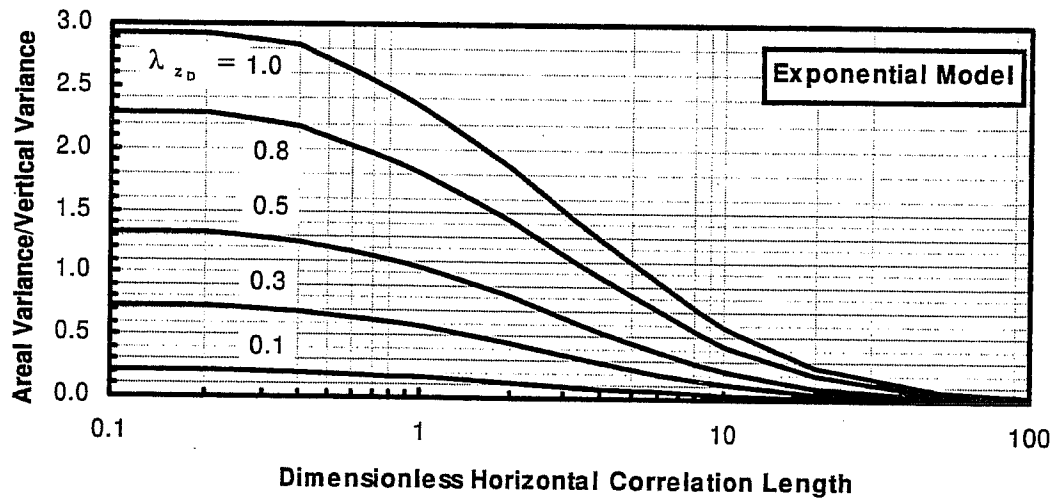

Figure 4. Autocorrelation chart for exponential semivariogram model from 50 realizations.

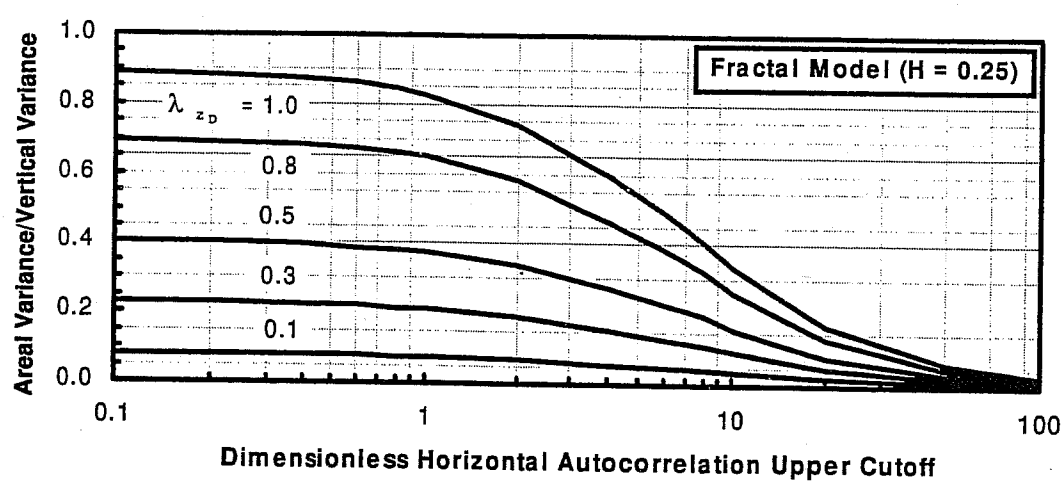

Figure 5. Autocorrelation chart for fractal semivariogram model obtained from 50 realizations.

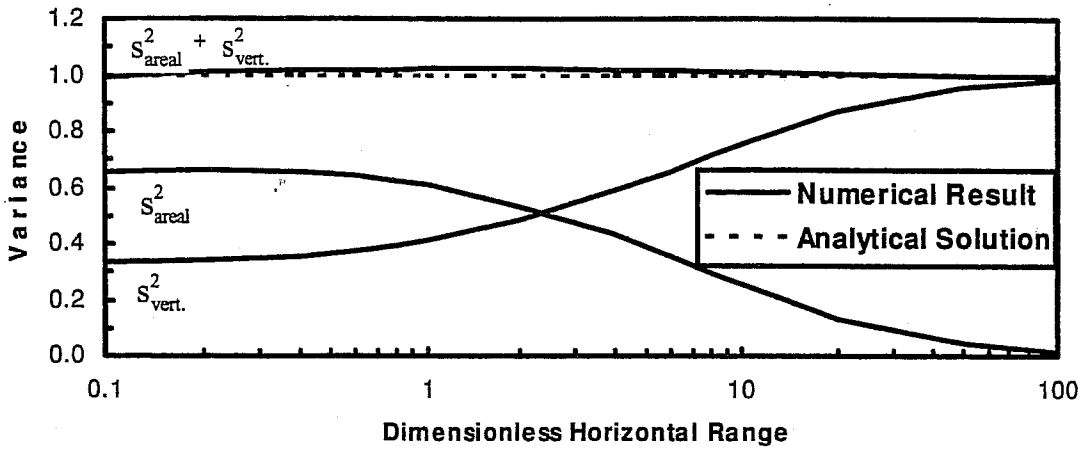

Figure 6. Analytical validation (exponential model, λ_{z_D} = 0.8, and 50 realizations).

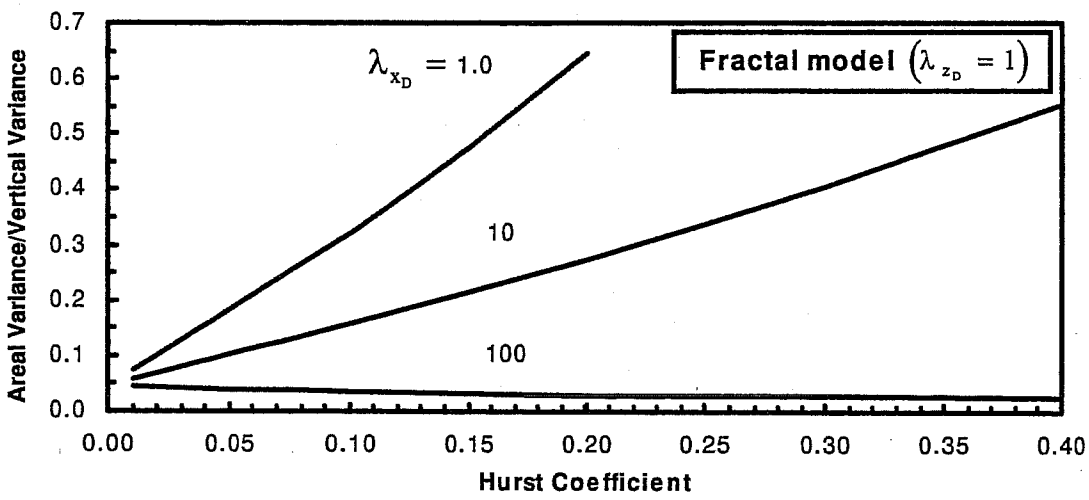

Figure 7. Estimation of s^2_{areal} / s^2_{vert} sensitivity to the Hurst coefficient for different truncated ranges.

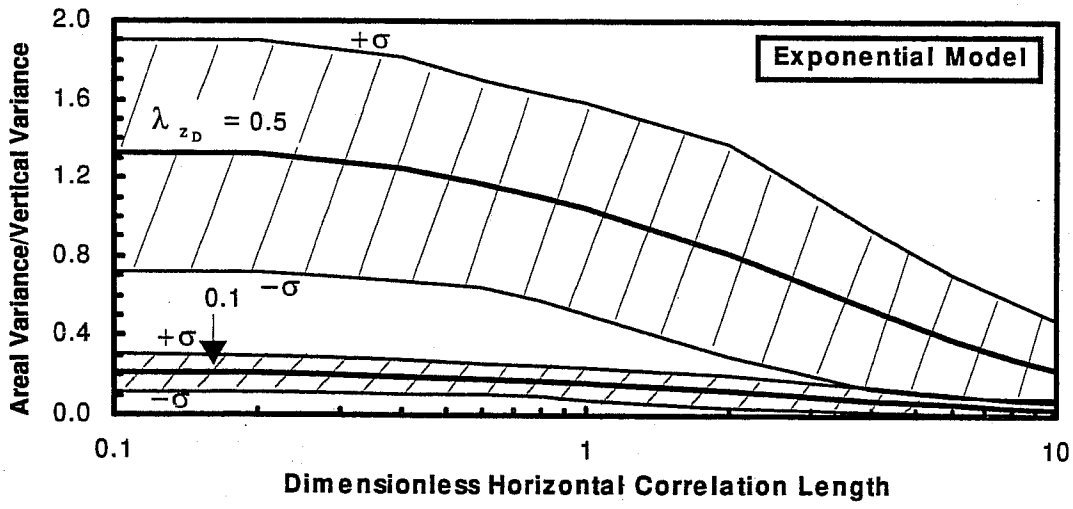

Figure 8. Variability (expressed as ± 1 standard deviation) of s^2_{areal} / s^2_{vert} among the 50 realizations.

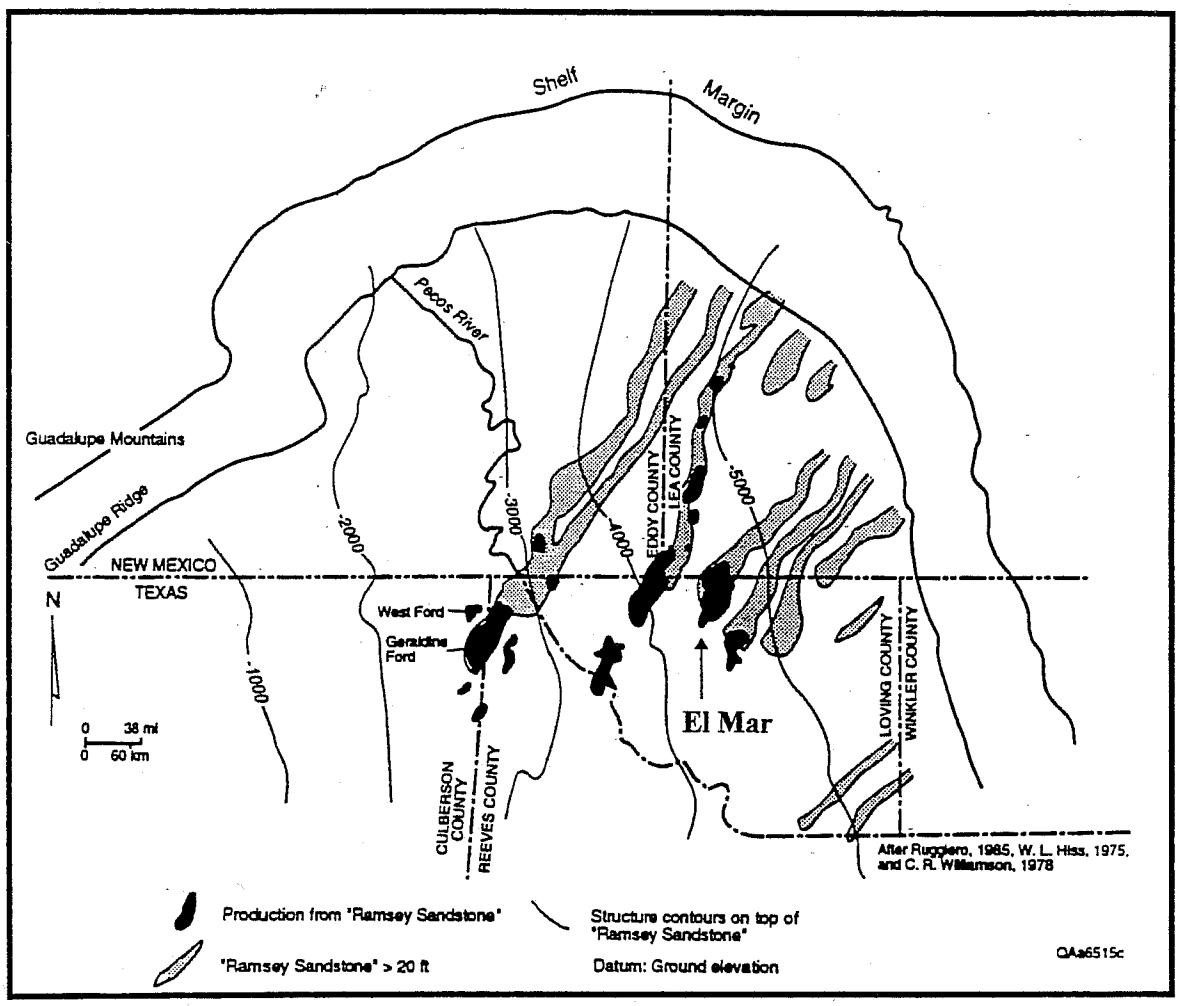

Figure 9. Map of the Delaware basin (from Dutton *et al.* (1996)).

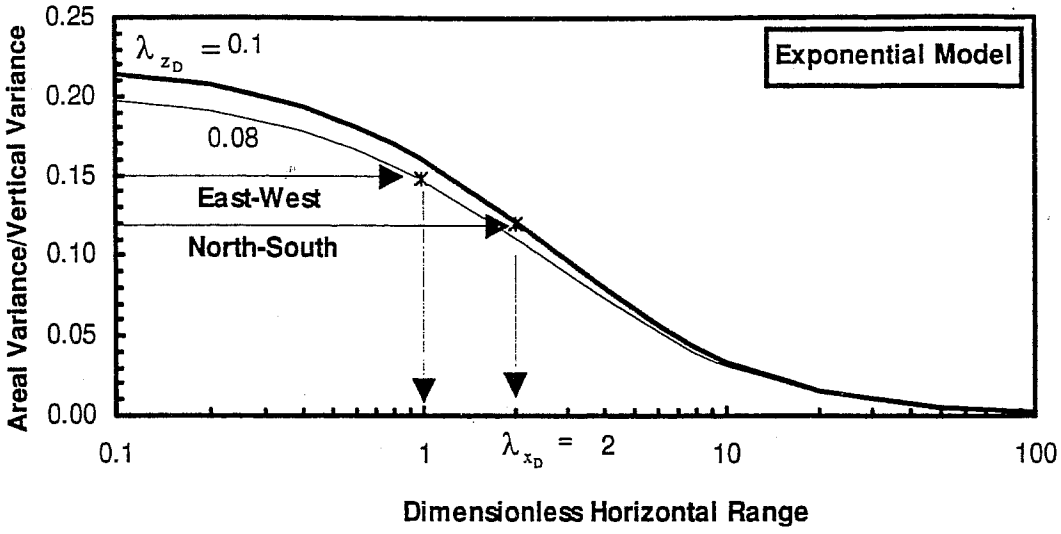

Figure 10. Determining λ_{x_D} for the North-South and the East-West sections of El Mar field.

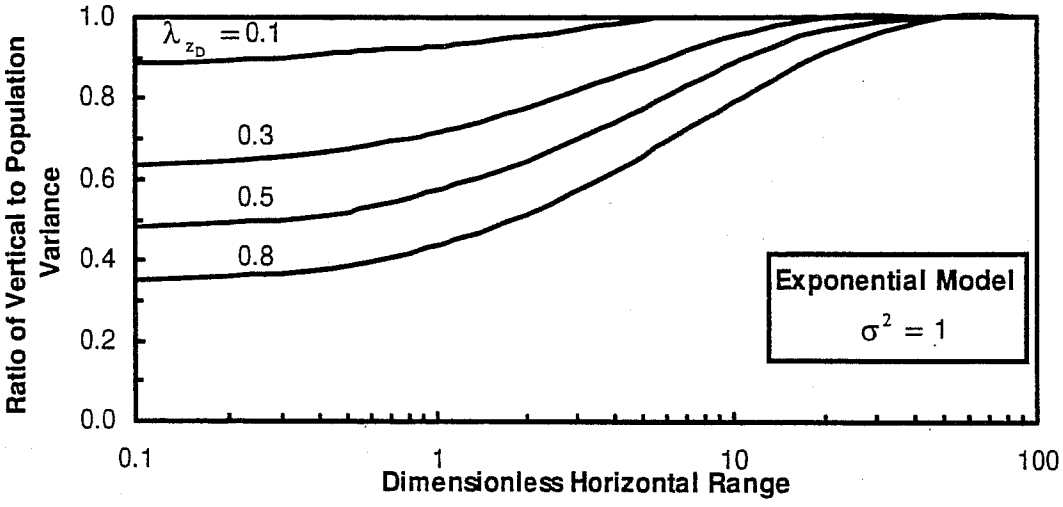

Figure 11. Differences between the vertical (sample) and population variance caused by autocorrelation.

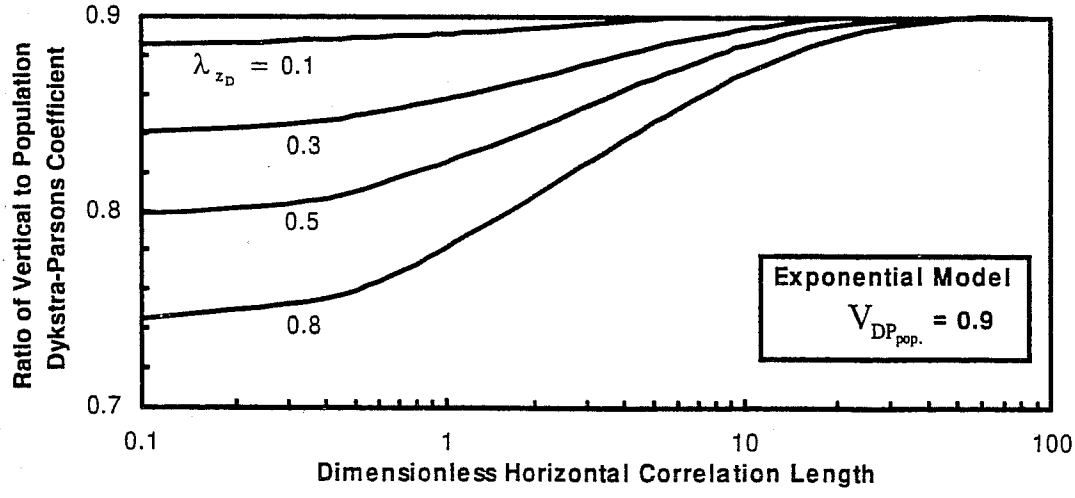

Figure 12. Differences between the vertical (sample) and population V_{DP} caused by autocorrelation

EXTRACTING MAXIMUM PETROPHYSICAL AND GEOLOGICAL INFORMATION FROM A LIMITED RESERVOIR DATABASE

Maqsood Ali, Adwait Chawathé, Ahmed Ouenes, Martha Cather, and William. W. Weiss

New Mexico Petroleum Recovery Research Center
New Mexico Institute of Mining and Technology
Socorro, New Mexico

ACKNOWLEDGMENTS

This research was funded by the Department of Energy (contract no. DE-AC22-93BC14893), State of New Mexico, Landmark Graphics Corporation (Halliburton), Texaco and Yates Petroleum. The authors greatly appreciate the financial support.

ABSTRACT

The characterization of old fields lacking sufficient core and log data is a challenging task. This paper describes a methodology that uses new and conventional tools to build a reliable reservoir model for the Sulimar Queen field. At the fine scale, permeability measured on a fine grid with a minipermeameter was used in conjunction with the petrographic data collected on multiple thin sections. The use of regression analysis and a newly developed fuzzy logic algorithm led to the identification of key petrographic elements which control permeability. At the log scale, old gamma ray logs were first rescaled/calibrated throughout the entire field for consistency and reliability using only four modern logs. Using data from one cored well and the rescaled gamma ray logs, correlations between core porosity, permeability, total water content and gamma ray were developed to complete the small scale characterization. At the reservoir scale, outcrop data and the rescaled gamma logs were used to define the reservoir structure over an area of ten square miles where only 36 wells were available. Given the structure, the rescaled gamma ray logs were used to build the reservoir volume by identifying the flow units and their continuity. Finally, history-matching results constrained to the primary production were used to estimate the dynamic reservoir properties such as relative permeabilities to complete the characterization. The obtained reservoir model was tested by forecasting the waterflood performance and which was in good agreement with the actual performance.

INTRODUCTION

In an ideal situation, the data required for detailed reservoir characterization range from regional to field-scale to small-scale, and consist of lithological description, petrophysical properties, fluid properties, well-test, production, and pressure data. Optimal data density is also crucial in addition to the variety and quality of data, and is governed by the type and scales of heterogeneity. Adequate data density is needed so that statistically significant conclusions can be drawn. However, in actual reservoir characterization problems neither all types of data nor the appropriate data density may be available.

A large number of oil and gas fields developed prior to 1970's lack modern logs as well as sufficient core material. The economic constraints and risks involved prohibit both small and large operators from spending large sums of money on drilling new wells, coring, logging, and running special well test operations in these old

fields. The characterization of such fields using available information is a challenging task, and no proven methodology is available in the industry. Also, the production data available from these fields are sometimes not reliable. Under these circumstances the simulation/history-matching process may result in petrophysical properties (porosity, permeability, relative permeabilities, etc.) far removed from reality.

This paper describes the methodology employed for the reservoir characterization of an old field - the Sulimar Queen. This field is deficient in core material, modern logs, and complete production data. The Sulimar Queen field is located in the Chaves County, southeast New Mexico (Figure 1). The reservoir is present in the upper Queen Formation called the "Shattuck Member". The Shattuck member was deposited in mixed lagoonal-sabkha-eolian environment, is internally complex and can only be successfully exploited if the distribution of individual porosity and permeability units within the reservoir is clearly understood.

For the characterization of the field, the only control points available consisted of *one core, core reports from two wells, and modern log suites from four wells.* From the rest of the field only *old gamma ray and neutron logs* were available. Neutron logs, because of their wide scale ranges and anomalous high and low porosity values, were discarded and were not used in this study (Ali et al., 1996). Two additional cores were obtained from the adjacent fields, and additional outcrop studies were conducted to supplement the database (Figure 1). Cores and logs from the adjacent fields were collected to capture the regional trend, so that the relationships developed in the Sulimar Queen field could be verified.

SMALL-SCALE HETEROGENEITY STUDY

The first objective was to analyze the scale of heterogeneity in the vertical direction from the available cores. Permeability measurements were made using a computer controlled minipermeameter (Suboor and Heller., 1995), and approximately 5,000 permeability measurements were made. Permeability measurements were made on a square grid with an interval of 12.5 mm, which created five vertical permeability profiles along the length of the core. The average of the five profiles for the three cores are shown in Figure 2 (also refer to Figure 3). The permeability varied from less than 0.1 md to 500 md, and the scale of permeability heterogeneity was the same for three cores (Figure 2). This similarity suggested that the vertical permeability heterogeneity in the Sulimar Queen and adjacent fields may be caused by the same depositional and diagenetic events. This regional trend provided the first confirmation of the assumption that the data from the adjacent fields may be used.

The producing zone of the Shattuck member consists of greenish brown, greenish gray, gray, brown, red, very fine-grained sandstone. It is bounded at the top and the bottom by anhydrite (Figure 2). The permeability heterogeneity is caused by minor changes in the depositional environment. Minor changes in the lithology are evident from the changes in the permeability (Figure 2). Permeability measurements made on a smaller-scale also improved the lithologic description of the core. On the basis of permeability distribution, the reservoir was divided into two separate layers, an upper high permeability layer (zone 1) with one low permeability subzone (subzone A) and a lower tighter layer (zone 2) as illustrated in Figure 2.

Improving the quantity and quality of petrographic data:

The problem was to collect enough samples for the petrographic analysis, so that the control of petrographic elements such as porosity types, pore morphologies, mineralogy, textures, and type, amount, and distribution of clay and cement in creating permeability heterogeneity can be determined. Conventionally,

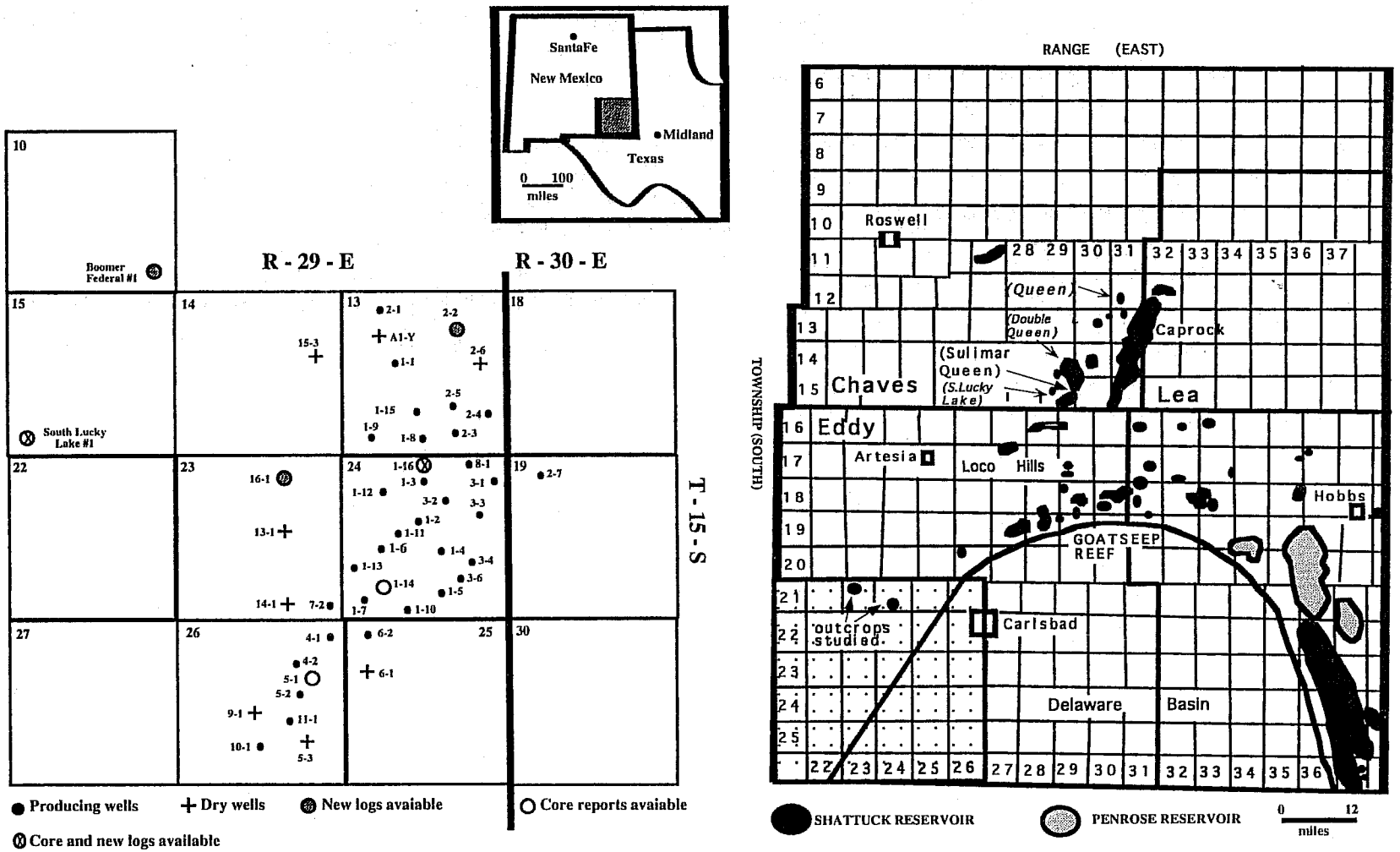

Figure 1: Showing the locations of the Sulimar Queen, South Lucky lake, Queen, and other Queen fields field and the outcrops relative to Goat Seep Reef. Distribution of the wells in the Suliamr Queen field is also shown.

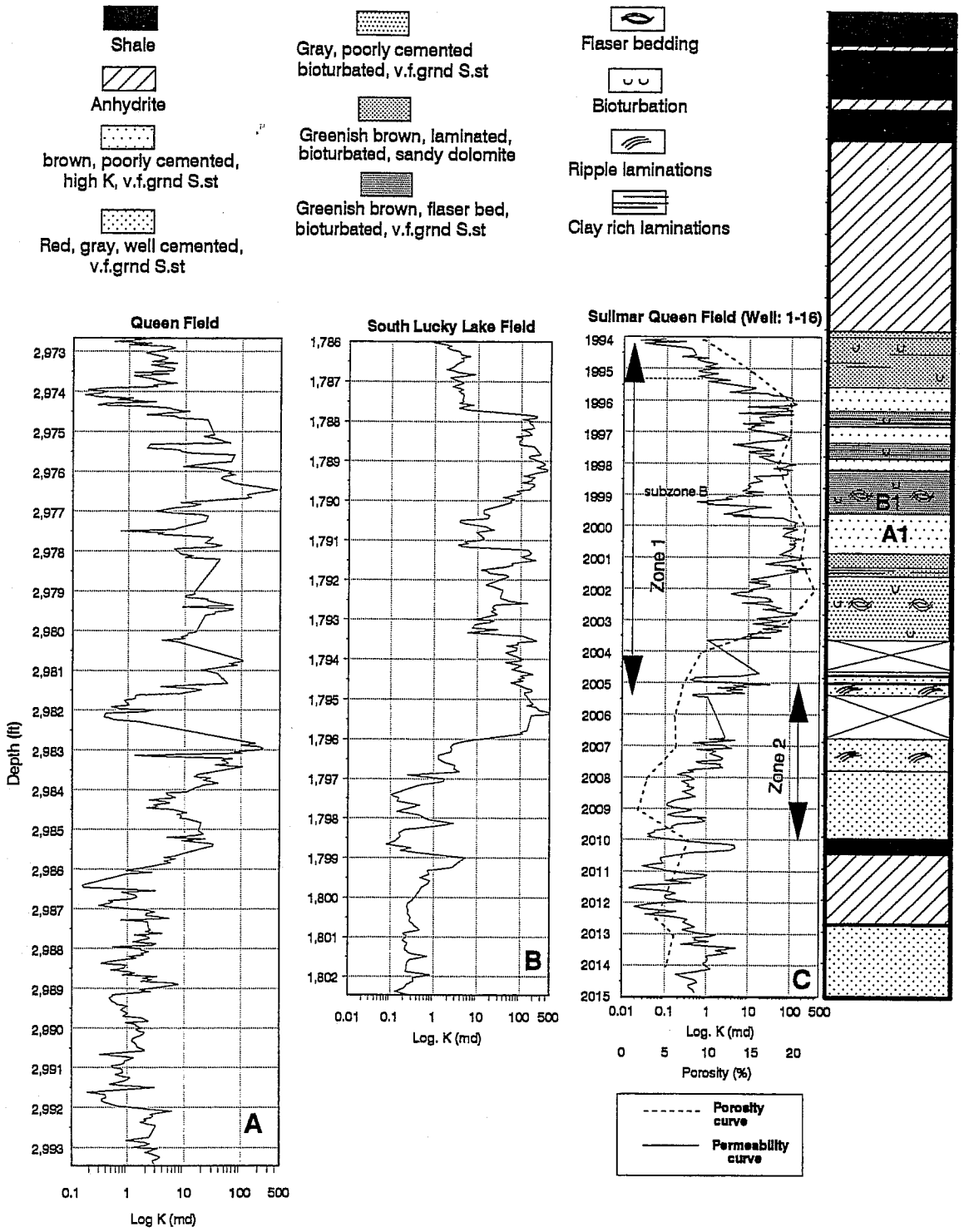

Figure 2: Permeability distribution in the cores from Queen (A), South Lucky Lake (B), and Sulimar Queen field (C). Core description from the Sulimar Queen field is also shown along side the permeability distribution. Note the similar permeability distribution especially between South Lucky Lake (B) and Sulimar Queen field (C).

relationships between permeability and petrographic elements are determined by using core plugs and thin sections, but there is a large difference in their respective volumes of investigation. Permeability varies from point to point within most core plugs. Therefore, a thin section prepared from the edge of that core plug may not contain the petrographic elements that are representative of the core plug's permeability. Consequently, such correlations may be misleading. Because of the destructive nature and the size, core plug analysis also restricts the detailed investigation of permeability heterogeneities on small-scale, especially in sedimentary structures with dimensions less than 2.5 cm. In the Shattuck member, permeability heterogeneities exist on a small-scale (Figure 2) and the whole range of permeability distribution cannot be sampled using core plugs. A new methodology was developed by utilizing a fine scale grid (on which permeability measurements were made with a minipermeameter) based on the premises that: (1) the area of investigation of minipermeameter is very small and can be examined in thin sections, and (2) each thin section contains many permeability points (Figure 3). The advantage of collecting a large set of data points is that detailed statistical analyses can be done and the effects of each petrographic element on permeability can be determined. This, also, helps assess the effects of diagenesis and porosity evolution on permeability more accurately.

According to Goggin et al. (1988), the effective radius and depth of investigation of a minipermeameter probe tip is four times the internal radius of the probe tip. However, it was found during the calibration and permeability measurements with the minipermeameter, the area immediately under and around a probe tip exerts the main control over the permeability. After careful examination, it was decided that, for a probe tip with inner radius of 0.125 inches (3.125 mm), the area of the thin section to be analyzed should have a diameter of 0.4 inches (10 mm). Depending on the number of permeability points located on each thin section, the thin section was divided into that many equal parts and petrographic data was collected from each part separately (Figure 3). With this new method, data equivalent to 7 thin sections on the average, were collected from one thin section which would not have been possible using the conventional core plugs. The minipermeameter, in addition to providing large amount of permeability data and resolving small-scale heterogeneity, also provided the opportunity to collect more petrographic data using few thin sections. Because of the similarity of the areas of investigation of both, the thin sections and the minipermeameter, the correlations established between permeability and petrographic elements were also more accurate than the correlations obtained from conventional core plugs.

Petrographic Analysis:

Thirty-eight thin sections were made from the cores and total of 267 data points were obtained. The petrographic elements collected for each permeability point were: total porosity, total secondary porosity, secondary intergranular porosity, microporosity, intraconstituent porosity, moldic porosity, microfractures, quartz, feldspar, rock fragments, anhydrite, dolomite, detrital clay, dead oil, pore size, grain size, grain sorting, pore sorting, and pore interconnection. Detailed petrographic analysis also helped determine the paragenetic sequence, porosity evolution, and the depositional environment. A generalized paragenetic sequence is shown in Figure 4. Petrographic analysis was done to establish the ranking of each petrographic element in controlling the permeability. In addition to simple regression analysis, a newly developed fuzzy logic algorithm was also used to determine the importance (ranking) of each petrographic elements in controlling the permeability (Table II and Figure 5). Depending on the ranking, the permeability may be estimated by

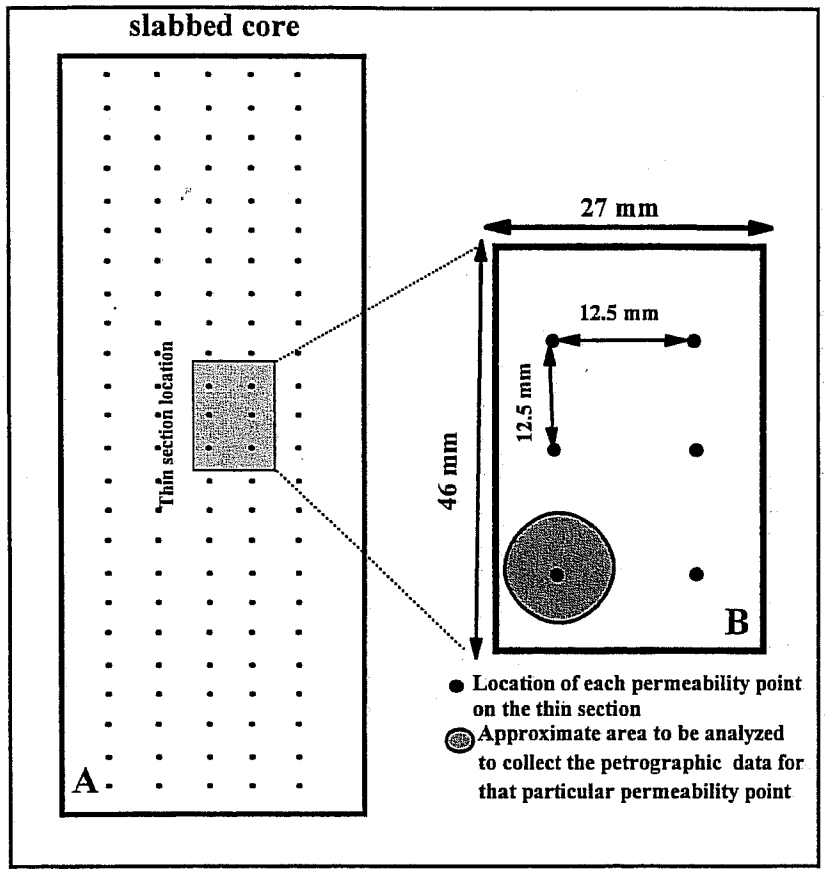

Figure 3: (A) Grid on which permeability measurements were made. Five vertical profiles were generated by this grid. The average of the five profiles is shown in Figure 2. Thin section location is also shown. (B) Distribution of permeability points on the thin section.

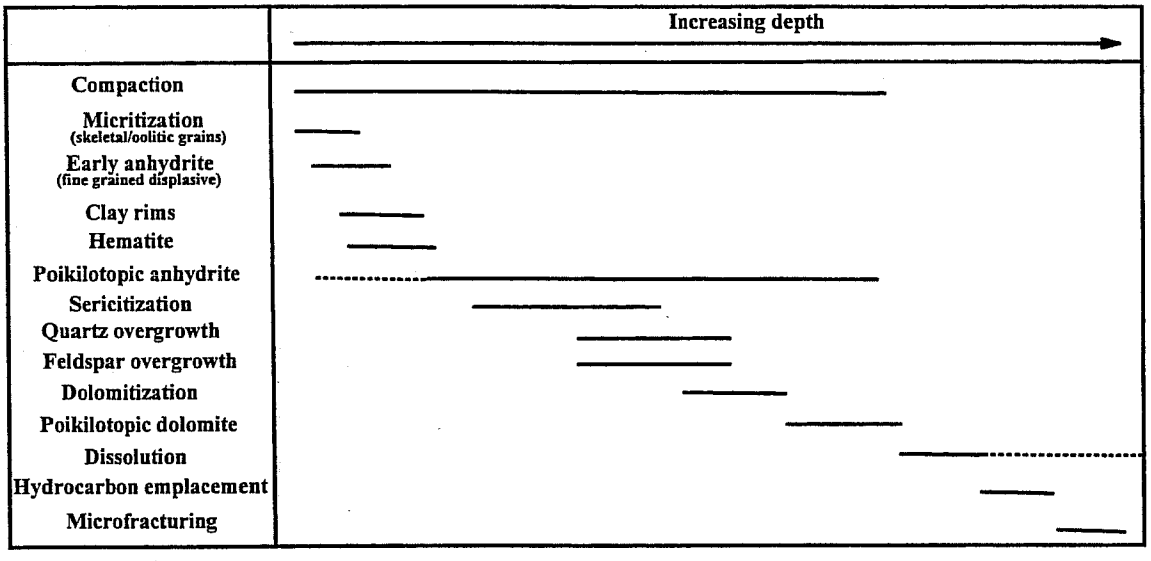

Figure 4: Generalized paragenetic sequence for the Shattuck member, Sulimar Queen Field.

using only the most important petrographic elements. In old fields, where the samples are scarce or not suited for making permeability measurements, thin section analysis may be used to estimate the permeability. The results of the fuzzy logic algorithm were in excellent agreement with conventional regression analysis. The advantage of using this new algorithm lies in the speed of analysis.

The petrographic analysis also indicated that quartz and feldspars are the dominant detrital grains, whereas, anhydrite and dolomite are the dominant cements. Both quartz and feldspar overgrowths are ubiquitous throughout the reservoir but never exceeded 2%. Most of the feldspar grains are altered (sericitized) and majority of the intraconstituent porosity is present among the partially dissolved feldspar grains especially in zone 1. Quartz and feldspar grains are also coated with clay and hematite. These clay rims consist of authigenic chlorite (Haynes, 1978). Hematite is more conspicuous in the low permeability part (zone 2), where it coats the grain and also stains the anhydrite (poikilotopic) cement. Both quartz and feldspar ranked in the middle with respect to controlling the permeability based on the fact that as their percentage increases, the percentage of anhydrite and dolomite cement decreases. The rock fragments consist of clay, dolomite (dolomicrite), and metamorphic rock fragments (zone 1). Rock fragments do not exert much control over the permeability because of their low percentage and fine sand size. Only when clay fragments form the pseudomatrix as they get squeezed between the harder grains, both porosity and permeability are reduced. Detrital clay may have originally been carbonate clay which was diagenetically altered to dolomicrite. Detrital clay (now dolomicrite) could be easily identified due to its exclusive presence in the primary pores. Detrital clays are present in substantial amounts only in the thinly laminated poorly sorted silty sandstone zones not thicker than 2 inches (zone 1). This is the reason why clay does not affect the permeability and is close to the bottom of the conventional ranking (Table I). Cement is present in the form of anhydrite and dolomite. Anhydrite is present in three morphologies: (1) fine crystalline nodules, mainly in the upper silty-shaly zone at the top of the Shattuck Member and in small amounts in zone 2 (Figure 2), (2) coarse, pore filling crystals, and (3) large patches of poikilotopic crystals surrounding several grains. It is the poikilotopic morphology which has affected the permeability especially in zone 2. Dolomite is present in two morphologies: (1) micritic dolomite, probably formed by the dolomitization of the carbonate mud, and (2) large poikilotopic patches. The presence of the inclusions of dolomicrite and anhydrite in the poikilotopic dolomite suggest that poikilotopic dolomite post-dates both of them. Dolomite and anhydrite are distributed in the form of irregular patches (2 - 4 mm in diameter) throughout the reservoir zone. This patchy distribution is probably due to the heterogeneous dissolution pattern. Both dolomite and anhydrite have also replaced the detrital grains. Although, based on the correlation coefficient and fuzzy logic, dolomite seems to more important than anhydrite in controlling permeability, it should be the opposite. This inverse ranking of dolomite and anhydrite is due to a 1.5 ft. thick low porosity and permeability layer of clastic dolomite at the top of the Shattuck Member which contains as much as 50% dolomite. In the rest of the reservoir zone, the amount of dolomite never exceeded 15 %. Because of this biased distribution, dolomite seems to have more control over permeability (Figure 5E). The dead oil present reduced the porosity and the interconnection between the pores and, therefore, its effect on the permeability was also acknowledged.

Among the porosities, the secondary intergranular porosity is the most dominant type and exerts the most influence on the permeability (Table I and Figure 5K). As the dissolution increases, the secondary intergranular porosity increases and the interconnection between the pores becomes good.

Petrographic elements	Amount (Ranges)	Correlation (R^2) with permeability	Correlation (R^2) with total ϕ	Ranking based on the R^2 with permeability
Secondary intergranular ϕ	0 - 27%	0.75	0.91	1
Total Secondary ϕ	0 - 27%	0.71	0.97	2
Total ϕ	0 - 27%	0.70	-	3
Pore size (microns)	0 - 70 µm	0.70	0.81	4
Quartz	0 - 75%	0.47	0.37	5
Feldspar	0 -26%	0.43	0.33	6
Dolomite	0 - 55%	-0.36	-0.26	7
Grain size (microns)	0 - 120 µm	0.30	0.25	8
Intraconstituent ϕ	0 - 3.5%	0.21	0.36	9
Primary ϕ	0 - 4%	0.17	0.20	10
Moldic ϕ	0 - 3%	0.13	0.14	11
Anhydrite	0 - 40%	-0.12	-0.07	12
Dead oil	0 - 11%	0.11	0.09	13
Micro- ϕ	0 - 5.5%	-0.10	-0.03	14
Clay	0 - 21%	-0.06	-0.13	15
Rock Fragments	0 - 9%	0.01	-0.06	16

Table I: Summary of the petrographic elements and their relationship (R^2) with permeability and total porosity. The ranking shows the importance of that petrographic element in controlling the permeability as determined by the conventional regression analysis.

As the amount of secondary porosity increases, so does the pore size. This explains why the pore size is very important in controlling the permeability (Figure 5M). The relationship between the grain size and permeability is not very good (Table I and Figure 5N). The larger size grains are present among the well-sorted part of the reservoir (zone 2) were affected by early anhydrite cementation and almost all the original porosity was lost. The moderately-sorted lagoonal sandstones (zone 1) were not affected by early cementation and enough primary porosity was available for the fluids responsible for dissolution to move freely through the system and produce secondary porosity.

The Fuzzy Logic Algorithm:

As indicated earlier, a new fuzzy logic algorithm was applied to determine the ranking of the petrographic elements with respect to permeability. The following paragraphs briefly describe the application of the fuzzy logic algorithm, and Table II shows the comparison between the conventional ranking and the fuzzy logic ranking.

All the petrophysical attributes examined under the thin section contribute to permeability. Although, this is true we are also aware that each attribute alters permeability in a unique manner. It is difficult to accurately

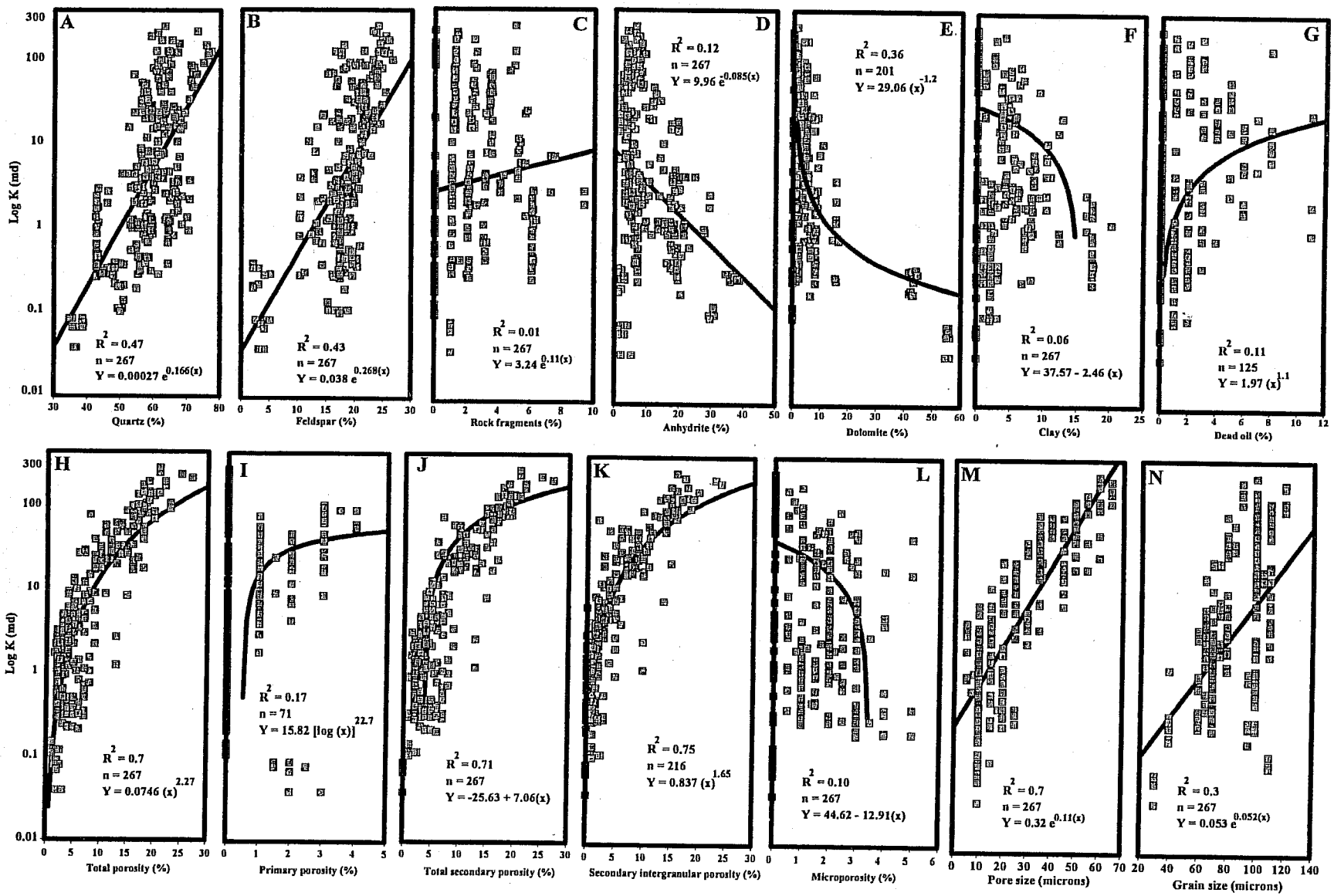

Figure 5: Relationships between permeability and different petrographic elements in the Shattuck Member, Sulimar Queen and South Lucky Lake fields.

quantify the non-linear interaction between each of the petrophysical parameters with permeability. The fact that permeability is affected differently by each attribute brings out the question of orthogonality of the petrophysical attributes with respect to each other. Truly dependent attributes should alter permeability in a similar fashion.

Facing the dilemma of not knowing the explicit relationship between the petrophysical attributes and permeability, the question of the most significant attributes that contribute to permeability was resolved using the fuzzy logic algorithm. This data-directed algorithm compares the effect of each individual input parameter (the petrophysical measurement) on the output (the minipermeameter permeability). Briefly, the algorithm achieves this comparison by building fuzzy membership functions for each of the input parameter. The fuzzy membership functions are then defuzzified using the centroid defuzzification rule to plot fuzzy curves. The range of each of these fuzzy curves on the ordinate reflects the effect of each input parameter on the output (Figure 6). Details of the fuzzy logic algorithm are beyond the scope of this paper and the interested reader is referred to Lin (1994). Our objective in this study was to rank the petrophysical attributes in a descending order of their influence on the permeability of the sample.

Figure 6 shows the fuzzy curves resulting from the Fuzzy Logic method. The first row, represents the petrophysical parameters which have the largest influence on the permeability. This is evident from the range of each fuzzy curve on the corresponding ordinate. For example, the fuzzy curve for total porosity exhibits a range of approximately 160, whereas, feldspar and anhydrite exhibit ranges of approximately 90 and 45 respectively. Here, total porosity has greater influence than feldspar which, in turn, affects permeability more than anhydrite.

Prior to generating the fuzzy curves for these petrophysical attributes, histograms were plotted for each attribute. The histograms ensure that the data have approximately gaussian distribution. Heavily skewed data result in erroneous results from the fuzzy logic algorithm. Histograms for moldic porosity and intraconstituent porosity were skewed even after normalization and hence the fuzzy logic results pertaining to these parameters were considered inconclusive. These parameters were eliminated from analysis. Table II compares the ranking obtained from the fuzzy logic algorithm with conventional regression analysis. It is evident from Table II that the most important petrographic elements (ranking 1 to 5) controlling permeability are accurately predicted by the new algorithm. From Table II, we can also see that the fuzzy logic algorithm ranked microporosity in the 6th place. From conventional ranking, we see that microporosity was ranked 8th. In the case of Sulimar Queen, we know that microporosity should affect permeability more than dolomite which appears to be in agreement in the fuzzy logic prediction.

It is important to realize that the conventional ranking technique compares the best regression models for different petrographic parameters. These regression models do not have the same polynomial order and hence the comparison is not entirely equitable. The fuzzy logic algorithm compares all the parameters on the same basis and hence is more superior in that aspect.

From the petrographic analysis, we concluded that zone 1 is the main reservoir since it was not affected by anhydrite cementation. Zone 1 also indicated the effects of dissolution and thus has the highest porosity and permeability. This detailed petrographic analysis also helped to understand the subtle changes in the depositional environment and the development of the depositional model.

Petrographic elements	Ranking due to regression	Ranking due to fuzzy logic
Secondary intergranular ϕ	1	1
Total secondary ϕ	2	2
Total ϕ	3	3
Quartz	4	4
Feldspar	5	5
Dolomite	6	7
Anhydrite	7	9
Microporosity	8	6
Clay	9	8
Rock fragments	10	10

Table II: Comparison of conventional and fuzzy logic based ranking of petrographic elements.

LOG ANALYSIS

As mentioned previously, only four modern log suites were available, and the rest of the field contained only old gamma ray and neutron logs. Due to the absence of other logs (e.g., resistivity, sonic, density, etc.) and the unreliability of the old neutron logs; correlations between core porosity, permeability, water saturation, and petrographic elements had to be made with gamma ray logs in order to predict these properties in the uncored wells. Both, the old and new logs, were digitized on 0.5 feet interval.

Developing relationships between gamma ray and porosity, total water content, and permeability:

In the Sulimar Queen and adjacent fields, a negative correlation was observed between old gamma ray (API) and neutron (API) values. This correlation implied that porosity increases with the increase in gamma (Ali et al., 1996). Although, old neutron and gamma ray logs were not reliable, this behavior still helped to understand the overall relationship between gamma ray values and porosity. A positive correlation was also observed between core porosity and gamma ray in the Sulimar Queen field (Figure 7A) as well as in the Queen field (Figure 7B) which is located 20 miles northeast of Sulimar Queen field. Similar relationships between gamma ray and porosity in the Sulimar Queen and adjacent fields suggested a possible regional trend. This increased our confidence in using the correlation between core porosity and gamma ray, developed in one well (Well 1-16) to be used for predicting porosity throughout the field (Figure 7A). The correlation may be expressed as:

$$\phi = 0.334\, e^{0.0526(\gamma)} \qquad (1)$$

where "ϕ" is the porosity in percent and "γ" represents the gamma ray value in the API units.

This relationship was only good for the *sand portion of the Shattuck member* as determined from the core description. In the Shattuck zone, the gamma ray values were not be controlled by the amount of clay but

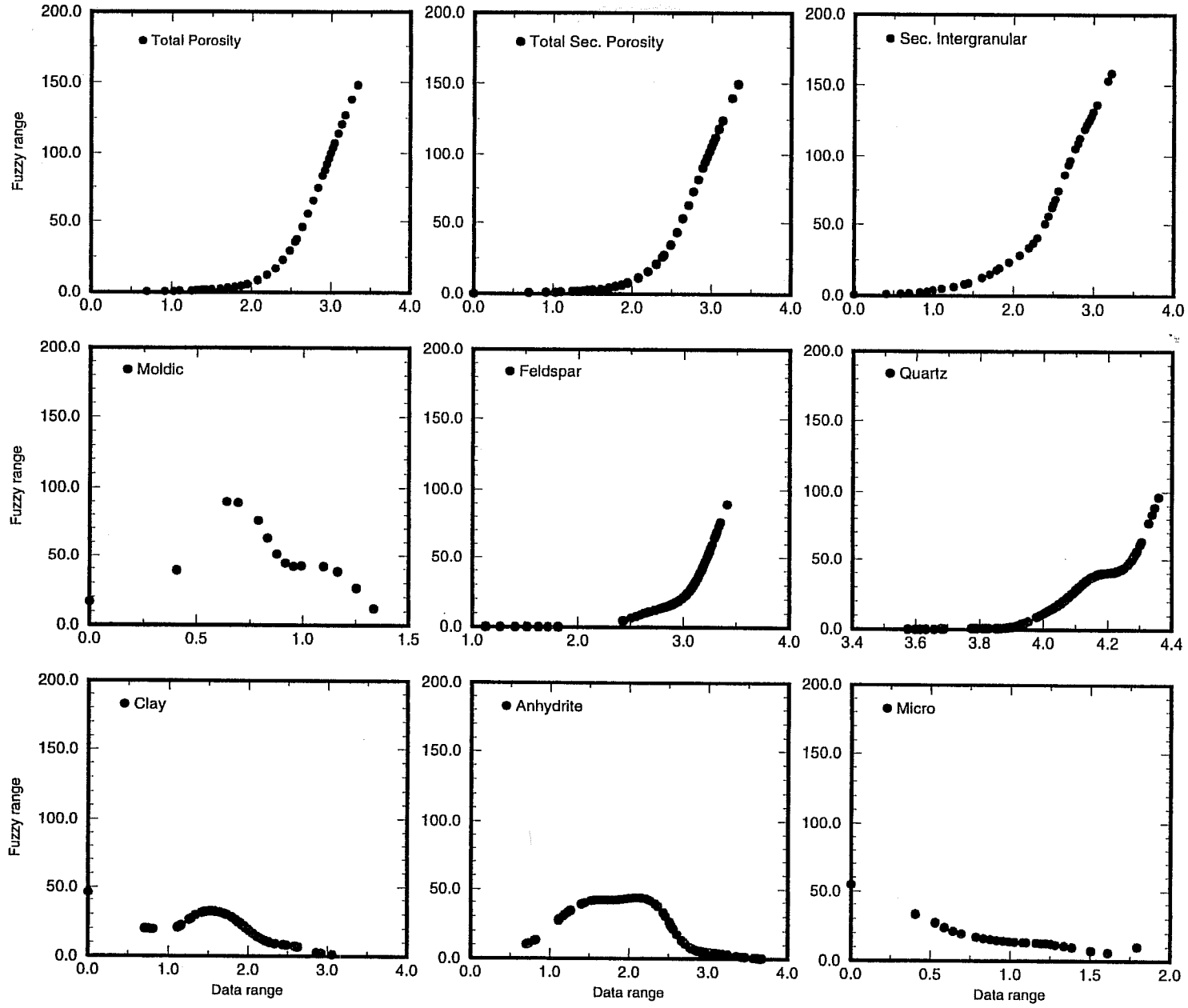

Figure 6: Fuzzy curves for various petrographic elements. The importance of each element is decided by the range of its fuzzy curve.

by the amount of potassium feldspar (confirmed by petrographic and XRD analysis) and uranium (confirmed by the spectral gamma ray log from one well in the Queen field) (Figure 8A). Unfortunately, the spectral gamma ray log was not available from well 1-16 in which core porosity, water saturation, and permeability data were available (Figure 8C). This uranium was assumed to be present in the formation water since gamma ray values are proportional to the total water content (W_{TC}) (Figure 9A). Similar relationships were also observed in the Queen (Figure 9B) and adjacent fields, again implying a regional trend. These trends emphasized that the relationship developed in only one well could be applied with reasonable confidence throughout the field (Ali et al., 1996).

The total water content represents the percentage of the total rock volume occupied by the water. The conventional way of representing the water saturation (S_W) as the percentage of porosity occupied by water was not used because of its inadequacy in conveying the amount of water present. For example, a 5% porosity rock with water saturation of 90% contains less volume of water than 20% porosity rock with only 35% water saturation. If we use the conventional representation of the water saturation the relationship between gamma ray response and volume of water could not be identified correctly. We suggest using total water content (W_{TC}) instead of conventional water saturation (S_w) in order to understand the relationship between the gamma ray response and the control of radioactive dissolved species in the water. The following relationship developed in well 1-16 was then used with caution to predict the total water content (W_{TC}) (Figure 9A):

$$W_{TC} = 4.6\ 10^{-5}\ \gamma^{2.9} \qquad (2)$$

Here, "W_{TC}" is the total water content in percentage, and "γ" the gamma ray value in API units. Once the total water content is calculated, then water saturation for particular a porosity can be calculated using:

$$S_W = [W_{TC}/\phi]\ X\ 100 \qquad (3)$$

Improving the reliability of old gamma ray logs:

The old gamma ray logs had varying scale ranges, therefore, a comparison of gamma ray API values from different wells was meaningless (Ali et al., 1996). Also, porosity and total water content obtained from the *unscaled* old gamma ray logs using the relationships developed in well 1-16 (Equations 1 & 2) were erroneous. Because of the different scale ranges of the old gamma ray logs, the extrapolation beyond the range of original data values (Well 1-16) yielded wrong results. In order to make old gamma ray logs useful and reliable, they had to be rescaled to the same datum so that the information provided by each well became comparable.

The old gamma ray logs were rescaled using the methodology proposed by Barrett (1994). In this methodology, modern logs are needed to determine the representative value ranges and the average high and low values in the zone of interest in that area. The average high and low gamma ray values were determined from the four modern logs available in the field. These values were 80.5 API and 12 API units (Ali et al., 1996) respectively. Using these average values, all the old gamma ray logs were rescaled. Example of the rescaled logs from well 1-14 and 5-1 are shown in Figure 10. The increase in the reliability of the old gamma ray logs after rescaling is also evident from the improved correlation coefficient between the core porosity and

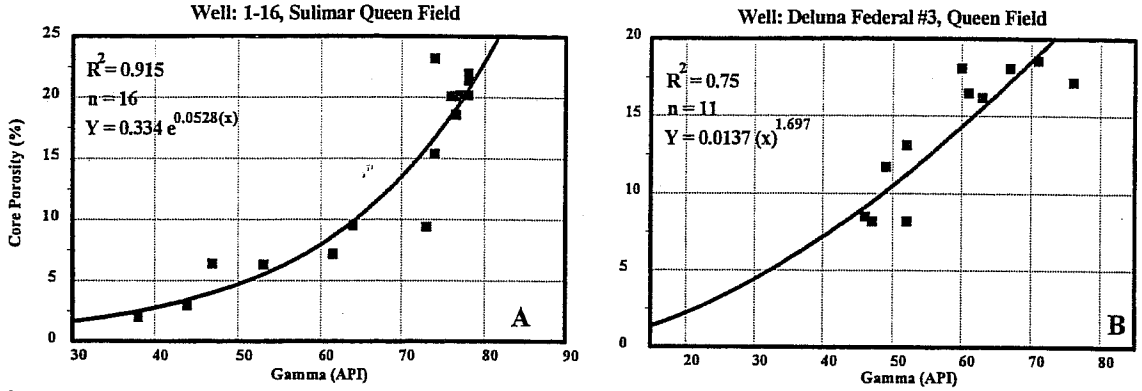

Figure 7: Plots showing the relationship between gamma ray values and core porosity in the Sulimar Queen (A) and the Queen field (B).

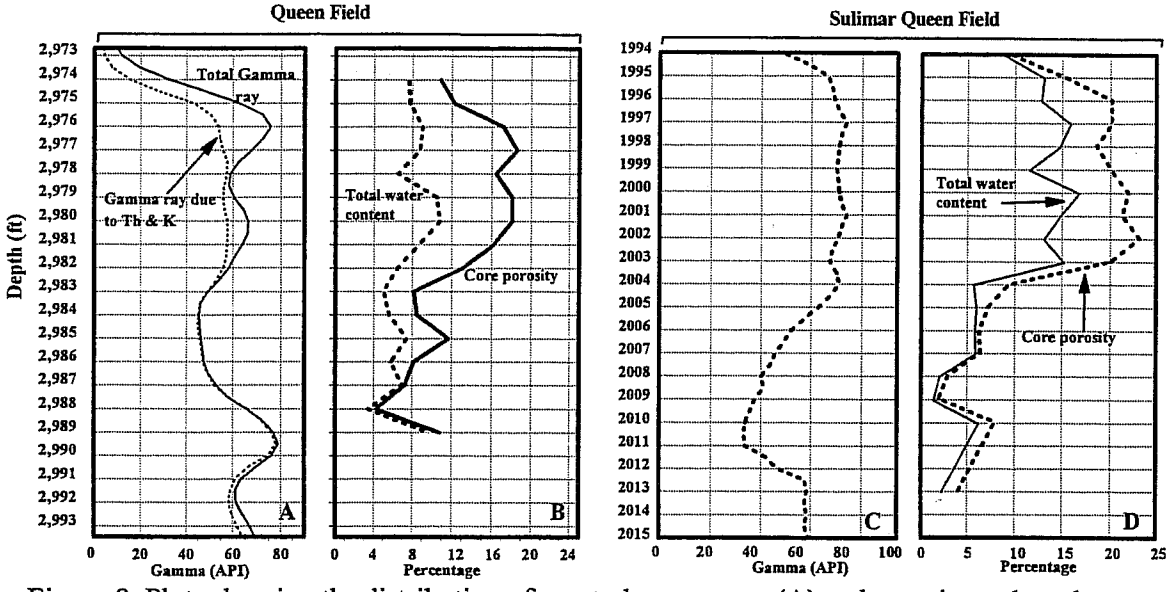

Figure 8: Plots showing the distribution of spectral gamma ray (A) and porosity and total water content (B) in the Queen field. Also shown is the gamma ray log (C) and porosity and total water content (D) in the Sulimar Queen field. As the porosity and total water content increases so does the gamma ray value.

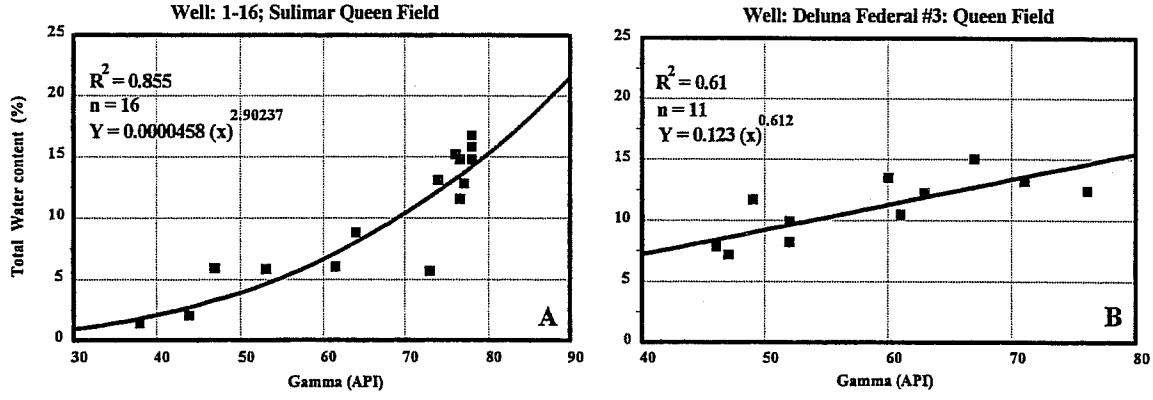

Figure 9: Plots showing the relationship between total water content and gamma ray values in the Sulimar Queen (A) and the Queen field (B).

the gamma ray values (Figure 11). The gamma ray derived porosity and total water content using Equations 1 and 2 were compared with the core porosities and total water content in wells 1-14 and 5-1 for reliability (Figures 12 and 13). Porosity calculated from the rescaled gamma ray logs also captured the presence of individual high and low porosity zones which were not distinguishable in the porosities obtained from unscaled gamma ray logs (Figure 14).

Air permeability and porosity also indicated a positive relationship in the Sulimar Queen field (Figure 15A). Similar relationships were also observed in the adjacent fields (Ali et al., 1996). A positive correlation was also observed between gamma derived porosity and permeability (Figure 15B). The relationship between gamma ray derived porosity and permeability is more useful (Figure 15B) because it can predict the whole range of original permeability distribution as opposed to one obtained from cores (Figure 15A). The whole range of permeability values could not be predicted using the gamma ray values because the maximum gamma ray reading was 80 API. This corresponds to a permeability of approximately 40 md while the maximum core permeability 116 md.

DEPOSITIONAL ENVIRONMENT

Two opposing interpretations for the deposition of the Queen Formation are available in the literature. Boyd (1958), Pray (1977), and Sarg (1977) proposed an aqueous "all wet" depositional model. They attribute the deposition in a subsiding lagoon based on the lack of evidence for extensive subaerial exposure in the Queen or the adjacent formations in the Guadalupe Mountains in Texas and New Mexico. On the other hand, Silver and Todd (1969), Mazzullo (1984) (1985), and Malicse and Mazzullo (1990) suggested an eolian/continental environment. During Guadalupian time, the northwest shelf was a flat, slowly subsiding platform to the north of the Delaware Basin (Figure 1). During Queen deposition, a broad lagoon was present between carbonate sand shoals and the land - sea margin (Ball, 1971).

Our depositional model was constructed after assimilating all the information from the cores, petrographic analysis, logs, lithologic description of the cores and chip analysis (Haynes, 1978), and the outcrop data. In the Sulimar Queen and the South Lucky Lake fields, the Shattuck Member was deposited in a mix of coastal sabkha, shallow lagoon (with variable energy and depth), and eolian (dry eolian sand sheets of Mazzullo, 1990) (Figure 16). These environments were established based on the variations in grain size and sorting, poorly developed sedimentary features (flaser bedding, ripple laminations, cross laminations, bioturbation, and haloturbation), and the distribution of overlying and underlying anhydrite (Figure 16).

Coastal Sabkha is the deflation flat present behind the lagoon. Well-sorted sandstone underlying the bottom anhydrite was deposited in the sabkha and exhibits haloturbation due to the growth of the displasive anhydrite nodules. This coastal sabkha is overlain by lagoonal deposit comprising of anhydrite, shaly-siltstone, and well-sorted, structureless red sandstones. These sandstones were probably deposited when sand was blown into the lagoon as the desert (sand sheet) environment encroached onto the lagoon. In the case of zone 2, these sandstones are well cemented by the anhydrites and have the lowest porosity and permeability. They also do not indicate effects of haloturbation. Another important observation which suggests a lagoonal deposition is the regional extent of this anhydrite. Overlying is a three feet sequence of well sorted eolian sandstones with weakly developed cross-stratifications and asymmetric wind ripples. Both lagoonal and eolian sandstones are very well cemented by anhydrite and have very low clay content and porosity. The combined distribution of

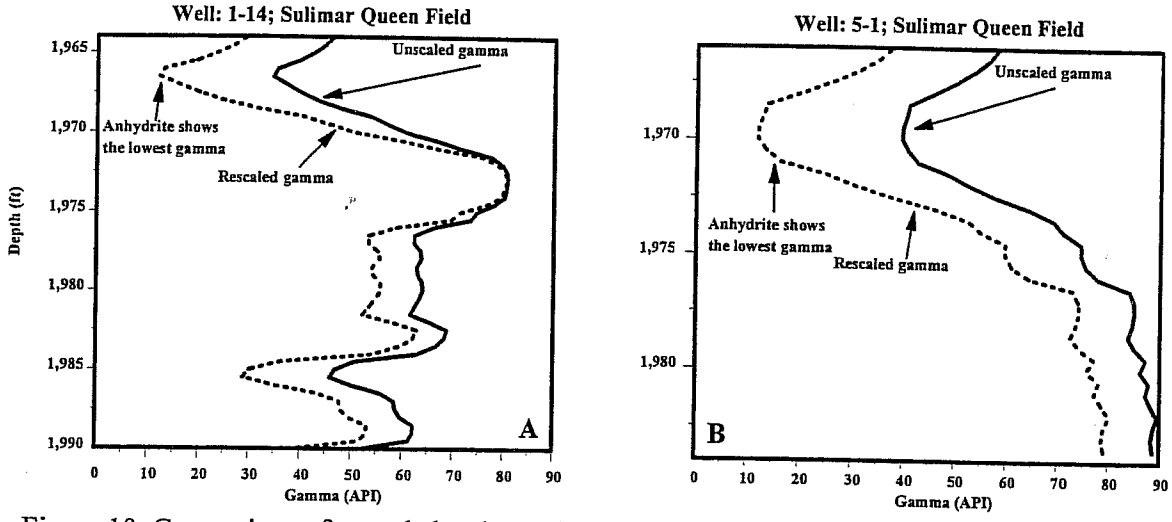

Figure 10: Comparison of unscaled and rescaled gamma ray logs. The rescaled logs have the minimum of 12 API and maximum of 80 API values. Note the presence of anhydritic portion in the rescaled gamma ray logs which were not easily identifiable in unscaled logs.

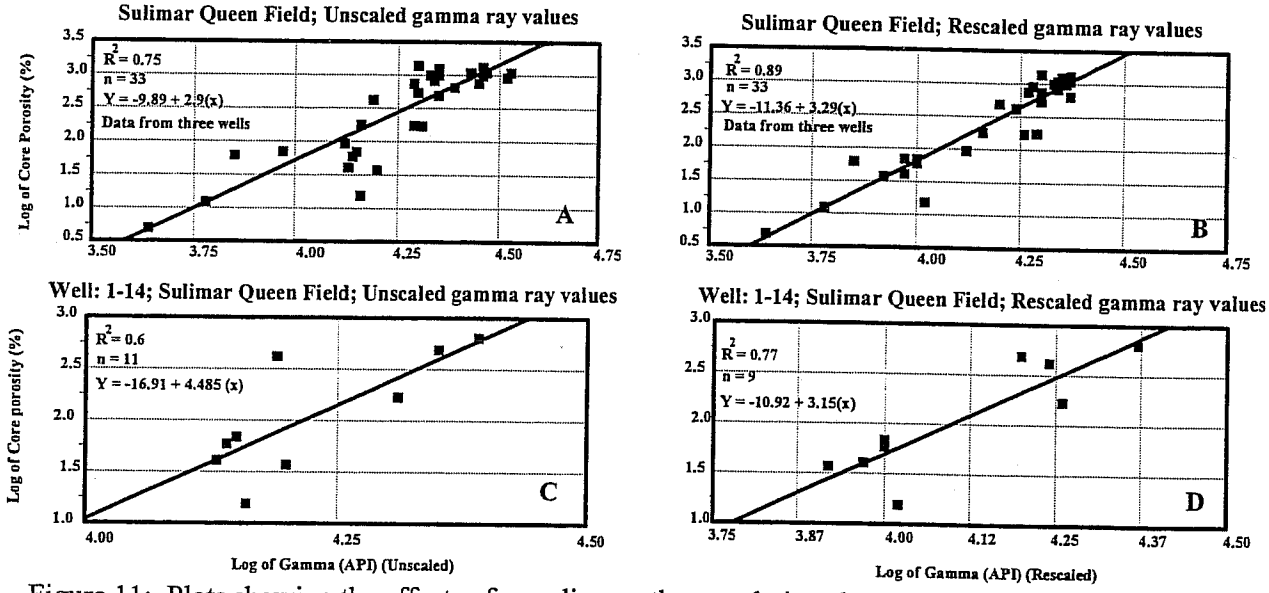

Figure 11: Plots showing the effects of rescaling on the correlations between core porosity and gamma ray values. Note the improvement of correlation from (A) to (B) and (C) to (D).

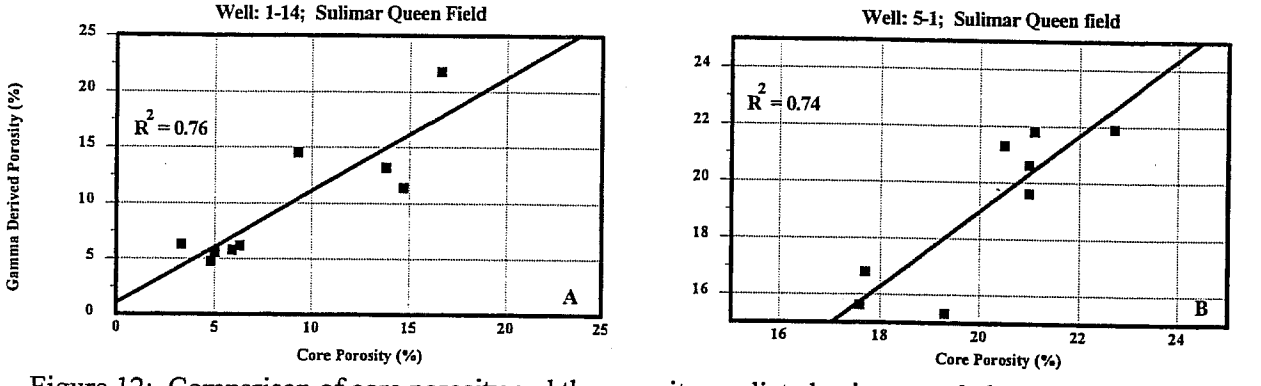

Figure 12: Comparison of core porosity and the porosity predicted using rescaled gamma ray logs in the Sulimar Queen Field.

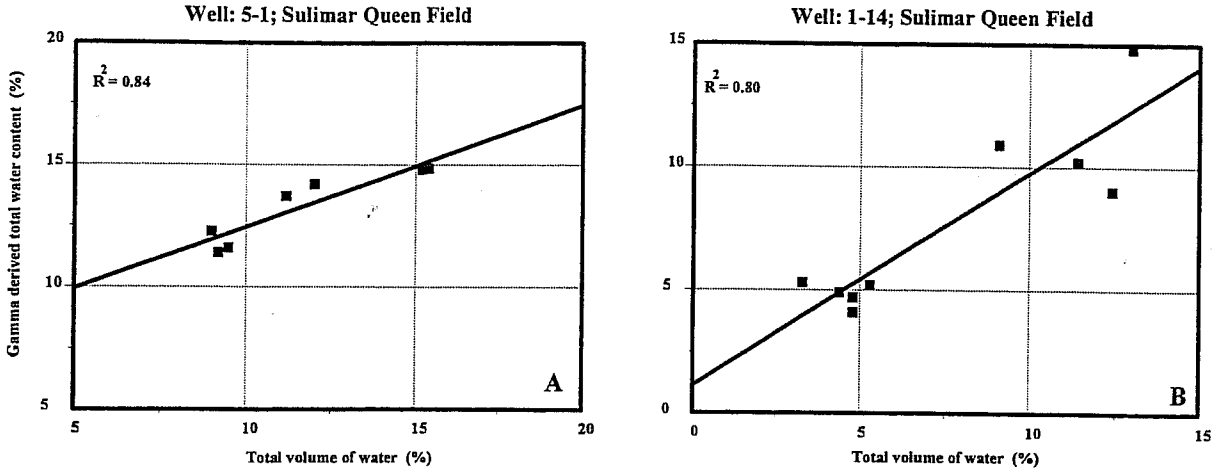

Figure 13: Comparison of core derived and rescaled gamma ray logs derived total water content. Note a strong correlation in both wells.

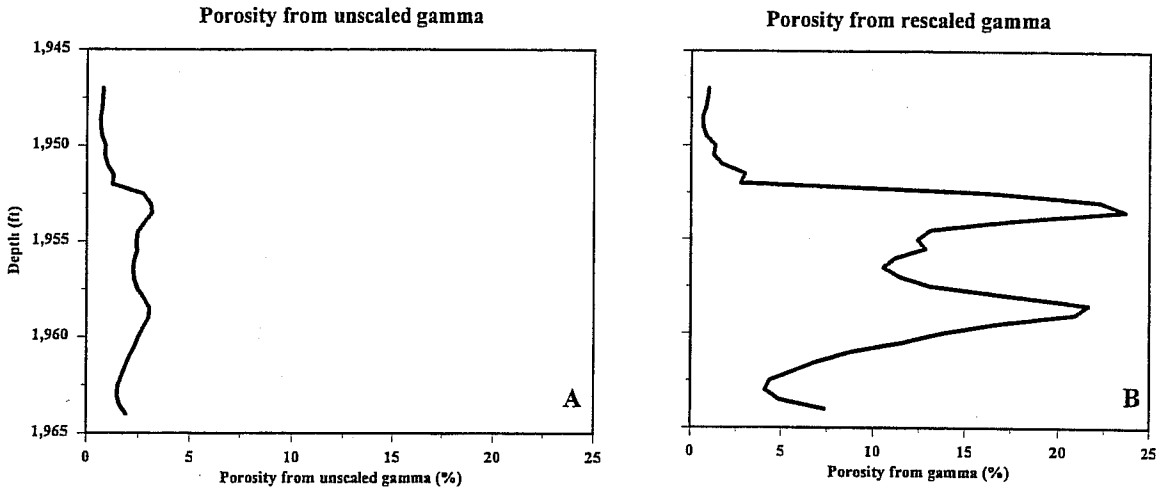

Figure 14: Comparison of porosity distribution as calculated from unscaled (A) and rescaled (B) gamma ray logs in well 5-2. High and low porosity zones are clearly visible in the porosity derived from rescaled gamma ray log (B).

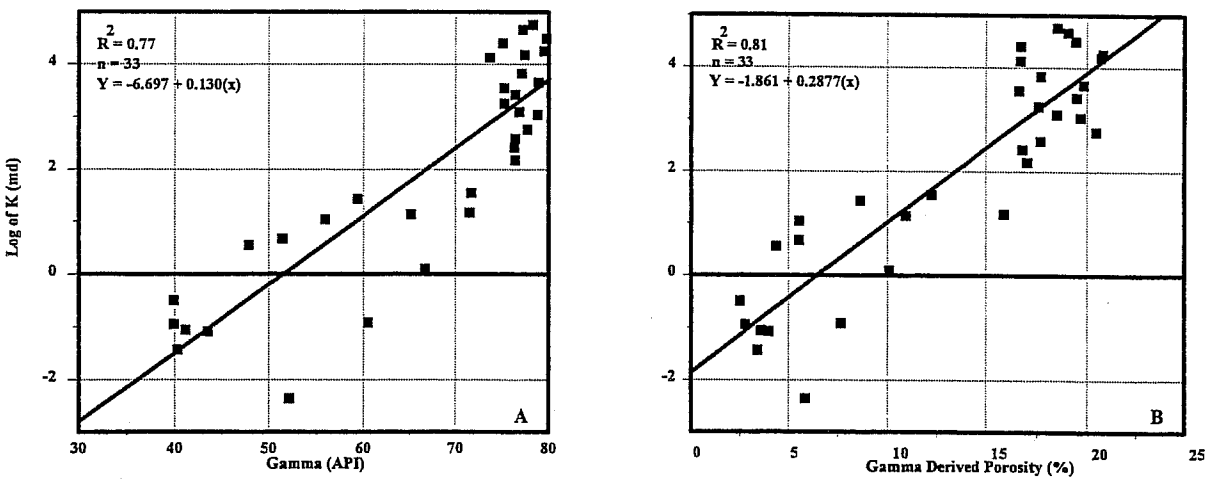

Figure 15: Plots showing the positive correlation between Gamma (API) values and permeability (A), and gamma ray derived porosity and permeability (B) in well 1-16 in the Sulimar Queen field.

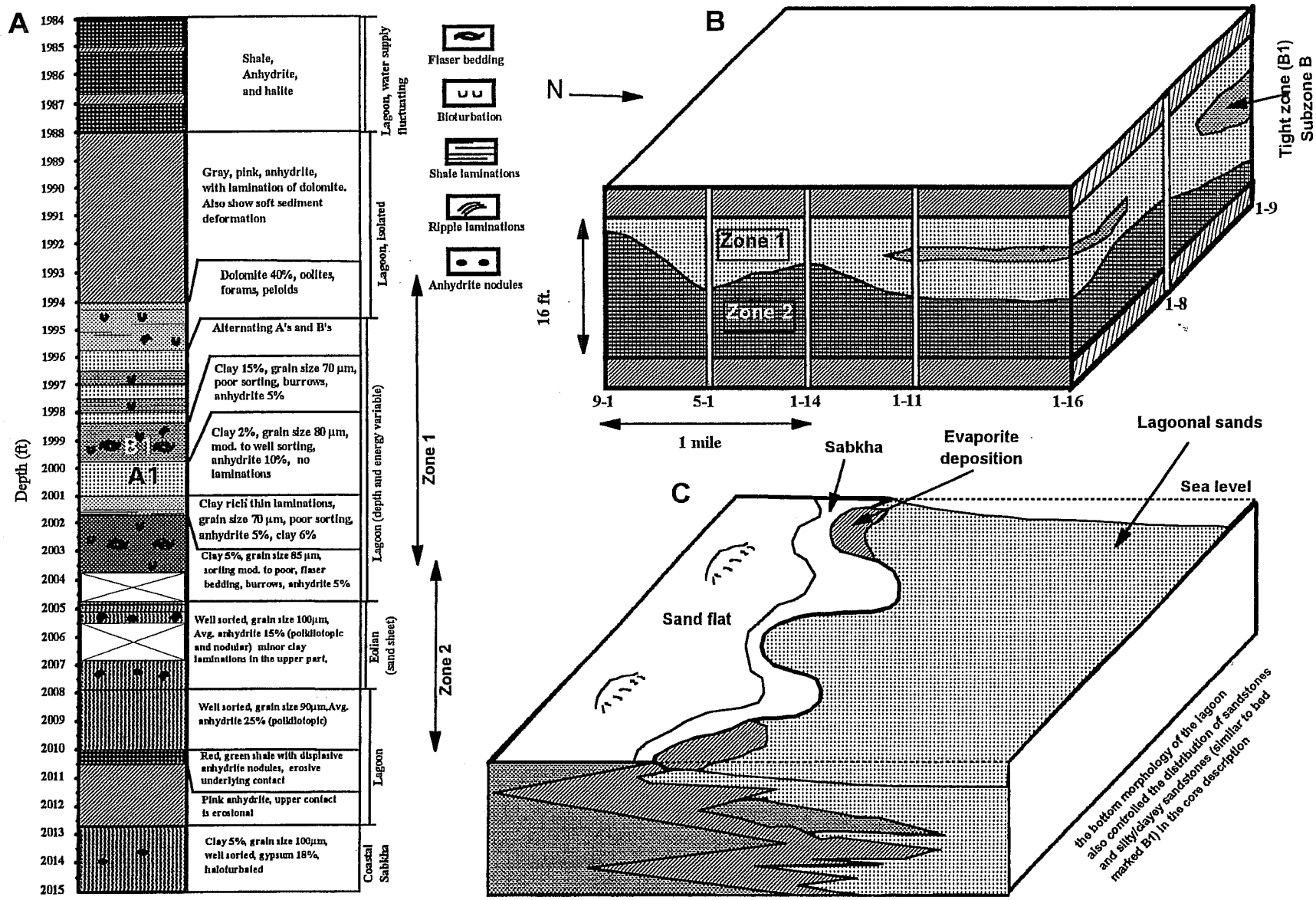

Figure 16: (A) Core description along with inferred depositional environments. (B) Block diagram of the Sulimar Queen field showing the distribution of the zone 1, zone 2, and low permeability subzone B1 within zone 1. (C) Generalized depositional model for the Shattuck zone in the Sulimar and adjacent fields. The interfingring of different environments created the present distribution of the Shattuck Member.

the bottom lagoonal and overlying eolian sandstones (zone 2, Figure 16) can be traced throughout the field because of their low gamma ray values (API). These sandstones thicken and completely replace the overlying lagoonal reservoir facies forming a trap in the western part of the field.

Zone 1 was deposited in a shallow lagoon with variable depth and energy level and displays moderate-sorting. This zone also has the highest porosity and permeability and forms the main pay. This zone probably escaped the early pervasive cementation by anhydrite and later porosity enhanced by dissolution. Zone 1 (Figure 16) lacks evidence of subaerial exposure and sedimentary structures typical of sabkha, fluvial, or eolian environments. The absence of curled clay flakes, clay pebbles, mud cracks with sandy infills, cross stratification, channel or flood plain deposits supports its deposition in a lagoon. Also, the eolian sands interbedded with beds of aquatic origins should show effects of fluvial erosion and wind deflation, which are also absent in zone 1. The alternating clay rich beds (B1) (Figure 16) containing thin laminations of clayey-silty sandstone with the featureless moderately-sorted sandstone beds (A1) (Figure 16) suggest a minor fluctuation in the energy of the lagoon. Zone 1 grades upward through sandy dolomite into anhydrites that precipitated in the lagoon. This transition was observed in the cores from Sulimar Queen as well as the adjacent fields. This regional extent of anhydrite points towards the deposition in a lagoon instead of local ponds or salinas. The absence of fossils suggest the conditions were hypersaline.

The Shattuck Member in the Sulimar Queen and adjacent fields was deposited in a mixed lagoonal-sabkha-eolian environment. The Sulimar Queen and adjacent fields were formed due to combining affects of lagoon bottom morphology, migration of different depositional environments in response to minor sea level fluctuations, the distribution of lagoonal anhydrite and anhydrite cemented lagoonal and eolian sandstone, minor structural features, and most importantly the development of secondary porosity.

NUMERICAL SIMULATION OF THE SULIMAR QUEEN

The overall objective of this project was to characterize the Sulimar Queen from a limited dataset. The confirmation of successful characterization is accomplished through a reliable reservoir model which honors most static (petrophysics and geology) and dynamic (production and pressure) data, and results in a reasonably accurate forecast of the reservoir performance.

The following paragraphs explain the stages of data integration which resulted in successful reservoir characterization. The old gamma ray and neutron logs (unscaled) were only useful for detecting the radioactive Shattuck sand, and were treated as perforating logs. Rescaling the logs provided improved correlations to predict porosities in the pay zone. The process of rescaling also improved the log signatures for detecting the anhydrite sequences bounding the pay sand which helped in delineating the sand thickness and the top of the structure for the 36 wells present in the field. Once the top of the structure was accurately identified in all the wells, a simple geostatistical mapping algorithm was applied to obtain a smooth fieldwide top of the structure. Using geologic input, this structure was modified manually (Figure 17). The initial porosity field distribution was also estimated using the same geostatistical mapping technique. The permeability control points in the field were obtained from inverse DST tests which were performed at many wells. Using an analytical k-ϕ relationship for each layer, derived from well 1-16, the initial permeability map was obtained.

The rescaling of the logs indicated the presence of a thin, tight zone which separated zones 1 and 2. The outcrop histograms also suggested three distinct lithological units (DOE Report). The proposed geologic model

and some of the well logs indicated that this zone may not be continuous throughout the field. Since the tight zone was thin and assumed to be discontinuous, the final simulation model comprised two layers only. The upper simulation flow layer representing the zone with high permeability and the lower flow layer for the low permeability zone. The thin, tight zone was combined with the lower layer.

The PVT analysis performed on oil samples collected from an adjacent field was used as initial PVT data in the simulator. This PVT data was unable to explain the large gas production in the initial producing life of the field. This is because the reservoir was initially assumed to be undersaturated. Careful analysis of the structure and production (GOR) profile indicated the presence of a gas cap. This was later confirmed independently (Lemay, 1996). Since, the only accurate measurement in the field was the oil production, this was used as an inner boundary condition constraint in an automatic history matching algorithm developed at the Petroleum Recovery Research Center. Based on this constraint, a good history-match was obtained for the primary production. The waterflood forecast obtained by using the reservoir model derived after primary production history-match is shown in Figure 18.

We considered the Sulimar Queen to be successfully characterized based on the detecting and locating the previously unconfirmed gas cap, combined with a consistent geologic description and reasonable simulation forecasts.

CONCLUSIONS:

In this study, new techniques were applied for improving the quantity and quality of data for better reservoir characterization of old fields.

1. The minipermeameter is useful in capturing the small-scale heterogeneities. Permeability measurements made on fine grids also improve the lithologic description of the cores.
2. Combination of minipermeameter and petrographic analysis allows the collection of large amount of petrographic data using fewer thin sections. The control of different petrographic elements on permeability can be easily and accurately determined. Correlations developed between the permeability and petrographic elements are also reliable.
3. The newly developed fuzzy logic algorithm is a fast, unbiased and reliable method for establishing the importance of each petrographic element on permeability.
4. Rescaling of the old logs improves their reliability. In the Shattuck Member, porosity, permeability, and water saturations could be estimated using the gamma ray logs.
5. Maximum geological and petrophysical information was gathered from the limited database by combining small-, medium-, and large-scale data obtained from minipermeameter, cores, petrographic analysis, and logs. The distribution of the different zones was mapped successfully in the field and a depositional model was developed.
6. Using this data, a successful characterization of the Sulimar Queen was obtained and confirmed through a good history-match of the primary production and a reasonably accurate forecast of the waterflood performance.

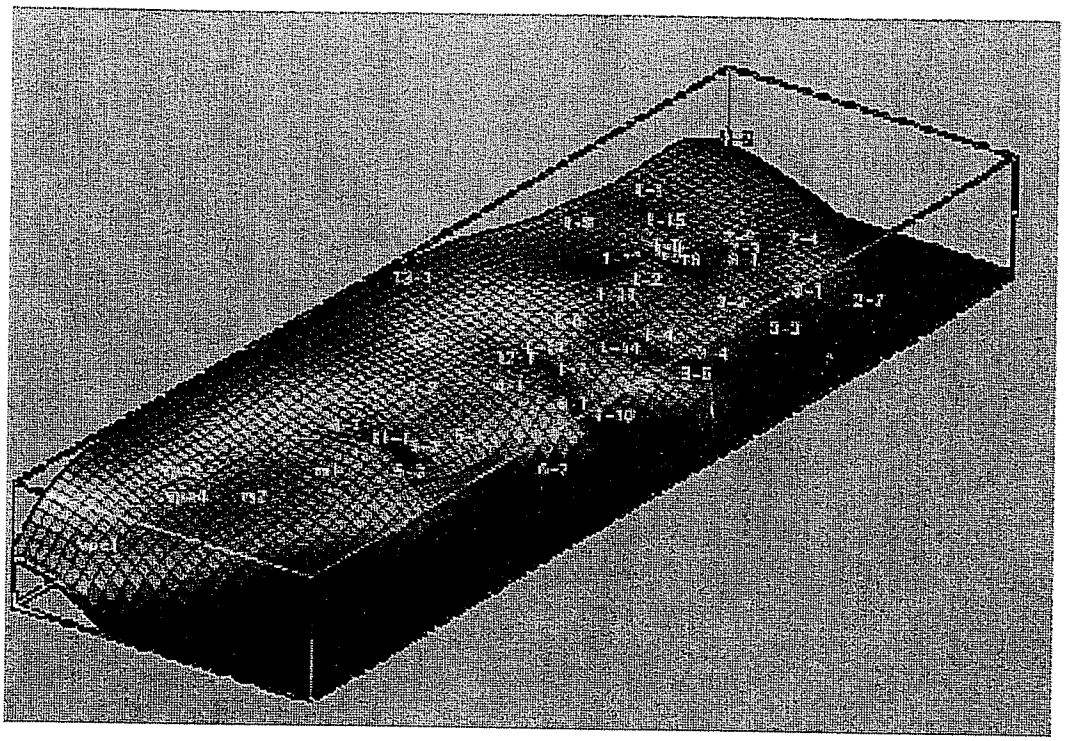

Figure 17: Top of the Sulimar Queen structure predicted using a simple geostatistical method and manually adjusted to geologic input.

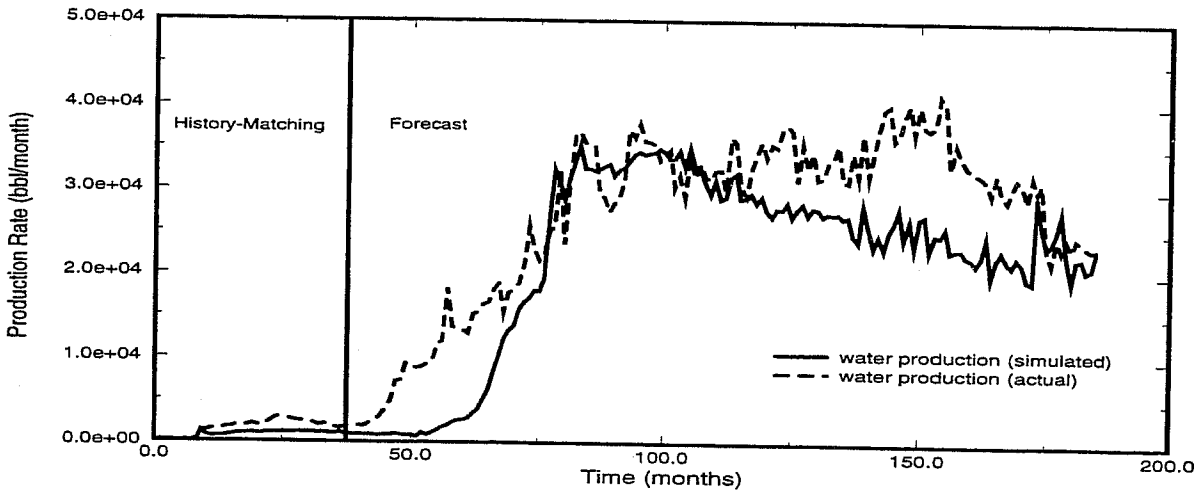

Figure 18: Waterflood history–match and forecast.

REFERENCES CITED

Ali, M., Chawathé, A., Ouenes, A., Weiss, W.,1996, Improved log analysis for the characterization of the Sulimar Queen field, southeast New Mexico: PRRC Report No. 96-33, pp. 32.

Balls, S. M., Roberts, J. W., Norton, J. A., and Pollard, W. D., 1971, Queen Formation (Guadalupian, Permian) outcrops of Eddy County, New Mexico, and their bearing on recently proposed depositional models: American Association of Petroleum geologists Bulletin, v. 55, p. 1348 - 1355.

Boyd, D. W., 1958, Permian sedimentary facies, central Guadalupe Mountains, New Mexico, New Mexico Bureau of Mines and Mineral Resources bulletin. 40, pp. 100.

Barrett, G. D., 1994, Use of computers to perform old log analysis: SPE Computer Applications, August, p. 9 - 12.

Goggin, D. J., Thrasher, R. L., and Lake, L. W., 1988, A theoretical and experimental analysis of minipermeameter response including gas slippage and high velocity flow effects: In Situ, v. 12 (1&2), p. 79 - 116.

Haynes, L. Cynthia, 1978, Sandstone diagenesis and development of secondary porosity, Shattuck Member, Queen Formation, Chaves County, New Mexico: M.A., Thesis, The University of Texas at Austin, pp.148.

Lemay, William, 1996, Personal Communication

Lin, Yinghua., 1994, Input identification of Modeling with fuzzy and neural systems: Ph.D., Dissertation, New Mexico Institute of mining and Technology, Socorro, New Mexico, pp. 89.

Martin, D. F., Buckley, J., Weiss, W. W. and Ouenes, A., 1996, Integration of advanced geoscience and engineering techniques to quantify interwell heterogeneity, Quarterly Technical Report submitted to DOE under contract no. DE-AC22-93BC14893.

Mazzullo, J. M., Williams, M., and Mazzullo, S. J., 1984, The Queen formation of Millard Field, Pecos county, Texas: Its lithologic characteristics, environment of deposition, and reservoir petrophysics: Transactions southwest section American Association of Petroleum Geologists, publication 84-78, p. 103 - 110.

Mazzullo, S. J., and Hendrick, C. L., 1985, Road log and locality guide, lithofacies, stratigraphy, and depositional models of the back-reef Guadalupian section (Queen, Seven Rivers, Yates, and Tansill Formations), SEPM Field Guidebook, p. 1 - 30.

Pray, L. C., 1977, The all wet, constant sea level hypothesis of Upper Guadalupian, shelf and shelf edge strata, Guadalupe Mountains, New Mexico and Texas: West Texas Geological Society, Special Publication 77 - 16.

Sarg, J. F., 1977, Sedimentology of the carbonate-evaporite facies transition of the Seven Rivers formation (Guadalupian, Permian) in southeast New Mexico: SEPM Permian basin section, special publication, 77 - 16, p. 451 - 478.

Silver, B. A., and Todd, R. G., 1969, Permian cyclic strata, northern Midland and Delaware Basins, west Texas, and southeastern New Mexico: American Association of Petroleum Geologists bulletin, v. 53, p. 2223 - 2251.

Suboor, M. A., and Heller, J. P., 1995, Minipermeameter characteristics critical to its use: In Situ, v. 19 (3), p. 225 - 248.

Towards an Integrated Petrophysical Tool for Multiphase Flow Properties of Core Samples

Roland LENORMAND

Institut Français du Pétrole
Rueil Malmaison 92852 cedex FRANCE
e-mail: roland.lenormand@ifp.fr

Abstract

This paper describes the first use of an Integrated Petrophysical Tool (IPT) on reservoir rock samples. The IPT simultaneously measures the following petrophysical properties:

- Complete capillary pressure cycle: primary drainage, spontaneous and forced imbibitions, secondary drainage (the cycle leads to the wettability of the core by using the USBM index);
- End-points and parts of the relative permeability curves;
- Formation factor and resistivity index.

The IPT is based on the steady-state injection of one fluid through the sample placed in a Hassler cell. The experiment leading to the whole Pc cycle on two reservoir sandstones consists of about 30 steps at various oil or water flow rates. It takes about four weeks and is operated at room conditions..

Relative permeabilities are in line with standard steady-state measurements. Capillary pressures are in accordance with standard centrifuge measurements. There is no comparison for the resistivity index, but the results are in agreement with literature data. However, the accurate determination of saturation remains the main difficulty and some improvements are proposed.

In conclusion, the Integrated Petrophysical Tool is as accurate as standard methods and has the advantage of providing the various parameters on the same sample and during a single experiment. The IPT is easy to use and can be automated. In addition, it can be operated in reservoir conditions.

1. Introduction

The purpose of reservoir models is to simulate fluid displacements in very complicated rock geometry. The flow equations are based on Darcy's law which includes both fluid and rock properties. The basic

equations can be written for two immiscible fluids (1 and 2) flowing in a porous medium with porosity ø and permeability K. At any point x of the medium:

$$u_1 = \frac{K Kr_1}{\mu_1} (\rho_1 g - \frac{dP_1}{dx})$$

$$u_2 = \frac{K Kr_2}{\mu_2} (\rho_2 g - \frac{dP_2}{dx})$$

In these equations, u is the filtration velocity (volume flow rate per unit surface area), μ and ρ the viscosity and density of the fluids, Kr is the relative permeability, g the gravity constant and P the pressure.

For two immiscible fluids that are both in continuous phase, the difference of pressure is equal to the capillary pressure:

$$Pc = P_1 - P_2$$

The monophasic permeability K depends only on the rock structure. In reservoir engineering it is assumed that the capillary pressure (Pc) and the relative permeabilities (Kr) do not depend on fluid viscosities, flow rate and pressure. These petrophysical parameters are only functions of the fluid saturation and displacement history.

The purpose of petrophysical measurement is to determine the capillary pressure (Pc) and relative permeability curves (Kr) as functions of saturation. In addition, electrical properties (formation factor and resistivity index I_R) are determined for the calibration of log data.

The petrophysical measurement methods have been developed over several years. However, there is still on-going research to improve not only the accuracy but also the speed and automation of measurements. One approach is to measure different parameters during the same experiment with the same sample ("integrated measure"). The purpose is not only to reduce cost but also to increase the representativeness by using the same sample.

In this paper, I will first recall the standard and integrated methods for measuring Pc and Kr curves. I will then describe the original method developed for the simultaneous measurement of the three properties : Pc, Kr, I_R. Finally, I will present and discuss the results obtained with two reservoir samples.

2. Measurement of Petrophysical properties

Let us recall the notations which are commonly used in petroleum engineering.

2.1. Definitions

It is now recognized that most reservoirs are not strongly water-wet (Anderson, 1986; Cuiec, 1991). Consequently, the definitions for capillary pressure must be valid for any type of wettability. In core analysis, the following definitions are generally used (Lenormand et al., 1993):

- *Reference fluid.* One of the fluids is arbitrarily chosen as the "reference". The reference fluid is water when oil and water are involved, and the liquid for liquid/gas systems.
- *Capillary pressure* is defined as: Pc=P(non-ref)-P(ref).
- A *drainage* is a displacement where the saturation of the reference fluid is decreasing; an *imbibition* is a displacement where the saturation of the reference fluid is increasing.
- A *Pc(S) curve* is an equilibrium curve obtained by a succession of displacements with small increments of pressure (or flow rate).

We will now take the example of oil and water systems. This set of definitions leads to the different parts of the Pc cycle shown in figure 1.

1) Primary drainage (Pc>0) : oil is displacing water
2) Positive imbibition, also called "spontaneous" imbibition
3) Negative imbibition, also called "forced" imbibition
4) Negative (secondary) drainage
5) Positive (secondary) drainage.

Let us now describe the different methods used for measuring capillary pressures.

2.2. Porous Plate

The capillary pressure is balanced by the *static* pressure difference between the fluids. The fluids are injected through two semipermeable porous plates to measure the positive and negative parts of the capillary pressure curve. The displacements are controlled by the pressure difference between the fluids which is increased step by step during drainage and decreased during imbibition. With the two semipermeable plates, this difference can take any positive or negative values and the whole Pc cycle can be measured (curves 1 to 5, fig. 1). When equilibrium is reached, the saturation is uniform along the sample and its value can be deduced from the effluent production.

Recently, the Porous Plate method has been improved by replacing the porous plates by very thin micropore membranes which are much more permeable (Longeron et al., 1994). The equilibrium time is around 100 times faster. A complete cycle takes only a few weeks instead of several months with the standard porous plates, and with the same accuracy.

2.3. Centrifuge

The capillary pressure is balanced by the pressure difference due to centrifuging (see for instance O'Meara et al, 1988). The pressure profile in each fluid can be related to the rotation speed and to the fluid density. In drainage, for instance, the sample is immersed in oil and Pc is assumed to be zero at the outlet. In any section of the sample, the pressure is known, but the saturation must be calculated from the effluent production by using the general flow equations (Forbes, 1991). Corrections for radial effects have also been proposed (Forbes et al., 1994).

2.4. Semidynamic method

The capillary pressure is balanced by the viscous pressure drop (Lenormand et al., 1993, 1995). The experimental set-up is described in Figure 2. It consists of a standard core-holder with no semipermeable membrane and a separator used to measure the fluid production. The saturations are either measured in different sections of the sample (conductivity, X-ray, γ-ray, etc.) or calculated using a method described in the next section.

For positive capillary pressures, oil is injected through the sample and water only "washes" the outlet face in order to establish the continuity between water inside the sample and the outlet. The first role of this circulation is to maintain the pressure Pw in water at a known and measured value (atmospheric pressure, or any fixed back-pressure). The second role is to allow water to invade the sample when the pressure in oil is decreased (imbibition).

An increase in the oil flow rate displaces water and the level of the meniscus in the fluid separator rises. When the steady state is reached, water is no longer produced, and therefore there is no pressure gradient in the water phase. The water pressure Pw is uniform along the sample, but there is a gradient in the oil that is flowing (Fig. 3). The pressure Po in the oil phase is measured either at the entrance or at any position along the sample. From the values of Pw and Po, we can calculate the capillary pressure defined as Pc=Po-Pw.

The primary drainage curve is obtained by increasing the oil flow rate from zero in a sample initially saturated with water to a maximum value corresponding to the irreducible water saturation (Fig. 3). Imbibition is obtained by decreasing the oil flow rate. During all these displacements, the water flow rate is kept constant at a low level to prevent any disturbance of the flow in the sample (negligible pressure drop) but high enough to wash the oil in the outlet.

The negative part of the Pc curve is obtained by permuting the roles of oil and water. The pressure measured inside the core is then the water pressure.

2.5. Relative permeability measurements

The relative permeabilities (Kr curves) are generally measured separately from capillary pressures using one of these two methods :

- transient displacement. A high flow rate displacement is performed and capillary pressure is neglected for interpretation.
- steady-state displacements. The two fluids are injected together. and generally saturation is assumed to be uniform along the core. More accurate results are obtained by using local saturation measurements (X ray, γ ray, etc. .)

2.6. Simultaneous determination of petrophysical properties

In core analysis, there is a general trend towards the simultaneous determination of relative permeabilities and capillary pressure curves during the same experiment.

A few years ago, several studies (Richmond and Watson, 1988, Chardaire-Rivière, 1992) were devoted to the simultaneous determination of capillary pressure curves (Pc) and relative permeabilities (Kr) by automatic history matching during core flood experiments. It is now recognized that it is more accurate to measure the capillary pressure separately. However, the Kr functions can be derived using the transient of the production. Several papers have been published for the various methods. For the centrifuge method: O'Meara and Crump, 1985; Nordtvedt et al., 1993; Nimmo, 1990 with local saturation measurements using resistivity. For the "porous plate" or "membrane" method: Jennings et al., 1985; Longeron et al., 1994; Christoffersen, 1995. In the membrane method, the transient is often used to estimate the equilibrium saturation (Guo and Hammervold, 1993). However, the method is not accurate due to the high hydraulic resistance of the membrane and the presence of the second fluid

(Lenormand *et al.* 1996). A new method combines the membrane method and a continuous injection (Kokkedee and Boutkan, 1993; Kokkedee, 1994).

With the membrane method, a simultaneous Pc and resistivity index is also available (Fleury and Longeron, 1996).

2.7. Discussion

In order to design an integrated tool that can perform simultaneous measurements of the Pc and Kr curves and the resistivity index, we have looked at the drawbacks and advantages of the various methods:

- the porous plate and membrane methods are not suitable for Kr measurements.
- the centrifuge method cannot measure the positive imbibition and the negative drainage. In addition the method is limited for high pressure and temperature.

Consequently, we preferred use the semidynamic method for an integrated petrophysical tool (IPT).

3. The Integrated Petrophysical Tool (IPT)

3.1. Principle of the IPT

The semidynamic method allows the complete Pc cycle to be determined. During the same experiment, it is also possible to detemine parts of the Kr curves by steady measurement. In addition, resistivity indices are easily measured.

During positive capillary pressure measurements, oil is flowing through the samples. Consequently, there is a direct measurement of permeability to oil provided that saturations are known. If we note S_0 the inversion point (corresponding to Pc=0 during imbibition), Kr(oil) is measured for $S<S_0$ and Kr (water) for $S>S_0$ (Fig. 4).

In this study, we used a cell with 6 pressure taps along the sample (Fig. 5). For electrical measurement, the current is injected through the end-pieces and tensions are measured using the pressure taps. The effluent volume, leading to the average saturation, is measured by an accurate capacitance method in the tube separator.

Local saturation at the entrance is calculated from the average saturation using the following method.

3.2. Calculation of the local saturation

The first version of the semidynamic method had the drawback of requiring saturation measurement at a few points along the sample. For this purpose, we used an ultrasonic technique, which is accurate but impossible to use with gas and difficult to incorporate in an automatic set-up. The problem has been solved by calculating the saturation from the average saturation. This new approach is based on an analytical calculation that only use the entrance pressure and average saturation (Ramakrishnan and Capiello, 1991). The calculation is the following.

Darcy's law is written below for two immiscible phases (fluids 1 and 2) flowing in direction x (without gravity)

$$q_1 = -K\frac{Kr_1}{\mu_1}A\frac{\partial P_1}{\partial x} \qquad q_2 = -K\frac{Kr_2}{\mu_2}A\frac{\partial P_2}{\partial x}$$

q is the volume flow rate, P the pressure, K and Kr are the single-phase and relative permeabilities; μ the viscosity and A the cross section area of the sample. When the steady-state is reached, only fluid 2 (oil, for Pc>0) is flowing at a uniform flow rate q_2 and water is no longer produced (q_1=0). The pressure P_1 in water is then uniform and will be taken as a reference (P_1=0). The relative permeability Kr_2 can be written as a function of the capillary pressure $Pc = P_2 - P_1$. Darcy's law is rewritten as:

$$q_2\, dx = -K\frac{Kr_2(Pc)}{\mu_2}A\, dPc$$

and then integrated between the entrance (x=0), where Pc=Pe and outlet (x=L), with Pc(L):

$$q_2\, L = K\frac{A}{\mu_2}\int_{Pc(L)}^{Pe} Kr_2(Pc)\, dPc$$

The originality of Ramakrishnan's calculation is to consider the series of experiments performed at different flow rates. The entrance pressure Pe is then a function of the flow rate q_2. The capillary pressure Pc(L) at the outlet remains constant and equal to zero as in centrifuge experiments (O'Meara *et al.*, 1988). Equation 4 is then differentiated with respect to Pe :

$$\frac{dq_2}{dPe} = \frac{KA}{L\mu_2} Kr_2(Pe)$$

This equation gives the relative permeability of the injected fluid as a function of the derivative of the entrance pressure:

$$Kr_2 = \frac{L\mu_2}{KA} \frac{dPe}{dq_2}$$

The local water saturation S can be derived from the average saturation <S> by using the same technique:

$$L < S > = \int_0^L S\, dx$$

This equation is rewritten by using Pc as the variable instead of x :

$$< S > = \frac{KA}{L\mu_2 q_2} \int_{Pc(L)}^{Pe} S(Pc)\, Kr_2(Pc)\, dPc$$

and by differentiating with respect to the entrance pressure Pe:

$$S(Pe) = \frac{L\mu_2}{KKr_2(Pe)A} \frac{d(< S > q_2)}{dPe}$$

We have simplified this equation by differentiating the product and replacing Kr by its value :

$$S(Pe) = < S > + q_2 \frac{d < S >}{dq_2}$$

For each flow rate, the entrance saturation S(Pe), together with entrance pressure Pe gives a point on the Pc curve (since the pressure in water is taken as reference, Pe=Pc).

For Ramakrishnan and Capiello, the method was applicable mainly for relative permeability, since the average saturation is too difficult to measure experimentally. In this paper we will show that the capillary pressure curve can also be measured. We have tested this method using simulated data as well as real experiments with saturation measurement using a CAT scanner (Lenormand et al., 1995).

4. Results

4.1. Procedure

Sample 1 and 2 are two reservoir sandstone cores of diameter 4 cm and length 8 cm. They are first cleaned with toluene and isopropanol to remove crude oil. Then, the samples are saturated with brine and the displacements are started at room conditions (20 C and exit at atmospheric pressure). The injection flow rates range from 5 to 1000 cm^3/hour. The rate used for washing the outlet is always 20 cm^3/hour. The duration for the whole cycle (primary drainage, positive and negative imbibition, secondary drainage) is about one month.

Table 1 Fluid and rock properties.

Rock samples		sample #1	sample #2
	porosity	0.22	0.22
	solid density (g cm^{-3})	2.65	2.70
	water permeability (m^2)	0.125 10^{-12}	1.19 10^{-12}
Paraffinic Oil	viscosity (Pa s)	1.3 10^{-3}	1.3 10^{-3}
Brine	viscosity (Pa s)	1 10^{-3}	1 10^{-3}
	salinity (g/l)	120	25

4.2. Capillary pressures

Capillary pressure curves are first displayed using the average saturation: pressure difference between the two faces of the sample vs. average saturation (Fig. 6). The maximum capillary pressure is higher for sample #1 which is less permeable.

Then the local saturation at the entrance is calculated using Ramakrishnan's equations. Using a 3rd order polynomial for the average saturation <S> vs. Ln (Q) produces a good fit (Fig. 7). Other methods (spline) lead to similar results. The drainage Pc curve with local saturation is shown in Fig. 8. For both samples, the shape of the "local" curve is not altogether satisfactory. The correction due to the derivative is too large and leads to a non monotonic variation in saturation. This effect had not been observed with the simulated cases. It may be due to an incorrect fluid distribution at the inlet and outlet leading to 2-dimensional flow effects and fluid trapping. For imbibition and second drainage, the local and average curves are very close (Fig. 9).

The shapes of the Pc curves show that both samples are water-wet.

4.3. Electrical Properties

We first measured the formation factor when the samples are saturated with brine.

sample #1 : F_R=18.9; Archie exponent m=1.94

sample #2 : F_R= 17 ; Archie exponent m=1.90

For the resistivity index, we have tried to use the theoretical calculation to derive resistivity at the entrance using the global resistivity. The results are not favorable. In fact, this method corresponds to a "two electrode" measurement with additional contact resistance due to the presence of oil covering the electrodes. It is well established that "four electrodes" are needed to ensure correct measurement (Sprunt et al., 1990; Fleury and Longeron, 1996) This is achieved by measuring the potential along the core. We used both the average saturation (sample 1) and the saturation calculated at the center of the core using a numerical simulator (sample 2). The resistivity index is then close to the results of standard methods with a saturation exponent close to 2 (Fig. 10).

4.4. Relative Permeabilities

The Kr determination using the analytical calculation and the overall pressure drop. is not possible. The cause may be the same as for electrical measurements, i. e, an additional pressure drop at the contact between the end-piece and the sample. We also used the local measurements.

For sample 2, the whole oil Kr curve is determined during drainage and only the end points during imbibition (Fig. 11). The results are very similar to direct measurements by the standard steady state method, using the same set-up (Fig. 11).

For sample 1 (Fig. 12), the oil Kr is accurately determined, but for water there is only one value, since the negative Pc curve is vertical (water-wet sample). The low value for Kr (water) is also consistent with water wet samples.

5. Discussion

The capillary pressure curves were compared to centrifuge measurements. For both samples, the pressure level is the same. However, the residual saturation differs by 0.1 for sample 1. The analysis of our experimental set-up shows a lack of accuracy in saturation measurement. In addition, there is a

difference for the saturations derived from a Karl-Fisher titration at end of experiment. The problem is not due to the capacitance measurement of the effluent volume. The main reasons are the following :

1) some leaks in the fittings, especially at high pressure during negative imbibition,
2) dead volumes in pressure sensors, tubing and fittings,
2) leaks in the piston seals of the syringe pumps,
3) difficulty to measure the sample pore volume in the conditions of the experiment (effect of confining pressure, for instance).

We have studied the different causes of error and proposed improvements for subsequent measurements. For instance, we have designed an "in-situ" gas porosimeter to measure the pore volume.

The design of the groove on the end-piece is still a problem. We used a spiral groove to prevent any fluid trapping. The surface of the groove is not large enough and the flow is not uniform at the entrance and exit of the sample. The addition of a metallic screen may improve the flow but will increase the possibility of trapping .

We have shown that local electrical and pressure measurements along the sample are needed. There is no technical difficulty with these measurements, even at high pressure and temperature. For interpretation of the local measurements, we have shown that the average saturation was close to the local saturation in the center. In the future, it would be more accurate to have a 1-D numerical simulation of the flow and adjust the Kr to have the best fit with local measurements.

6. Conclusion

This paper describes the first use of an Integrated Petrophysical Tool (IPT) on two reservoir rock samples.

The IPT is based on the steady-state injection of one fluid through the sample placed in a Hassler cell. The experiment leading to the whole Pc cycle consists of about 30 steps at various oil or water flow rates. It takes about four weeks to measure the following petrophysical properties:

- Complete capillary pressure cycle: primary drainage, spontaneous and forced imbibitions, secondary drainage
- End-points and parts of the relative permeability curves;
- Formation factor and resistivity index.

Relative permeabilities agree with steady-state measurements. and Capillary pressure with centrifuge measurements. There is no comparison for resistivity index, but the results are in agreement with literature data. For these experiments, special attention must be paid to the precise determination of effluent production. Above all, any fluid leakage must be avoided.

In conclusion, the Integrated Petrophysical Tool is as accurate as standard methods and has the advantage of providing the various parameters on the same sample and during a single experiment. The IPT is easy to use and can be automated. In addition, it can be operated at reservoir condition.

References cited

Anderson, W. G., "Wettability literature survey: Part 2. Wettability measurement", 1986, Journal of Petroleum Technology, p. 1246.

Chardaire-Rivière, C. Chavent, G. , Jaffre J. and Liu J., 1990, Multiscale estimation of relative permeabilities and capillary pressure, SPE 20501.

Christoffersen, K. R., 1995, "Gas/Oil Capillary Pressure of Chalk at Elevated Pressures", SPEFE, sept. , p. 153-159.

Cuiec, L., "Evaluation of Reservoir Wettability and its Effect on Oil Recovery", 1991, Interfacial Phenomena in Petroleum Recovery, Ed. N.R. Morrow, M. Dekker Inc., New-York, p. 319-376.

Fleury, M. and Longeron, D., "Combined resistivity and capillary pressure measurements using micropore membrane technique", 1996, presented at the meeting of Society of Core Analysts, Montpellier, France.

Forbes, P., "Simple and accurate methods for converting centrifuge data into drainage and imbibition capillary-pressure curves", 1991, SCA Conference Paper, 9107.

Guo, Y. and Hammervold, W. L.,1993, "Equilibrium Time and Accuracy of Capillary Pressure Measurements Using Diaphragm Method", paper presented at the SPWLA Annual Symposium, Calgary.

Jennings, J. W., McGregor, D. S. and Morse, R. A., 1985, "Simultaneous Determination of Capillar Pressure and Relative Permeability by History Matching," paper SPE 14418, Las Vegas.

Kokkedee J.A. and Boutkan, V. K., 1993, "Towards measurement of Capillary Pressure and relative Permeability at Representative Wettability", 7th European EOR Symposium, Moscow.

Kokkedee J.A., 1994, "Simultaneous Determination of Capillary Pressure and Relative Permeability of a dispplaced Phase", paper SPE 28827, European Conference, London.

Lenormand R., Eisenzimmer A and Zarcone C., A novel method for the determination of water/oil capillary pressures of mixed wettability samples, paper SCA 9322, 1993.

Lenormand R., Eisenzimmer A. and Delaplace Ph., "Improvements of the Semi-Dynamic Method for Capillary Pressure Measurements", 1995, presented at the meeting of Society of Core Analysts, San Francisco.

Lenormand R., Delaplace Ph. and Schmitz P. "Can we really measurethe relative permeabilities using the micropore membrane method?", 1996, presented at the meeting of Society of Core Analysts, Montpellier, France.

Longeron, D.G., Hammervold, W.L., and Skjaeveland, S.M.: "Water-Oil Capillary Pressure and Wettability Measurements Using Micropore Membrane Technique", SCA 9426 in Proceedings of the 1994 International Symposium of the Society of Core Analysts, Stavanger, Norway, Sept.

Nimmo, J. R., 1990, "Experimental testings of transient Unsaturated Flow Theory at Low Water Content in a Centrifugal Field", Water Resources Research, Vol. 26, N° 9, p. 1951-1960.

Nordtvedt, J. E., Gerardo Mejia, Pin-Huel Yang and A. T. Watson, 1993, "Estimation of Capillary Pressure and Relative Permeability Functions from Centrifuge Experiments", SPERE, p. 292-298.

O'Meara D. J., Hirasaki G. J and Rohan J. A.: "Centrifuge Measurements of Capillary Pressure", 1988, SPE paper 18296.

O'Meara, D. J. and Crump, J. G., 1985, "Measuring Capillary Pressure and Relative Permeability in a Single Centrifuge Experiment", SPE 14419.

Ramakrishnan T.S. and Capiello A. , A new technique to measure static and dynamic properties of a partially saturated porous medium, Chem. Eng. Sci., 1991, p. 1157-1163.

Richmond P.C. and Watson A. T., Estimation of multiphase flow functions from displacement experiments, SPERE, 1990, 121-127.

Sprunt, E. S., Maute, R. E. and Rackers, C. L., "An interpretation of the SCA electrical resistivity study", the Log Analyst, pp. 76-88, 1990.

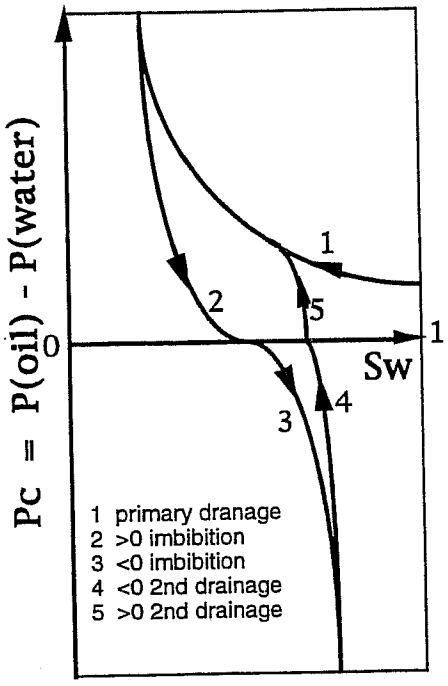

Fig. 1 - Definition of the various capillary pressure curves

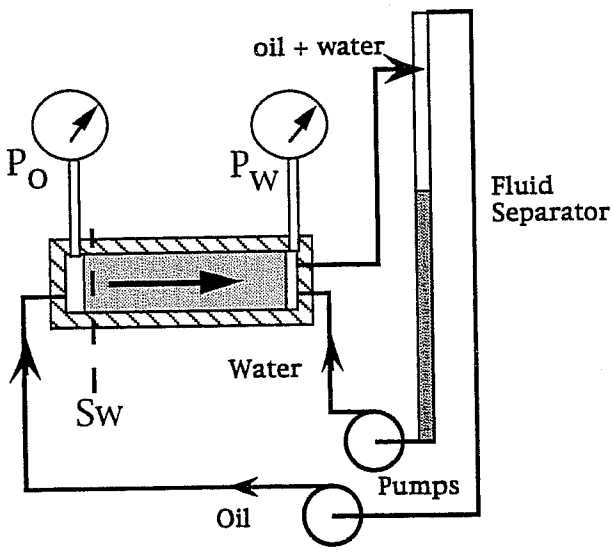

Fig. 2 - Principle of the experimental set-up for measurements using the semidynamic method.

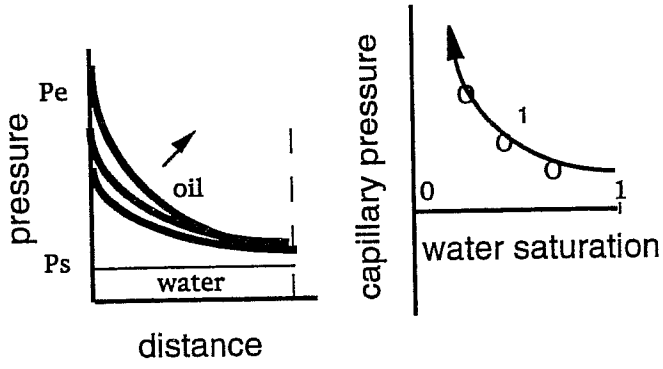

Fig. 3 - Pressure profiles and corresponding points on the Pc curves during an IPT measurement.

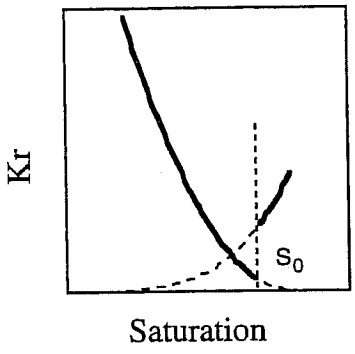

Fig. 4 - Parts of the Kr curves determined during an IPT measurement.

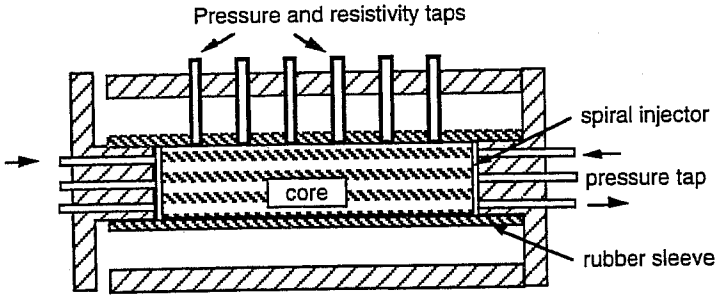

Fig 5 - Core-holder for the Integrated Petrophysical Tool

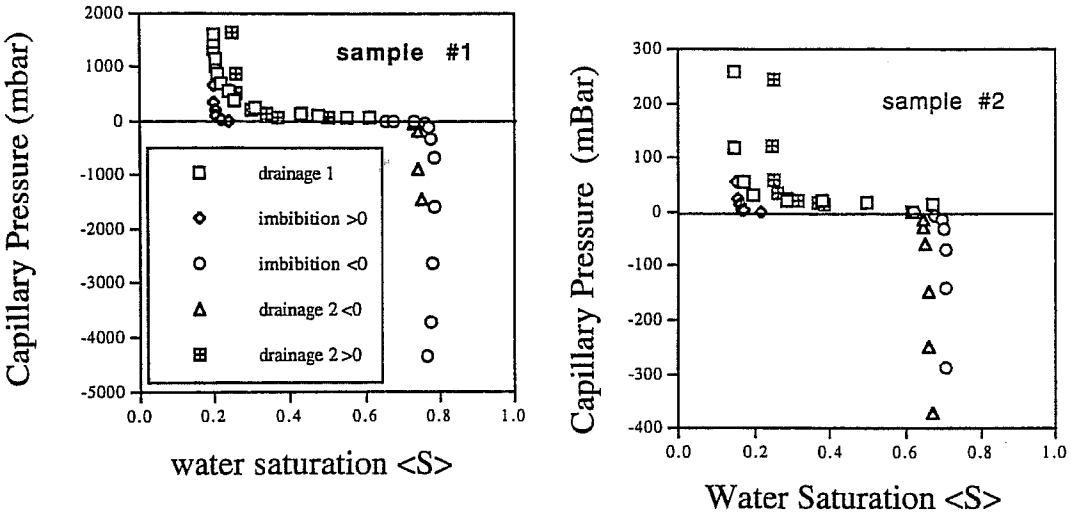

Fig. 6 - Capillary pressure cycles with average saturation.

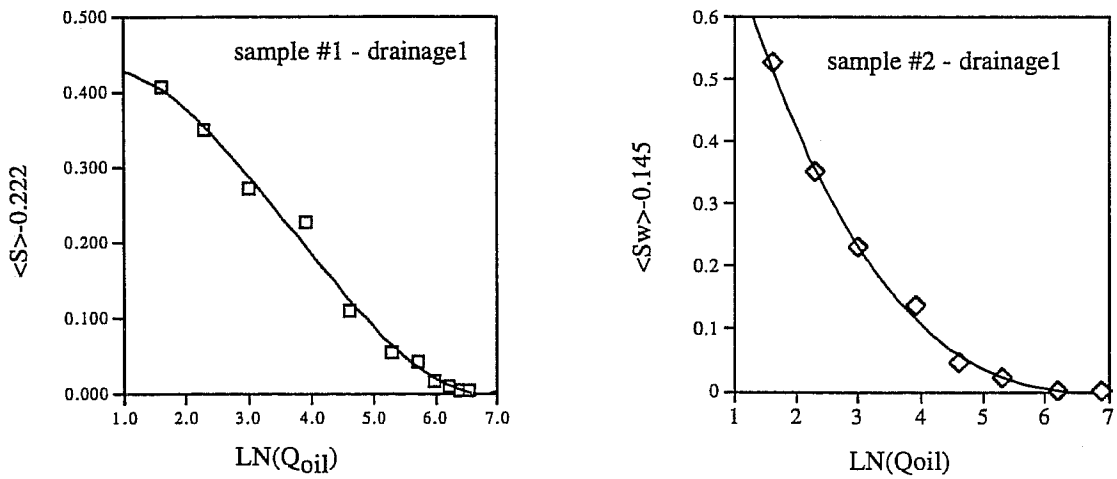

Fig. 7 - Calculation of the local saturation: approximation of <Sw> vs LN (Q) by a 3rd order polynomial.

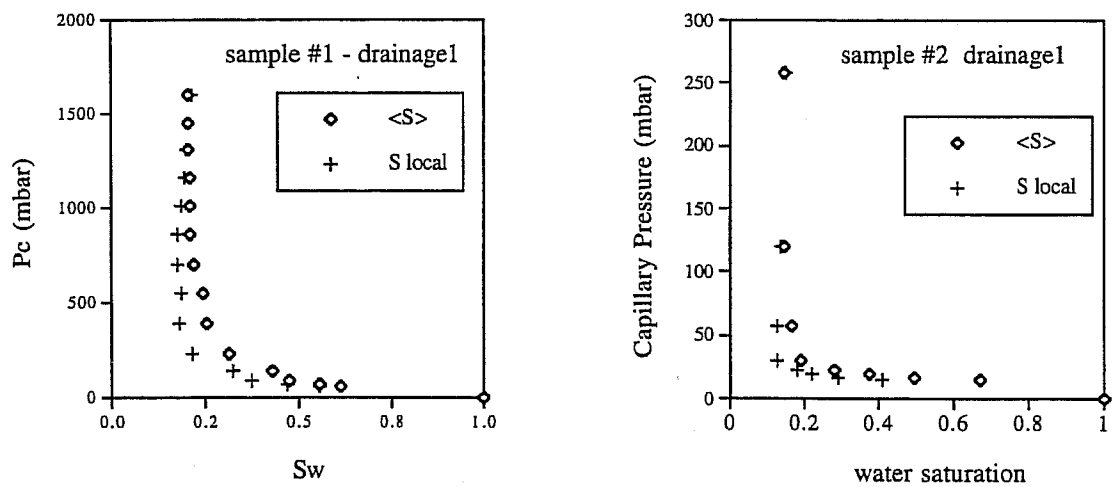

Fig. 8 - Primary drainage Pc curves: Average and local saturation

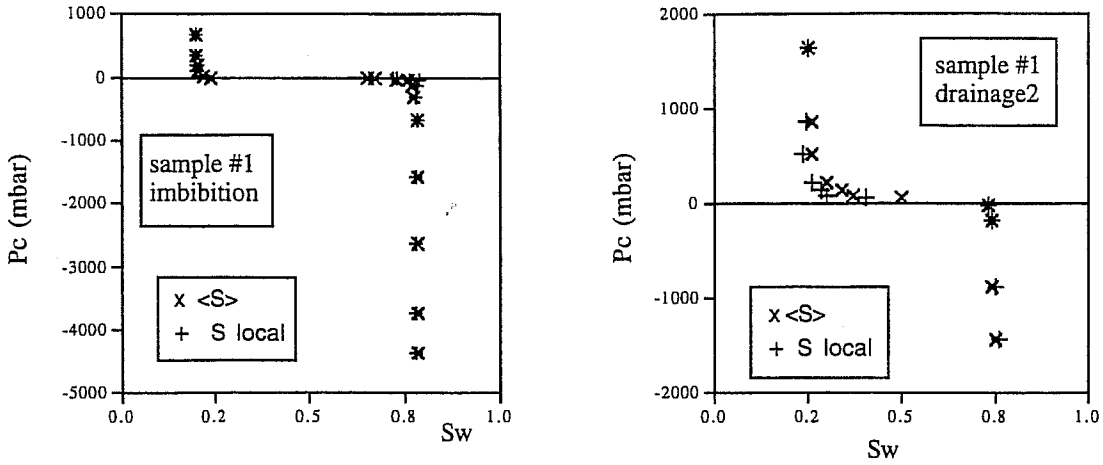

Fig. 9 - Capillary pressure with local saturation for imbibition and second drainage (sample #1).

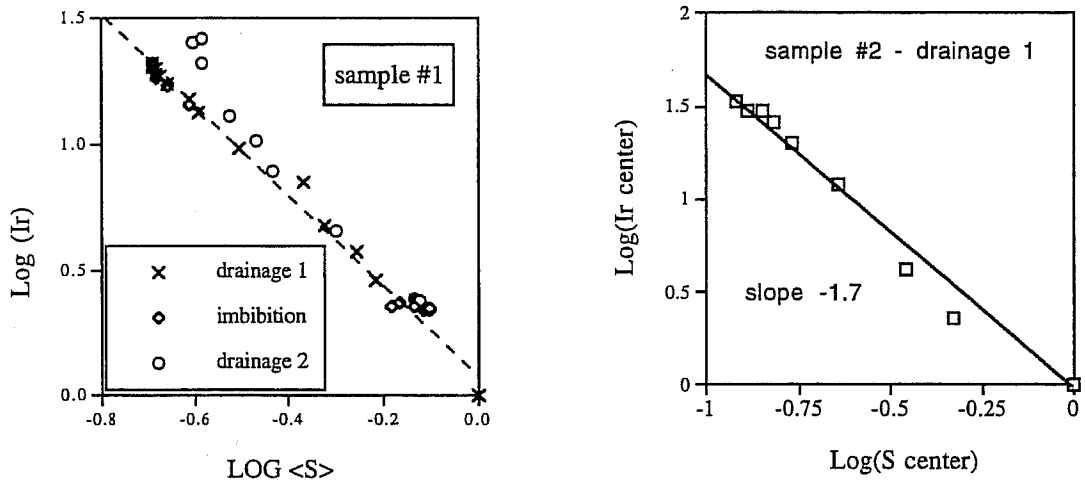

Fig. 10 - Resistivity index measurements.

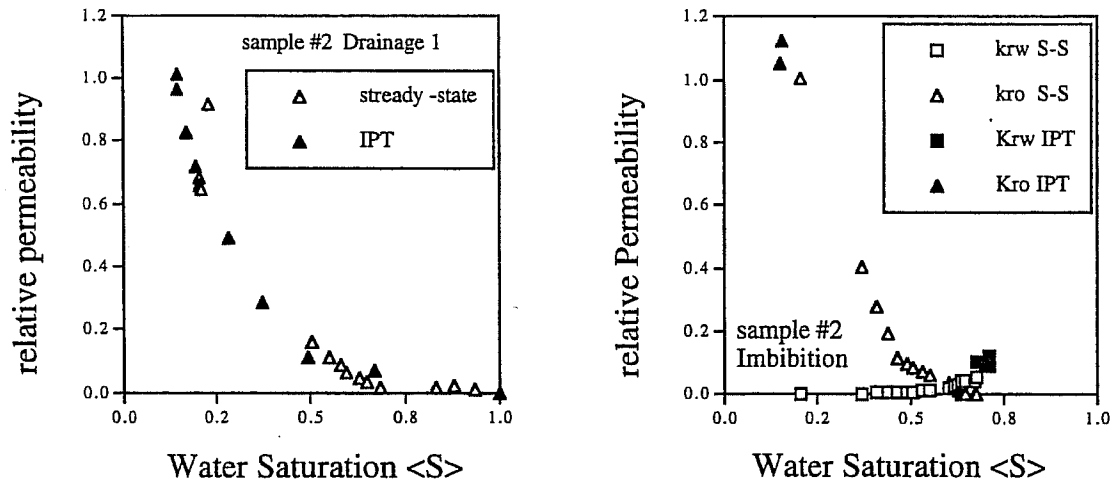

Fig. 11 - Relative permeability. Comparison between steady-state (S-S) and IPT measurements.

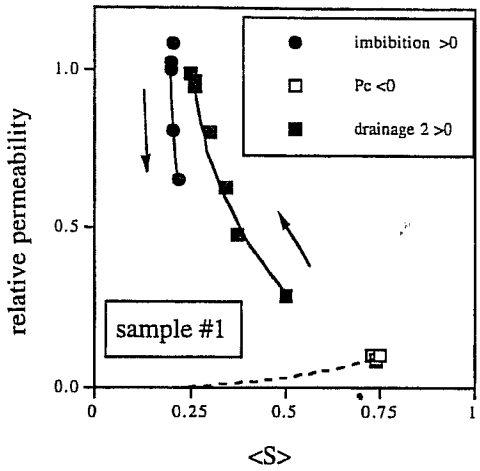

Fig. 12 - Relative permeability measurements for sample #1 (IPT)

FLOW UNITS FROM INTEGRATED WFT AND NMR DATA

E. Kasap, M. Altunbay and D. Georgi

Western Atlas Logging Services

ABSTRACT:

Reliable and continuous permeability profiles are vital as both hard and soft data required for delineating reservoir architecture. They can improve the vertical resolution of seismic data, well-to-well stratigraphic correlations, and kriging between the well locations. In conditional simulations, permeability profiles are imposed as the conditioning data. Variograms, covariance functions and other geostatistical indicators are more reliable when based on good quality permeability data.

Nuclear Magnetic Resonance (NMR) logging and Wireline Formation Tests (WFT) separately generate a wealth of information, and their synthesis extends the value of this information further by providing continuous and accurate permeability profiles without increasing the cost. NMR and WFT data present a unique combination because WFTs provide discrete, in situ permeability based on fluid-flow, whilst NMR responds to the fluids in the pore space and yields effective porosity, pore-size distribution, bound and moveable fluid saturations, and permeability. The NMR permeability is derived from the T_2-distribution data. Several equations have been proposed to transform T_2 data to permeability. Regardless of the transform model used, the NMR-derived permeabilities depend on interpretation parameters that may be rock specific.

The objective of this study is to integrate WFT permeabilities with NMR-derived, T_2 distribution-based permeabilities and thereby arrive at core quality, continuously measured permeability profiles. We outlined the procedures to integrate NMR and WFT data and applied the procedure to a field case. Finally, this study advocates the use of hydraulic unit concepts to extend the WFT-NMR derived, core quality permeabilities to uncored intervals or uncored wells.

INTRODUCTION

Over the years traditional reservoir characterization techniques have evolved into a multi-disciplinary process. Geostatistical techniques provide a framework for integrating all available engineering and geoscience data over multiple scales while honoring the petrophysical well data and geological and sedimentological models.

Well logs provide direct measures of reservoir formation properties and are a vital source for hard and soft data required for delineating reservoir architecture. They are used to improve the vertical resolution of seismic data[1-5], well-to-well stratigraphic correlations[6-7], and kriging between the well locations. In conditional simulations, well log porosity profiles are imposed as the conditioning data and the sand-to-shale ratios from well logs are maintained throughout the relevant vertical cross-sections. Well-log measured heterogeneity in a vertical cross-section is used to generate variograms, covariance functions and other geostatistical indicators within a single well or between well pairs. Corbett, et al.[8] incorporated wireline formation pressure test data into a reservoir characterization study to identify connectivity between the adjacent zones.

Recently, great effort has been dedicated to the integration of well logs into seismic data.[1-5] Conventionally seismic data has been used to delineate reservoir structure (lateral extent), but its vertical resolution is limited. Yang, C. T. et al.[2] pointed out that generally it is difficult to identify beds thinner than 25 ft from 3-D seismic signals. Although seismic data is routinely and effectively used to estimate the structure of the reservoir bodies, it typically plays no role in the essential task of estimating rock properties, which are measured or computed from well logs. In the presence of 3-D seismic surveys and logged wells, the simultaneous analysis of seismic-attribute data and borehole data often leads to better estimates of property distributions in comparison with estimates generated from either seismic or well data alone.[1-8]

Porosity and permeability are the key reservoir properties needed for proper reservoir description and simulation. Porosity is routinely available from wireline log data and, in conjunction with 3-D seismic data, can be used to generate excellent reservoir porosity models. Until recently, cores were the only source of permeability data measured on a

small enough scale to provide critical reservoir heterogeneity data. Usually permeability is derived from core based permeability-porosity cross-plots. However, such an approach is flawed as the porosity-permeability correlations are often poor and core data may be sparse and expensive to obtain.

Newly developed Nuclear Magnetic Resonance (NMR) logging techniques do provide vertically continuous pore-size distributions, but do not measure permeability directly. Transient pressure tests are the only direct, in situ measurement that can yield formation permeability. Well tests assess the largest possible scale and average all vertical variations in permeability. Wireline Formation Tests (WFT) access a limited volume of the reservoir and are well suited for characterizing reservoir heterogeneities. They also measure on a scale that closely matches the measurement scale of NMR logs.

The objective of this study is to integrate WFT-calculated permeabilities with NMR-derived permeabilities and, thereby, arrive at core quality, continuously measured permeability profiles, without increasing the cost. NMR and WFT data present a unique combination because WFTs provide discrete, in situ permeability measured through fluid-flow and NMR logs provide continuous T2 distributions. This study outlines a procedure to integrate NMR and WFT data and illustrates its application to a field study. The study extends the Hydraulic Unit concepts of Amaefule et al.[9] to the WFT-NMR derived, core quality permeabilities to uncored intervals or uncored wells.

WIRELINE FORMATION TESTS

When a WFT probe is set against the formation and a measured volume of fluid is withdrawn, a wireline formation test is initiated. Pressure changes are continuously recorded throughout the test. Decreasing pressure is sometimes followed by a stabilized flow period when the drawdown period is extended and permeability of the formation is high enough to supply fluid at a rate equal to that required by the pump withdrawal. The buildup period starts when the fluid withdrawal stops and ends when the system pressure reaches the formation fluid pressure.

Figure 1 shows a WFT test repeated three-times. This particular test was performed at a depth of 8775 ft. Approximately thirty tests at ten depths were performed. Permeability, undisturbed formation pressure (P*) and fluid compressibility can be extracted from transient-measured pressures and drawdown rates. Shown in Fig. 2 are the calculated P*s at ten vertical depths, which shows an excellent correlation between the depth and formation pressure indicating a constant pressure gradient. The calculated slope of -3.62 translates to an in situ API gravity of 90.8 which may be indicative of solution gas in the oil under the reservoir conditions. Alternatively the reservoir oil might also contain large quantities of light hydrocarbon components.

In addition to P*, WFTs can provide a direct measure of near wellbore permeability. Although WFTs are short (seconds to a minute), tests cannot feasibly be conducted continuously, because the time to set the tool and the time for the pressure to stabilize before ending the test are too long to permit "continuous" permeability profiling. Figure 3 shows ten permeability values calculated at ten vertical depths. The figure indicates that ten measurements of permeability are not sufficient to delineate reservoir heterogeneity, although 10 pressure values are quite satisfactory for calculating reservoir fluid pressure gradient and in situ API gravity. However, even though WFT-measured permeabilities are too sparse to produce a continuous profile, they are curretnly the most reliable in situ measured permeability obtainable on a small enough scale to permit the identification of local heterogeneity.

In the following section, we discuss the calculation of P* and permeability from WFTs. New concepts and analysis techniques, combined with 3-D numerical studies, have recently been reported in the literature.[10-15] 3-D numerical simulations have also contributed to the diagnosis of WFT-related problems and the improved analysis of WFT data. We first review, the Formation Rate Analysis Technique (FRAT), a new technique that combines drawdown and buildup data analysis.

Formation Rate Analysis

Kasap et al.[10-11] proposed FRAT for the entire WFT to obtain permeability and P*. FRAT combines the drawdown and buildup data into a single plot where both the drawdown and buildup periods are well represented by straight lines with identical slopes. The geometric factor (G_O) concept[16] is the foundation of FRAT, from which we obtain both P^* and permeability. G_O is calculated for modified hemispherical-flow geometry, which does nor require a cavity in the formation, nor a probe seal of infinite extent. In Darcy's equation with this modified hemispherical geometry for isothermal, steady-state

flow of a liquid, the dimensionless G_O replaces the factor 2π that would apply for true semi-infinite, hemispherical-flow geometry.

During the drawdown period, fluid will be withdrawn at a rate of q_{dd}. The accumulation rate, q_{ac}, is the difference between the formation flowrate, q_f, expressed with Darcy's equation, and drawdown rate of the pump. The pressure-transient theory for slightly compressible liquids can be derived from the definition of isothermal compressibility:

$$q_{ac} = C_t V_{sys} \frac{\partial P(t)}{\partial t}. \quad (1)$$

The rate q_{ac} for all practical purposes, is equal to the difference between q_f, the volumetric rate flowing through the rock adjacent to the packer probe (Darcy flux), and q_{dd}, the drawdown rate of the pump. Thus, we can rewrite the Darcy equation and account for the WFT drawdown, stabilized flow and buildup data:

$$P(t) = P^* - \left(\frac{\mu}{kG_o r_i}\right)\left(C_t V_{sys} \frac{\partial P(t)}{\partial t} + q_{dd}\right) \quad (2)$$

Note that the terms within the last parentheses in Eq. 2 correspond to the accumulation and drawdown rates, respectively. The two terms act against each other, and their difference, in essence, is the flowrate from the formation. Eq. 2 provides a means to estimate formation permeability and P^* from drawdown or/and buildup data. A plot of $P(t)$ vs. Formation Rate, which is given in Eq. 2 as

$$q_f = \left(C_t V_{sys} \frac{\partial P(t)}{\partial t} + q_{dd}\right) \quad (3)$$

should approach to a straight line with a negative slope and intercept P^* at the P(t) axis. The absolute value of the slope, m, is

$$m = \frac{\mu}{kG_o r_i},$$

and permeability is calculated from

$$k = \frac{\mu}{G_o r_i m}. \quad (4)$$

We note that Eq. 2 does not require a constant drawdown rate as long as q_{dd} is continuously recorded.

Theoretically, both drawdown and buildup should have the same slope and should go through the same straight line. However, during the early stages of the drawdown period when the flow is being established and during the early stages of the buildup period when the flow is adjusting to the changing flow conditions, the actual pressure vs. formation rate plot may deviate from the assumed pseudo-steady state solution.

Field Tests

We illustrated FRAT with two field examples collected with the Reservoir Characterization Instrument (RCI℠)[17]. Test A6-4 was chosen because it shows a stabilized flow during the drawdown period and test A7-2 was chosen because it is representative of many wireline formation tests.

Figure 4 shows pressure versus formation rate and its best-fit straight line. The slope of the straight line is directly related to permeability and the intercept with the vertical axis is P*. When the probe radius of 2.25 cm, a viscosity of 0.75 cp and G_o of 4.27 are used a permeability of 70.1 mD is calculated.

This calculation can be performed in real time with every new pressure value measured by using weighted averages of formation rate. A plot of such a calculation is shown in Fig. 5. Figure 5 indicates that calculated permeability stabilizes within a very short period of time and remains constant for the drawdown and buildup periods at around 69.5 mD. Figure 5 also shows the corresponding formation rate, calculated by using Eq. 2, and indicates that during the test formation rate nearly stabilizes due to high permeability and low drawdown rate.

Formation rate analysis is also applied to A7-2 test, (the first repeat test, Fig. 1). The FRAT plot, shown in Fig. 6 indicates very little scatter in the data. Using the same viscosity, probe radius and G_o as in the A6-4 test, the calculated permeability and P*, based on the best-fit straight line, are 10.1 mD and 4627.7 psi, respectively. For the formation rate calculations a system volume of 267 cc and fluid compressibility of $6.8 \cdot 10^{-4}$/psi were used. Figure 7 shows the continuously calculated permeability and flow rate. The figure indicates that for this test the formation rate did not stabilize; nevertheless, the calculated permeability is not affected and reaches a constant value immediately after the start of the test and remains constant at that value throughout the drawdown and buildup periods.

Numerical Simulations

In this section, we use numerical simulations to verify the FRAT results. A 3-D finite-element scheme applied to the diffusivity equation in Cartesian coordinates is used to calculate transient pressures due to the flow in the near-wellbore region of the formation. The details of the simulator are given in previous publications.[10-13]

Figure 8 shows the comparison of pressure versus time plot from the field data, and the numerical simulation data for the A6-4 test. We used measured drawdown rates at the pump and the information given in Table 1 for this simulation. The figure shows that the permeability of 69.5 mD used in the simulation (FRAT permeability is 70.1 mD) satisfactorily matches the pressure response of the formation. The match between the field data and the numerical simulation data is excellent.

Numerical simulations were also conducted for the A7-2 test (Fig. 1, the first repeat test) by using the FRAT-obtained permeability and the continuously measured drawdown pump rate. Simulation results and field data are compared in Fig. 9. The results indicate that the simulation run with the FRAT permeability match well the field data.

These field test studies confirm that FRAT analysis correctly predicts formation permeability and undisturbed formation pressure. WFTs can very accurately provide fluid type, density and location and formation permeability and pressure.

Table 1- Numerical Simulation Parameters

	Value
Flow Line Volume (cm^3)	267.1
Wellbore Radius (cm)	15
Outer Boundary, r_e (cm)	230
Probe Radius (cm)	1.27
Pay Thickness (cm)	242.25
Duration of Drawdown (s)	5
Porosity	0.15
Fluid Viscosity (cp)	0.75
Reservoir Pressure, P* (atm)	315.116
Total Compressibility (/atm)	$1.x10^{-4}$

NMR LOGGING

The earliest industry workers[18-20] recognized the potential for NMR measurements to provide porosity, pore-size distribution and permeability. Initial attempts to make downhole NMR measurements proved cumbersome. However, in the early 1990's a new magnet configuration[21] greatly simplified the measurement and significantly increased the data quality. Today in many areas of the world NMR logs are run routinely as part of the open hole formation evaluation suite.

NMR logs provide the petrophysicist two types of data:

- mineralogy independent porosity
- T2 distributions

The NMR measurement essentially counts the number of hydrogen protons aligned with an external magnetic field, and then monitors the dephasing of the protons' spins with time. The number of protons initially aligned with the external magnetic field is proportional to the porosity, while the change in amplitude of subsequent echoes, known as the transverse relaxation, is characterized by a quasi-exponential decay with a characteristic time, T2 (Fig. 10). The initial NMR signal amplitude only depends on the hydrogen proton density in the pore space, as the measurement is insensitive to the hydrogen in the rock matrix (e.g., OH^- groups in clays) and is, thus, a mineralogy independent measure of porosity.

To measure T2-decay, a series of evenly spaced radio frequency, (RF) pulses are used to rephase the transverse magnetization. These RF pulses essentially recall the NMR signal, which is then referred to as an echo. In a gradient-magnetic field or in a heterogeneous magnetic field the apparent T2-decay rate depends on the inter-echo spacing (TE). However, for liquids, diffusion effects are minimal for commonly used inter-echo times (e.g., 0.6 and 1.2 ms.); however, they can be important for very light hydrocarbon liquids and gasses.[22]

The dominant factor on the T2-relaxation process is controlled by nuclear magnetic interactions occurring on the pore wall. Including diffusion effects, the T2 relaxation is well described by:

$$\frac{1}{T2} = \frac{1}{T2_{bulk}} + \frac{\lambda}{T2_{surf.}}\frac{S}{V} + \frac{1}{T2_D} \qquad (5)$$

where:

$T2_{bulk}$	=	relaxation time of the bulk fluids in the pore space
$T2_{surf.}$	=	relaxation time of the fluid in a few molecular layers next to the pore surface
λ	=	thickness of the surface fluid layer
S, V	=	pore surface and pore volume, respectively
$T2_D$	=	relaxation time due to diffusion

If diffusion effects are negligible, and because the bulk T2 for water is of the order of seconds while the observed T2 is only a few hundred milliseconds or less, then the above can be approximated by:

$$\frac{1}{T2} = \rho_s \frac{S}{V} \tag{6}$$

where:

ρ_s	=	surface relaxivity (0.003 - 0.03 cm/s) - clastics
	=	surface relaxivity (< 0.003 cm/s) - carbonates

In water filled pore systems, T2 is a measure of the S/V ratio. Large pores will have a small surface-area-to-pore-volume ratio and long T2's, while small pores will have a large surface-area-to-pore-volume ratio and will exhibit short T2's. Rocks with a spectrum of pore sizes give rise to a corresponding spectrum of T2 relaxation times (Fig. 11).

The NMR echo data from the logging tool are converted to a T2 spectrum that is closely related to the pore-size distribution for a single-phase fluid. The T2 spectrum derived from the echo data, measures the porosity fraction associated with each T2. The integral of the T2 spectrum, (the sum of the porosities at each T2), is the NMR porosity. However, the real benefit from NMR logging derives not just from the NMR porosity, but from the partitioning of the T2 spectrum into fast decaying fluids (bound and irreducible water) and free fluids.[23] Generally, clay bound water relaxes in a few milliseconds or less,[24] and, thus, if we log with a short enough TE (~0.6 ms) and faithfully record the early echoes, the integral from 0 to 4 ms will be a measure of the clay bound water. For clastics, the integral of the T2 spectrum from 4 to ~32 ms is a measure of the irreducible water and the remainder, e.g. 32 ms to ∞, is the moveable fluid fraction. The T2-time separating the moveable and irreducible fluids is referred to as the T2-cutoff time.

In clastic systems, the NMR T2 data has been used successfully to estimate permeability.[25] Several models are currently used to derive permeability from T2 spectra. Timur[19] (1968) recognized the relationship between moveable fluids and permeability.

$$k = 0.136 \frac{\phi^{4.4}}{S_{wir}^{2}} \tag{7}$$

Kenyon[26] and others have related permeability to the mean T2. This approach is formulated as:

$$k_{NMR} = C \cdot T2_{gm}^{2} \cdot \phi^{4} \tag{8}$$

The constant C may need to be adjusted for different reservoirs and formations.

Coates[27] put forward a permeability model which incorporates both the moveable and bound fluid fractions and does not explicitly depend on the mean T2.

$$k = \left(\frac{100\phi}{C}\right)^{4} \left(\frac{S_{moveable}}{S_{wir}}\right)^{2} \tag{9}$$

where:

$S_{moveable}$	=	Movable fluid saturation = $(1-S_{wir})$
S_{wir}	=	Bulk volume irreducible fluid saturation
C	=	Formation specific constant

This is particularly advantageous in the presence of hydrocarbons. In a water wet system, if liquid hydrocarbons are present then Eq. 5 does not simplify to Eq. 6, because the hydrocarbons are shielded from the rock surface and do not undergo surface relaxation. If a rock contains both water and oil, the pore space occupied by hydrocarbons will no longer exhibit the T2 relaxation associated with the S/V ratio of these pores and the mean T2 will be anomalously large compared to the mean T2 for a water saturated rock. Thus, Eq. 8 will over estimate the permeability in hydrocarbon zones whilst permeability calculated with the Coates' equation, Eq. 9, will be relatively unaffected by hydrocarbons.

RCI CALIBRATION OF NMR PERMEABILITY

The NMR signal is obtained from the fluids in the pores of a porous media. To interpret this signal a good understanding of the relationship between the signal, the rock matrix and the fluids is required. An accurate interpretation of the NMR data also requires calibration of the processing parameters (e.g. T2-cutoff

time, coefficients and exponents in the permeability model). Where available, core data are the natural source for the calibration data. However, advancements in logging technology, specifically in WFT tool-design, has moderated this requirement, and provided an alternative solution to interpretation calibration for most fields where cores are unavailable or too expensive to obtain.

In this study, RCI generated permeability values are used to calibrate the coefficient in the Coates' equation. Plotted in Fig. 12 are the RCI permeabilities and the MRIL® permeabilities for different values of C. To determine the best Coates constant, we have summed the absolute value of the difference between the RCI and MRIL permeabilities and plotted the sum versus the C-value (Fig. 13). The optimum C for this formation is obtained from the minimum at 14.5. Calibration of the coefficient in Coates bound-water permeability model via RCI data makes it possible to translate the NMR log responses into an accurate permeability profile for the formation despite the lack of core data.

DETERMINATION OF FLOW UNITS

"A flow unit is a volume of reservoir rock within which geological and petrophysical properties that affect the fluid flow are internally consistent and predictably different from properties of surrounding rock volumes".[28] Flow units are extensively used in reservoir characterization studies and in numerical simulations for performance predictions and reserve estimations. Two key elements for deriving the flow-unit profiles are accurate permeability and effective porosity profiles. RCI-calibrated MRIL permeability and MRIL porosity meet this requirement, and, hence, enable the flow unitization process.

Permeability and porosity data from a control well or interval are processed to determine RQI, the Reservoir Quality Index[9] (Figs 14a and b).

$$RQI = 0.0314\sqrt{\frac{k}{\phi}} \qquad (10)$$

Then a transformation of RQI to hydraulic units is performed by employing the hydraulic unitization technique as outlined below.

Traditional plots of permeability versus porosity (Fig. 14a) have little petrophysical and no mathematical justification. Usually, log-normally distributed permeability is plotted against normally-distributed porosity in a semi-logarithmic format to reduce the scatter. The underlying assumption for this plot is the capillary-tube model from which the Kozeny-Carman equation stems.

$$k = \frac{1}{8}\phi\frac{r^2}{\tau^2} \qquad (11)$$

When capillary-tube geometry is assumed, the r^2 term is replaced with an expression for the specific surface area, S_{gv}:

$$k = \frac{\phi_e^{\,3}}{(1-\phi_e)^2}\frac{1}{F_s\tau^2 S_{gv}^2} \qquad (12)$$

where:

k	=	RCI calibrated MRIL permeability, cm^2
ϕ_e	=	effective Porosity (MRIL MPHI)
τ	=	tortuosity
F_s	=	shape factor
S_{gv}	=	specific surface area, cm^{-1}

This equation can be rewritten as:

$$k = \frac{\phi_z}{K_z S_{gv}^2} \qquad (13)$$

where:

ϕ_z	=	normalized ϕ ratio, $\phi^2/(1-\phi)^2$
K_z	=	Kozeny-Carman Constant, $F_S\,\tau^2$

In reality, tortuosity and shape factor vary from one sample to another reflecting formation heterogeneity; therefore, the traditional permeability versus porosity cross-plots show scatter, even in semi-logarithmic space. Therefore, any transform equation derived from this approach (via statistical best fit-line) is prone to have unacceptable error. Assuming that the Kozeny-Carman constant is a single "universal" constant has proven unacceptable. The hydraulic unitization concept assigns a different constant for each hydraulic (flow) unit to account for variations in the pore-space attributes. To apply the hydraulic unitization methodology, we apply the following steps:

1. Algebraic manipulation of the Kozeny-Carman equation yields the following when both sides of the original equation are divided by porosity and raised to the power of 0.5 :

$$\sqrt{\frac{k}{\phi_e}} = \frac{1}{S_{gv}}\frac{\phi_e}{K_z^{0.5}(1-\phi_e)} \qquad (14)$$

2. Taking logarithms of both sides of the above equation results in a ***straight-line relationship***:

$$\log\left[\sqrt{\frac{k}{\phi_e}}\right] = \log\left[\frac{1}{S_{gv}\ K_z^{0.5}}\right] + \log\left[\frac{\phi_e}{(1-\phi_e)}\right]$$

$$y = b + mx \qquad (15)$$

3. The left-hand side of the above equation (with the proper conversion factor for permeability - cm^2 to $microns^2$) yields the RQI (Fig. 14b).

The relationship of K_z and S_{gv} to permeability and porosity remains constant for data points with similar pore-space attributes. Therefore, when RQI is plotted versus normalized porosity in logarithmic space, data fall on a straight-line with a 45° slope. Where this straight line intersects the y-axis (x =1) the intercept is equal to $\log(1/SgvK_z^{0.5})$. This intercept is called the Flow Zone Indicator (FZI). Samples with similar pore space attributes exhibit similar y-intercepts. They remain within a confidence envelope (set by the required data accuracy) around a 45° straight-line. Pore-space attributes control intrinsic flow properties; samples with similar y-intercepts belong to the same hydraulic unit. Any large deviation from this straight line indicates the existence of a separate hydraulic unit for which the relationship between K_z, S_{gv}, porosity and permeability is different.

To identify the correct number of hydraulic units (i.e. to draw the correct number of straight-lines with the prescribed 45° slope through the data), cluster analysis is used (Fig. 15). The analysis is based on deciding the optimum center for each data cloud and isolating that set of data with a cluster identification tag. The clustering algorithm used for the RCI-calibrated-MRIL data maximizes the between-cluster distance and minimizes the within-cluster variations. It should be noted that cluster analysis introduces a bias to the determination because the number of clusters should be known prior to clustering. This bias is later eliminated from the determination of flow units via sensitivity analysis.

Sensitivity Analysis

Independent input variables used in the flow-unit formulation have associated uncertainties and known inaccuracies. Because of these uncertainties adjoining hydraulic units may not be statistically independent. If the computed uncertainties for adjoining hydraulic units overlap, the two units are merged.

In this study, error margins are calculated for RQI and FZI based on the rms (root mean square) equation and recommended API practices for permeability and porosity determinations. The following rms equation applies, if:

$$y = f(x_1, x_2, x_3, \ldots, x_n)$$

then, the error in y-function can be calculated:

$$\Delta Y = \pm\left(\begin{array}{l}\left((\partial Y/\partial x_1)\,\Delta x_1\right)^2 + \ldots \\ +\left((\partial Y/\partial x_n)\,\Delta x_n\right)^2\end{array}\right)^{0.5} \qquad (16)$$

where:

$\partial Y / \partial x_i$ are partial derivatives of the function with respect to its independent variables. Δx_i are uncertainties associated with independent variables.

With the above equation, an error margin is calculated for each cluster. These margins are used to establish whether clusters are truly independent. Then clusters with similar means are merged into one unique flow unit (Figs 16 and 17). Redundant clusters are eliminated. Clusters with more than 20 % variation are isolated and then reanalyzed to refine the clustering. Thus, the bias introduced initially into the analysis is eliminated. At this stage of unitization, flow units are plotted in depth format with available wireline logs (Fig. 18).

Further study is planned for deriving permeability and MBVI transform equations by using the flow unit profiles generated from RCI-calibrated MRIL permeability and conventional logs. This hopefully will permit us to derive MRIL equivalent irreducible water saturation and permeability profiles for adjoining cased wells from conventional log data.

CONCLUSIONS

In this study, we used RCI pressure transient permeabilities to calibrate MRIL derived permeabilities. The constant in the Coates equation was changed from a generic 10 to the reservoir specific 14.5. We then used the hydraulic units concept to classify the reservoir into six distinct flow units based on the MRIL effective porosity and RCI calibrated MRIL permeabilities

We conclude from this work, that

1. WFT data analyzed with FRAT simultaneously provides excellent pressure data for fluid identification and permeabilities.
2. WFT permeabilities are ideally suited for calibrating NMR permeabilities.
3. WFT-calibrated, NMR-permeability profiles are an excellent source of reservoir heterogeneity data.
4. MRIL effective porosity and RCI-calibrated MRIL-permeability data can provide core-quality in situ data in reservoir flow unit studies.

NOMENCLATURE

C_t	compressibility factor, *1/psi*
F_s	shape factor
G_o	geometric factor
k	permeability, *mD*
K_z	Kozeny-Carman Constant
P	pressure, *psi*
q	volumetric flowrate, cm^3/s
r_i	packer-probe radius, *cm*
S	pore surface area, cm^2
S_{gv}	specific surface area, cm^{-1}
t	time, *s*
$T2_{bulk}$	bulk fluid relaxation time, *ms*
$T2_{surf.}$	Surface relaxation time, *ms*
$T2_D$	relaxation time due to diffusion, *ms*
V	pore volume, cm^3
V_{sys}	system volume, cm^3
ϕ	porosity, *fraction*
ϕ_e	effective porosity, *fraction*
ϕ_z	normalized ϕ ratio
λ	thickness of the surface fluid layer
μ	viscosity of fluid, *cp*
ρ_s	surface relaxivity, *cm/s*
τ	tortuosity

Subscripts

ac	accumulation
dd	drawdown
f	formation

ACKNOWLEDGMENTS

We gratefully acknowledge the assistance of J. Michaels and M. Moody with data collection and preparation, and D. Oliver and T. Jbeili for editorial assistance. Finally, we thank Western Atlas Logging Services for permission to publish this paper.

REFERENCES

1. Araktingi, U. G., Bashore, W. M.,Tran, T. T. B., and Hewett, T. A., " Integration of Seismic and Well Log Data in Reservoir Modeling," Reservoir Characterization III, Edited by B. Linville, T. E. Burchfield and T. C. Wesson, PennWell Publishing Co., 1993, p515-554.
2. Yang, C. T., Chopra, A. K., J. Chu, Huang, X., and Kelkar, M. G.,"Integrated Geostatistical Reservoir Description Using Petrophysical, Geological and Seismic Data for Yachheng 13-1 Gas Field," SPE 30566, presented at the SPE Annual Technical Conference and Exhibition, 22-25 October, Dallas, Texas, 1995.
3. Yang, A-P. and Gao, Y.,"Reservoir Characterization by Integrating Well Data and Seismic Attributes," SPE 30563, presented at the SPE Annual Technical Conference and Exhibition, 22-25 October, Dallas, Texas, 1995.
4. Schultz, P.S., Ronen, S., Hattori, M., Mantran, P., Hoskins, J., and Crobett, J., "Seismic-Guided Estimation of Reservoir Properties," SPE 28386, presented at the SPE Annual Technical Conference and Exhibition, 25-28 September, New Orleans, LA, 1994.
5. Hand, J. L., Moritz, A.L., Jr., Yang, C-T., Chopra, A. K., "Geostatistical Integration of Geological, Petrophysical, and Outcrop Data for Evaluation of Gravity Drainage Infill Drilling at Prudhoe Bay," SPE 28396, presented at the SPE Annual Technical Conference and Exhibition, 25-28 September, New Orleans, LA, 1994.
6. Johann, P., Fournier, F., Souza, O., Eschard, R. and Beucher, H. "3-D Stochastic Reservoir Modeling Constrained by Well and Seismic Data on a Turbidite Field," SPE 36501, presented at the SPE Annual Technical Conference and Exhibition, 6-9 October, Denver, CO, 1996.
7. Reedy, G. K., and Pepper, C. F.; "Analysis of Finely Laminated Deep Marine Turbidites: Integration of Core and Log Data Yields a Novel Interpretation Model," SPE 36506, presented at the SPE Annual Technical Conference and Exhibition, 6-9 October, Denver, CO, 1996.
8. Corbett, C., Solomon, G. J., Kartikay, S., Ujang, S. and Ariffin, T.; " Application of Seismic-Guided Reservoir Property Mapping to the Dulang West Field, Offshore Peninsula Malaysia," SPE 30568, presented at the SPE Annual Technical Conference and Exhibition, 22-25 October, Dallas, Texas, 1995.
9. Amaefule, J. O., Altunbay, M., Tiab, D., Kersey, D. G., Keelan, D. K.; "Enhanced Reservoir Description: Using Core and Log Data to Identify

Hydraulic (Flow) Units and Predict Permeability in Uncored Intervals/Wells", SPE 26436, 68th Annual SPE Conference, Oct. 1993.

10. Kasap, E., Huang, K., Shwe, T. and Georgi D.; "Robust and Simple Graphical Solution for Wireline Formation Tests: Combined Drawdown and Buildup Analysis," SPE paper 36525, presented at the SPE Annual Technical Conference and Exhibition, Denver, Colorado, 6-9, 1996, Vol. Ω, p343-357.

11. Kasap, E., and Georgi, D., Micheals J., and Shwe, T.; "A New Simplified, Unified Technique for the Analyses of Wireline Formation Test Data," paper presented at the 1996 SPWLA Annual Logging Symposium, New Orleans, LA, June 16-19.

12. Huang, K., Samaha, A., and Kasap, E.; "Dimensionless Parameters for Interpretation of WFT Data: Simulations and Experiments," paper presented at the 1996 SPWLA Annual Logging Symposium, New Orleans, LA, June 16-19.

13. Samaha, A., Huang, K., Kasap, E., Shwe, T., and Georgi, D.; "Near Wellbore Permeability and Damage Measurements: Experiments and Numerical Simulations for Interpretation of WFT Data," SPE 35150 presented at the SPE 1996 International Symposium on Formation Damage Control in Lafayette, Louisiana, U.S.A. 14-15 February.

14. Waid, M. C., Proett, M.A., Chen, C.C., and Ford, W.T.: "Improved Models for Interpreting the Pressure Response of Formation Testers," paper SPE 22754 presented at the 1991 SPE Annual Technical Conference and Exhibition, Dallas, TX, Oct. 6-9.

15. Proett, M. A. and Chin, W. C.,; "Supercharge Pressure Compensation Using a New Wireline Testing Method and Newly Developed Early Time Spherical Flow Model," paper SPE 36524 presented at the 1996 SPE Annual Technical Conference and Exhibition, Denver, CO, Oct. 6-9.

16. Goggin, D. J., Trasher, R. L., and Lake, L. W.; "A Theoretical and Experimental Analysis of Minipermeameter Response Including Gas Slippage and High Velocity Flow Effects," In Situ 12, No. 1 and 2 (1988) 79-116.

17. Micheals, J., Moody, M. and Shwe, T.; "Wireline Fluid Sampling," paper SPE 30610, presented at the SPE Annual Technical Conference and Exhibition, Dallas, TX, October 22-25, 1995.

18. Brown, R.J.S., Gamson, B.W.; "Nuclear Magnetism Logging", SPE 1305-G, Dallas, Tx, October 4-7, 1959

19. Timur, A.; "Pulsed Nuclear Magnetic Resonance Studies of Porosity, Movable Fluid, and Permeability of Sandstones", Trans. AIME, v. 246, p. 775, 1969

20. Seevers, D.O.; "A Nuclear magnetic Method for Determining the Permeability of Sandstones", Trans. SPWLA, v.6, Sec. L, 1966

21. Miller, M.N., Paltiel, M.E., Gillen, J. Granot and J.C. Bouton; "Spin Echo Magnetic Resonance Logging: Porosity and Free Fluid Index Determination", SPE 20561, 65 th Annual Tech. Conf., New Orleans, Sep 23-26, 19990

22. Akkurt, R., Vinegar, H.J., Tutunjian, P.N., and Guillory, A.J.; "NMR Logging of Natural Gas Reservoirs", Paper N, Presented at the 36th Annual Logging Symposium, SPWLA, Paris, France, 1995.

23. Starley, C., Morris, C. E., Kenyon, W. E. and Howard, J. J.; "NMR in Partially Saturated Rocks: Laboratory Insights on Free Fluid Index and Comparison With Borehole Logs," paper CC, presented at the 32nd Annual Logging Symposium, SPWLA, Midland, TX, June 16-19, 1991.

24. Prammer, M. G., Drack, E. D., Bouton, J. C., Gardner, J. S. and Coates, G. R., "Measurements of Clay-Bound Water and Total Porosity by Magnetic Resonance Logging; " SPE 36522, presented at the SPE Annual Technical Conference and Exhibition, 6-9 October, Denver, CO, 1996.

25. Kubica,P.; "Statistical Tests of Permeability Estimates Based on NMR Measurements", SPWLA 36 th Annual Logging Convention, Paper VVV, June 26-29, 1995.

26. Kenyon, W.E., Day, P.I., Straley, C., Willemsen, J.F.; "A Three-Part Study of NMR Longitudinal Relaxation Properties of Water-Saturated Sandstones", SPE Formation Evaluation, September 1988.

27. Coates, G.R., Miller, M., Gillen, M., Henderson, G.; "An Investigation of a New Magnetic Resonance Imaging Log", SPWLA Convention in Midland, Tx, June 18, 1991.

28. Ebanks, W. J., Jr.; "Flow Unit Concept-Integrated proach to Reservoir Description for Engineering Projects", ARCO Oil and Gas Company, Plano, TX.

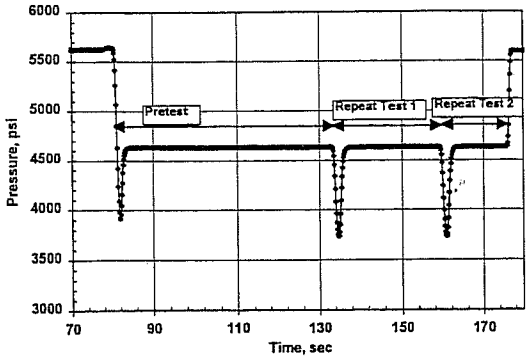

Figure 1. Pressure versus time from a WFT showing a pretest and two repeated tests.

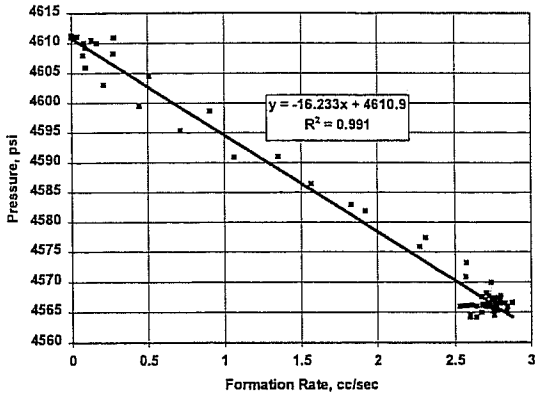

Figure 4. Pressure versus formation rate plot for Test A6-4 and its best fit straight line. A permeability of 70.1mD is calculated from the slope.

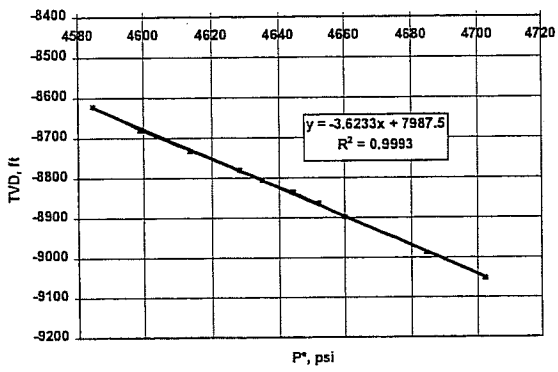

Figure 2. Depth versus formation pressure obtained from a WFT. The calculated pressure gradient corresponds to 90.8 API gravity formation fluid.

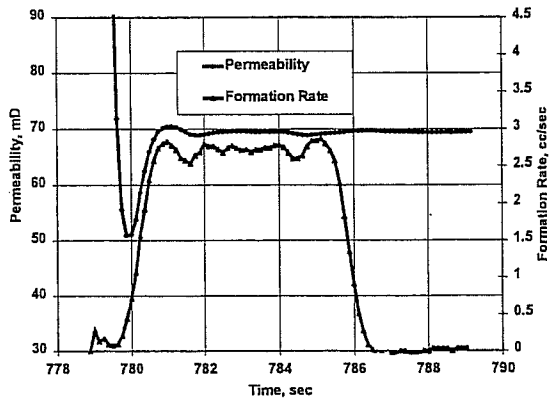

Figure 5. Continuously calculated formation rate and permeability from FRAT (Test A6-4).

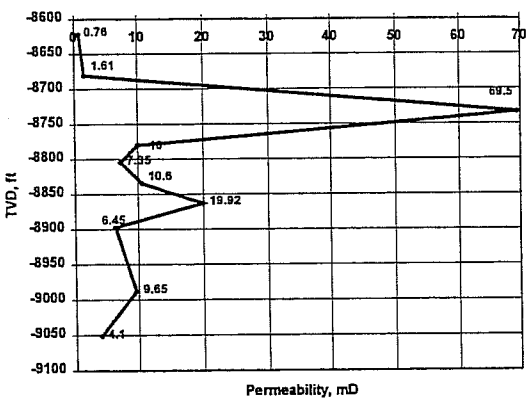

Figure 3. Permeability profile at Well A, obtained with RCI.

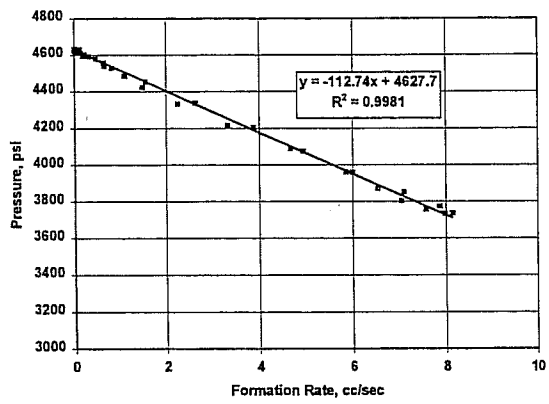

Figure 6. Pressure versus formation rate for Test A7-2 and its best-fit straight line. A permeability of 10.1mD is calculated from the slope.

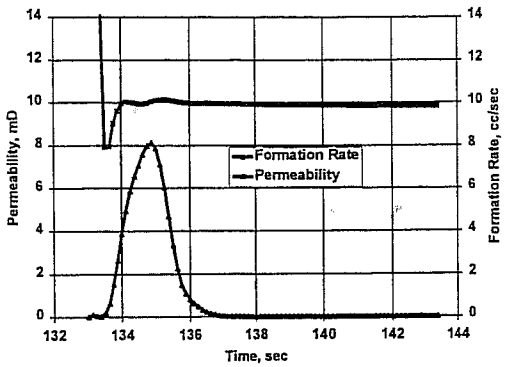

Figure 7. Continuously calculated formation rate and permeability from FRAT (Test A6-4).

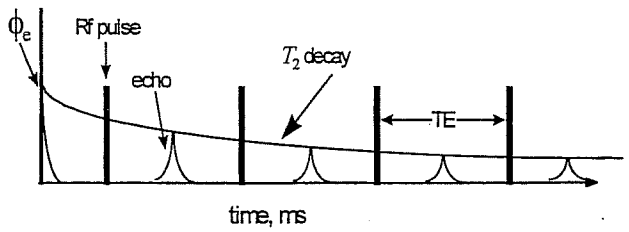

Figure 10a. Schematic of NMR data acquisition.

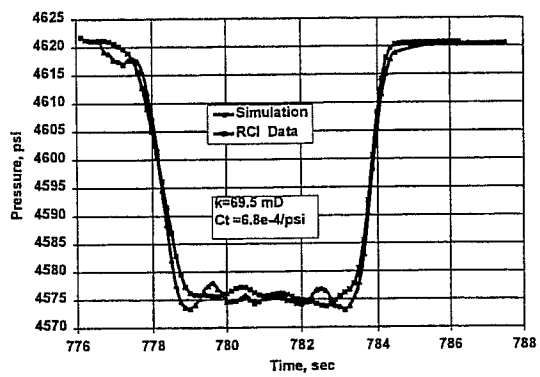

Figure 8. Comparison of transient pressures from RCI with the pressures from numerical simulation for Test A6-4.

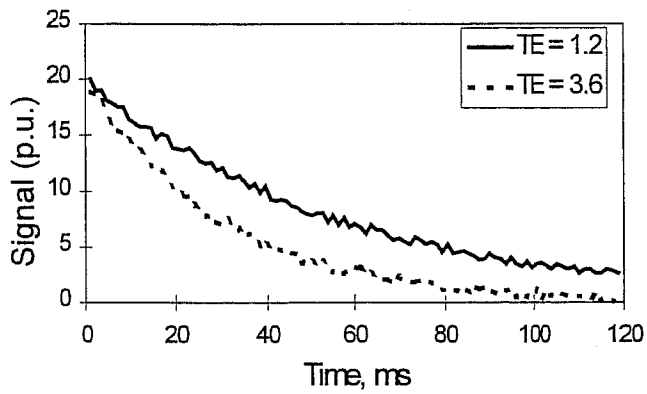

Figure 10b. Typical NMR echo data.

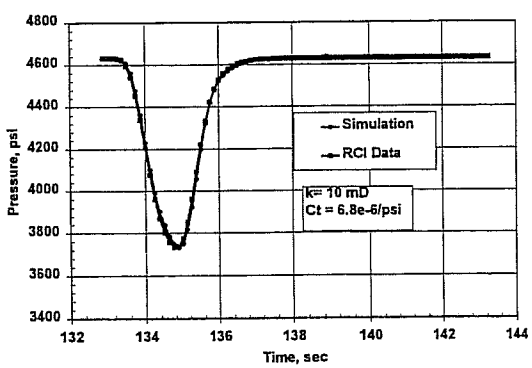

Figure 9. Comparison of transient pressures from RCI with the pressures from numerical simulation for Test A7-2.

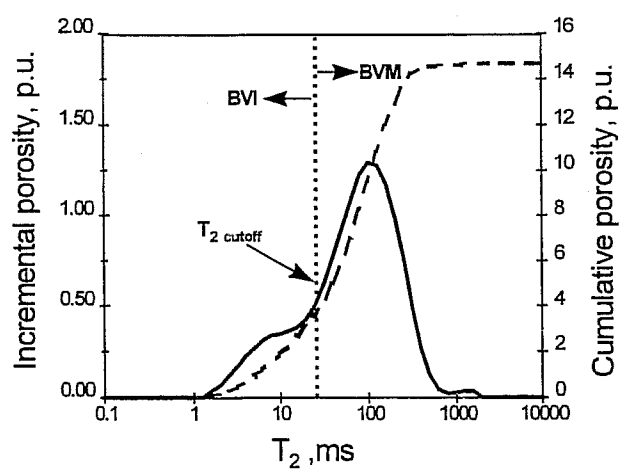

Figure 11. T2 spectrum with indicated T2 cutoff.

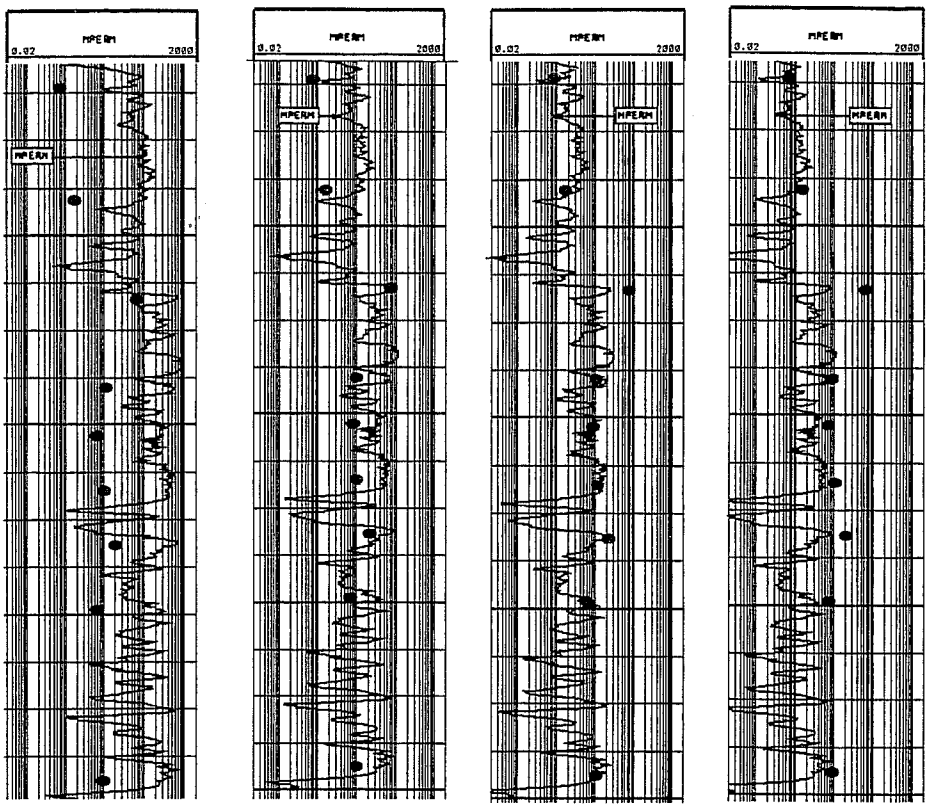

Figure 13. Calibration of C based on RCI permeabilities.

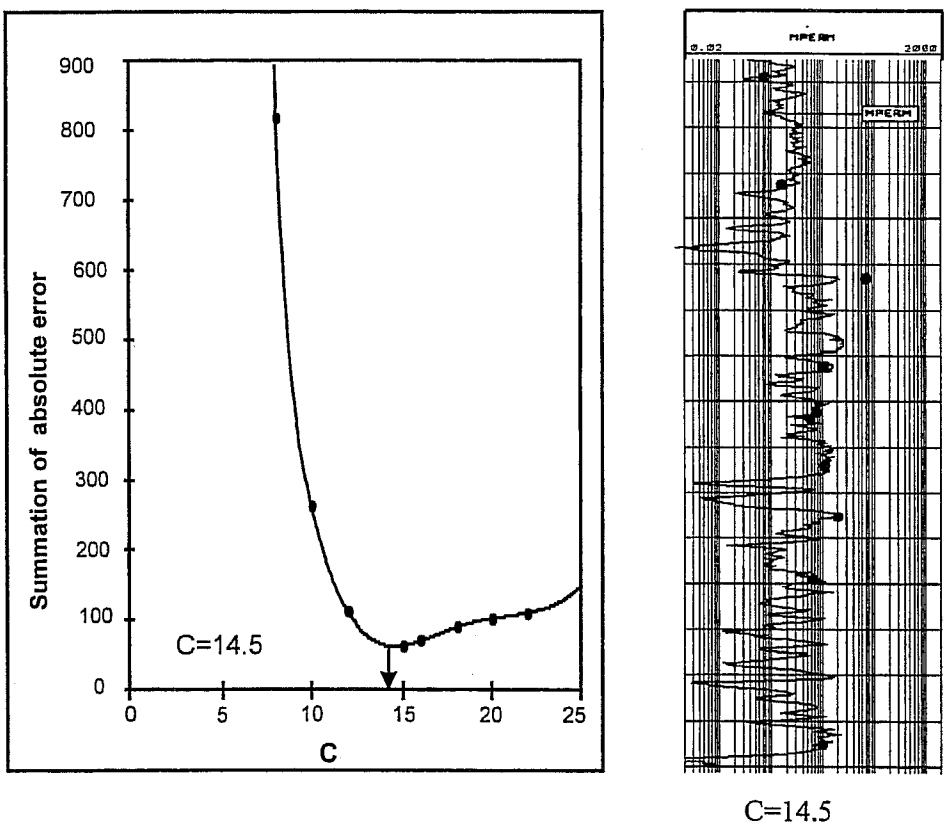

Figure 14. Proper selection of C minimizes error for permeability estimation

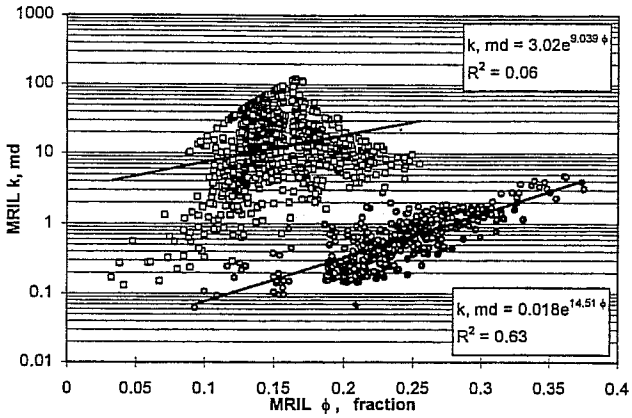

Figure 14a. Permeability versus porosity relationship.

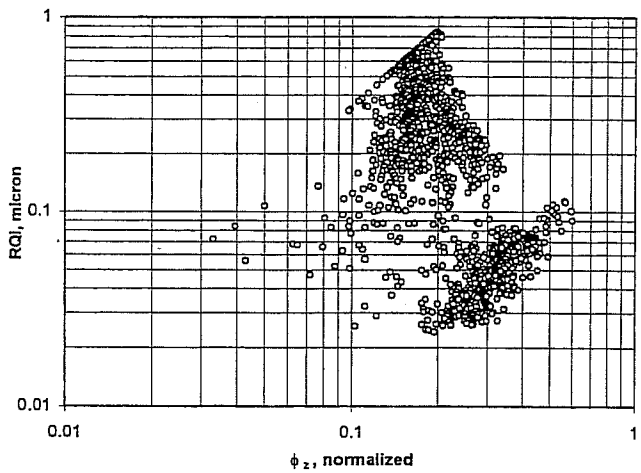

Figure 16. Sensitivity analysis of the clustering-results produce the unique classification of flow (hydraulic) units.

Figure 14b. Reservoir Quality Index versus normalized porosity.

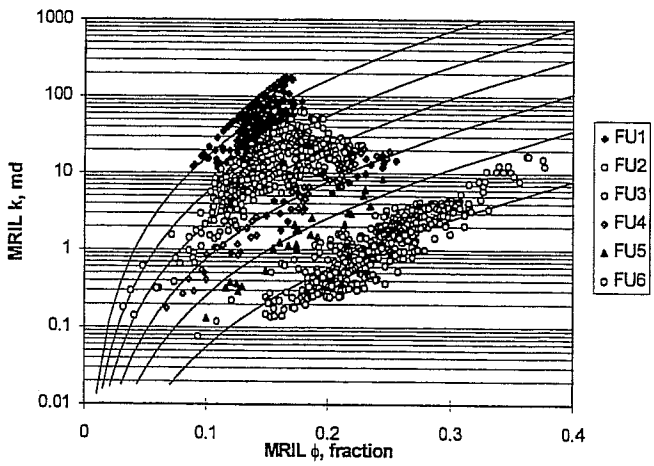

Figure 17. Traditional permeability versus porosity plot for the six unique flow units.

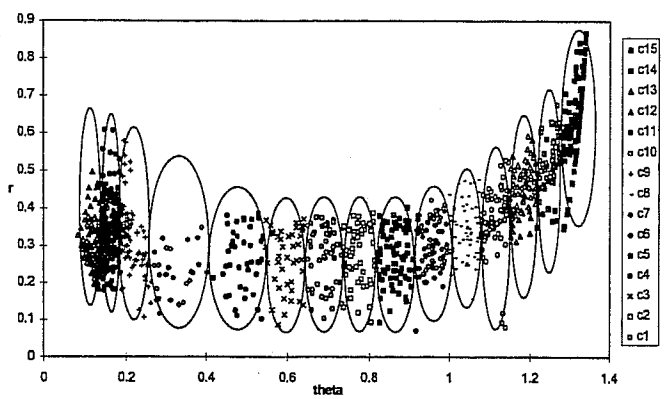

Figure 15. Cluster analysis maximizes between-cluster distance and minimizes within cluster variations.

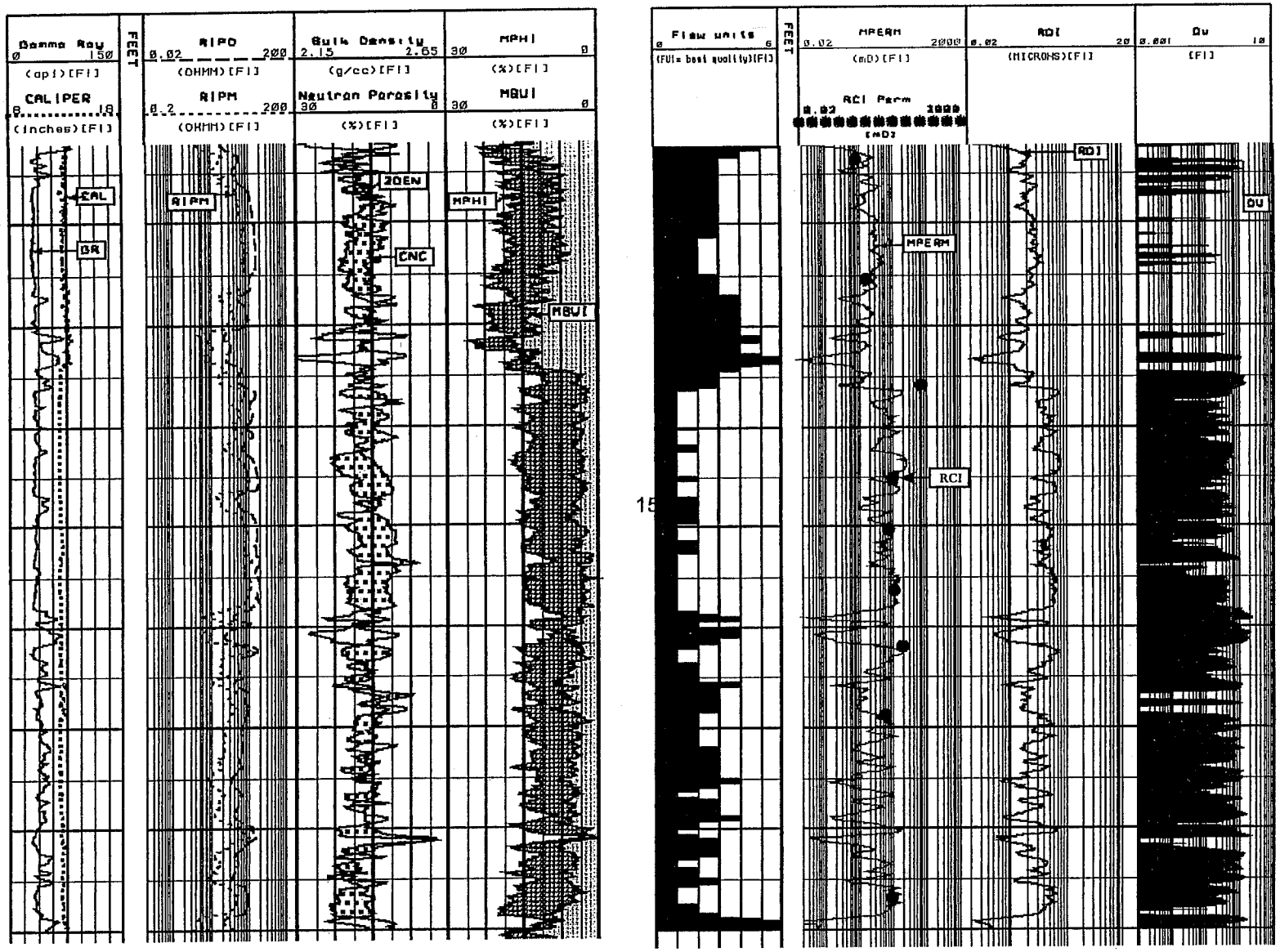

Figure 18. RCI-calibrated MRIL permeability and hydraulic unitization with conventional log data enable the derivation of permeability transform equations for the neighbouring cased-wells.

New Developments in High Resolution Borehole Seismology and their Application to Reservoir Development and Management

Björn N.P. Paulsson

Chevron Petroleum Technology Company
1300 Beach Blvd., La Habra, CA 90631-6374

Abstract

Single-well seismology, Reverse Vertical Seismic Profiles (VSP's) and Crosswell seismology are three new seismic techniques that we jointly refer to as borehole seismology. Borehole seismic techniques are of great interest because they can obtain much higher resolution images of oil and gas reservoirs than what is obtainable with currently used seismic techniques. The quality of oil and gas reservoir management decisions depend on the knowledge of both the large and the fine scale features in the reservoirs. Borehole seismology is capable of mapping reservoirs with an order of magnitude improvement in resolution compared with currently used technology. In borehole seismology we use a high frequency seismic source in an oil or gas well and record the signal in the same well, in other wells, or on the surface of the earth.

Introduction

Borehole Seismology has been regarded as a promising technique for reservoir imaging. In Figure 1 the resolution and measurement length are given for a number of seismic techniques including borehole seismic techniques. The combination of large measurement

lengths and high resolution is the reason for the current interest in Borehole seismology. In the first quarter of 1997 we are deploying a new, powerful, yet non-destructive borehole seismic source, and a new receiver system, the combination of which has a projected capability of handling source-receiver spacing of more than 2,000 meters and well depths as great as 6,100 meters.

This advanced borehole seismic data acquisition system consists of a powerful, clamped, swept-frequency, vibratory source which is non-destructive, a multi-level (up to 100 levels) receiver string of clamped, three-component geophones, and an acquisition system for Reverse VSP's. The downhole vibrator produces high quality *S*-waves, with controlled polarization, as well as *P*-wave direct arrivals and reflections. The radiation pattern of the two different actuators which will be part of the three component source are shown in Figure 2 and the measured force from both the prototype and the new actuators together with the modeled force of the new actuator are shown in Figure 3.

An early prototype of the clamped hydraulic downhole vibrator produced wide bandwidth (10 - 640 Hz) seismic data in the crosswell mode (Paulsson *et al.,* 1994), Figure 4. The data from this prototype source routinely contained high quality transmitted *P*-waves and *S*-wave arrivals as well as *P*- and *S*-wave reflections. This source was used to produce cross well seismic images which contained high resolution information about the reservoir as seen in Figure 5.

The new advanced borehole seismic source will be significantly more powerful, controllable, and deployable than the early prototype. The source in a Single well configuration is shown in Figure 6 and in a Reverse VSP/Cross well configuration in Figure 7.

We anticipate that borehole seismology will soon be used in management of both new and mature reservoirs. There are two different classes of applications for the borehole seismic techniques. The first is monitoring and evaluation of improved or enhanced oil recovery efforts such as water, steam or CO_2 floods using time-lapse methods. The process of injecting steam, water or CO2 into a rock formation will change both measured P and S wave velocities and can therefore be monitored using borehole seismology. A second application is reservoir characterization, whereby we determine with much greater resolution the architecture of the reservoir, including the continuity of bedding, the direction of fractures and fault planes, and the lateral variability of porosity. This will allow for the accurate positioning of directional or in-fill wells.

Development and Production Seismology

The primary task of the emerging field of high resolution development and production seismology is to map fine-scale geological heterogeneities to lower the risk of proper placement of new wells, re-drilling of existing wells and to improve the recovery of the hydrocarbon resources. Improved understanding and delineation of reservoirs lowers the economic risk, allowing for the operation of smaller, more marginal fields and the

identification of bypassed pockets of oil and gas in larger fields. In most producing reservoirs, an improved description is needed to manage production effectively. In many cases it is desirable to have greater resolution than 3-D surface seismic data can provide, and/or larger area coverage than well-logging techniques provide. Borehole seismology fills the resolution and coverage gap between 3-D seismology and well logging techniques, which makes it complementary to these proven methods. Furthermore, borehole seismology can provide accurate formation velocity information for improved processing of 3-D seismic data and for determining petrophysical parameters. One particularly important application for borehole seismic data is in areas where reliable surface seismic data can not be collected.

Surface seismic data account for the most of the worldwide geophysical activity in oil fields. However, higher resolution of the reservoir can be achieved by placing the seismic source and the receivers in boreholes near the reservoir. This has been demonstrated over the last twenty years with experimental crosswell seismology, the most tested of the three new borehole seismic techniques. The primary reasons for the superior performance of these borehole methods are:

- The avoidance of a near-surface weathering layer allows the use of seismic frequencies more than an order of magnitude higher than is possible using surface techniques.
- The avoidance of the near-surface weathering layer makes it possible to record high quality *S*-wave data routinely.

- The recording environment is very quiet.
- The transducers are closer to the targets.

The resolution of various seismic methods and their corresponding measurement lengths are shown in the Table. The measurement length is the distance over which the seismic energy propagates in a particular method and is a partial indication of how much of the reservoir is actually sampled by this technique.

Seismic Technique (Hz)	Measurement Length (m)	Resolution (m)
Ultra sonic on core (10^5-10^6)	.01 - 0.1	.001 - .01
Sonic logs (1,000 - 10,000)	0.1 - 3	.01 - 0.1
Crosswell seismology (10-2,000)	10 - 2,000	1 - 5
Single-well seismology (10-1,000)	10 - 1,000	1 - 5
Reverse VSP (10 - 500)	100 - 3,000	2 - 10
VSP (10 -100)	100 - 5,000	10 - 50
Surface Seismology (10 - 100)	100 - 10,000	20 - 50

When using the single-well acquisition geometry, the seismic source and the receiver array are placed in the same vertical or deviated well shown in Figure 8. This technique is suitable for mapping features at depth which are parallel or sub-parallel to the well used for the survey. Application examples include, for vertical wells, salt dome flanks or fault surfaces, and for deviated wells, horizontal or near horizontal lithology boundaries.

Single well seismic methods will provide a new type of high frequency seismic data which have previously been unavailable. The technology for deploying well logging tools in horizontal wells has been developed over the last few years and includes the use of coiled tubing, regular tubing, and newly developed well tractors. The same technology will be used for the single-well seismic system. Figure 9 shows a cross section through the Bayou Choctaw Salt Dome Site where a consortium of companies are testing and evaluating single well seismic imaging.

For Reverse VSP's, Figure 8, seismic energy is transmitted from the borehole to an array of geophones on the surface of the earth or on the sea floor, in the case of offshore wells. We have observed that considerably higher seismic frequencies can be recorded in the Reverse VSP configuration compared with the conventional VSP technique. This is most likely due to the better coupling of a seismic source in a well compared to the surface where the source coupling is a major issue. It is also likely that it will be more cost effective in many situations to deploy an array of receivers at the surface for reverse VSP's, than it will be to establish multiple shot points on the surface in the case of a conventional walkaway VSP.

For the third borehole seismic technique, crosswell seismology, Figure 8, we can construct two-dimensional velocity images for the region between pairs of wells using travel time tomography, and two dimensional reflection images using migration techniques. The combination of these two image types can be a very powerful tool in key areas of the reservoir and it offers resolution on the scale of 1 to 2 meters.

We believe that borehole seismology will eventually be an integrated part of the oil and gas reservoir production process and that it will fundamentally change the way we are using seismic methods. Much of the processing will be done in the field to provide fast results. We will compute velocity tomograms and eventually, the reflection images in the field. This is a departure from the processing approach of surface seismic data used for development purposes. In this sense, borehole seismology will be more like well logging, where the preliminary results are delivered in the field. Client reservoir engineers and geologists will be able to change the direction and the scope of the survey based upon initial results. This will make the borehole seismic imaging of oil and gas reservoirs a dynamic, client driven process.

Summary

We have developed a downhole seismic source which has the potential to make borehole seismology into an economic and widely used technique for oil and gas reservoir characterization. The new tool has an effective force output which will allow it to be used in large well spacing and in reservoirs with highly attenuating sediments. It also has a very broad seismic bandwidth, which allows us to achieve both long range and high resolution using the same source tool. Since the source is clamped, the tool can also be used in gas-filled wells. This feature also helps to minimize tube waves during single-well seismic surveys. The source system design includes 3-component motion providing for multi-component data. The advanced borehole seismic system is also the first system

in the oil and gas industry where both the source and the receivers operate on fiber optic wirelines. Data examples from the new system will be presented in 1997.

References

The Steepbank Crosswell Seismic Project: Reservoir Definition and Evaluation of Steamflood Technology in Alberta Tar Sands, Paulsson, B.N.P., Fairborn, J.W., Meredith, J.A., Wang, Z., Geophysics: The Leading Edge of Exploration, July 1994.

Acknowledgment

The following individuals are acknowledged for contributing substantially to the development of the downhole seismic vibrator: Robert Heming and Frank McCaffery with Chevron, Marion Scott, Bob Cutler and Chad Harding with Sandia National Laboratories, Frank Bernhard and Glen Kirkendall with E-Systems, Sen Chen with Exxon Production Research Company, Tim Fasnacht with Gas Research Institute, John Giles and Kim Mitchell with Pelton Company, Henry Tan with Amoco, Dale Cox with Conoco and Jack Cole with University of Arkansas.

Figure captions

Figure 1. Resolution and Measurement Length for Different Seismic Techniques

Figure 2. Radiation Patterns for Different Actuators

Figure 3. The Hydraulic Vibrator Axial Force Output

Figure 4. Steepbank Cross Well Seismic Data

Figure 5. Steepbank Cross Well Seismic Tomograms

Figure 6. Single Well Configuration of the Downhole Seismic Vibrator

Figure 7. Reverse VSP/Cross Well Seismic Configuration of the Downhole Seismic Vibrator

Figure 8. Borehole Seismology

Figure 9. The Bayou Choctaw Salt Dome Site

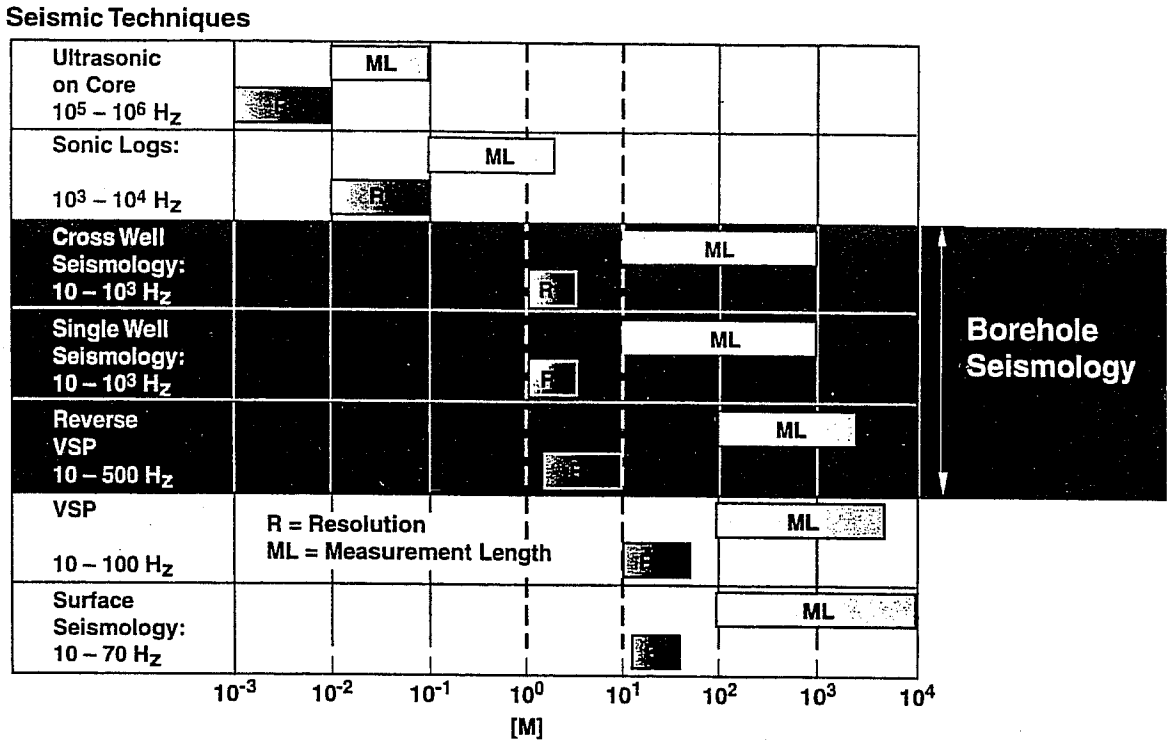

Figure 1. Resolution and Measurement Length for Different Seismic Techniques

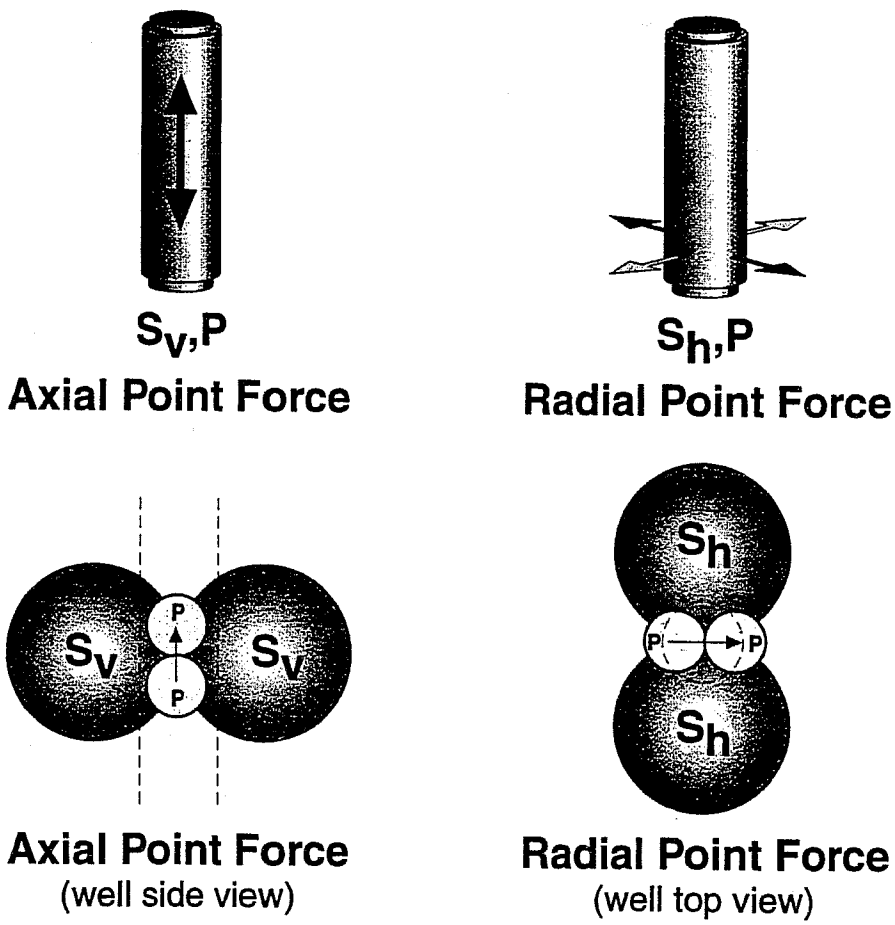

Figure 2. Radiation Patterns for Different Actuators

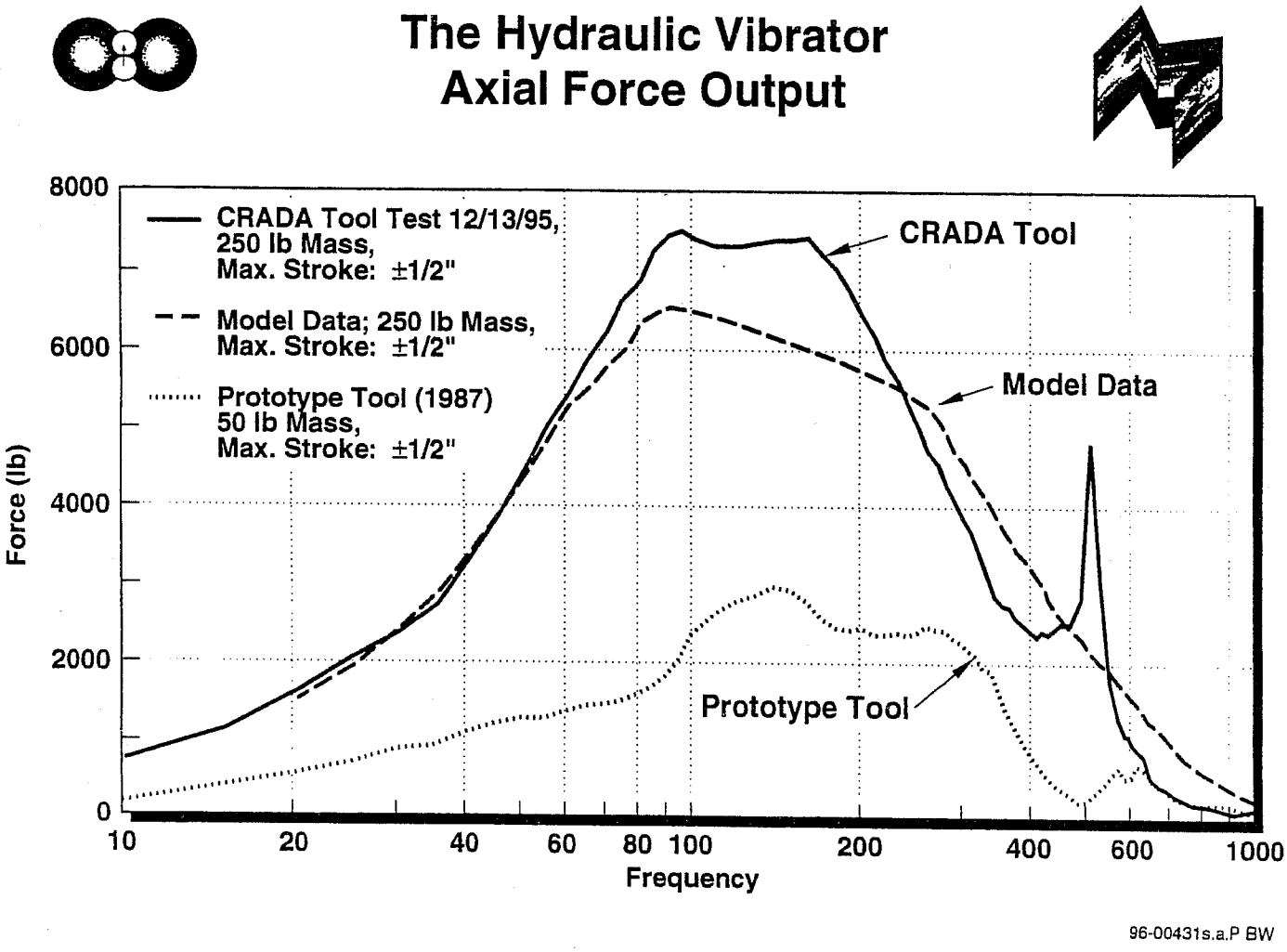

Figure 3. The Hydraulic Vibrator Axial Force Output

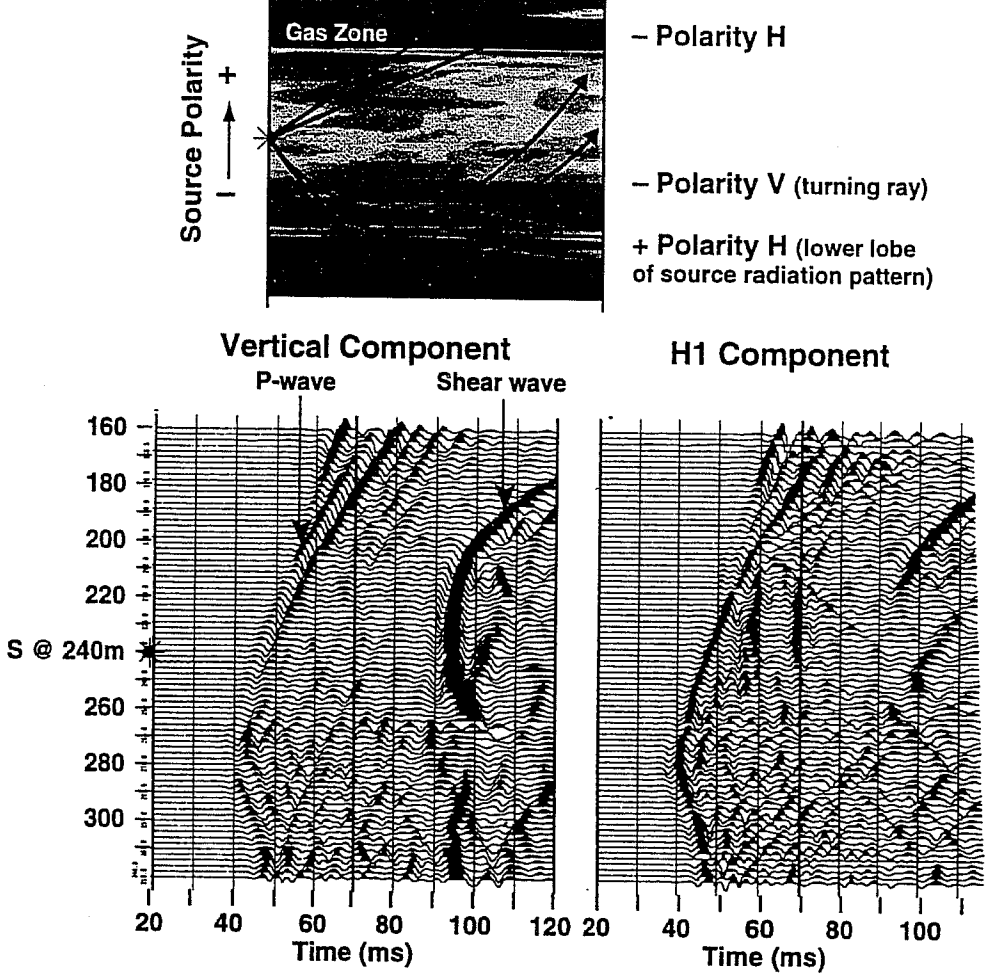

Figure 4. Steepbank Cross Well Seismic Data

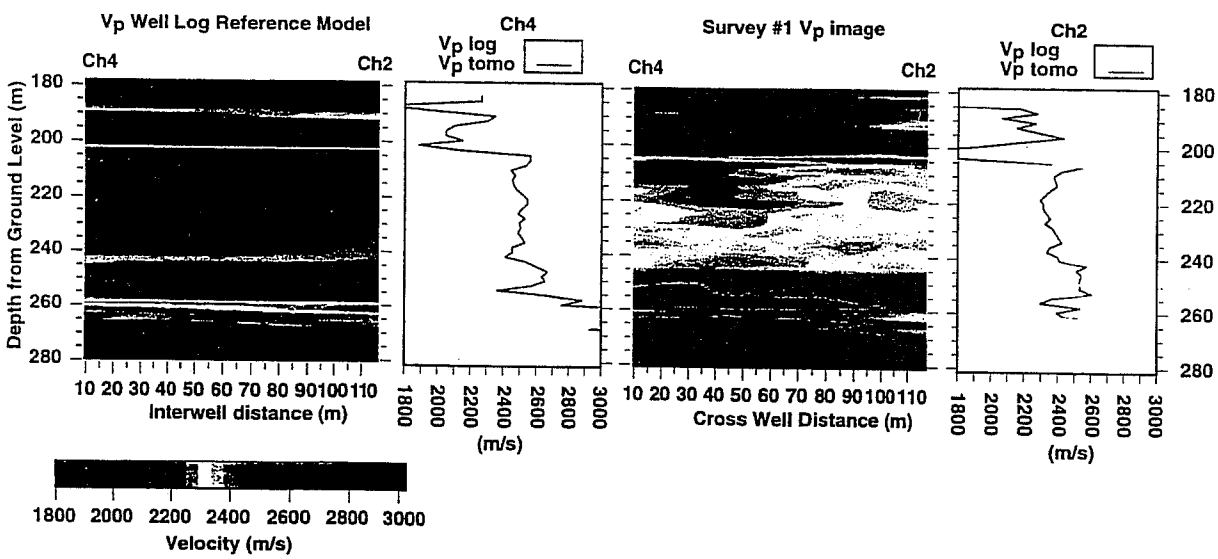

Figure 5. Steepbank Cross Well Seismic Tomograms

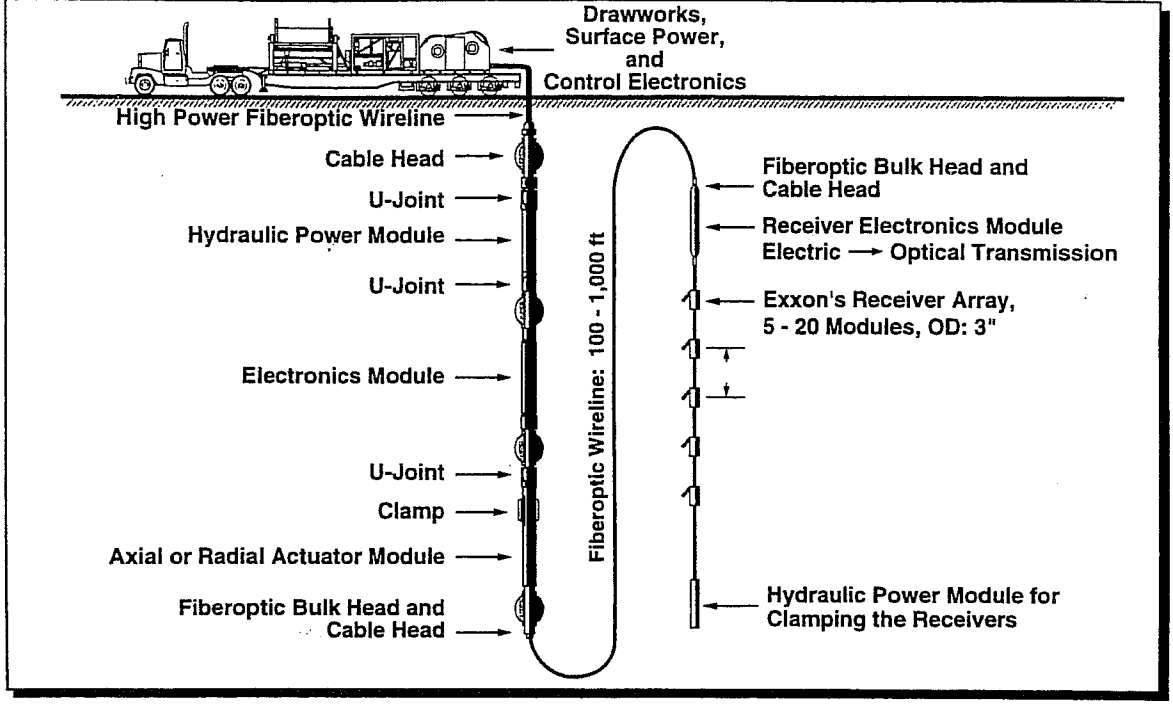

Figure 6. Single Well Configuration of the Downhole Seismic Vibrator

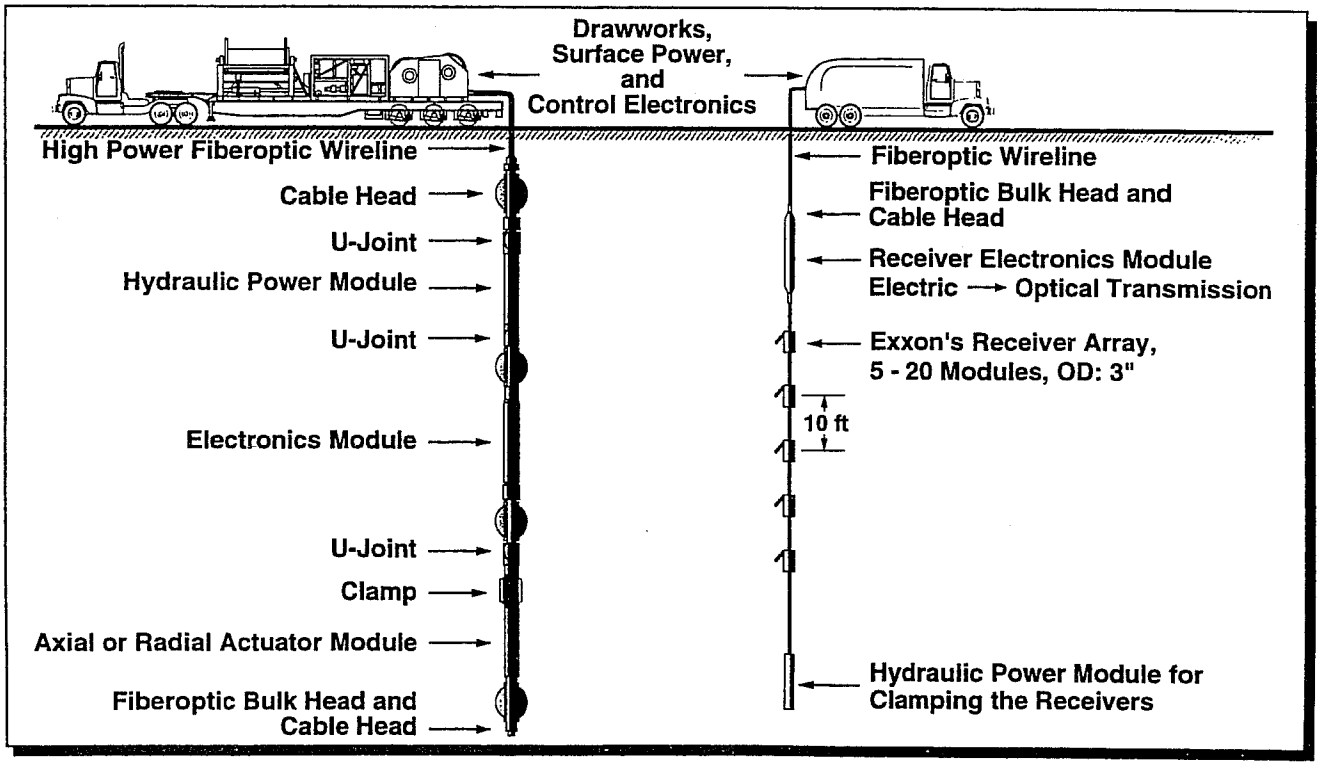

Figure 7. Reverse VSP/Cross Well Seismic Configuration of the Downhole Seismic Vibrator

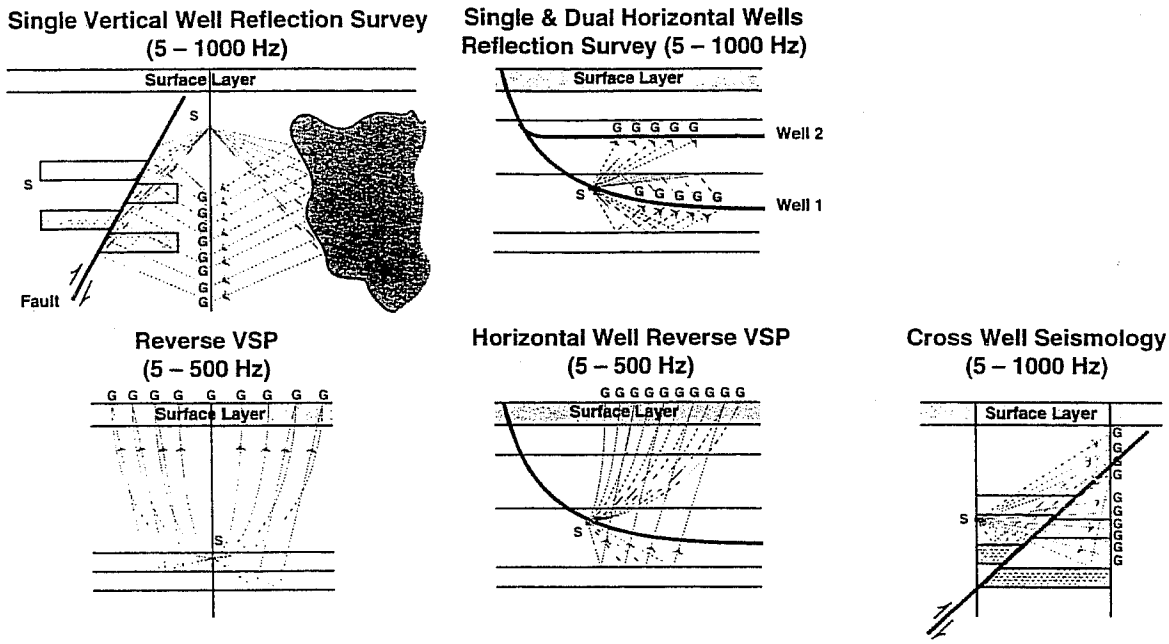

Figure 8. Borehole Seismology

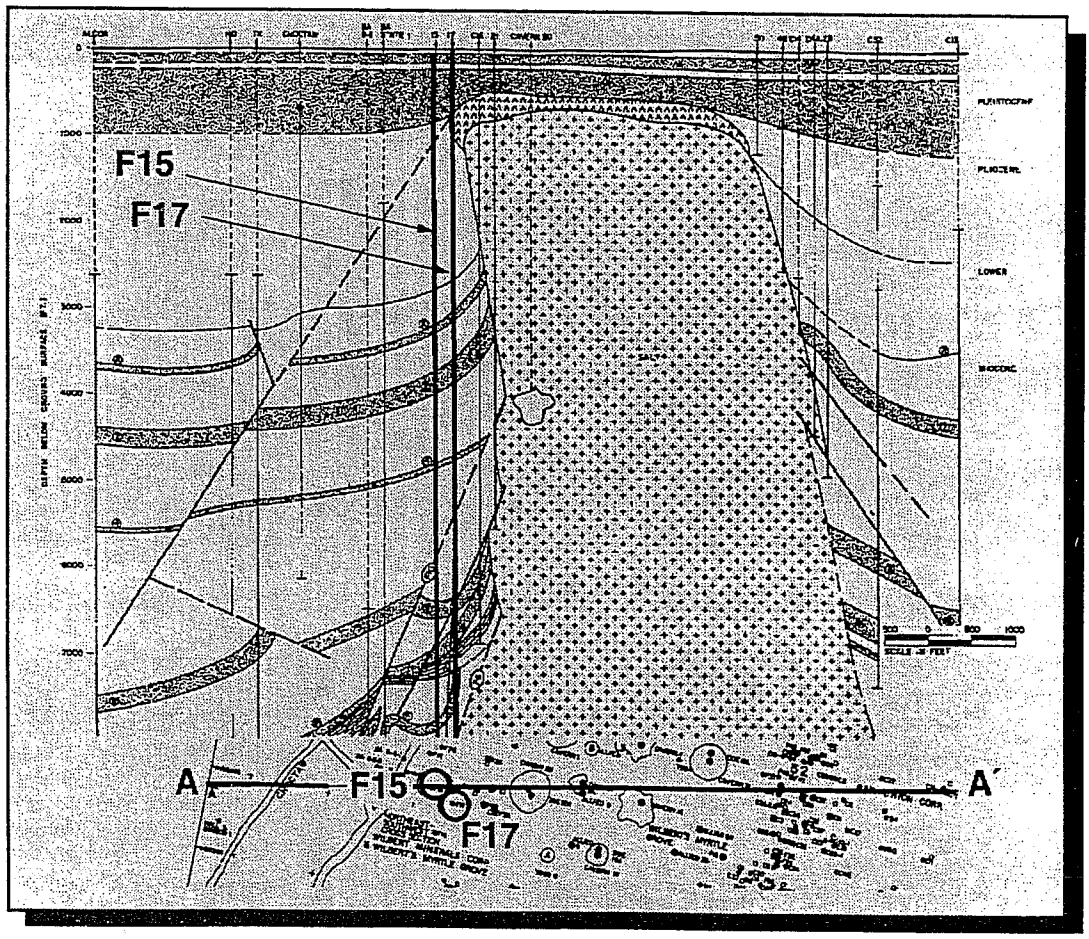

Figure 9. The Bayou Choctaw Salt Dome Site

A Direct Method For Determining Complete Positive And Negative Capillary Pressure Curves For Reservoir Rock Using The Centrifuge

E. A. Spinler - Phillips Petroleum Co., Bartlesville, OK

B. A. Baldwin - Phillips Petroleum Co., Bartlesville, OK

Acknowledgments

The authors thank Phillips Petroleum Co. for permission to publish this extended abstract and thank D. M. Chancellor for his mechanical assistance in building equipment for this work, J. C. Stevens for performing the centrifuging and R. L. King for assistance with magnetic resonance imaging.

Abstract

A method is being developed for direct experimental determination of capillary pressure curves from saturation distributions produced during centrifuging fluids in a rock plug. A free water level is positioned along the length of the plugs to enable simultaneous determination of both positive and negative capillary pressures. Octadecane as the oil phase is solidified by temperature reduction while centrifuging to prevent fluid redistribution upon removal from the centrifuge. The water saturation is then measured via magnetic resonance imaging. The saturation profile within the plug and the calculation of pressures for each point of the saturation profile allows for a complete capillary pressure curve to be determined from one experiment. Centrifuging under oil with a free water level into a 100 percent water saturated plug results in the development of a primary drainage capillary pressure curve. Centrifuging similarly at an initial water saturation in the plug results in the development of an imbibition capillary pressure curve. Examples of these measurements are

presented for berea sandstone and chalk rocks.

Background

Knowledge of capillary pressure for each specific rock/oil/water combination is important for predicting potential hydrocarbon recovery from a reservoir. Capillary pressure is a measure of the interaction between fluids and the rock pore surface. The strength of the interaction varies with the fluid saturations, the interfacial tension between the fluids, the pore structure and the wettability of the pore surfaces. A measure of the capillary pressure can be calculated from the force exerted by the density difference between retained fluids at each height above or below the free water level. Knowing the fluid saturations as a function of the height above and below the free water level permits the determination of a capillary pressure curve for any given reservoir rock/fluid system. However, in practice this has been difficult, of uncertain accuracy, or very time consuming to experimentally determine.

Capillary pressure curves are typically determined by either mercury intrusion, porous plate/membrane or centrifuge methods. Mercury intrusion, although rapid, provides questionable results due to the use of mercury in a vacuum to mimic water/oil behavior. It's methodology limits the technique to primary drainage and possible positive imbibition capillary pressures. Porous plate/membrane methods can generate all the capillary pressure curves, but to reach an apparent equilibrium saturation can take days to months per pressure point for 5 to 8 data points. This delays the availability of the results and limits the number of tests which can be made. The lengthy experimental time also increases the chance for mechanical failure. The centrifuge method is normally only used to determine drainage or negative imbibition curves. It takes days to months to complete a test. The limitation of most centrifuge methods is that they only provide an indirect, or assumed/calculated, measure of saturation at the inlet face of a rock plug based on the amount of fluid expelled from the rock. Numerous methods over the past 50 years have been proposed for

approximating the inlet saturation from centrifuge effluent volumes, but in every case, the model chosen influences the results.

A capillary pressure curve that is determined from the measured oil/water saturation profile under a known pressure gradient as measured from a free-water level would ideally mimic the reservoir. The methodology as proposed herein does provide such positive and negative capillary pressures for both drainage and imbibition. Furthermore, the method appears to be accurate, rapid and robust.

Methodology and Results

The method under development *directly* measures the oil/water saturation distribution in a rock plug which has been established via a known fluid differential pressure by centrifuging. *Direct* measurements of the saturations is possible by a number of different techniques, but for this study, magnetic resonance imaging was used because it provides high spatial resolution. Previously, the authors (Baldwin et al., 1996) had discussed some of the different methods by which magnetic resonance images of the saturations within rock plugs could be measured. All saturations for this work were determined by imaging the liquid water phase while the oil phase was solid and does not image. The saturation profile was established and locked in place, by cooling, while in the centrifuge. The measurement of the complete oil/water saturation profile determined with more than a hundred measurements within a rock plug has an advantage over other typical techniques which measure saturations one point at a time.

An additional advantage is that both the positive and negative portions of the capillary pressure curve can be measured simultaneously by positioning the free water level along the length of the plug as shown in Figure 1. The capillary pressure is zero at the free water level. Drainage or imbibition is achieved by centrifuging the plug under hydrocarbon or water when starting the plug at an appropriate saturation state. The sequence of the centrifuge steps is important because it

determines the direction of fluid flow and possible hysteresis. Capillary pressure as a function of position in the plug and the achievable pressure range is calculated from the speed of the centrifuge, the height above the free water level, the fluid density difference and the sample length.

Water and octadecane which has a melting point of about 27 degrees Celsius were used. Other hydrocarbons which are solid at the ambient temperature in the magnetic resonance imager would also work. When one phase is frozen, the relaxation time in the magnetic resonance imager is so short that it is not imaged. Thus, in this system only the water was imaged. Because the hydrocarbon was frozen in place while centrifuging, redistribution of the water in the plug when handled at normal ambient temperature will not occur. The small volume change created by the contraction of the hydrocarbon during freezing can be easily corrected. One disadvantage is that the water as the wetting phase had a relaxation time that was dependent on the size of the pore spaces it occupied. In chalks with a relatively narrow pore size distribution, this was not a problem. However, sandstones with a broad pore size distribution had relaxation times for the lower water saturations that were significantly shorter than those for high water saturation and consequently affected the image intensity. A correction (Baldwin, et al., 1991) was calculated for this effect in the sandstones by using T1 mapping where the relaxation time was measured on a pixel by pixel basis and extrapolated back to zero relaxation time to minimize the relaxation effect on intensity. This procedure produced a porosity map where intensity was proportional to the water saturation.

Laboratory experiments for this study consisted of preparing both a berea sandstone plug and a reservoir chalk plug. These plugs were selected because they have a great disparity in rock properties (Table 1) and it was intended to evaluate the methodology for both. The reservoir chalk plug was previously cleaned by extraction with mild solvents. No cleaning was necessary for the berea plug.

Each plug was initially saturated with 100% of the water phase. The experimental work with each plug was done separately, but the steps were basically the same. Once placed in their centrifuge

holders, water and octadecane (warmed to slightly above its melting point) was added.. No oil imbibition was expected to occur, nor was it observed, since both samples were water-wet. The final free water level height was adjusted by adding the appropriate amounts of each fluid. This position was expected to change since one fluid will be expelled from the rock during the test while the other will enter. Movement of the free water level was minimized by having the volume of bulk fluids around the plugs significantly greater than the pore volume of the rock plugs as indicated in Figure 1. Centrifuging at a temperature above the melting point of octadecane was conducted for an appropriate amount of time, 1 day intervals for the berea and 3 day intervals for the chalk. At the end of the centrifuging time, but while still centrifuging, the sample was cooled to solidify the oil, but not the water. When the oil phase in the sample was frozen in approximately 4 hours, it was removed from the centrifuge and imaged for saturation. The centrifuge procedure was repeated until the saturation profiles in the plugs were observed to be stabilized. The height of the free water level was locked in place by the frozen oil phase and becomes part of the image. Distances from the free water level for each pixel of the intensity image were determined and local pressures calculated from standard centrifuge equations. Local pressures determine the capillary pressure at any point on the image from the free water level. Capillary pressure curves as measured by this method for primary drainage of berea sandstone and reservoir chalk are shown in Figures 2 and 3. The scatter in capillary pressure data for the berea reflects the less uniform porosity distribution found in the sandstone as compared to the chalk. Note, however, that for these tests, the image represented only a 4 millimeter slice through each plug. Averaging or imaging more of the plug by MRI can further smooth the capillary pressure curves.

Following the determination of the primary drainage capillary pressure curve, the plugs were centrifuged under 100 percent oil phase and inverted as necessary to drive the plugs to a relatively uniform initial water saturation. The plug at initial water saturation was then centrifuged with a free water level near the center of the plug. Again centrifuging of the plugs continued until the saturation profiles were observed to be stable. The resultant primary imbibition capillary pressure

curve are illustrated in Figures 4 and 5 for the berea sandstone plug and the reservoir chalk core plug, respectively.

Centrifuging under 100 percent oil phase can establish a relatively uniform residual oil saturation before the development of the secondary drainage capillary pressure curves. This can be repeated, as well as the imbibition step above, to obtain a set of hysteresis capillary pressure curves. Secondary drainage curves for these plugs will be developed in future papers on this methodology.

The time needed to complete each step of the above test depended on how rapidly the fluids reached their equilibrium saturation in the centrifuge. This was largely determined by the permeability of the rock. This was especially true for low permeability chalk which had to be centrifuged up to 12 days to obtain and verify a stabilized saturation profile compared to up to 2 days for the berea sandstone. The total experimental time to generate equilibrium primary drainage and primary imbibition capillary pressure curves in this study took approximately 1 week for the berea sandstone plug and approximately 1 month for the low permeability chalk plug.

Conclusions

1. Direct measurement of the saturation distribution in centrifuged rock plugs by magnetic resonance imaging or other means eliminates the need for assumed or indirect determination of fluid saturations.
2. Placement of the free water level along the length of rock plugs allows for the simultaneous development of both the positive and negative capillary pressures for drainage and imbibition.
3. Freezing of the oil phase during centrifuging allows for handling and determination of the water saturation in rock plugs without fluid redistribution.
4. The combination of centrifuging for pressure and direct measurement of the resulting saturation distribution can provide a rapid, accurate and robust laboratory method for determining

capillary pressure curves in porous media.

References Cited

1. Baldwin, B. A. and Yanánashi, W. S., Sept.-Oct.1991. Capillary-pressure determinations from NMR images of centrifuged core plugs: berea sandstone: The Log Analyst p. 550-556.

2. Baldwin, B. A. and Spinler, E. A. , 1996, A direct method for simultaneously determining positive and negative capillary pressure curves in reservoir rock: 4th International Symposium on Evaluation of Reservoir Wettability and Its Effect on Oil Recovery proceedings.

Figure Captions

Figure 1: Schematic of plug with free water level and large cell volume in centrifuge.

Figure 2: Primary drainage capillary pressure curve for berea plug bc.

Figure 3: Primary drainage capillary pressure curve for chalk plug 10052b.

Figure 4: Imbibition capillary pressure curve for berea plug bc.

Figure 5: Imbibition capillary pressure curve for chalk plug 10052b

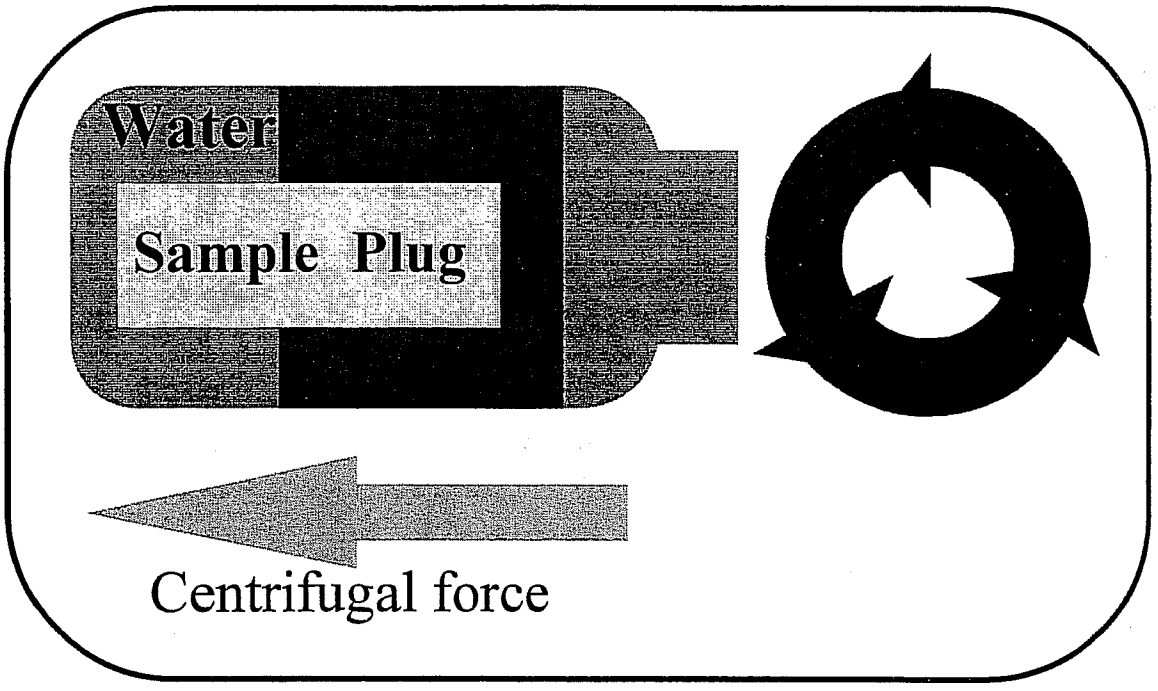

Figure 1.

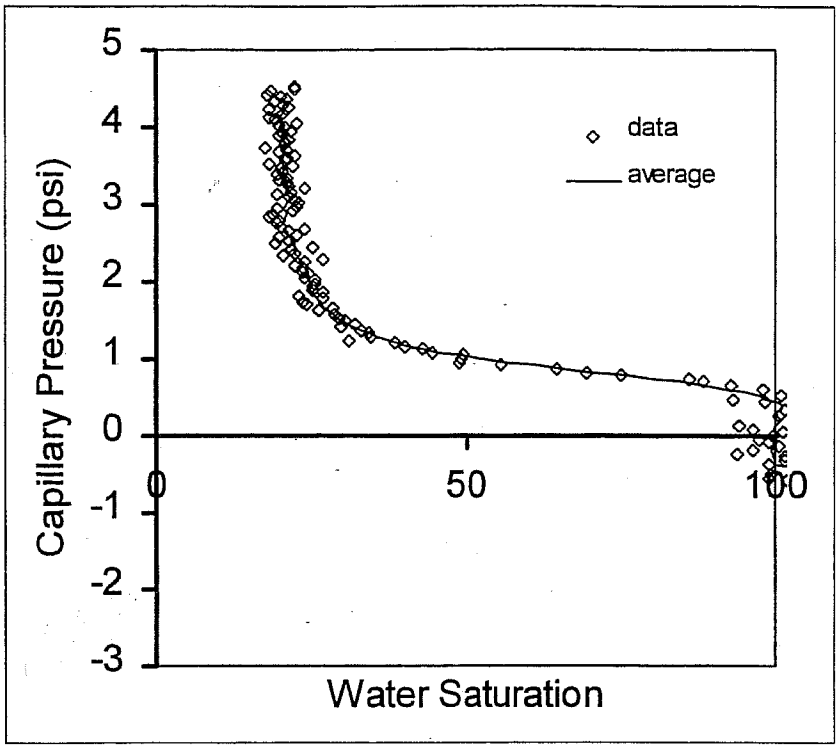

Figure 2.

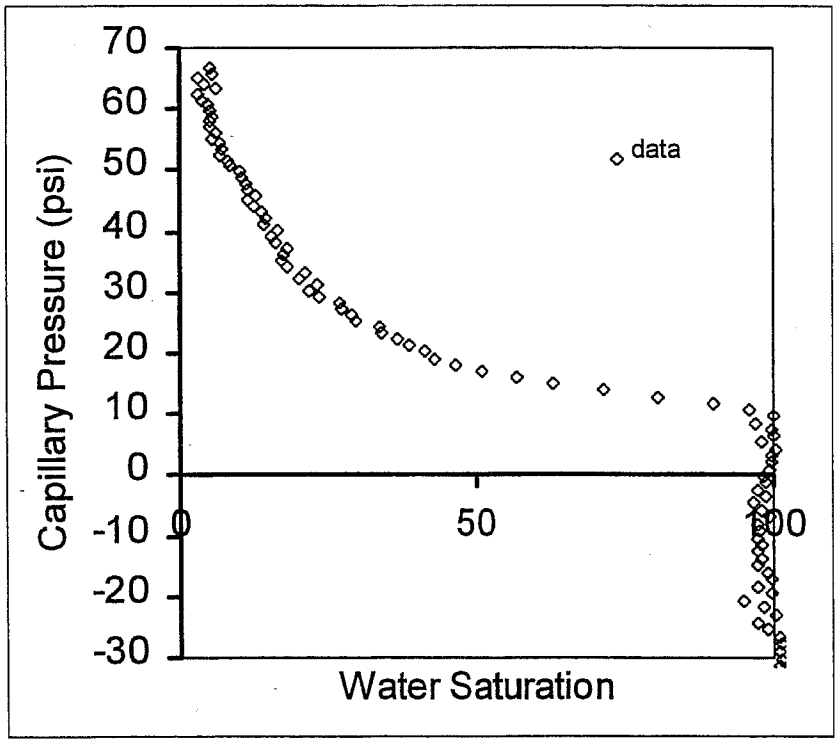

Figure 3.

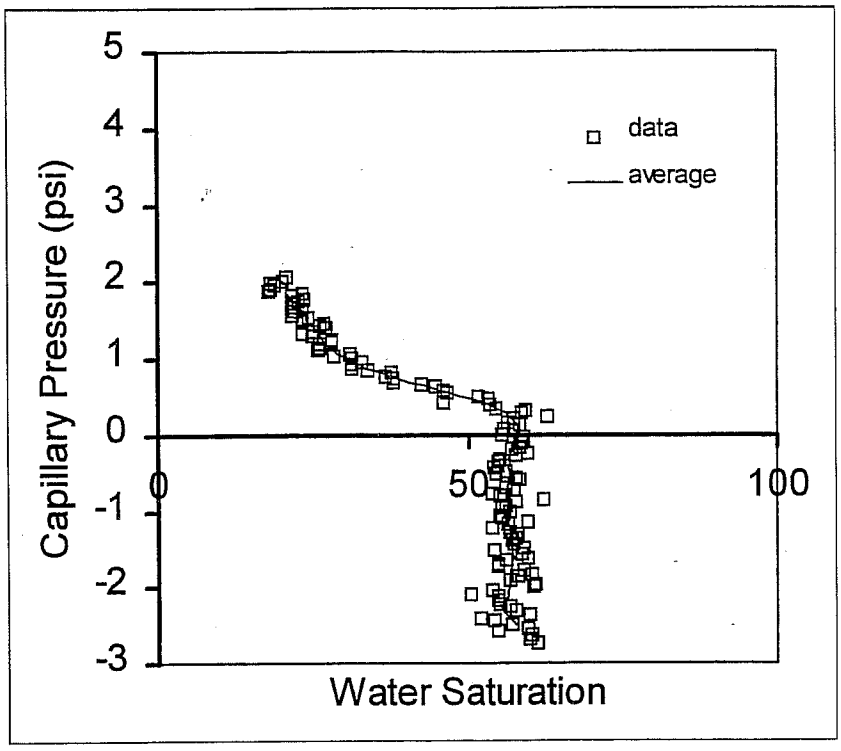

Figure 4.

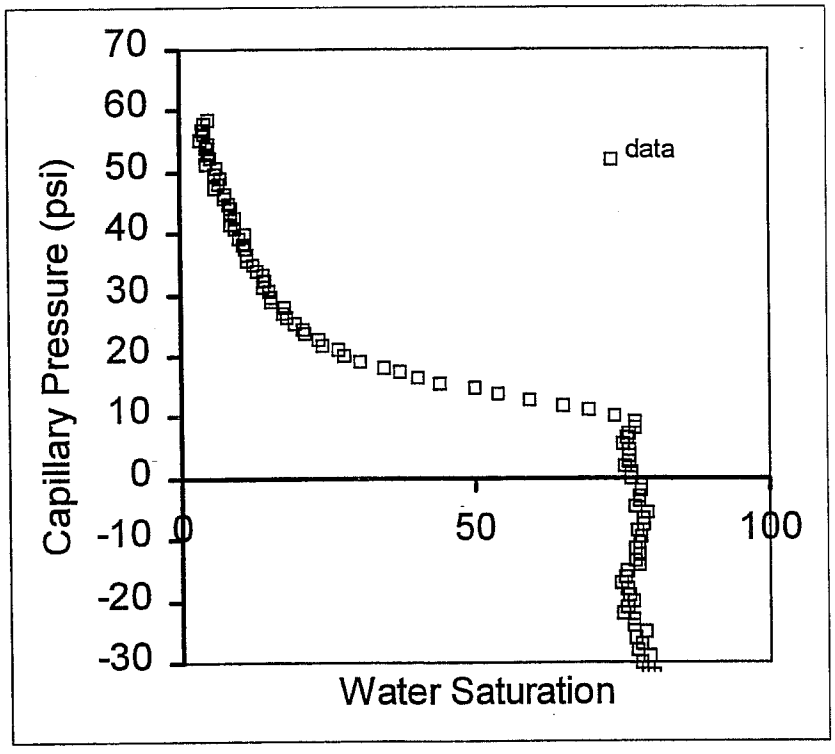

Figure 5.

Table 1 - Petrophysical Properties

Plug #	Type	Length (cm)	Diameter (cm)	Porosity (fraction)	Permeability (md)
bc	berea	4.68	2.54	0.21	~ 600
1052b	chalk	3.94	2.54	0.33	~ 5